Development and application of an artificial allylic aminase for *in vivo* catalysis purposes.

Inauguraldissertation zur Erlangung
der Würde eines Doktors der Philosophie
vorgelegt der Philosophisch-Naturwissenschaftlichen
Fakultät
der Universität Basel

Von

Alain Baiyoumy

2023

Genehmigt von der Philosophisch-Naturwissenschaftlichen Fakultät auf Antrag von

Erstbetreuer: Prof. Dr. Thomas R. Ward

Zweibetreuer: Prof. Dr. Olivier Baudoin

Externe Experte: Prof. Dr. Clemens Mayer

Basel, den 20. Juni 2023

Prof. Dr. Marcel Mayor

Abstract

Natural enzymes have evolved to catalyze numerous reactions displaying unmatched selectivity and activity. Furthermore, nature has evolved many enzymes to work in a cascade, affording complex molecules from the simple starting material. However, the evolutionary process endowing these enzymes with such abilities took millions of years. This timescale does not match the demand for efficient catalytic systems to resolve societal problems in ecology, medicine, and pharmacology. Artificial metalloenzymes (ArMs) are an exciting solution since they combine the chemical versatility brought by a synthetic catalyst within a natural protein optimizable *via* a quick mutagenesis campaign. These two pivot points give artificial metalloenzyme great flexibility in terms of optimization since chemical fine-tuning and bio-engineering can be done to reach the maximal potential of ArMs. This inspired the research presented in this thesis which aims to present the development of a new class of ArMs.

Contents

Chapter 1 Introduction: CpRu-Catalyzed Deallylation Reactions for Biological Applications

Alain Baiyoumy, Robin Vinck, Thomas R. Ward*

University of Basel, Department of inorganic chemistry, Mattenstrasse 24a, 4058 Basel, Switzerland.

KEYWORDS metal-based catalysis, *in cellulo* catalysis, Au-nanoparticules, Artificial Metalloenzyme, auxotrophic rescue, fluorescence, drug releasing, SCNP

Author contribution

AB carried out literature research and wrote the manuscript with input from RV and TRW. RV wrote the manuscript and revised the manuscript. TRW revised the manuscript.

Abstract:

In vivo transition metal catalysis offers promising perspectives in various areas of research, including targeted drug uncaging for precision medicine and imaging. This emerging field was pioneered by Meggers. In 2006, he reported the deallylation of various carbamate-protected probes using chloro(1,5-cyclooctadiene)(η^5-pentamethylcyclopentadienyl)ruthenium (**[Cp*Ru(cod)Cl]** hereafter) as a catalyst, both under physiological conditions and, most remarkably, *in cellulo*. This landmark publication sparked interest from the chemical biology community. However, performing *in vivo* catalysis is a challenging endeavor. Indeed, living systems did not evolve to tolerate noble metal catalysts. Precious metals are typically thiophylic and thus often poisoned by thiol-containing biomolecules present in the cytosol. Since then, much research has been conducted around cyclopentadienyl and pentamethyl cyclopentadienyl Ru-based catalysts for biological applications. However, efforts to further develop or improve this catalytic system remain scarce, and investigations concerning the catalyst's stability and degradation mechanism are limited. The most studied reaction using these systems is the deallylation of N-allyloxy-protected substrates as initially published by Meggers and co-workers in 2006. Mascarenas and co-workers have recently used these systems to perform ruthenium-catalyzed thioalkyne-azine cycloadditions (RuAtAC) and [2+2+2] cycloadditions in the presence of living cells. Despite its promising applications, this catalytic system presents some limitations, and many groups have encountered challenges including catalyst degradation and cytotoxicity. This review summarizes the applications of CpRu-based catalysts in chemical biology and outlines possible avenues to expand and improve the performance of such systems in a biological setting.

INTRODUCTION

In contrast to natural enzymes, homogeneous catalysts heavily rely on platinum-group metals to forge C–X bonds.[1,2] In this context, numerous catalytic C–C cross coupling reactions have been developed. Many chemists have worked on the development and application of these versatile bond-forming reactions using specifically tailored metal catalysts.[3] Among these reactions, one should mention: the Suzuki-Miyaura[4], Mizoroki-Heck[5], Negishi[6], Sonogashira[7], Kumada-Tamao-Corriu[8], Migita-Kosugi-Stille[9], Tsuji-Trost[10], Buchwald-Hartwig[11], Ullmann[12], Castro-Stephens[13], Glaser[14], Hiyama[15], Fukuyama[16], Cadiot-Chodkiewicz[17], and Hirao cross-coupling[18]. These efforts culminated with the 2010 Nobel Prize in chemistry, awarded to Heck, Negishi and Suzuki.[19]

For the purpose of this review, the so-called Tsuji-Trost reaction, also known as metal-catalyzed allylic substitution, will be presented in more detail as it is the reaction catalyzed by the so-called "Meggers catalyst" which has found widespread applications for the deprotection of allylcarbamate-protected cargoes in a cellular environment.[20–22] Early developments of the allylic substitution were reported by Jiro Tsuji in 1965[23] with the functionalization of diethyl malonate using stoichiometric amounts of $[Pd(Cl)(allyl)]_2$ as allyl donor, Scheme 1.[23] The first catalytic allylic-substitution was reported in 1970 by Hata and Atkins.[24,25] They performed the allylic amination of diethylamine using $[Pd(acac)_2]$ as a catalyst, and allylic alcohol or allyl ether as allyl source to generate the corresponding π-allyl complex (π-allyl hereafter). In 1972, Trost revealed the influence of the nucleophile's hardness on selectivity between branched or linear products, used in combination with an unsymmetrical allyl moiety.[26] Building on this work, Tsuji showed in 1985 that the formation of an η^3-allyl complex using a chiral allyl moiety proceeds with inversion of configuration.[27] Importantly, he showed that a soft nucleophile (for example carbon from enolates, electron-rich double bonds, or thiols) is added directly to the carbon of the coordinated η^3-allyl complex, without prior coordination to the metal. This results in a Walden-inversion at the center undergoing substitution. In contrast, a hard nucleophile coordinates to the metal center, followed by reductive elimination, thus resulting in retention of configuration. In 1997, Takeuchi revealed three important factors influencing the regioselectivity (*i.e.* the branched vs. linear ratio) of the allylic substitution reaction: i) the steric interactions between the incoming nucleophile and the allylic termini, ii) the charge distribution of the π-allyl ligand on the metal center, and iii) the stability of the η^2-alkene-metal complex that results from the nucleophilic addition to the η^3-allyl moiety.[28] The rules determined by Takeuchi are applied to iridium-based catalysts, they are also applicable to other metal-based catalysts but not equally, one of the rules might be more important for Ru-based catalysts. While early work on the Tsuji-Trost reaction focused mostly on Pd-based catalysts, it was later realized that other metals were equally versatile (e.g., Mo, Ir, Ru).[29] The historical development of the metal-catalyzed allylic substitution and its postulated mechanism are presented in Scheme 1.

a)

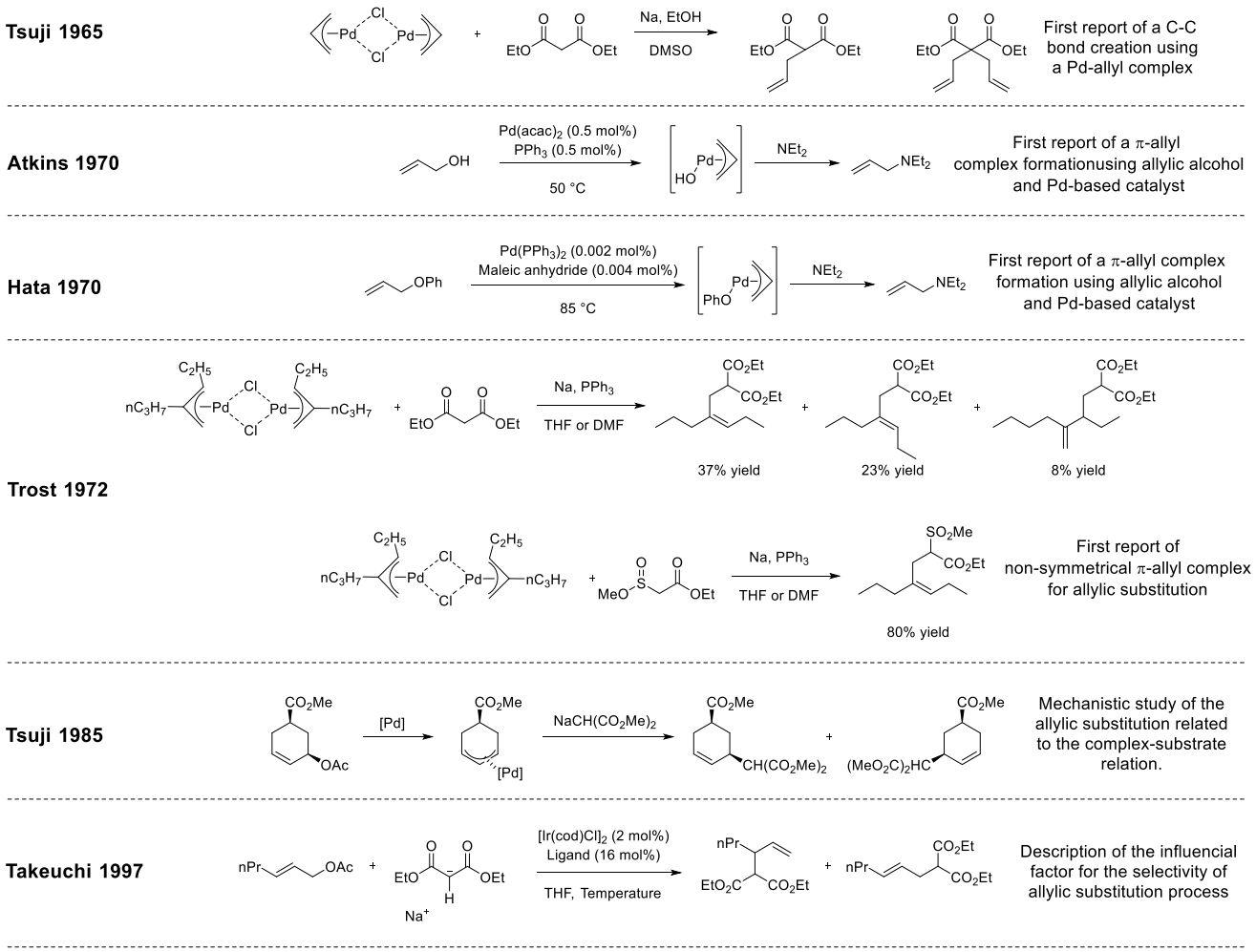

b)

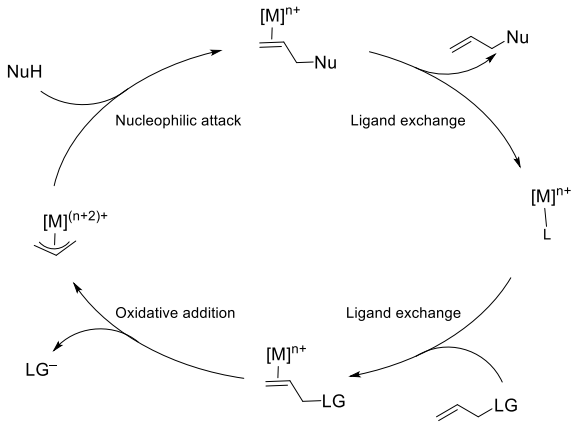

Scheme 1: a) Early milestones of metal-catalyzed allylic substitution [23–28] b) generally accepted mechanism for the allylic substitution with soft nucleophiles. [27]

In the case of ruthenium, Itoh was the first to report on the use of CpRu piano-stool complexes as catalysts performing η^3-allyl complex formation from allylic halide (Cp: η^5-cyclopentadienyl, C_5H_5).[30] Ru-arene have also been reported as catalyst to perform in cellulo catalytic hydrogenation. These are not covered in this review.[31–33]

The selectivity for branched or linear products resulting from an allylic substitution depends on the structure of the catalyst. [Cp*Ru]-catalyst precursors (Cp*: η^5-pentamethylcyclopentadienyl) tend to produce the branched product, while the selectivity of [CpRu]-catalyst precursors is harder to predict.[34] In the context of chemical biology, it is noteworthy that such [CpRu] piano-stool complexes display remarkable stability in water.[35]

Since this first publication, many different ligands have been used in conjunction with CpRu-complexes.[36] In their initial study, Streu and Meggers reported that **[Cp*Ru(cod)Cl]** (cod: η^4-1,5-cyclooctadiene) catalyzes the deallylation of allylcarbamate-protected amines under biocompatible conditions (*i.e.* in the presence of water, air and thiols).[20] Notably, they described the uncaging of the N-allyloxycarbamate-protected rhodamine **1** in the presence of mammalian cells and of thiophenol, Scheme 2. Strikingly, the reaction performed much better in the presence of thiophenol than in its absence, highlighting its relevance for in cellulo catalysis. This observation is not fully understood, but many groups have reported the use of thiols to efficiently quench the η^3-allyl intermediate.[37,38] The reaction is conveniently monitored by fluorescence resulting from the uncaging of rhodamine **2** in the cytosol of HeLa cells.

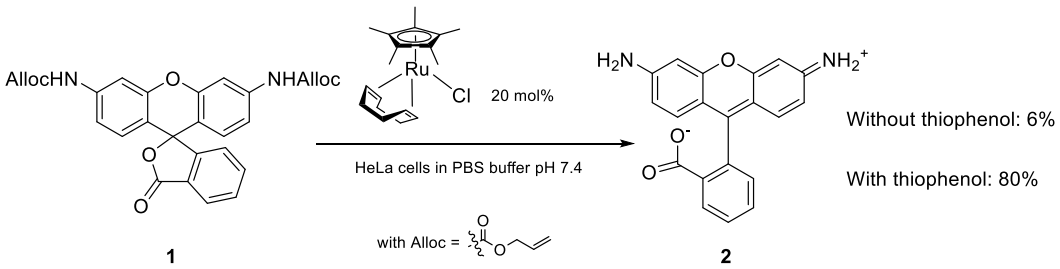

Scheme 2: Catalytic deallalytion of the caged rhodamine **1** in the presence of HeLa cells.

Instead of uncaging a fluorophore, Scheme 2, one can envisage adapting this system towards the uncaging of a biologically active moiety, either in cellulo or in vivo. Upon catalytic deallylation of the substrate, an active molecule (referred to as cargo hereafter) may be released.

A recent review has described in a more general terms the use of metal complexes for catalytic and photocatalytic reactions in living cells.[39] Herein, we present a comprehensive overview of the research triggered by the seminal study from Streu and Meggers,[20] with a focus on in vitro, in cellulo and in vivo applications of [CpRu]-containing complexes. This review is organized as follows: 1] Early milestones on catalyst development, 2] Study and development of the catalytic system, 2.1] Development of new detection methods for *in cellulo* and *in vivo* applications, 2.1.1) Fluorescence monitoring, 2.1.2) Bioluminescence monitoring, 2.1.3) Auxotrophic rescue monitoring, 2.1.4) Cell viability monitoring 3] Further improvement of the catalytic activity *via* chemical modification of the catalyst, 3.1) modification of the first coordination sphere of the complex, 3.2) Formation of artificial metalloenzymes, 3.3) Formation of catalytic nanoparticles, 4] Diversification of the chemical reactivity of previously described complexes 5] Reported and future applications, 5.1) *in vitro* catalysis, 5.2) *in cellulo* catalysis, and 5.3) *in vivo* catalysis**.** This review ends with an outlook.

1.1 Early milestones of catalyst development

Building upon a publication by Kitamura and co-workers,[40] the first improvement on the original **[Cp*Ru(cod)Cl]** catalyst was reported by Meggers in 2014.[41] It included the following features: a quinoline-2-carboxylic acid (QA hereafter) as chelating ligand and a Cp ligand instead of the original (cod) and Cp*-moiety respectively. The resulting **[CpRu(QA)(Solv)]PF_6** (Solv = solvent) complex displayed remarkable features for in cellulo deallylation, including high turnover numbers (TON hereafter) and a tolerance against thiols, including glutathione (GSH hereafter). The relevance of GSH is linked to its presence in most mammalian cells with concentration varying between 0.1 and 10 mM.[42] Glutathione act as a redox buffer in the cytosol.[43] **[CpRu(NMe_2-QA)]PF_6** (**Ru1**) was applied to the catalytic uncaging of the alloc-protected rhodamine **3** and doxorubicin in HeLa cells, inphosphate buffer using 20 mM of catalyst **Ru1**, Scheme 3.

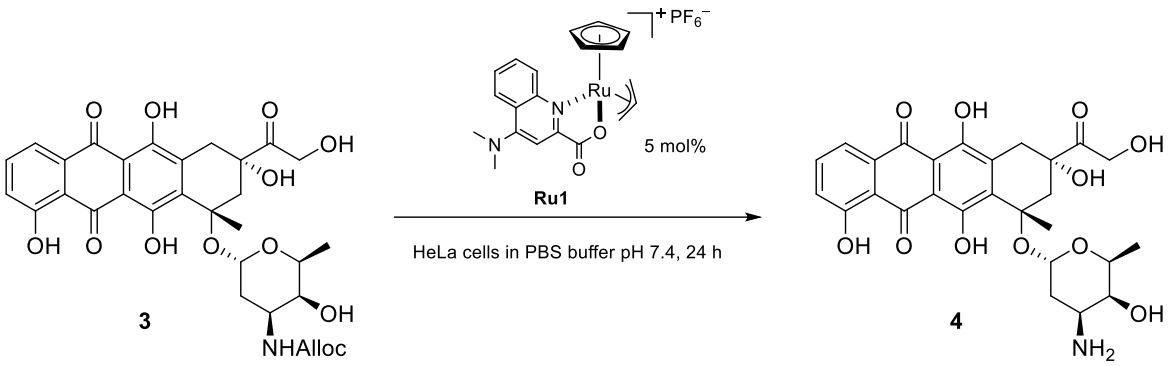

Scheme 3: Catalytic deallylaltion of caged doxorubicin **3** in HeLa cells using **Ru1**.

Using **Ru1**, Meggers and co-workers achieved a TON of up to 270 with a catalytic loading of 0.1 % (i.e. 0.5 mM). Meggers and co-workers demonstrated the beneficial role of electron-donating groups on the QA ligand on the reaction outcome (including reaction rate, TON). Interestingly, Kitamura and co-workers reported an opposite trend (i.e. that electron-withdrawing groups are beneficial for activity).[44] Inspired by previous works from Kitamura and co-workers, Meggers proposed a catalytic cycle, Scheme 4.[45] They highlighted the influence of the nucleophile on the reaction mechanism: for strong nucleophiles, the rate-limiting step is the formation of the η^3-allyl complex, whereas for weak nucleophiles, the rate-limiting step is the attack of the nucleophile on the π-allyl complex. The reader is referred to the papers from Kitamura's group for a thorough description of this system. [46–48]

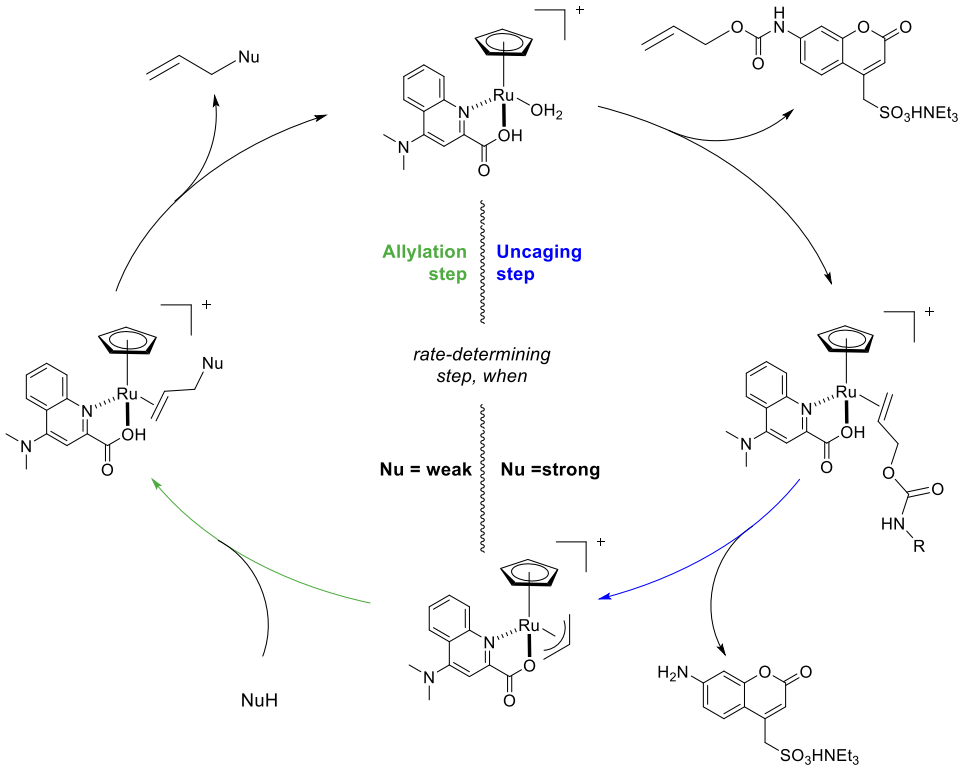

Scheme 4: Catalytic cycle proposed by Meggers for the deallylation of allyl-carbamates, emphasizing the role of the nucleophile.[22]

In 2017, Meggers and co-workers further improved these [CpRuL$_3$]-based complexes for the in cellulo deallylation of allyl-carbamate-protected cargoes.[49] The use of a substituted 8-hydroxyquinolic (HQ hereafter) ligand in place of QA ligands led to a remarkable improvement in the catalytic performance of the corresponding complex. Depending on the nature of the substituent on the HQ moiety, the TON of **[CpRu(HQ)(Allyl)]PF$_6$** (**Ru2**) was up to five times higher than that of **Ru1**, accompanied with a thirty-fold higher reaction rate. In contrast to the QA-based system, electron-withdrawing substituents led to higher TON. For instance, using *p*-CO$_2$Me-HQ (**Ru3**) led to a 10-fold increase in TON compared to the unsubstituted HQ. However, this trend was only valid to a certain extent. They therefore proposed the existence of an optimum electron-withdrawing effect beyond which the activity of the catalyst eventually decreases, Figure 1.

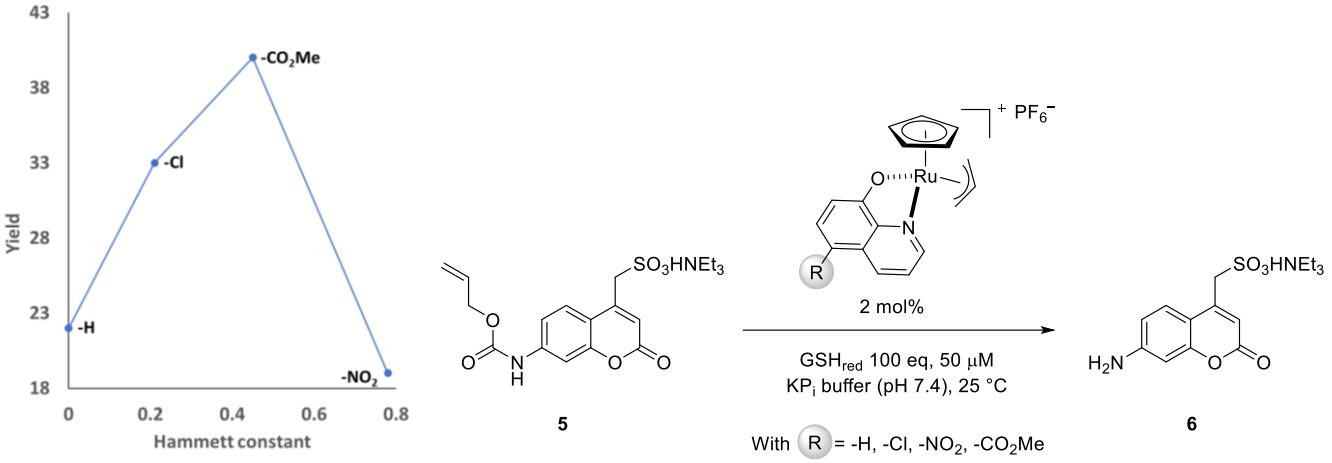

Figure 1: Deallylation yield as a function of the Hammett constant, highlighting the importance the electron-withdrawing substituent on catalyst activity.

Although **Ru2** is more active than its predecessors, it was also found to be significantly cytotoxic, 50-51 with an IC_{50} of 70 nM on HeLa cells (IC_{50} is the concentration needed to induce a decrease of 50% of the cell viability).[50] Its use in cellulo at high catalytic loadings is thus rendered problematic.

In recent years, considerable efforts have been invested into applying the three catalytic systems reported by Meggers **[Cp*Ru(cod)Cl]**, **[CpRu(X-QA)(allyl)]PF_6** (X = -H, -OMe or -NEt_2) and **[CpRu(X'-HQ)(Allyl)]PF_6** (X' = -H or CO_2Me) to uncage various allyl-carbamate protected cargoes, either under physiological conditions or *in cellulo*.[50–57] In addition to using free complexes, different approaches have been pursued to expand the versatility of these Ru-based complexes. For example, the first coordination sphere has been subjected to many changes, from ligand functional group diversification to catalyst modification. Within functional group diversification, simple to complex variations have been attempted. Mascarenas and co-workers studied the ability of modified complexes to be accumulated in different cell compartments. This compartmentalization endows the cell with a different catalytic environment.[58,59] In another approach, Duhme-Klair and co-workers combined **Ru2** derivatives with siderophores to enable endow the resulting catalyst to penetrate into the cytoplasm of Gram-negative bacteria.[60] Many groups investigated the effect of modifying the catalyst's second coordination sphere. Ward, Trefzer, and Tanaka investigated second coordination sphere effects through the assembly of artificial metalloenzymes (ArMs hereafter).[61–69] Rotello and Zimmermann investigated the formation of immobilized Ru-catalysts on gold nanoparticles[70–74] or single-chain nanoparticles (*vide infra)*.[75,76]

Capitalizing on the remarkable tolerance towards cellular debris present in cell lysate, other catalytic in cellulo applications of [CpRu]-derived complexes have been reported including: RuAtAC,[77] [2+2+2] cycloadditions,[78,79] Alder-ene reaction,[79] redox isomerization. [80] These reactivities are also presented in this review.

Despite the apparent diversity of biochemical applications for Ru-based complexes, the reported transformations for in cellulo applications predominantly involve ring-closing metathesis (RCM) of olefins,[81] transfer hydrogenation,[31–33] and the deallylation of alloc-protected substrates.[20–22,37,38,58–60,63,69,72,82–99] This review focuses on the reactions catalyzed by the three types of catalyst published by Meggers and co-workers: i) **[Cp*Ru(cod)Cl]**, ii) **[CpRu(X-QA)(allyl)]PF_6** and iii) **[CpRu(X'-HQ)(Allyl)]PF_6**. In the following sections we discuss several applications of transformations catalyzed by Ru-based complexes, as well as some of their potential limitations. We also outline future perspectives for the improvement of these exciting yet complex systems.

1.2 Study and development of the catalytic system

Variation of the structures of the three piano stool complexes has opened the door to various *in vitro, in cellulo,* and *in vivo* applications. Various substrates were selected based on their specific and straightforward readout. These readouts are based either on the photophysical properties or on a biological response. The main readouts used *in cellulo* and *in vivo* catalysis are fluorescent detections, bioluminescent detection, auxotrophic rescue, and cell viability. The latter two last strategies rely on cell viability triggered by either the formation/release of an essential metabolite or an essential xenobiotic or by the release of a cytotoxic drug. A list of the Ru-based deallylation catalysts tested under biologically-relevant conditions is presented in Figure 2.

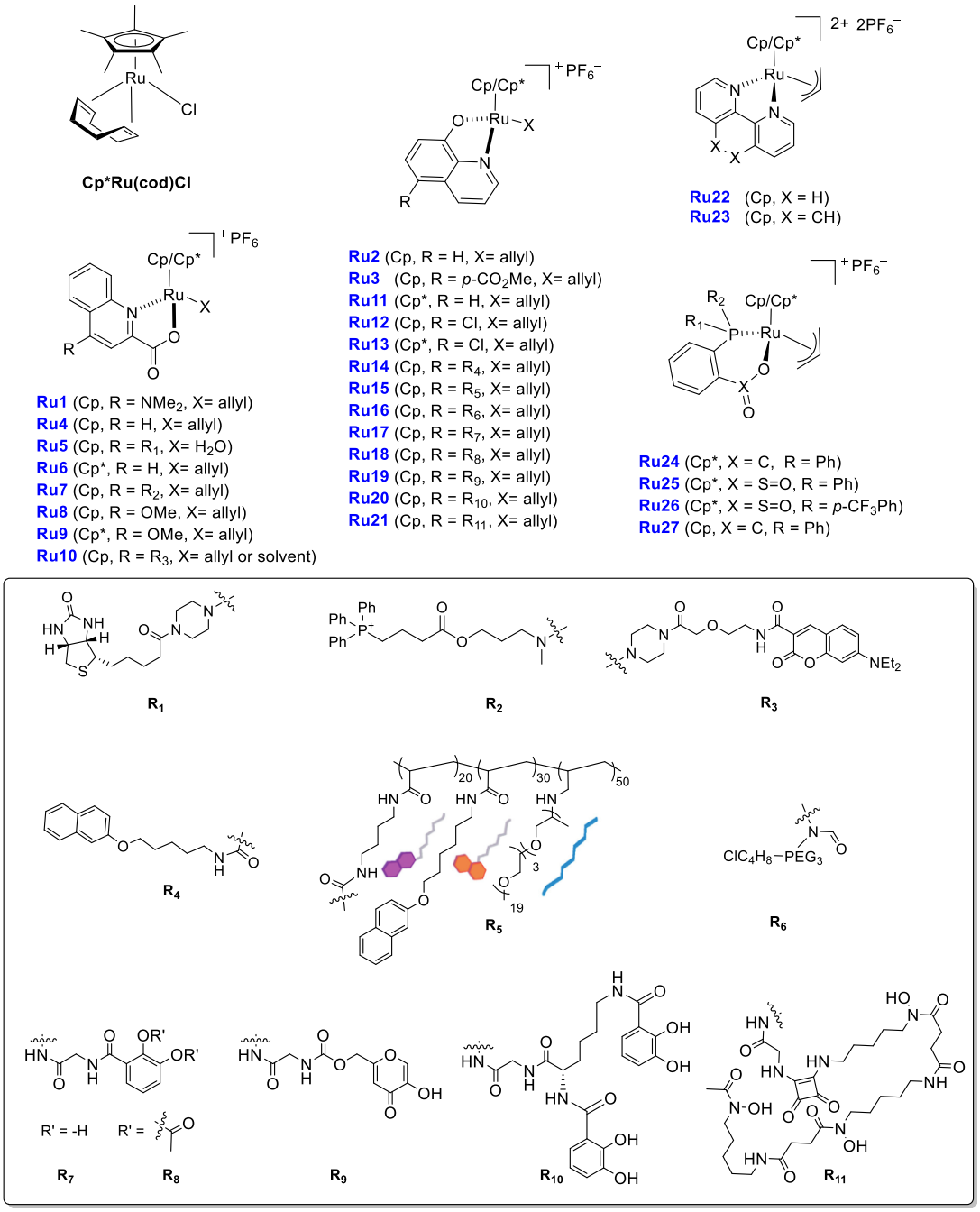

Figure 2: Summary of the Ru-based deallylation catalysts presented in this review.

Some of the major challenges with *in cellulo* and *in vivo* catalysis include: i) determination of the localization and the concentration of the (active) catalyst, and ii) the quantification of product. We summarize below the most promising methods that have been developed and applied in this context.

1.2.1 Development of new detection method for *in cellulo* and *in vivo* study.

1.2.1.1 Fluorescence monitoring

A straightforward means to quantify the concentration of an analyte *in cellulo* is to rely on monitoring a fluorescent signal. This signal can be produced either by i) the (uncaged) product itself or ii) the expression of a fluorescent probe *that is up-regulated by an inducer which is results from the Ru-catalyzed deallylation reaction*.

In 2014, Mascarenas and co-workers used **[Cp*Ru(cod)Cl]** to catalyze the deallylation of alloc-protected small DNA-binding molecules *in cellulo*.[82] For this purpose, they selected a probe that becomes fluorescent upon deallylation and binding to the DNA of chicken embryo fibroblast (CEF) cells. Phenyl azo-pentadiamidine (**8a**), 4',6-diamidino-2-phenylindole (**10**), and ethidium bromide (**12**) were selected as DNA binding molecules. The catalyst's activity was determined for all substrates and their respective binding affinity, Scheme 5.

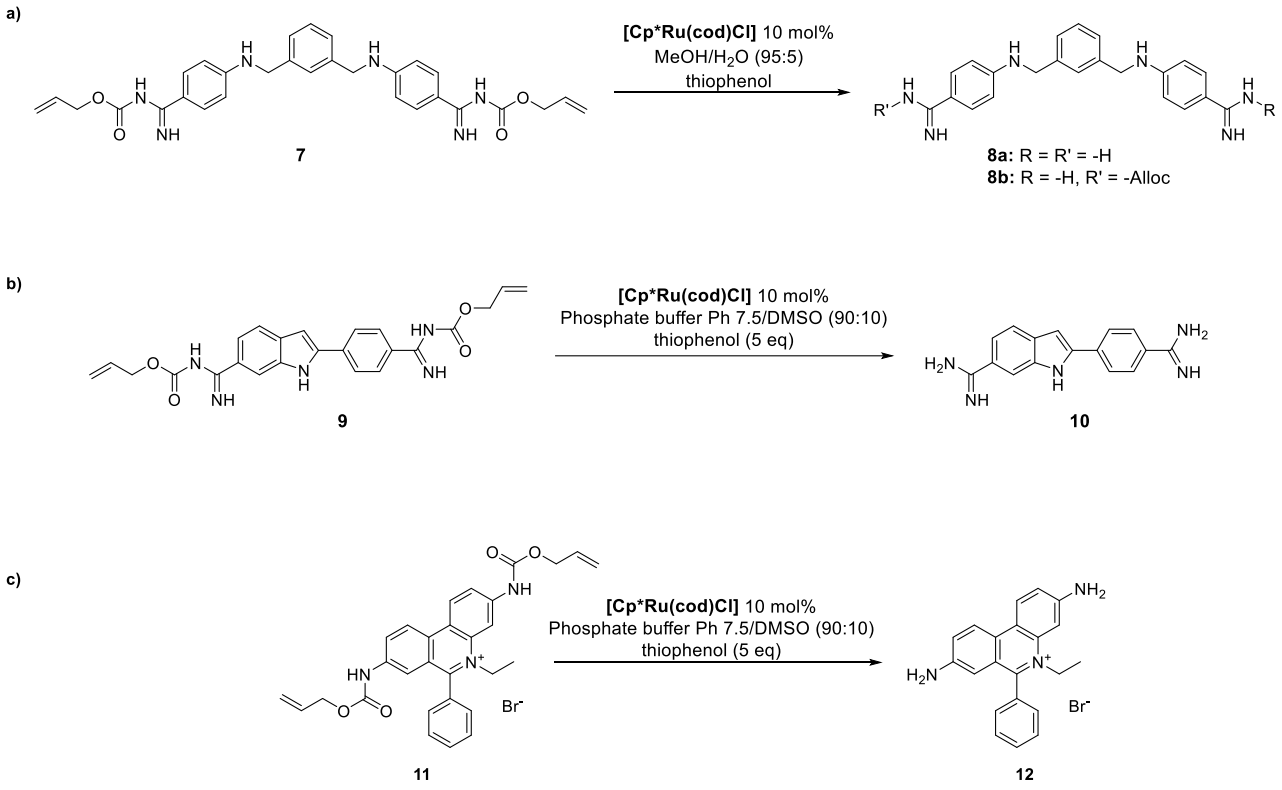

Scheme 5: Ru-catalyzed deallylation of DNA-binding probes: a) **7**, b) **9** and c) **11**

As an extension of this work, Mascarenas and co-workers relied on **Ru7** to accumulate in the mitochondria, thanks the presence of a phosphonium targeting moiety.[58] Premliminary experiments revealed that catalyst **Ru7** was much more active than of **Ru1** for the deallylation of compound **1**, Scheme 10.

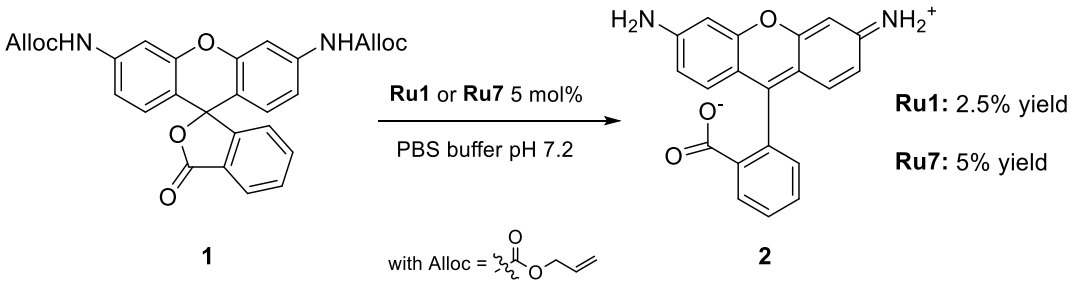

Scheme 10: Catalytic activity of **Ru1** and **Ru7** for the deallylation of substrate **1**

Next, the authors studied the compartmentalization *in cellulo* of two distinct metal-catalyzed reactions. The deallylation of pro-fluorophore **15** by **Ru7**, and the Au-catalyzed hydroarylation of the coumarin precursor **13** to afford **16**, Scheme 6.[59]

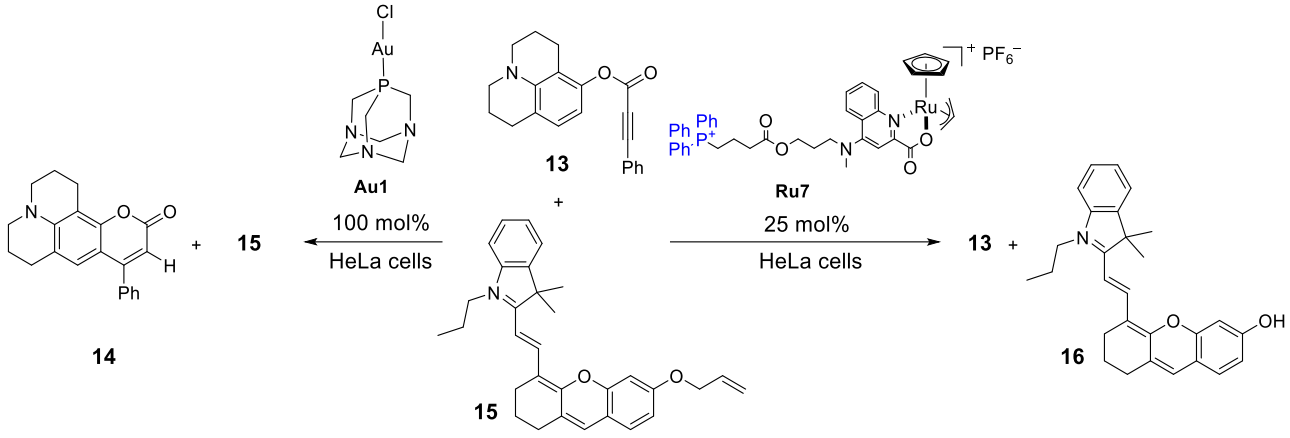

Scheme 6: Bio-orthogonal metal-catalyzed reactions performed in cellulo.

The fluorescent properties of select proteins as also been used for the quantification Ru-catalyzed deallylation. For example, Mayer and co-workers used the [CpRu]-catalyzed uncaging reaction to produce a non-canonical amino acid in *E. coli* triggering the production of the green fluorescent protein (GFP hereafter). The advantage of this method is the direct quantification of the catalytic activity *via* fluorescence. The *in cellulo* expressed GFP contains a non-cannonical amino acid (ncAA) which results from Ru-catalyzed uncaging of the corresponding alloc-protected ncAA, Figure 3.[84]

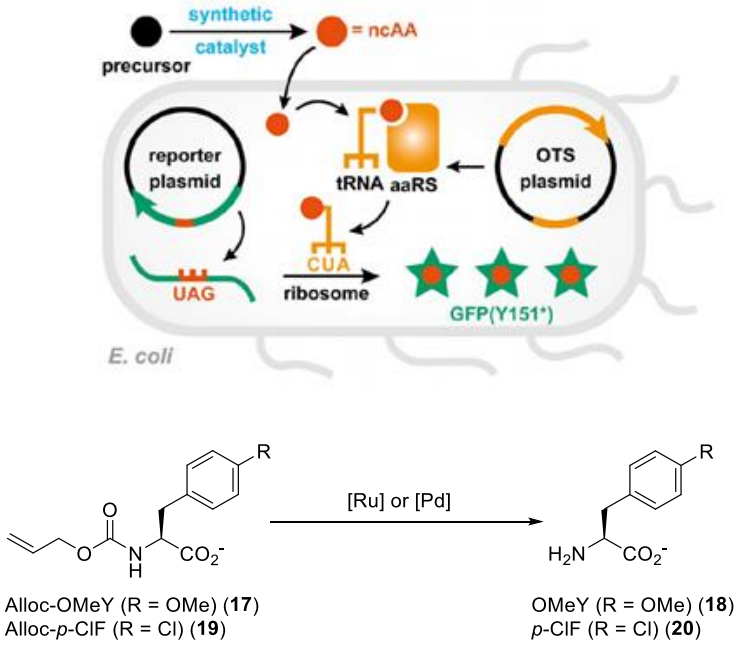

Figure 3: Upon deallylation, the non-canonical phenylalanine amino (ncAA) acid is incorporated in a green fluorescent protein (GFP), enabling a direct readout of Ru-catalyzed deallylation *in cellulo*.

To compare the efficiency of various Ru-deallylation catalysts, Vrabel and co-workers used the caged resoruferins **21**, **22**, and **23** and determined the resulting fluorescence of resorufin **24** obtained under different catalytic conditions.[98] The authors included a self-immolating ethylenediamine moiety between the protecting group and the resorufin fluorophore, Scheme 7.

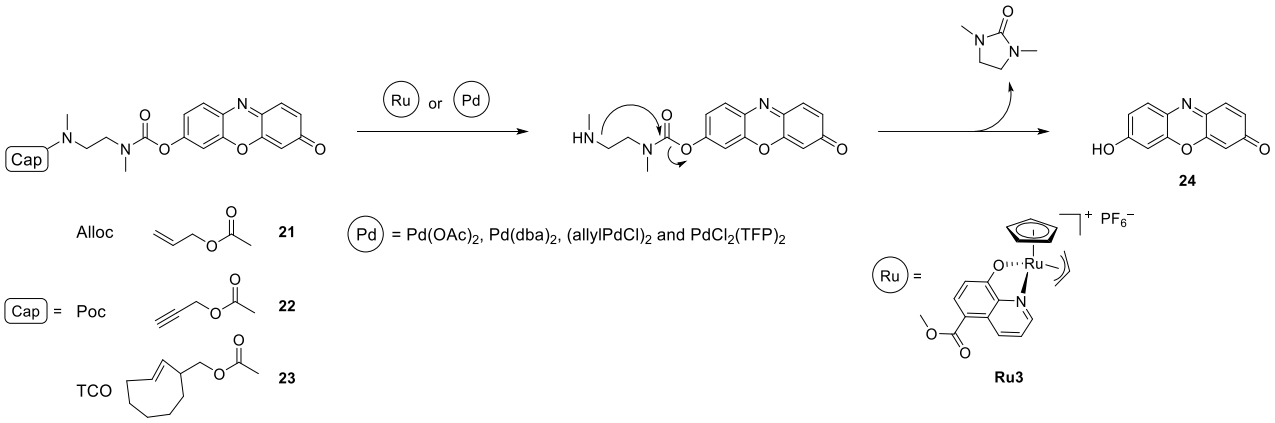

Scheme 7: Metal-catalyzed uncaging of resorufin via a self-immolating moiety.

1.2.1.2 Bioluminescence monitoring

Bioluminescence is the production and emission of light by a living organism. The light emitted by a bioluminescent organism is produced by energy released from chemical reactions occurring inside the organism. Capitalizing on this concept, a few groups have used this readout method to determine the efficiency of their catalytic system. Wender and co-workers reported a system relying on a **[CpRu(OMe-QA)Allyl]PF_6 Ru8** catalyst to uncage via deallylation the alloc-aminoluciferine **25** to afford aminoluciferine **26** in the presence of 4T1 cells, a mouse breast cancer cell line, transfected with the gene of click-beetle luciferase, Scheme 8. Luciferase is an enzyme that catalyzes luciferin's conversion into oxyluciferin, accompanied with a luminescent signal. The authors could thus monitor in real-time the catalytic uncaging via luminescence spectroscopy.[37]

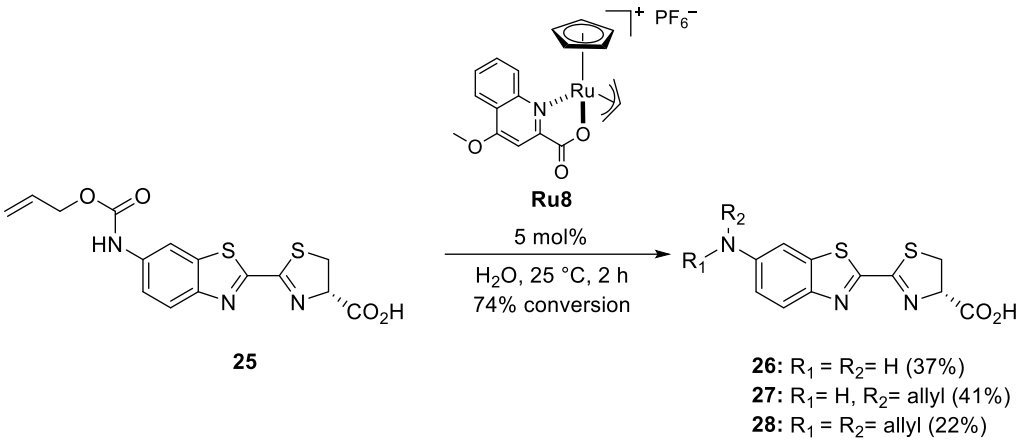

Scheme 8: Upon Ru-catalyzed deallylation of compound **25**, the formation of various derivatives of aminoluciferine were detected, highlighting the complexity of the reaction.

Ward and co-workers also have exploited the possibility of producing a bioluminescent signal to quantify the efficiency of their catalytic system.[95] In this study, they used an ArM-based catalyst endowed with cell penetrative properties to perform the deallylation of compound **29**. Upon deallylation, a gene-switch leads to the production of compound **30** and a photon, Scheme 9. This work will be discussed in the artificial metalloenzyme chapter.

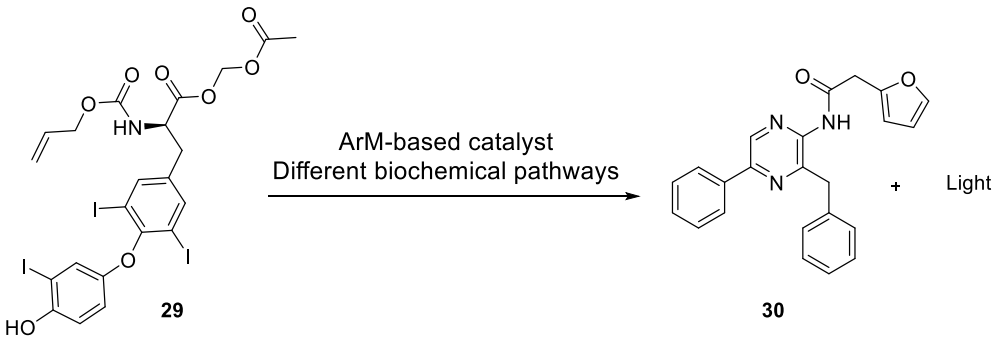

Scheme 9: ArM-based *in cellulo* deallylation of **29** followed by multiple biochemical pathways finally affording **30** and light, enabling the monitoring of the reaction.

1.2.1.3 Auxtrophic rescue monitoring.

Auxotrophy is the inability of an organism to produce a particular organic compound essential for its growth. Complementing the organism with a means to produce this compound enables to rely on selection to monitor the efficiency of the auxotrophic rescue. [53,83] The organic compound may be either be an essential metabolite or a xenobiotic, Figure 4.

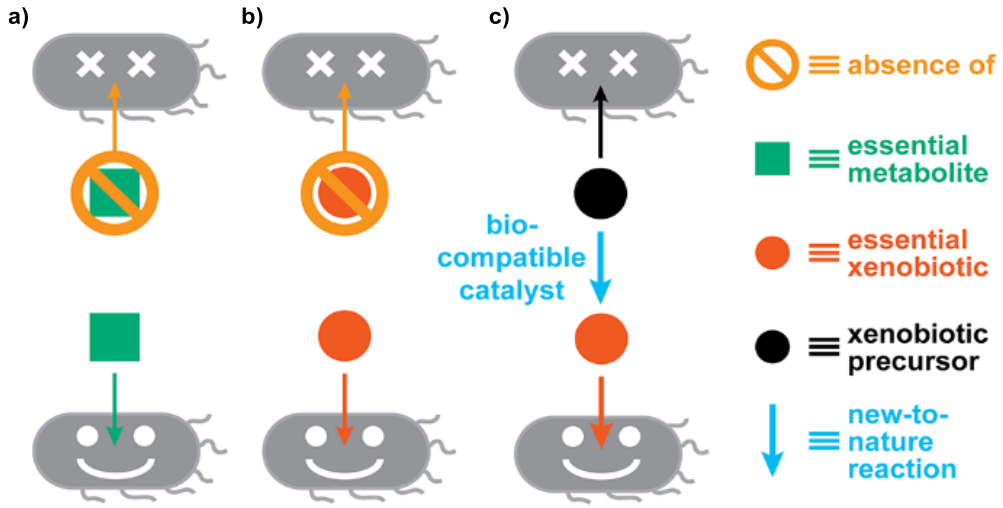

Figure 4: Supplementing auxotrophic cells with an essential metabolite or xenobiotic enables to apply selection schemes to the assay. a) For a natural auxotroph, an essential metabolite is provided to the organism that is not able to biosynthesize it. b) Synthetic auxotrophs are engineered to require xenobiotics such as ncAAs or unnatural nucleobases. c) Implementation of a bio-orthogonal catalytic to perform an auxotrophic rescue.

Balskus and Mayer have exploited this principle to develop different auxotrophic systems. Balskus relied on an *E. coli* auxotroph that could not produce *p-aminobenzoic acid (PABA)* as a result of a single gene deletion (either Δ*pabA* or Δ*pabB)*, Figure 5a.[53] Mayer and co-workers relied on a β-lactamase variant (TEM-1.B9) whose ampicillin degradation capacity required the presence of either 3-iodo-L-tyrosine (3iY) or 3nitro-L-tyrosine (3nY)). These xenobiotics were preduced via a Ru-catalyzed uncaging of the corresponding alloc-protected ncAAs, Figure 5b.[83]

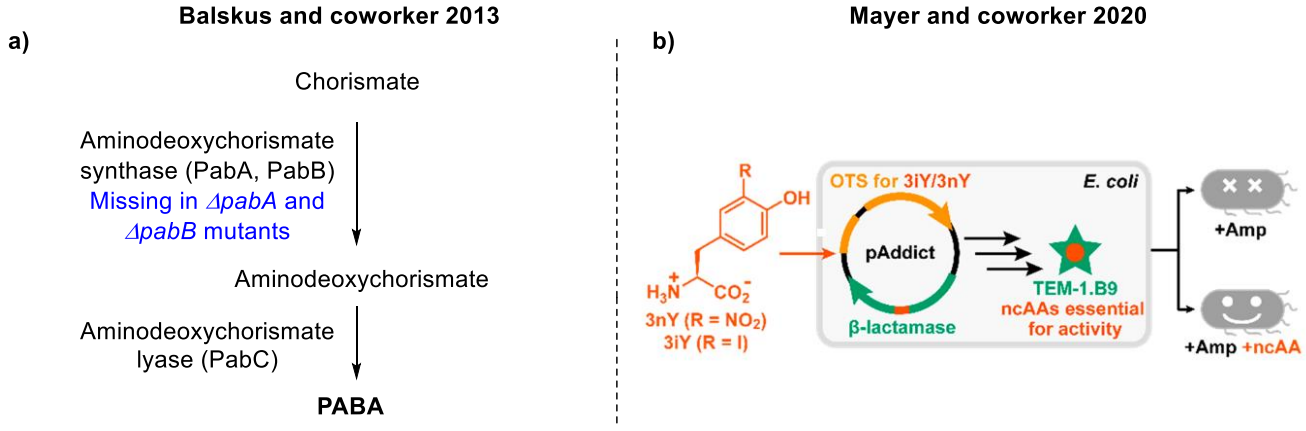

Figure 5: The two auxotrophic systems developed by Balskus and Mayer, respectively. **a)** Biosynthesis of aromatic metabolites in *E.coli* from chorismate. **b)** pAddict plasmid containing a

-lactamase variant triggered when either 3iY or 3nY are incorporated. This selectivity is brought by an orthogonal translation system (OTS) selective for either of these ncAAs.

Balskus and co-workers reported the use of a biocompatible uncaging reaction catalyzed by **[Cp*Ru(cod)Cl]** that converts alloc-PABA **31** into PABA **32** to rescue the auxotrophic *E. coli* strain, Scheme 10a. Mayer and co-workers relied on **Ru8** to uncage of **33** and **34**, Scheme 10b. They quantified the conversion of **33** into 3nY **34** by monitoring the culture's optical density (i.e. OD_{600}).

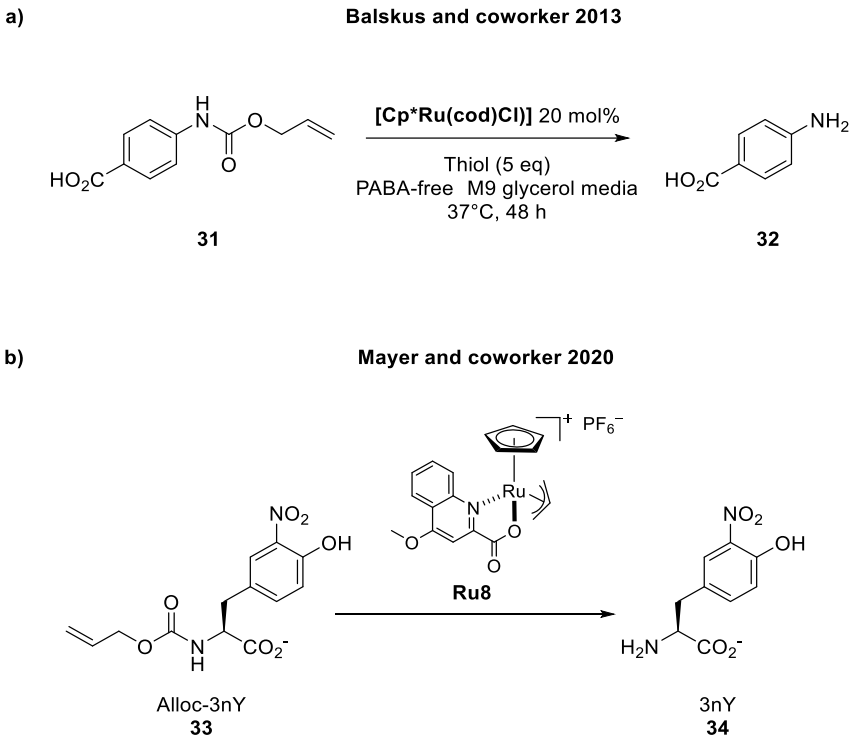

Scheme 10: Evaluating the efficiency of an auxotrophic rescue on different *E. coli* strains *via* two pathways. **a) 31** Uuncaging of *PABA* **32** using **[Cp*Ru(cod)Cl]** and a **32**-free M9 glycerol media**. b)** Uncaging of **33** using **Ru8** as catalyst affording **34**.

1.2.1.4 Cell survival/viability monitoring.

This method consists of determining the cell viability after treating cells with a pro-drug that, following its Ru-catalyzed uncaging, releases the active drug. The extent of viability (as determined by the OD_{600} enables the quantification of the catalytic efficiency. Different groups have adopted different strategies that rely on this method. Tanaka, Duhme-Klair and Rotello exploited this quantification method to estimate the efficiency of their system. Tanaka and co-workers have

developed an ArM-catalyzed deallylation of a pro-apoptotic peptide **35** which, upon deallylation, functionalizes the surface of the tumor cell SW620.[69] As a result, the organism triggers the apoptosis of the corresponding cell, thus decreasing the cell viability of the tumor cells SW620, Scheme 11. This study was also applied *in vivo*, thus enabling the authors to quantify survival and tumor volume.

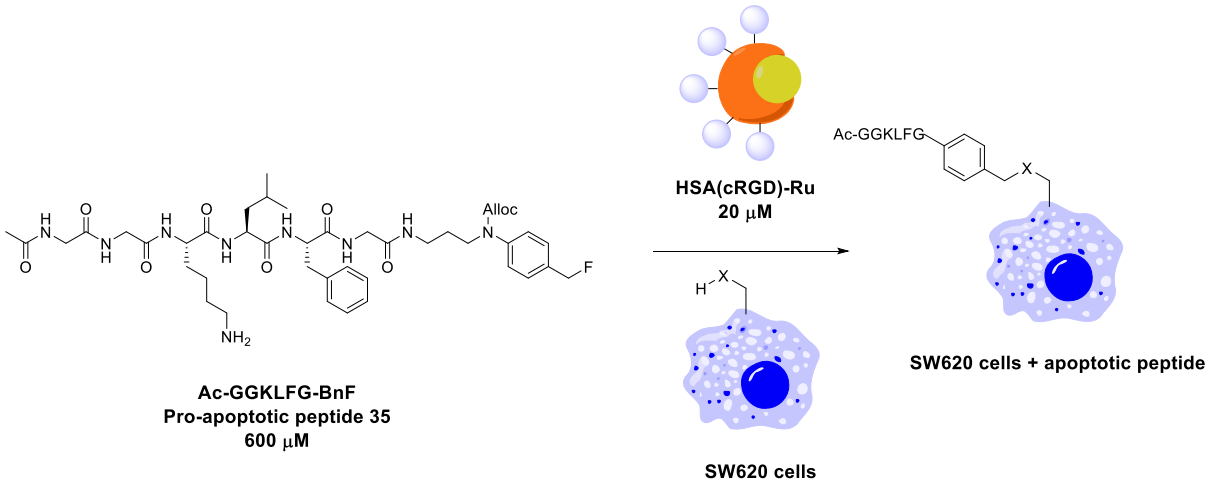

Scheme 11: Cytotoxicity assay of **HSA(cRGD)-Ru** using SW620 cells. Deallylation of the pro-apoptotic peptide **35** using **HSA(cRGD)-Ru** results in surface functionalization of **SW620** and cell death.

Similarly, Rotello and co-workers took advantage of this detection method to estimate the efficiency of their catalytic system for intra or extracellular catalysis.[72] They developed nanoparticles that can either penetrate or not into HeLa cells. In addition, they evaluated the potency of ZnS-supported nanoparticles the same way, Scheme 12.[100] These studies will be discussed in the corresponding part of the review.

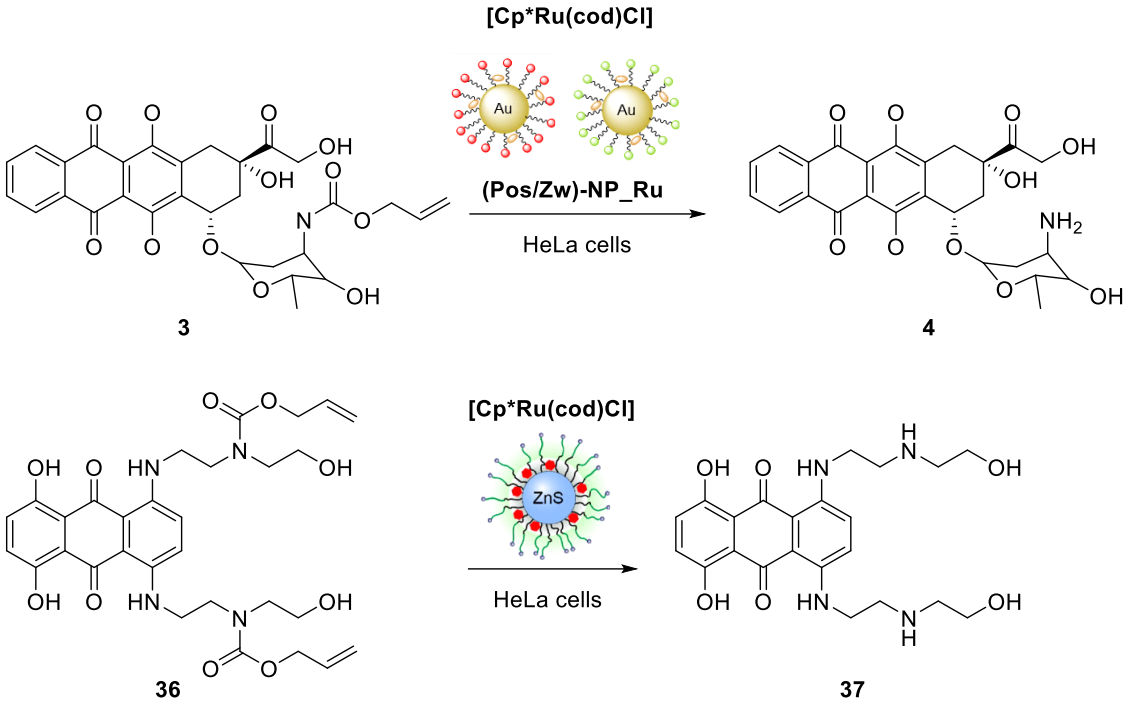

Scheme 12: Application of the developed (**Pos**/**Zw**)-**NP_Ru** for the deallylation of pro-doxorubicin **3** in the presence of HeLa cells and ZnS-based nanoparticles functionalized with **[Cp*Ru(cod)Cl]** for the deallylation of pro-mitoxantrone **36**.

Duhme-Klair and co-workers evaluated the possibility of catalyzing the deallylation of pro-drugs pro-moxifloxacin **38** and **39** into moxifloxacin **40**. In this study, they used **Ru17-21** aiming to increase their cellular uptake in *E. coli* cells, Scheme 13. They determined the most promising siderophore-ruthenium catalyst **Ru18** resulting in the highest cell viability.

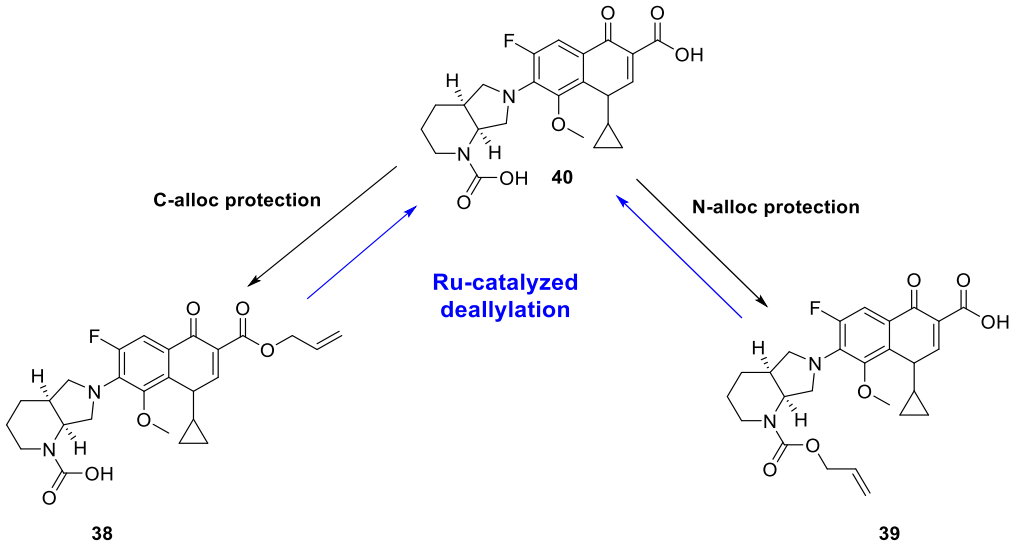

Scheme 13: Structure of the different components of the catalytic system used in this study. The alloc-protected forms of moxifloxacin **38** and **39** are uncaged and afford the antibacterial molecule moxifloxacin **40**. Catalysis is performed using the siderophore Ru**17-21**, endowing the catalyst with cell penetrative properties.

The previously described detection methods endow researchers with powerful tools to quantify the catalytic performance and optimize it. Capitalizing on these methods, many groups have worked on the improvement of three initial catalytic systems: i) **[Cp*Ru(cod)Cl]**, ii) **[CpRu(X-QA)(allyl)]PF6,** and iii) **[CpRu(X'-HQ)(Allyl)]PF6**.

1.3 Further improvement of the catalytic activity *via* chemical modification of the catalyst

1.3.1 Modification of the first coordination sphere of the complex.

Few groups have worked on modifying the ligand to modulate the activity or the vectorization of the catalyst. These modifications rely on the variation of the bidentate ligand, either **QA** or **HQ**, *via* functional group modifications or by entirely modifying the bidentate ligand. The η^5-Cp was also compared with η^5-Cp* to estimate the influence of this ligand on catalysis. Relying on their elegant screening platform, see Figure 7, Mayer and co-workers screened a broad palette of [83]of Ru- and Pd-based catalysts to determine which was the least cytotoxic and which led to the highest fluorescence resulting from the *in cellulo* expression of GFP, Figure 37.[84] The catalysts **$Pd(OAc)_2$, [Cp*Ru(cod)Cl], $[CpRu(MeCN)_3]PF_6$ and $[Cp*Ru(MeCN)_3]PF_6$** proved less active than **Ru2/4/6-9/12-14**. Importantly, the **HQ**-based catalysts **Ru2/12-14** displayed marked cytotoxicity above a 12.5 mM. Accordingly, the **QA**-based catalysts **Ru4-8/2-7** (QA-based) are more attractive for work in the presence of *E. coli* cells, Figure 7. Whether such cytotoxicity is also observed with other cell types may be worthy of thorough investigation.

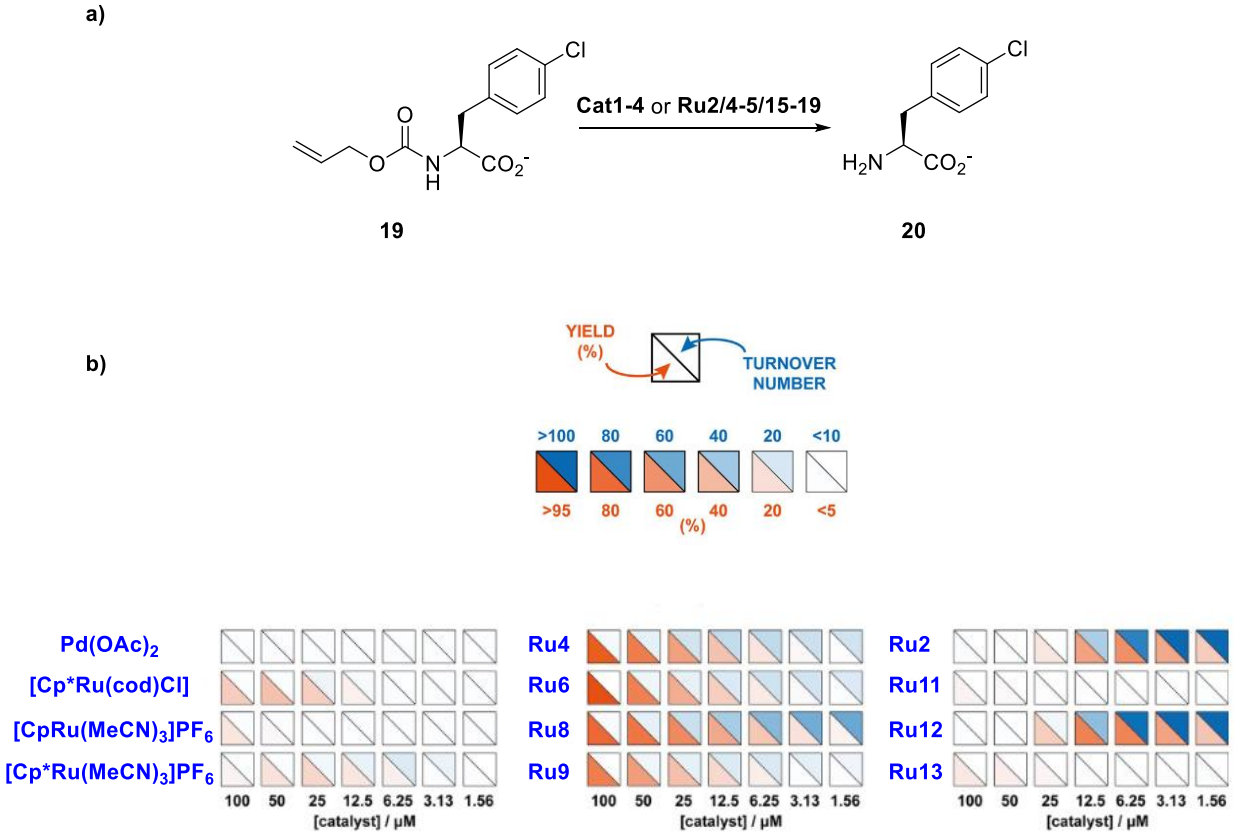

Figure 7: Screening platform developed by Mayer and co-workers enabling to determine the best biocompatible catalyst for the deallylation of alloc-protected ncAA **19**. **a)** Catalytic deallylation of pro-ncAA **19**. **c)** Yield and TON for the various catalysts at different concentrations are displayed as a fingerprint.

The nature of the organic co-solvent appeared to influence the outcome of the reaction. The author determined that, combined with **Ru8**, DMSO gave the best results in the uncaging of **19**. Importantly, **Ru8** kept >50% of its initial activity after 3 hours of incubation prior to catalysis, illustrating its slow decay over time. The authors did not investigate other complexes' stability or further investigate the degradation mechanism of **Ru8**. Similarly, Okamoto and co-workers have screened multiple complexes to find the best candidate for their one-pot multiple peptide ligations.[38] To develop this method, a library of complexes was synthesized to evaluate their catalytic potency toward the conversion of pro-peptide **41** into peptide **42** and, thus, their stability in the reaction conditions, Figure 8b and c.

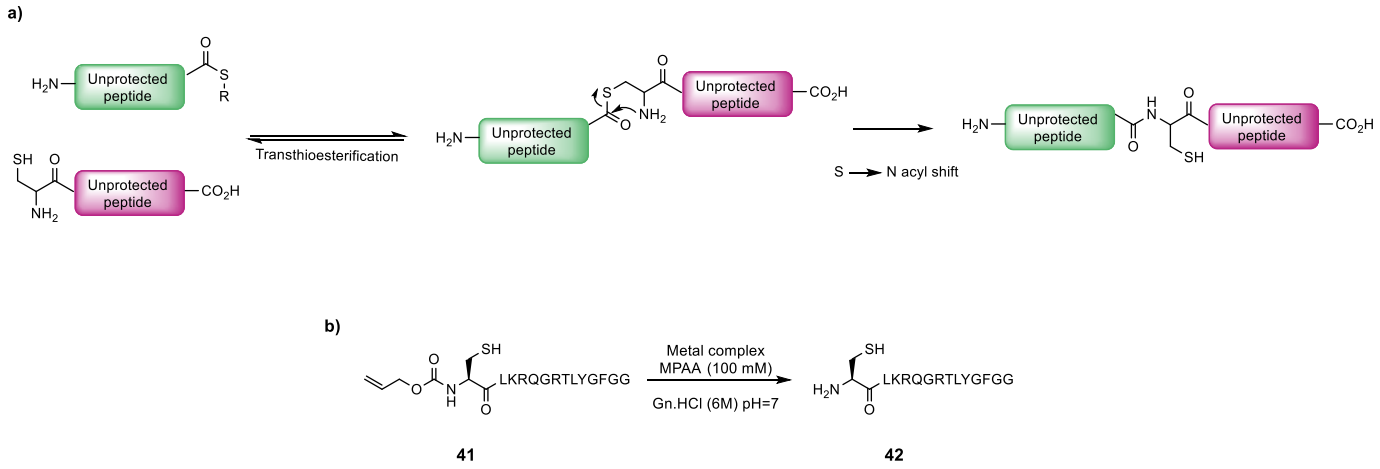

Figure 8: Native Chemical Ligation (NCL)resulting from a Ru-catalyzed deallylytion of an alloc protected *N*-terminal cysteine, **a)** NCL mechanism**.** b) alloc-protected peptide used in the study. (Gn·HCl = Guanidinium hydrochloride and MPAA = 4-mercaptophenylacetic acid).

This screening campaign revealed that **Ru1**, **Ru4**, and **Ru27** were the most efficient affording 70, 56, and 72 TON, respectively (with a 1 % catalyst loading). The authors attributed the difference between **Ru1** and **Ru4** to a difference in electron density at the metal center resulting in higher stability of **Ru4** towards 4-mercaptophenylacetic acid. The difference between **Ru1**/ **Ru4** and **Ru27** was suggest to result from steric hindrance, leading to a reduced rate achieved with **Ru27** but increasing its stability towards MPAA. This study suggests that the higher electrophilicity of **Ru1** and **Ru4** increases the reactivity of the corresponding η^3-allyl complexes towards nucleophiles and decreases the stability of the complexes towards MPAA. Interestingly, MPAA benefitted the catalysis by minimizing the transfer of an allyl moiety to the protein after deallylation.

Mascarenas and Duhme-Klair modified the first coordination sphere of catalyst **Ru1**. They aimed to endow the catalyst with new properties like mitochondrial accumulation or cell penetration. Mascarenas and co-workers developed a derivative of **Ru1** to favor its accumulation in mitochondria.[58] One of the methyl groups of the amine moiety was replaced with a triphenylphosphonium moiety affording **Ru7**. This triphenyl phosphonium has been reported to act as a particularly efficient mitochondria-targeting moiety.[101] For the preliminary experiment, the catalytic activity of the phosphonium-modified catalyst **Ru7** was found to be much higher than that of **Ru1**, Scheme 15. The reasons for this difference remain to be clarified. Of note, both catalysts

were used in water, PBS, or lysates to convert the pro-rhodamin **1** into rhodamine **2** giving 2%, 2.5%, and 0.4% for **Ru1** and 6%, 5%, and 5% for **Ru7**.

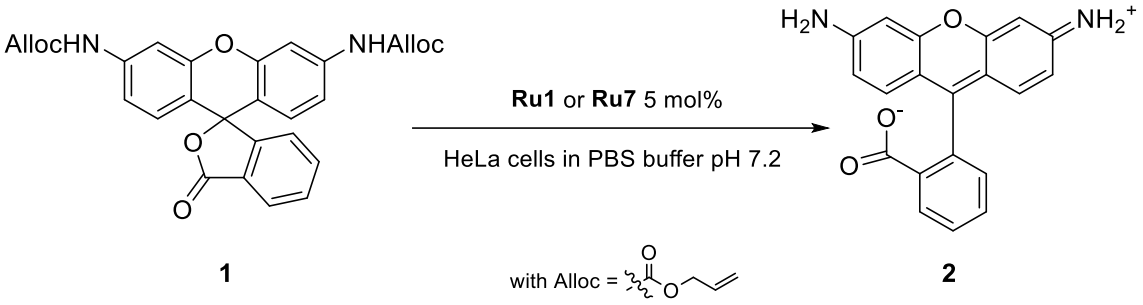

Scheme 15: Substrate **1** was used as a test substrate to compare the deallylation activity of **Ru1** and **Ru7**.

An elegant strategy to render Ru-deallylation catalysts more cell permeable was explored by Duhme-Klair and co-workers. With this goal in mind, they used siderophores covalently linked to the catalyst aiming to increase the cellular uptake in *E. coli*, Scheme 13. They identified **Ru18** as the most promising siderophore-ruthenium catalyst for this purpose.

The improvement of the catalytic activity *via* modification of the second coordination sphere was explored by Ward, Tanaka, Trefzer, Rotello, and Zimmermann. Two distinct strategies were pursued: i) formation of artificial metalloenzymes and ii) formation of catalytic nanoparticles.

1.3.2 Formation of artificial metalloenzymes

Capitalizing on the versatility of the biotin-streptavidin couple, the Ward group has extensively used this system to assemble artificial metalloenzymes (ArMs hereafter). Linking a CpRu-moiety to a biotin ensures that, upon mixing with streptavidin, the metal is nearly irreversibly anchored within streptavidin. The deallylase activity of the ArM may be fine-tuned either by variation of the linker between the biotin and the CpRu moiety or by genetic engineering of the host protein.

Although CpRu-deallylation catalysts have been reported to tolerate mM concentration of reduced thiols (e.g. glutathione), our initial studies focused on assembling and compartmentalizing the ArM either i) on the surface of *Chlamydomonas reinhardtii* or ii) *E.* Coli, or in the periplasm of *E.coli*, Figure 13.[-96,102] These compartments contain significantly lower concentrations of reduced thiols and circumvent the challenge of importing the cofactor and substrate into the cytoplasm.

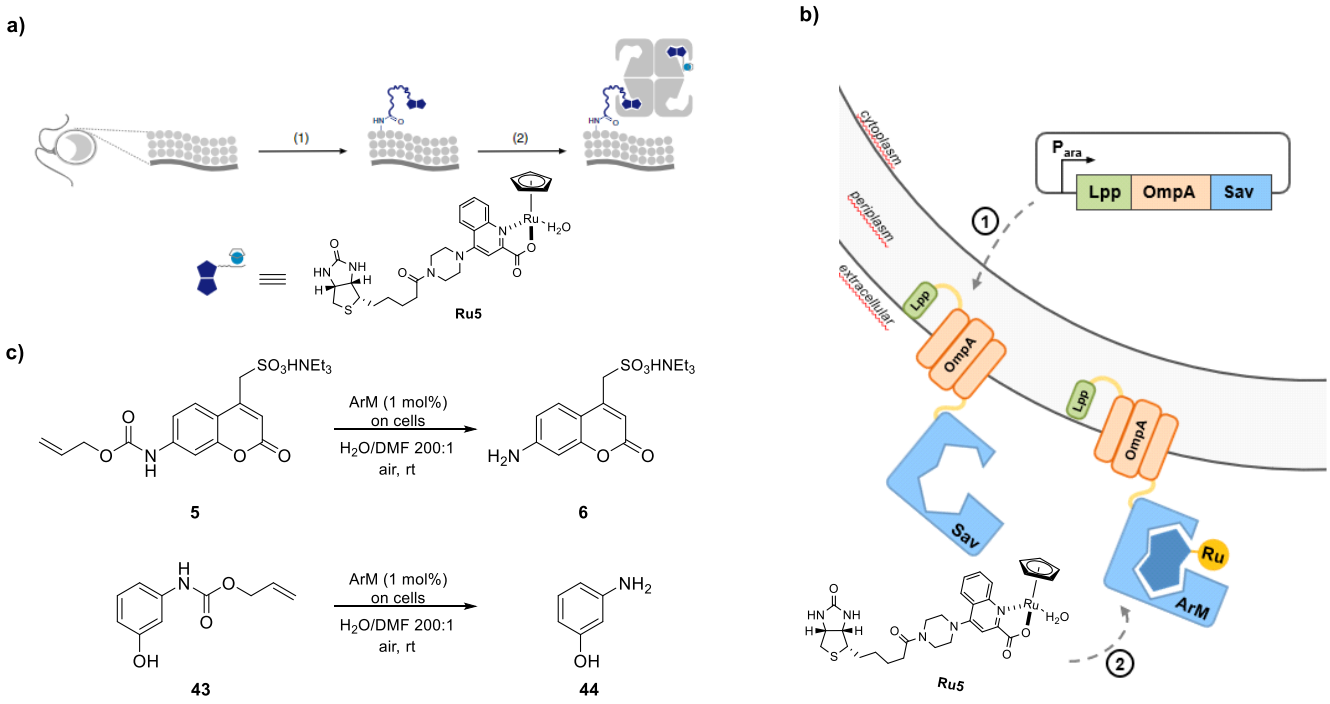

Figure 10 : Summary of the surface display strategies used to assemble ArMs at the surface of various cells. a) Surface functionalization of *Chlamydomonas reinhardtii* by a biotinylated moiety (1), thus allowing the supramolecular anchoring of Sav and the subsequent immobilization of a biotinylated cofactor forming the ArM at the surface of the cell (2). b) *E. coli* surface display strategy, Sav was genetically engineered at its C-terminus to include a truncated *E. coli* lipoprotein (Lpp) fused to the amino terminus of the five β-strand of the outer membrane protein OmpA β-strand from the five constitutive (1), thus allowing the assembly of the ArM at the surface by addition of the corresponding biotinylated cofactor (2). c) Catalytic uncaging of substrates **5** and **43** used in the different studies.

Perhaps the most versatile feature of ArMs is the possibility of improving the catalytic performances (TON, ee, etc.) *via* the modification of amino acid residues in the proximity of the cofactor. For streptavidin (Sav hereafter), two positions are often selected for mutagenesis, e.g. S112, and K121, as highlighted by the X-ray the ArM **Ru5** · S112M-K121A, Figure 11.

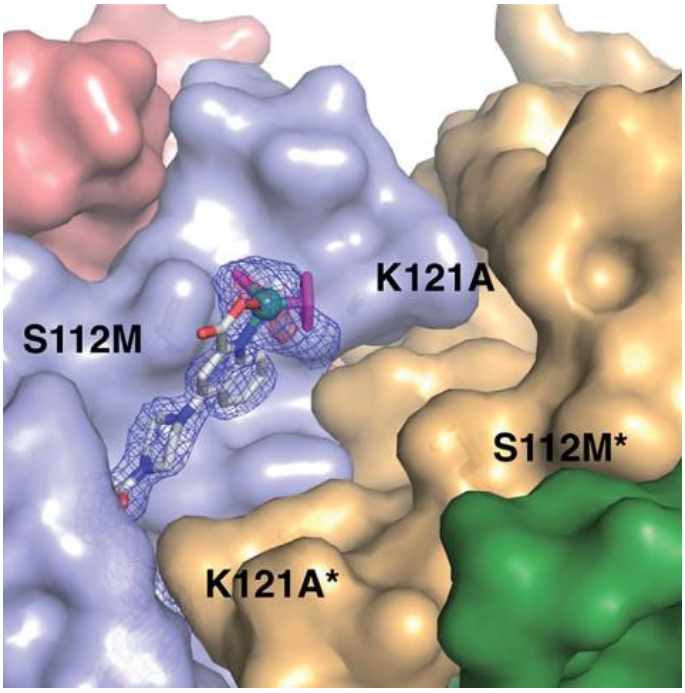

Figure 11: Close-up view of **Ru5** · Sav S112M-K121A (PDB 6FH861[61]). The four monomers of Sav are displayed as color-coded accessible surface, the biotinylated cofactor **Ru5** as stick with the Ru as a sphere.

The potential of Sav *E. coli* surface-display was highlighted for the deallylation of various substrates, either affording a fluorescent coumarin **6**, or for the upregulation of a protein as a result of the uncaging of *m*-aminophenol **44,** which turns on the overexpression of the reporter GFP, Figure 10b and c. [90,96,102] Mutagenesis studies, relying on *E. coli* surface display, revealed marked differences with results obtained with purified Sav samples. Careful analysis of surface-displayed samples led us to conclude that the homotetrameric nature of Sav was sometimes compromised when Sav was displayed on the surface of *E. coli*.[96] An alternative approach was reported by Gademan and cowokers, relying on *Chlamydomonas reinhardtii*. In this study, they covalently functionalized its cell surface with biotin. Next they added Sav, followed by the biotinylated catalyst **Ru5**. They could show that the resulting cells were endowed with deallylase activity, which could be monitored by the fluorescence resulting from the uncaging of coumarin **6**.

An alternative application of surface functionalization was reported by Tanaka and co-workers to target tumor cells. Their study used cRGD peptides-coated human serum albumin (HSA) as host protein for **Ru10**. cRGD peptides display high affinity for integrins, which are often overexpressed at the surface of tumor cells. As a result, the ArM accumulated on the surface of tumor cells. Next,

addition of a pro-apoptotic peptide **35** led to cell death as a result of deallylase activity by **Ru10** · HSA(cRGD), Scheme 11. [69] Finally, the surface functionalization strategy **Ru10**·HSA(cRGD) combined with the pro-apoptotic peptide was applied for *in vivo* tumor therapy using mice bearing SW620 tumors. Co-injection of **Ru10**·HSA(cRGD and **35** revealed the suppression of tumor growth while used separately they did not influence its growth.

In parallel to the *E. coli* surface-display efforts, compartmentalization of ArMs in the intracellular environment was investigated. While ArM-based cell surface catalysis was explored and developed, in the meantime, some investigations about intracellular ArM-based catalysis were undertaken. Two directions were followed: i) development of cell penetrative ArM and ii) periplasmic protein expression and subsequent formation of ArM in the periplasm. The Matile, Fussenegger, and Ward groups further teamed up to develop a cell penetrative artificial deallylase (ADAse hereafter) to perform catalysis in mammalian cells.[95] They ensure cell penetration by fluorescence, Figure 14. Capitalizing on the tetrameric nature of Sav, the remaining biotin binding sites can be equipped with **Ru5**, thus ensuring the introduction of the ADAse in the cytosol of HEK 293 T-cells, Figure 12.

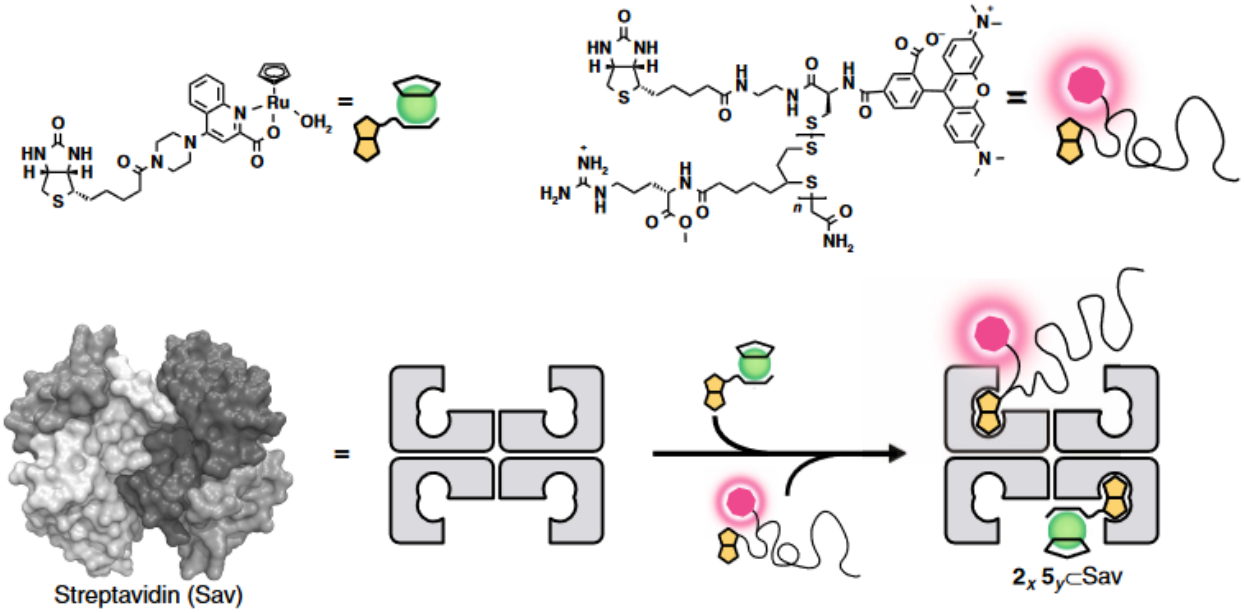

Figure 12: Formation of the cell-penetrating ArM bearing a fluorophore for fluorescent monitoring and a polydisulfide peptide for the cell penetrative properties.

They used HEK 293T cells that were engineered with a T3-gene switch consisting of two plasmids. The uncaging of the T3 hormone by **Ru5** leads to the upregulation of luciferase (sec-nluc) *via* the binding of the T3 hormone to the TSR thyroid hormone receptor. The corresponding luciferase

expression levels were be monitored by the luminescent signal emitted in the presence of furimazine **29-2**, which, as a result of sec-nluc releases the pyrazine **30**, along with CO_2 and a photon. *In vitro* screening of the ADAse revealed that **Ru5**·Sav S112A had the highest TON with the caged T3-substrate **29**, Figure 13.

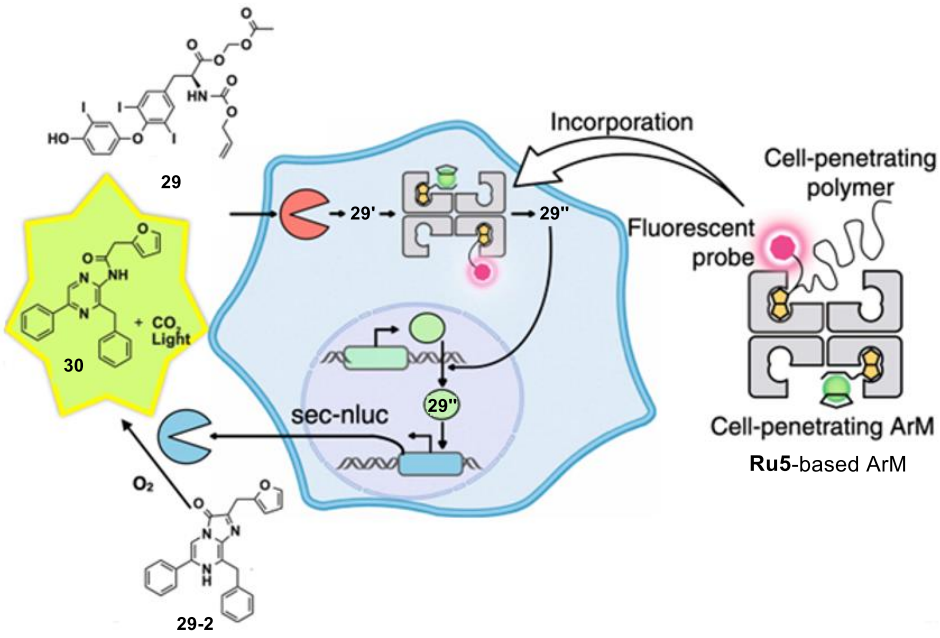

Figure 13: An enzyme cascade within HEK 293 T cells. The fully assembled ADAse was introduced in the cells thanks to a fluorescently-labeled cell-penetrating polydisulfide. The deallylation of the caged T3-hormone by **Ru5**-based ArM upregulates the expression of sec-luc, which can be monitored by luminescence, using furimazine **29-2** as a substate.

Capitalizing on this work, Matile and Ward improved the covalent disulfide exchange module responsible for the uptake of the ADAse in mammalian cells. For this purpose, they tested various benzopolysulfanes-based (BPS hereafter) cell-penetrating moieties.[63] Upon varying the polysulfane ring size and the number of sulfur atoms, they identified the seven-membered ring pentasulfane BPS5 **45**. This cell-penetrating moiety was biotinylated and added to Sav. Next, the **Ru5** cofactor was added to assemble the cell-penetrating ADAse affording **47**. After incubation with HeLa Kyoto cells, and thorough washing to remove the cofactor in the medium, substrate **1** was added. Rapid appearance of fluorescence could be observed by fluorescence microscopy. Again, thorough control experiments led the authors to conclude that i) the ADAse is indeed internalized and ii) the uncaging event occurs in the cytosol of the HeLa Kyoto cells, Figure 14.

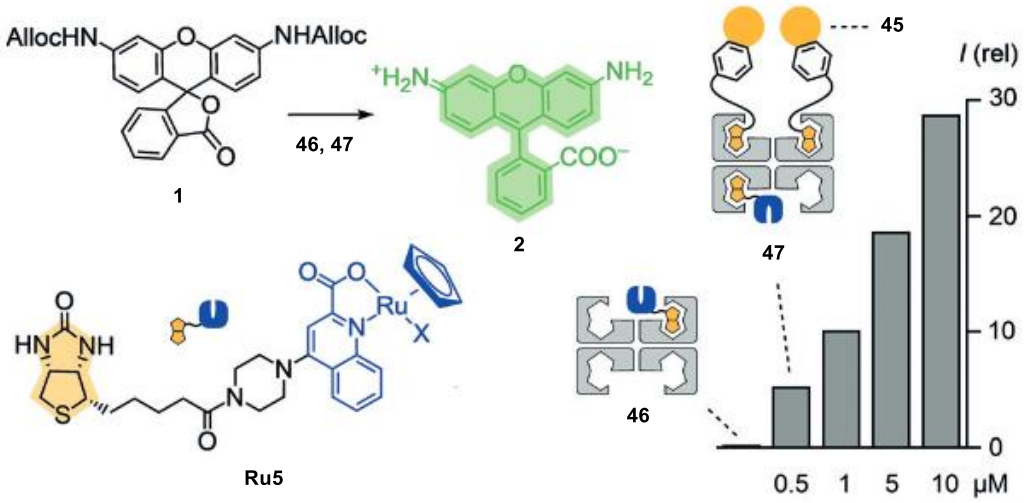

Figure 14: Improvement of the *in cellulo* uptake of an ADAse based on the biotin-streptavidin technology. The screening of various benzopolysulfanes led to the identification of BPS5 **45** *as* the most efficient.

Another strategy to obtain cell penetrative ArM is incorporating them into cell penetrative capsules. Capitalizing on this concept, Trefzer and co-workers developed a nanoreactor using a self-assembly of encapsulin from M. *smegmatis* ($^{Strep}ENC_{SM}$).[68] This strategy allows the incorporation of an encapsulin-based nanoreactor containing an HaloTag-based ArM. This assembly of encapsulin and protein allows the structure to host an organometallic cofactor resulting in a nanoreactor. This nanoreactor was then used to perform new-to-nature reactions under biologically relevant conditions or *in cellulo*. The nanoreactor was assembled by the encapsulation of HT as host protein incorporating a ruthenium-based cofactor **Ru16 forming** $^{Strep}ENC_{SM}${HT-**Ru16**} **used for the deallylation of 48**, Figure 15.

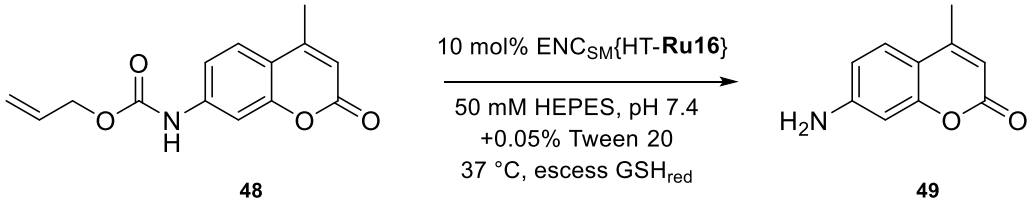

Figure 15: Catalytic deallylation of alloc-protected methyl-aminocoumarin and catalytic activity comparison of the different constituents of the nanoreactor **a)** Catalytic deprotection of alloc-aminocoumarin. **b)** Comparison of the activity of the nanoreactor encorporating the ArM.

A drastic increase in activity was observed when the reaction was performed under anaerobic conditions, highlighting that the cofactor is not extremely air-tolerant. However, the encapsulation of the cofactor is beneficial for the stability of the cofactor. This nanoreactor construct was applied to *in cellulo* catalysis on mouse monocytes J774A.1. They incubated a monolayer of cells with $^{Strep}ENC_{SM}$\{HT-**Ru16**\} for 24 hours and, after washing the cells, added pro-methylcoumarin **48** to the cell supernatant. The corresponding blue fluorescence resulting from uncaged aminocoumarin **49** was observed in the cells in the shape of a vesicle formed by with $^{Strep}ENC_{SM}$\{HT-**Ru16**\}, highlighting the potency of this nanoreactor. Indeed, using **Ru16** alone, no fluorescence could be detected *in cellulo*.

Another strategy explored by Ward and Jeschek to perform *in cellulo* catalysis with ArM is to express Sav directly in the periplasm of *E. Coli*. They combined this strategy with a double mutant library containing the four hundred Sav isoforms resulting from saturation mutagenesis at positions Sav S112X-K121X' for the deallylation of caged aminocoumarin **5** and alloc-indole **50**, Figure 16a. [65] As can be appreciated, the identified best mutants for both substrates were quite similar, highlighting the broad substrate scope of the ADAse, compartmentalized in the periplasm of *E. coli*. Most importantly, the double mutants identified in the *in cellulo* screening could be validated with purified Sav variants. Up to 15-fold improved activity vs. Sav WT could be found for the uncaging of aminocoumarin **5** in the presence of **Ru5** · Sav S112M-K121W, Figure 16.

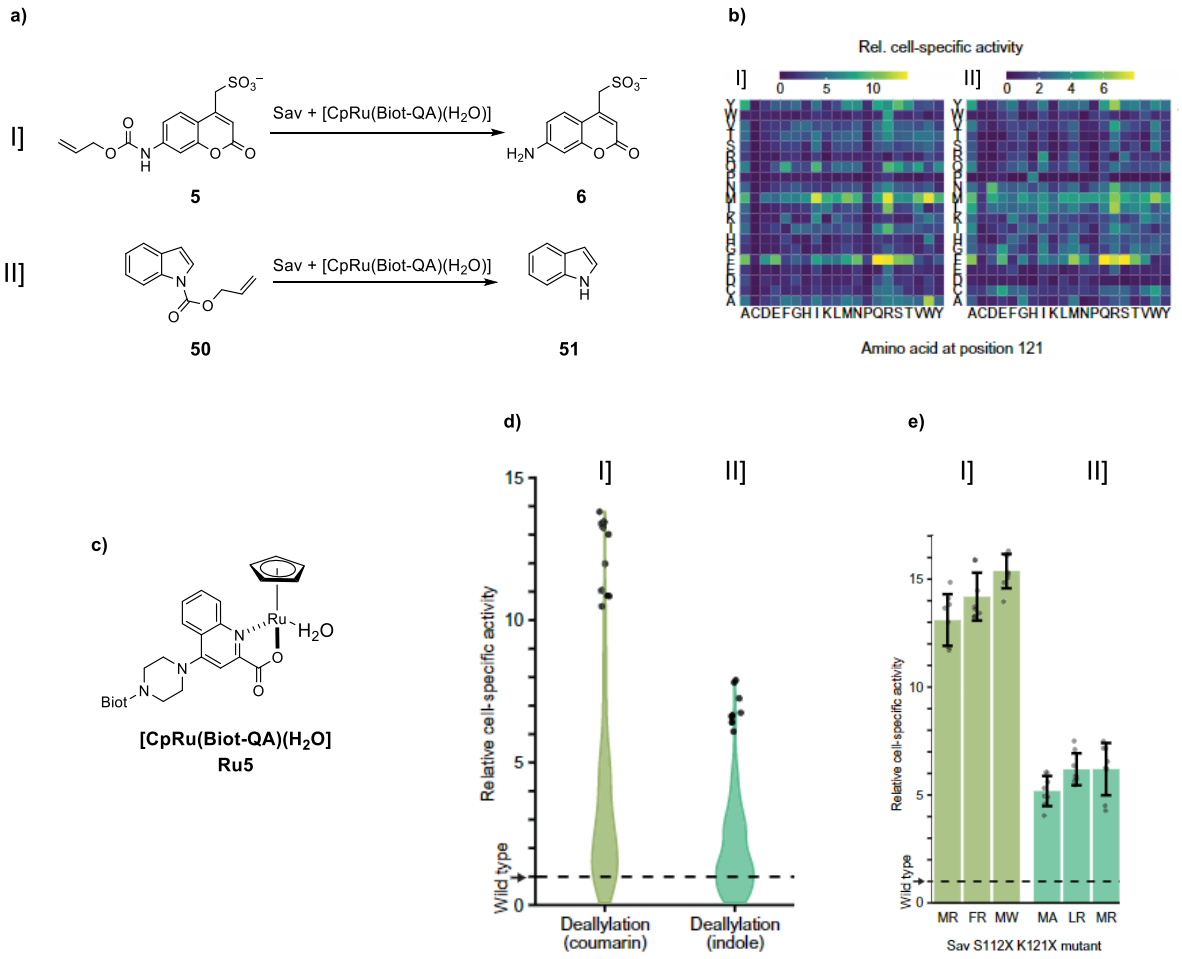

Figure 16: Directed evolution an ADAse based on the biotin-streptavidin technology **a)** Substrates selected for the deallylation reactions. **b)** Heat-map of the cell-specific activity of the 400 double mutant ADAses at positions 112 and 121 normalized to the activity of the wild-type Sav (S112-K121). **c)** Structure of the biotinylated Ru-cofactor **Ru5** used in this study. **d)** Activity distribution in the Sav mutant library for the two ADAses reactions. Violins comprise 400 double mutants, with the 10 most active ArMs depicted as circles. **e)** Validation of *in cellulo* hits from the 400 mutant screens, using purified Sav double mutants. The amino acids designate mutants in positions 112 and 121.

This extensive library of 400 mutants can be screened in only one week using an automatized sequence of three steps: incubation with the cofactor, washing, and substrate addition. Up to eight 96-well plates can be screened simultaneously. Nevertheless, this high-throughput screening platform faces time and material limitations as the number of mutations increase. For example, 3 simultaneous mutation sites result in 8000 possible mutants, and 4 mutation sites result in 160000

possible mutants, which would take more than a lifetime to screen with the previously described methodology. Ward and Dittrich explored fluorescence-activated cell sorting (FACS) to address this challenge. For this, water-in-oil-in-water double emulsions droplets (DEs) produced by microfluidics allowing ultra-high-throughput screening were used.[93] To validate the potential of this methodology, the Ward and Dittrich groups selected the ADAse based on the biotin-streptaviding technology, Figure 17.

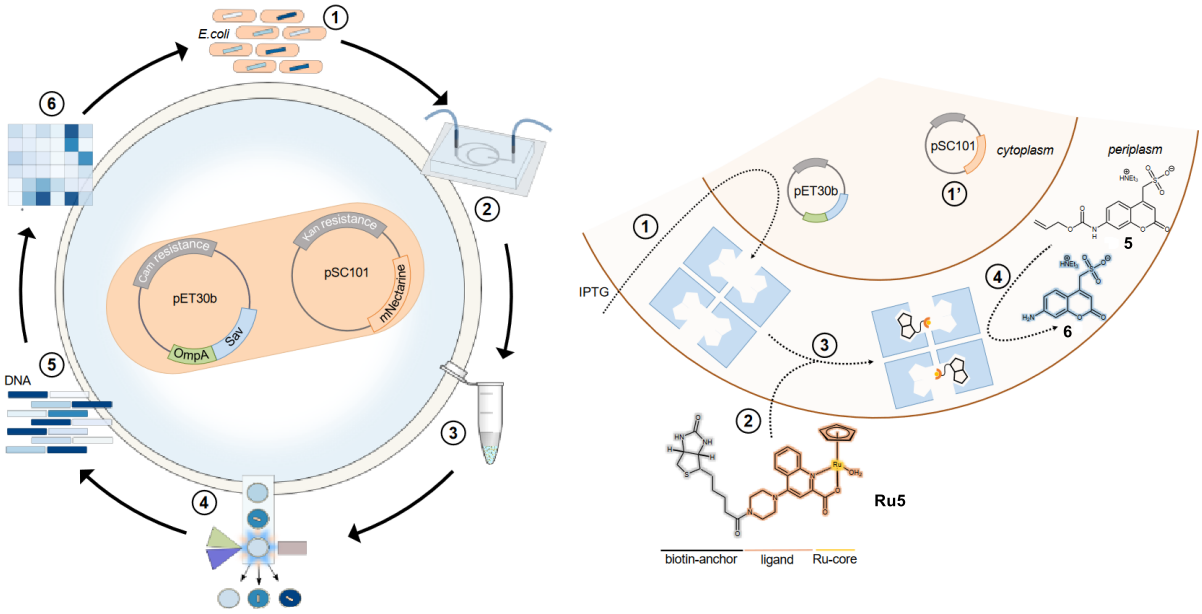

Figure 17: Directed evolution of an ADAse using a microfluidics-based screening assay. **a)** Steps required to implement a high-throughput screening of an *E.coli* library endowed with ADAse activity. **b)** ArM's assembly in the periplasm of *E. coli* and the catalytic deallylation of caged coumarin **5**.

Despite the high dilution of the cells required to minimize the encapsulation of > 1 *E. coli* cell per droplet, roughly 1200 *E. coli* cells can be incorporated in Des per second, thus enabling the screening of large libraries in a fully automated fashion. For example, a 1 million variant library would require less than 15 minutes to be analyzed and sorted by FACS with this methodology. This strategy was tested with the 400 double mutant library that was developed for the streamlined 96 well plate screening, Figure 16b. By subjecting the same 400 mutant library to the DE microfluidic screening and sorting by FACS, we were delighted to identify the same five best mutants, that were identified during the 96 well plate screening, Figures 16 and 18.

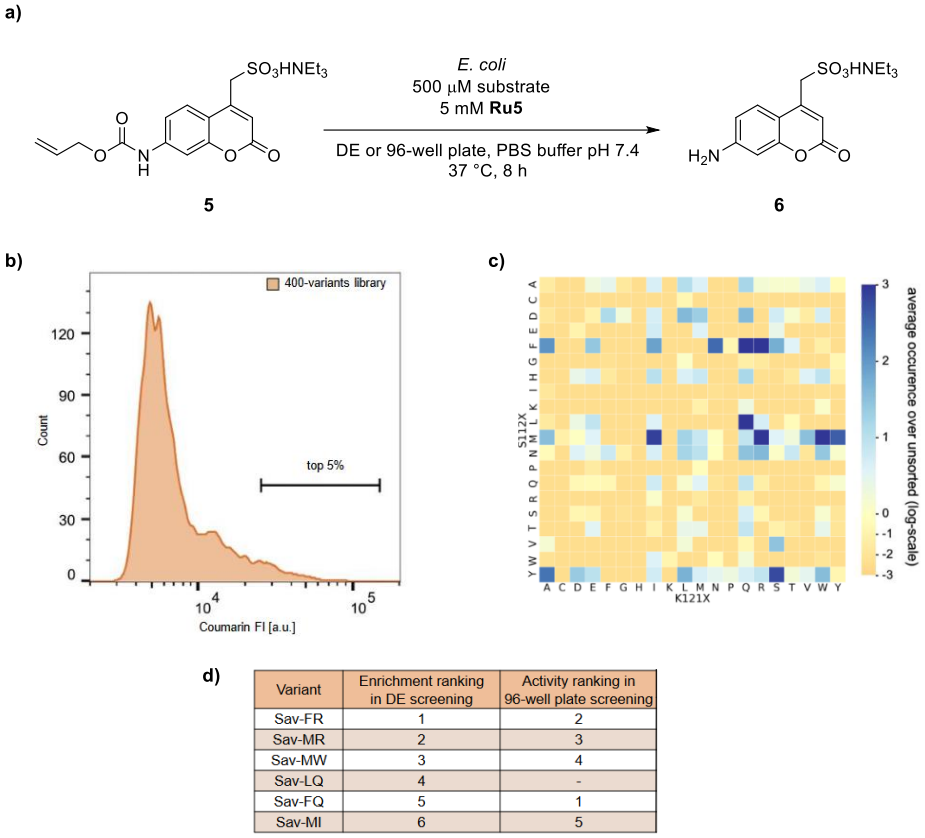

d)

Variant	Enrichment ranking in DE screening	Activity ranking in 96-well plate screening
Sav-FR	1	2
Sav-MR	2	3
Sav-MW	3	4
Sav-LQ	4	-
Sav-FQ	5	1
Sav-MI	6	5

Figure 18: Screening results comparison between DEs and 400-variant library. **a)** ArM catalyzed deallylation. **b) fluorescence profile of the DE sorting by FACS. C)** Heat-map resulting from the FACS sorting, followed by next-generation sequencing to determine the ADAse activity of each DE droplet. **d)** Comparison of the five best mutants determined by DEs FACS sorting and the 400-variant library.

The use of ArM presents numerous exciting features like increased cofactor stability, enantioselectivity, and increased TON, for example. Moreover, many proteins have been described as potential host proteins for forming ArM.[103–110] Nevertheless, one of the limitations of the ArM technology is the need to synthesize the corresponding cofactor. Each cofactor requires a specific anchoring system with one linker and a metal catalyst. To accelerate the assembly of ArMs is to anchor the CpRu moiety to an aminoacid directly bound to the protein scaffold. With this goal in mind, the Ward group evaluated the potential of unnatural, unnatural amino acids (UAA). For this purpose and inspired by the **Ru2** cofactor bearing a hydroxyquinoline ligand reported by Meggers, the Ward group evaluated the potential of two UAAs equipped with a hydroxyquinoline moiety (either **HQ-Ala1** and **HQ-Ala2**, respectively).[111,112] Using a Halotag protein (HT) endowed with

either **HQ-Ala1** or **HQ-Ala2 in combination with an equivalent of [CpRu(MeCN)$_3$]$^+$. Three positions** (F144, A145, and M175) in the hydrophobic cleft of Halotag **were mutated with HQ-Ala1** either **HQ-Ala2**. The resulting six ADAses were tested for the uncaging of caged coumarin **5**, Figure 19. Compared to wild-type (WT) HT treated with **[CpRu(MeCN)$_3$]PF$_6$** and **5**, the increase in fluorescence was only modest: five for WT vs. eight **HQ-Ala1** TON after eight hours, Figure 19. Strikingly, the Ru concentration (by ICP-MS) only differs by 20%, between WT-HT and HQ-Ala1-HT, suggesting that the **[CpRu(MeCN)$_3$]PF$_6$**-binds to multiple Lewis-basic residues on the surface of HT. The corresponding CpRu-HT are capable of uncaging the aminocoumarin **5**, albeit with very modest TONs.

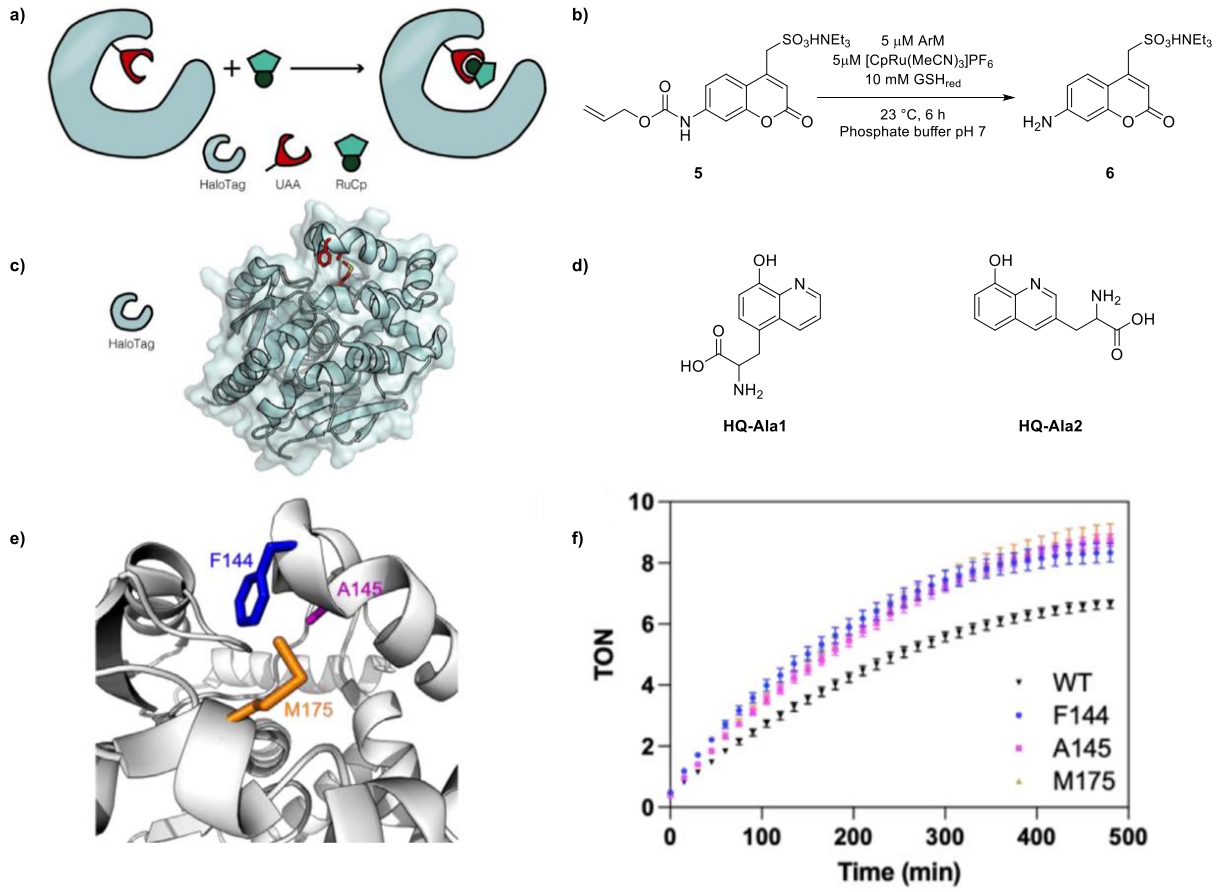

Figure 19: An ADAse based on incorporating a hydroxyquinoline-bearing unnatural amino acid in HaloTag. **a) HQ-Ala1** or **HQ-Ala2** are incorporated into HaloTag by amber stop codon suppression. Incubation with [CpRu(MeCN)$_3$]$^+$ affords an ADAse **b)** Deallylation reaction catalyzed by the ADAse to afford aminocoumarin **6**. **c)** Cartoon representation of a crystal structure of HaloTag (PDB: 5Y2Y102). **d)** Structures of the two metal-chelating UAAs used in this project. **e)** Close-up view of

the hydrophobic binding cleft of HaloTag (PDB: 6U32103) highlighting the positions selected for incorporation of of HQ-Ala1. **f)** Fluorescence monitoring of the uncaged aminocoumarin **6** in the presence of HaloTag-WT, HaloTag-F144-HQ-Ala1, HaloTag-A145-HQ-Ala1 and HaloTag-M175-HQ-Ala1.

1.3.3 Catalytic nanoparticles loaded with Ru-based deallylation catalysts

Toward new *in cellulo* applications of Meggers-type catalysts, Rotello and co-workers and Zimmerman and co-workers have compartmentalized ruthenium catalysts within nanoparticles (NPs).[72,85–89,113,114] This methodology was previously evaluated – albeit without the ruthenium catalyst– to enable DNA or drug release resulting from different triggers.[115–118] Rotello and co-workers developed a protein-sized catalytic system based on a gold nanoparticle core endowed with functional monolayers.[86] These monolayers consist of three essential components, Figure 20a-b:

1. A hydrophobic alkane chain for the catalyst encapsulation
2. A tetra(ethylene glycol) unit to provide biocompatibility[119]
3. A dimethyl-benzyl ammonium group to ensure water solubility and to enable binding to the non-toxic Cucurbit[7]uril (CB[7] here after) acting as a gate-keeper [120,121]

To evaluate the potential of these NPs, the authors selected the ruthenium-catalyzed deallylation applied to different substrates, as displayed earlier in this review. Rotello and co-workers assembled catalytic nanoparticles by immobilizing a ruthenium catalyst in an AuNP. The ruthenium catalyst **[Cp*Ru(cod)Cl]** is located in the hydrophobic monolayer of the NP, affording the corresponding **NP_Ru**. They introduced a gatekeeper by shielding the surroundings of the active with **CB[7],** affording **NP_Ru_CB[7].** Upon adding 1- adamantylamine (ADA), which binds tightly to **CB[7]**, upregulates the deallylation activity of the **NP_Ru_CB[7]**, Figure 20c.

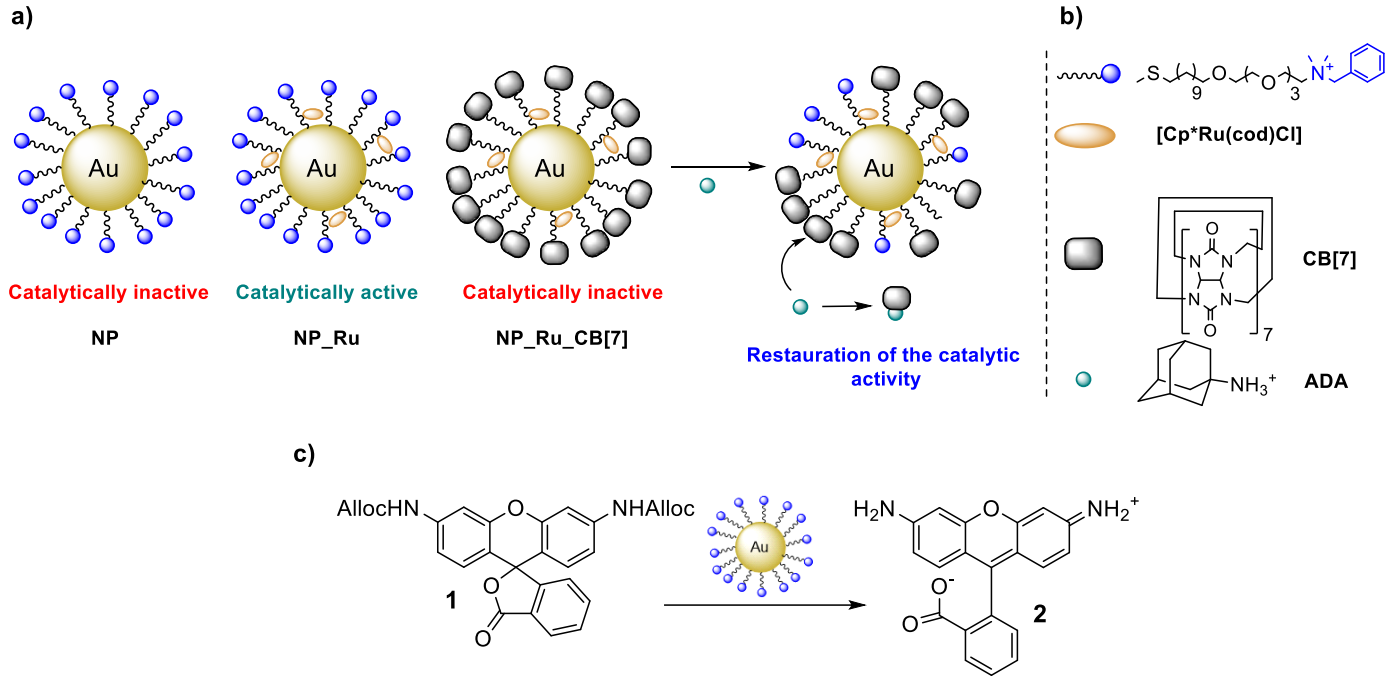

Figure 20: a) NP, catalyst embedded in the **NP** giving **NP_Ru**, and **CB[7]-**capped catalyst-embedded **NP_Ru** affording **NP_Ru_CB[7]** and the regeneration of the catalytic activity via the use of 1-adamantylamine **ADA**. **b)** Structure of the different constituent of the nanoparticules. **c)** Intracellular catalysis with **NP_Ru** converting the caged dye **1** into Rhodamine **2**.

Another way to modulate the activity of the **NP_Ru** is to modify the monolayer, Figure 21a, c-d. The structure of the protecting monolayer is affected by various non-covalent interactions. i) The long hydrophobic segments interact with each other via attractive van der Waals forces ii) The alkylammonium groups experience electrostatic repulsion with neighboring cationic groups. These two opposite forces govern the degree of compaction of the nanozyme monolayer and, as a result, their kinetic behavior. Rotello and co-workers investigated the influence of the hydrophobicity of the alkyl group of the ammonium group on the catalytic activity.[71] Various alkyl and aryl groups were evaluated. Only **TTMA**, **DMBzA**, and **DMTolA** were soluble in PBS and thus selected, Figure 21b. The hydrophobicity of the alkylammonium group influenced the kinetic behavior, the size of the nanozyme (NZ) and the ruthenium uptake was modified.

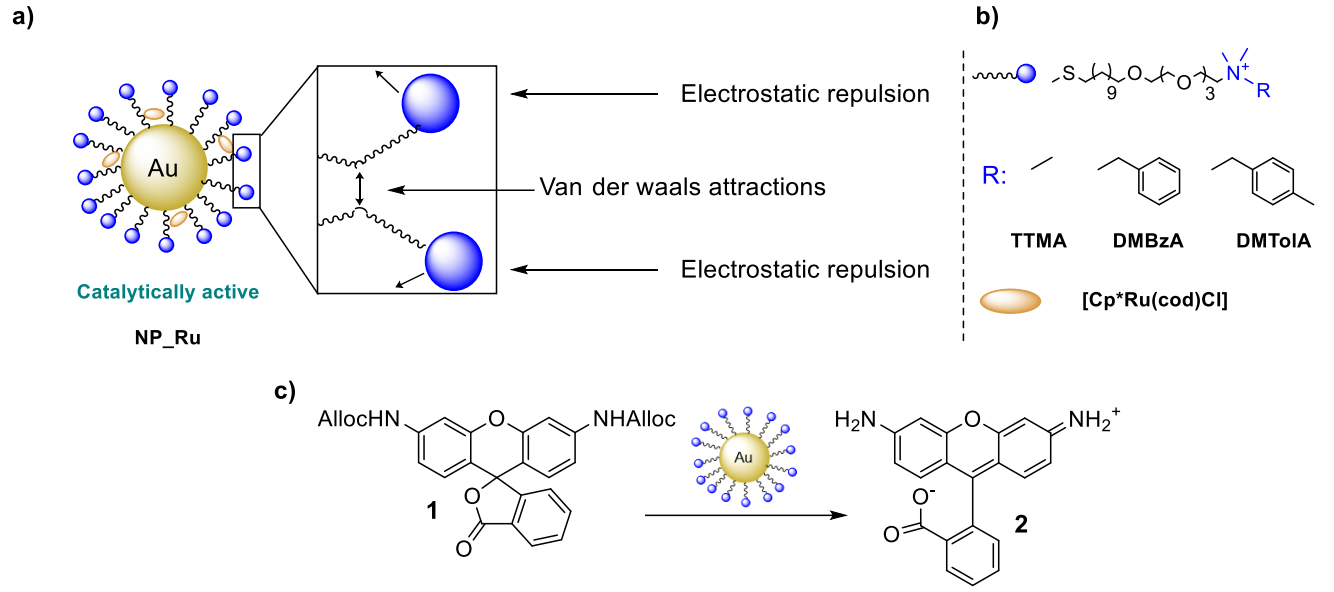

Figure 21: Schematic representation of the NPs. **a)** Structure of the NP scaffolds endowed with an ammonium group. Counteracting forces affecting the degree of compaction of the **NP_Ru**. **b)** Structure of the different constituent of the NPs as well as the different alkyl group used to modulate the compaction of **NP_Ru**. **c)** Uncaging reaction of pro-rhodamine **1** used in this study to validate the concept.

As reported by Rotello and co-workers, an increasing concentration of substrate for **TTMA-NP_Ru DMBzA-NP_Ru, DMMTolA-NP_Ru** as well as **DMBzA-NP_Ru** leads to a decrease in reaction rate as well as substrate inhibition. The authors hypothesize that at high substrate concentration, non-selective binding of the substrate with empty/inactive cavities in the **NP** produces antagonistic effects, reflected by allosteric regulation of catalysis. In contrast, **DMTolA-NP_Ru** displays Michaelis-Menten saturation kinetics with no substrate or product inhibition. These results suggest that higher monolayer compaction from increased hydrophobicity leads to a classical Michaelis-Menten behavior. Next, Rotello and co-workers modified the alkylammonium headgroups to favor cellular uptake of NZs, thus enabling either intracellular- or extracellular catalysis.[72] To achieve this goal, the ammonium headgroups were modified to be either positively charged (**Pos-NP_Ru**) or zwitterionic (**Zw-NP_Ru**), Figure 22a. In the former case, cellular uptake occurs, thus leading to intracellular catalysis. In the latter case, the **Zw-NZ** does not penetrate cells, leading to extracellular catalysis, Figure 22b.

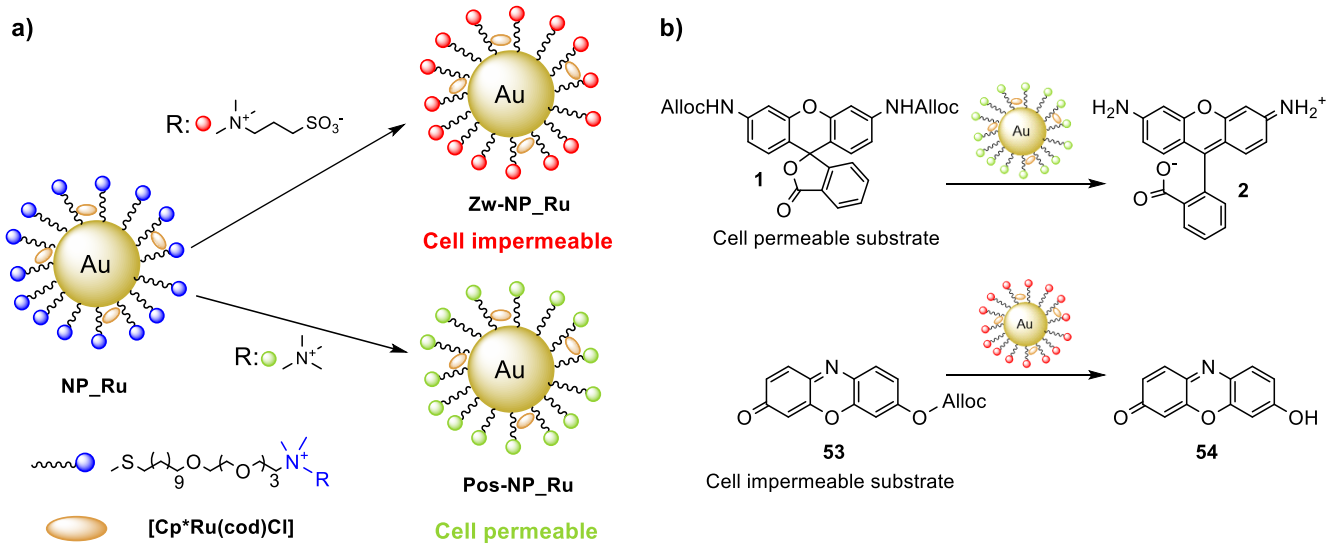

Figure 22: The charge of the ammonium headgroups of **NP_Ru** enable the localization of catalysis. **a)** Structure of the charged **NP_Ru**. **b)** Substrates used for intra- or extracellular (**Pos**/**Zw**)-**NP_Ru**-catalyzed uncaging. **c)** The surface charge of (**Pos**/**Zw**)-**NP_Ru** determines the level of internalization and thus the localization of the uncaging reaction.

Firstly, the activity of these (**Pos**/**Zw**)-**NP_Ru** was evaluated and compared to the corresponding (**Pos**/**Zw**)-**Au_NP** and the substrate alone. Only the condition (**Pos**/**Zw**)-**NP_Ru** + **1** leads to an increase in fluorescence. Secondly, confocal microscopy was performed, and analyzed the reactions in the presence of living cells. The caged substrate **1** and **53** were selected according to two criteria: i) significant differences in emission wavelength to identify unambiguously both fluorophores ii) different cell penetration properties (**1** can penetrate the cells while **2** cannot) to monitor extra- versus intracellular catalysis. The compartmentalization of catalysis could be readily monitored, confirming the validity of the designed systems. Next, they used the caged doxorubicin **3** to afford doxorubicin **4** in the presence of the (**Pos**/**Zw**)-**NP_Ru** in HeLa cells, Scheme 16. The confirmed that intracellular catalysis is more efficient than extracellular catalysis for releasing doxorubicin.

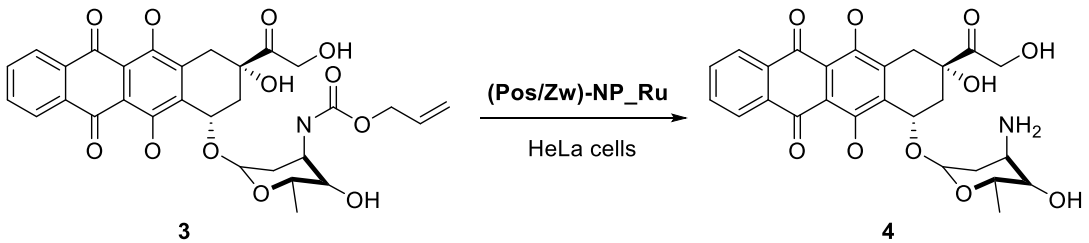

Scheme 16: Application of the developed (**Pos**/**Zw**)-**NP_Ru** for the deallylation of caged doxorubicin **3** in the presence of HeLa cells.

In 2020 Rotello and co-workers demonstrated the possibility of controlling the extracellular catalytic activity of the **NP_Ru** through binding to a protein to form Corona-**NP_Ru**, Figure 23.[74] The interaction between the protein and the corresponding **NP_Ru** govern the subsequent denature and thus the corresponding intra or extracellular activity. Formation of a hard corona structure from **NP_Ru-1** and the protein that inhibits the extracellular activity. Formation of a soft corona structure from **NP_Ru-2** and the protein that reduced extracellular activity. Corona-free-**NP_Ru-3** displaying high extracellular activity and enable to interaction the protein.

To study the efficacy of the different nazozymes, **[CpRu(8-HQ)(allyl)]PF$_6$** was selected as it was reported by Meggers to be more active for the *in cellulo* deallylation of allyl-carbamate protected cargoes. [49]

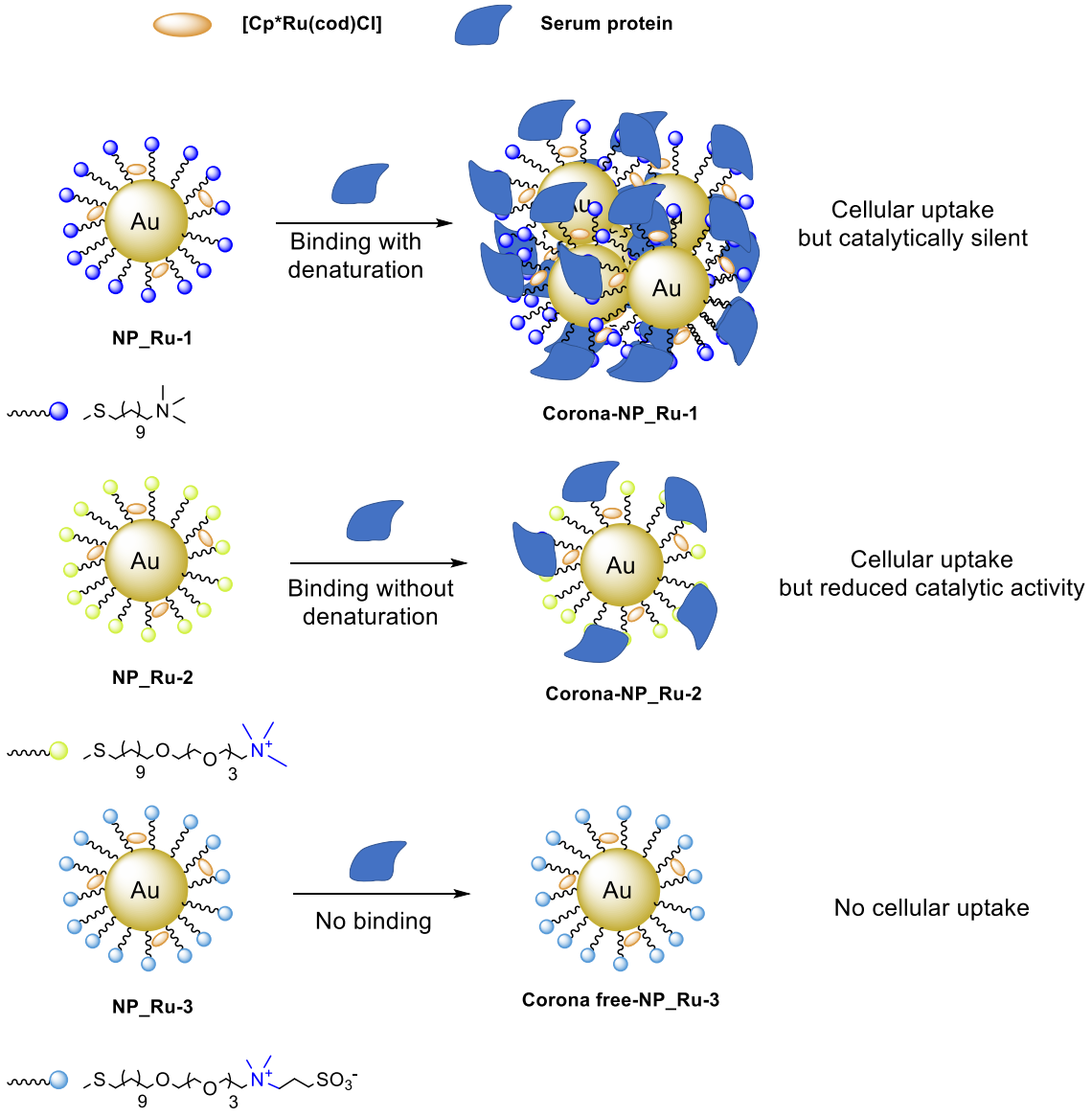

Figure 23: The interaction of **NP_Ru** with serum proteins determines the cellular uptake and deallylation properties of the nanozyme.

The length of the linker (the part between the thiol and the charged moiety) modulates the interaction between the serum protein and the hydrophobic surface, thus influencing the degree of protein denaturation. The shorter the linker, the more pronounced the denaturation, i.e. higher denaturation for **Corona-NP_Ru-1** than for **Corona-NP_Ru-2**. The sulfonate group in **NP_Ru-3** prevents protein interaction thus preventing **Corona-free-NP_Ru-3 preventing internalization in cells via endocytosis**. The catalytic activity of these **NP_Ru** was evaluated *for* the deallylation of pro-rhodamine **1**, Scheme 17. The authors used bovine serum albumin as an interacting protein to form the corresponding corona scaffold. The catalytic efficiency of **Corona-NP_Ru-1** and **Corona-NP_Ru-2** is reduced in the presence of plasmatic proteins in agreement with the compaction degree expected by the authors.

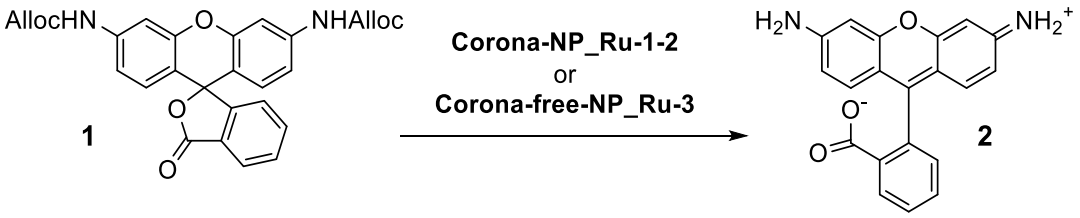

Scheme 17: Influence on bovine serum on the uncaging efficiency of Ru-loaded nanoparticles.

The reversibility of the corona scaffold formation was explored. Treatment of the **Corona-NP_Ru** with trypsin led to the recovery of catalytic activity. Adding a trypsin inhibitor minimized the digestion of the corona protein, thus minimizing the NZ activity, Figure 24.

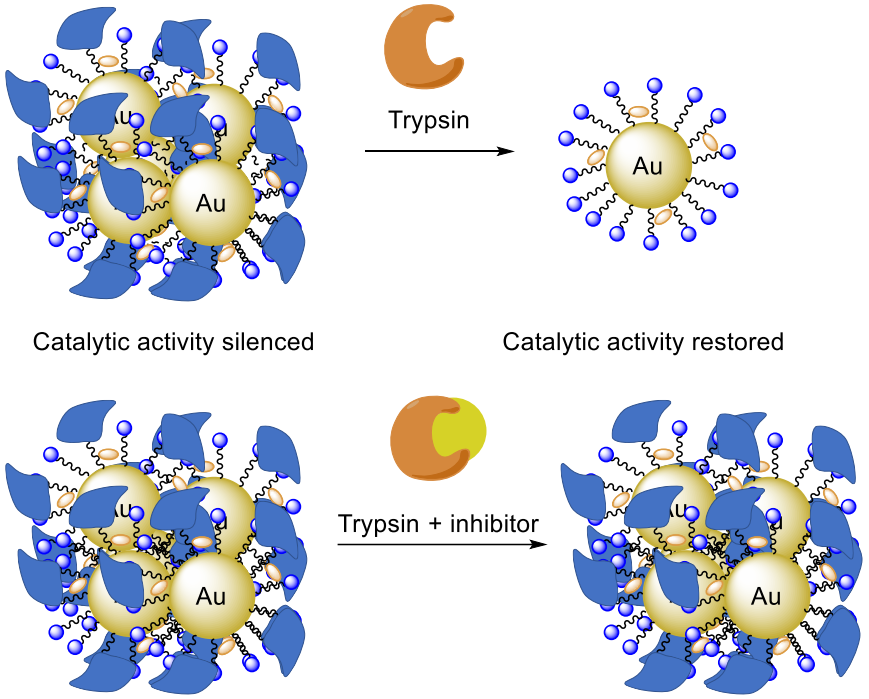

Figure 24: Upregulation of deallylation catalysis by NZ surrounded by a protein corona.

The reversibility of the binding of the corona-protein is very promising for *in cellulo* catalysis as it enables the controlled release of a drug, as highlighted with HeLa cells. Importantly, the design of the linker may allow modulating the compaction of the NZ. This, in turn, regulates the degree of silencing and partly restores the catalytic activity. After varying different parameters on their **Au_NP**, Rotello and co-workers developed ZnS-based nanoparticles for the deallylation of either pro-rhodamine **1** or pro-mitoxantrone **52**, Figure 18.[100] They observed lower cytotoxicity from ZnS-based nanoparticles and a high degradability compared to their previous system based on **Au_NP**. Furthermore, they capitalize on the effect of thiols to rationalize the increase of catalytic activity when **[Cp*Ru(cod)Cl]** was taken up by ZnS since their degradation releases thiolate surface thus acting as nucleophilic surfaces.

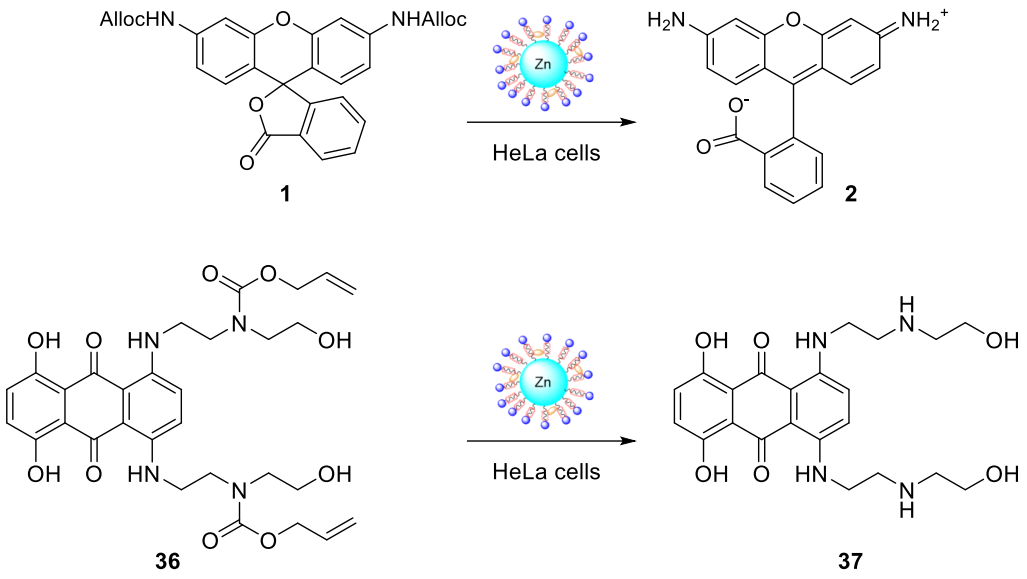

Scheme 18: ZnS-based NZ for the **[Cp*Ru(cod)Cl]**-catalyzed *in vivo* uncaging of fluorophores and drugs as promising substitute for **Au_NPs**.

In a similar manner using nanoparticles, Zimmerman and co-workers. Examined the potential of single-chain nanoparticles (SCNPs hereafter) for tandem catalysis.[75] The triblock oligomer **56** was synthesized via reversible addition-fragmentation chain-transfer polymerization (RAFT) by amine-functionalization of pPFPA100 with the sequential addition of building blocks **54**, **55**, and Jeffamine M-1000. The catalytic activity of SCNP **Ru15** was installed by treatment of **56** with **[CpRu(MeCN)$_3$]PF$_6$** in MeCN and was monitored by ^{1}H NMR, Scheme 19.

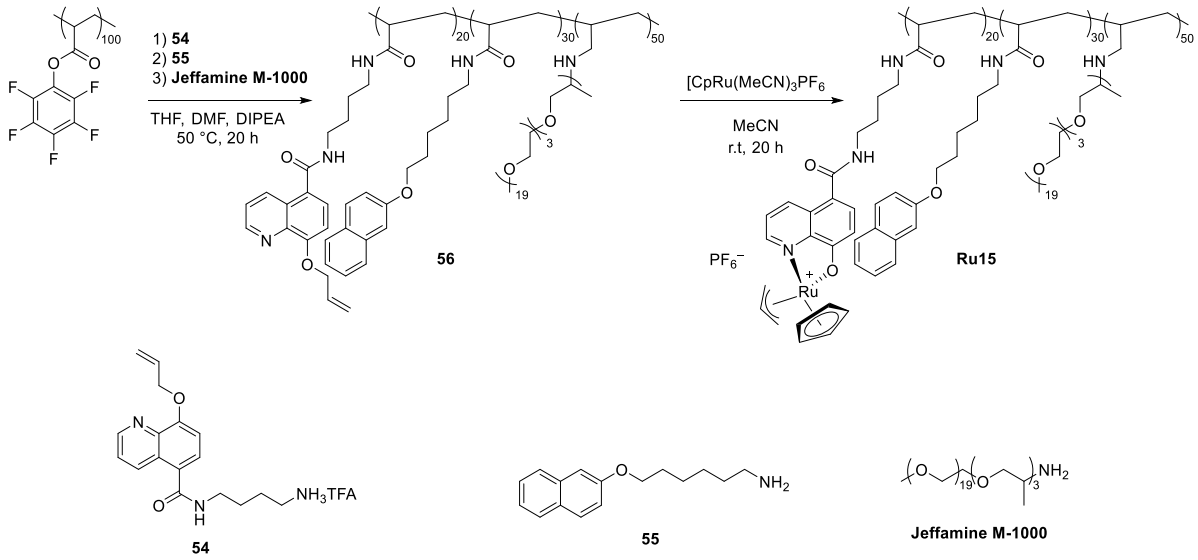

Scheme 19: Synthesis and installation of catalytic activity of SCNP upon addition of **[CpRu(MeCN)$_3$]PF$_6$** to the triblock copolymer bearing alloc-protected hydroxyquinoline moieties.

Next, the catalytic performance of **Ru15** was compared to that of the free catalyst **Ru3**, Scheme 20.

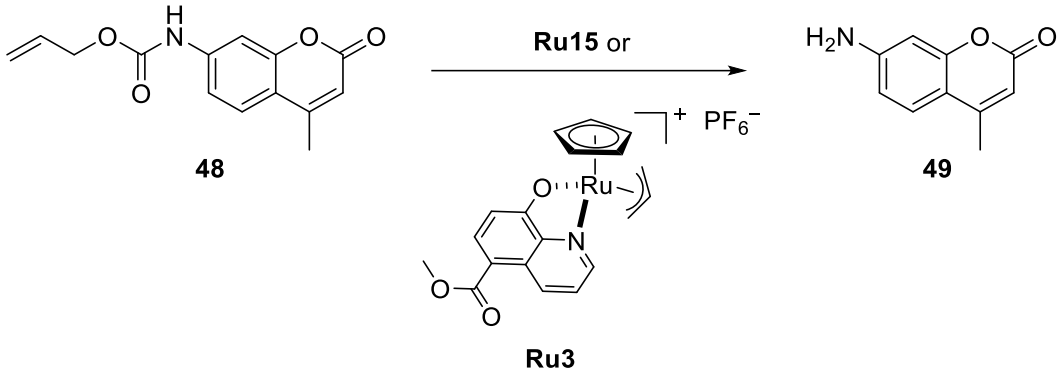

Scheme 20: The deallylation of caged aminocoumarin **48** catalyzed by either **Ru3** or **Ru15**, highlighting the potency of SCNP for catalysis.

The results reveal that the hydrophobic cavity provided by **Ru15** benefits catalysis. Accumulation of the substrate in the hydrophobic pocket of the polymer-embedded catalyst **Ru15** increases the local concentration of the substrate. This is reflected by an increase in the deallylation rate. The sugar-protected umbelliferone **57** can be involved in tandem catalysis, beginning with the deallylation affording **58** which, gets deglycosylated with β-galactosidase (β-gal), Scheme 21.

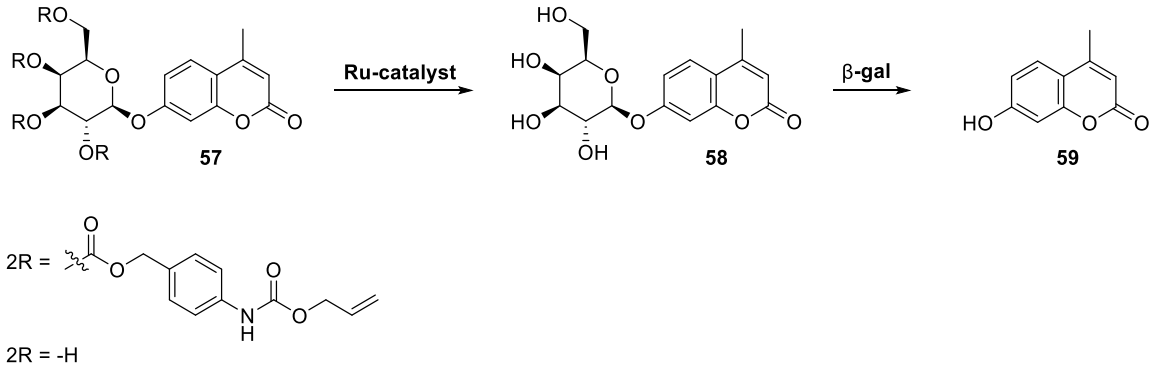

Scheme 21: Tandem catalysis using **Ru15** or **Ru3** and β-gal to afford methyl-umbelliferone **49** as a result of Ru-catalyzed deallylation, self-immolation and deglycosylation.

One limitation of the previous study is the covalent anchoring of the CpRu-moiety within the SCNP, which limits possible variation of the catalyst. To circumvent this limitation, Zimmerman and co-workers anchored via non-covalent interactions the CpRu moiety to *the* SCNPs. They used it for

uncaging purposes under biologically-relevant conditions. These were equipped with non-covalently anchored **Ru14**, Scheme 22.

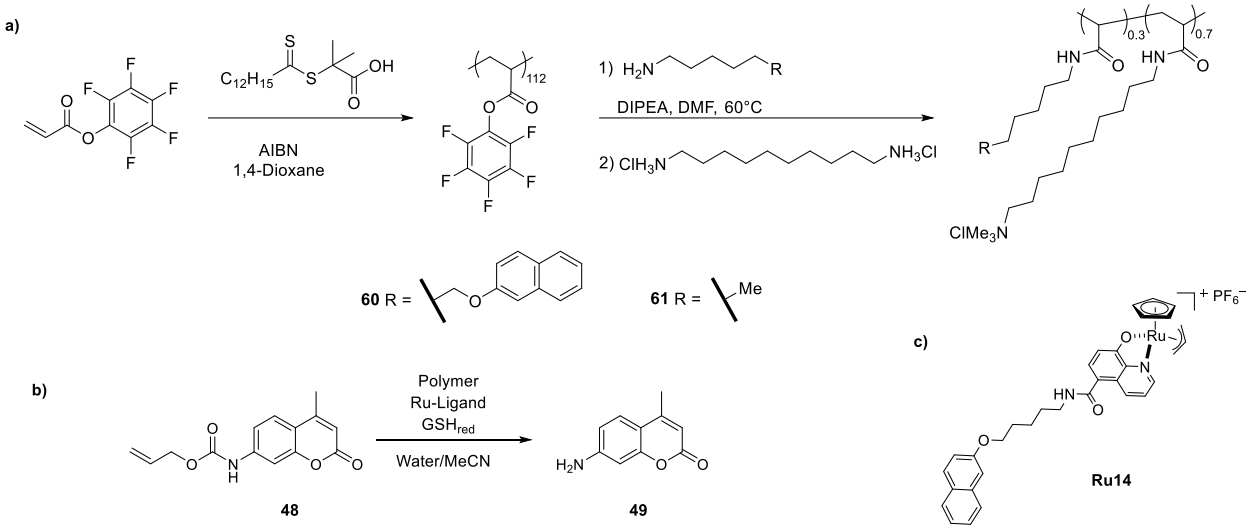

Scheme 22: Development and application of the SCNP strategy for catalysis. a) synthesis of the two SCNP scaffolds with varying degrees of hydrophobicity **60** and **61** for the supramolecular anchoring of CpRu-based deallylation catalysts. b) Ru-catalyzed deallylation reaction of caged coumarin **48** was performed under biologically-relevant conditions. c) Structure of **Ru14**.

It is hypothesized that SCNPs are monomeric below the critical micellar concentration (CMC). The NZ **Ru29** –which consists of **Ru14** + **60** was selected as it proved more active than **Ru30** (**Ru14** + **61**). Supramolecular anchoring was ensured by tethering a naphthyl-moiety to the **Ru3** *to afford* **Ru14**. The catalyst modification with a hydrophobic side chain increases its uptake by SCNP **60**, as reflected by the catalysis results. GSH, proposed to act as a nucleophile in the deallylation reaction, was added to the medium to mimic the cytosol.

As the NZs can be tuned to penetrate the cells, many applications may be envisioned, including auxotrophic rescue and biochemical pathway regulation. A possible application of SCNPs could be the addition of a chiral moiety in the single polymer chain, which could endow the nanoreactor with a chiral environment that could enable enantioselective catalysis.

1.4 Diversification of the chemical reactivity of previously described catalysts

In addition to their allylic-substitution catalytic activity, CpRu-based catalysts have proven versatile for a variety of in cellulo catalyzed transformations.

The first report of a new chemical transformation catalyzed by **[Cp*Ru(cod)Cl]** was described by Teply and co-workers. They demonstrated the potential of **[Cp*Ru(cod) Cl]** to catalyzed [2+2+2] cycloadditions in different media.[79] They observed that the [2+2+2] cycloaddition of alkyne **62** is air-tolerant and proceeds in aqueous media, Scheme 24a. They extended the scope of [2+2+2] cycloaddition to synthesize pyridine derivatives from alkyne **64** and malonitrile **65**, Scheme 24b. Also, alder-ene type reaction was performed with alkyne **67** and vinyl alcohol **68** affording a mixture of aldehydes, Scheme 24b-c. They also attempted enyne-diazo fusion with the alkyne **72** and the diazo compound **73** to afford bicyclic cyclopropanes aiming to extend the scope of bio-tolerant transformations catalyzed by **[Cp*Ru(cod)Cl]**, Scheme 24d. The main challenges encountered with the above reactions was related to the low solubility of the substrates, products, and catalysts. They eventually developed a [2+2+2] cycloaddition using the dicationic water-soluble tri-yne **76** in *E. coli* cell lysates with 1% acetone to solubilize the catalyst [**Cp*Ru(cod)Cl]**, Scheme 24e.

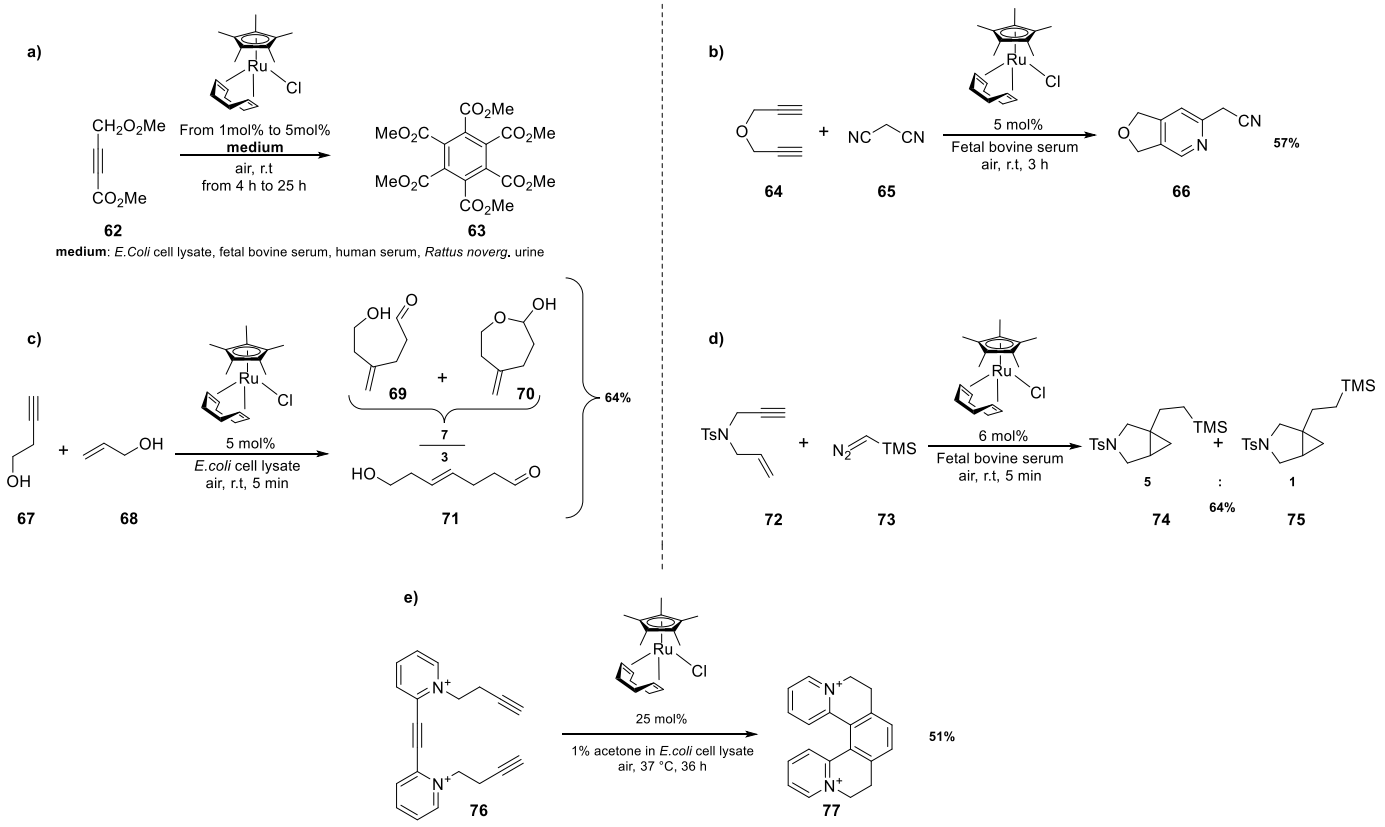

Scheme 24: Applications of **[Cp*Ru(cod)Cl]** for cycloaddition reactions.

All transformations gave yield ranging from 52% to 76% from isolated yield, even in cell lysates.[122] This work paved the way for diversifying Ru-based catalyst uses in biologically relevant mediums. Capitalizing on this work, Mascarenas and co-workers reported on an intracellular Ru-catalyzed [2+2+2] cycloaddition reaction to afford a variety of fused polycyclic compounds.[123] As polycyclic compounds, anthraquinones appeared as attractive targets as i) their aggregation results in an increase in fluorescence (i.e. aggregation-induced emission), and ii) they are not internalized in cells. Additionally, anthraquinones are bioactive, and their current therapeutic use includes constipation, arthritis, multiple sclerosis, and cancer.[124] They selected di-yne **77** and ene-yne **78** as they both accumulate in HeLa cells, and the resulting fluorescent anthraquinone **79** can easily be monotored, Scheme 25.

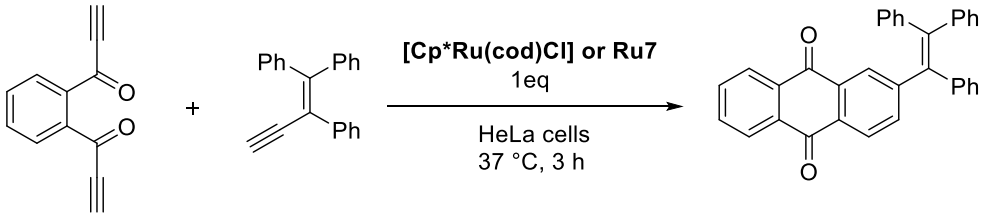

Scheme 25: [2+2+2] Cycloaddition of **77** with **78** in HeLa cells using either **[Cp*Ru(cod)Cl]** or **Ru7** to afford **79** which aggregates and produces fluorescence.

Aiming to diversify the chemical versatility for in cellulo catalysis, Mascarenas and co-workers demonstrated the efficiency of a Ru-based catalyst for Ruthenium(II)-promoted azide-thioalkyne cycloaddition (RuAtAC).[77] Click chemistry is a powerful method to functionalize biomolecules thanks to its high chemoselectivity. For example, the copper-catalyzed azide-alkyne cycloaddition enables the modification of peptides, nucleic acids, and carbohydrates. In addition, they observed that RuAtAc occurred without cross-reactivity with CuAAC rendering these two processes bio-orthogonal. Capitalizing on this finding, they developed an *in cellulo* tandem CuAAC/RuAtAc reaction within *E.* coli cells, Scheme 26.

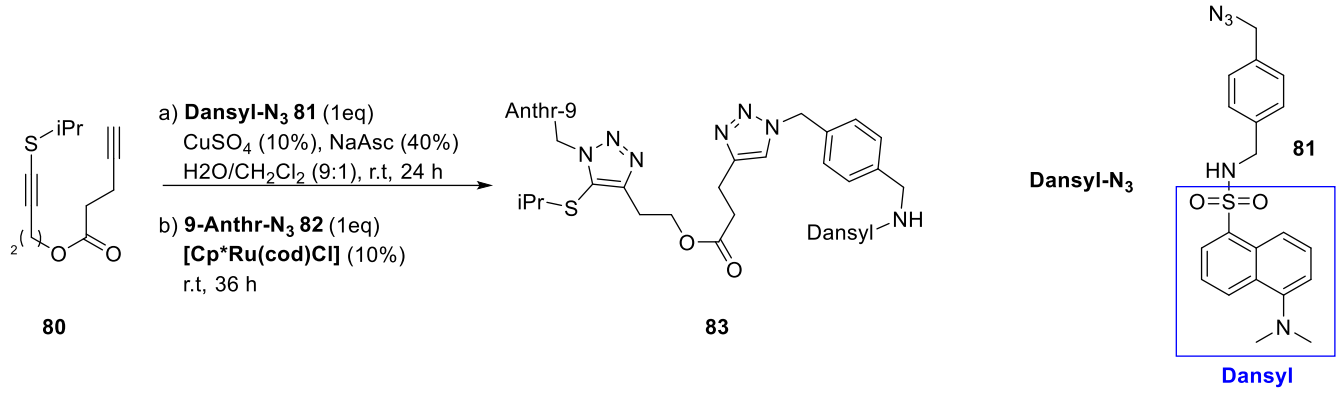

Scheme 26: Tandem CuAAC/RuAtAc cascade enabled by the bio-orthogonality of the two metal-catalyzed processes. (with Anthr = anthracene).

Finally, Mascarenas reported an elegant Ru-catalyzed *in cellulo* redox-isomerization of allylic alcohol **84** to afford the fluorescent ketone **85**, Scheme 27.[125] Interestingly, the selected Ru(IV)-complex proved suitable for the redox isomerization of an allylic alcohol in HeLa cells. The mechanism of the reaction is not fully elucidated, but the authors hypothesized that the reaction is initiated *via* aquation of the precatalyst, followed by coordination of the allylic alcohol. Follows a β-hydrogen abstraction and migratory insertion to afford the corresponding ketone **85**.

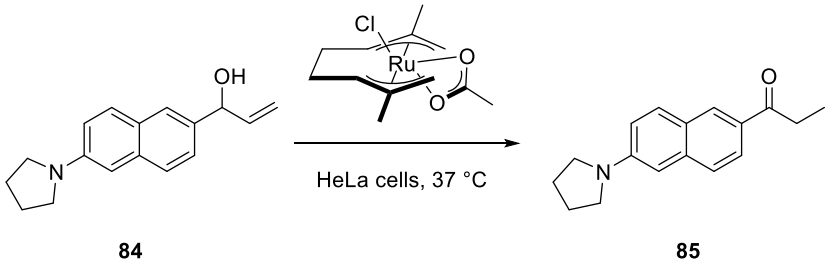

Scheme 27: Biocompatible, redox-neutral allylic alcohol isomerization, catalyzed by a Ru(IV)-catalyst.

1.5 Reported and future applications

1.5.1 *In vitro* catalysis

The development of *in vitro* catalytic reactions represents an important milestone towards *in cellulo* catalysis. These inspiring results have inspired the scientific community to highlight the tolerance of CpRu-based catalysts towards complex biological media.

All transformations gave yield ranging from 52% to 76% from isolated yield, even in cell lysate medium containing thiols known to poison metal-based catalysts.[122] This work paved the way for diversifying Ru-based catalyst uses in biological media.

Protein functionalization is a field of high interest as such minor modifications often significantly affect the biological response of the protein. For example, the methylation of histone lysines has been shown to induce gene silencing or activation. [126,127] In 2010, Schultz and co-workers investigated the possibility of deallylating alloc-methyl lysine in modified myoglobin using **[Cp*Ru(cod)Cl]**, Scheme 28.[99]

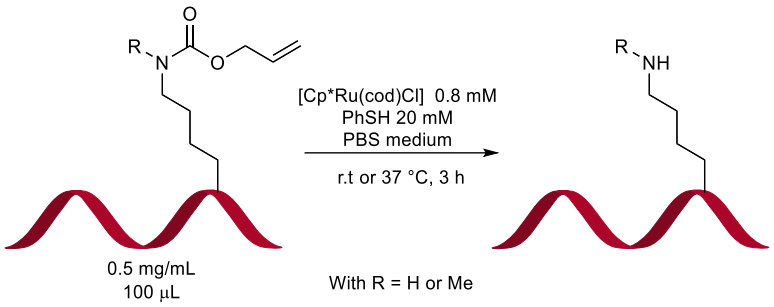

Scheme 28: [Cp*Ru(cod)Cl] catalyses the deallylation of an alloc-protected lysine in myoglobin.

The expression of a protein bearing an alloc- protected UAA (lysine here), followed by its catalytic uncaging, highlighted the possibility of performing this type of reaction on proteins in an aqueous media.

1.5.2 *In cellulo* catalysis

Researchers have worked for decades on developing and applying *in cellulo* new-to-nature reactions. This field opens the door to implementing the unnatural chemical pathway within living entities, endowing them with new features. A direct pharmaceutical application *in cellulo* catalysis is the possibility of releasing a drug from a pro-drug in the organism using new-to-nature catalysis. Ideally, the pro-drug should be significantly less cytotoxic and should not be metabolized by the organism, offering temporary protection during its vectorization. This is one possible application among many others rendering this research topic significant. Different readouts have been developed, rendering the *in cellulo* catalytic activity quantification accessible. It should be emphasized however that fluorescence readout in a cellular environment can be viewed as semi-quantitative at best.

Mascarenas and co-workers have applied their DNA-intercalating deallylation reaction on chick embryo fibroblast cells.[82] For their *in cellulo* study, they selected substrates **9** and **11** as the corresponding DNA-intercalating products **10** and **12** are fluorescence, Scheme 5. Importantly, the products **10** and **12** display a characteristic emission pattern upon intercalation in DNA. They then studied the possibility of compartmentalizing the catalyst within HeLa cells.[58] **Ru7** was developed to accumulate in the mitochondria of HeLa cells, but **Ru7** was challenging to detect since its spectroscopic characteristics do not allow direct visualization. Thus, they developed **Ru28** to highlight its accumulation in the mitochondria, Scheme 29.

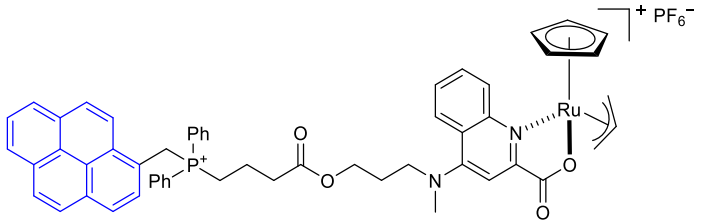

Ru28

Scheme 29: Structure of the pyrene derivative of the ruthenium complex **Ru28**, leading to accumulation in the mitochondria and enabling a strightforward visulation.

Capitalizing on this work, they revealed the possibility of simultaneously performing two orthogonal reactions within one HeLa cell.[59] The Au-catalyzed reaction took place in the periplasm of HeLa cells, while the Ru-catalyzed reaction took place in the mitochondria, Scheme 6.

Additional limitations were reported *in cellulo* by different groups. Wender and co-workers developed a bioluminescent readout system in 4T1 cells possessing the gene of click-beetle luciferase, allowing them to produce bioluminescence as a result of the uncaging of substrate **25** to afford the bioluminescent aminoluciferin **26**.[37] During their study, they observed the formation of a side product arising from a side reaction of **26** on the CpRu(η^3-allyl) intermediate, affording **27** and **28**. To minimize the formation of these undesirable allylation products, the authors evaluated the effect of pH, temperature, buffer, and external nucleophile, Scheme 30.

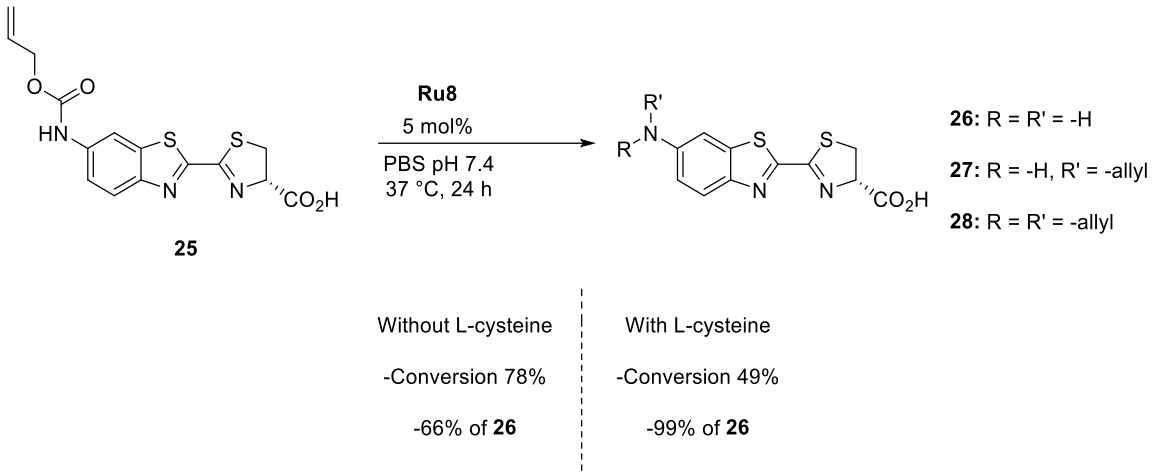

Scheme 30: Product distribution from the Ru-catalyzed cleavage of alloc-luciferine **25**. In the presence of L-cysteine, the conversion of **25** to **26** using **Ru8** decreases but prevents the formation of a side allylated product.

To estimate the TON *in cellulo*, the authors incrementally varied the concentration of substrate **26** while maintaining the concentration of the catalyst. The increase in luminescence was correlated to the increase in substrate **26** concentration, suggesting that the reaction is indeed catalytic. The experimental setup also strongly suggested that, under their reaction conditions, the catalytic deallylation step took place extracellularly, which contrasts with Meggers's findings. Another limitation encountered by Mayer, Vrabel, Tanaka, and Duhme-Klair is related to i) the stability of the CpRu-complexes in the presence of air, and ii) the observed cytotoxicity of the CpRu. In their study in *E. coli*, Mayer observed that **Ru2**, **Ru11-13** catalysts are cytotoxic, Figure 2. He additionally found that the activity of the QA-based catalysts decay upon exposure to air. Similar observations were reported by Vrabel and co-workers while performing the **Ru3**-catalyzed deallylation of substrates **21**, **22**, and **23** in HeLa cells.[98] They observed a decrease in the catalytic activity complex **Ru3** was incubated in air for 1 hour prior to catalysis. They also determined that **Ru3** has cytotoxicity with IC50 = 70 mM for HeLa cells. While developing the ArM-based surface functionalization of SW620 cells, Tanaka and co-workers observed that the catalytic activity of **Ru10** disappeared after 2h upon exposure to air. Additionally, they observed that an ArM, resulting from anchoring **Ru10** in HSA is markedly more stable towards air that the free cofactor. Finally, Duhme-Klair and co-workers, compared the **Ru2**-catalyzed deallylation of pro-moxifloxacin **38** with and without air, concluding that the catalyst is indeed air-sensitive. Accordingly, they focused their

subsequent work on hypoxic environments, such as intestinal bacteria, including *E.* coli K12, Scheme 13.

1.5.3 *Critical analysis of the potential of in vivo catalysis for therapeutic applications*

Among the diverse *cellulo* applications mentioned in this review, the controlled release of a cytotoxic drug through catalytic uncaging of a non-toxic prodrug to treat cancer is arguably the most promising but perhaps the most challenging. The catalytic deallylation strategy may fill a gap in personalized medicine by circumventing some challenges in chemotherapies based on antibody-drug conjugates (ADCs). ADCs, consist of a cytotoxic (or cytostatic) drug appended to an antibody with a high affinity for an antigen overexpressed by cancer cells. This antigen is usually a protein expressed at the cancer cell's surface. Following administration of the ADC to the patient, the antibody accumulates at the tumor site and is subsequently internalized by cancer cells. The cytotoxic drug is then released inside the cell, thus providing a cancer-targeted effect while sparing healthy tissues. While several ADCs have reached the market, demonstrating their high therapeutic potential, this strategy has flaws. ADCs are known to poorly and slowly diffuse in the highly-dense tissues characterizing solid tumors, preventing the drug from reaching some tumors. This poor penetration is partly due to the capture of the ADC in perivascular tumor cells, a phenomenon often referred to as the "binding site barrier effect".[128] They have also been associated with off-target toxicity due to a premature release of the drugs.[129] Moreover, the number of drug molecules that can be appended to the antibody without compromising its binding affinity is limited. In commercialized ADCs, this drug-antibody ratio rarely exceeds 4.[130] Replacing the cytotoxic payload in ADCs with a catalyst able to convert a virtually unlimited number of non-toxic prodrugs into chemotherapeutic drugs appears as a logical step up. This strategy is not exactly new, with the first *in vivo* examples of antibody-directed enzyme prodrug therapies (ADEPT) dating back to 1988.[131] However, in ADEPT, the catalytic unit consists of an enzyme, often of bacterial origin. In addition to the potential immunogenicity of this enzyme, the size of these antibody-enzyme conjugates may hamper their diffusion in cancer tissues to an even greater extent than for ADCs.[132] But as highlighted in this review, metal-based catalysts have recently demonstrated their efficiency in biological environments, including mammalian cells.[133,134] To date, most of the proof-of-concepts were demonstrated in isolated 2D mammalian cell cultures. However, examples demonstrating a real therapeutic potential in animal models remain scarce.[135,136] This is probably due to additional challenges. First, plasma is a highly complex and oxygenated medium containing a high

concentration of plasmatic proteins, which can deactivate the catalyst and prevent the prodrug from coming into contact with the catalyst. One could argue that promising results were previously obtained in mammalian cell culture media. However, these media usually contain only up to 10% of serum. Secondly, the reaction must be compatible with very low concentrations of the catalyst. As mentioned earlier, antibodies diffuse poorly in tumor tissues. Therefore, the catalyst concentration that can be realistically accumulated in the tumor is expected to be extremely low. *In vivo* data acquired using radiolabeled therapeutic antibodies suggest that of the injected dose, only 0.01%/g of tissue eventually reaches the inside of the tumor. This would correspond to a maximal antibody concentration in the range of 100 nM at the surface of the tumor following the administration of a pharmacologically relevant dose of a therapeutic antibody.[137] Finally, the reaction should also be compatible with low concentrations of substrate. In principle, caging a cytotoxic drug with an allyl or alloc group should decrease its biological activity by reducing its interaction with its biological target. However, it is unrealistic to expect that a small caging group, such as allyl, will completely suppress the cytotoxicity of the corresponding prodrug. In addition, the spontaneous uncaging of the prodrug *via* natural xenobiotic metabolism may also occur. For these reasons, the prodrug should be administered at low doses to avoid adverse effects, and its concentration in the tumor will remain low.

Recently, Zong-Wan Mao and co-workers applied the catalytic deallylation of an alloc-protected gemcitabine prodrug using a derivative of **Ru3**. Once coupled to the antibody Trastuzumab, the catalyst should bind to the Human Epidermal Growth Factor Receptor 2 (HER2), overexpressed at on the surface of some cancer cell, and selectively release gemcitabine in the vicinity of tumors. Following a set of experiments *in cellulo* validating the ability of the antibody-catalyst conjugate to accumulate at the surface of HER2 positive cells selectively and to uncage alloc-gemcitabine, an *in vivo* proof of concept was obtained in a zebrafish embryo xenograft model.[138] However, the data provided suggest that the biological effect is poorly correlated to the catalytic properties of the conjugate. Indeed, in the cytotoxicity experiment, the viability of HER2-positive cells treated with only 0.2 μM of the conjugate and 4 μM of alloc-gemcitabine was equal to the viability of cells treated with 4 μM of gemcitabine. The alloc-gemcitabine and the conjugate alone being non-toxic at these concentrations, one can assume that close to 100% of conversion of the alloc-gemcitabine was achieved. However, such a high conversion could only be neared by the authors *in vitro*, at a catalyst concentration of 10 μM, which is very far from the concentration of catalyst realistically

accumulated at the surface of cells. Indeed, following incubation of cultured cells with 1 μM of the conjugate, the amount of ruthenium was around 50 ng/107 cells (0.5 nmol/10^7 million cells), as revealed by inductively coupled plasma mass spectrometry (ICP-MS). Therefore, assuming that the accumulation was the same in the cytotoxicity experiment (even though the initial conjugate concentration was 5 times lower) and that the well volume was 100 μL, the corresponding concentration of Ru in wells could be expected to be around 2 nM at best. It is thus unreasonable to claim that a 5000 times lower catalyst concentration *in cellulo* may lead to the same conversion achieved *in vitro*. One could argue that the remarkable cytotoxicity achieved in this study could be due to a combination of the individual cytotoxicity of the alloc-gemcitabine and the antibody-catalyst conjugate, maybe marginally complemented by the uncaging of the prodrug.

While this study provides some evidence of the therapeutic potential of this strategy, it mostly reveals what features such a catalyst/prodrug system should display before even envisaging its *in vivo* evaluation:

1) Given the deficient concentration of antibody-catalyst conjugate one could hope to accumulate at the tumor, the catalyst should achieve very high TONs (at least > 1000) in biologically relevant conditions, *i.e.*, low concentration of the prodrug in 100% oxygenated plasma. This implies the catalyst should be stable in plasma for several days or weeks. Indeed, therapeutic monoclonal antibodies can have plasmatic half-lives of several weeks.[139] Before treating the patients with the caged drug, one should wait until most of the antibody has been excreted to minimize the systemic release of the cytotoxic drug.

2) The drug should be significantly more toxic than the prodrug to achieve acceptable toxicity in cancer cells, even with low TONs, without causing off-target toxicity. Ideally, the drug should have an IC50 100 times lower than the prodrug. This can be achieved by screening the cytotoxicity of many known drugs and their corresponding prodrugs or by designing a new prodrug/drug couple from scratch. Alternatively, larger constructs in which a single deallylation event would lead to the release of several cytotoxic drugs would be of interest.

3) The prodrug should be stable to metabolism to prevent any activation, especially in the liver, which would lead to hepatotoxicity. This can be easily assessed *in vitro* using hepatic microsomes.

These main features are necessary for such strategies to succeed early in their development. Therefore, we encourage scientists working in this exciting field to rigorously put their system to the test to validate the above features prior to evaluating these *in vivo*.

1.6 Conclusion

Over the past sixteen years, [Cp/Cp*Ru]-based catalysts have demonstrated their potential for *in cellullo uncaging reactions*. Biorthogonal uncaging reactions have been studied using ruthenium catalysts, opening the way for the selective release of drugs. In particular, CpRu-based systems have performed well in deallylation reactions for numerous substrates in various cells and organelles. Furthermore, it was shown that the catalytic activity could easily be modulated by nanoenzymes or ArMs formation. Both strategies have demonstrated promising features, acting like microreactors or increasing the catalyst stability against biological media. However, despite good performances, the use of these complexes remains restricted due to their limited stability and cytotoxicity.

Nevertheless, only a handful of reactions exploiting this catalytic system have been developed so far. This contrasts with the range of transformations catalyzed by similar metal complexes. The rich chemical toolbox accessible via ruthenium catalysis will undoubtedly be applied in *cellulo* to diversify the use of new-to-nature reactions in living organisms. Despite its wide applications *in cellulo*, more detailed studies on the *in vivo* fate of the complex are required. For instance, the oxygen-sensitivity of the complex needs to be further investigated to allow the community to design the next generation catalysts with significantly improved biocompatibility and catalytic performance in terms of TONs at low catalyst- and substrate concentrations.

Chapter 2: Goal of the thesis

This thesis aims to use the potential of artificial metalloenzymes to implement a new-to-nature reaction within living organisms. The choice turned toward developing an artificial allylic aminase to perform the bioorthogonal enantioselective N-hetero cyclization. The artificial system used a Cp-based Ru^{II} catalyst and streptavidin as the host protein. Chapter 3 presents a direct *in vivo* application of this system for deallylation, which uses the exact mechanism as allylic amination. Chapters 4 and 5 will present the subsequent study of catalyst limitations and substrate design influence, respectively.

Chapter 3: Directed Evolution of a Surface-Displayed Artificial Allylic Deallylase Relying on a GFP Reporter Protein

Alain Baiyoumy[†,ϕ], Jaicy Vallapurackal[†,ϕ], Fabian Schwizer[†,#,ϕ], Tillmann Heinisch[†,⊥], Tsvetan Kardashliev[‡], Martin Held[‡], Sven Panke[‡] and Thomas R.Ward[†,*,∇]

[†] University of Basel, Department of Chemistry, Mattenstrasse 24a, 4058 Basel, Switzerland.

[‡] ETH Zürich, D-BSSE, Mattenstrasse 26, 4058 Basel, Switzerland.

[∇] National Competence Center in Research (NCCR), Molecular Systems Engineering, Basel, Switzerland.

[ϕ] Contributed equally to this work.

This chapter has been published in *ACS Catal.* 2021, 11, 17, 10705–10712

DOI: 10.1021/acscatal.1c02405

Author contribution

General concepts and idea by T.R.W. Cloning of the constructs and library creation by T.H., T.K., and F.S. A.B. and F.S. performed the *in vivo* and *in vitro* experiments. A.B. performed the *in vitro* experiments and molecule characterizations via HPLC. J.V. designed and performed the cross-linking experiments. T.R.W., A.B. and J.V. wrote the manuscript. All authors reviewed the manuscript and the SI.

Abstract:

Artificial metalloenzymes (ArMs) combine characteristics of both homogeneous catalysts and enzymes. Merging abiotic and biotic features allows for the implementation of new-to-nature reactions in living organisms. Here we present the directed evolution of an artificial metalloenzyme based on E. coli surface-displayed streptavidin (Sav^{SD} hereafter). Through the binding of a ruthenium-pianostool cofactor to Sav^{SD}, an artificial allylic deallylase (ADAse hereafter) is assembled, which displays catalytic activity towards the deprotection of alloc-protected 3-hydroxyaniline. The uncaged aminophenol acts as a gene switch and triggers the over-expression of a fluorescent GFP reporter protein. This straightforward readout of ADAse activity allowed the simultaneous saturation mutagenesis of two amino acid residues in Sav near the ruthenium cofactor, expediting the screening of 2762 individual clones. A 1.7-fold increase of in vivo activity was observed for Sav S112T-K121G compared to the wild-type Sav (wt-Sav). Finally, the best performing Sav isoforms were purified and tested in vitro. For Sav S112M-K121A, a total turnover number of 372 was achieved, corresponding to a 5.9-fold increase vs. wt-Sav. To analyze the marked difference in activity observed between the surface-displayed and purified ArMs, the oligomeric state of Sav^{SD} was determined. For this purpose, crosslinking experiments of E. coli cells over-expressing Sav^{SD} were carried out, followed by SDS-PAGE and Western blot. The data suggest that Sav^{SD} is most likely displayed as a monomer on the surface of E. coli. We hypothesize that the difference between the in vivo and in vitro screening results may reflect the difference in oligomeric state of Sav^{SD} vs. soluble Sav (monomeric vs. tetrameric). Accordingly, care should be applied when evolving oligomeric proteins using E. coli surface-display.

2.1 Introduction

Artificial metalloenzymes[140] (ArMs) are formed by the incorporation of a synthetic cofactor into a natural host protein.[141,142] Artificial metalloenzymes combine the advantages of synthetic transition metal catalysts (e.g. broad range of reactivities[143–151], large substrate scope, wide choice of metals) with the benefits of enzymes (e.g. high selectivity, high TON, aqueous compatibility, directed evolution, etc.).[152–159] Hence, such entities can be optimized by combining both chemical and genetic means, which significantly broadens the range of possible optimization approaches.[160] The effect of the chemical or biological modifications can then be evaluated *via* a high-throughput screening using various analytical readouts, including fluorescence or UPLC-MS.[161,162]

Building on the pioneering work of Meggers[163,164] we performed the *in vivo* deallylation of an alloc-protected aminocoumarin **5** moiety using an artificial allylic deallylase (hereafter ADAse).[165] The catalytic system, comprising an air and thiol tolerant ruthenium (II) complex **1**,[166] is anchored within Sav displayed on *E. coli*'s outer-membrane.[165,167] The efficiency of this system was improved *via* iterative saturation mutagenesis of the position S112 and K121.[168–170] The reaction was monitored via the fluorescence of the uncaged aminocoumarin **4**, Figure 1. We know from previous Sav-ArM evolution campaigns, that the iterative site-saturation mutagenesis at positions S112 and K121 often leads to significant improvement in catalytic performance, as these two positions lie in close proximity to the cofactor.[160,165,171]
The possibility of expressing a protein at the surface of a cell[172–175] caught our attention since, relying on this process, we could avoid issues encountered using periplasmic or cytoplasmic expression (reductive conditions, limited accessibility of the substrates and cofactors etc.). Previous studies have highlighted the possibility of performing chemical transformations such as polymerization[175], deallylation[176–179], hydrolysis[180], hydroarylation[181], carbene insertion[182,183] in living cells environment and performing the uncaging of a fluorophore or an inducer in living cells.[165,184,185] More recently, we engineered a gene circuit in the cytoplasm of mammalian cells[186]. Based on these results, we aimed to develop a gene switch based on the regulatory protein DmpR[187–190] to promote the production of a protein of interest and allow us to monitor the improvement of the system via fluorescence. Building on these results, we set out to engineer and optimize an ArM whose activity could induce the overexpression of a reporter protein in *E. coli*. With this goal in mind, we selected the [CpRu]-catalyzed deallylation of amines, as pioneered by Meggers. We opted for an *E. coli* surface display of Sav to evolve the ADAse activity, relying on a fluorescent readout caused by the up-regulation of a green fluorescent protein reporter protein (GFP hereafter).

2.2 Results and discussion

To up-regulate the GFP reporter protein in *E. coli*, we selected a DmpR-regulated GFP construct, whereby binding of various aniline derivatives to the DmpR regulator, turns-on the over-expression of GFP, which can be conveniently used as read-out of ADAse activity, Figure 1. As a first step, we tested the induction capacity of various polar benzene derivatives in the presence of reporter cells equipped with the DmpR-regulated GFP plasmid, Figure 2a. Both 2-methylphenol and 3-

hydroxyaniline **2** performed best, as reflected by the GFP fluorescence observed in the reporter cells. As allylcarbonates (to protect 2-methylphenol) are more prone to spontaneous hydrolysis than allylcarbamates (to protect 3-hydroxyaniline), we selected the *N*-allylcarbamate-3-hydroxyaniline **3** for further studies. Next, we spiked the DmpR-GFP equipped reporter-cells with the wild-type ADAse consisting of cofactor **1** · wt-Sav, Figure 2b. We were pleased to observe the following trends: i) the alloc-protected aniline **3** does not lead to marked GFP-fluorescence in the reporter cells, ii) the cofactor **1** alone is not very active at deprotecting compound **3**, and iii) cofactor **1** · wt-Sav leads to increased GFP-fluorescence (1.8-fold vs. cofactor **1** alone). The GFP fluorescence produced in the presence of cofactor **1** · wt-Sav corresponds to the equivalent of spiking GFP-expressing cells with >100 μM 3-hydroxyaniline **2**. Based on these findings, we engineered a system based on two plasmids: Lpp-OmpA-Sav[167,191] and DmpR-GFP[187,189,190], thus allowing us to screen and optimize the ADAse activity using a single cell. Lpp-OmpA-Sav regulates the expression and translocation of Sav to the surface of *E. coli* cells and is induced by *L*-arabinose, Figure 1. DmpR-GFP expresses a GFP reporter-protein via the binding of an inducer to the DmpR regulator Figure 1.

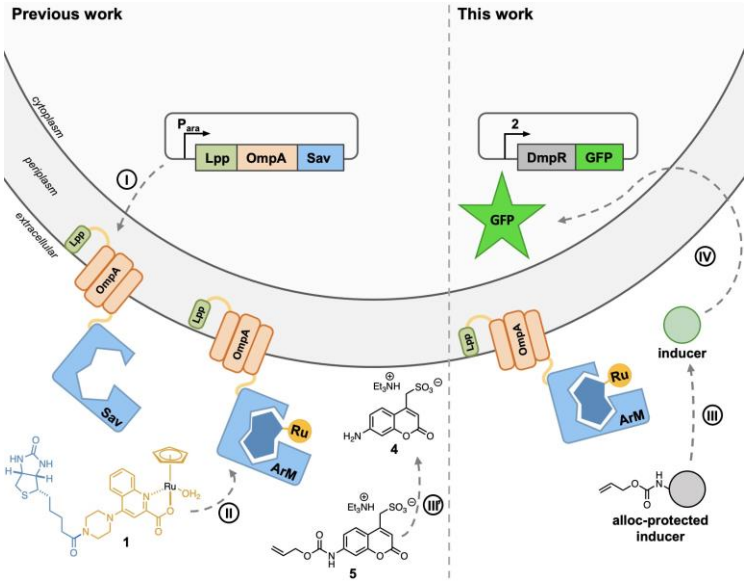

Figure 1 Comparison of the previous and the current strategies for the optimization of ADAses using an *E. coli* surface-display construct. I) expression, translocation and integration of the Lpp-OmpA-Sav construct on the outer membrane of *E. coli* cells. For clarity only one streptavidin (Sav) monomer is displayed. II) The biotinylated cofactor **1** binds to Sav to afford the ADAse. Previous work: III') uncaging of the protected substrate **5** to yield the fluorescent coumarin **4**. This work: III)

uncaging of an alloc- protected inducer in the presence of the ADAse releases the inducer; IV) the inducer diffuses into the cytoplasm of *E. coli* cells and induces the expression of GFP.

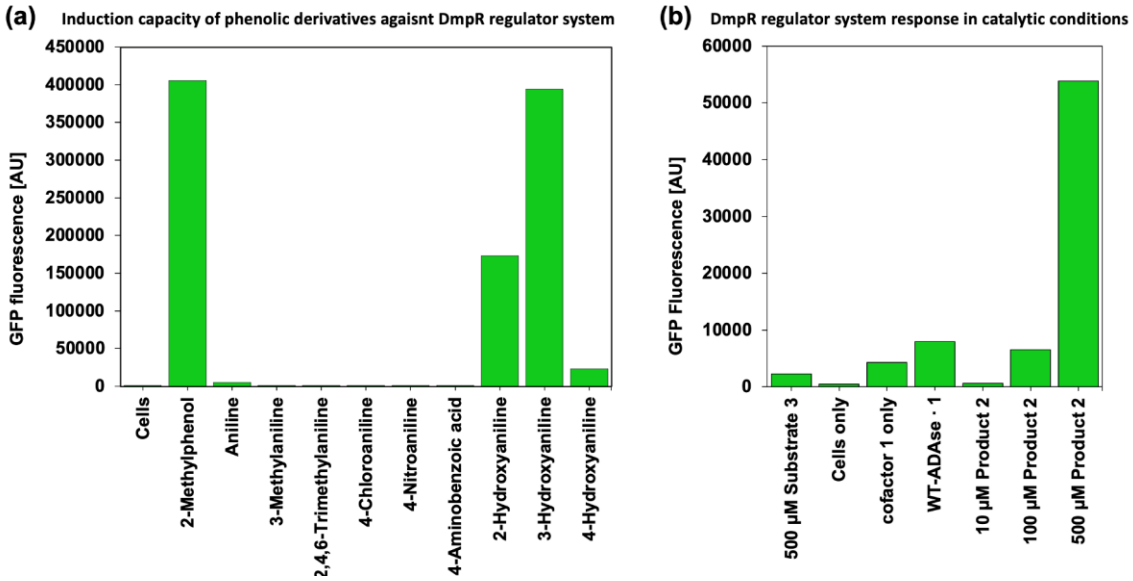

Figure 2. (a) Induction capacity of various phenols and anilines for the DmpR regulator system. Reaction steps: i) *E. coli* DH5α cells containing the DmpR-GFP reporter plasmid were cultivated in LB-medium at 30 °C to a cell density of OD_{600} = 0.6. ii) Dilution of the cells to OD_{600} = 0.05-0.08, followed by addition of 500 µM caged inducer. iii) Incubation at 30°C, 200 rpm shaking. iv) Analysis of the fluorescence intensity of the cells by flow cytometry (the median value of the fluorescence intensity is displayed). **(b)** Performance of purified ADAses in the presence of reporter cells. Conditions: 500 µM substrate **3**, 5 µM ruthenium cofactor **1**, 2.5 µM wt-Sav, 30 °C, 9 h. Preparation of reporter cells (see **SI**).

Next, we combined the previously designed *E. coli* surface-displayed ADAses with the deprotection of caged inducer **3** and the subsequent expression of GFP, Figure 3a. Control experiments revealed a modest background fluorescence for cells containing an empty vector (i.e. Lpp-OmpA plasmid without Sav gene), 2 µM cofactor **1** and 500 µM caged substrate **3**, Figure 3b. Gratifyingly, in the presence of the assembled ADAse **1** · wt-Sav, a 1.7-fold increased fluorescence was observed. The observed fluorescence is comparable to a GFP expression level in the presence of ~50 µM 3-hydroxyaniline **2**. These highlight the reliability of the surface-displayed ADAse for screening purposes.

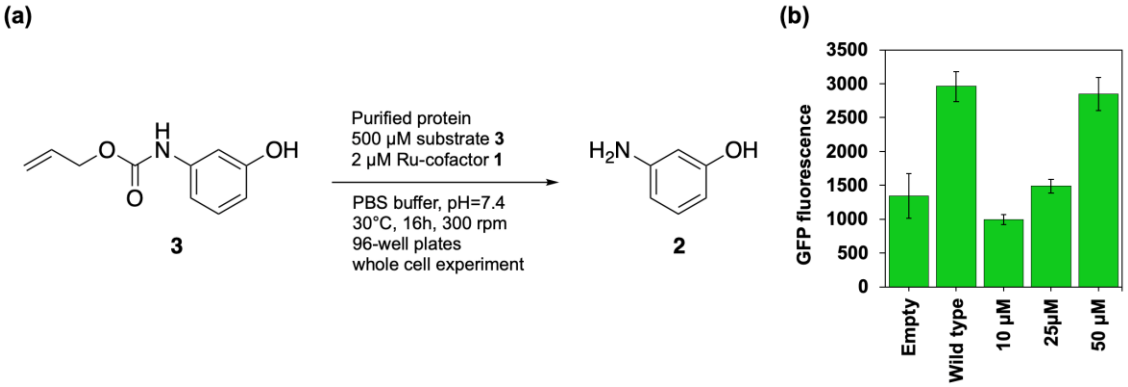

Figure 3. (a) Reaction scheme and conditions for the allylic deallylation of the substrate **3** to the 3-hydroxyaniline **2**. Reaction conditions: 500 µM substrate **3**, incubation of cells with 2 µM cofactor **1**, 30 °C, 16 h. Preparation of catalysis cells using a normalized OD (see SI). **(b)** Control experiments to validate the screening strategy: cells expressing Sav S112M-K121A were spiked with 10 µM, 25 µM or 50 µM product **2**. GFP-fluorescence determined in a plate reader at: $\lambda_{ex.}$ = 475 nm, $\lambda_{em.}$ = 509 nm.

To validate the GFP-reporter strategy, we optimized the performance of the surface-displayed ADAse by simultaneously randomizing both S112 and K121 positions, Figure 4. Simultaneous saturation mutagenesis of two residues yields a library containing 20^2 = 400 different mutants in one pot. The screening effort (i.e. the oversampling) can be reduced by a factor ~1.8 (1724 colonies instead of 3066 colonies with a sequence coverage of 95%) when using the degenerate codon DNK instead of NNK[19]. This library comprises of 17 different amino acids at each position (Gln, Pro and His are missing), leading to a total number of 17^2 = 289 individual mutants.

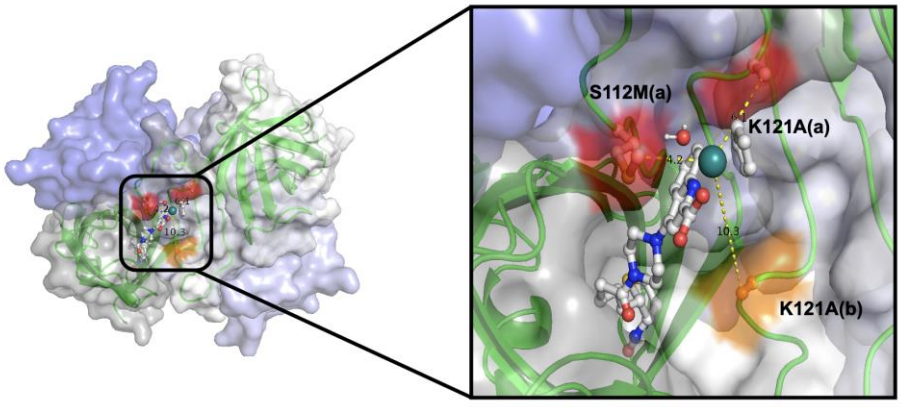

Figure 4. Crystal structure of the ADAse [CpRu(QA-Biot)(OH_2)] **(1)** · Sav S112M-K121A (PDB 6FH8[165]).The four monomeric units are displayed as transparent surface in grey, white, blue and

light blue. The mutated positions (S112M^a and K121A^a of monomer A) are highlighted in red and the position K121A^b of monomer B faces the active site is highlighted in orange (only in one of the two symmetry-related monomers). The biotinylated ruthenium complex is displayed as ball and stick. Color code: C = grey, N = blue, O = red, S = yellow, H = white, Ru = dark green sphere. The cofactor **1** is anchored in the Sav monomer A (grey). The closest C$_\beta$-residue to Ru (dark green sphere) is K121A (red) of Sav monomer A (blue).

The corresponding Sav library was assembled by Gibson assembly including a synthesized part of the Sav gene that carried the required mutations at its center (90 base pair length, DNK codons in positions S112 and K121) into the Lpp-OmpA plasmid (see SI). Analysis of the library revealed a good statistical distribution of the different amino acids, Figure S7. However, the library contained a background of 42% (i.e. original Lpp-OmpA plasmid, frame shifts, stop codons, inserts, unclear sequencing results). Thus, a coverage of 93.8% is predicted for a total of 2762 screened individual colonies.[192] The 2762 colonies were tested and the 100 most active clones were sequenced (see SI for details). The 100 clones were retested in order to exclude false positives. Out of these 100 clones, the 10 best mutants (Sav K121D, K121E, K121G, K121N, S112M-K121R, S112M-K121T, S112T-K121A, S112T-K121G, S112T-K121N and S112T-K121T) were selected for protein expression in the cytoplasm, purification and *in vitro* characterization.

Since almost all double mutants were more active than wt-Sav, we also tested the corresponding single mutants (i.e. Sav S112M, S112T, K121A, K121G, K121N, K121R and K121T) in order to identify potential synergetic effects. In addition, streptavidin wild-type (wt-Sav), mutant S112M-K121A (i.e. the best mutant identified in previous work[7]) as well as the cofactor **1** alone were included in the *in vitro* catalysis validation (Figure 5). Comparison of the *in vivo* and *in vitro* ADAse activities revealed striking differences, Figure 5. Although variable expression levels may account for marked differences *in vivo* enzymatic activities,[165] past experience with Sav expression levels[170] led us to investigate an alternative hypothesis. Indeed, we surmised that fusing each Sav monomer (16.7 kDa) with a hydrophobic Lpp-OmpA insert (15.3 kDa) may affect the quaternary structure of surface-displayed Sav. Since two monomers of Sav make up the biotin-binding vestibule, (Figure 4), the oligomeric nature of Sav may strongly affect which close-lying mutation of surface-displayed Sav (quaternary structure unknown) is indeed present in purified, tetrameric Sav samples.[167,193,194]

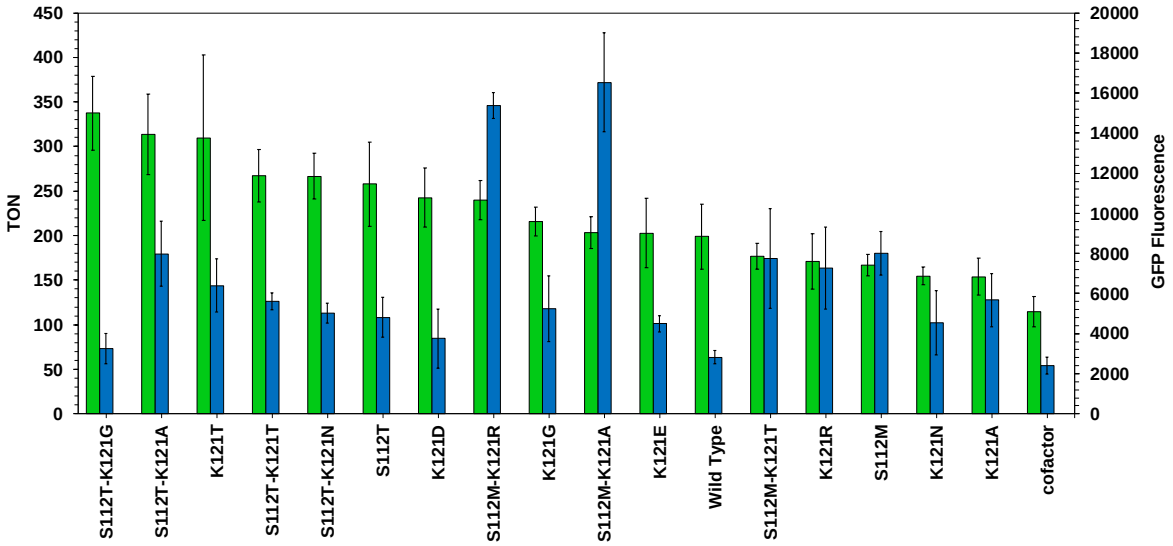

Figure 5. Directed evolution of artificial allylic deallylases for the uncaging of protected aniline **3**. *In vitro* catalysis (blue bars): Substrate **3** (500 µM), cofactor **1** (1 µM), purified Sav isoform (2 µM biotin-binding sites), PBS-buffer (1x, pH 7.4), 30°C, 18 h, 300 rpm shaking. Total turnover number (TON) determined by HPLC (Figure S3 and Figure S4). Error bars = standard deviation from triplicate measurements. *In vivo* catalysis (green bars): 500 µM substrate **3**, incubation of cells with 2 µM ruthenium cofactor **1**, 30°C, 16 h. Preparation of catalysis cells (see SI). GFP-fluorescence determined with a plate reader at: λex. = 475 nm, λem. = 509 nm. Displayed values are normalized for the optical cell density (OD_{600}).

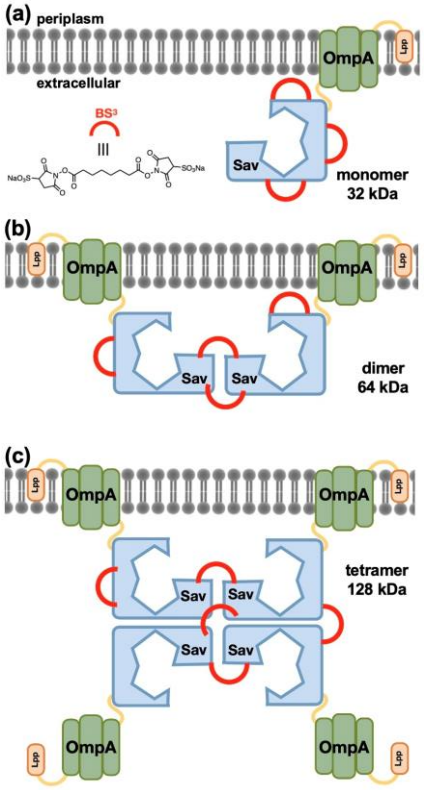

Figure 6. Schematic representation of Sav^{SD} using the Lpp-OmpA display system and the crosslinking approach**. (a)** Crosslinking with bis(sulfosuccinimidyl) suberate (BS^3), which mainly targets lysines, fixes the oligomeric state of the surface-displayed Sav^{SD}. Subsequent lysis of the cell membrane, releases the crosslinked constructs into solution that are analyzed by SDS-PAGE and western blot (see Figure 7). Depending on the surface-displayed quaternary structure of Sav^{SD}, three different sizes, **(a)** 32 kDa, **(b)** 64 kDa and **(c)** 128 kDa can be expected for the monomer, dimer and tetramer, respectively.

To assess the quaternary structure of surface-displayed Lpp-OmpA-Sav, we set out to: i) treat the *E. coli* cells with a crosslinking agent, ii) lyse the cells and iii) analyze the protein-content by SDS-page and Western blot to identify the Sav-containing bands. Although surface display is a widely used strategy in protein expression and optimization, the quaternary structure of oligomeric, surface-displayed, proteins should to be addressed on a case-to-case basis.[191,195,196]

To minimize the adventitious assembly of homotetrameric Sav following cell lysis and workup, the cells were treated with bis(sulfosuccinimidyl) suberate (BS^3), a protein cross-linking agent,[197] to fix the oligomeric state of Sav^{SD} prior to cell lysis, Figure 6. Similar studies have highlighted the crosslinking of *E. coli* outer membrane proteins using cleavable crosslinkers to yield oligomeric proteins.[198–200] Exploratory crosslinking experiments highlighted the superiority of the anionic BS^3

vs. the commonly used glutaraldehyde.[197,198] The Sav^{SD} as well as the empty vector as negative control– were expressed in *E. coli* at 25 °C for 24 h in shaking flasks. The cells were harvested and the pellets were washed with PBS, and resuspended in PBS before cross-linking with BS^3 (8 mM, 30 min, 25°C) (See SI for details). The cross-linking was quenched by addition of 1 M Tris-buffer, the cell suspension centrifuged, the supernatant discarded and the cell pellet was resuspended in lysis buffer, which is supposed to release the Sav from the cellular environment and render it in the supernatant. The suspension was centrifuged and the supernatant was set aside for analysis. One part of the supernatant was loaded onto the gel (Figure 7, lane 6/9) and one part was denatured (SDS sample buffer, 95 °C, 30 min), Figure 7, lane 7/10. The remaining cell pellet was resuspended in 8 M urea to ensure the recovery of any additional protein that might have been retained in the cell debris from lysis, centrifuged and the supernatant was subjected to analysis, Figure 7, lane 8/11. For comparison, purified protein wt-Sav (pp-Sav) was subjected to cross-linking with BS^3. The resulting protein samples were analyzed by SDS-PAGE, Figure 7. To validate the BS^3 crosslinking strategy, control experiments using purified wt-Sav were carried out. The pp-Sav samples that were first denatured and then crosslinked, mainly appear as monomers and partly as dimers, Figure 7, lane 5. In contrast, the denatured pp-Sav sample that was not crosslinked, mainly migrates as monomer, dimer, as well as tetramer and higher oligomers on the SDS-PAGE, Figure 7, lane 2. Importantly, the pp-Sav samples that were crosslinked before the denaturation step retain the tetrameric structure, Figure 7, lane 4. We thus conclude that BS^3 crosslinking strategy permanently fixes the oligomeric state of Sav which is not affected by subsequent denaturation.

For Sav^{SD}, the electrophoresis results performed on a crosslinked Sav^{SD} sample, strongly suggest that Sav^{SD} is present as a monomer on the surface. Indeed, the denatured samples (Figure 7, lane 10 and 11) display a prominent band at about 32 kDa, which corresponds to the molecular weight of monomeric Sav^{SD} (Lpp-OmpA-Sav 31.925 kDa). In contrast, for the non-denatured Sav^{SD} sample (Figure 7, lane 9) faint bands at higher molecular weight are visible. Despite the chaotropic nature of the SDS-page analysis, the remarkable stability of homotetrameric Sav drives its oligomerization (tetramer and higher oligomers), as observed for the pp-Sav, Figure 7, lane 1-5.[201] Based on these qualitative observations, we hypothesize that the Lpp-OmpA-Sav is not displayed as a homotetramer on the outer membrane of *E. coli*. Accordingly, care should be applied when optimizing the performance of surface displayed oligomeric (artificial) enzymes, especially if their active site lies at the interface between monomers, as is the case for streptavidin, Figure 4.

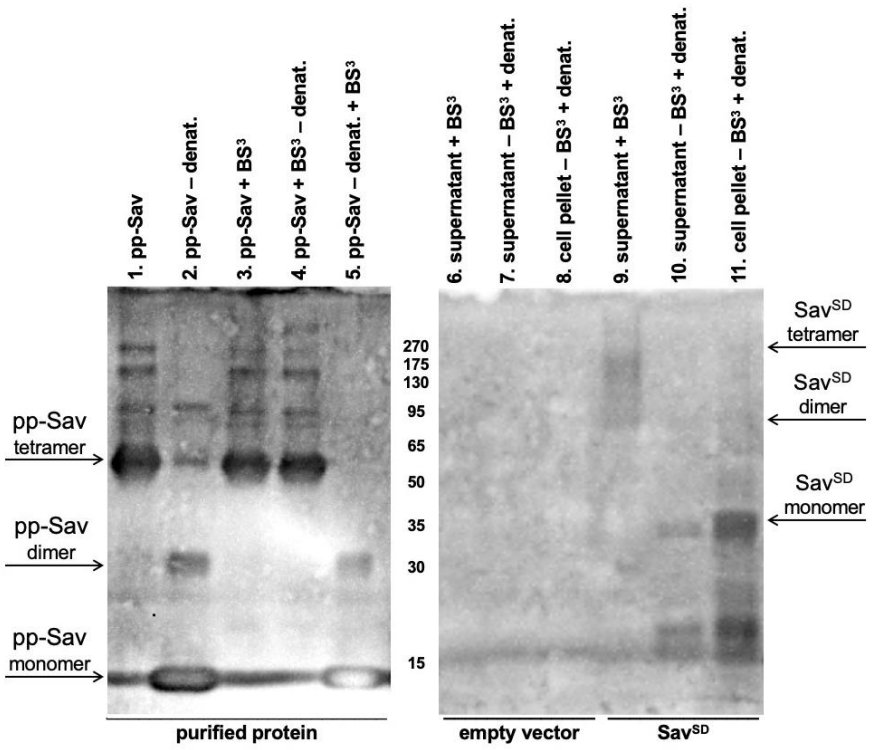

Figure 7. Western blot analysis of the quaternary structure of Sav^{SD}. Crosslinking of Sav^{SD}, followed by SDS-PAGE (14% polyacrylamide gel) and western blot (anti-Sav rabbit polyclonal antibody used at a 1:200 dilution). Lane 1 and 2 weren't cross-linked. For lane 3 to 11, except for lane 5, all samples were crosslinked with BS^3 prior to any additional treatment. All denatured samples were treated under the same conditions: SDS sample buffer, 95°C, 30 min. 1) pp-Sav, 2) denatured pp-Sav, 3) crosslinked pp-Sav, 4) crosslinked and then denatured pp-Sav, 5) denatured and then crosslinked pp-Sav, 6) empty vector, supernatant, 7) empty vector, denatured supernatant, 8) empty vector, denatured cell pellet 9) Sav^{SD}, supernatant, 10) Sav^{SD}, denatured supernatant, 11) Sav^{SD}, denatured cell pellet.

2.3 Conclusion

An *E. coli* surface-displayed artificial allylic deallylase has been engineered to turn on a gene-switch leading to the upregulation of GFP. The ADAse activity was genetically optimized by simultaneous site saturation mutagenesis of positions S112 and K121. The most active surface-displayed ADAase (Sav- S112T-K121G) revealed a 1.7-fold improvement compared to the wild type Sav ADAse. Validation of surface-displayed ADAse activity, performed on purified Sav samples revealed marked differences between Sav^{SD} and pp-Sav data. Using pp-Sav, the best variant was Sav S112M-K121A

with a 5.9-fold increased (and TON = 372) catalytic activity compared to the ADAse based on wild type. The differences in activity between surface-displayed ArMs and purified samples–reflected by GFP fluorescence and 3-hydroxyaniline **2** detected by HPLC may be the result of multiple parameters: i) Sav^{SD} expression levels, the presence of side-products, including the formation of *N*-allylated 3-hydroxyaniline[6] and iii) oligomeric nature of Sav^{SD}. Experimental evidence presented herein strongly supports the latter hypothesis.

2.4 Supplementary information

Instruments and materials

All commercially-available chemicals were purchased from Sigma-Aldrich, Acros Organics, Fluka, Fluorochem or Merck and used without further purification. Deuterated solvents were purchased from Cambridge Isotope Laboratories Inc. The water was purified with a Milli-Q-System (Millipore). Antibiotics were purchased from Applichem GmbH, DNase I was from Roche Diagnostics AG, IPTG was from Apollo Scientific, biotin-4-fluorescein was from ANAWA Trading SA and Agarose/SDS-PAGE markers were from New England BioLab Inc. Restriction enzymes, DNA polymerases and ligases were purchased from New England BioLab Inc. Antibodies were purchased from GenScript. The nitrocellulose membrane was purchased from GE Healthcare. The Pierce™ Silver Stain kit was purchased from Thermo Fisher Scientific. Primers were ordered from Microsynth AG. The double site saturation library was purchased from EUROFINS. Thin layer chromatography (TLC) was performed on Merck TLC Silica gel 60 F254 plates, using a UV-detector (254 nm or 360 nm). Basic $KMnO_4$ solution was used for the staining. Column chromatography was performed using silica gel (Merck Silica gel 60 (0.040-0.063 mm)). NMR spectra were recorded on a 400 MHz and 500 MHz Bruker Advance spectrometer at room temperature and evaluated with MestReNova. Chemical shifts (δ) are quoted in parts per million (ppm) and referenced to the residual solvent peaks. Scalar coupling (J) is reported in Hertz (Hz). High resolution mass spectra (HRMS) were measured on a Bruker maXis 4G. Mass-spectral analysis of the expressed streptavidin mutants was performed on a Bruker Daltonics, ESI/micrOTOF MS. Fluorescence/Absorbance spectroscopy was performed on a TECAN infinite M1000 Pro. PCR reactions were performed with an Eppendorf Mastercycler Gradient. Agarose gel electrophoresis chambers and SDS gel electrophoresis chambers and were purchased from Bio-Rad Laboratories Inc. The gels were visualized with the software Quantity One.

DNA sequencing (Sanger cycle sequencing/capillary electrophoresis) was performed by Microsynth AG. *E. coli* BL21(DE3) were purchased from Stratagene (Agilent), *E. coli* NEB5α cells were purchased from New England Biolabs and *E. coli* TOP10(DE3) cells were a gift from Dr. Markus Jeschek (DBSSE ETH Zürich, Switzerland). Cells were chemically treated according to the Hanahan method using RbCl. Affinity column chromatography (purification of the expressed streptavidin mutants) was performed on an Äktaprime Plus chromatography system, using a 2-iminobiotin sepharose column. Flow cytometry analysis was performed on a BD LSR Fortessa SORP (Special Order Research Product). High-throughput screening was performed with a Voaflo96 pipetting station from Integra.

Synthesis

Expression and purification of streptavidin isoforms

Streptavidin isoforms were expressed in *E. coli* BL21(DE3) cells containing pET11b_SAV plasmids and purified as described elsewhere.[202] The number of free biotin-binding sites was determined by titration with biotin-4-fluorescein.[203]

Synthesis of the biotinylated ruthenium cofactor

The biotinylated ruthenium cofactor **[CpRu(QA-Biot)(OH$_2$)] 1** was prepared *in situ* by mixing solutions of **[CpRu(MeCN)$_3$]PF$_6$** and biotinylated ligand **6** in a 1:1 ratio in DMF and subsequent incubation for 10 min at room temperature (Figure S1). The biotinylated ligand **6** was synthesized as described by Heinisch *et al.*[102]

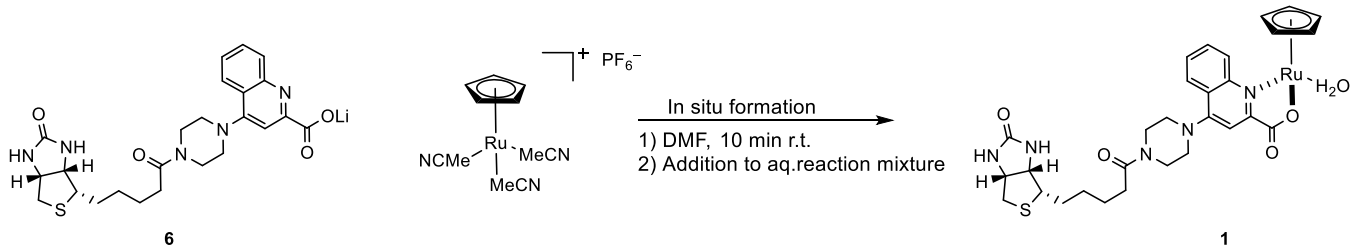

Figure S1: *In situ* formation of the biotinylated ruthenium cofactor **[CpRu(QA-Biot)(OH$_2$)]** (**1**).

Synthesis of the caged hydroxyaniline substrate 3

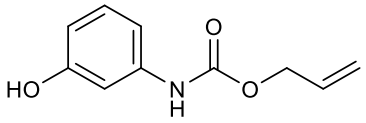

At 0°C, allyl chloroformate (3.90 ml, 4.42 g, 36.7 mmol, 2.0 eq.) was added dropwise to a stirred suspension of 3-aminophenol (**2**, 2.00 g, 18.3 mmol, 1.0 eq.) in a mixture of dry diethyl ether (100 ml) and dry THF (20 ml). A white precipitate was formed immediately. The reaction mixture was stirred an additional 2 h at room temperature. The precipitate was removed by filtration. The filtrate was evaporated under reduced pressure. The resulting brown oil was solubilized in diethyl ether (20 ml) and the resulting organic phase was washed with solutions of HCl (1 M, 20 ml), saturated $NaHCO_3$ (20 ml) and water (20 ml). The organic phase was dried over Na_2SO_4 and the solvent was evaporated to yield a brown oil. The residue was purified by flash column chromatography (SiO_2, ethyl acetate/cyclohexane 1:3) to afford the product as a white crystalline solid (**3**, 792 mg, 4.1 mmol, 22% yield). NMR and HRMS spectra are displayed in Figure S2.

^{1}H NMR (500 MHz, Chloroform-*d* δ/ppm): 7.30 (s (broad), 1H, **10**), 7.13 (t, *J* = 8.1 Hz, 1H, **7**), 6.81 (s (broad), 1H, **NH**), 6.68 (ddd, *J* = 8.0, 2.1, 0.9 Hz, 1H, **6**), 6.58 (ddd, *J* = 8.1, 2.4, 0.9 Hz, 1H, **8**), 6.52 (s (broad), 1H, **OH**), 5.95 (ddt, *J* = 17.2, 10.4, 5.7 Hz, 1H, **2**), 5.36 (dq, *J* = 17.2, 1.5 Hz, 1H, **1**), 5.26 (dq, *J* = 10.4, 1.3 Hz, 1H, **1**), 4.67 (dt, *J* = 5.7, 1.4 Hz, 2H, **3**). Solvents: Chloroform (7.26), cyclohexane (1.43).

^{13}C NMR (126 MHz, Chloroform-*d* δ/ppm): 156.77 (1C, **9**), 153.62 (1C, **4**), 138.69 (1C, **5**), 132.07 (1C, **2**), 129.98 (1C, **7**), 118.54 (1C, **1**), 110.86 (1C, **8**), 110.58 (1C, **6**), 106.03 (1C, **10**), 66.17 (1C, **3**). Solvents: Chloroform (77.28, 77.03, 76.77).

HRMS (ESI-MS, pos.) m/z: $[M + H]^+$ calculated for $C_{10}H_{12}NO_3$: 194.0812, found: 194.0811.

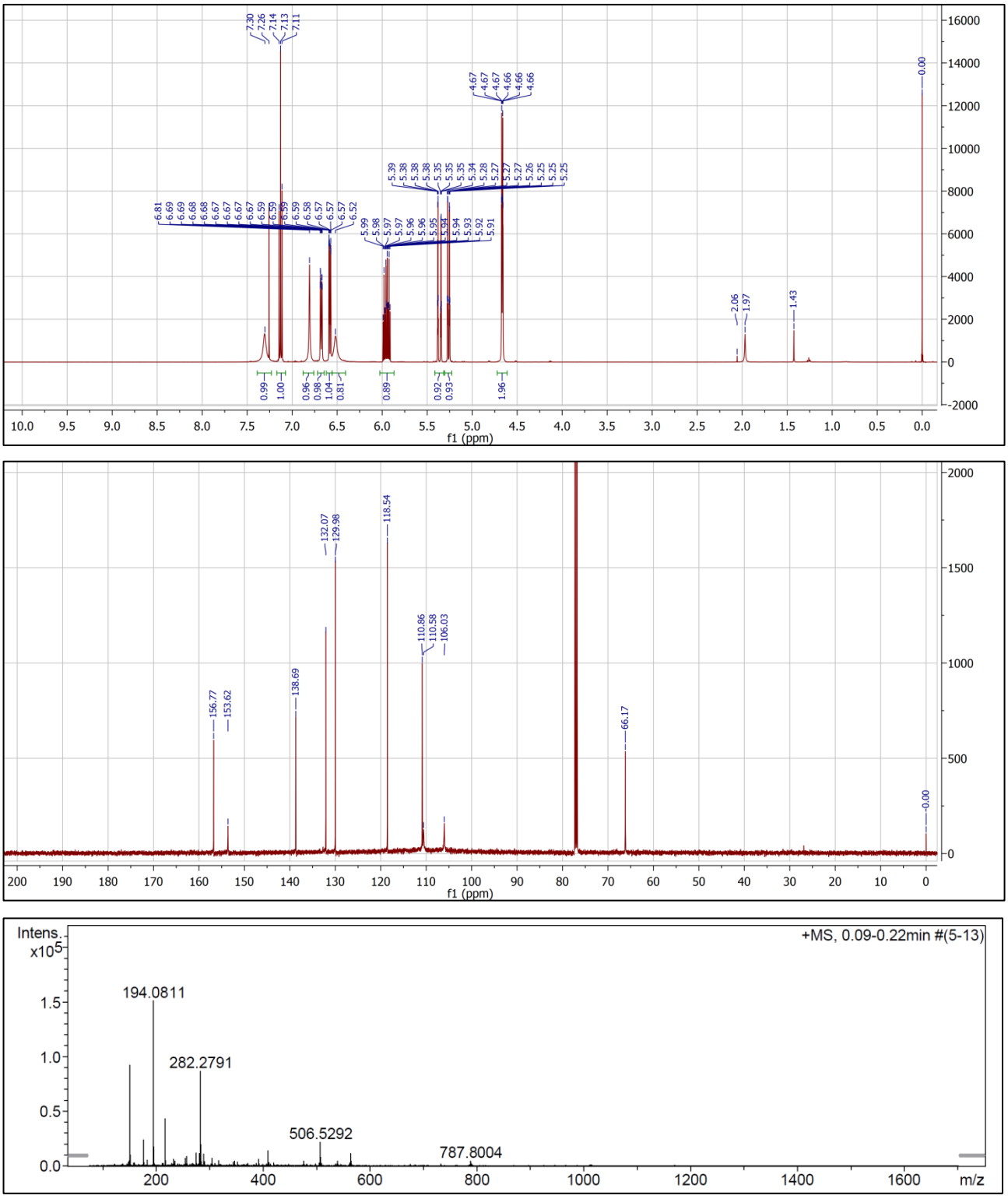

Figure S2: a) ^{1}H-NMR, b) ^{13}C-NMR and c) HRMS spectrum of compound **3**.

Design of a caged DmpR substrate

Induction capacities of various phenols and anilines

E. coli DH5α cells containing the DmpR/GFP reporter plasmid were cultivated in LB-medium at 30°C to a cell density of OD_{600} of 1. The cell culture was diluted to OD_{600} = 0.05-0.08 in fresh media and aliquoted (1 mL) in fresh tubes. Each tube was supplemented with the putative inducer (500 µM) and incubated overnight at 30°C, 200 rpm (12-13 h). The GFP fluorescence intensities and OD_{600} values of appropriately diluted samples were recorded in a Tecan M2000 microtiter plate reader; the OD-normalized fluorescence intensity values obtained with each putative inducer are displayed in Figure 2a.

In vitro catalysis

Stock solutions

Biotinylated ligand **6**:	5 mM in DMF
[CpRu(MeCN)$_3$]PF$_6$:	5 mM in DMF
Ruthenium cofactor **1**:	0.2 mM in DMF (4 µL of ligand **6** stock was mixed with 4 µL **[CpRu(MeCN)$_3$]PF$_6$** stock and 92 µl DMF and incubated for 5 min)
Sav isoform:	0.4 mM free biotin-binding sites in PBS-buffer
Substrate:	50 mM substrate **3** in DMF
Product:	20 mM product **2** in DMF
Internal standard:	12.5 mM phenol in DMF
Inhibitor:	10.4 mM potassium isocyanoacetate in water
PBS buffer:	50 mM NaH_2PO_4/Na_2HPO_4 (set to pH 7.4), 0.9 % NaCl

Catalysis experiment

Buffer (245 µL), protein (1.25 µL, 2 µM final concentration) and ruthenium cofactor **1** (1.25 µL, 1 µM final concentration) were added in this order to a 2 mL vial. The solution was incubated at room temperature for 10 min (formation of the ADAse). The substrate **3** (2.5 µL, 500 µM final concentration) was added (1.5% final DMF content). The vials were closed and incubated in a thermoshaker (30°C, 18 h, 300 rpm shaking). The inhibitor was then added to the reaction (240 µL, 5 mM final concentration). Accordingly, no catalytic activity for cofactor **1** · Sav-S112M-K121A

spiked with inhibitor was detected[95]) followed by the internal standard (10 µL, 250 µM final concentration). The sample was then subjected to HPLC analysis Figure S3. The peak areas of the product and the internal standard in the HPLC chromatogram were integrated and the total turnover number (TON) was determined by comparison to a calibration curve displayed in Figure S4.

Evaluation by HPLC

Solvents:	MilliQ-water +3% MeCN + 0.1% TFA (Solvent A)
	MeCN + 0.1% TFA (Solvent B)
Column:	Agilent Eclipse XDB-C18, 5 µm particles, 4.6 x 150 mm
Oven temperature:	40°C
Flow rate:	1 ml/min
Run time:	22 min
Gradient:	0 min (10% B), 5 min (10% B), 7 min (30% B), 15 min (30% D), 17 min (10% B), 22 min (10% B)
Injection volume:	10 µL
Absorption:	280 nm
Retention times:	Product **2**: 1.82 min, Internal standard (Phenol): 9.49 min, Substrate **3**: 11.77 min

a)

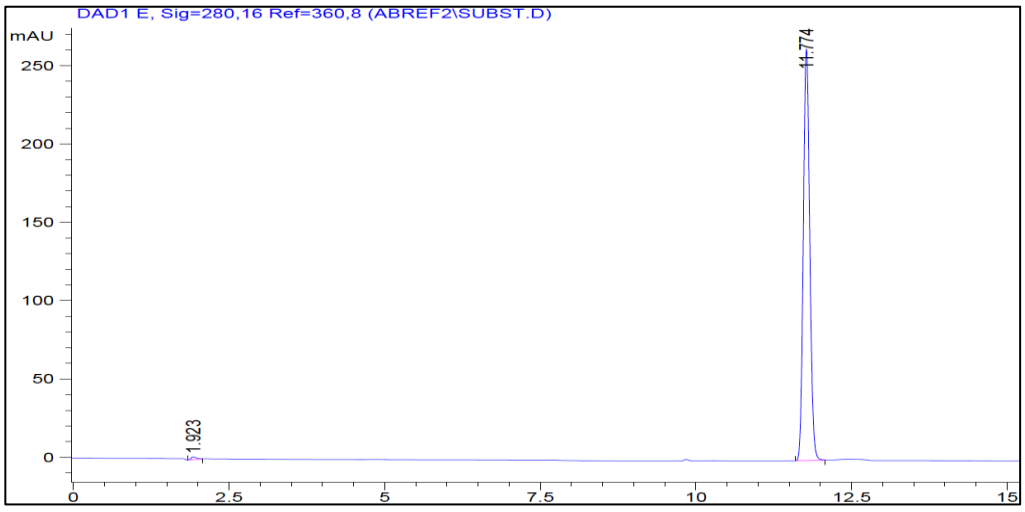

b)

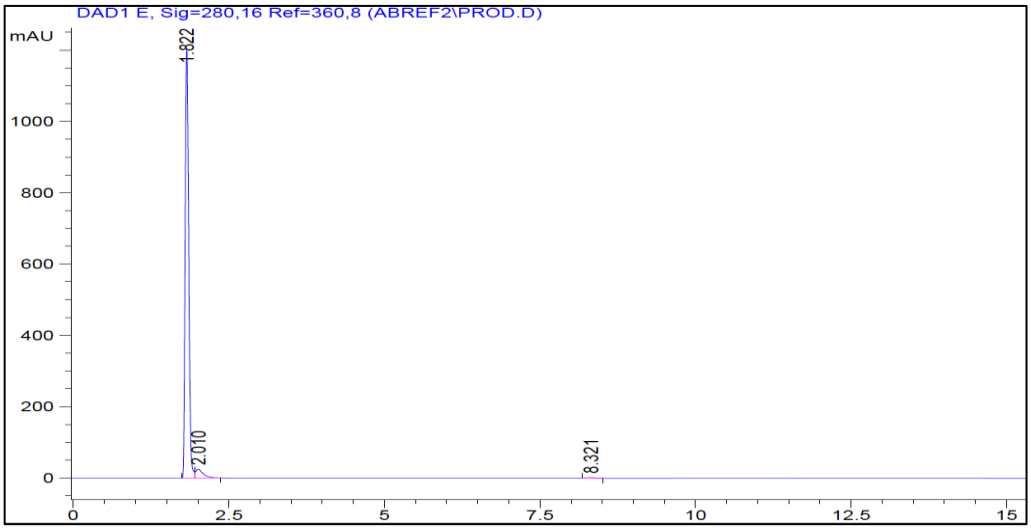

c)

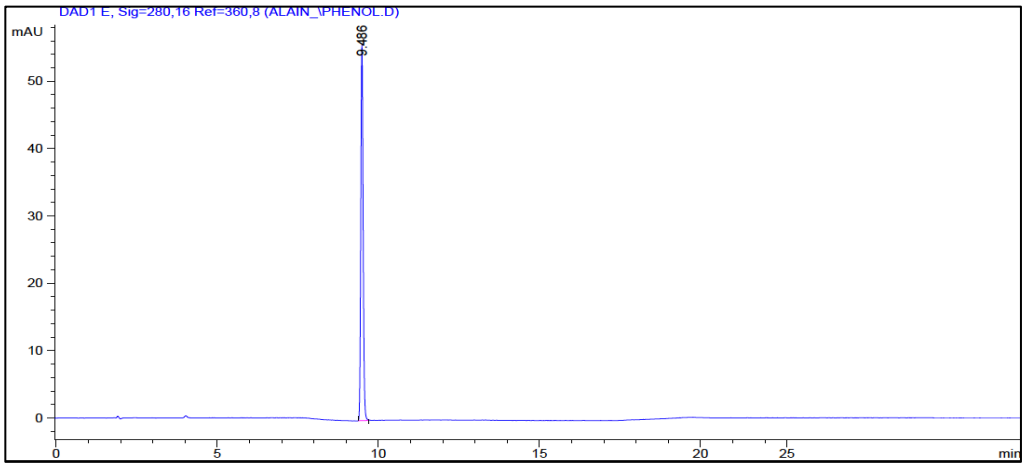

Figure S3: HPLC chromatogram (absorption at 280 nm) of a) Substrate **3**, b) Product **2** and c) Internal standard.

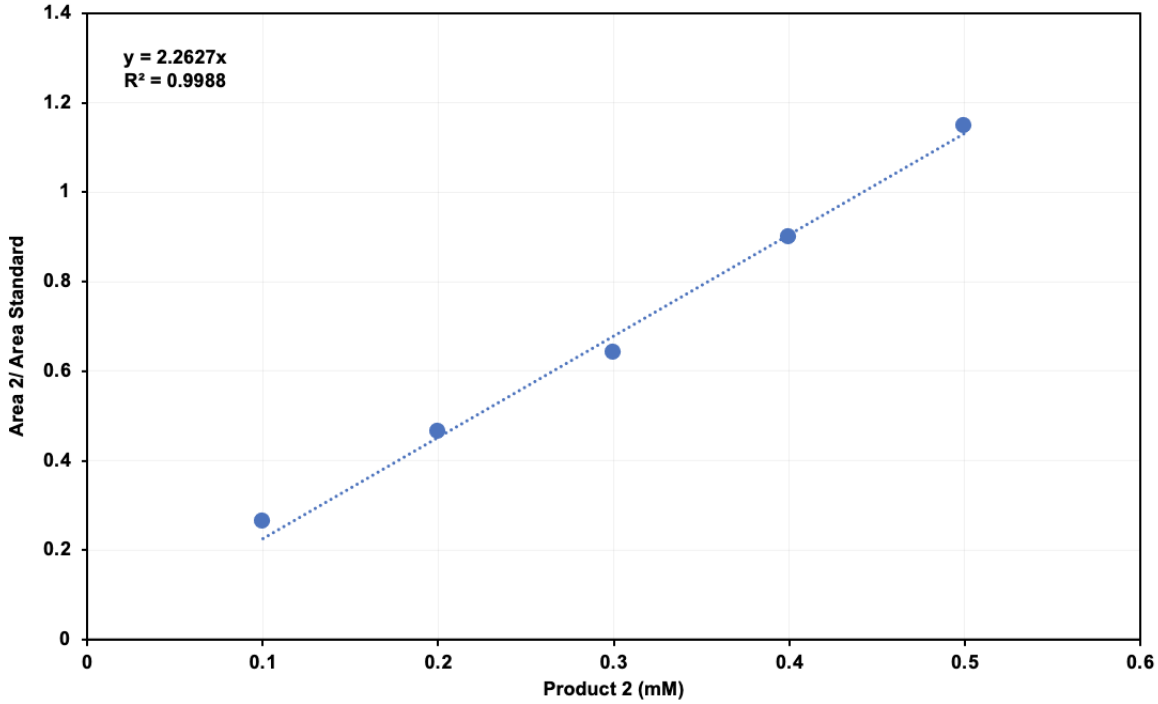

Figure S4: Calibration curve of product **2** as a function of the peak areas of the product and the internal standard determined by HPLC.

Design, cloning and transformation of streptavidin and reporter plasmids

Summary of plasmids used in this study

Table S1: Plasmids composition.

Abbreviation	Plasmid backbone	Gene	Inducer	Resistance marker	Origin of replication
P1	pSEVA	DmpR	3-OH-anilline	Ampicillin	p15A
P2	pBAD33	Lpp-OmpA-Sav	L-arabinose	Chloramphenicol	pBR322

Cloning of reporter plasmid P1

Double-stranded synthetic DNA fragment encoding the *dmpR* gene (codon-optimized) from *Pseudomonas sp.* and promoter sequences P_r and P_o from *Pseudomonas sp.* was purchased from IDT DNA. The fragment was introduced in a modified pSEVA131 backbone (p15a ori, ampicillin antibiotic cassette, promoterless *sfgfp*) by Gibson assembly method. The expression of the fluorescent protein is controlled by the P_o inducible promoter. Vector amplification was achieved using the Phusion high-fidelity PCR mastermix with GC buffer, primers (5`-GGATCCTAATTAATTAAAGGCATCAAATAAAACG) and (5`-CTTGGACTCCTGTTGATAGATC). The inserted sequence was confirmed after plasmid isolation using QIAquick Miniprep plasmid purification kit.

Cloning of Sav display plasmid P2

For streptavidin expression and insertion into the outer membrane, a fusion construct consisting of the *E. coli* lipoprotein (Lpp), a truncated version of the *E. coli* outer membrane protein A (OmpA) and full-length streptavidin (Sav) was cloned into an *L*-arabinose inducible pBAD33 vector backbone as described by Heinisch *et al.*[102]

Preparation of GFP reporter cells (NEB5α-P1):

Plasmid **P1** was transformed into chemically competent NEB5α (NEB) cells following the manufacturer´s protocol.

Preparation of catalytically competent GFP reporter cells (Top10(DE3)-P1-P2)

Plasmids **P1** (1 µL of ~100 ng/µL stock solution) and **P2** (1 µL of ~100 ng/µL stock solution) were co-transformed into chemically competent Top10(DE3) cells (50 µL) by heat shock treatment (42 °C) and cells were incubated on LB-agar$_{cam,amp}$ plates (35 µg/mL chloramphenicol, cam; 50 µg/mL ampicillin, amp) overnight at 37 °C.

Catalysis with GFP reporter cells

Stock solutions

Biotinylated ligand **6**:	5 mM in DMF
[CpRu(MeCN)$_3$]PF$_6$:	5 mM in DMF
Ruthenium cofactor **1**:	1 mM in DMF (20 µL of ligand **6** stock was mixed with 20 µL **[CpRu(MeCN)$_3$]PF$_6$** stock and 60 µl DMF and incubated for 5 min at room temperature)
Sav isoform:	2 mM free biotin-binding sites in water
Substrate:	10 mM substrate **3** in DMF
Product:	10 mM product **2** in DMF
LB-phosphate buffer:	50 mM NaH_2PO_4/Na_2HPO_4, pH 7.4 (10.1 mL Na_2HPO_4 (200 mM), 2.4 mL NaH_2PO_4 (200 mM) and 37.5 mL LB medium were mixed together)

Preparation of GFP reporter cells (NEB5α-P1)

NEB5α_pDmpR cells were freshly picked from an LB-agar$_{amp}$ plate or from a glycerol stock to inoculate LB$_{amp}$ medium for preparation of an overnight culture. In the next morning, in a 250 mL baffled shake flask 20 mL LB$_{amp}$-medium were inoculated with the overnight culture (600 µL) and incubated at 37 °C, 250 rpm, until ~OD$_{600}$ = 0.6 was obtained (~2.5 h). Prior to the catalysis experiments the GFP reporter cells were stored on ice.

Catalysis experiment

In a 96-well plate deep well plate, Sav (2 mM, 2.5 µL of stock solution; 10 µM final concentration) were mixed with Ru-cofactor (2.5 µL, 1 mM; 5 µM final concentration). The mixture was incubated for 5 min. Next, substrate **3** (25 µL, 10 mM; 500 µM final concentration), LB-phosphate (20 µL) and reporter cells (450 µL) were added and the plate covered with a porous seal to start the reaction. The plate was incubated (30 °C, 300 rpm). After 9 hours, aliquots of the reaction were transferred to a TECAN plate reader to determine the GFP fluorescence (excitation: 488 nm, emission: 509 nm) and the OD_{600}.

Double site saturation mutagenesis library generation

A double site saturation mutagenesis library of Sav including positions S112 and K121 was selected for the optimization of ADAse displayed on the *E. coli* surface. A two-step process was anticipated as a suitable library generation strategy:

generation by the company EUROFINS of a Sav gblock library of a 90 bp length and comprising DNK codons in positions S112 and K121 and
Gibson assembly of **P2** plasmid backbone and the Sav gblock library.

To reduce the screening effort, a focused Sav gblock library was designed containing degenerate codons DNK in both positions S112 and K121. The degenerate codon DNK codes for all 20 amino acids except Gln, Pro and His. Gibson assembly was carried out with the **P1** backbone (obtained by PCR amplification with primers Gibson_backbone_fw and Gibson_backbone_rv) and the Sav gblock library to obtain the library for the in vivo screening.

DNA sequence of Sav – turquoise = gblock library purchased from Eurofins, and red = positions S112 and K121.

catgaccggtggccagcagatgggtcgtgatcaggcaggtattaccggcacctggtataatcagctgggtagcacctttattgttaccgcaggc
gcagatggtgcactgaccggtacgtatgaaagcgcagttggtaatgcagaaagccgttatgttctgacaggtcgttatgatagcgcaccggca
accgatggtagcggcaccgcactgggttggaccgttgcatggaaaaataactatcgtaatgcacatagcgcaaccacctggtcaggtcagtat
gttggtggtgcagaagcacgcattaatacccagtggctgctgaccagcggcaccaccgaagcaaatgcctggaaaagcaccctggttggtcat

gataccttaccaaagttaaaccgagcgcagcaagcattgatgcagcaaaaaaagccggtgtgaataatggtaatccgctggatgcagttcag cag

Primers used:

Gibson_backbone_fw: caaccaccacgtcttcgtgcgtaattatgggtcacc

Gibson_backbone_rv: gttggtcatgataccttaccaaagttaaaccgagcgc

PCR reaction to amplify P2 backbone with Gibson primers

To amplify the **P2** plasmid backbone a PCR reaction was carried out using the conditions depicted in Table S and Table S.

Table S2: General PCR conditions.

Reagents	**1 PCR reaction (µL)**
Q5 buffer, 5x	5
dNTPs (10 mM)	0.5
Gblock_backbone_fw (10 µM)	0.5
Gblock_backbone_rv (10 µM)	0.5
Plasmid prep template **P2** (25 ng/µL)	1
Q5 Hot Start DNA polymerase (2 U/µL)	0.25
ddH_2O	15.25
DMSO (8% final)	2
Total volume	25

Table S3: General PCR thermocycling protocol.

Initial denaturation		95 °C	2 min
25 cycles	Denaturation	95 °C	30 s
	Annealing	70 °C	15 s
	Extension	72 °C	5 min
Elongation		72 °C	10 min

Hold	8 °C	

After the PCR, DpnI (10 units) was added to the sample in order to digest the template **P2**. The mixture was incubated at 37°C for 2 h followed by incubation at 80°C for 20 min (heat inactivation of the digestion enzyme). The sample was then purified following the manufacturer´s protocol (Macherey-Nagel Nucleo Spin PCR clean up).

Gibson cloning of Sav gblock library into backbone P2

For a final amount of ~4000 clones 4x 20 µL Gibson reaction were set up in parallel using a 5-fold excess of the Sav gblock library (insert, 0.15 pmol final amount per 20 µL reaction) vs. the PCR amplified **P2** backbone (0.03 pmol final amount per 20 µL reaction). The Gibson reaction was carried out following the manufacturer´s protocol (New England Biolabs; incubation at 50°C for 60 min).

Transformation of Sav library plasmid P2 and GFP reporter plasmid P1 into Top10(DE3) cells

The transformation procedure was carried out in two steps. First, the Gibson-assembled Sav library plasmid **P2** was transformed with *E. coli* DH5α cells, and then isolated. In parallel, chemically-competent *E. coli* Top10(DE3) cells which already contain the GFP reporter plasmid **P1** were prepared. Finally, the isolated **P2** plasmid was transformed with the Top10(DE3) cells.

A volume of 2 x 5 µL Gibson reaction mixture was transformed with 2 x 50 µL chemically ultra-competent *E. coli* DH5α cells (New England Biolabs) using a heat shock method (42 °C). Afterwards, the cells were taken up in 2 x 1 mL LB-medium (containing 34 µg/ml chloramphenicol) and 2 x 50 µL thereof were transferred onto LB-agar$_{cam}$ plates and incubated at 37 °C overnight. The remaining 2 x 950 µL were incubated overnight (37 °C, 250 rpm). On the two LB-agar plates ~2500 colonies were counted, which corresponds to a total number of ~47000 individual clones present in the liquid culture. The plasmids were then isolated following the manufacturer´s protocol (Macherey-Nagel Nucleo Spin Plasmid kit). A minimal amount of the isolated plasmid (1 ng) was transformed into chemically competent *E. coli* TOP10(DE3) cells (50 µL) which already contain the **P1** plasmid using a heat shock method (42 °C). In this way it should be guaranteed that the final cells only

contain one individual streptavidin clone per cell. Afterwards, the cells were taken up in 1 mL LB-medium (containing 34 µg/mL chloramphenicol and 100 µg/mL ampicillin) and 20 µL thereof were transferred onto LB-agar$_{Cam, Amp}$ plates and incubated at 37 °C overnight. The remaining 980 µL were incubated overnight (37 °C, 250 rpm). On the LB-agar plate ~70 colonies were counted, which corresponds to a total number of ~3400 individual clones present in the liquid culture.

Sequencing and evaluation of the library

2 x 96 colonies from the final library (section 0) were sequenced and the amino acid distributions at the positions S112 and K121 were evaluated (Figure S5). 58% of the sequenced colonies were desired single or double mutants, 12% contained the initially used template (K121A), 17% contained a frame shift within the gene, 4% contained an unwanted stop codon or an insert and 9% of the sequencing gave unclear results.

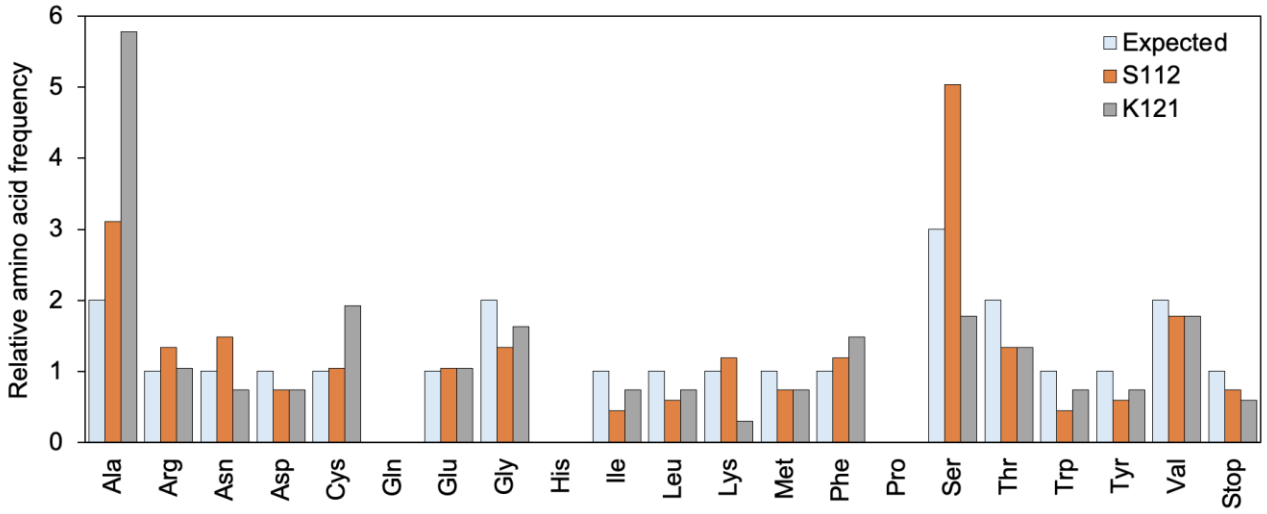

Figure S5: Amino acid distribution of the prepared streptavidin double site saturation library at positions S112 and K121.
The relative amino acid frequencies calculated from 162 sequenced colonies are displayed. The expected amino acid frequencies were calculated based on the degenerate codon DNK.

We applied the following equation to calculate the number of transformants which need to be tested in order to obtain a certain coverage of the library (Equation S1).[204]

$$T = -V * \frac{1}{S} * \ln(1 - P_i)$$

Equation S1: Estimation of the number of colonies to be screened to reach a certain coverage of the library.

T: Number of transformants to be tested, V: Number of variants within the library, S: Percentage of correct sequences within the library, P_i: Percentage of coverage.

Two degenerate DNK codons at the positions S112 and K121 lead to a total number of variants within the library of V = 24^2 = 576. With S = 58% of correct sequences in the library and a total number of T = 2762 analyzed transformants, we obtained a percentage of coverage of P_i = 93.8%.

High throughput screening of surface-displayed ADAses

The 96-well plate assay was carried out following a modified protocol described by Jeschek *et al.*[94]

Stock solutions:

Biotinylated ligand **6**:	5 mM in DMF
[CpRu(MeCN)$_3$]PF$_6$:	5 mM in DM
Ruthenium cofactor **1**:	2 mM in DMF (e.g. 60 µL of ligand **6** stock was mixed with 60 µL **[CpRu(MeCN)$_3$]PF$_6$** stock and 30 µl DMF and incubated for 5 min at room temperature)
PBS buffer:	50 mM NaH_2PO_4/Na_2HPO_4 (set to pH 7.4), 0.9 % NaCl
LB medium:	10 g/L tryptone, 5 g/L yeast extract, 10 g/L NaCl, 100 µg/mL ampicillin, 34 µg/mL chloramphenicol
Modified Studier 5052 medium:	25 mM Na_2HPO_4, 25 mM KH_2PO_4, 50 mM NH_4Cl, 5 mM Na_2SO_4, 2 mM $MgSO_4$, 0.5% glycerol, 15 g/L tryptone and 10 g/L yeast extract, 100 µg/mL ampicillin, 34 µg/mL chloramphenicol
Cofactor buffer (2 µM):	2 µM ruthenium cofactor **1** in PBS buffer
Atto 565-Biotin buffer (2 µM):	2 µM Atto 565-Biotin in PBS buffer
Substrate buffer (500 µM):	500 µM substrate **3** in modified Studier 5052 medium

Cell cultures and protein expression:

All pipetting steps were performed with a 96-well pipetting station from Integra.
In a 96-flat well-plate, 120 µL of LB-medium were inoculated with fresh colonies of Sav cells (Top10(DE3): pBAD33_Lpp-OmpA-Sav + pDmpR_GFP). Each 96-flat well plate contained 90 colonies and 6 control samples (3x: empty cells; 3x: Sav S112M-K121A). After incubation overnight (37 °C, 200 rpm), 100 µL of LB-medium were added to the preculture plate. 300 µL of modified Studier 5052 medium were filled into a fresh 96-deep well plate and then inoculated with 10 µL preculture. The main cultures were incubated at 37 °C for 3.75 h at 380 rpm followed by addition of 30 µL of a 2 % L-arabinose solution (0.2 % final concentration) and incubation for 4 h at 25 °C and 380 rpm. The optical density OD_{600} of the culture after streptavidin expression was determined to be 7 – 8.

Cofactor loading:

The plate was centrifuged (5 min, 10°C, 3.200 g), the supernatant was discarded and the pellets were resuspended in 600 µL ice-cold PBS buffer. In case of a subsequent determination of the streptavidin expression level, an aliquot of 50 µL was transferred into a new 96-deep well plate (was only done for the final hits). The plate was centrifuged (5 min, 10°C, 3.200 g), the supernatant was discarded and the pellets were resuspended in 600 µL cofactor buffer. The cells were incubated on ice for 30 min. Finally, the plate was centrifuged (5 min, 10°C, 3.200 g), the supernatant was discarded and the cell pellets were washed 2 x in 600 µL ice-cold PBS buffer.

Catalysis:

The pellets were resuspended in 200 µL substrate buffer (or modified Studier 5052 medium containing a defined amount of product **2**), the 96-deep well plate covered with a porous cover slide and incubated at 30 °C, 380 rpm for 16 h. The optical density OD_{600} of the culture at the beginning of the catalysis was determined to be 11-12. After the catalysis, 10 µL of the reaction mixture were mixed with 190 µL PBS buffer in a transparent 96-flat well plate. The optical density OD_{600} of the

cells as well as the GFP fluorescence (excitation = 475 nm, emission = 509 nm) were measured using a TECAN plate reader.

Determination of the relative Sav expression levels:

The plate containing the 50 µL aliquots (from section 0) was centrifuged (5 min, 10°C, 3.200 g), the supernatant was discarded and the pellets were resuspended in 50 µL Atto 565-Biotin buffer. The cells were incubated on ice for 30 min. The plate was centrifuged (5 min, 10°C, 3.200 g), the supernatant was discarded and the cell pellets were washed 2 x in 600 µL ice-cold PBS buffer. The pellets were resuspended in 200 µL PBS buffer and 150 µL of the cell suspension was transferred into a flat 96-well plate. The Atto 565 fluorescence of cells was measured in a plate reader (TECAN, excitation at 565 nm and emission at 590 nm, Figure S6).

Evaluation of the screening results

The variation of ADAse activity/GFP expression level of a 96-deep well plate containing 96 times the wt-Sav ADAse was determined. No notable discrepancy of the GFP expression level vs. position within the 96-well plate was observed.
The 10 best hits from the library screening (K121D, K121E, K121G, K121N, S112M-K121R, S112M-K121T, S112T-K121A, S112T-K121G, S112T-K121N, S112T-K121T), the according single mutants (S112M, S112T, K121A, K121R, K121T) as well as the wild-type (wt-Sav), the mutant S112M-K121A and the empty vector control were selected and rescreened (Figure S6)

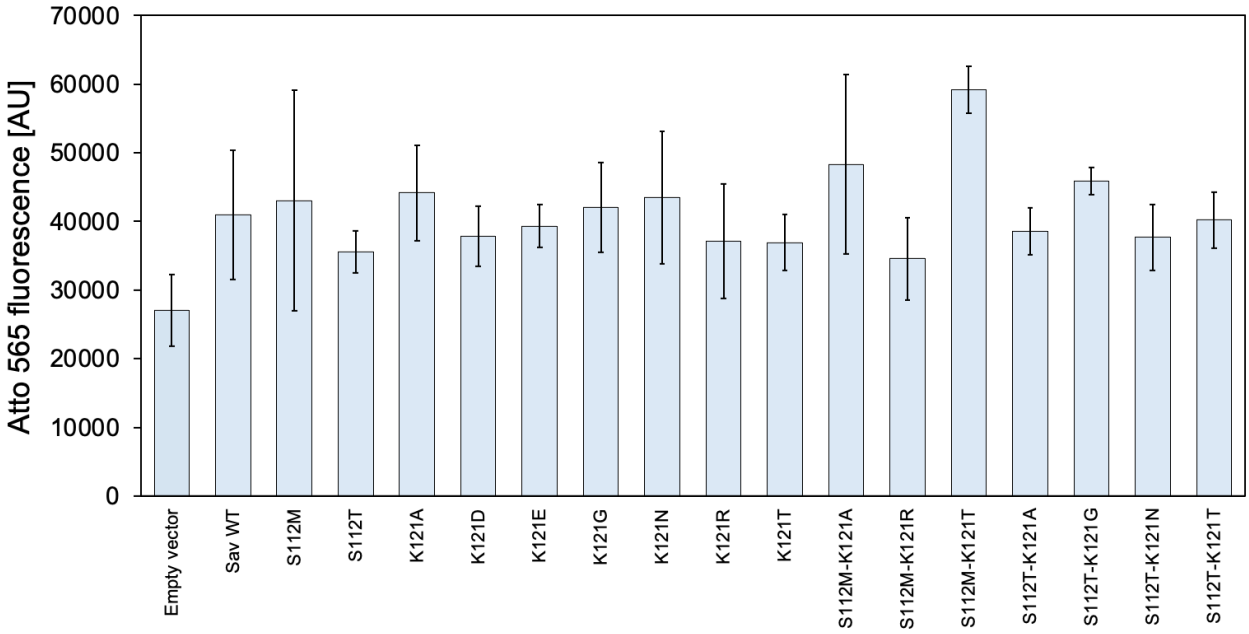

Figure S6: Determination of the relative Sav expression levels on the surface of *E. coli* cells.
The relative Sav concentrations on the *E. coli* cell surface were determined via labelling with the biotinylated Atto 565-Biotin dye (section 0). Displayed are the mean values of the Atto 565-fluorescence (excitation = 565 nm, emission = 590 nm) ± 1 standard deviation of a measurement with eight repetitions.

Crosslinking Experiments

Preparation of the crosslinked samples

Precultures of *E. coli* TOP10(DE3) cells containing the plasmid for the Lpp-OmpA-Sav, and the empty vector, were prepared in LB-medium (34 µg/ml chloramphenicol) and incubated overnight at 37°C and 300 rpm shaking in a 15 mL culturing tube. The modified Studier 5052 medium (25 mL, 34 µg/ml chloramphenicol) was inoculated to an OD_{600} of 0.05 in a 250 mL baffled shake flask. The main culture was incubated (37°C, 300 rpm) until an OD_{600} of 0.4 – 0.8 was obtained (~2 h). The Sav expression was induced by addition of 0.2% L-arabinose and Sav was expressed for 24 h at 25°C and 300 rpm.

Cells (OD_{600} = 5.0) from the cultivation were transferred into Eppendorf tubes, spun down and washed with ice-cold PBS (2x 500 µL). The pellets were then resuspended in 100 µL PBS and crosslinked with BS^3 (40 µL from a 25 mM stock solution, 8 mM final concentration) and incubated at room temperature for 30 min before the crosslinking was terminated with Tris-buffer (1 M, pH 7, 150 µL). The cell suspension was centrifuged and the supernatant discarded. Following, B-PER (200 µL) was added to the pellet and incubated for 1 h at 30 °C. After incubation, the samples were clarified by centrifugation (21'100 g, 15 min). The supernatant was separated and 10 µl were directly taken for analysis (sample 1). 10 µL were denatured in SDS sample buffer (6 x Lämmli Buffer, 95 °C for 30-45 min) to give sample 2. The remaining pellet was resuspended in urea (200 µL, 8 M in 20 mM Tris-HCl buffer) and incubated for 30 min at 37°C. After incubation, the samples were clarified by centrifugation (21'100 g, 15 min) and the supernatant was denatured (6 x Lämmli Buffer, 95 °C for 30-45 min) to give sample 3.

Purified protein controls

All control samples were prepared from purified and lyophilized wt-Sav (pp-Sav). A stock solution of pp-Sav (2 mg/mL) was prepared in PBS. For samples **2-6**, 10 µL of the stock solution was crosslinked with BS^3 (4 µL from a 25 mM stock solution, 10 mM final concentration) and incubated on ice (5 min). The reaction was terminated with Tris-buffer (1 M, pH 7, 10 µL). If B4F was added, B4F (2 µL) and Lämmli-buffer (20 µL, 6x conc.) otherwise only Lämmli-buffer (20 µL, 6x conc.) were added. If the probe was denatured, the sample was incubated at 95 °C for 30-45 min prior to the loading on the gel. Sample **e)** was first denatured, then crosslinked and B4F added.

SDS-PAGE and Western Blot

Two identical gels were loaded with 10 µL of each prepared sample and then run at 140 V for ~50 min. After completion, one gel was stained with a Pierce™ Silver staining kit according to manufacturer's protocol.

The second gel was transferred to a nitrocellulose membrane at 45 V overnight. After completion of the transfer, the membrane was quickly rinsed with water and blocked with TBST (Tris-buffered

saline + 0.5% Tween 20) containing 4% BSA (25 mL) at RT for 1.5 h. After rinsing the membrane twice with TBST the membrane was incubated in fresh TBST (20 mL) containing the primary antibody (100 µL of a polyclonal serum). After thorough washing with TBST (4 x 10 min) the membrane was incubated in fresh TBST (20 mL) containing the secondary antibody fused with HRP (10 µL). After washing the membrane with TBST (4 x 10 min) the detection was carried out according to manufacturer's protocol.

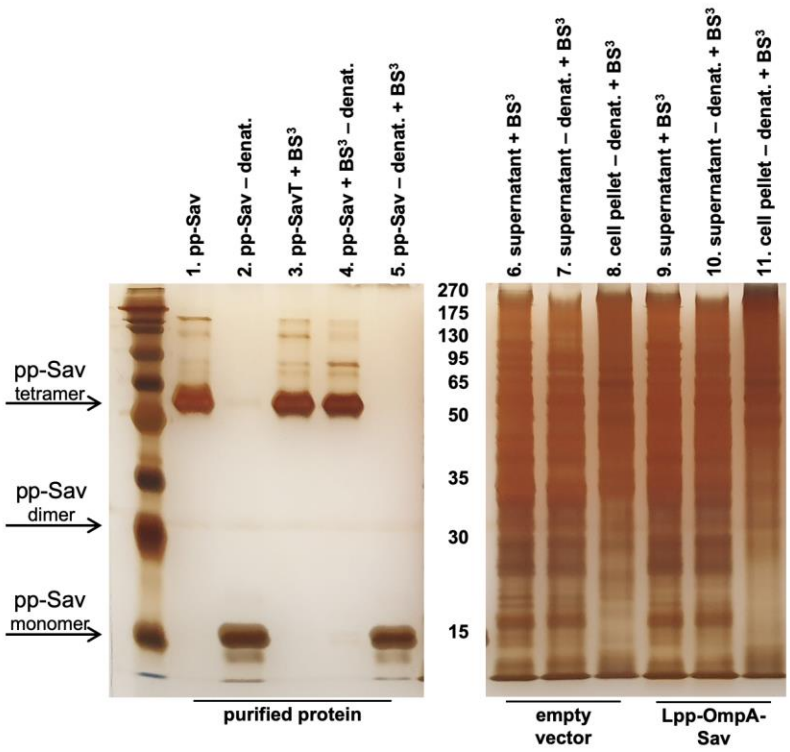

Figure S10. SDS-PAGE analysis of the quaternary structure of Sav^{SD} (visualized by silver staining). Lane 1 and 2 weren't cross-linked. For lane 3 to 11, except for lane 5, all samples were crosslinked with BS^3 prior to any additional treatment. All denatured samples were treated under the same conditions: SDS sample buffer, 95°C, 30 min. 1) pp-Sav, 2) denatured pp-Sav, 3) crosslinked pp-Sav, 4) crosslinked and then denatured pp-Sav, 5) denatured and then crosslinked pp-Sav, 6) empty vector, supernatant, 7) empty vector, denatured supernatant, 8) empty vector, denatured cell pellet 9) Sav^{SD}, supernatant, 10) Sav^{SD}, denatured supernatant, 11) Sav^{SD}, denatured cell pellet.

Deconvoluted mass spectra of the purified proteins

K121D (expected MW: 16412.82 g/mol)

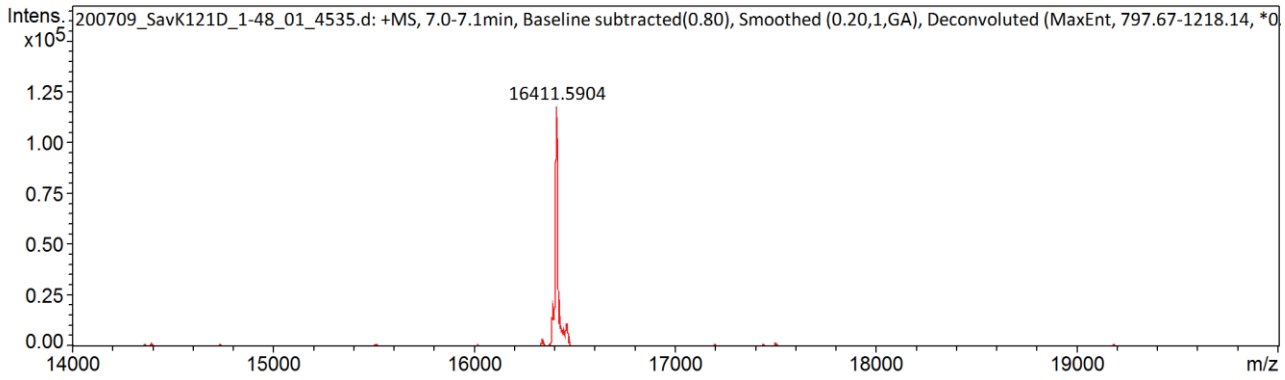

K121E (expected MW: 16426.84 g/mol)

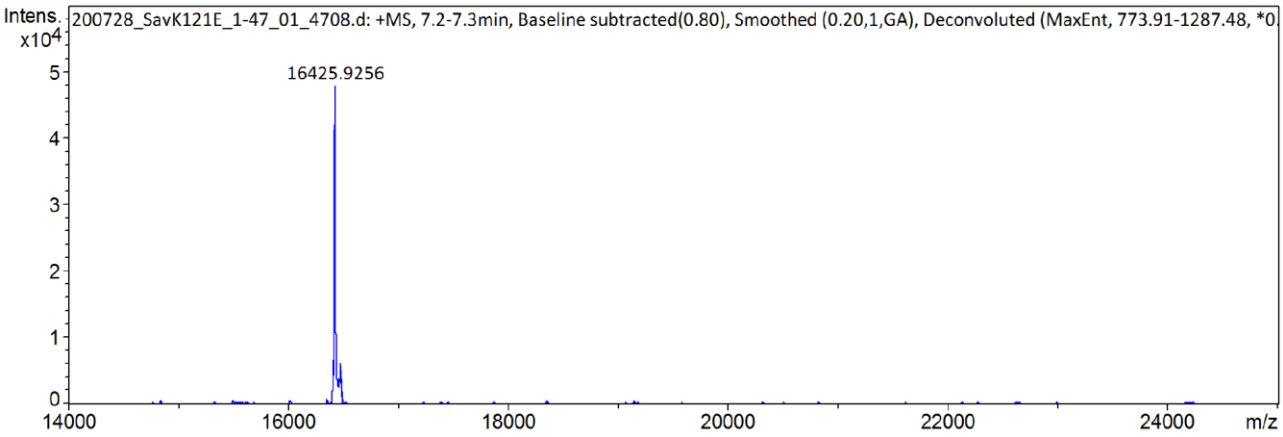

K121G (expected MW: 16354.78 g/mol)

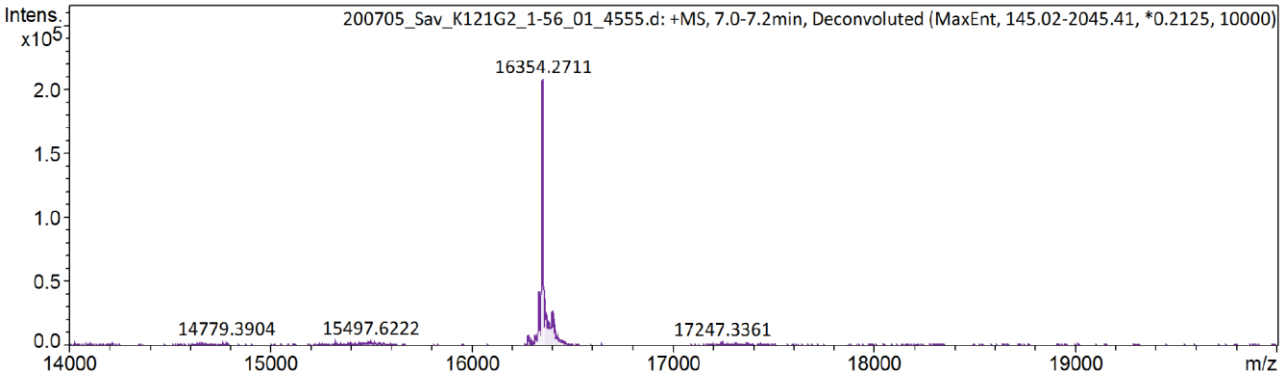

K121N (expected MW: 16411.83 g/mol)

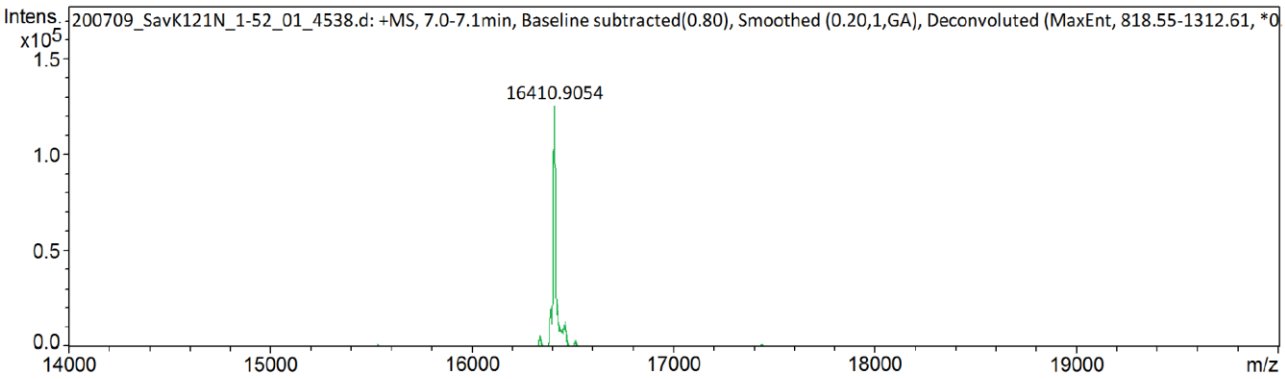

S112M-K121R (expected MW: 16498.03 g/mol)

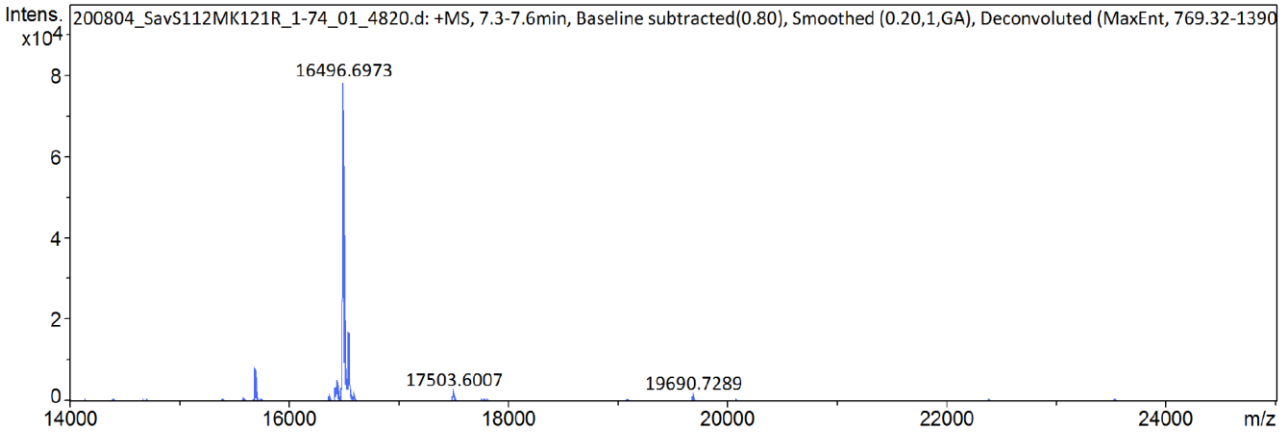

S112M-K121T (expected MW: 16442.95 g/mol)

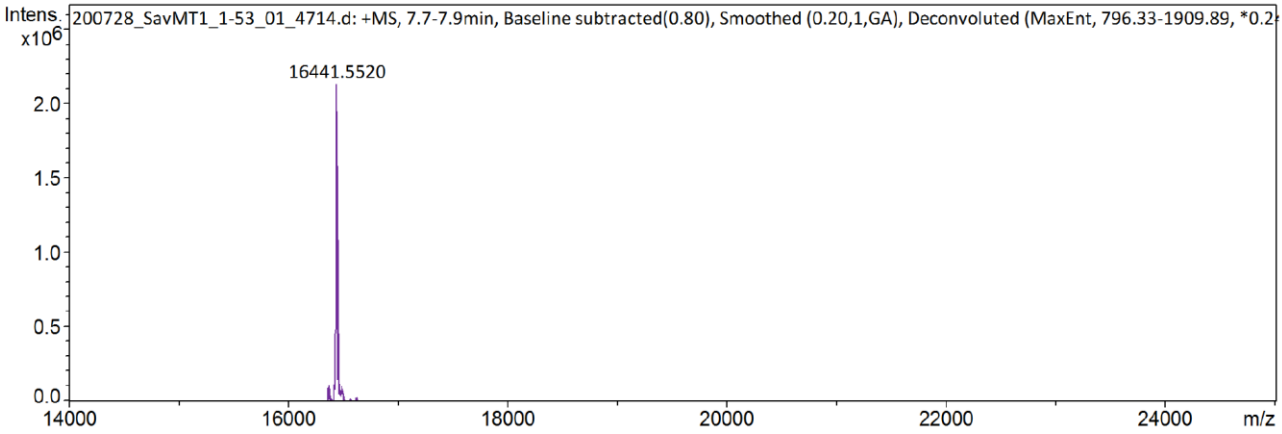

S112T-K121A (expected MW: 16382.83 g/mol)

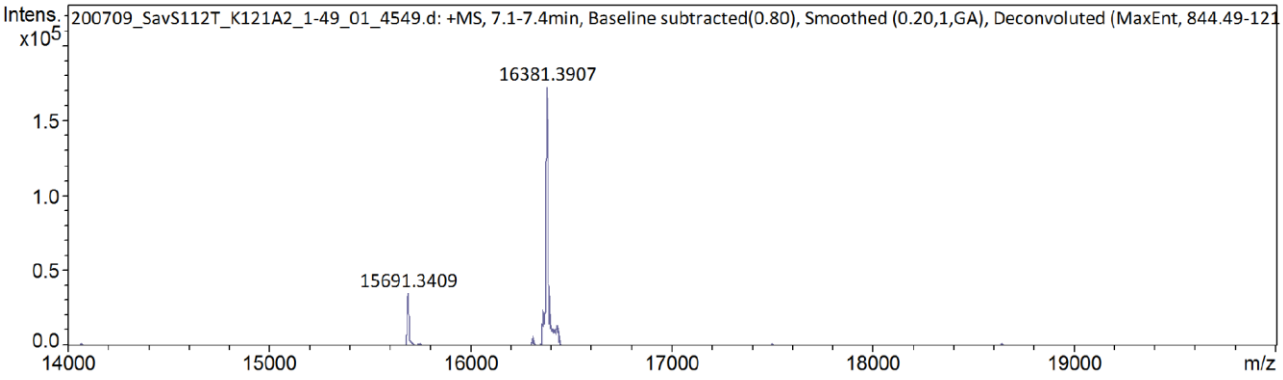

S112T-K121G (expected MW: 16368.81 g/mol)

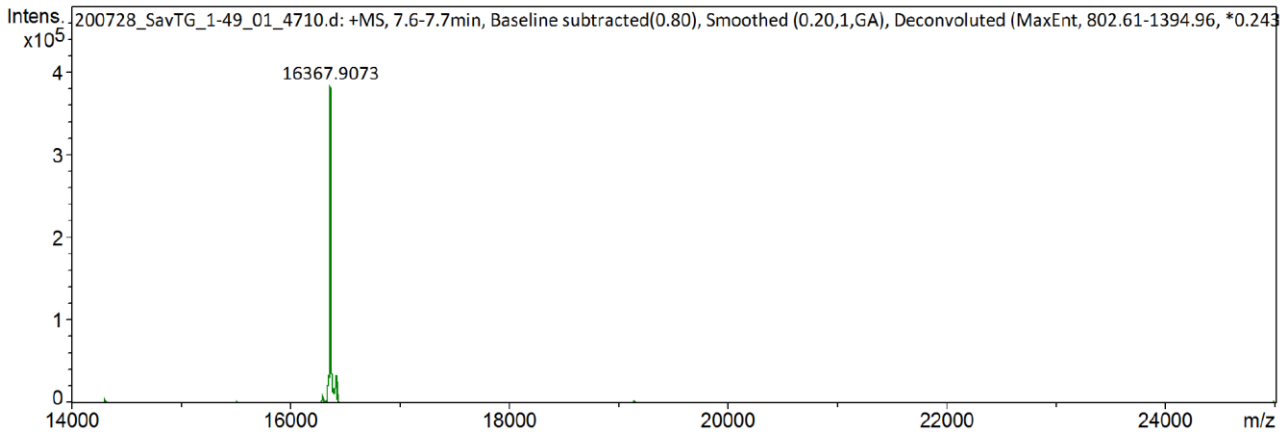

S112T-K121N (expected MW: 16425.86 g/mol)

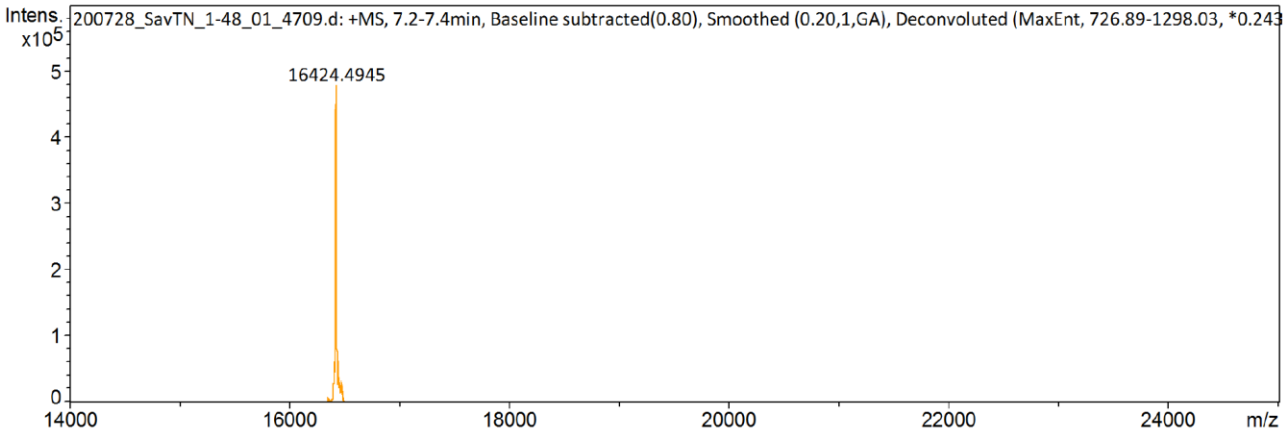

S112T-K121T (expected MW: 16412.86 g/mol)

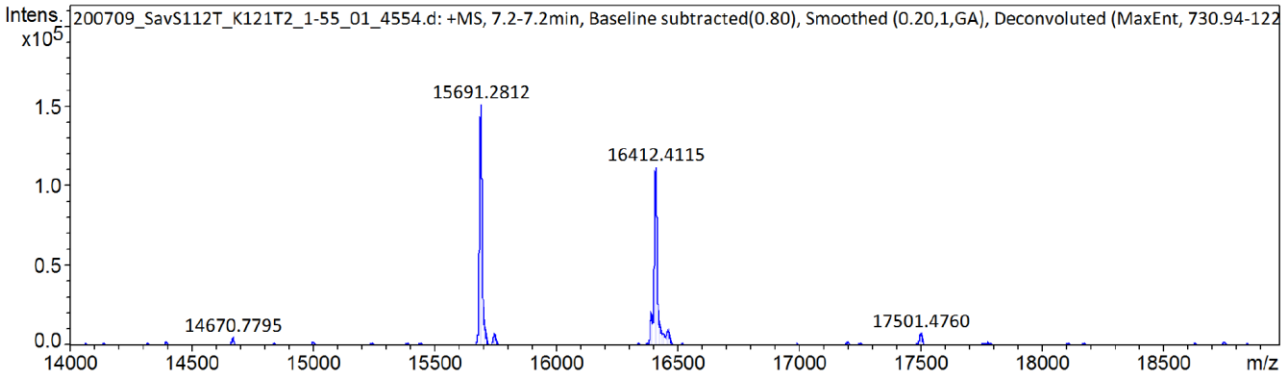

Chapter 4: The two Janus faces of CpRu-based deallylation catalysts and their application for in cellulo prodrug uncaging.

Alain Baiyoumy, Robin Vinck, Thomas R.Ward*

University of Basel, Department of Chemistry, Mattenstrasse 24a, 4058 Basel, Switzerland.

Author contribution

AB conceived the project, performed all in vitro experiments, developed the analytical methods, and wrote the manuscript with input from RV and TRW. RV carried out all the in cellulo experiments and the associated analytics, and revised the manuscript. TRW conceived and supervised the project and revised the manuscript.

The two Janus faces of CpRu-based deallylation catalysts and their application for in cellulo prodrug uncaging. 92

Abstract

In the past 16 years, metal-catalyzed deallylation has proved helpful in the study of biological processes in cellulo and the early development of innovative therapeutic catalytic strategies. This reaction is catalyzed by a class of Ru(II)-precatalysts and has been claimed to be compatible with air, water, and thiol-containing compounds such as glutathione. However, little is known about the actual influence of biological components on the outcome of this reaction. The results presented herein show that the co-solvent used in this reaction can drastically affect the stability of the complex in air and so the conversion, while the presence of glutathione helps reduce the formation of allylated by-products. In addition, while this catalyst class has been described as air-stable, we show this is not the case. In the presence of air, the complex is deactivated and oxidizes thiol into disulfide. A mechanism for this degradation pathway is proposed.

3.1 **Introduction**

In 2006, Meggers and co-workers reported the use of [Cp*Ru^{II}(cod)Cl] (Cp* = cyclopentadienyl and cod = cyclooctadiene) to catalyze the deprotection of alloc-protected amines in the presence of thiol and air.[205] In 2014, Meggers reported the use of [CpRu^{II}(NMe$_2$-QA)(solv)] (QA = quinaldic acid) **1** or [CpRu^{IV} (NMe$_2$-QA)(η^3-allyl)] **2** for the same reaction and proposed a catalytic cycle, Figure 1.[41]

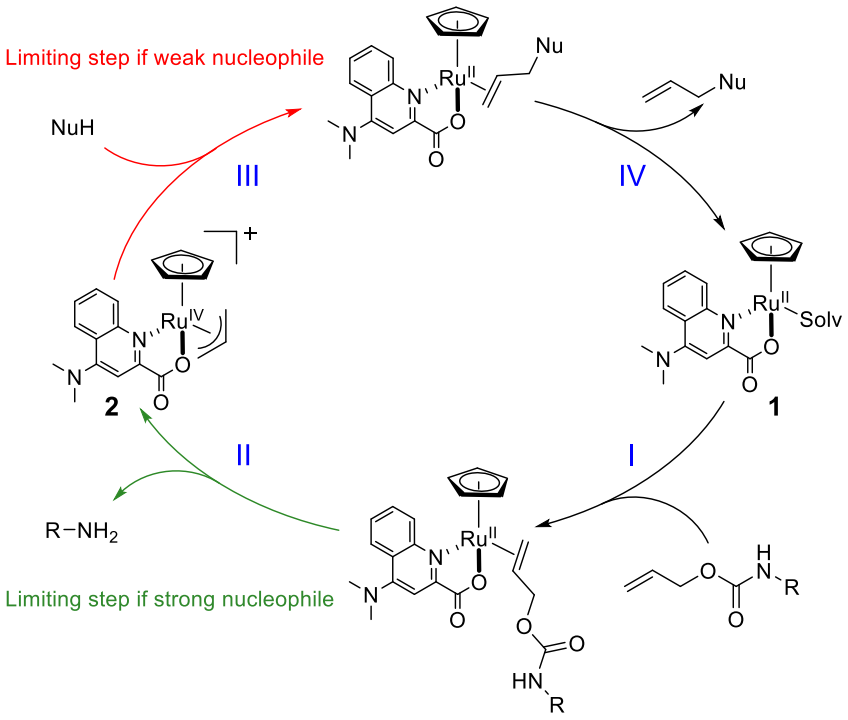

Figure 1: Proposed mechanism for the Ru-catalyzed deallylation of Alloc-protected amines. **I**] Coordination of the alloc-protected amine to **1**. **II**] Oxidative addition of the allyl moiety to the Ru(II)-center affording the Ru(IV)(η^3-allyl) complex **2** and the uncaged amine R-NH$_2$. **III**] Nucleophilic addition on **2** resulting in a coordinated Ru(II)(η^2-alkene) complex. **IV**] Regeneration of the Ru(II) catalyst by alkene-displacement by the solvent (solv). Adapted from Meggers and co-workers.[22]

In 2009, Kitamura and co-workers investigated how the substituent on the chelating ligand affects catalytic activity.[44] They found that electron-withdrawing groups are beneficial to the activity. However, Meggers and co-workers found that electron-donating groups are beneficial to activity. This difference may be caused by the different substrates used in these studies:[41] According to Meggers' work, a strong donating group on the ligand benefits the deallylation of electron-poor allylic substrates. In Kitamura's case, electron-withdrawing solid groups on the ligand favored the reaction for electron-rich allylic substrates.

§

While thiols are generally poisonous to soft-metal-based catalysts, the CpRu-based deallylation catalysts reported by Meggers were shown to maintain their activity *in cellulo*, despite the presence of millimolar concentrations of reduced glutathione (GSH hereafter) in the cytoplasm of aerobic cells [41,49,56,57,62,65,68,69,206,207]. The functionalization of η^3-allyls with thiols nucleophiles using these catalysts was described.[48,208] This inspired multiple studies, whereby derivatives of catalysts **1** or **2** were used to uncage *a* variety of alloc-protected cargoes *in cellulo*, including fluorophores, drugs, hormones, amino acids, etc.[54,56,57,61,62,64–69,76,206,207,209–212]

In 2010, Waymouth and co-workers formulated a more detailed description of the catalyst's behavior in the presence of solvent and oxygen.[213] They also showed that the reaction did not proceed to completion in the presence of oxygen, possibly due to the oxidative degradation of the ruthenium complex. This suggested a possible competition between catalyst oxidative degradation and deallylation reactions. Wender and co-workers also observed another issue with the system, arising from a side reaction linked to the nucleophilic nature of the uncaged amine. Indeed, the uncaged primary amine may act as a parasite nucleophile, which attacks the η^2-alkene to afford the corresponding (di)- allylated amine. Aiming to improve the performance of CpRu(II)-based deallylation catalysts, we set out to investigate how the presence of GSH, O_2, and the nature of the co-solvent affect the reactivity and the stability of Ru(II) intermediate **1** and the resulting product distribution, using a coumarin derivative as a substrate.

3.2 **Results and Discussion**

It has been observed, both in our lab and elsewhere, that air affects Ru-catalyzed reactions involving η^3-allyl precursors. Moreover, the solvent also has a pronounced effect on the reactivity and stability of the complex in the presence of air.[84] To probe this further, we performed a set of ^{1}H NMR experiments in the presence/absence of air and using different organic co-solvents. The resulting ^{1}H NMR spectra highlight the strong influence of the solvent on the stability of catalyst **1**, Figure 2.

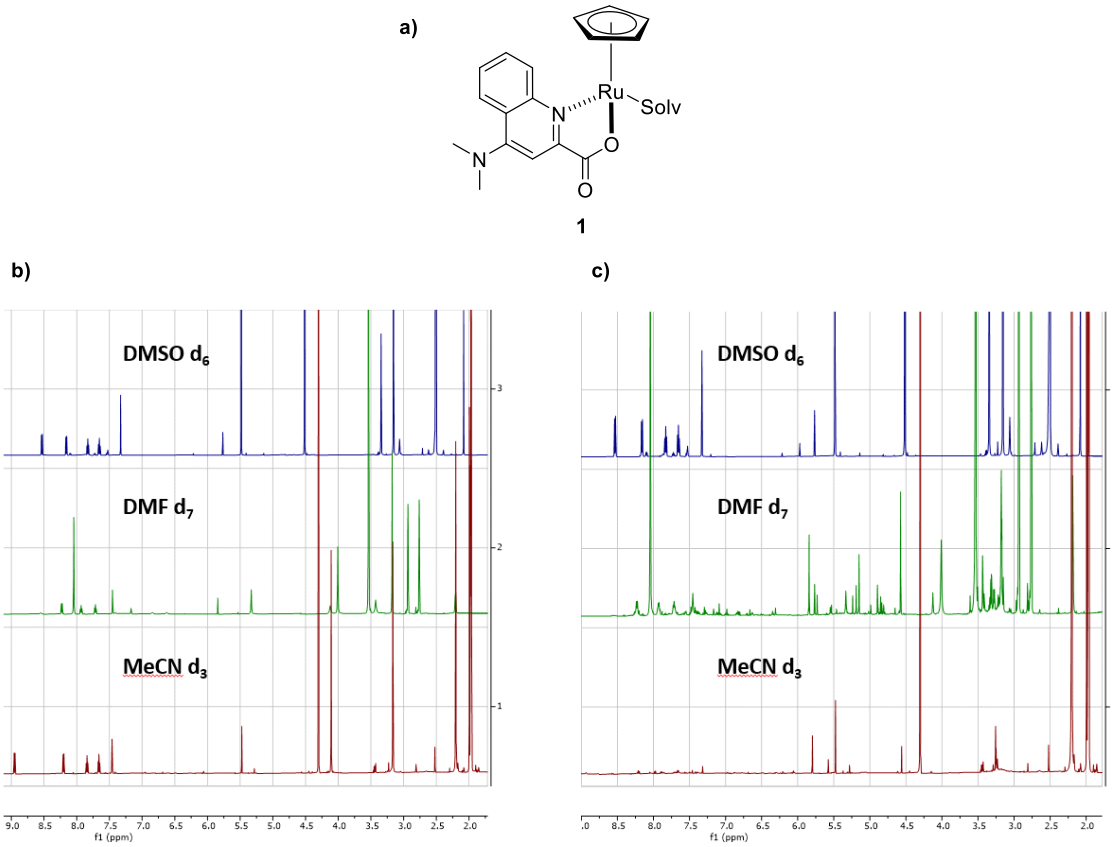

Figure 2: ^{1}H NMR spectra of catalyst **1** recorded in different deuterated solvents: **a)** Structure of catalyst **1. B)** ^{1}H NMR recorded in the absence of air. **C)** ^{1}H NMR recorded following 15 min of exposition to air. Additional peaks can be observed in the case of MeCN and DMF, but not in DMSO.

Figure 2b) displays the ^{1}H NMR of **1** recorded in different solvents without air. Figure 2c) displays the NMR spectrum of the same sample exposed to air for 15 minutes. An apparent degradation of **1** is observed when DMF and MeCN are used as solvents. The NMR spectrum recorded in DMSO remains unchanged following exposure to air, raising the question of the solvent`s influence on the stability of the complex.

According to Meggers, the Ru-based catalytic deallylation reaction is more efficient in the presence of thiols, which act as strong nucleophiles. Thiols react faster than water or the reaction product with the allyl from Ru(IV) intermediate **2** and thus regenerate **1** more quickly, Figure 1.[41,49] This finding sparked our interest since thiols, such as reduced glutathione (GSH), are present at high concentrations in intracellular environments and have thus impeded our work on intracellular catalysis using artificial metalloenzymes.[92] We thus set out to probe the mechanistic role of thiols, specifically glutathione, in more detail.

First, the stability of Ru(II) intermediate **1** in the presence of GSH was evaluated in deuterated water by mixing GSH (100 eq. vs. **1**) with Ru(II) intermediate **1** in the presence/absence of air.

While no significant change was observed in the ^{1}H NMR spectrum in the absence of air, the oxidized form of GSH, GSSG, was detected in the presence of air, Figure 3. Thus, in air and Ru(II) intermediate **1**, GSH is oxidized into GSSG. In the absence of air, it remains in its reduced form. Ru(II) intermediate **1** is required for this oxidation process as triplet dioxygen does oxidize GSH (see Supporting Information).

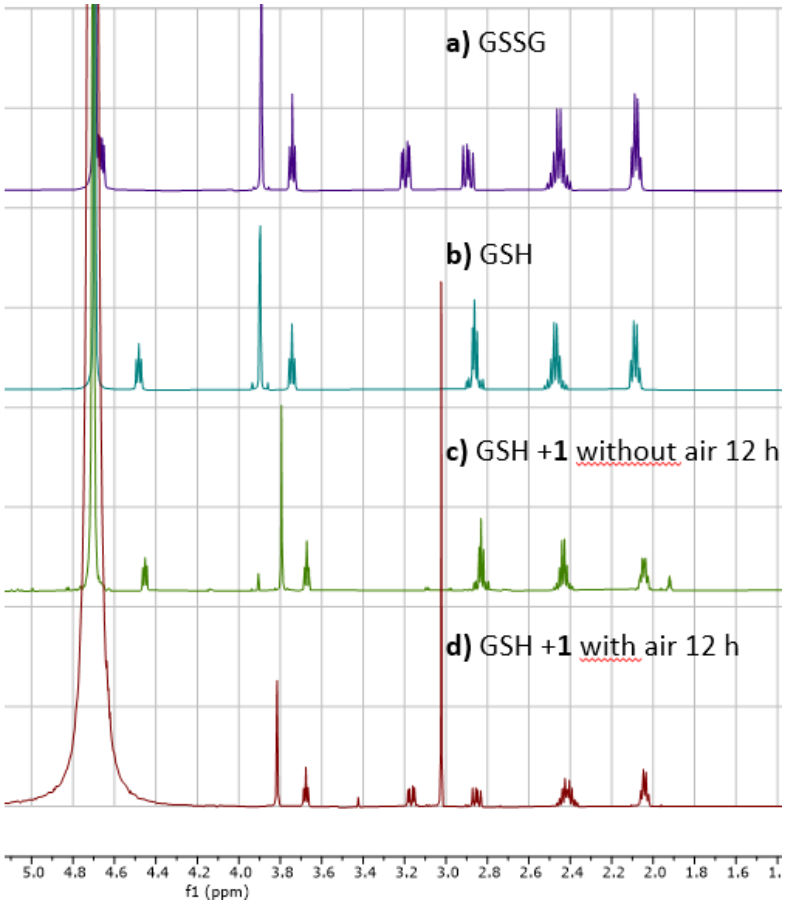

Figure 3: ^{1}H NMR spectra of GSSG, GSH, and the conditions used to study the formation of GSSG from GSH in D_2O + 1% co-solvent (here, MeCN). a) ^{1}H NMR of GSSG. b) ^{1}H NMR of GSH. c) ^{1}H NMR of GSH + 5 mol% **1** without exposure to O_2 and d) ^{1}H NMR of GSH + 5 mol% **1** after exposure to O_2. The signal at 3.02 ppm corresponds to the NMR standard dimethylsulfone. Sample preparation: total volume 500 µL, 475 µL D_2O, 20 µL GSH (50 mM stock solution), 5 µL (10 mM stock solution) prepared in inert conditions. After the reaction, 100 µL of dimethylsulfone (6 mM stock) was added to the tube (with exposure to air).

These results show that GSH is oxidized into GSSG in the Ru(II) intermediate **1** and air presence. If the complex itself can oxidize GSH in cellulo, it could support the use of this catalyst for the uncaging of a cytotoxic drug.[214] Indeed, it has been shown that the oxidation of GSH into GSSG inside cells can affect its redox balance, eventually leading to cell death.[215] The release of a cytotoxic drug from a non-cytotoxic pro-drug would thus be combined with the perturbation of

the redox environment of the cells by oxidizing GSH into GSSG. However, for this to be useful, the reaction should be catalytic. A set of reactions was therefore performed with different complexes to investigate whether GSH oxidation is indeed catalytic, Figure 4.

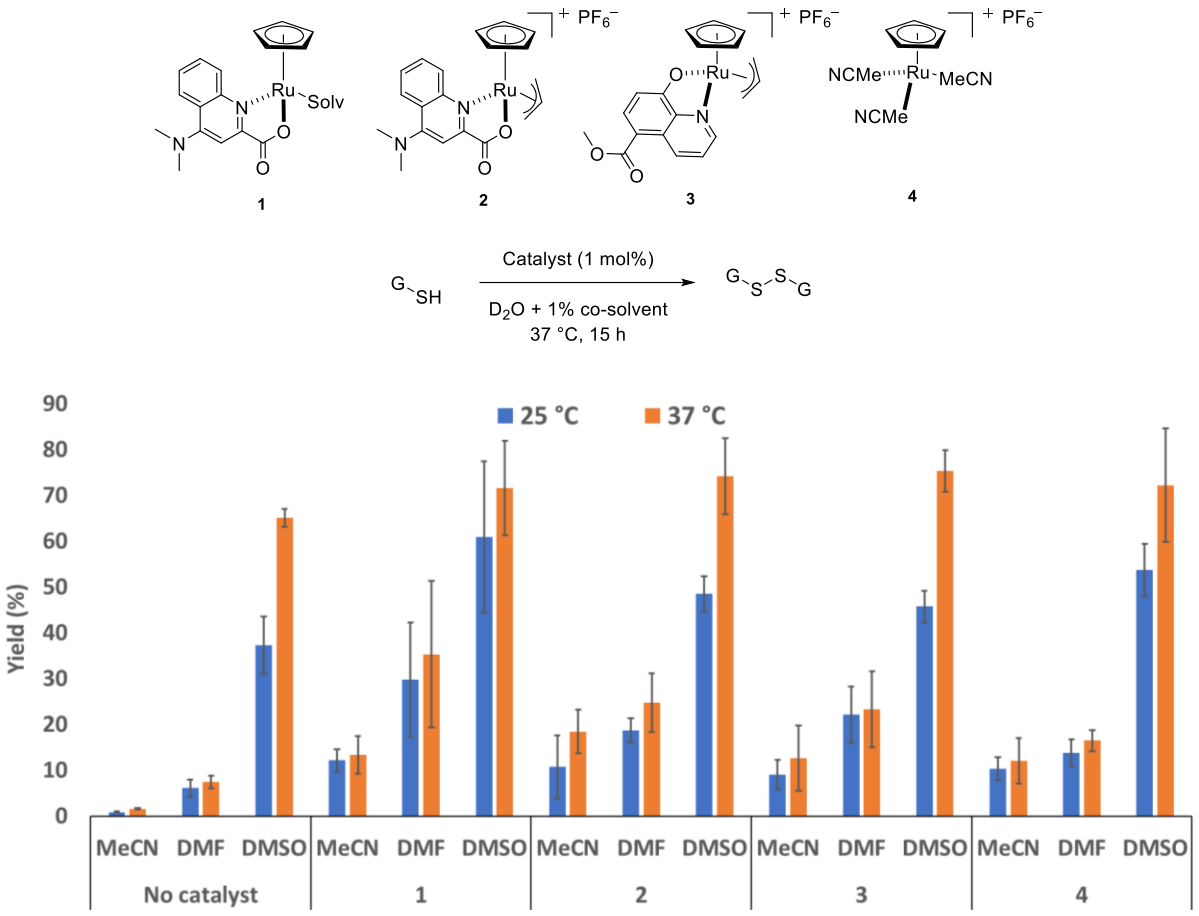

Figure 4: ^{1}H NMR-Quantification of glutathione oxidation catalyzed by CpRu catalysts **1-4**. Three parameters were varied, temperature, co-solvent, and catalyst. Reaction conditions: [GSH] = 10 mM; [CpRu(QA)(] **1** = 1 mol%, co-solvent = 1%; final volume = 500 µL.

The results in Figure 4 indicate that GSH oxidation, in the case of MeCN and DMF, is enhanced by catalysts **1**-**4**. This suggests that the Ru-based catalyst activates oxygen, enabling the oxidation of thiols. This oxidative process could partly explain why these deallylation catalysts have been reported to be active *in cellulo* and even mammalian cells. Indeed, the Ru-catalyzed oxidation of GSH may minimize the detrimental effect of GSH on the soft metal center. Strikingly, when DMSO is used as a co-solvent, GSH is oxidized even without any catalyst. It should be noted that Walker and co-workers have previously reported the spontaneous oxidation of DMSO by GSH.[216] To exclude the role of contaminants present in DMSO, we confirmed this reactivity by performing the reaction with five different sources of DMSO and in the absence of oxygen, Figure S4. The effect of oxygen on the catalytic deallylation reaction remains to be elucidated. With this goal in mind, we

narrowed the study to catalysts **1** and **2** bearing a quinaldic acid chelate and their precursor **4**, as HQ-based complexes have been reported to be cytotoxic.[84,98]

The Ru-catalyzed deallylation of the alloc-protected coumarin **5** was selected as a test reaction to study the influence of oxygen on the reaction. The use of DMSO as a co-solvent was inspired by Meggers's standard conditions, even though DMSO spontaneously oxidizes GSH. We then compared the catalytic activities of catalyst **1**, **2**, and **4** in DMSO for the deallylation of **5** in the presence and absence of glutathione and air, Figure 5 (see Table S1 for details). Based on the results presented above, using DMSO as a co-solvent might affect the concentration of reduced GSH in the reaction mixture. However, the concentration of DMSO used was fourteenfold that of GSH (140 mM vs. 10 mM for GSH), thus favoring the formation of GSSG.

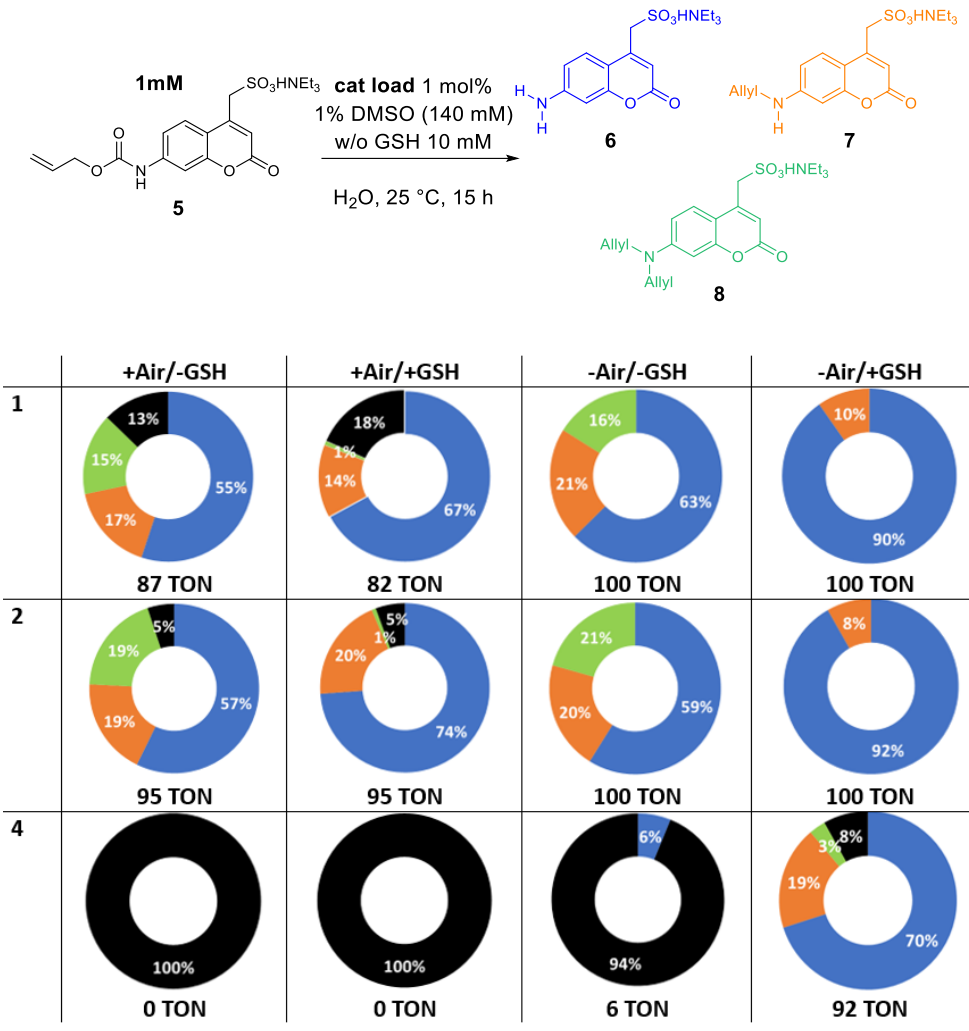

Figure 5: Deallylation of the alloc-protected coumarin **5** with CpRu-based catalysts in 1% DMSO in water, highlighting the distribution of the various aminocoumarin products **6-8.**

Much information can be extracted from this experiment. Firstly, the catalytic activity with **1** and **2** is partly decreased, and **4** severely so, by the presence of air. Ru(II) intermediate **1** is more sensitive to the presence of air than Ru(IV) intermediate **2**, probably due to the difference between Ru^{II} and Ru^{IV} stability against oxygen.[217] Secondly, the product repartition is dependent on the presence of GSH. The formation of product **8** is prevented when GSH is used, while product **7** is always formed even in the presence of GSH. Additionally, GSH forms an active catalyst with pre-catalyst **4** without air but loses its activity when exposed to air. Finally, the presence of GSH does not impede the overall conversion. However, the potential role of GSH here is highly attenuated by the large consumption of GSH by DMSO, leaving only a fraction of the initial GSH loading.

A possible explanation for forming products **7** and **8** could be the following. The formation of product **7** occurs during the deallylation step. Product **6** is formed and remains near the CpRu(IV) **2,** preferentially acting as a nucleophile. This contrasts the formation of product **8,** which requires intermediate **7** to act as a nucleophile while remote from the CpRu(IV) **2** moiety.

The presence of air does not affect the catalyst when DMSO is used as a co-solvent, which is reflected in Figure 8. Nevertheless, the ^{1}H NMR spectrum of Ru(II) intermediate **1** in DMF or MeCN displayed a lack of stability against oxygen. We then investigated the influence of these solvents as co-solvent of the reaction using Ru(II) intermediate **1** as a catalyst, Figure 9.

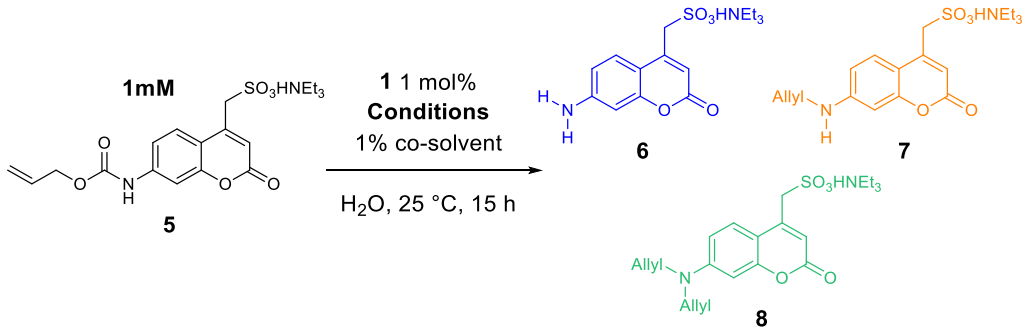

§

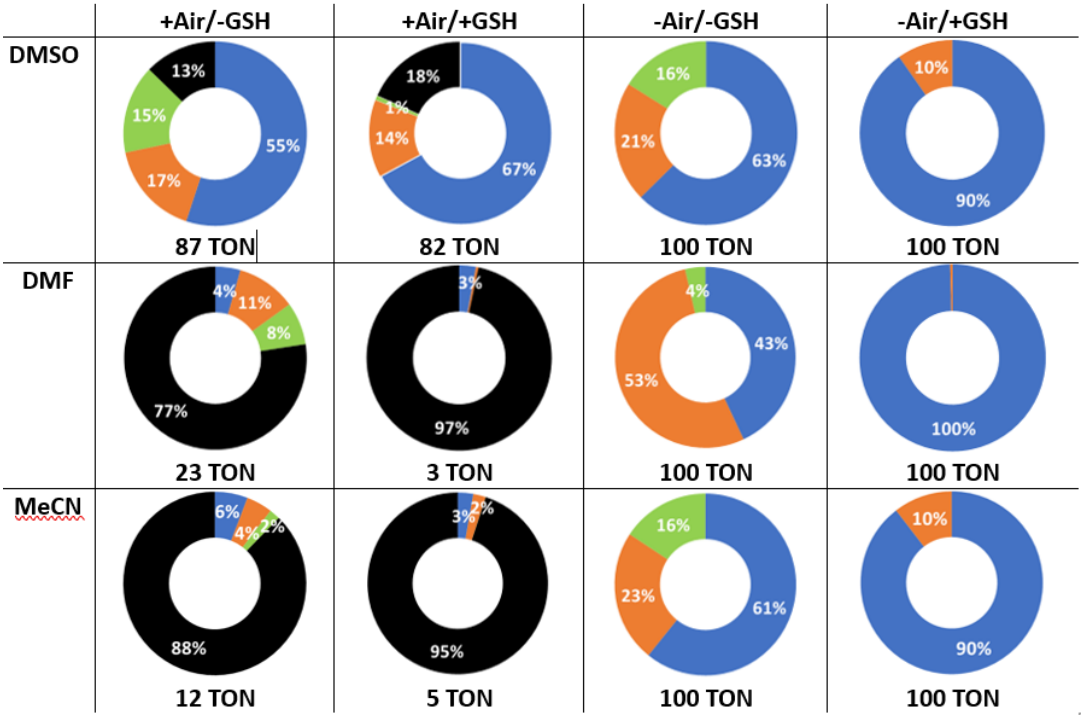

Figure 6: Deallylation reaction in different solvents illustrates the product conversion and distribution with the respective TON) indicated for each condition.

The data from Figure 6 show that the co-solvent's nature has a noticeable effect on reactivity (detailed results in Table S2). As was highlighted above by ^{1}H NMR, the catalyst is less stable in MeCN and DMF in the presence of air, revealing variable stability, possibly due to the coordination strength of the solvent. For MeCN and DMF, more monoallylated amine **7** is produced without GSH. Additionally, the diallylated amine **8** is barely detectable in the presence of GSH. In the case of DMSO, the same trend is observed when GSH is used, even if DMSO, might consume a part of GSH, Figure 6. Although the presence of GSH improved the selectivity, it decreased the overall conversion for DMF and MeCN, Figure 6. Even though GSH reduces the overall conversion, the increase in selectivity renders the reaction monitoring more accessible. As a result, the presence of GSH in cells is beneficial since it minimizes the formation of (di)-allylated amine-products **7-8**.

From the previous experiments (Figure 4- 6), the following information can be gathered: i) The formation of GSSG from GSH requires O_2 unless DMSO is used as a co-solvent. ii) The deallylation proceeds better when DMSO is used as a co-solvent. iii) GSH provokes a slight decrease in the overall conversion but drastically increases the selectivity of the reaction. As a result, three reactions occur in the presence of air and GSH: i) deallylation. ii) disulfide formation. iii) oxidative degradation of the complex. These three processes compete with each other during catalysis. If these reactions compete, the oxygen consumption rate should vary in the presence or absence of **5** and GSH. To further investigate this theory, oxygen consumption (oxygraphs) monitoring

during catalysis was carried out using an oxygen-sensing probe and different reaction conditions, Figure 7.

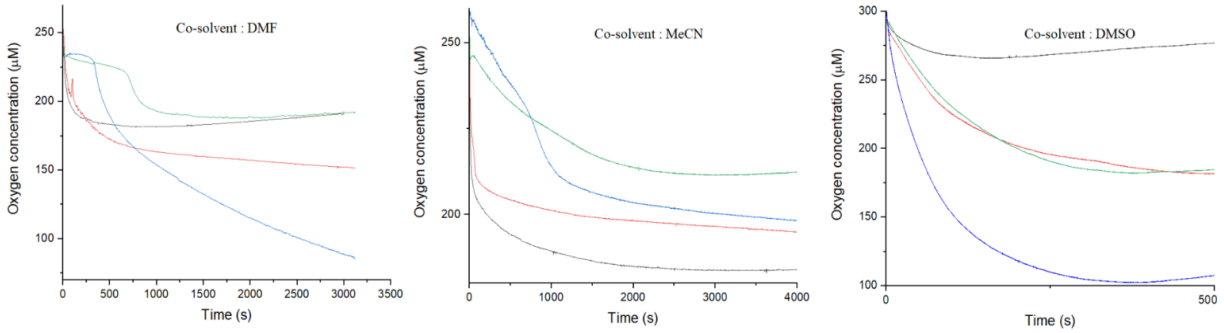

Figure 7: Oxygraphs measurement of Ru(II) intermediate **1** in different conditions in water with 1% co-solvent and no head space (GSH 10 mM, substrate **5** 1 mM and Ru(II) intermediate **1** 0.1 mM). The black curve corresponds to Ru(II) intermediate **1** alone. The red curve corresponds to Ru(II) intermediate **1** in the presence of GSH. The blue curve corresponds to Ru(II) intermediate **1** in the presence of GSH and substrate **5**. The green curve corresponds to Ru(II) intermediate **1** in the presence of substrate **5**.

The oxygraphs obtained reveal a high similarity for the evolution of the oxygen consumption rate when MeCN and DMF are used as co-solvents. In the presence of the Ru(II) intermediate **1** alone, the oxygen consumption is rapid, and the Ru(II) intermediate **1** is almost wholly consumed after 3 and 1.5 minutes in DMF and MeCN, respectively, since 75 mM of oxygen was consumed for both conditions. If we consider a stoichiometry of 1:1 for Ru(II) intermediate **1** to air, from 100 mM of Ru(II) intermediate **1** initially added, 75% were consumed in the abovementioned timescale. On the other hand, when Ru(II) intermediate **1** is used in the presence of GSH (red curve), the oxygen rate consumption is lowered due to a possible coordination between GSH and Ru(II) intermediate **1**. This coordination prevents the oxidative degradation of Ru(II) intermediate **1** via the formation of GSSG. This leads to an increased lifetime of Ru(II) intermediate **1** in the presence of air. Oxygen consumption was recorded for 2 hours and 7.5 hours in DMF and MeCN, respectively. When Ru(II) intermediate **1** is used with caged substrate **5**, the oxygen consumption is lower than in the previous two cases since the deallylation does not require oxygen. The initial profile features a fast decrease in oxygen concentration. It then stabilizes before decreasing again for DMF. The oxygen concentration decreases for around 30 minutes. A similar pattern is observed in MeCN. After 50 minutes, no oxygen consumption was apparent. This supports a potential competition between the catalyst's oxidation and the CpRu-catalyzed deallylation of caged coumarin **5**. When Ru(II) intermediate **1** was used in the presence of GSH and substrate **5**, the oxygen consumption rate was even slower than in the previous cases. In the case of DMF, a transient plateau was again

observed, but for a lower duration. We hypothesize that GSH induces a different competition between the deallylation reaction and the formation of GSSG. The oxygen decrease was visible for 5.5 hours for MeCN and DMF.

Regarding the oxygraphs for the condition where DMSO was used as a co-solvent, a low and slow decrease in oxygen concentration was observed over 4 h for catalyst **1** alone. The behavior was almost identical when Ru(II) intermediate **1** was used in the presence of GSH or substrate **5**. Both the nucleophile and substrate lead to a slow consumption of oxygen over 11 hours. When Ru(II) intermediate **1** was used with GSH and substrate **5**, the oxygen consumption was faster than for the conditions mentioned above and lasted for ten hours. Introducing a substrate or thiol may induce a ligand exchange from DMSO with the Lewis-basic reagent. This ligand exchange promotes the formation of an intermediate, which may be affected by oxygen. Nevertheless, the incomplete conversion of GSH into GSSG excess O_2 reveals that Ru(II) intermediate **1** for this transformation degrades into fewer active species. The oxygraphs are an efficient means to quantify the oxygen consumption but do not give any insight into the nature of the degradation product.

The oxygen sensitivity of Ru(II) intermediate **1** is apparent by the naked eye as revealed by a rapid color change from red to brown to green upon exposure of Ru(II) intermediate **1** solution to air. This suggests that Ru(II) intermediate **1** is converted into different species in the presence of oxygen. To monitor the evolution of these species, UV-Vis monitoring was carried out under different conditions, Figure 8. Ru(II) intermediate **1** was dissolved in DMSO, DMF, or MeCN in the presence or absence of air and/or GSH and diluted with water to mimic the catalytic conditions, Figure 8 (The reader can also refer to Figure S5-11 for the UV-vis spectrum in the presence of GSH).

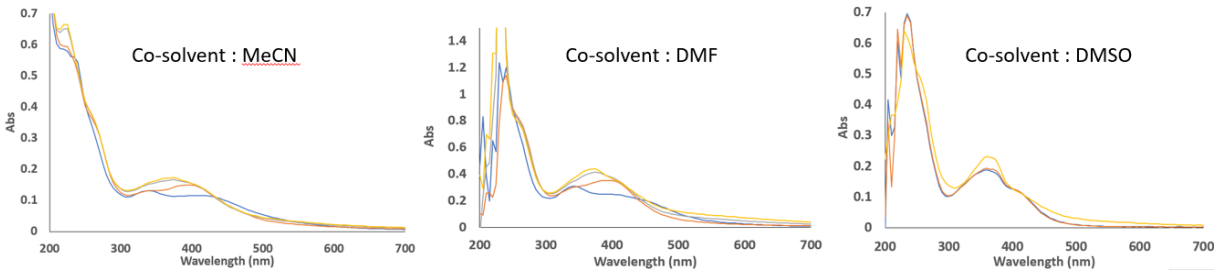

Figure 8: UV-Vis spectrum of Ru(II) intermediate 1 in water and 1% of co-solvent. The blue curve represent Ru(II) intermediate 1 without air. The orange curve represent Ru(II) intermediate 1 after 1h exposure to air. The grey curve represent Ru(II) intermediate 1 after 2h exposure to air. The yellow curve represent Ru(II) intermediate 1 after 15h exposure to air.

Irreversible changes in the UV-Vis spectra after air exposure highlight its gradual conversion to an oxidized species. The interaction of Ru(II) intermediate **1** with oxygen was similar in MeCN and DMF according to the UV-vis spectrum. For both co-solvents, λ_{abs} displayed a notable variation and the corresponding absorbance. They stabilized after 2h, meaning that the final state of the complex is reached after 2h following exposure to air. Nevertheless, the spectrum in the presence of DMSO displayed increased stability upon oxygen exposure. Ogo and Ferraro have previously reported different studies on various [Cp*Ru]-based complexes and their reactivity with O_2, Figure 9a.[218–220] These studies led them to conclude that, in the presence of O_2, a [Cp*Ru]-peroxo complex is endowed with oxidative properties. The resulting peroxo-complexes catalyzed the oxidation of phosphite, phosphine, and guanosine-5'-monophosphate (GMP). Based on their work, we propose a similar pathway to rationalize the reactivity of Ru(II) intermediate **1** in the presence of air. A first intermediate is formed upon exposure of Ru(II) intermediate **1** to oxygen (**9** hereafter). It can be converted back to Ru(II) intermediate **1** in the presence of a reductant, Figure 9b.[33–35] After 2 h of exposure, a second hypothetical intermediate is formed since further variation of λ_{abs} was observed (**10** or **11** hereafter). No further modification of the UV-Vis spectrum was observed, even upon standing overnight. This suggests that **10** or **11** is the final state of the catalyst. Considering the oxidation of **9** to **11**, two hypotheses can be formulated: formation of a decarboxylated peroxo-ruthenium(IV) core (**11-1**) or oxidation of the ligand (**11-2**), Figure 9b.

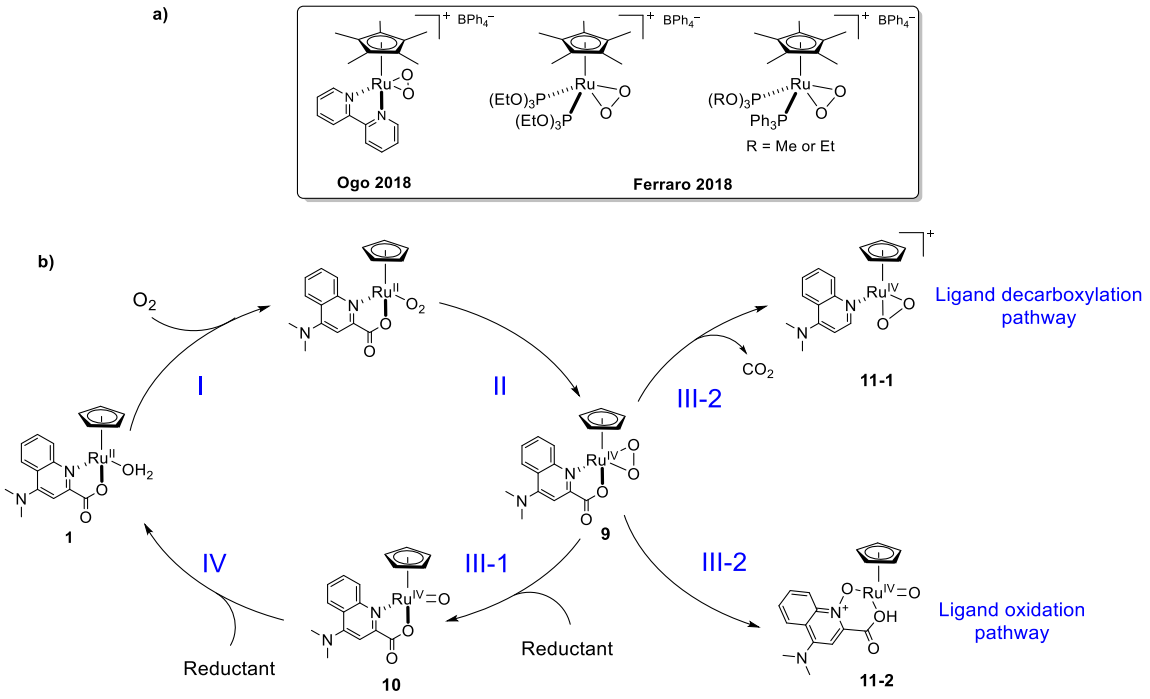

Figure 9: Oxidative deactivation of Ru(II) intermediate **1** in the presence of dioxygen. Starting on the left with Ru(II) intermediate **1**, I) Ligand substitution with O_2. II) Oxidation of the catalyst with O_2 forming a Ru(IV) peroxo intermediate **9**. III-1) Conversion of **9** into **10** by action of a reductant.

IV) Reduction of **10** into Ru(II) intermediate **1** via reduction. III-2) Proposed irreversible degradation pathway via decarboxylative degradation affording **11-1** or via ligand oxidation pathway affording **11-2**.

In the case of the formation of an oxidized species **11-1** form, a decarboxylative pathway would be required to convert **9** to **11-1** irreversibly. The regeneration of **1** from **9** requires a reductant, water itself might act as a reductant, leading to the formation of H_2O_2. To investigate the possible

H_2O_2 formation, an assay using Horseradish Peroxidase (HRP hereafter) was performed. This assay did not reveal the formation of H_2O_2, Figure S12-14. However, another reducing agent may be responsible for this transformation. Regarding the ligand, the pyridine moiety could form an N-oxide species, which inhibits the catalytic process. To confirm this hypothesis, an MS-MS experiment was carried out with the oxidized complex to investigate the location of the oxidation site, Figure S15-19. The MS-MS experiment revealed that the ligand is not oxidized in the presence of oxygen. Nevertheless, fragments presenting a peroxo and an oxo structure, as well as a decarboxylated ligand, were identified from mass-matching. This supports the hypothesis of a coupled oxidative-decarboxylative deactivation of Ru(II) intermediate **1**. Nevertheless, MS-MS analysis also revealed that the η^5-cyclopentadienyl moiety was absent from these fragments. Loss of the Cp-moiety may be part of the deactivation pathway. Overall, two hypotheses about the deactivation of the catalyst can be made. i) Cp-Removal and ii) ruthenium oxidation. Moreover, the regeneration of Ru(II) intermediate **1** from **9** *via* **10** requires a reductant. Unfortunately, water itself does not act as a reductant since the HRP experiment did not reveal the formation of H_2O_2. However, another reductant in this study fulfills the requirement since we have demonstrated that GSH is converted into GSSG in the presence of air and Ru(II) intermediate **1**. As a result, based on

the data gathered in this study and the literature, we propose a mechanism combining the deallylation reaction and the catalyst oxidation pathway, Figure 10.

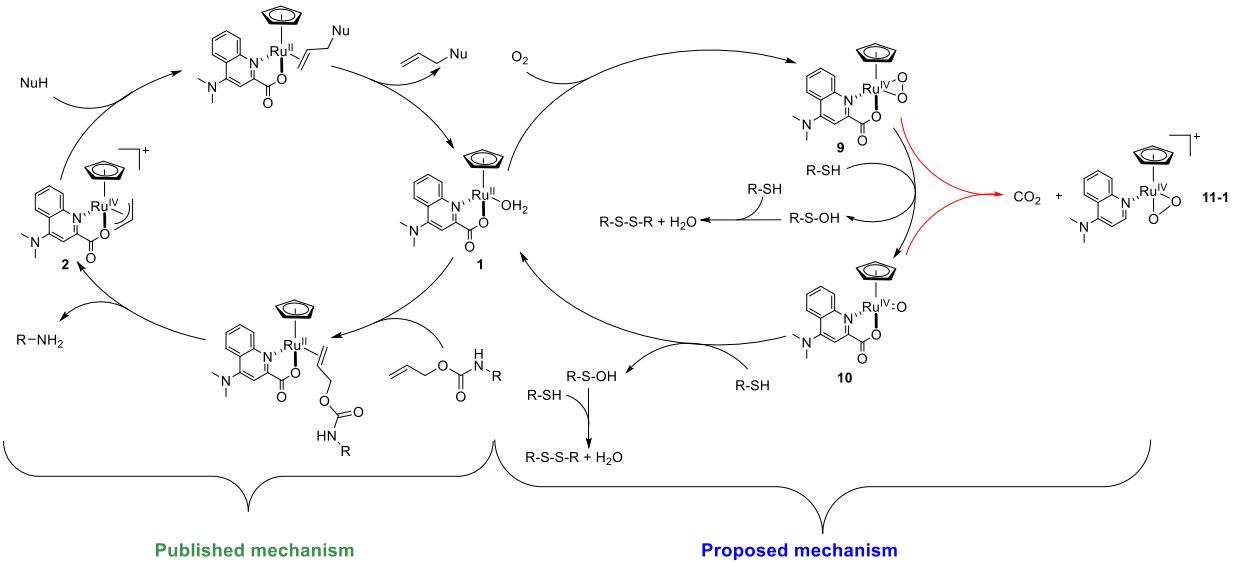

Figure 10: The proposed combination of two catalytic cycles. On the left is the catalytic cycle proposed by Meggers, and on the right is a mechanism for the thiol oxidation and possible degradation of the complex, resulting in an inactive ruthenium species. From this cycle, it is possible to regenerate the active catalyst.

This experiment disproved the formation of **11-2** but was consistent with the formation of **9** and **10** and a hypothetical degradation through **11.** According to the mechanism outlined in Figure 10 and previous work,[37] thiols decrease the overall conversion for the deallylation process. This might be due to a possible competition between deallylation and thiol oxidation. Considering that the degradation pathway still occurs, this affects the deallylation, resulting in a reduced conversion. It was shown above that the glutathione present in the intracellular medium does not affect the reaction. On the contrary, it reduces the parasitic allylated product. However, there are also thiols in the extracellular medium. This is the case, for example, with albumin, which has a cysteine (cysteine 34) exposed to the solvent. This cysteine is often used to carry out Michael additions in situ.[221] We tested the effect of bovine serum albumin (BSA) on the reaction, Figure 11.

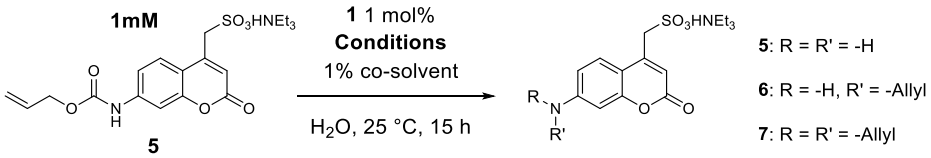

§

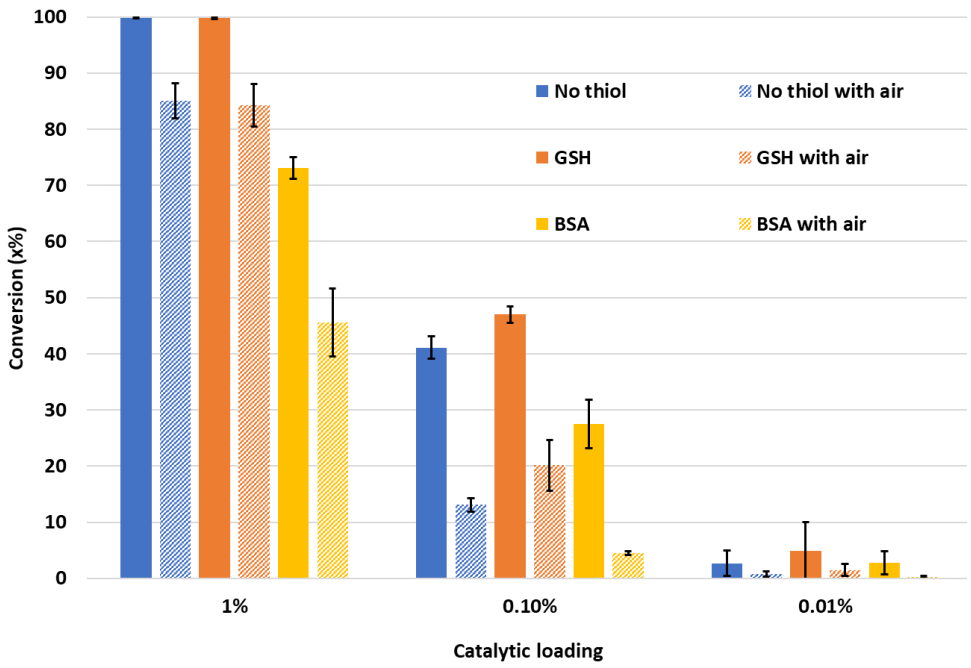

Figure 11: Determination of the total conversion of the deallylation of substrate **5** using catalyst **1** under different conditions (BSA = bovine serum albumin).

The conversion in the presence of BSA is lower than in the presence of GSH. We hypothesize that BSA binds via hydrophobic interactions to the Ru(II) intermediate **1** or the substrate **5.** Indeed, the primary function of albumin is to adsorb hydrophobic substrates to vectorize them in the organism. This effect may be problematic for reactions occurring in the extracellular medium. As described previously, one of the most ambitious applications for these CpRu-based deallylation catalysts is their use to uncage cytotoxic drugs via deallylation.[21] To do so, it is highly desirable to accumulate the catalysts at the cell surface or in the cytosol of cancer cells. Essential features of such catalysts include i) non-toxicity, ii) efficient uncaging of prodrugs in the presence of oxygen, as well as, all metabolites present either in the extracellular medium or the cytosol, and iii) maintaining high catalytic activity at low concentrations (i.e. < 5 mM). Meggers and co-workers reported that analogs of Ru(IV) intermediate **3** were 10 times more efficient than analogs of Ru(IV) intermediate **2** at uncaging alloc-protected amines in biological media.[21] Building on these findings, Mao and co-workers uncaged an alloc-protected gemcitabine prodrug in a zebrafish embryo xenograft model.[222] However, catalyst **3** was also highly cytotoxic in HeLa cells, with an IC_{50} of 70 nM.[216] The increase in activity of catalyst **3** may be counterbalanced by its increased cytotoxicity. To test this hypothesis, we compared the cytotoxicity of Ru(IV) intermediate **2** and **3** in CT26 cells (mouse colon carcinoma cell line). To mimic the experimental conditions reported by Meggers and co-workers to assess the efficiency of Ru(IV) intermediate **2** and **3**, the experiments with CT26 cells were performed in the presence of air and 0.5 % v/v of DMSO.[21] As

summarized in Figure 12a, Ru(IV) intermediate **3** is only slightly more cytotoxic than Ru(IV) intermediate **2**, with IC_{50}s of 360 ± 2 and 531 ± 8 nM, respectively. To compare the efficiency of Ru(IV) intermediate **2** and **3** in the presence of CT26 cells, we used the alloc-gemcitabine **12** previously described by Mao and co-workers.[222] The cytotoxicity of gemcitabine **13** and its caged analog **12** was determined. Gemcitabine **13** was about 500 times more toxic than alloc-gemcitabine **12**, with IC_{50} of 12.1 ± 0.2 nM and 5.86 ± 0.05 μM, respectively, Figure 12b. Next, an experiment was initiated by incubating CT26 cells with 1 μM of alloc-gemcitabine **12** –where no cytotoxicity was observed. Then, the CT26 cells were treated with increasing concentrations of either Ru(IV) intermediate **2** or **3** in the presence of 1 μM of alloc-gemcitabine **12**, Figure 12c. To minimize the cytotoxicity effect of the Ru(IV) intermediate **2** or **3**, their concentration was kept below 100 nM. As can be appreciated in Figure 12d, the catalytic activity of both deallylation Ru(IV) intermediate **2** and **3** is similar. A significant reduction in cell viability was only observed at a catalyst concentration > 50 nM for both catalysts. At a catalyst concentration of 100 nM, corresponding to a 10% catalyst loading, the cell viability was reduced to 64% and 56% for Ru(IV) intermediate **2** and **3**, respectively. Under these conditions, we can safely assume that neither the Ru(IV) intermediate **2 or 3** nor the alloc-gemcitabine **9** contribute significantly to the reduction in cell viability. Inspection of Figure 10A reveals that such a reduction of cell viability is observed with a concentration of gemcitabine **13** in the 10 nM range. Under these experimental conditions [substrate **12**] = 1mM, [Ru(IV) intermediate **2** or **3**] = 100 nM, [product **13**] = 10 nM–, we conclude that the conversion is roughly 1%, which corresponds to a TON = 0.1! We cannot exclude at this stage that the cytotoxicity observed in this assay results from a synergistic combination of the individual cytotoxic effects of the prodrug **12**, gemcitabine **13**, and the Ru(IV) intermediate **2** or **3**.

These control experiments reveal that, while analogs of Ru(IV) intermediate **3** have been reported to be more efficient than analogs of Ru(IV) intermediate **2** *in vitro*, significant improvement in catalytic activity in biological media is required before they can be considered safe for clinical applications in medicine.

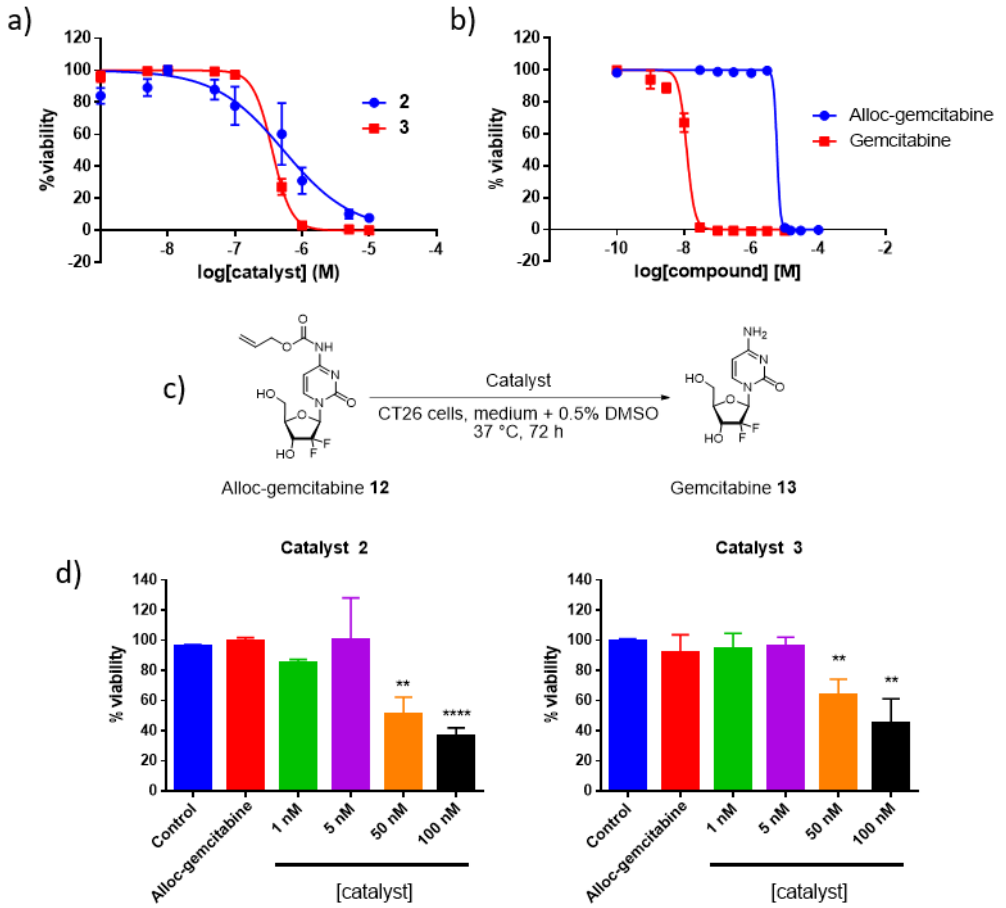

Figure 12: CT26 cell viability assays in the presence of alloc-gemcitabine **12**, Ru(IV) intermediate **2** or **3** and gemcitabine **13 a)** CT26 cells viability following 72 h of incubation with Ru(IV) intermediate **2** or **3**. **b)** CT26 cells viability following 72 h of incubation with alloc-gemcitabine **12** or gemcitabine **13**. **c)** Deallylation of caged-gemcitabine **12** to gemcitabine **13**, catalyzed by Ru(IV) intermediate **2** or 3. **d)** CT26 cells viability following 72 h of incubation with 1 µM of alloc-gemcitabine **12** and increasing concentrations of Ru(IV) intermediate **2** or **3**. **** $P < 0.0001$, ** $P < 0.01$ (unpaired t-test).

3.3 **Conclusion**

Since its initial report by Meggers in 2006, the CpRu-catalyzed deallylation system presented herein has been widely applied in chemical biological applications. Over the years, the system has revealed some of its limitations, including i) catalyst oxidation by dioxygen, ii) undesirable allylation of the uncaged amine present in the product iii) thiol oxidation, and iv) limited catalytic activity in (extra)-cellular media. Although qualitative, this study reveals that the catalysts **1-4** are

neither oxygen nor thiol-resilient. A complex kinetic interplay between catalyst oxidation and η^3-allyl formation is presented. Future work in the group will explore the relation between substrate complexity and catalytic outcome, which is necessary. While the *in cellulo* applications of these catalysts remain limited, they significantly contributed to the coming-of-age of *in cellulo* catalysis. A thorough understanding of the mechanism and the associated side reactions will eventually enable the field to reach its maturity.

3.4 Supplementary information

I] Synthesis of substrates and complexes:

1) Synthesis of ethyl 3-hydroxyphenyl)carbamate:

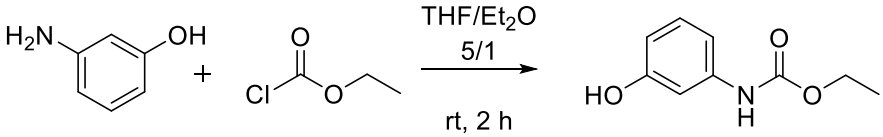

Reproduced from Griffiths and Rynckelynck. [223]

Ethyl chloroformate (11.7 g/10.3 mL, 1.2 eq) was added dropwise to a stirred suspension of 3-aminophenol (10g, 1eq) in 600 mL of a mixture of dry diethyl ether and dry THF (5:1). A white precipitate (probably the corresponding amine hydrochloride) formed quickly. The reaction mixture was stirred an additional 2 hours at room temperature. The hydrochloride was removed by filtration. The filtrate was evaporated under vacuum to give a colorless oil. The oil was solubilized in 300 mL diethyl ether and the resulting organic phase was washed with solutions of HCl (1 M, 200 mL), saturated NaHCO3 (200 mL) and water (200 mL). The organic phase was drier over Na_2SO_4 and the solvent was evaporated and the residue dried under high vacuum for 2hm wielding a colorless-white crystalline solid (8.8 g, 54.1%). The crude was directly used for the next reaction without further purification.

^{1}H NMR (500 MHz, Chloroform-*d*) δ 7.32 (s, 1H), 7.13 (t, *J* = 8.1 Hz, 1H), 6.70 – 6.62 (m, 2H), 6.57 (ddd, *J* = 8.2, 2.4, 0.9 Hz, 1H), 4.23 (q, *J* = 7.1 Hz, 2H), 1.31 (t, *J* = 7.1 Hz, 3H). δ=3.5 & 1.21 (diethylether).

§

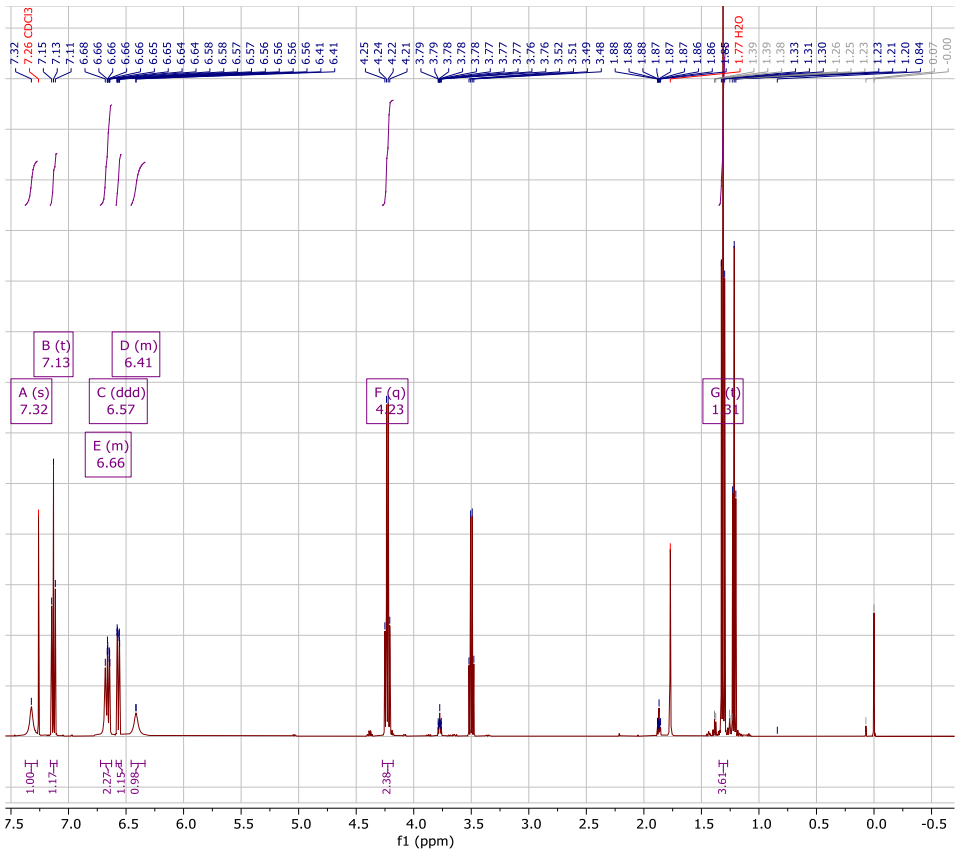

2) Synthesis of ethyl (4-(chloromethyl)-2-oxo-2H-chromen-7-yl)carbamate:

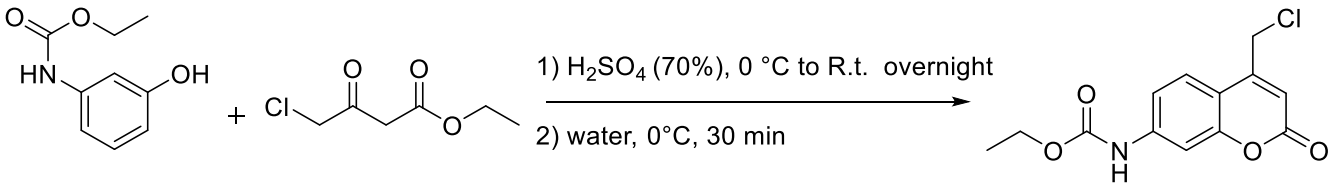

Pechmann condensation

Reproduced from Griffiths and Rynckelynck[223].

Ethyl 4-acetoacetate (8.799 g/7.27 mL, 1.1 eq) was added dropwise to a stirred suspension of 3-carboethoxyaminophenol (8.8 g, 1 eq) in sulfuric acid (70%, 250 mL)) on ice. The black mixture (probably the batch of Ethyl 4-acetoacetate was too old) was stirred overnight at room temperature. The dark orange mixture was then poured on ice water (400 mL) and stirred for 20 minutes. The precipitate (white greenish slurry) was then filtered and washed with methanol (75 mL) and chilled diethyl ether (2 times 75 mL). The solid was then dried overnight under high vacuum to afford a white solid (2 g, 14.6%). The crude was directly used for the next reaction without further purification.

§

^{1}H NMR (500 MHz, DMSO-d_6) δ 10.20 (s, 1H), 7.76 (d, J = 8.8 Hz, 1H), 7.60 (d, J = 2.1 Hz, 1H), 7.42 (dd, J = 8.8, 2.1 Hz, 1H), 6.51 (d, J = 0.8 Hz, 1H), 4.98 (d, J = 0.9 Hz, 2H), 4.17 (q, J = 7.1 Hz, 2H).

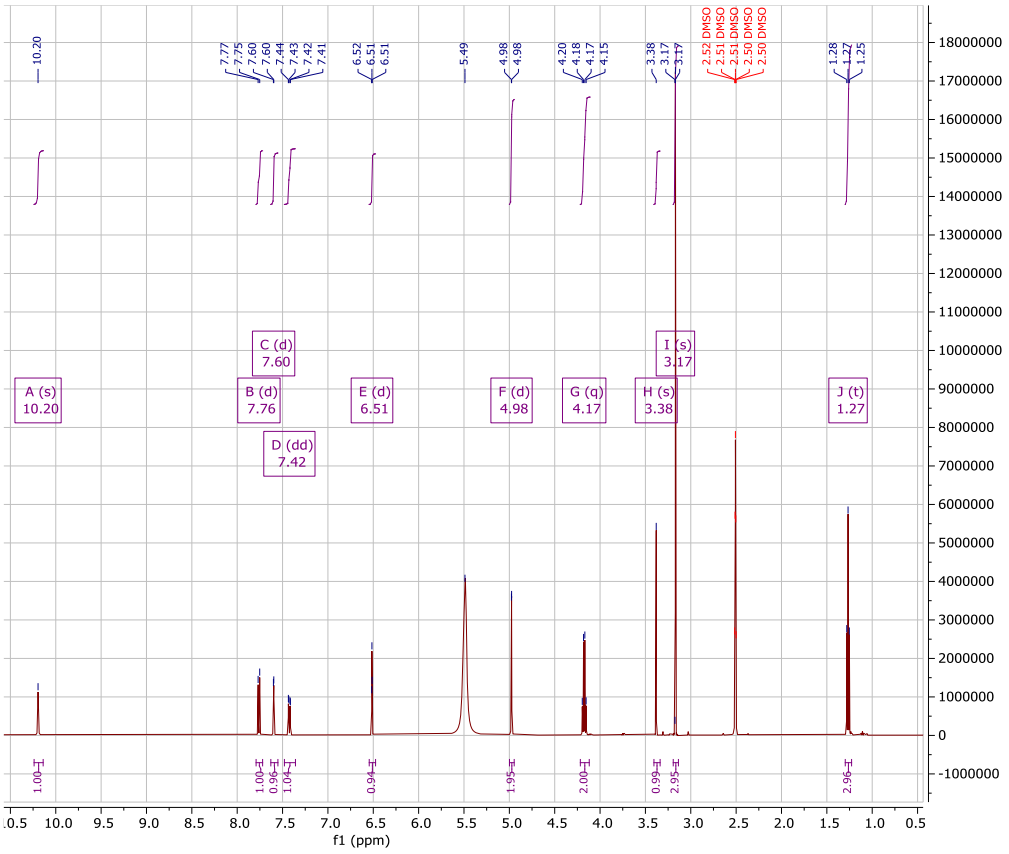

3) Synthesis of sodium (7-((ethoxycarbonyl)amino)-2-oxo-2H-chromen-4-yl)methanesulfonate:

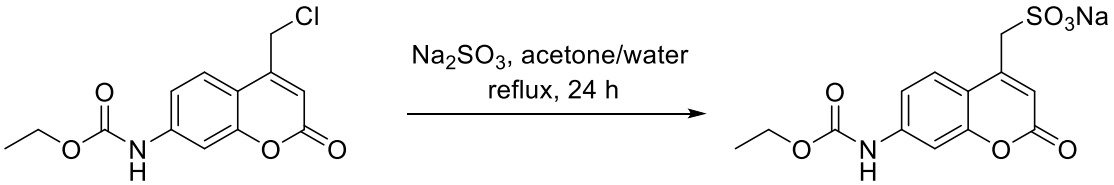

Reproduced from Griffiths and Rynckelynck[223].

A suspension of 4-chloromethyl-7-carbethoxyaminocoumarin (2 g, 1 eq) and Na_2SO_3 (3.694 g, 5 eq) in a mixture of acetone (35 mL) and water (25 mL) was stirred under reflux for 24 hours. After cooling, solvents were evaporated under vacuum to leave a yellowish-

white sticky mass. The mass was suspended in hot methanol (75mL) and filtrated while warm. The filtrate was dried over Na_2SO_4, solvent evaporated and the residue dried several hours at high vacuum to give a yellowish-white powder (2.48 g, 100%).

^{1}H NMR (500 MHz, DMSO-d_6) δ 10.12 (s, 1H), 9.89 (s, 1H), 7.85 (d, J = 8.8 Hz, 1H), 7.55 (d, J = 2.1 Hz, 1H), 7.34 (dd, J = 8.8, 2.2 Hz, 1H), 6.24 (s, 1H), 4.21 – 4.08 (m, 4H), 4.00 (s, 2H), 1.31 – 1.22 (m, 5H).

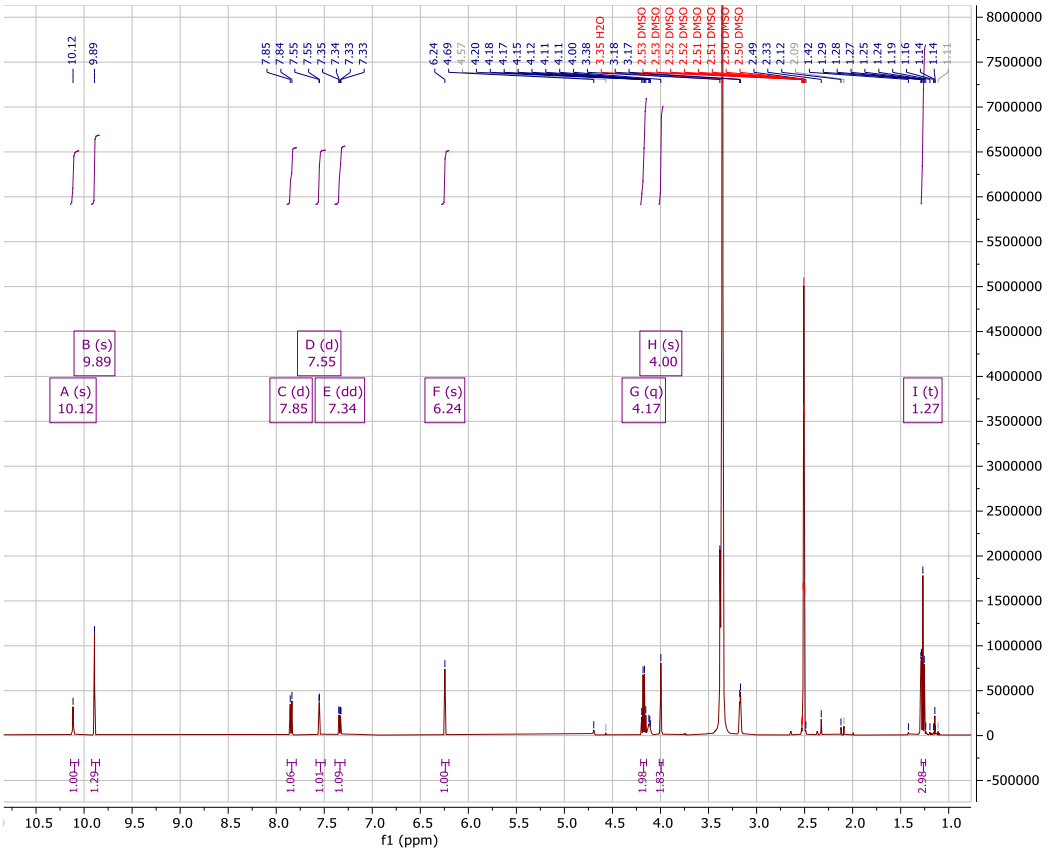

4) Synthesis of (7-amino-2-oxo-2H-chromen-4-yl)methanesulfonic acid:

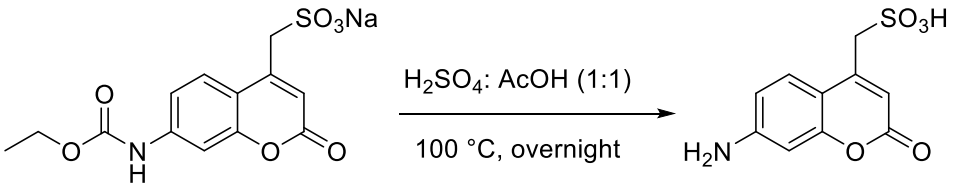

Reproduced from Griffiths and Rynckelynck[223].

Concentrated sulfuric acid (5 mL) and acetic acid (7.5 mL) were added to sodium 7-carbethoxyaminocoumarin-4-methanesulfonate (2.48 g, 1 eq) and the mixture was heated with stirring at 100 °C overnight (first green suspension which got solubilized upon heating). After cooling, the solution (dark-pink black) was poured into ethanol (75 mL)

and gave a beige precipitate. The solid was filtered off, washed with ethanol (once 20 mL) and dried at high vacuum to give a beige powder which was used without further purification.

^{1}H NMR (500 MHz, DMSO-d_6) δ 7.56 (d, J = 8.7 Hz, 1H), 6.52 (dd, J = 8.7, 2.2 Hz, 1H), 6.42 – 6.36 (m, 1H), 5.94 (s, 1H), 3.87 (s, 3H).

5) Synthesis of triethyl-l^5-azaneyl (7-(allylamino)-2-oxo-2H-chromen-4-yl)methanesulfonate:

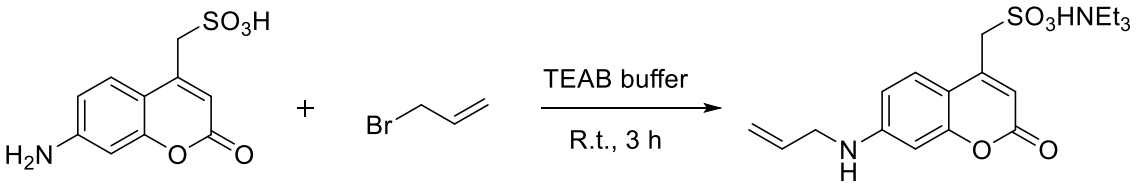

The (7-amino-2-oxo-2H-chromen-4-yl)methanesulfonic acid (crude from the previous reaction) (0.588 mmol, 1eq) was dissolved in triethylammonium bicarbonate buffer (TEAB, 3 mL), the mixture is bubbling, at the end of the bubbling allylbromide (0.502

mmol, 1 eq) was added to the reaction mixture and the solution was stirred for 3 h at room temperature. The reaction was then acidified to pH 4 using AcOH and then filtered. The reaction mixture was then purified by preparative reverse phase HPLC and the collected fraction were gathered and lyophilized to give a white powder (12 mg, 5.4% yield). (Low yield due to incomplete consumption of the starting material plus lack of selectivity of formation between mono and di-allylated product).

^{1}H NMR (500 MHz, Deuterium Oxide) δ 7.56 (d, *J* = 8.9 Hz, 1H), 6.72 (dd, *J* = 8.9, 2.3 Hz, 1H), 6.49 (d, *J* = 2.3 Hz, 1H), 6.15 (s, 1H), 5.97 (ddt, *J* = 17.3, 10.4, 5.2 Hz, 1H), 5.30 (dq, *J* = 17.3, 1.7 Hz, 1H), 5.22 (dq, *J* = 10.4, 1.6 Hz, 1H), 4.32 (s, 2H), 3.84 (dt, *J* = 5.2, 1.7 Hz, 2H), 3.20 (q, *J* = 7.3 Hz, 6H), 1.28 (t, *J* = 7.3 Hz, 9H).

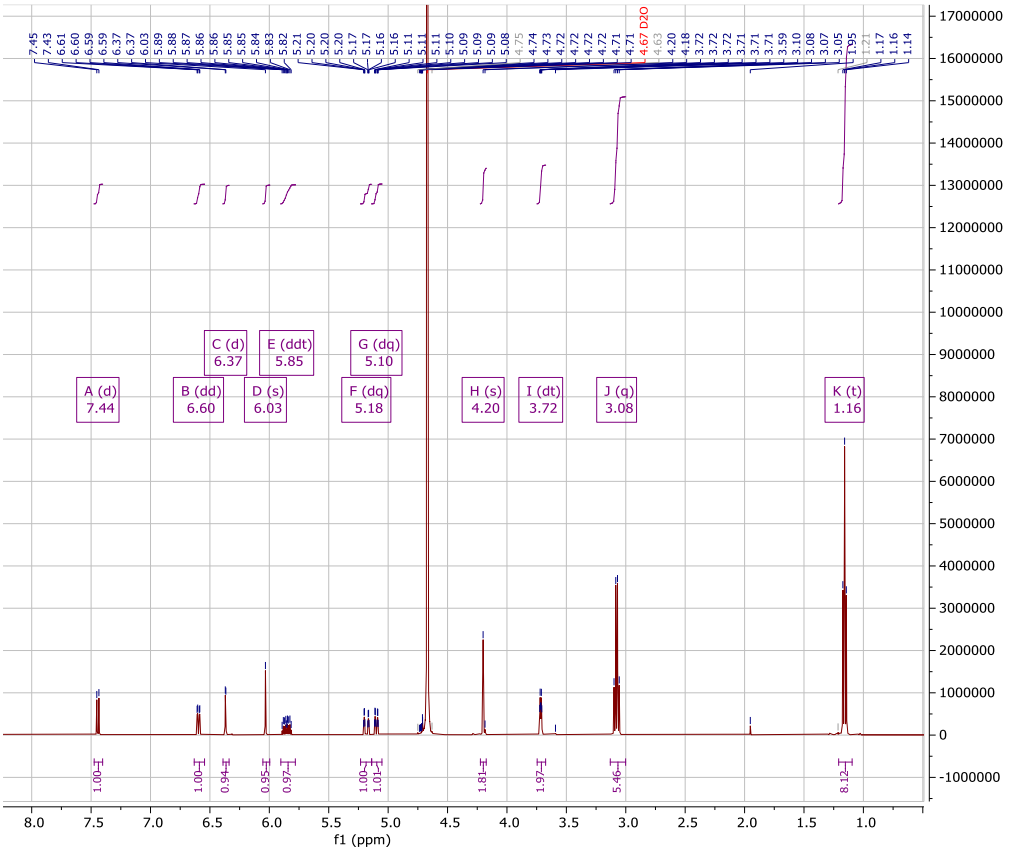

^{13}C NMR (126 MHz, D_2O) δ 164.8, 155.8, 152.7, 149.1, 134., 126.8, 116.1, 111.9, 109.9, 108.9, 97.7, 52.5, 46.6, 44.9, 8.2.

§

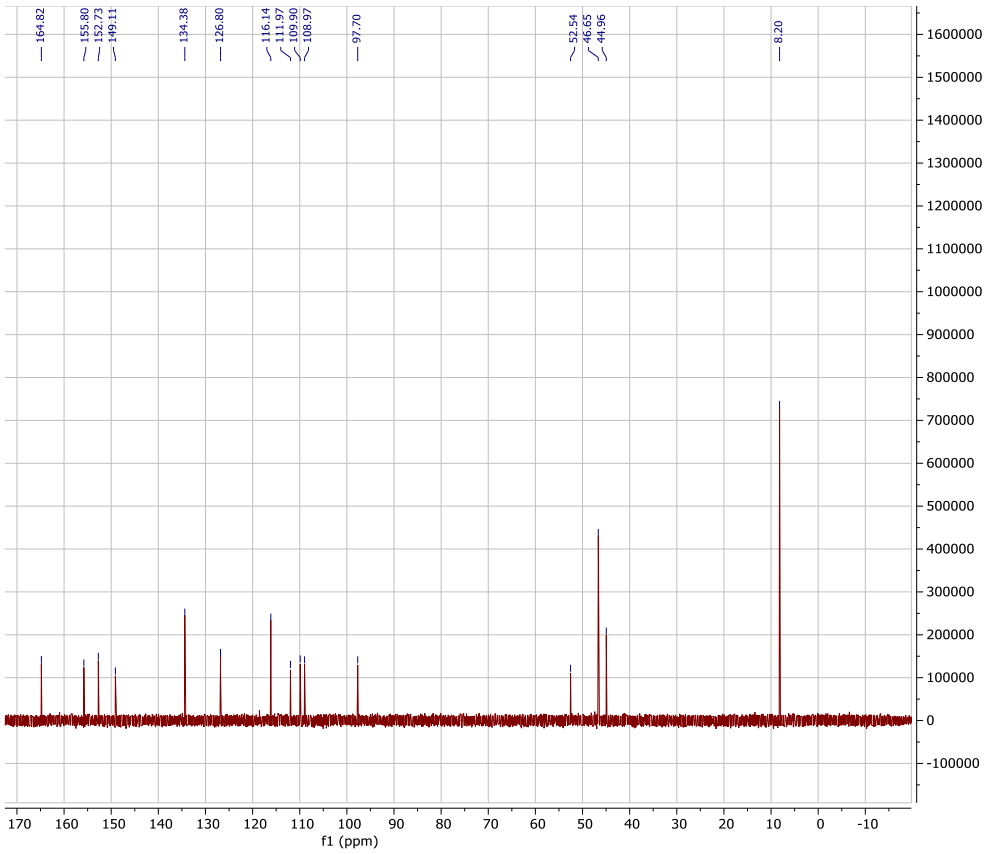

6) Synthesis of triethyl-l^5-azaneyl (7-(diallylamino)-2-oxo-2H-chromen-4-yl)methanesulfonate:

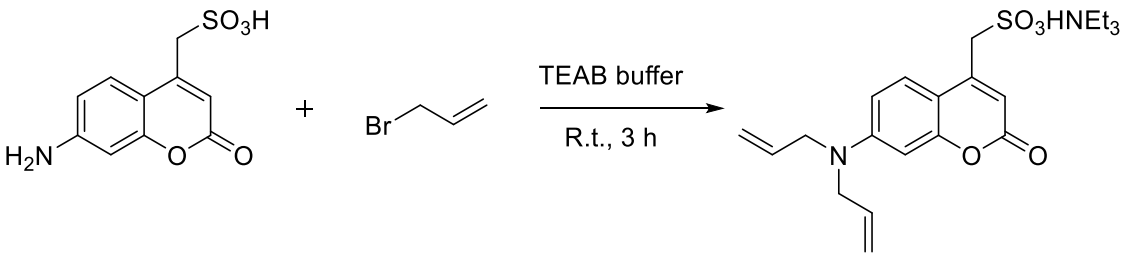

The (7-amino-2-oxo-2H-chromen-4-yl)methanesulfonic acid (crude from the previous reaction) (0.1963 mmol, 1 eq) was dissolved in TEAB (triethylammonium bicarbonate buffer, 3 mL), the mixture is bubbling, at the end of the bubbling allylbromide (0.9815 mmol, 5 eq) was added to the reaction mixture and the solution was stirred for 3 h at room temperature. The reaction was then acidified to pH 4 using AcOH and then filtered. The reaction mixture was then purified by preparative reverse phase HPLC and the collected fraction were gathered and lyophilized to give a white powder (10 mg, 10.8% yield).

§

The two Janus faces of CpRu-based deallylation catalysts and their application for in cellulo prodrug uncaging. 116

^{1}H NMR (500 MHz, Deuterium Oxide) δ 7.65 (d, *J* = 9.1 Hz, 1H), 6.84 (dd, *J* = 9.2, 2.6 Hz, 1H), 6.64 (d, *J* = 2.5 Hz, 1H), 6.17 (s, 1H), 5.95 (ddt, *J* = 17.2, 10.5, 4.6 Hz, 2H), 5.27 – 5.17 (m, 4H), 4.35 (s, 2H), 4.09 (dt, *J* = 4.1, 1.8 Hz, 3H), 3.24 (dq, *J* = 31.7, 7.3 Hz, 6H), 1.29 (t, *J* = 7.3 Hz, 8H).

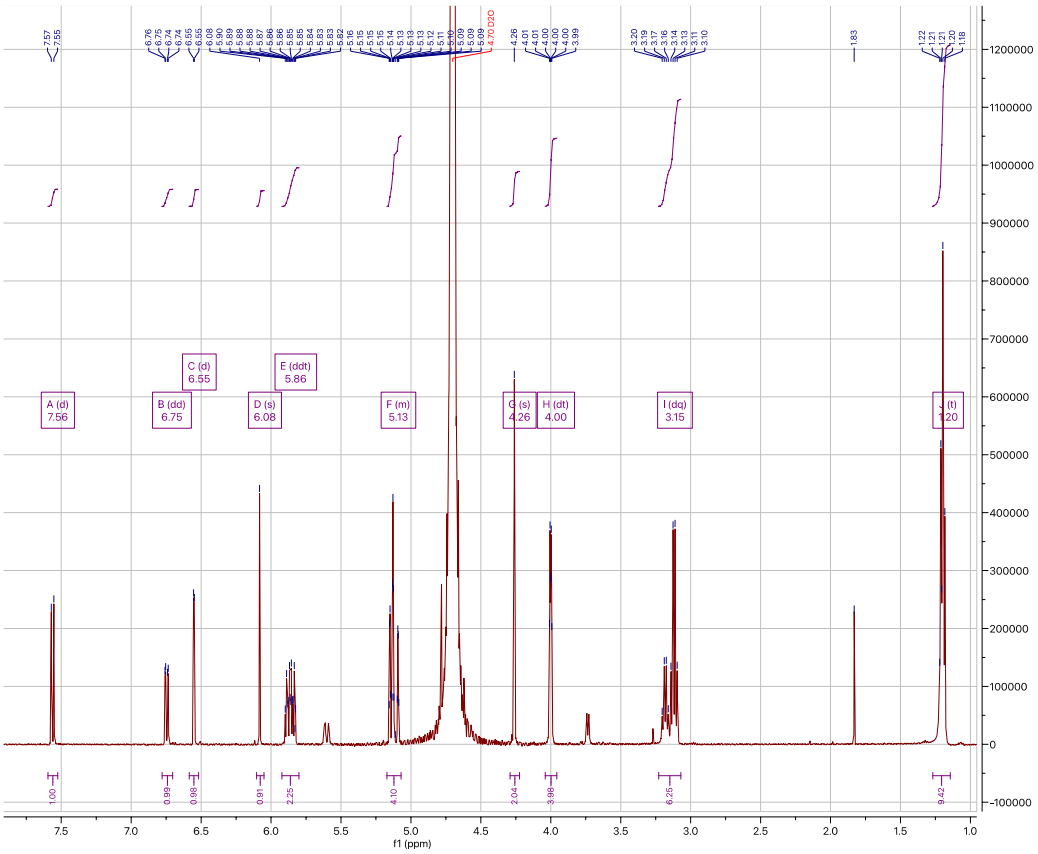

^{13}C NMR (126 MHz, D_2O) δ 165.0, 155., 152.2, 149.0, 132.7, 126.8, 115.9, 110.3, 109.6, 108.2, 97.8, 52.5, 52.5, 46.6, 8.2.

§

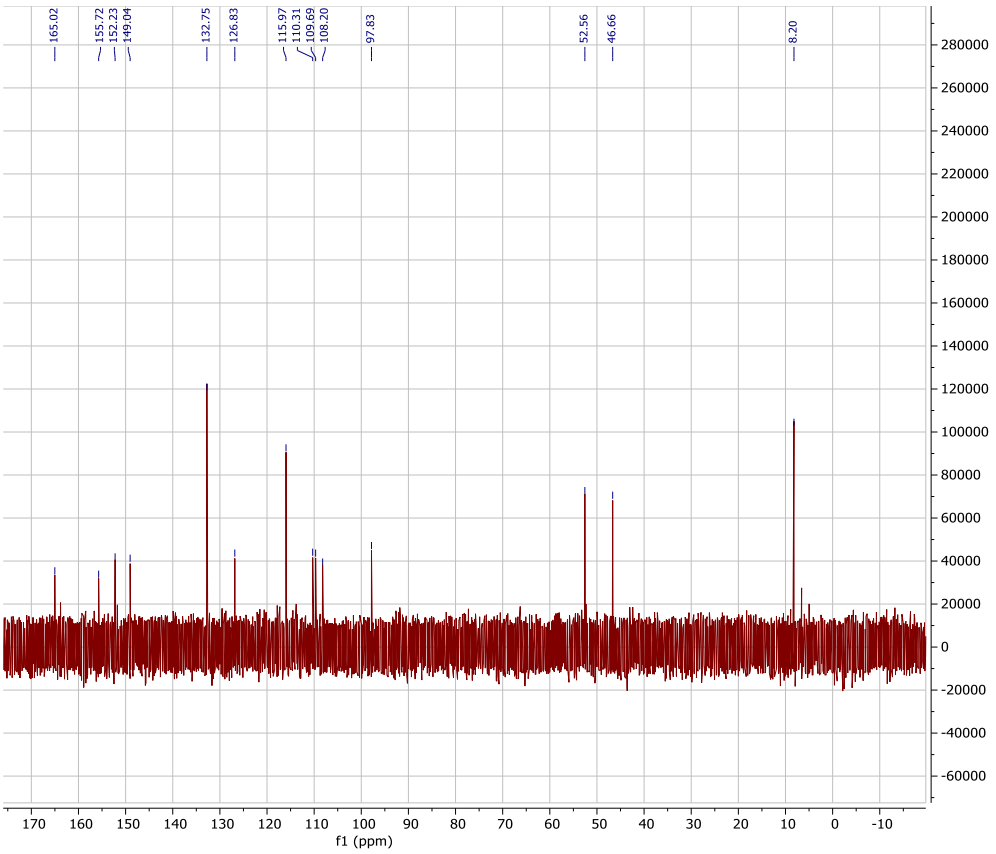

7) Synthesis of sodium triethyl-l^5-azaneyl (7-(((allyloxy)carbonyl)amino)-2-oxo-2H-chromen-4-yl)methanesulfonate:

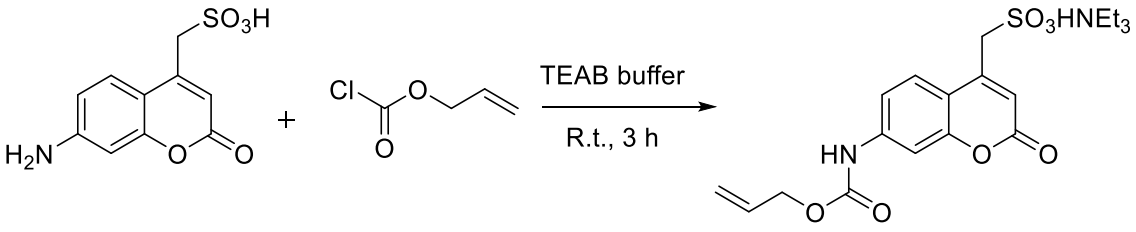

Reproduced from Meggers *et al*[22].

The (7-amino-2-oxo-2H-chromen-4-yl)methanesulfonic acid (crude from the previous reaction) (0.392 mmol , 1 eq) was dissolved in TEAB (triethylammonium bicarbonate buffer, 3 mL), the mixture is bubbling, at the end of the bubbling allylchloroformate (1.96 mmol, 5 eq) was added to the reaction mixture at 0 °C and the solution was stirred for 1.5 h at 0 °C and then 2 h at room temperature. The reaction was then acidified to pH 4 using AcOH and then filtered. The reaction mixture was then purified by preparative reverse

phase HPLC and the collected fraction were gathered and lyophilized to give a white powder (25 mg, 15% yield).

^{1}H NMR (500 MHz, Deuterium Oxide) δ 7.75 (d, *J* = 8.8 Hz, 1H), 7.42 (d, *J* = 2.2 Hz, 1H), 7.21 (dd, *J* = 8.8, 2.2 Hz, 1H), 6.44 (s, 1H), 6.04 (ddt, *J* = 17.3, 10.6, 5.4 Hz, 1H), 5.42 (dq, *J* = 17.3, 1.6 Hz, 1H), 5.33 (dq, *J* = 10.5, 1.4 Hz, 1H), 4.70 (dt, *J* = 5.3, 1.5 Hz, 2H), 4.41 (d, *J* = 0.7 Hz, 2H), 3.20 (q, *J* = 7.3 Hz, 6H), 1.28 (t, *J* = 7.3 Hz, 10H).

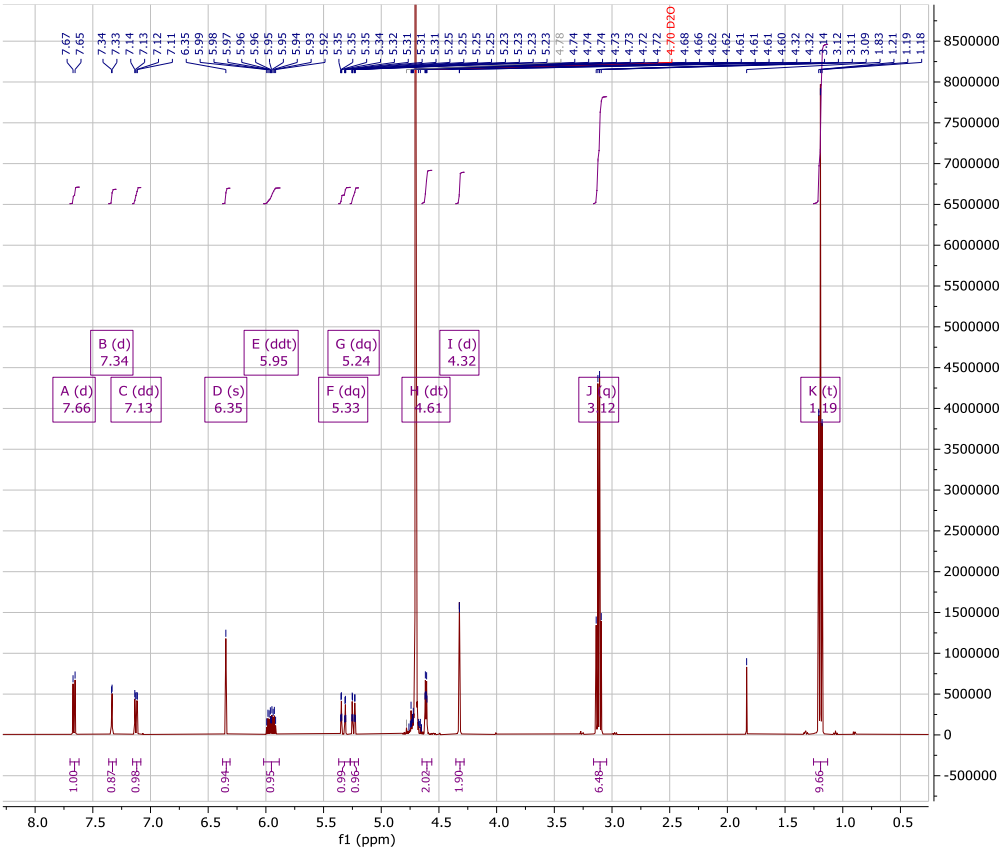

9) Synthesis of lithium 4-(dimethylamino)quinoline-2-carboxylate:

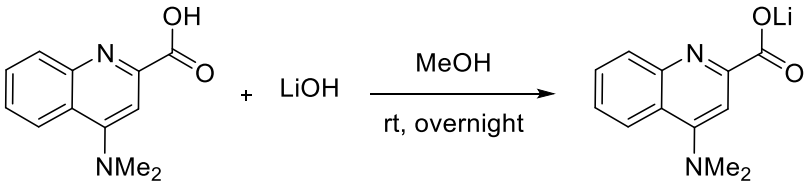

4-(dimethylamino)quinoline-2-carboxylic acid (1 eq, 1.16 mmol) was dissolved in methanol (4 mL) followed by LiOH (1 eq, 1.16 mmol) and the resulting solution was stirred at room temperature overnight. A white precipitate appeared, the mixture was

centrifuged, the solid and the supernatant were separated and the solid was washed with acetone and centrifuged again (3 x 2 mL).

The resulting product was obtained as a white powder (220 mg, 0.99 mmol, 85%).

NMR: ^{1}H NMR (500 MHz, DMSO) δ 8.06 (dd, *J* = 8.5, 1.3 Hz, 1H), 7.84 (d, *J* = 8.7 Hz, 1H), 7.66 (ddd, *J* = 8.3, 6.8, 1.4 Hz, 1H), 7.53 – 7.47 (m, 2H), 3.03 (s, 6H). The peak at 2.08 ppm correspond to acetone.

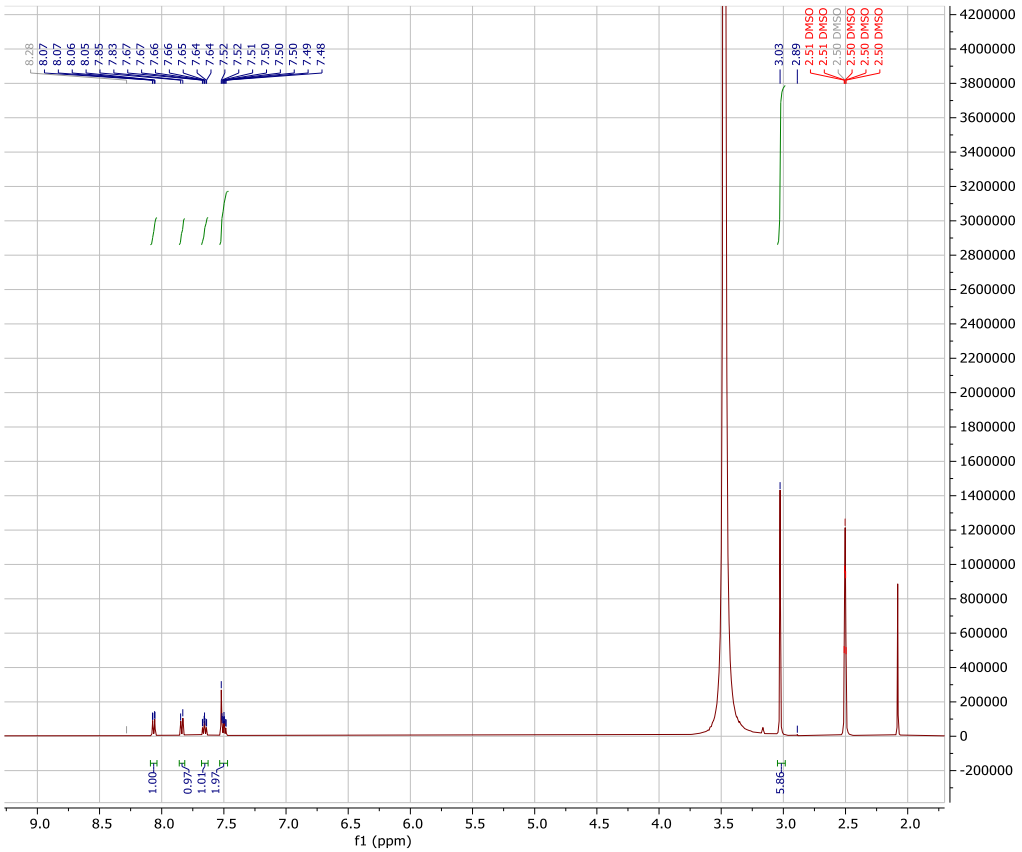

10) Synthesis of CpRu(NMe$_2$-QA)(MeCN):

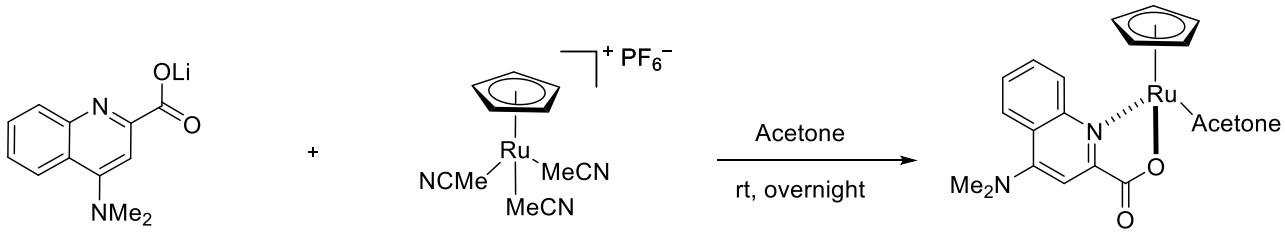

adapted from Meggers *et al.* [22]

Lithium 4-(dimethylamino)quinoline-2-carboxylate (15.3 mg, 1eq) and tris(acetonitrile)cyclopentadienylruthenium hexafluorophosphate (30 mg, 1eq) were

dissolved in acetone at room temperature overnight in the glovebox. The reaction mixture was then centrifuged to remove the white precipitate, the supernatant was collected and dried under vacuum. The resulting purple solid was washed with Et_2O (3 x 1 mL), the supernatant discarded and the solid dried under vacuum to afford a purple solid (24 mg, 79%).

^{1}H NMR (600 MHz, DMSO) δ 8.53 (dd, *J* = 8.8, 1.3 Hz, 1H), 8.16 (dd, *J* = 8.5, 1.4 Hz, 1H), 7.83 (ddd, *J* = 8.5, 6.8, 1.4 Hz, 1H), 7.65 (ddd, *J* = 8.3, 6.8, 1.3 Hz, 1H), 7.33 (s, 1H), 5.48 (s, 3H), 4.51 (s, 5H), 3.16 (s, 7H), 2.08 (s, 2H, free acetone).

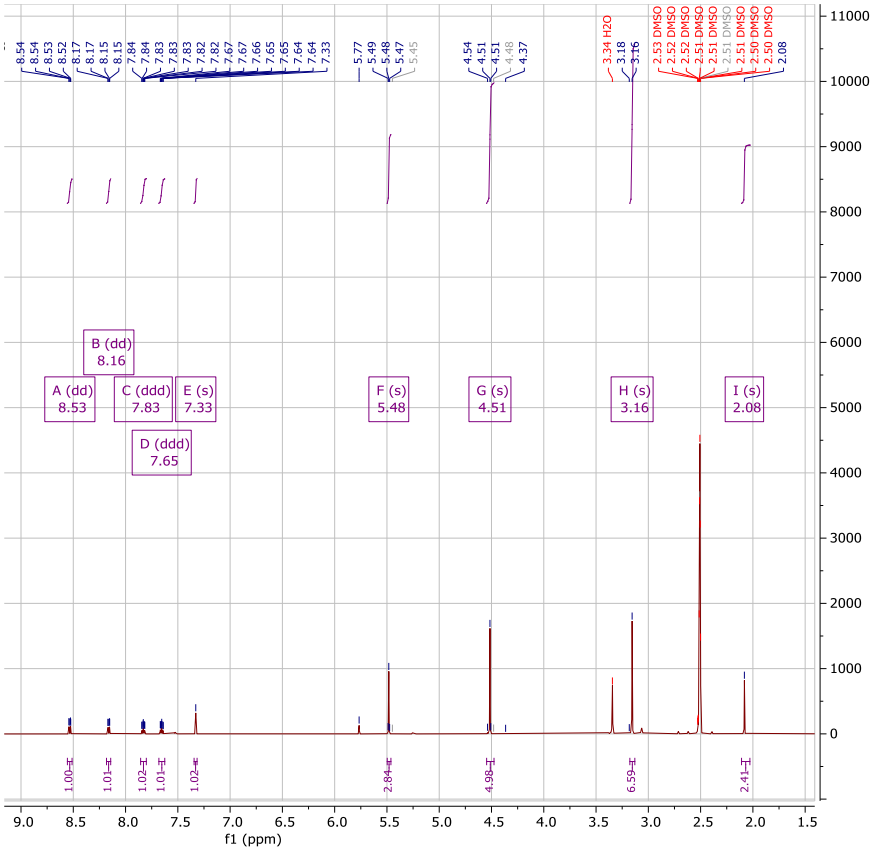

11) Synthesis of [CpRu(NMe$_2$-QA)(allyl)]PF$_6$:

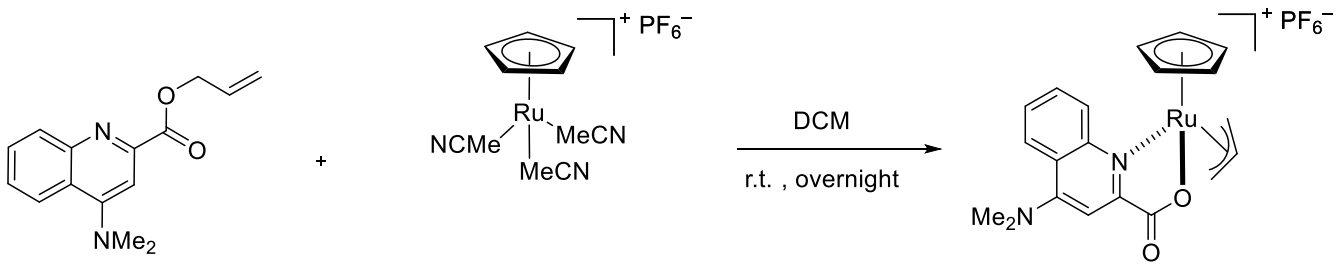

§

adapted from Meggers *et al.*[22]

Allyl 4-(dimethylamino)quinoline-2-carboxylate (17.7 mg, 1eq) and tris(acetonitrile)cyclopentadienylruthenium hexafluorophosphate (30 mg, 1eq) were dissolved in dichloromethane at room temperature overnight in the glovebox. The reaction mixture was evaporated and the resulting yellow solid was washed with Et_2O (3 x 1 mL). the was solid dried under vacuum to afford a yellow solid (31 mg, 79%).

^{1}H NMR (600 MHz, Acetonitrile-d_3) δ 8.24 (dd, J = 8.5, 1.5 Hz, 1H), 7.89 (ddd, J = 8.6, 6.8, 1.5 Hz, 1H), 7.69 – 7.58 (m, 2H), 7.30 (s, 1H), 6.10 (s, 5H), 4.55 (d, J = 10.9 Hz, 1H), 4.51 (tt, J = 10.8, 6.0 Hz, 2H), 4.32 (d, J = 10.7 Hz, 1H), 4.24 (dd, J = 6.1, 2.9 Hz, 1H), 4.03 (dd, J = 6.1, 2.9 Hz, 1H), 3.32 (s, 7H).

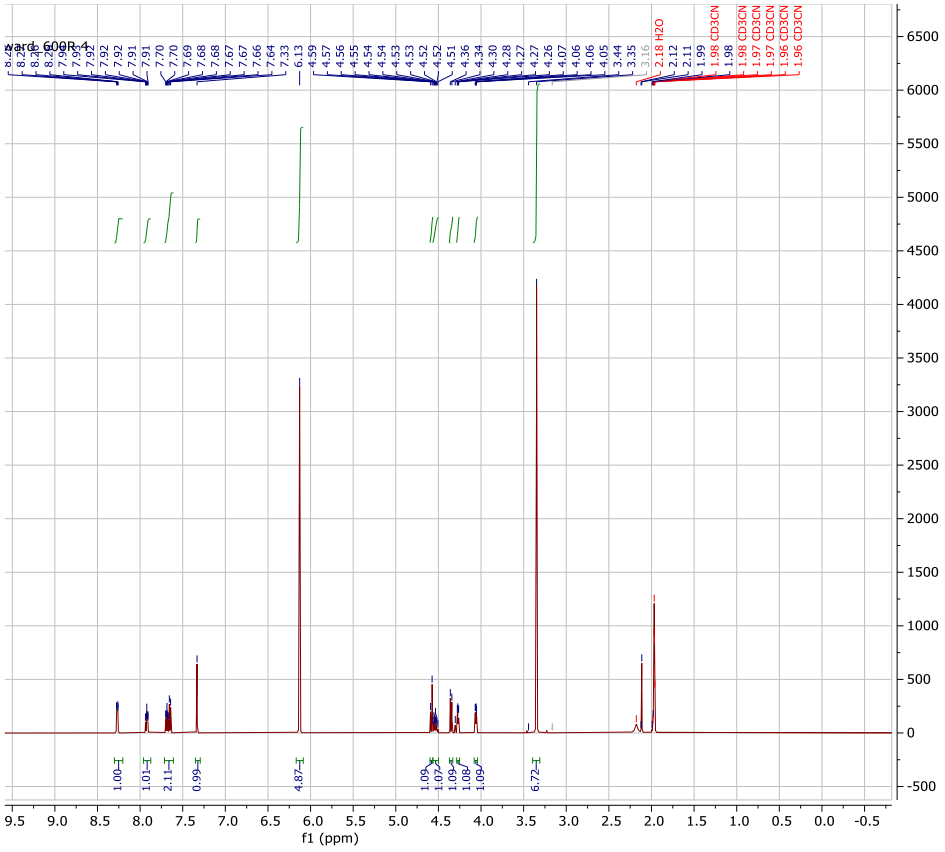

^{13}C NMR (151 MHz, CD_3CN) δ 132.0, 128.1, 127.2, 125.6, 123.3, 107.4, 102.7, 95.8, 69.1, 64.1, 43.3, 0.7, 0.6, 0.4, 0.3, 0.2.

§

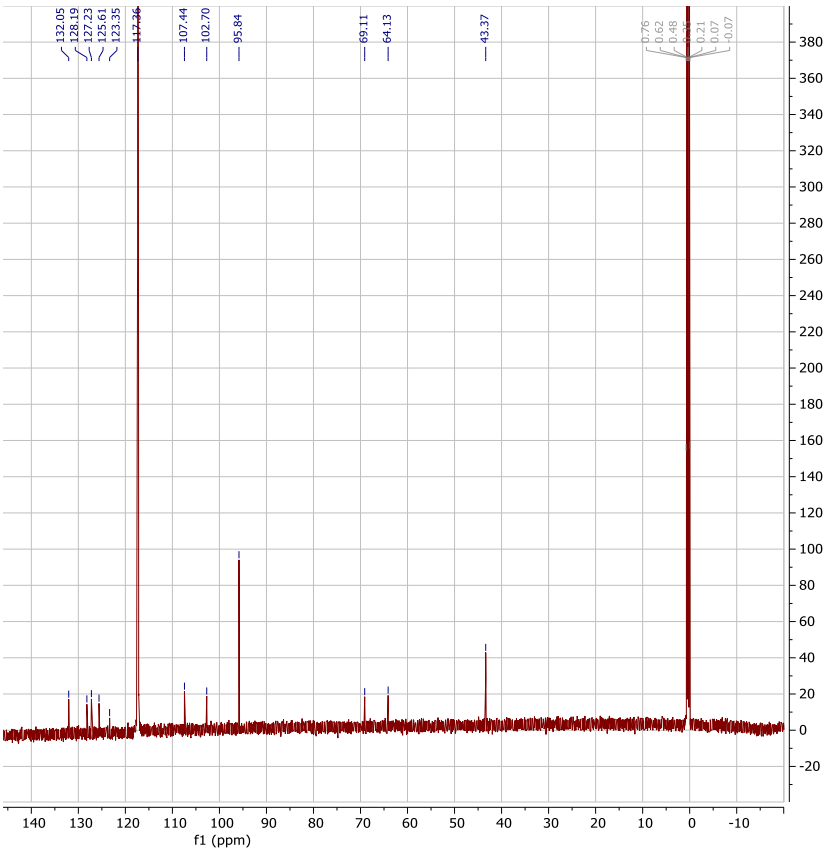

11) Synthesis of [CpRu(CO_2Me-HQ)(allyl)]PF_6:

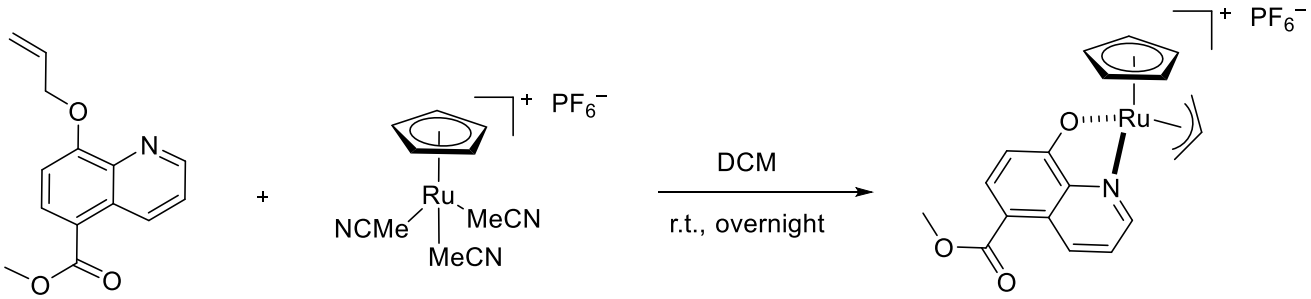

adapted from Meggers *et al.* [21]

methyl 8-(allyloxy)quinoline-5-carboxylate (16.8 mg, 1eq) and tris(acetonitrile)cyclopentadienylruthenium hexafluorophosphate (30 mg, 1eq) were dissolved in dichloromethane at room temperature overnight in the glovebox. The reaction mixture was evaporated and the resulting orange solid was washed with Et_2O (3 x 1 mL). the was solid dried under vacuum to afford an orange solid (32 mg, 83.7%).

The two Janus faces of CpRu-based deallylation catalysts and their application for in cellulo prodrug uncaging. 123

^{1}H NMR (600 MHz, Methylene Chloride-d_2) δ 9.72 (dd, J = 8.9, 1.1 Hz, 1H), 8.74 (dd, J = 5.1, 1.2 Hz, 1H), 8.25 (d, J = 8.6 Hz, 1H), 7.67 (dd, J = 8.8, 5.1 Hz, 1H), 6.95 (d, J = 8.6 Hz, 1H), 5.98 (s, 6H), 4.48 – 4.38 (m, 2H), 4.31 – 4.22 (m, 3H), 3.90 (s, 3H).

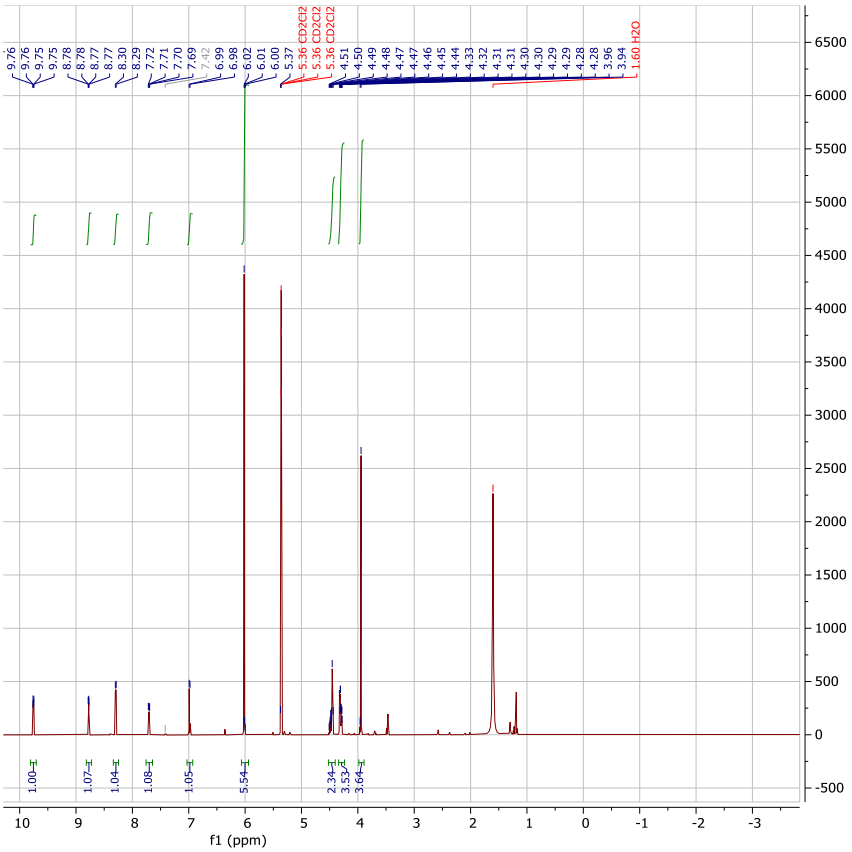

^{13}C NMR (151 MHz, CD_2Cl_2) δ 165.8, 155.1, 139.6, 136.0, 130.8, 125.3, 115.2, 111.3, 98.8, 95.6, 69.2, 64.0, 53.8, 53.6, 53.4, 53.2, 53.1, 51.8.

§

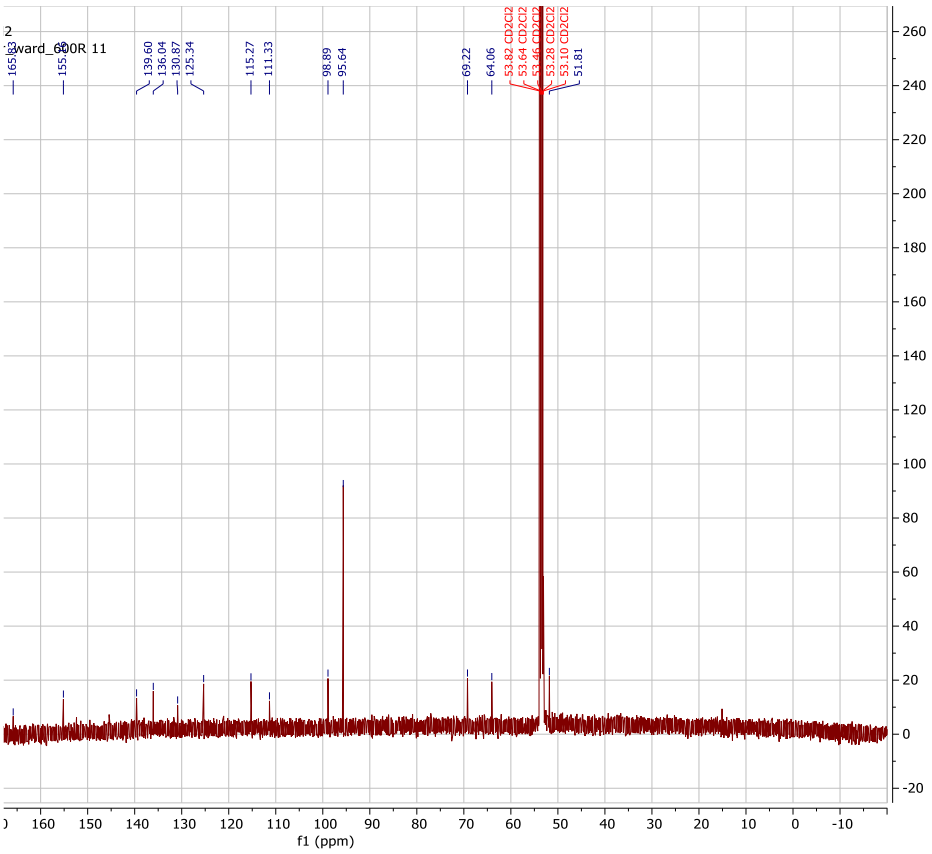

11) Synthesis S-allyl glutathione:

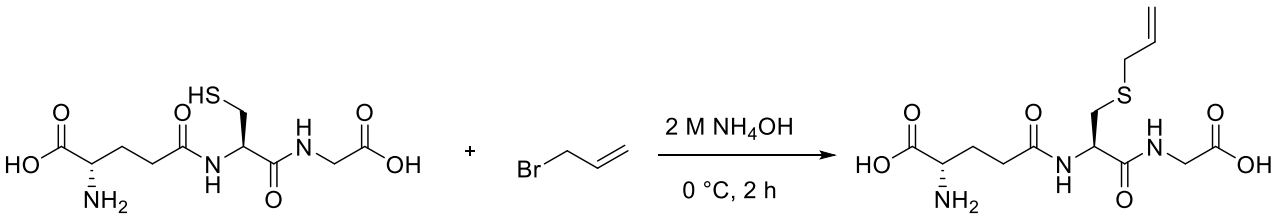

adapted from Palvannan *et al.*[224]

Glutathione (3.25 mmol, 1 eq) was dissolved in 2 M NH_4OH solution (24 mL) followed by the addition of allyl bromide (14 mmol, 4.3 eq) at 0°C, the resulting solution was stirred at 0 °C for 2 hours and filtered. The filtrate was concentrated *in vacuo* to a small volume and filtered. The solid was washed with ethanol and dried *in vacuo*. A white crude powder was obtained (1 g). Portion of this crude was purified by preparative liquid chromatography to afford a white fluffy powder.

^{1}H NMR (500 MHz, Deuterium Oxide) δ 5.84 (ddt, *J* = 17.2, 10.0, 7.2 Hz, 1H), 5.25 – 5.15 (m, 2H), 4.58 (dd, *J* = 8.6, 5.1 Hz, 1H), 3.87 (d, *J* = 3.7 Hz, 2H), 3.79 (t, *J* = 6.3 Hz, 1H), 3.22

(dt, *J* = 7.2, 1.1 Hz, 2H), 3.03 (dd, *J* = 14.2, 5.1 Hz, 1H), 2.84 (dd, *J* = 14.1, 8.7 Hz, 1H), 2.62 – 2.48 (m, 2H), 2.17 (td, *J* = 7.7, 6.3 Hz, 2H).

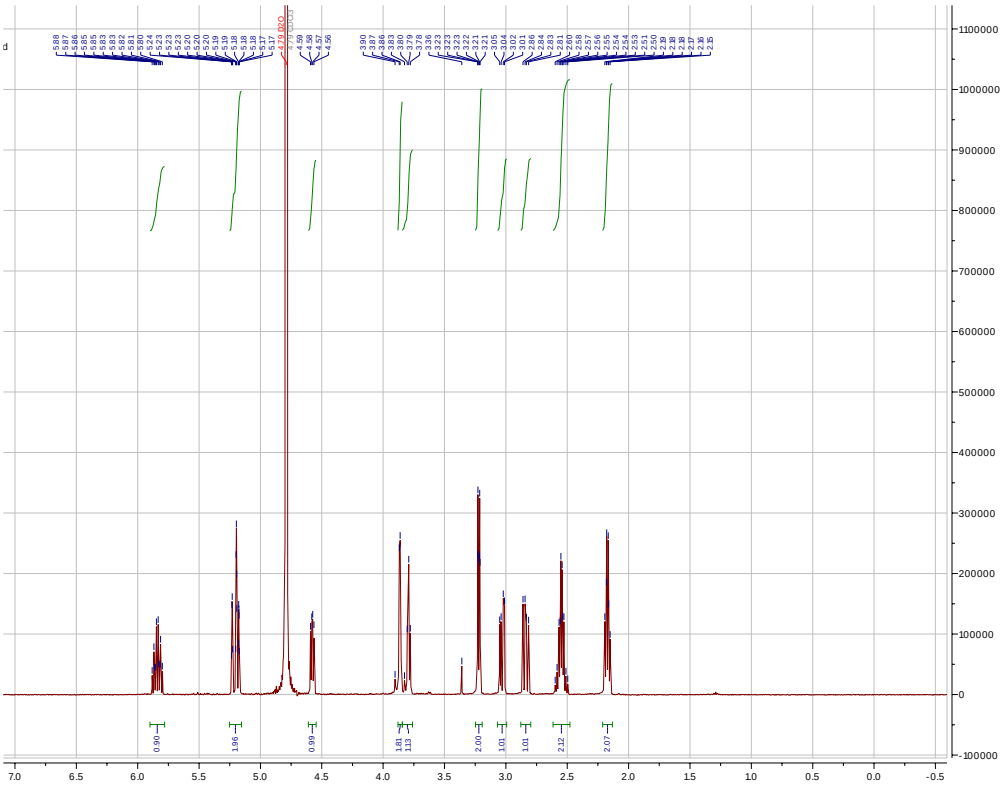

II] Ru-catalyzed deallylation and UPLC-MS monitoring:

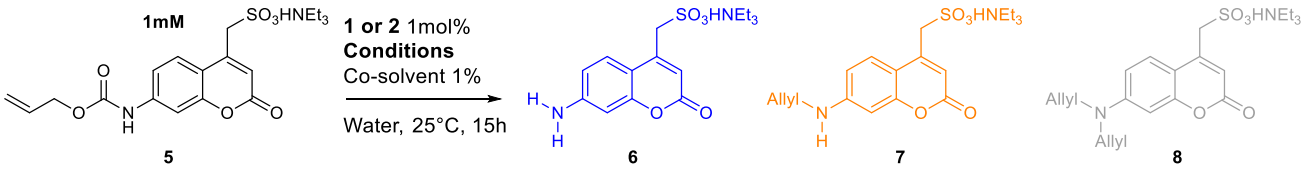

Conditions without glutathione:

In a 2 mL-vial, MQ-water (89 µL), along with a stock solution of substrate **5** (10 µL of a 10 mM stock solution in water, 0.1 µmol), and the catalyst **1** or **2** (1 µL of 1 mM stock solution, 0.001 µmol, in a given co-solvent (acetonitrile, DMF or DMSO)). The vial was placed in a thermoshaker at 25 °C and shaken at 600 rpm for 15 h. Then, part of the reaction mixture (25 µL) was diluted in a 2 mL-vial containing MQ-water/Acetonitrile (130 µL total, 50:50). The internal standard (10 µL of a 0.1 mM biphenyl stock solution, 0.001 µmol) was added,

the vial was vortexed and then transferred into another 2 mL-vial containing a 100 µL inlet. The resulting solution was subjected to UPLC-MS analysis.

Conditions with glutathione:

In a 2mL-vial was added 69 µL of MQ-water followed by 10 µL solution of **5** (10 µL of a 10 mM stock solution in water, 0.1 µmol), glutathione (20 µL solution of 50 mM stock solution in water, 1 µmol) and the catalyst **1** or **2** (1 µL of 1 mM stock solution, 0.001 µmol, in a given co-solvent (acetonitrile, DMF or DMSO)). The vial was placed in a thermoshaker at 25 °C and 600 rpm for 15 h. After 15 h, 25 µL of the reaction mixture was dissolved in a 2-mL vial containing 65 µL of MQ-water/Acetonitrile (50:50) and then The internal standard (10 µL of a 0.1 mM biphenyl stock solution, 0.001 µmol) was added , the vial was vortexed and then transferred into another 2mL-vial containing a 100 µL inlet and the final vial was subjected to UPLC-MS analysis.

	Average **5** (%)	Average **6** (%)	Average **7** (%)	Average **8**(%)	Average conversion (%)
1					
Air	12.75 +/- 0.9	55.11 +/- 0.95	16.61 +/- 0.12	15.53 +/- 1.58	87.25 +/- 0.9
Air + GSH	18.35 +/- 2.04	67.10 +/- 2.48	13.81 +/- 1.66	0.74 +/- 0.21	81.65 +/- 2.04
No air	0 +/- 0	62.66 +/- 0.57	21.26 +/- 0.21	16.08 +/- 0.4	100 +/- 0
No air + GSH	0 +/- 0	90.27 +/- 0.72	9.73 +/- 0.72	0 +/- 0	100 +/- 0
2					
Air	5.09 +/- 0.18	57.24 +/- 0.58	18.53 +/- 0.25	19.11 +/- 0.4	94.90 +/- 0.18
Air + GSH	5.58 +/- 0.52	73.87 +/- 0.2	19.72 +/- 0.46	0.81 +/- 0.09	94.413 +/- 0.52
No air	0 +/- 0	58.86 +/- 0.17	20.50 +/- 0.2	20.63 +/- 0.05	100 +/- 0
No air + GSH	0 +/- 0	91.74 +/- 0.51	8.25 +/- 0.51	0 +/- 0	100 +/- 0
4					
Air	100 +/- 0	0 +/- 0	0 +/- 0	0 +/- 0	0 +/- 0
Air + GSH	100 +/- 0	0 +/- 0	0 +/- 0	0 +/- 0	0 +/- 0
No air	93.83 +/- 0.25	6.16 +/- 0.25	0 +/- 0	0 +/- 0	6.16 +/- 0.25
No air + GSH	8.15 +/- 0.57	70.06 +/- 0.74	18.76 +/- 0.34	3.02 +/- 0.03	91.84 +/- 0.57

Table S1: Results from the catalyst 1,2 and 4 screening comparison. The results are from independent triplicates measured by UPLC.

	Average **5** (%)	Average **6** (%)	Average **7** (%)	Average **8**(%)	Average conversion (%)
DMSO					
Air	12.75 +/- 0.9	55.11 +/- 0.95	16.61 +/- 0.12	15.53 +/- 1.58	87.25 +/- 0.9
Air + GSH	18.35 +/- 2.04	67.10 +/- 2.48	13.81 +/- 1.66	0.74 +/- 0.21	81.65 +/- 2.04
No air	0 +/- 0	62.66 +/- 0.57	21.26 +/- 0.21	16.08 +/- 0.4	100.00 +/- 0
No air + GSH	0 +/- 0	90.27 +/- 0.72	9.73 +/- 0.72	0 +/- 0	100.00 +/- 0
DMF					
Air	77.44 +/- 0.94	4.44 +/- 0.56	10.58 +/- 0.44	7.54 +/- 0.26	22.56 +/- 0.94
Air + GSH	96.62 +/- 0.94	2.92 +/- 0.93	0.46 +/- 0.06	0 +/- 0	3.38 +/- 0.94
No air	0 +/- 0	43.04 +/- 3.13	53.35 +/- 2.43	3.62 +/- 0.7	100 +/- 0
No air + GSH	0 +/- 0	99.56 +/- 0.02	0.44 +/- 0.02	0 +/- 0	100 +/- 0
MeCN					
Air	87.66 +/- 1.89	5.82 +/- 3.3	4.61 +/- 1.7	1.90 +/- 1.15	12.34 +/- 1.89
Air + GSH	94.95 +/- 2.11	2.78 +/- 1.09	2.24 +/- 1.01	0.02 +/- 0.01	5.05 +/- 2.11
No air	0 +/- 0	60.80 +/- 2.78	23.52 +/- 2.22	15.68 +/- 0.75	100 +/- 0
No air + GSH	0 +/- 0	89.53 +/- 3.61	10.47 +/- 3.61	0 +/- 0	100 +/- 0

Table S2: Results from the co-solvent screening comparison. The results are from independent triplicates measured by UPLC.

UPLC-MS conditions:

Elution system:

A: MQ-water + 0.1% formic acid

B: Acetonitrile + 0.1% formic acid

Gradient used:

The flow was kept at 0.55 mL/min for the whole run.

Initial: 99% **A** /1% **B** => 1.5 min: 99% **A** /1% **B** =>4 min: 75% **A** /25% **B** =>6 min: 30% **A** /70% **B** =>9 min: 30% **A** /70% **B** =>9.5 min: 99% **A** /1% **B** =>10 min: 99% **A** /1% **B**

Standard curves:

The two Janus faces of CpRu-based deallylation catalysts and their application for in cellulo prodrug uncaging. 128

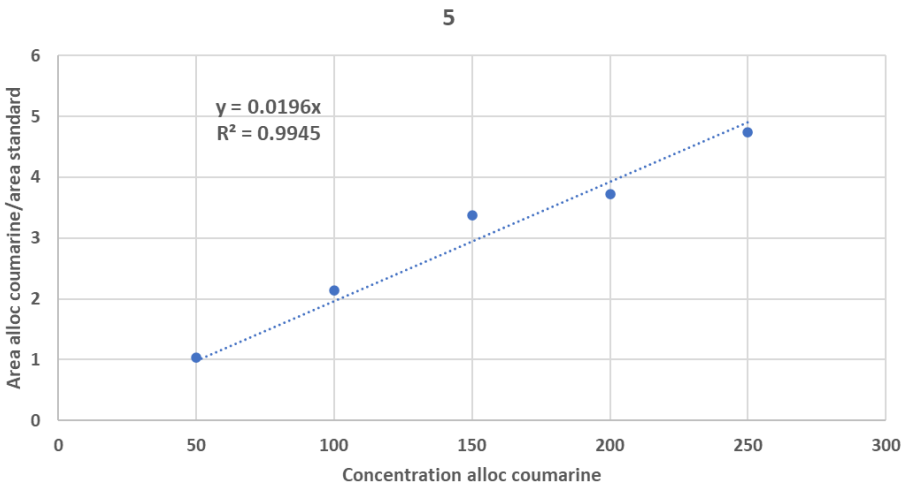

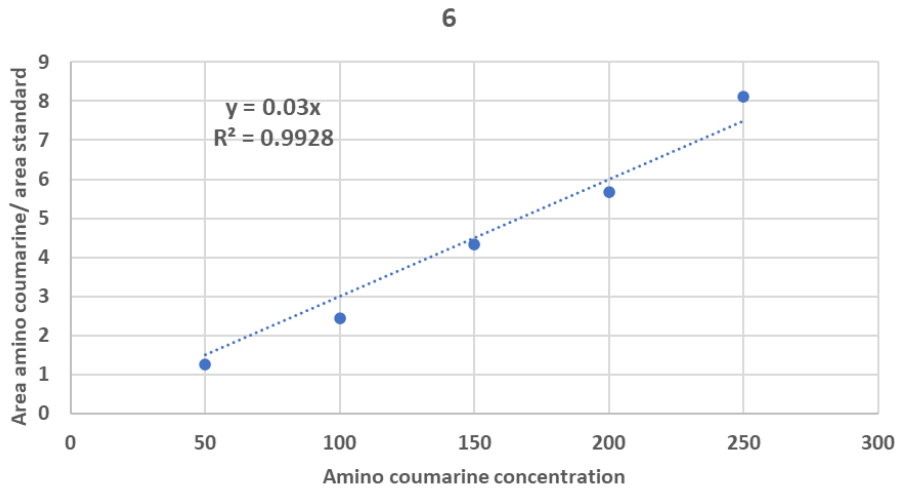

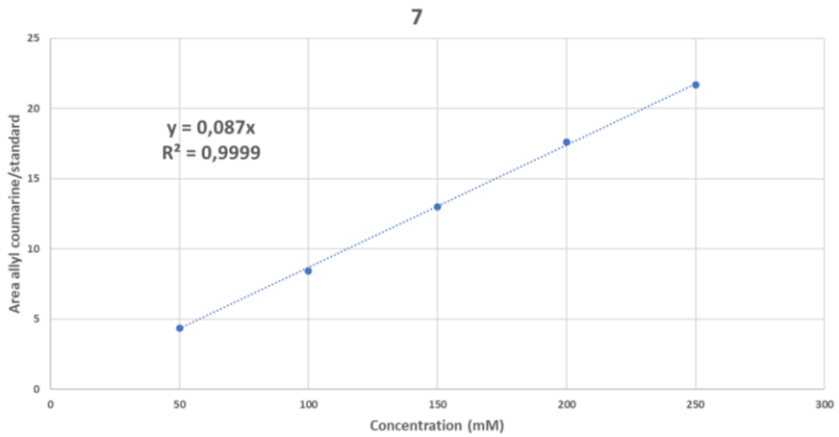

§

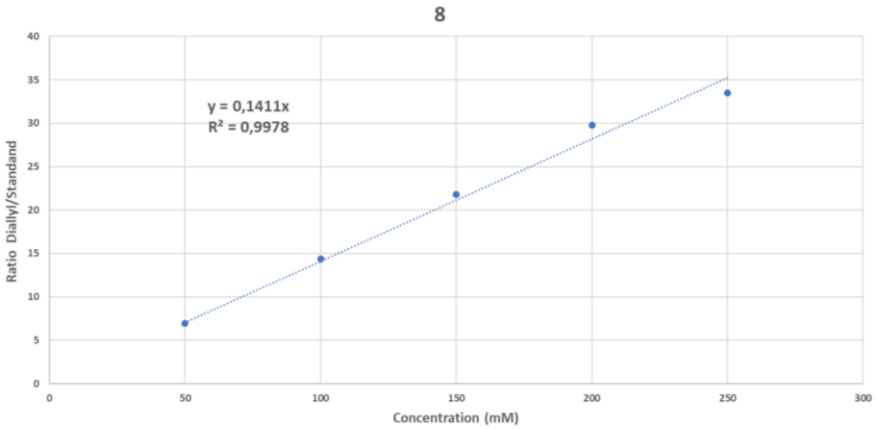

Figure S1: *Standard curve of **5**, **6**, **7** and **8**.*

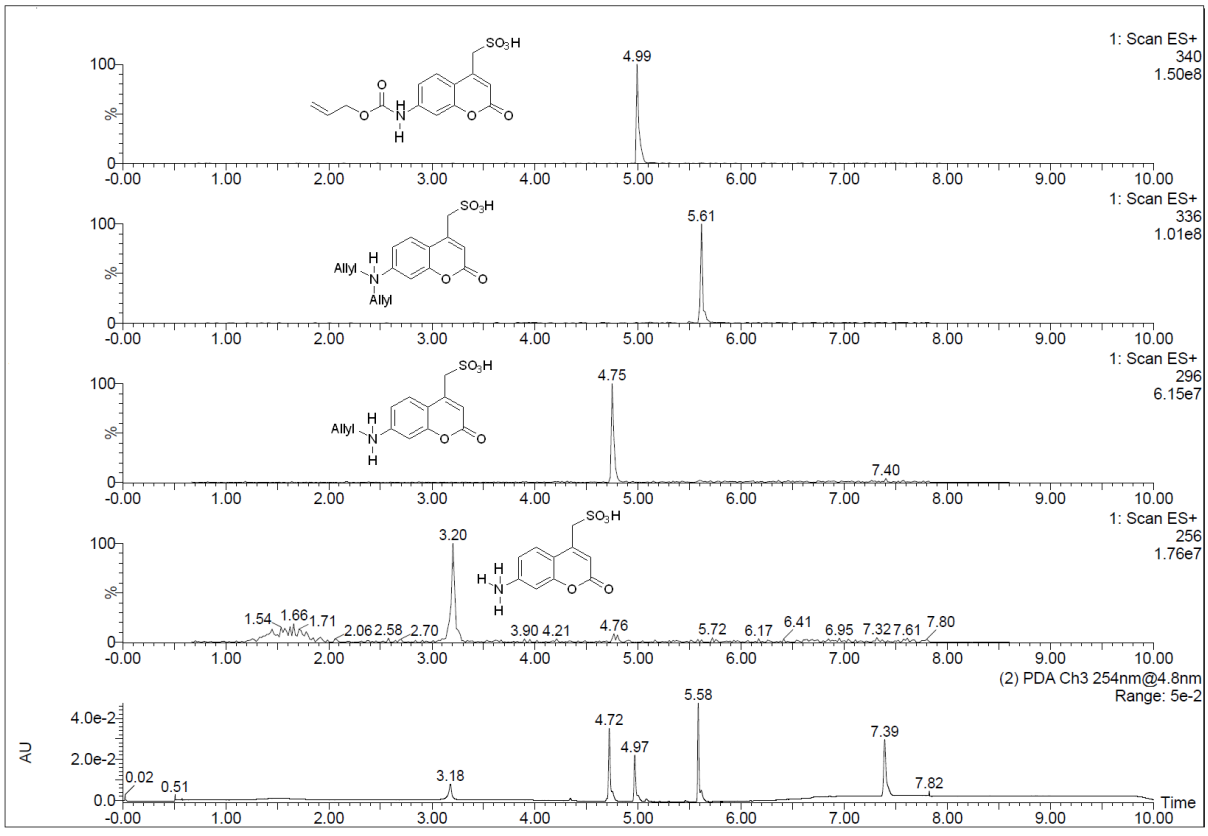

Figure S2: UPLC-MS traces of **5**, **6**, **7**, **8** and the corresponding MS analysis. The UV spectrum was taken at 254 nm. The last spectrum represents the analysis of a Ru-catalyzed deallylation reaction.

III] Glutathione oxidation monitored by ^{1}H NMR:

Influence of the co-solvent on 1 stability

A solution of 10 mM of catalyst **1** was prepared in the corresponding solvent (DMSO, DMF or MeCN) without air (in this experiment, samples were prepared in the gloveboxe having a N_2 atmosphere). A ^1H NMR was recorded for each solvent and afterward the corresponding NMR sample was exposed to air for 15 minutes prior resubmission to ^1H NMR .

Ru-catalyzed oxidation in the presence of air

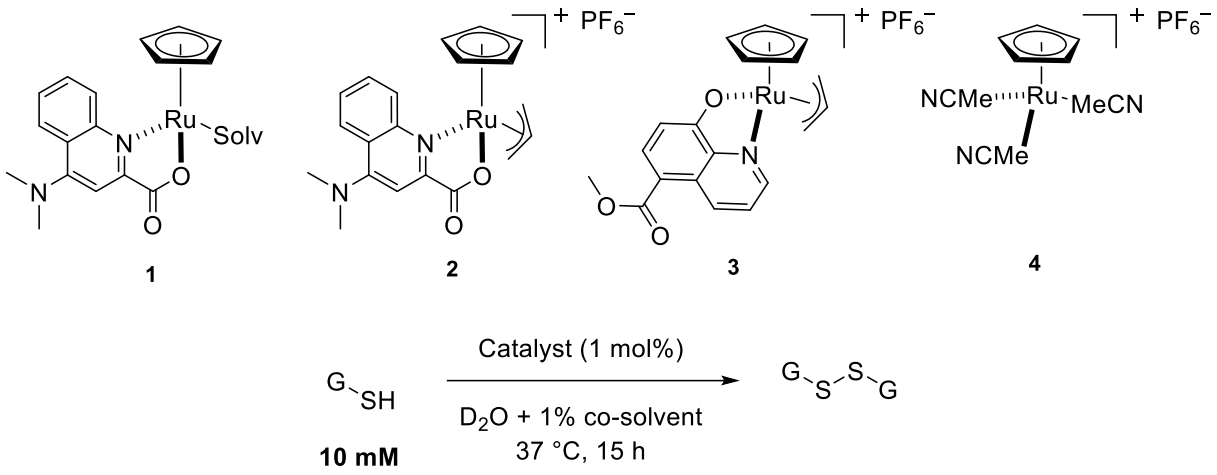

D2O (395 µL) was added to a 2mL vial followed by a solution of glutathione (100 µL, 50 mM stock solution in D_2O) and a solution of the corresponding catalyst (5 µL, 10mM stock solution in the corresponding deuterated co-solvent or not deuterated co-solvent). The resulting solution was placed in a thermoshaker and stirred at 300 rpm (37°C, 15h). Then, a solution of standard (100 µL, 6mM stock solution of Dimethyl sulfone in D_2O) was added to the vial, the resulting solution was vortexed, and subjected to a quantitative ^1H-NMR analysis using a relaxation delay time d_1=30s. The peak used for the quantification is the CH_2 proton in α-position of the disulfide bond.

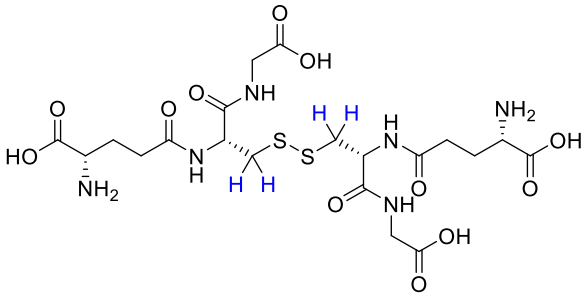

§

^{1}H NMR:

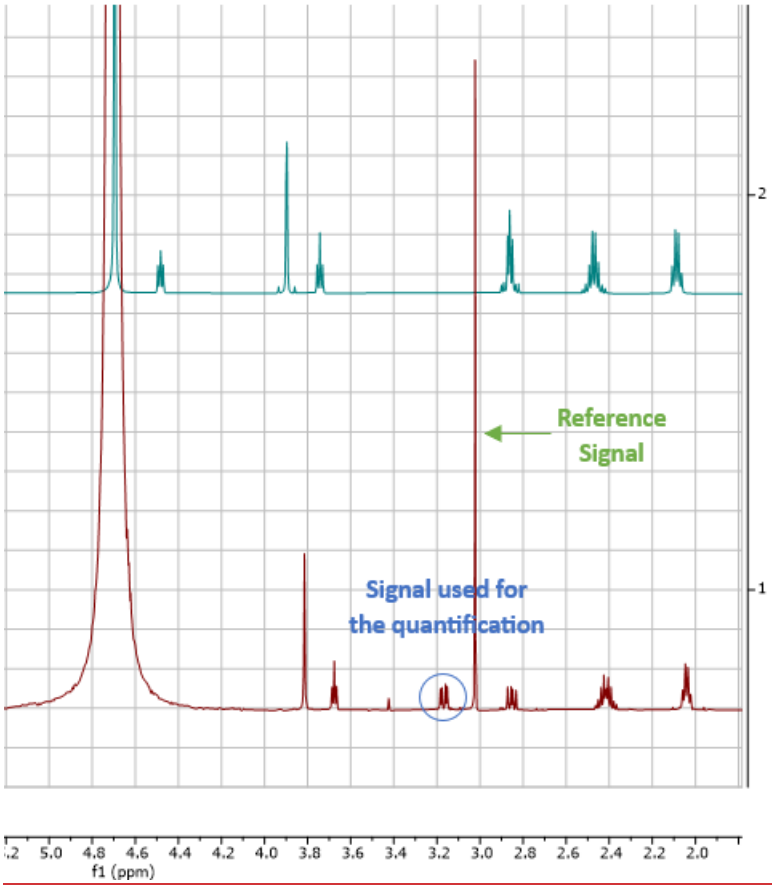

Figure S3: ^{1}H NMR of GSH and GSG respectively, highlighting the reference signal (dimethyl sulfone) and the methylene signal used for quantification of conversion.

Effect of DMSO on glutathione oxidation:

D2O (395 µL) was added to a 2mL vial followed by a solution of glutathione (100 µL, 50 mM stock solution in D_2O) and not deuterated DMSO (5 µL, coming from different sources). The resulting solution was put in a thermoshaker at 37°C for 15h. After 15h, a solution of standard (100 µL, 6mM stock solution of Dimethyl sulfone in D_2O) was added to the vial, the resulting solution was vortexed and then transferred into a 6mm NMR tube. The NMR tube was then subjected to a quantitative NMR analysis with d_1=30s.

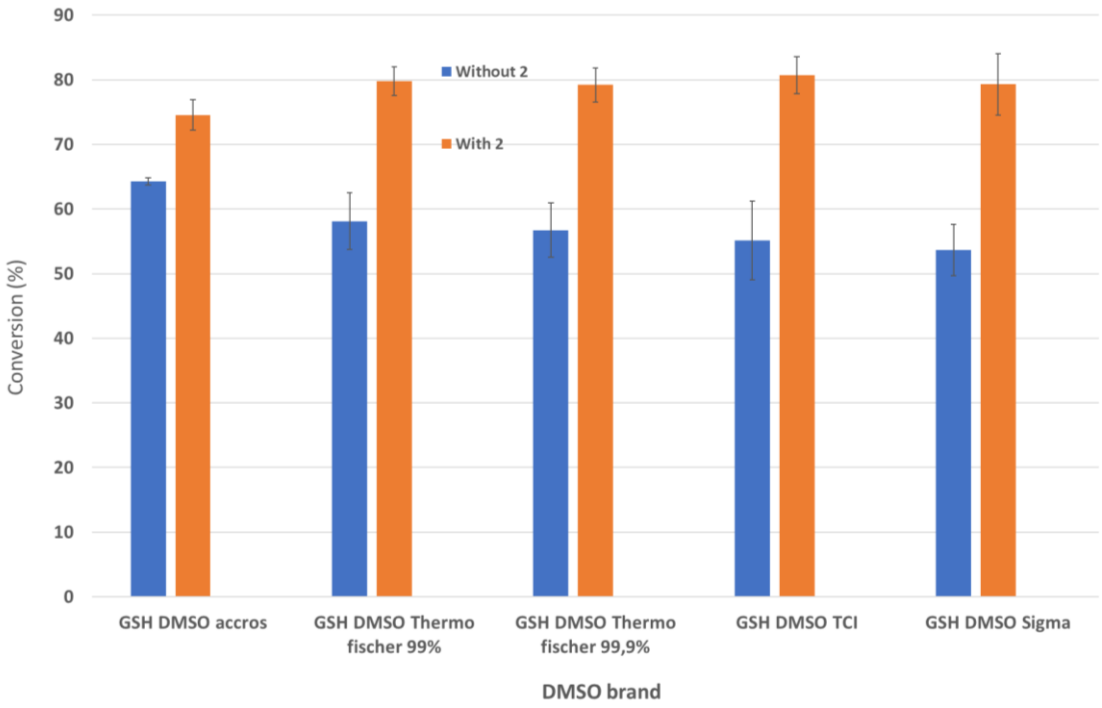

Figure S4: GSH conversion in the presence of different DMSO sources.

IV] Oxygen evolution experiment:

Experimental procedure:

Depending on the measurement, GSH could be added with or without **5**. The oxygraphs were measured with a catalytic loading of 1% versus GSH to mimic the NMR conditions.

360 µL of glutathione (1 eq, 18 µmol) were added in a 2-mL sealed cap vial followed by 180 µL of substrate **5** solution in water (0.1 eq, 1.8 µmol), the vial volume was then adjusted to 1782 mL with MQ-water prior sealing. Finally, once the probe is in place, 18 µL of catalyst **1** solution (in either MeCN, DMF or DMSO, 0.01 eq, 0.18 µmol) was added and the oxygen decay measured.

V] UV-vis experiment on 1 in different solvent:

10 µL of catalyst **1** solution (in either MeCN, DMF or DMSO, 0.1 µM) was added in a quartz-cuve for UV measurement and diluted with 990 µL of MQ-water. The UV-vis measurement were taken according to the condition displayed on each spectrum.

MeCN as co-solvent:

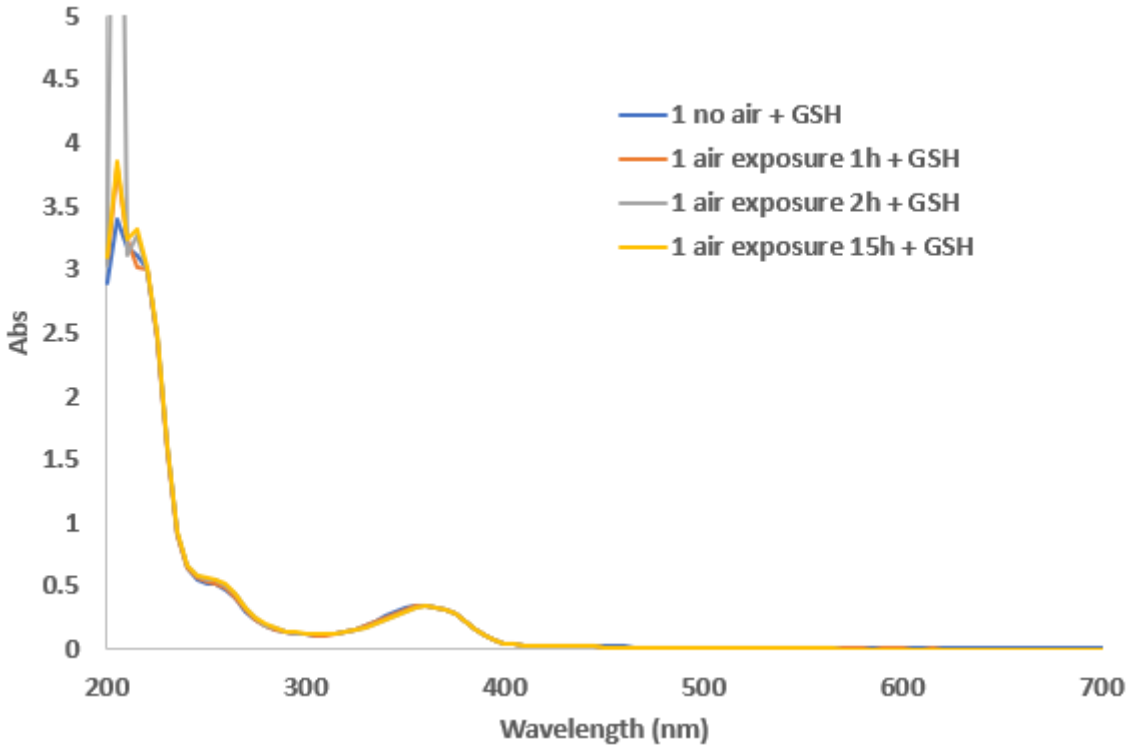

Figure S5: Evolution of **1** with GSH in the absence or presence of air. Superimposition makes the curves indistinguishable from each other.

DMF as co-solvent:

with GSH:

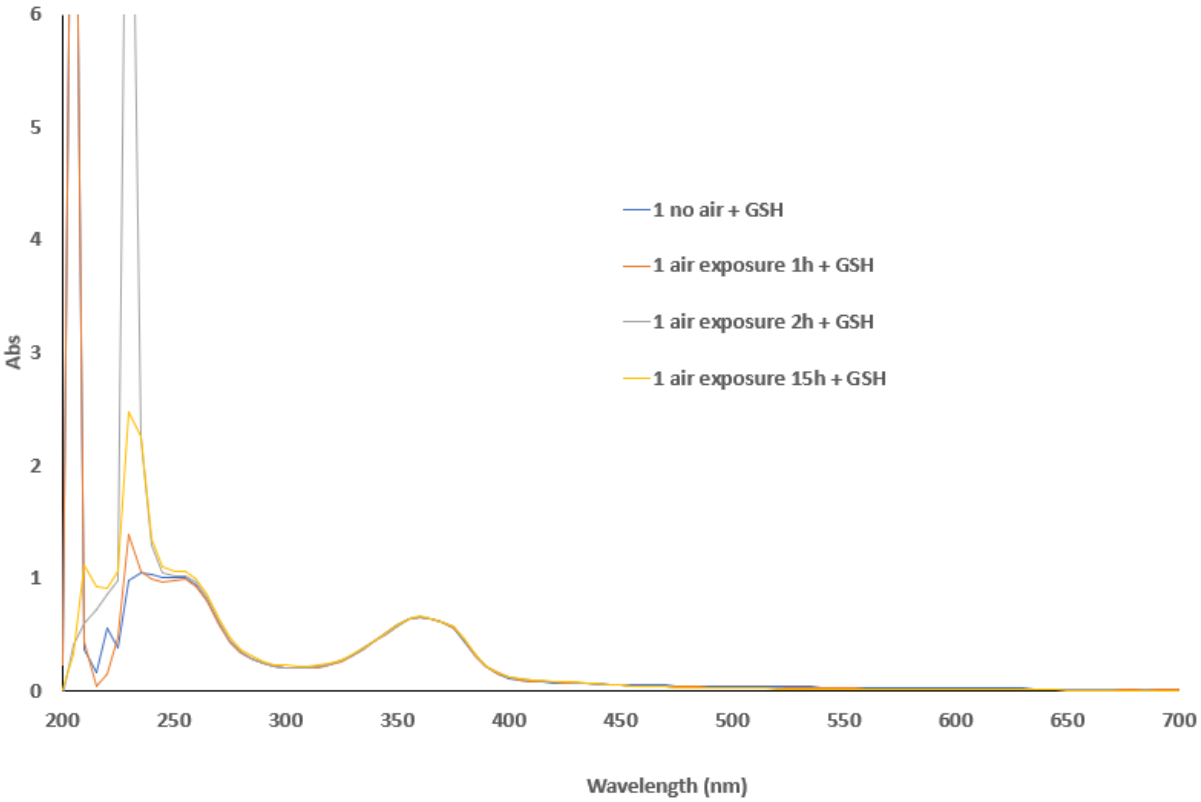

Figure S6: Evolution of **1** with GSH in the absence or presence of air. Superimposition makes the curves indistinguishable from each other.

DMSO as co-solvent:

with GSH:

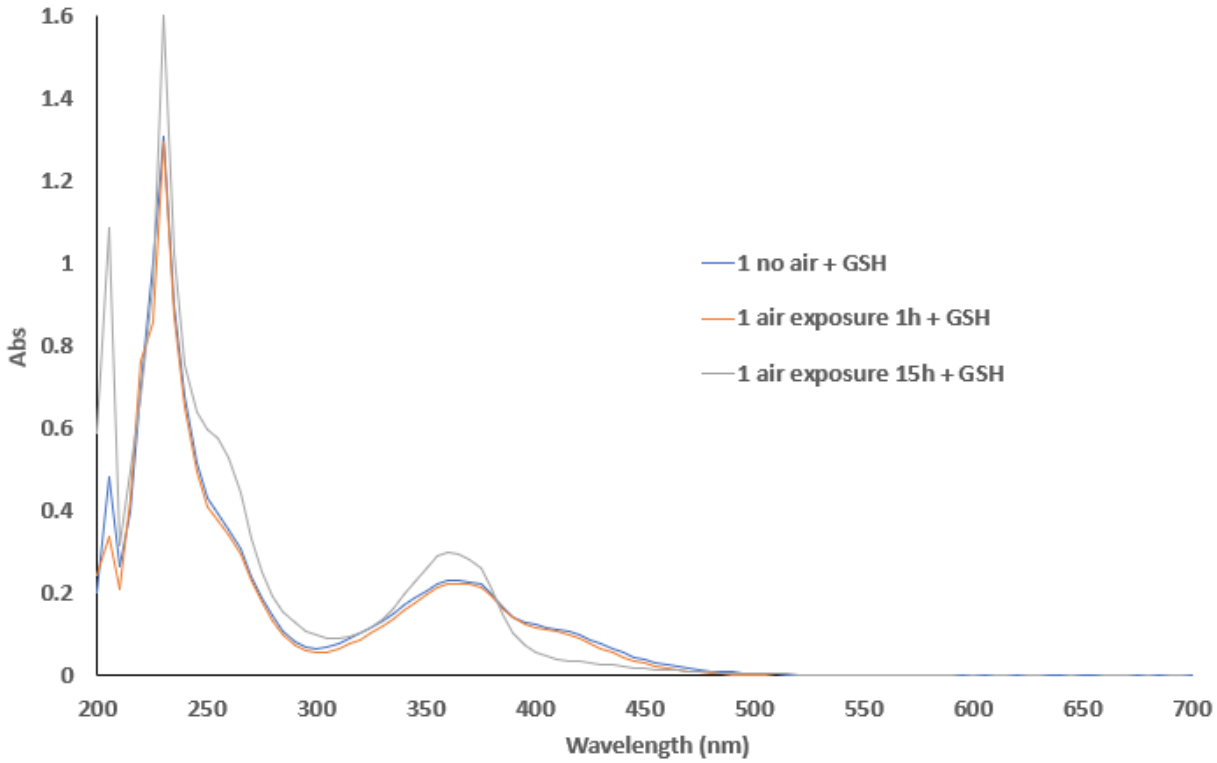

Figure S7: Evolution of **1** with GSH in the absence or presence of air.

UV-Vis spectrum profile comparison depending on the solvent:

Without air/GSH:

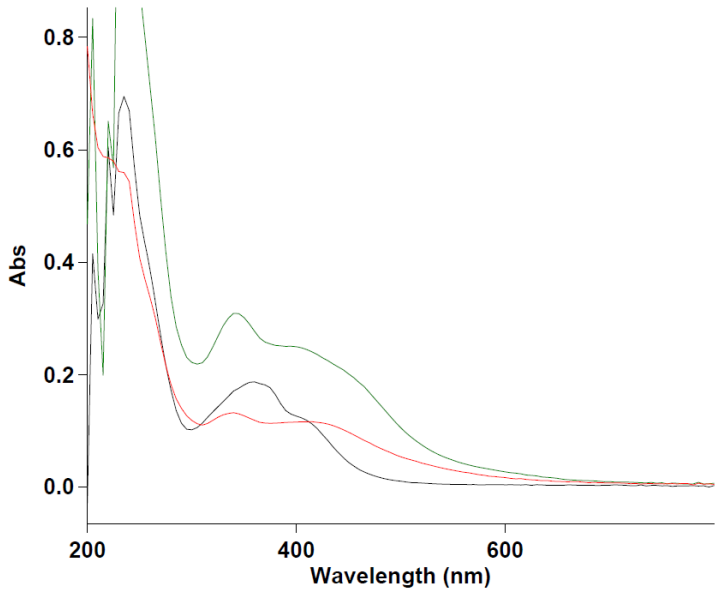

Figure S8: Evolution of the UV-Vis spectrum of **1** after one night (5h for MeCN). In black: DMSO, green: DMF and red: MECN.

§

Without air with GSH:

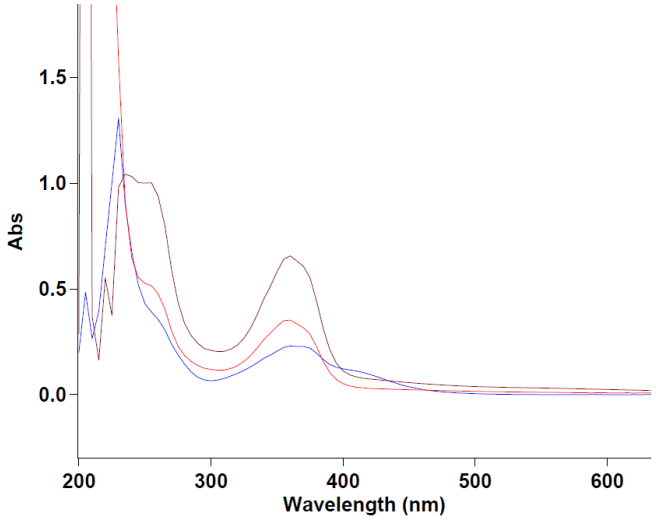

Figure S9: Evolution of the UV-Vis spectrum of **1** after one night (5h for MeCN). In blue: DMSO, brown: DMF and red: MECN.

With air without GSH:

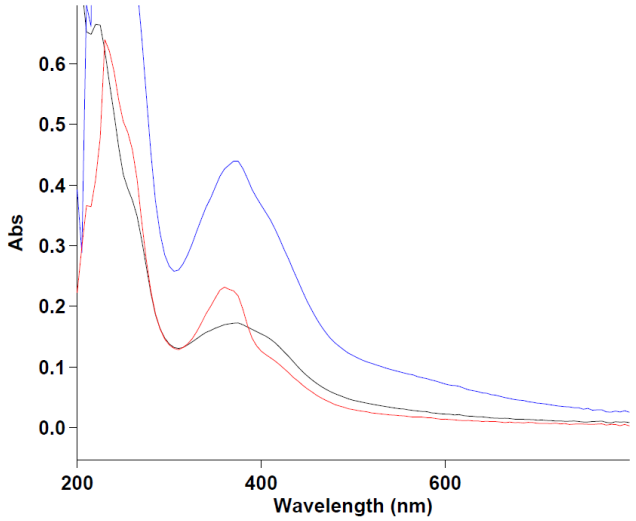

Figure S10: Evolution of the UV-Vis spectrum of **1** after one night (5h for MeCN). In red: DMSO, blue: DMF and black: MECN.

With air and GSH:

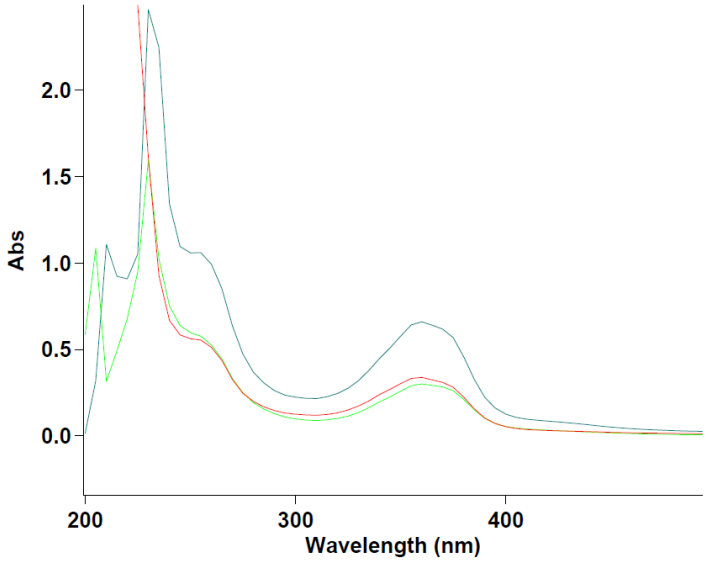

Figure S11: Evolution of the UV-Vis spectrum of **1** after one night (5h for MeCN). In green: DMSO, blue: DMF and red: MECN.

VI] H_2O_2 determination by HRP titration:

The quantification of H_2O_2 was carried out via a Horseradish Peroxidase assay using the oxidation of TMB as a quantitative readout for the presence of H_2O_2 the analysis of the oxidation product of TMB. Horseradish peroxide catalyses the oxidation reaction between TMB and H_2O_2 and from the oxidation product of TMB the quantification of H_2O_2 is followed. For the experiment different vials were prepared. One containing only [$CpRu^{II}(NMe_2\text{-}QA)(solv)$] **1** , one containing [$CpRu^{II}(NMe_2\text{-}QA)(solv)$] **1** and the TMB and a last one containing [$CpRu^{II}(NMe_2\text{-}QA)(solv)$] **1**, the TMB and the HRP and the reactions were shaken at 37°C at 700rpm for 1h30 in a thermoshaker.

Vial 1: [$CpRu^{II}(NMe_2\text{-}QA)(solv)$] **1** (5 µL, stock solution of 1 mM in DMF, final concentration 10 µM) was added in MQ-water (409 µL) in a 2mL vial equipped with a screw cap. After 1h30, TMB solution (5 µL, from a stock solution of 50 mM in DMF, final concentration 500 µM) and HRP solution (76 µL, 263 U/mL stock solution in water, final concentration 20 U/mL) were added to the vial. The solution was subjected to UV-Vis analysis to detect the presence of oxidized TMB (λ_{max} = 650 nm).

Vial 2: [$CpRu^{II}(NMe_2\text{-}QA)(solv)$] **1** (5 µL, stock solution of 1 mM in DMF, final concentration 10 µM) was added in MQ-water (414 µL) in a 2mL vial equipped with a screw cap followed by TMB solution (5 µL, from a stock solution of 50 mM in DMF, final

concentration 500 μM). After 1h30, HRP solution (76 μL, 263 U/mL stock solution in water, final concentration 20 U/mL) were added to the vial and the UV-vis measurement was done.

Vial 3: [$CpRu^{II}(NMe_2$-QA)(solv)] **1** (5 μL, stock solution of 1 mM in DMF, final concentration 10 μM) was added in MQ-water (414 μL) in a 2mL vial equipped with a screw cap followed by TMB solution (5 μL, from a stock solution of 50 mM in DMF, final concentration 500 μM). and HRP solution (76 μL, 263 U/mL stock solution in water, final concentration 20 U/mL) were added to the vial and the UV-vis measurement was done. After 1h30 the UV-vis measurement was done.

To confirm that the assay could indeed detect the formation of H_2O_2 identical three vials described above were spiked after 90 min with 10, 20 and 30 mM of H_2O_2. This was meant to mimic 1, 2 and 3 TONs..

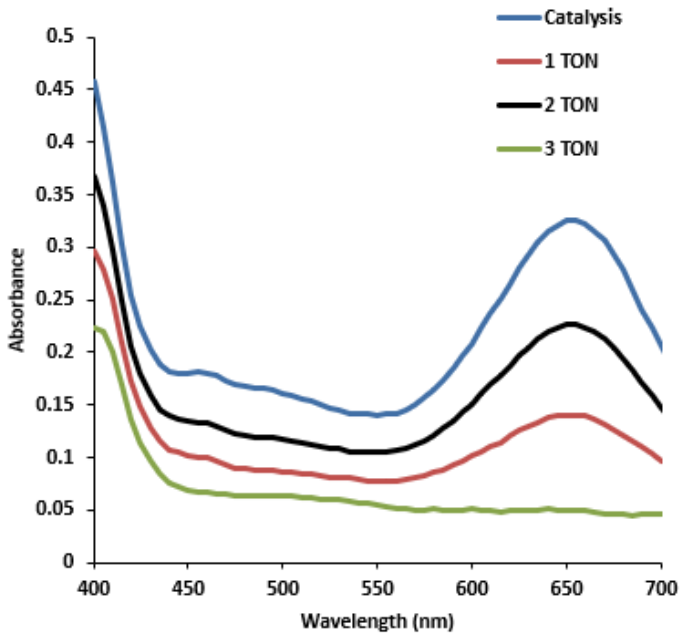

Figure S12: UV-Vis trace resulting from vial 1, spiked with varying amounts of H_2O_2. In green: catalysis result; in red: result mimicking the formation of 1 eq. H_2O_2 per cat **1**; in black: result mimicking the formation of 2 eq. H_2O_2 per cat **1** and in blue: result mimicking the formation of 3 eq. H_2O_2 per cat **1**.

§

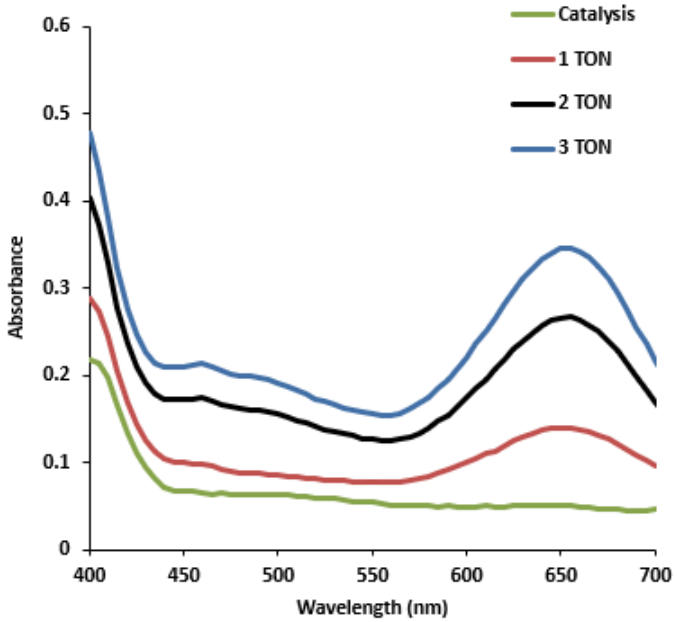

Figure S13: Result from vial 2 type preparation. In green: catalysis result; in red: result mimicking the formation of 1 eq. H_2O_2 per cat **1**; in black: result mimicking the formation of 2 eq. H_2O_2 per cat **1** and in blue: result mimicking the formation of 3 eq. H_2O_2 per cat **1**.

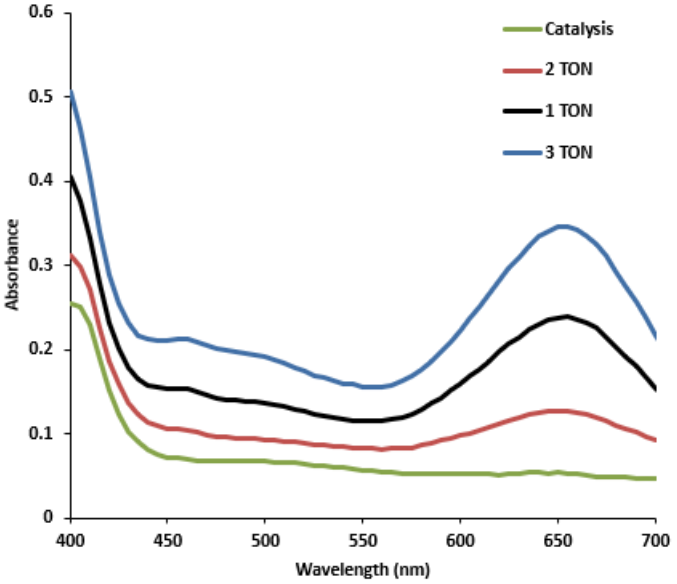

Figure S14: Result from vial 3 type preparation. In green: catalysis result; in red: result mimicking the formation of 1 eq. H_2O_2 per cat **1**; in black: result mimicking the formation of 2 eq. H_2O_2 per cat **1** and in blue: result mimicking the formation of 3 eq. H_2O_2 per cat **1**.

VII] MS-MS experiment to determine the oxidation site on the catalyst:

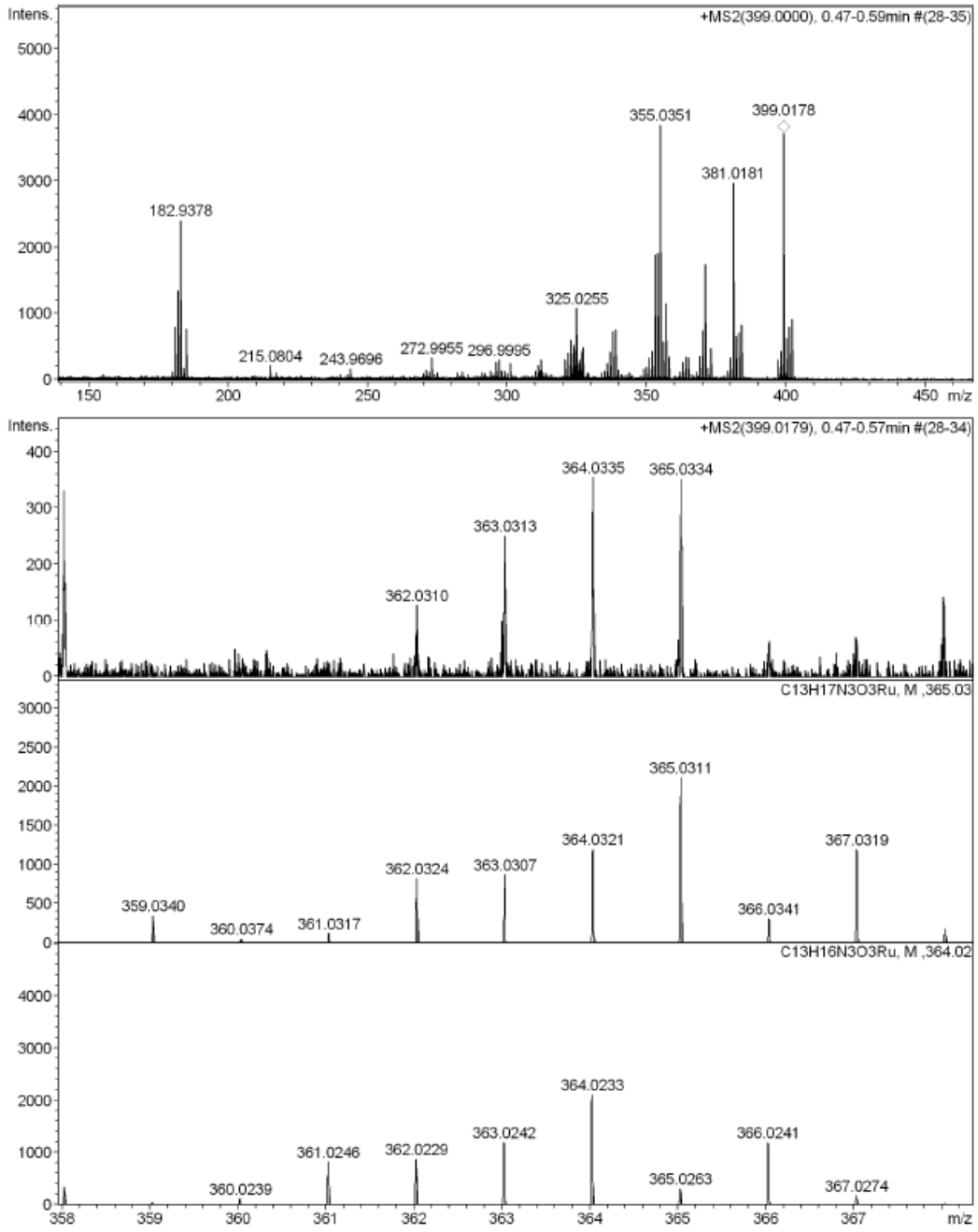

Measured m/z vs. theoretical m/z

Meas. m/z	#	Formula	Score	m/z	err [mDa]	err [ppm]	mSigma	rdb	e¯ Conf	z
355.0352	1	C 16 H 17 N 2 O Ru	100.00	355.0383	2.7	7.5	154.1	10.0	odd	1+
365.0334	1	C 13 H 17 N 3 O 3 Ru	100.00	365.0311	-2.2	-6.1	401.2	7.5	even	
371.0312	1	C 16 H 17 N 2 O 2 Ru	100.00	371.0332	1.7	4.4	163.8	10.0	odd	

Proposed adduct:

§

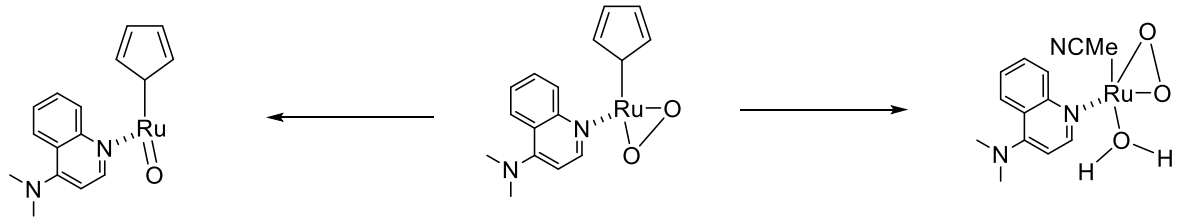

Chemical Formula: $C_{16}H_{17}N_2ORu$
m/z: 355.04 (100.0%)

Chemical Formula: $C_{16}H_{17}N_2O_2Ru$
m/z: 371.03 (100.0%)

Chemical Formula: $C_{13}H_{17}N_3O_3Ru$
m/z: 365.03 (100.0%)

Figure S15: MS-MS experiment of **1** in MECN, comparison of the measured mass with the proposed structure showing a match.

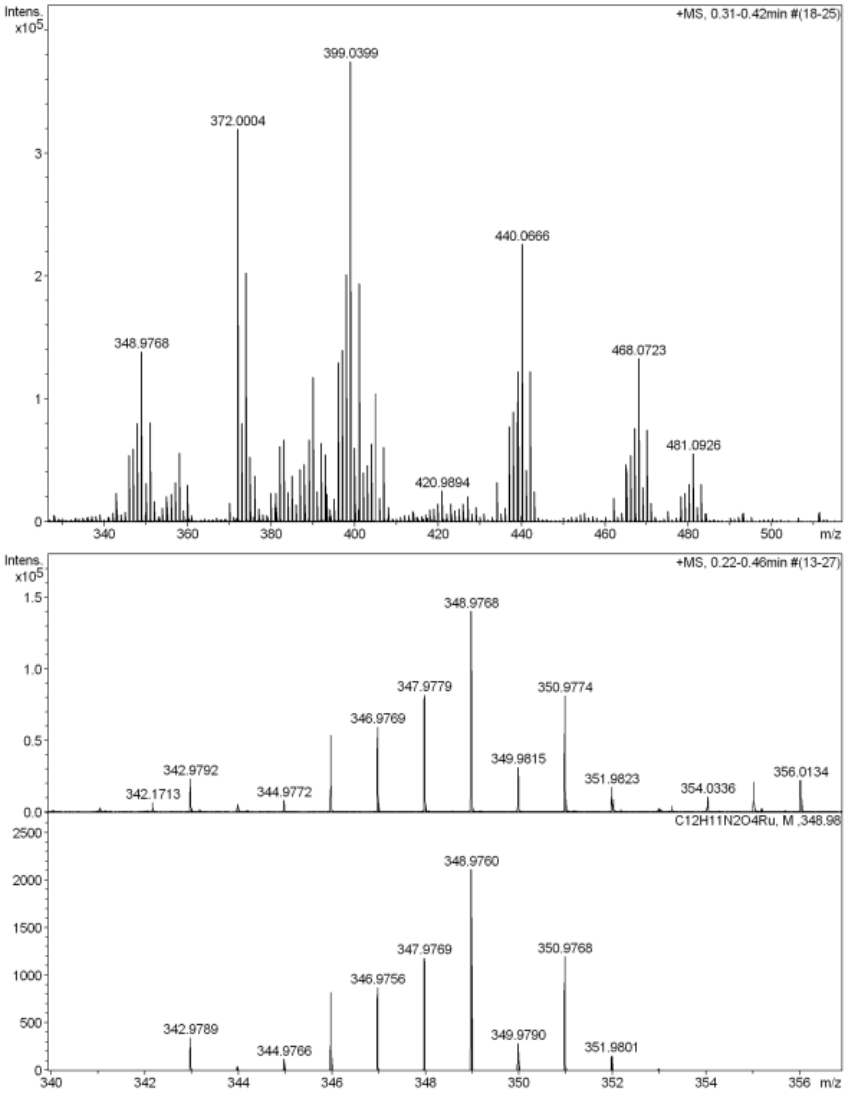

Measured m/z vs. theoretical m/z

Meas. m/z	#	Formula	Score	m/z	err [mDa]	err [ppm]	mSigma	rdb	e⁻ Conf	z
348.9768	1	C 12 H 11 N 2 O 4 Ru	100.00	348.9760	-0.8	-2.4	33.9	9.0	odd	1+

Proposed structure:

§

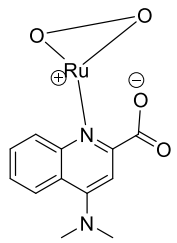

Chemical Formula: $C_{12}H_{11}N_2O_4Ru$
Exact Mass: 348,98

Figure S16: MS-MS experiment of **1** in MECN, comparison of the measured mass with the proposed structure showing a match

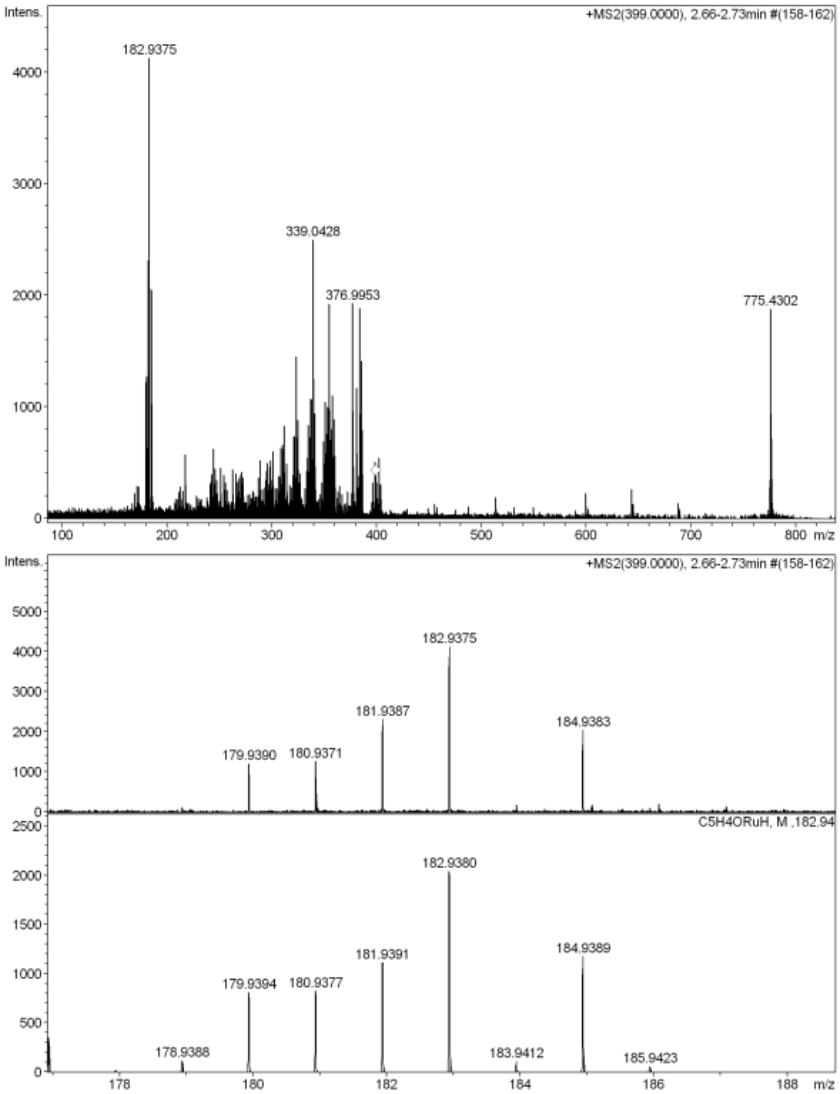

Measured m/z vs. theoretical m/z

Meas. m/z	#	Formula	Score	m/z	err [mDa]	err [ppm]	mSigma	rdb	e⁻ Conf	z
182.9375	1	C 5 H 5 O Ru	100.00	182.9380	0.3	1.7	135.7	4.0	odd	1+

§

The two Janus faces of CpRu-based deallylation catalysts and their application for in cellulo prodrug uncaging. 143

Proposed structure:

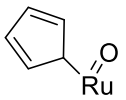

Chemical Formula: C_5H_5ORu
Exact Mass: 182.94

Figure S17: MS-MS experiment of **1** in MECN, comparison of the measured mass with the proposed structure showing a match

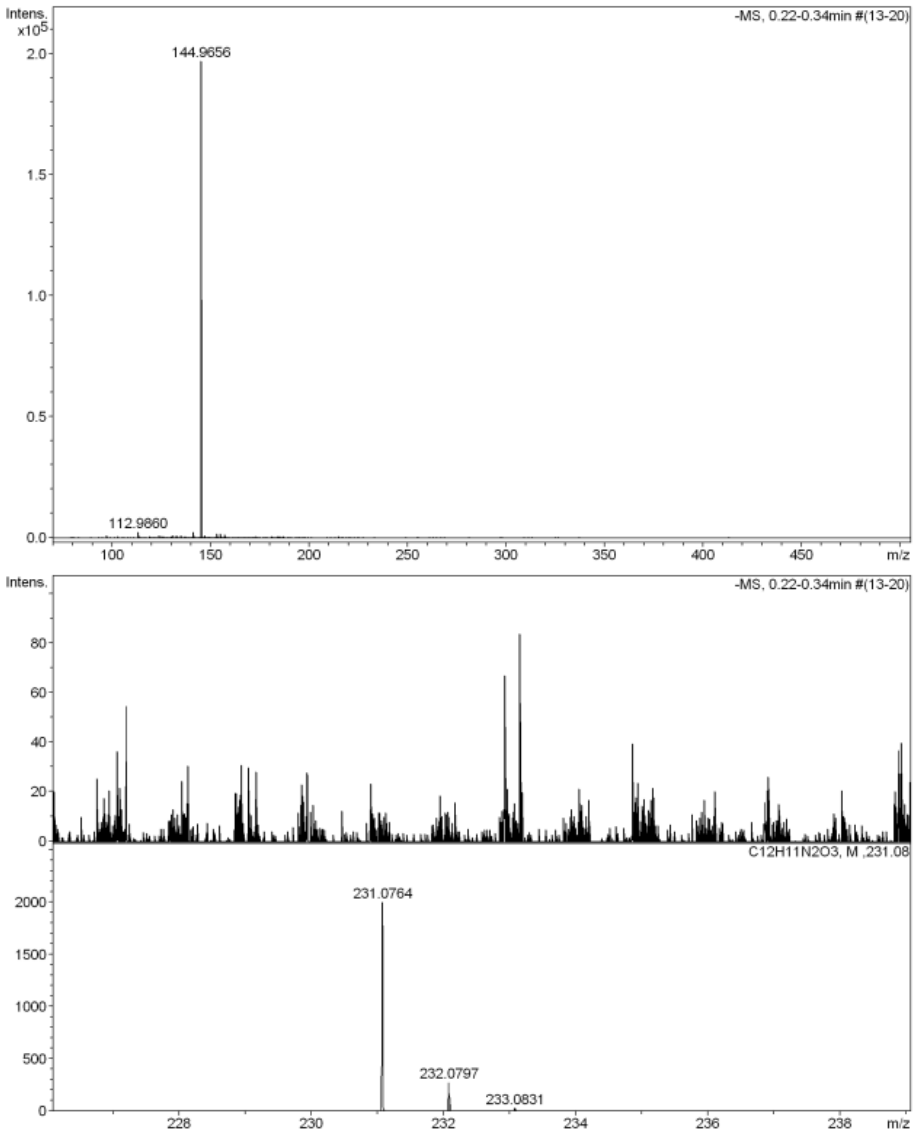

Proposed structure:

§

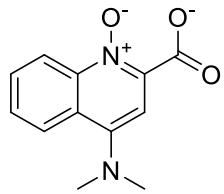

Exact Mass: 231,08

Not found.

Figure S18: MS-MS experiment of **1** in MECN, comparison of the measured mass with the proposed structure showing a mismatch

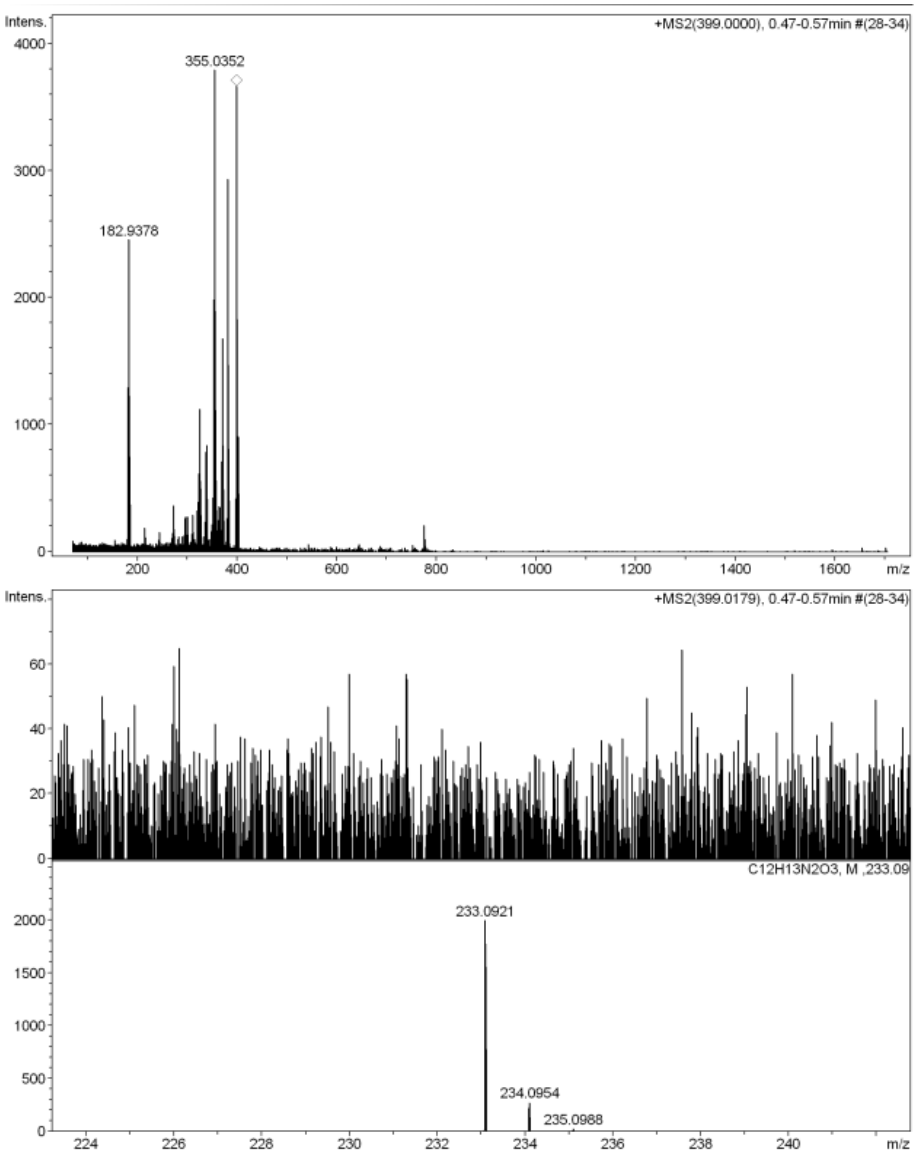

Proposed structure:

§

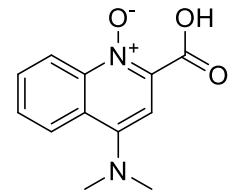

Exact Mass: 232,08

Not found.

Figure S19: MS-MS experiment of **1** in MECN, comparison of the measured mass with the proposed structure showing a mismatch

VIII] Cell experiments:

Cell culture:

CT26 cells were cultured in DMEM Glutamax medium (Gibco, Life Technologies, USA) supplemented with 10 % of fetal calf serum (Gibco) and 1% penicillin-streptomycin (Gibco) and maintained in a humidified atmosphere at 37 °C and 5 % of CO_2.

Cytotoxicity assay:

Cells were seeded at a 4,000 cells/well density in 96-well plates (100 µL/well) and were incubated at 37 °C, 5% CO_2 for 24 h. The medium was replaced by test compound dilutions in fresh medium (100 µL/well) and cells were incubated at 37 °C, 5% CO_2 for 72 h. The concentration of DMSO in each dilution was kept constant (0.5%). The medium was replaced with 100 µL of fresh medium containing resazurin (0.2 mg/mL). After 4h of incubation at 37 °C, 5% CO_2, plates were read using a Tecan Infinite M1000 PRO (Tecan Group AG) microplate reader (λ_{exc} = 540 nm; λ_{read} = 590 nm). Fluorescence data were normalized using untreated cells as 100% as negative controls, data were fitted using GraphPad Prism Software and IC_{50}s were calculated by non-linear regression.

Chapter 5: Ruthenium-catalyzed enantioselective allylic amination in biologically relevant conditions

Alain Baiyoumy, Giuletta Minzer, Thomas R. Ward.

Department of Inorganic chemistry 24a Mattenstrasse Basel 4058

Author contribution

AB conceived the project with TRW, synthesized substrate and cofactors, performed experiments, developed analytical methods, expressed protein and wrote the manuscript with input from TRW. GM synthesized ligands, performed catalysis with and without protein, expressed protein and performed the analysis of the catalysis. TRW supervised the project and revised the manuscript.

§

Abstract:

Within the last several years, numerous new-to-nature reactions have been accomplished in living systems using transition metal catalysts. Ruthenium compounds have attracted considerable attention for this purpose due to the balance they strike between good activity and biocompatibility. Here, we explore the ruthenium compound [CpRu(QA–NMe_2)solv]PF_6 (QA = 2-quinolinecarboxylate) (**Ru1**) as a catalyst for intramolecular allylic amination reactions *in cellulo*. Although **Ru1** is unstable under aerobic conditions, its stability can be improved by anchoring within the protein streptavidin to generate the artificial metalloenzyme (ArM) **biot-Ru-Sav**. Through judicious tuning of the substrate structure, it is possible to enhance the desired reactivity such that it can be achieved using the free **Ru1** catalyst in cell-free extract. Finally, through directed evolution, we identify several **biot-Ru-Sav** ArMs that perform the desired reaction in *E. coli.* cell lysate with moderate enantioselectivities and enhanced conversion rates.

4.1 Introduction

Since the 2006 discovery of Cp*Ru(cod)Cl (Cp* = pentamethylcyclopentadienyl, cod = 1,5-cyclooctadiene) as a robust catalyst for allylcarbamate cleavage *in cellulo*, ruthenium compounds have been widely studied as catalysts for transformations in biological systems.[20,214] Much of this chemistry has been developed using Cp*Ru(cod)Cl as well as Kitamura-type catalysts*[225,226] [CpRu(QA–R)allyl]PF_6 (Cp = cyclopentadienyl; QA = 2-quinolinecarboxylate)[22] and [CpRu(HQ–R')allyl]PF_6 (HQ = 8-hydroxyquinolinate), [21]developed by Meggers and colleagues. To date, deallylation, Ru(II)-promoted azide–alkyne cycloaddition,[77] [2+2+2] cycloaddition,[79,123] Alder-ene,[79] and redox isomerization[125] reactions have been explored with these three catalyst systems in biological media Scheme 1a-d. Nevertheless, different studies have reported some limitations linked to the stability of these complexes and their cytotoxicity.[60,84,98]

Our laboratory and others have also investigated ruthenium compounds as co-factors in artificial metalloenzymes (ArMs) for ring-closing metathesis and deallylation reactions.[91–

[96,102,227] Pioneered by Kaiser[228] and Whitesides[229] in the 1970s, ArMs are hybrid systems consisting of an organometallic co-factor embedded in a protein scaffold. They can combine the advantageous features of both homogeneous and enzymatic catalysis.[230] Capitalizing on the exceptional affinity of biotin for streptavidin, we have developed numerous new-to-nature reactions using ArMs consisting of a biotinylated co-factor embedded within streptavidin (Sav) scaffolds. Optimization of these systems can be readily carried out using chemical and genetic means by either tuning the biotin anchor or through mutations of the host protein.

We were interested in expanding the scope of *in cellulo* reactivity achievable with ruthenium-based catalysts. We drew inspiration from the ruthenium-catalyzed intramolecular allylic amination developed by Kitamura and co-workers, Scheme 1f, [231] which employs a CpRu/(*R*)-Cl-Naph-PyCOOCH$_2$CH=CH$_2$ catalyst (Naph = naphthalene; Py = pyridine). However, this reactivity proceeded efficiently only at temperatures ≥70 °C and in organic solvents when allylic alcohol derivatives were used as substrates.[232] To demonstrate analogous intramolecular allylic amination *in cellulo*, we initially sought a ruthenium catalyst that would be robust in air and water, in the presence of thiols, and operate efficiently at lower temperatures.[37,60,84,98] We turned to the compounds [CpRu(QA–R)L]PF$_6$ (R = –NMe$_2$) where L = solvent or allyl; Meggers have shown the latter to be robust and highly active for the cleavage of allyloxycarbonyl-protected amines under biological conditions. [22,135]

Here, we develop a biocompatible platform for intramolecular allylic amination using [CpRu(QA–NMe$_2$)solv]PF$_6$ (**Ru1**) as a catalyst, Scheme 1g. Through judicious substrate modification, it is possible to render the desired reactivity competitive with complex oxidation under aerobic conditions and in the presence of cell-free extract. Through the design and genetic optimization of an ArM featuring a biotinylated catalyst (**biot-Ru**) embedded in streptavidin, it is possible to improve the reaction conversion and enantioselectivity.

§

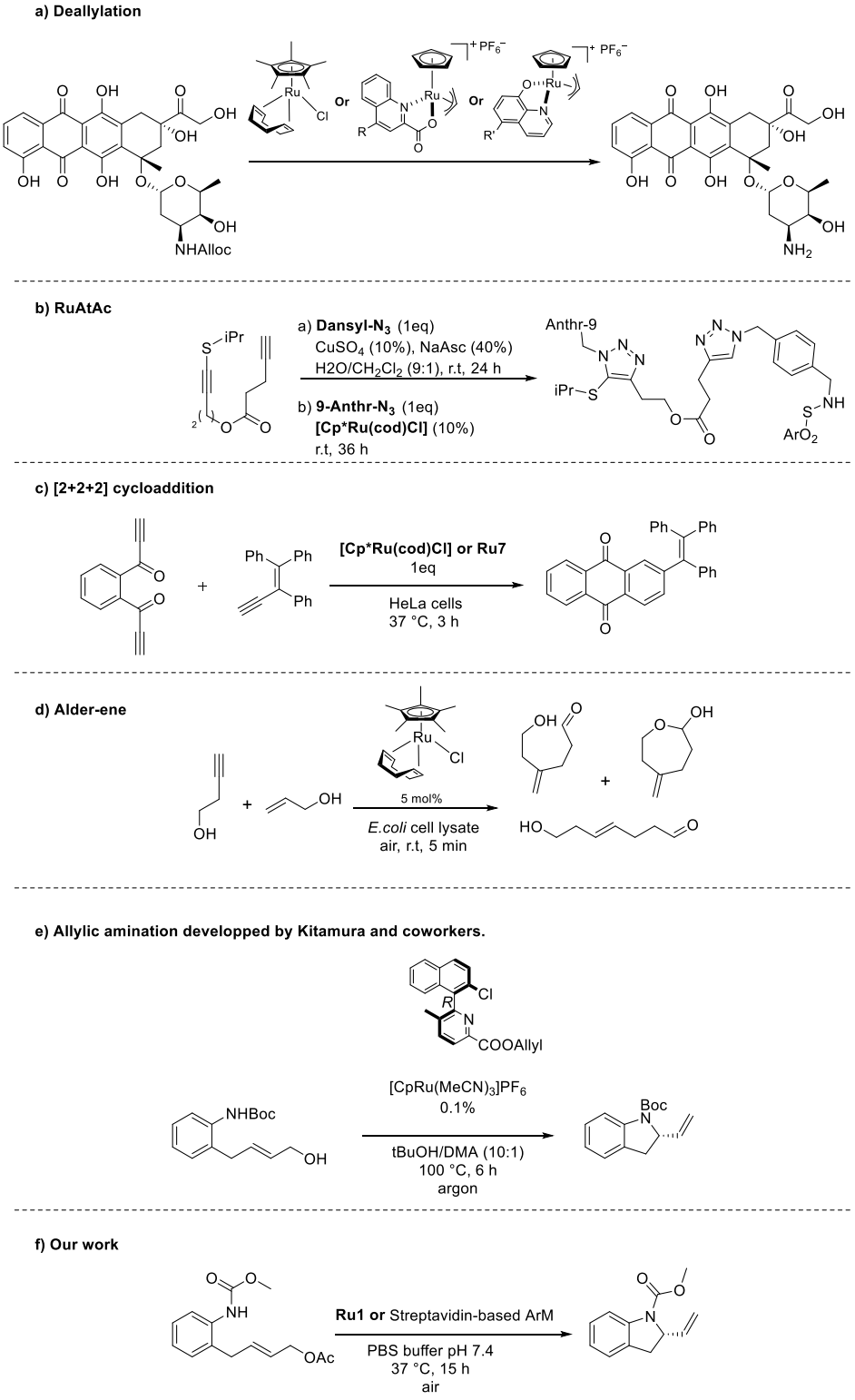

Scheme 1: Four prominent Ru-based compounds developed for *in cellulo* catalysis, the previous work from Kitamura and co-workers and our work **a)** an example of a deallylation reaction, with R = -H, -OMe or -NEt_2 and R' = -H, -4-Cl, -5-Cl, -CO_2Me and -NO_2.[21,22,72,100] **b)** RuAtAc developed by Mascarenas and co-workers.[233] **c)** [2+2+2]

cycloaddition developed by Mascarenas and co-workers[123] inspired from Teply and co-workers.[79] **d)** Alder-ene reaction developed by Teply and co-workers.[79] **e)** Allylic amination developed by Kitamura and co-workers.[231] **f)** Our work.

4.2 Results and Discussion

.

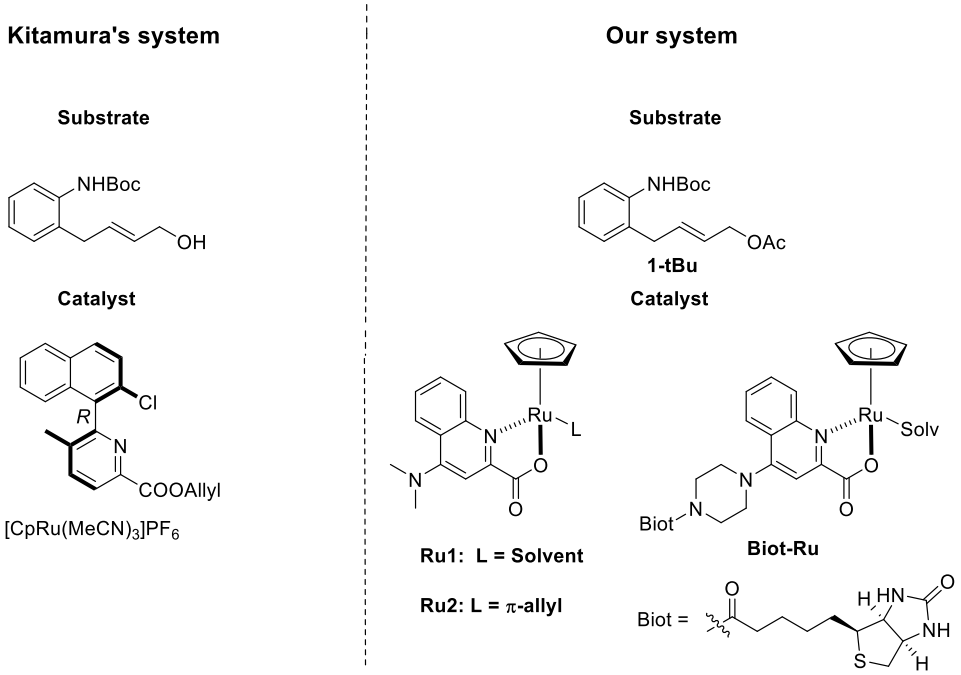

Scheme 3: Previous catalyst and substrate system used by Kitamura and co-workers (left) and the substrate and catalysts explored in this work (right).

We initially explored the *N*-allylation reaction with catalyst **Ru1** using the allylic acetate substrate **1-tBu**. Using 1 mol% **Ru1** under air-free conditions at 37 °C in phosphate-buffered saline (PBS, pH = 7.4) with 1.5% *N*,*N*-dimethylformamide (DMF) as co-solvent, a turnover number (TON) >80 was achieved (Figure 1). However, when the same reaction was performed with air, catalysis was effectively shut down. Using the biotinylated catalyst **biot-Ru**, low turnover could be achieved in air, and only slight improvement was observed when using a **biot-Ru–Sav** artificial metalloenzyme featuring the co-factor embedded in wild-type Sav.

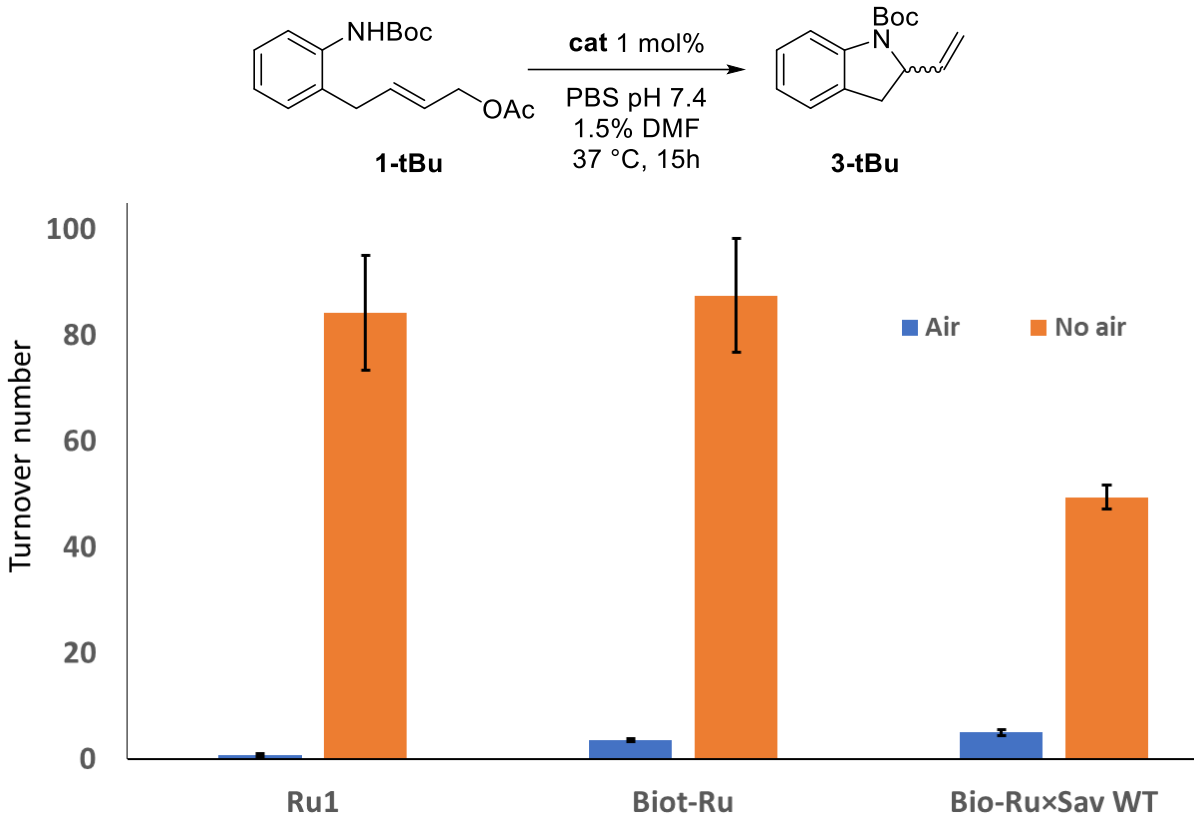

Figure 1: Results from preliminary analysis of the ruthenium-catalyzed allylic amination reaction carried out in PBS with 1.5% DMF at 37 °C using 1 mol% of **Ru1** (left), **biot-Ru** (middle), or **biot-Ru-Sav** (right) as catalyst. The influence of air on the reaction was studied and quantified by HPLC. Results represent the average value of triplicate repeats, and error bars represent the standard deviation between them.

Based on unpublished results from our group about the complex reactivity and stability, oxidation of ruthenium compounds in air is unavoidable but is in kinetic competition with the desired reactivity. Considering this, we envisioned two approaches to enhance the rate of the desired *N*-allylation: i) reducing the steric bulk of the aniline protecting group and ii) increasing the π-allyl formation capacity of the allylic system (Figures 2 and 3).
We initially explored changing the carbamate alkyl group from tert-butyl to methyl, ethyl, isopropyl, n-propyl, or n-butyl (substrates **1-Me** through **1-nBu**). Using the same suite of R groups, we also explored substrates featuring a urea functional group (substrates **2-Me** through **2-nBu**). Reactions were initially screened using **Ru1** with a lower catalyst loading of 0.1% to demonstrate the potency of this reaction for its eventual demonstration in cells, Figure 2. In unpublished work from our lab as well as a previous study from another

§

group,[84] the use of dimethyl sulfoxide (DMSO) as a co-solvent was found to enhance the stability of **Ru1**, and thus, all reactions were run in PBS with 1.5% DMSO instead of DMF.

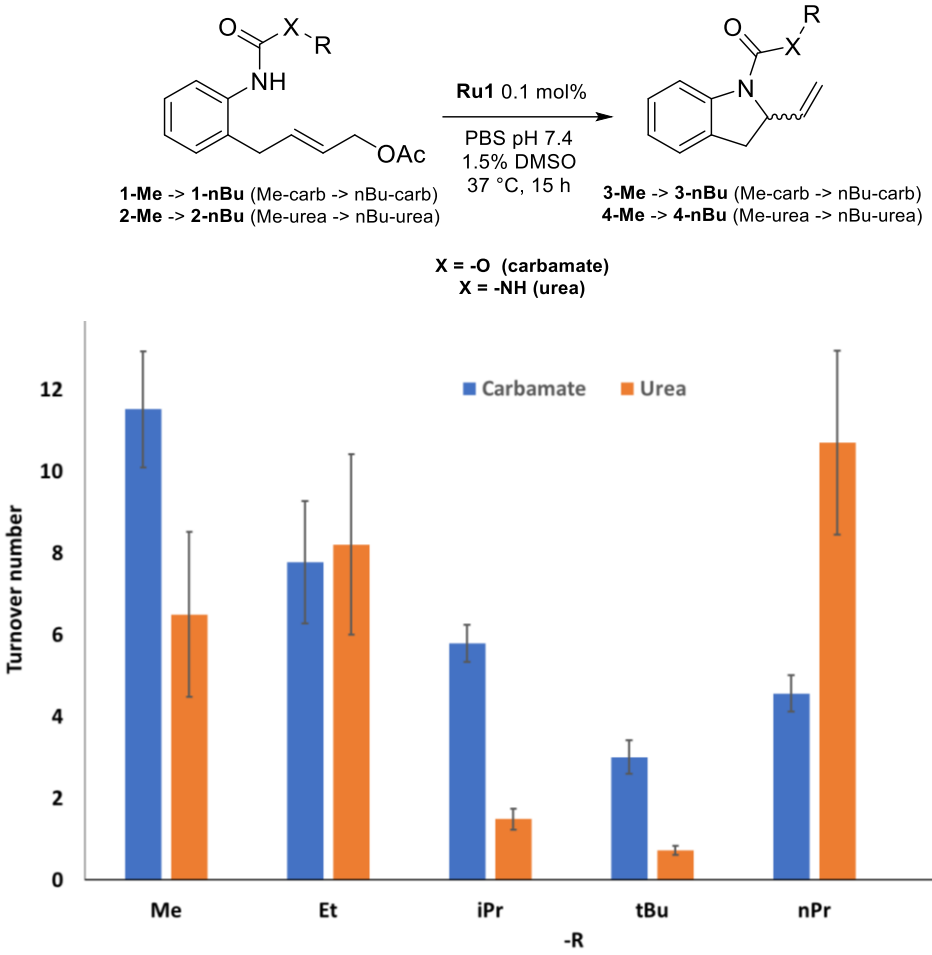

Figure 2: Impact of substrate electronics and steric bulk on the ruthenium-catalyzed allylic amination reaction. Results were obtained from HPLC. Results represent the average value of triplicate repeats, and error bars represent the standard deviation between them.

The results from screening the 12 substrates are given in Figure 2. In the case of the carbamate substrates, the reaction efficiency increased overall with decreasing alkyl group size from tert-butyl to methyl. The decrease in steric hindrance around the allylic system might explain the increase in catalytic activity by increasing the accessibility of the allylic system to the Ru complex. However, changing the alkyl group will also change the lipophilicity of the substrate and, therefore, its solubility in the aqueous reaction medium, and thus, the TONs in Figure 2 represent an interplay of substrate accessibility and solubility. The urea substrates were found to be much less soluble than the carbamate analogs, and thus, deciphering a trend in the corresponding TON is more complex.

§

Given these results, we selected substrate **1-Me** for subsequent exploration of the impact of the substrate leaving group on the reaction efficiency. Variants of **1-Me** featuring an amide or diethylphosphoryl leaving group (**1a** and **1b**, respectively; Figure 3) were explored. The highest TON was achieved with substrate **1b**, however, this result is ascribed to its instability under the reaction conditions—indeed**,** in pure buffer solution, **1b** was found to convert to **3-Me**. The turnover of substrate **1-Me** was slightly higher than **1a,** so substrate **1-Me** was chosen for further Sav-based ArM screening using **biot-Ru** as a co-factor.

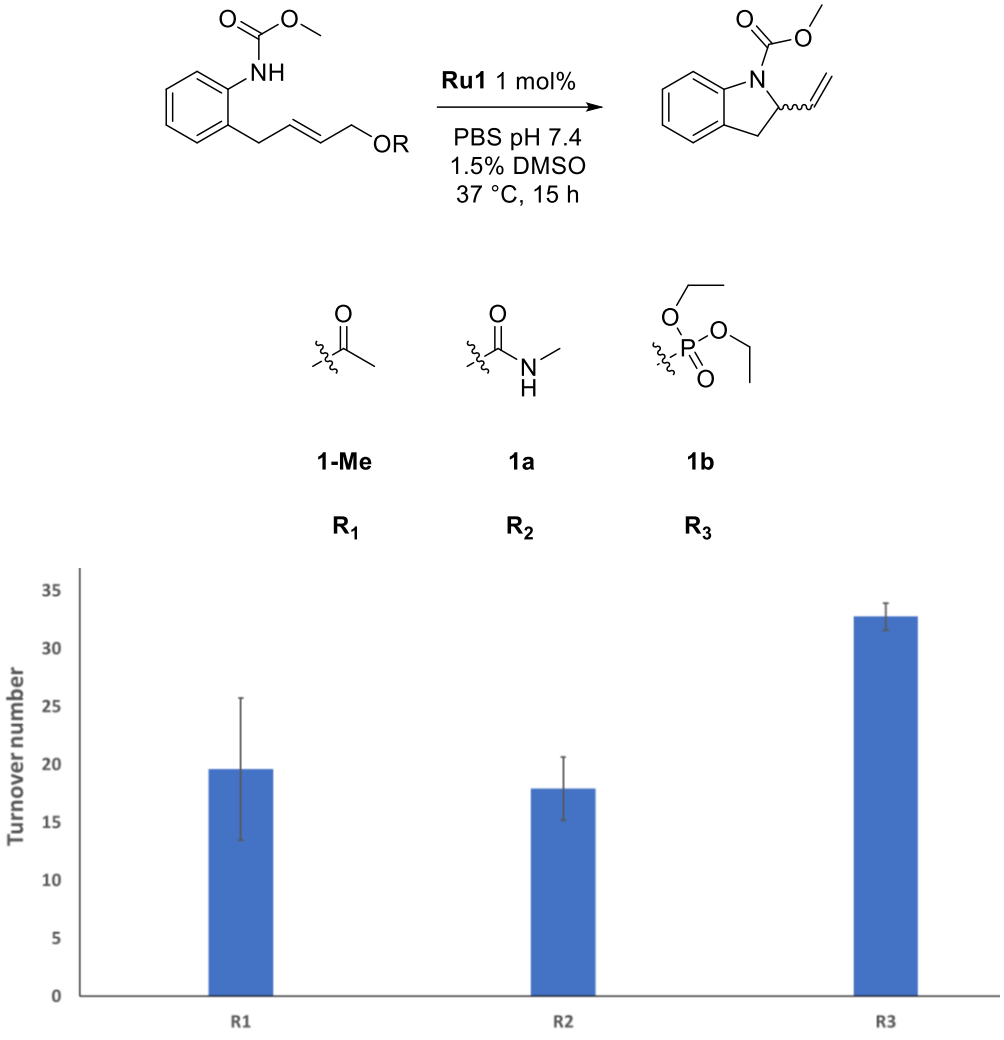

Figure 3: Impact of the substrate leaving group on the ruthenium-catalyzed allylic amination reaction. Analyses were performed using HPLC. Results represent the average value of triplicate repeats, and error bars represent the standard deviation between them.

We also designed a second co-factor, **biot-Ru-HQ** (Figure 4), which is based on the ruthenium hydroxyquinolate catalyst from Meggers and colleagues, Scheme 1.[21] We

§

selected a random pool of Sav mutants to screen the catalytic performance of ArMs featuring **biot-Ru** and **biot-Ru-HQ** co-factors. In our initial screenings, we found that DMF enhances the catalytic activity when used in the presence of protein, and so DMF was used as a co-solvent in all subsequent reaction studies, Figures S13–14.

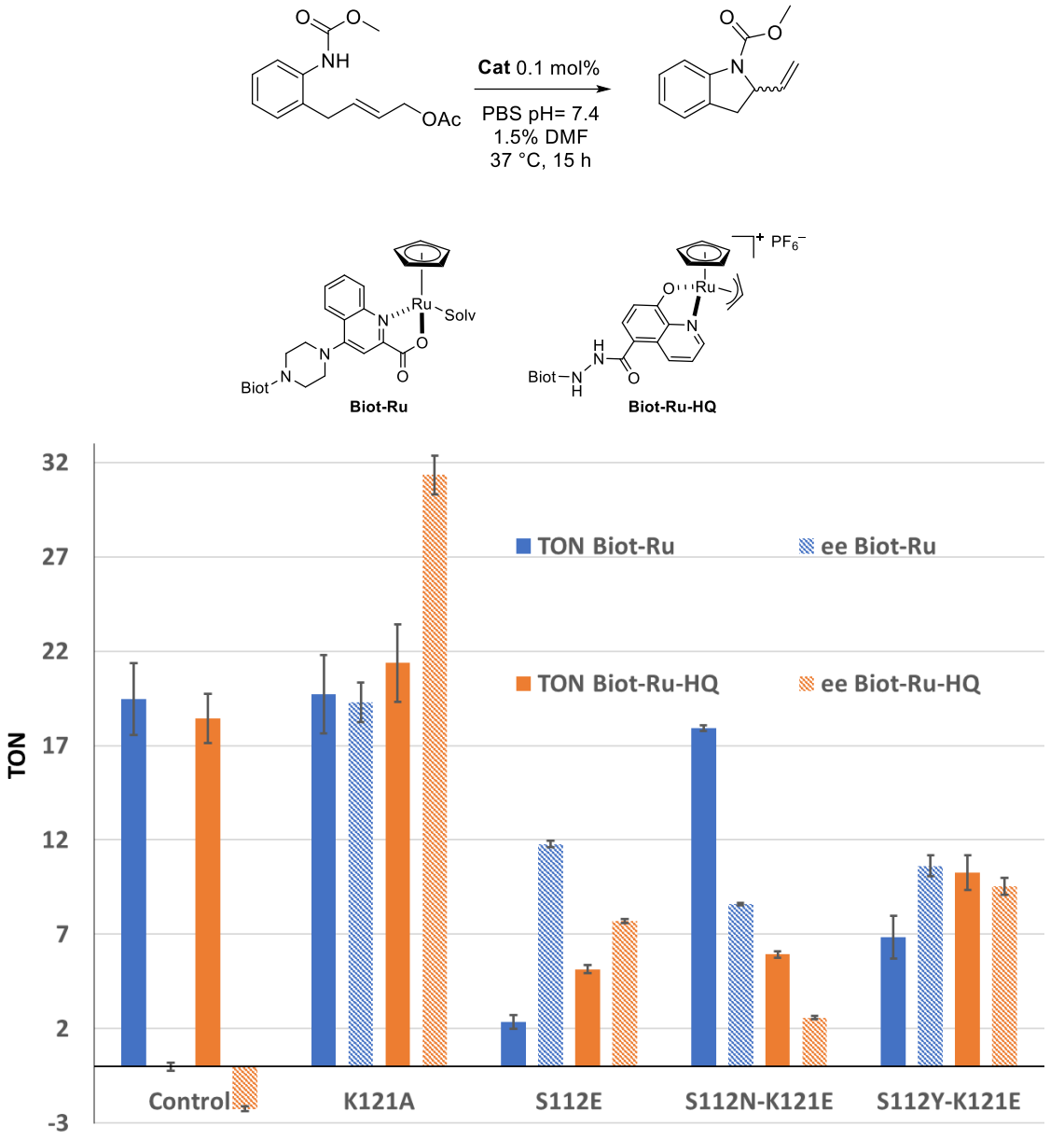

Figure 4: Results of ruthenium-catalyzed allylic amination using free **biot-Ru** or **biot-Ru-HQ** (control) or the same co-factors embedded in random Sav mutants. Analyses were performed using HPLC. Results represent the average value of triplicate repeats, and error bars represent the standard deviation between them.

§

As seen in Figure 4, similar activity was observed for both co-factors. As such, we selected **biot-Ru** for the remainder of this study, given its relatively simple synthesis, and because of concerns surrounding the potential cytotoxicity of hydroxyquinoline-based ligands such as in **biot-Ru-HQ**.[84,98]

As *E. coli* cells contain between 1-10 mM glutathione (GSH hereafter)[234], we decided to examine the activity of the **biot-Ru-Sav** system under more biologically relevant conditions by adding GSH to the reaction mixture. From an initial screening campaign without of thiol using a few mutants, S112A-K121E was found to afford the highest substrate conversion and product enantioselectivity (see Figures S13–14 in the Supporting Information for more details). With this mutant in hand, we used lyophilized cell-free extract from an empty *E.* coli vector to estimate the resilience of the catalytic system to intracellular conditions (5 mg/mL of cell-free extract in PBS was used). We evaluated the catalytic activity in 10 mM of glutathione (GSH hereafter), Figure 5.

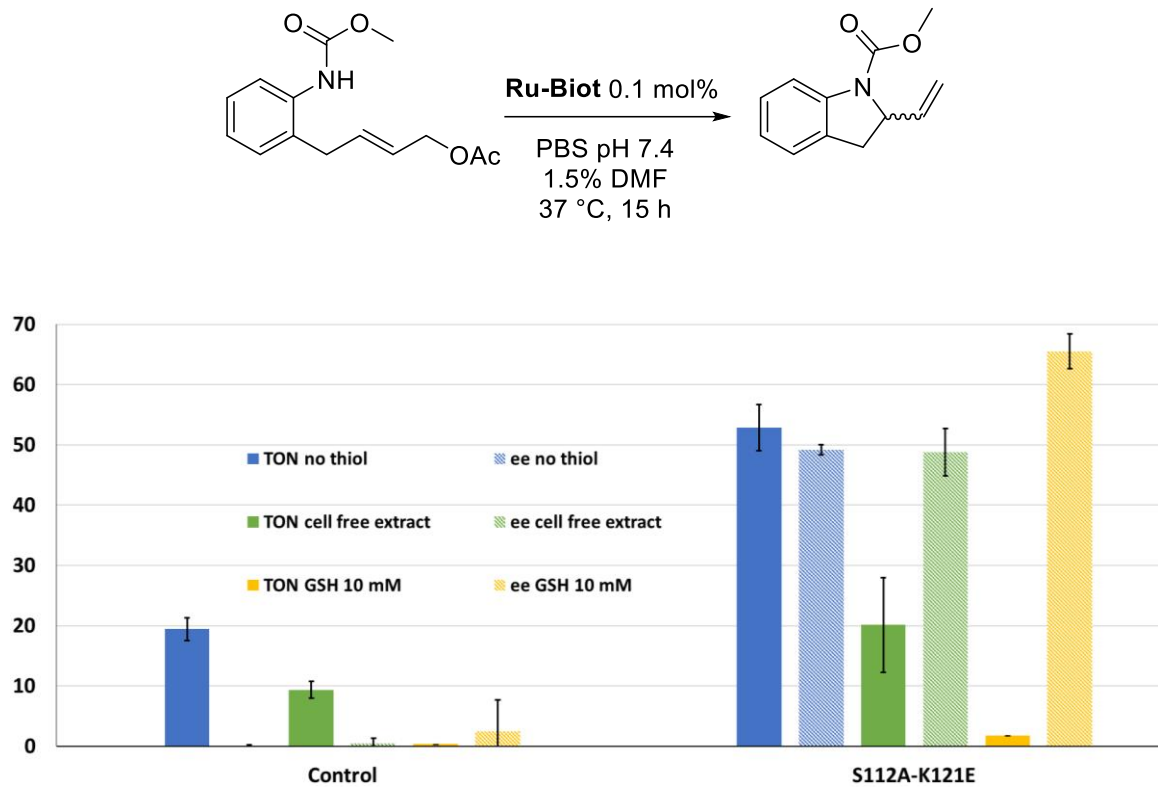

Figure 5: Impact of various thiol sources on ruthenium-catalyzed allylic amination using free biot-Ru (left, control) or biot-Ru embedded within a Sav S112A-K121E scaffold (right). Results represent the average value of triplicate repeats, and error bars represent the standard deviation between them.

§

It is clear from Figure 5 that high concentrations of thiols have a deleterious effect on the catalyst TON. Indeed, the reaction was nearly shut down with 10 mM of glutathione, Figure 5, solid yellow data. This may be due to a competition between nucleophilic attack by carbamate and glutathione, intermediate I-2, Scheme 4.

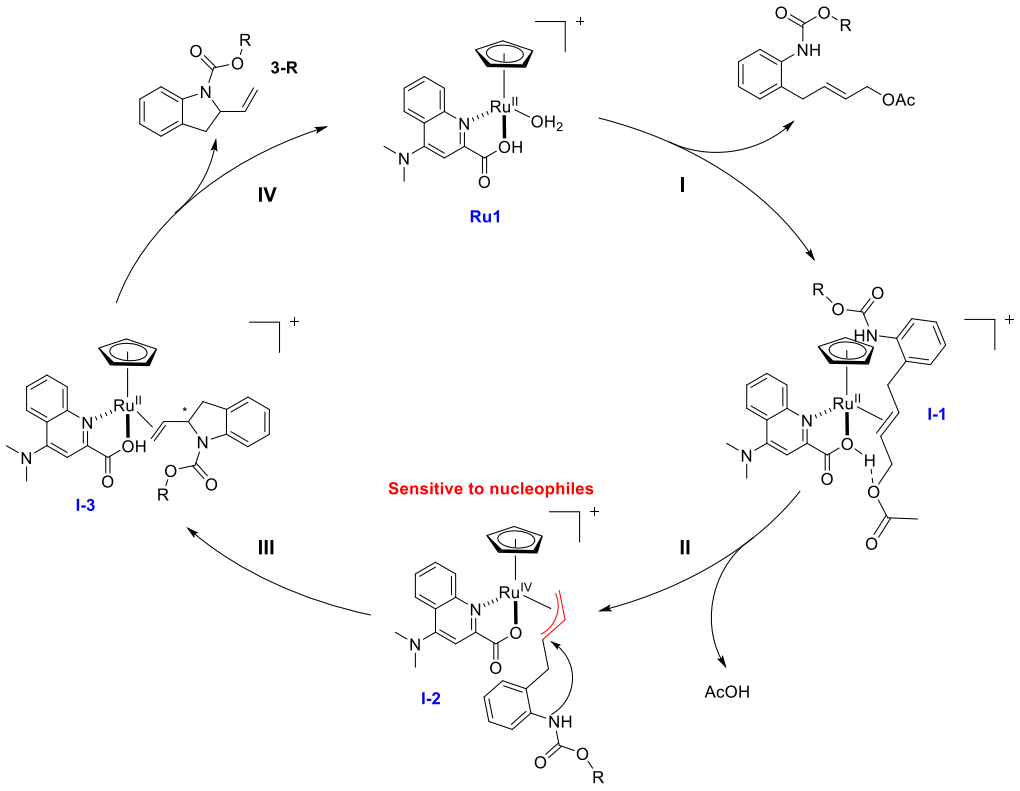

Scheme 4: Mechanism of the ruthenium-catalyzed allylic amination. I) **Ru1** interacts with the substrate through ligand exchange and forms **I-1**. II) Oxidative addition of the ruthenium complex forming the η^3-allyl complex **I-2** and acetic acid as a side product. III) Intramolecular allylic amination from the carbamate on the η^3-allyl intermediate forming **I-3**, IV) Ligand exchange of the desired product with the solvent forming **Ru1** and **3-R**.

However, the reaction was found to proceed (albeit with a low TON) in the presence of cell-free extract (Figure 5, solid green data), which suggested that it might be possible to perform the reaction in intracellular conditions. Toward this end, we tuned the activity of the ArM by genetic optimization using site saturation mutagenesis at positions S112 and K121 in Sav. Based on the above promising results obtained with mutant Sav S112A-

K121E and preliminary screenings with double mutant Sav S112A-K121N as well as Sav K121N, we decided to screen S112A-K121X and S112X-121N combinations to optimize our ArM. We were also interested in exploring Sav S112X-K121D mutants, given that D (aspartic acid) and N (asparagine) are structurally similar amino acids, but D bears a negatively charged side chain at physiological pH, Figure 6.

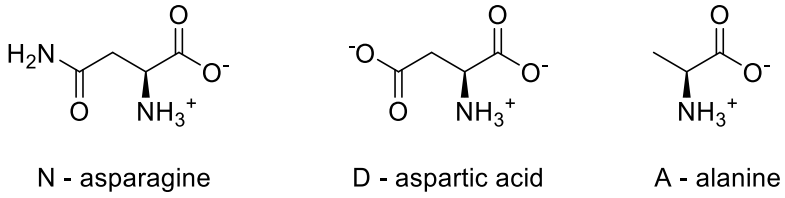

Figure 6: Illustration of the structures of different amino acid residues (at physiological pH) chosen for Sav mutant screening and ArM optimization.

The screening campaign used cell lysate from *E*. coli transformed with the corresponding plasmid. Figure 7 illustrates the adopted workflow from cytoplasmic expression to cell lysate isolation and the final results from the screening campaign.

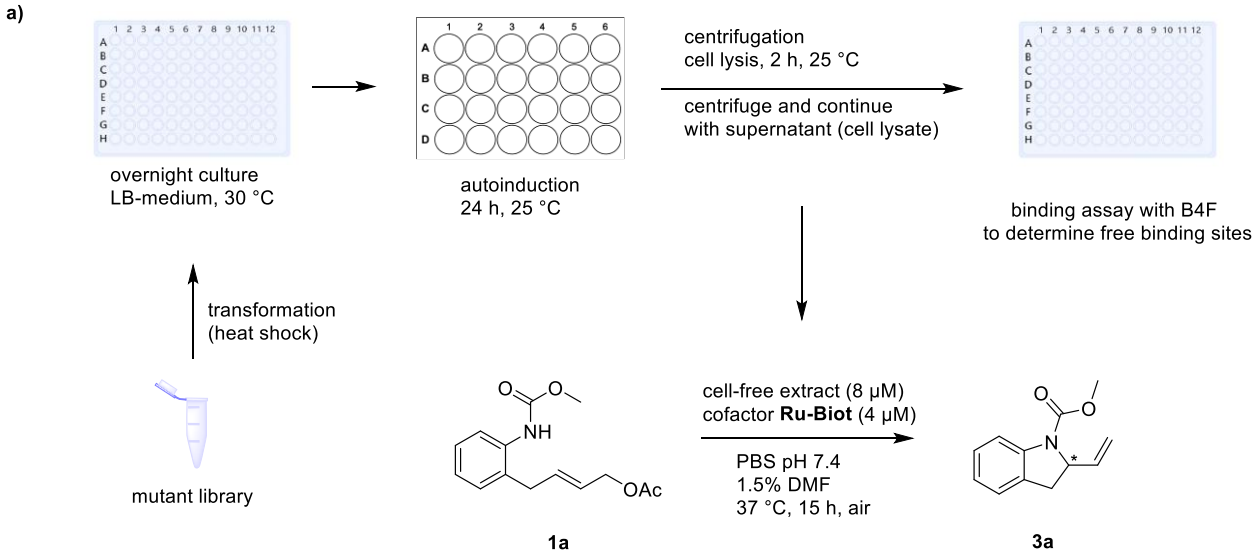

§

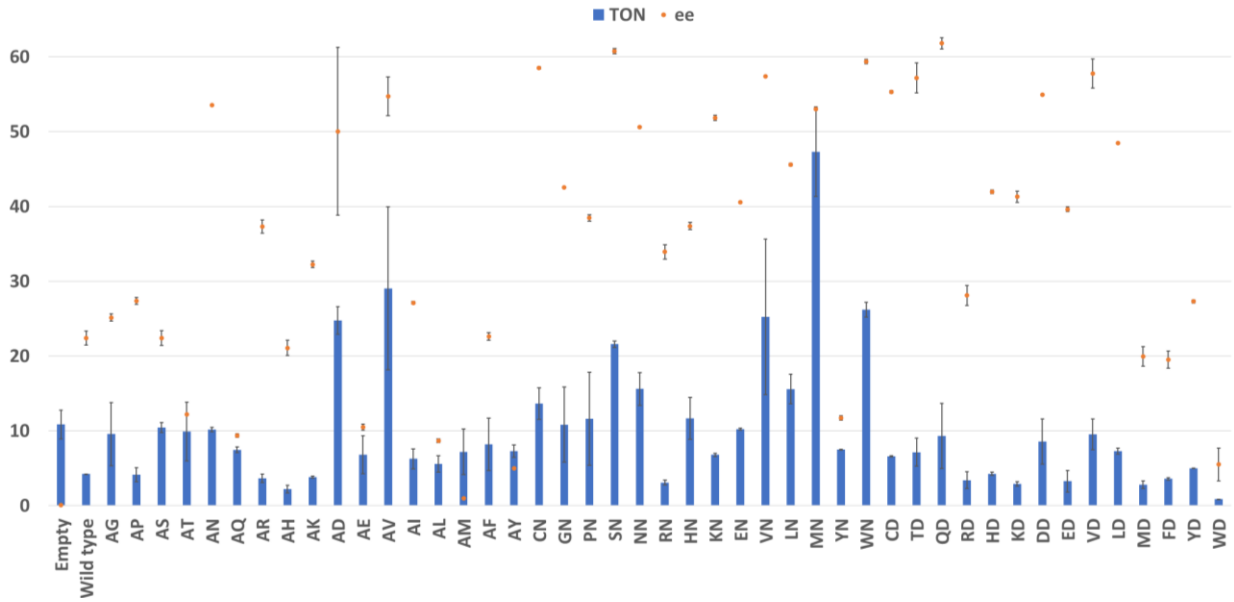

Figure 7: Presentation of the screening procedure as well as the results obtained. a) Workflow for the cytoplasmic expression of Sav in 24 well plates (upper) as well as the reaction condition for allylic amination (lower) and b) the corresponding screening results, represented in dual graph format with TON in blue bars and ee in orange dots. XY presents mutations S112X and K121Y. The mutants are classified in the following order: Special cases (C. G, P), amino acids with polar uncharged side chains (S, T, N, Q), amino acids with electrically charged side chains (R, H, K and D, E) and amino acids with hydrophobic side chains (A, V, I, L, M, F, Y, W). Results represent the average value of duplicate repeats, and error bars represent the standard deviation between them.

This campaign revealed that some synergistic effects are observed for some mutant combinations at position S112X-K121Y, which improve the enantioselectivity and/or the TON. In particular, for S112A-K121X mutants, the residues K121D, K121N, and K121V afforded the most significant improvement in enantioselectivity over wild type (WT). Of these, K121D and K121V afforded the best TON interestingly, S112A-K121E did not afford any improvement in enantioselectivity compared to WT. This difference between the purified protein presented before and this one is probably linked to the expression level of S112A-K121E in a 24-well plate. The majority of ArMs featuring Sav S112X-K121N mutants afforded enantioselectivities above 50%; of these, ArMs with S112W-K121N and K121N mutants performed most optimally, achieving enantioselectivities of approximately 60%.

§

Interestingly, relative to ArMs based on S112X-K121N mutants, ArMs featuring S112X-K121D mutants exhibited moderate enantioselectivity but much lower TONs. It is possible that the negatively charged aspartate stabilizes the π-allyl reaction intermediate and slows down the allylic amination kinetics such that the catalyst degradation is favored.[60,84,217] Finally, we found that an ArM featuring the Sav S112Q-K121D mutant affords the highest enantioselectivity (ee 62%, TON 9). In comparison, a Sav S112M-K121N scaffold afforded the optimal combination of activity and enantioselectivity with an 11.7-fold increase in activity compared to WT (53% ee, TON 47 versus 22% ee, TON 4 for Sav WT).

4.3 Conclusion

Herein, we report the first ruthenium-catalyzed allylic amination in *E. coli* cell lysate. Challenges include the limited substrate scope of such reactions, as well as the need for judicious catalyst design to achieve desired reactivity in biologically relevant conditions. However, these results also highlight the possibility of realizing more complex new-to-nature cell reactions. Future optimization of the presented system will benefit from a two-pronged approach involving further substrate design and optimization as well as new catalyst design for biological applications.

4.4 Supplementary information

I] Synthesis of substrates and complexes:

1) Synthesis of methyl (E)-2-(4-hydroxybut-2-en-1-yl)benzoate

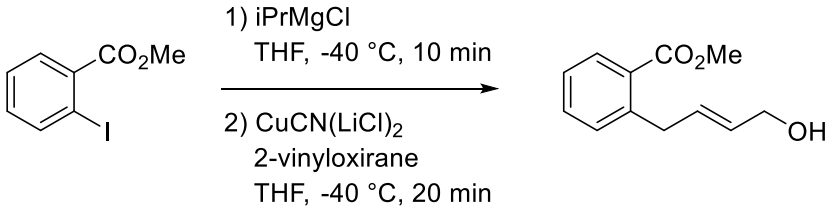

A solution of $CuCN(LiCl)_2$ was prepared in the absence of air in a sealed tube with CuCN (171 mg, 1.91 mmol), LiCl (162 mg, 3.82 mmol) in THF (4 mL) for 20 minutes.

Methyl 2-iodobenzaote (20g, 76.3 mmol) was dissolved in THF (70 mL), and the solution was cooled to -40°C. To this cooled solution was added iPrMgCl (2M in THF, 45.8 mL, 91.6 mmol). The resulting orange solution was stirred at -40°C for 20 minutes, and then the previously prepared $CuCN(LiCl)_2$ solution and 2-vinyloxirane (9.22 mL, 114 mmol) were added at the same temperature. After 20 minutes, a saturated solution of $(NH_4)_2SO_4$ (40 mL) was added. The mixture was warmed to room temperature and stirred for 30 minutes.

The resulting blue precipitates were removed by filtration using a frited funnel and vacuum. The recovered biphasic solution was separated using a separating funnel. The aqueous layer was washed 3 times with TFH (30 mL). The organic phases were combined and dried over Na_2SO_4 and concentrated under a vacuum to afford a crude oil of methyl (E)-2-(3-hydroxyallyl)benzoate. The crude was used for the next step without further purification.

13.1 g of crude product was recovered.

2) Synthesis of (E)-2-(4-hydroxybut-2-en-1-yl)benzoic acid

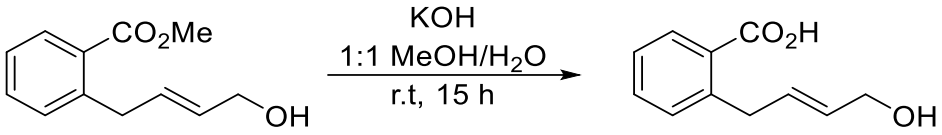

Methyl (E)-2-(4-hydroxybut-2-en-1-yl)benzoate (13.1 g, 63.5 mmol) and KOH (4.63 g, 82.6 mmol) were dissolved in MeOH/water (1:1, 120 mL). After 15 h stirring at r.t, the mixture was concentrated *in vacuo*. The residue was partitioned between ether (120 mL) and water (120 mL). The aqueous layer was washed with diethyl ether (40 mL), acidified by adding $NaHSO_4$, and extracted with EtOAc (3x 80 mL). The combined organic layers were washed with brine (80 mL). The organic solution was dried over Na_2SO_4, and then filtered over cotton. The organic phase was then reduced under vacuum to afford a pale yellow oil (15.5 g crude). The crude was directly used for the next step without purification.

3) Synthesis of (E)-2-(4-acetoxybut-2-en-1-yl)benzoic acid

§

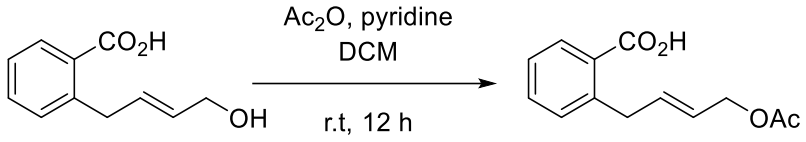

(E)-2-(4-hydroxybut-2-en-1-yl)benzoic acid (15.5 g, 80.6 mmol, contains impurities from the previous reaction) was dissolved in Py (6.51 mL, 80.6 mmol) and Ac2 O (7.57 mL, 80.6 mmol). The solution was stirred at rt for 12 h. The concentration of the whole mixture *in vacuo* afforded crude (E)-1-acetoxy-4-(2-carboxyphenyl)but-2-ene as pale yellow oil. The crude was purified by column chromatography with a gradient of AcOEt in cyclohexane from 20% to 60 In 35 column volume. The product was recovered firstly as transparent oil, which after one night in the freezer turned into a white solid (8 g).

NMR: ^{1}H NMR (500 MHz, CD_3CN) δ 7.91 (dd, *J* = 8.1, 1.4 Hz, 1H), 7.53 (td, *J* = 7.6, 1.5 Hz, 1H), 7.41 – 7.29 (m, 2H), 5.98 (dtt, *J* = 15.4, 6.6, 1.3 Hz, 1H), 5.60 (dtt, *J* = 15.6, 6.4, 1.5 Hz, 1H), 4.48 (dq, *J* = 6.3, 1.1 Hz, 2H), 3.81 – 3.73 (m, 2H).

4) Diversification via Curtius rearrangement

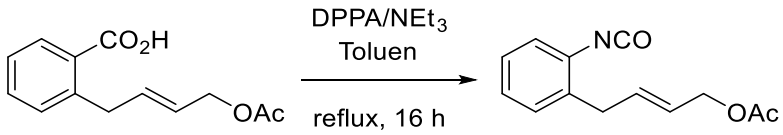

This step was the keystone of the synthetic diversification of the scaffold. Instead of performing the reaction in tBuOH from the original paper, we performed the reaction in toluene to trap the isocyanate and then quench with the corresponding nucleophile.

(E)-2-(4-acetoxybut-2-en-1-yl)benzoic acid (1 eq) was dissolved in toluene (1 mL per 50mg of starting material), followed by triethylamine (1.1 eq) and diphenyl phosphorylazide (DPPA) (1.1 eq). The reaction was stirred at reflux for 16h, and then the isocyanate was quenched with the corresponding nucleophile (1.2 eq). The crude was purified by column chromatography from a solid loading.

§

Purification method for carbamates: slow gradient of AcOEt in cyclohexane from 0% to 35%

Purification method for urea-containing molecules: slow gradient of AcOEt in cyclohexane from 5% to 35%

Nucleophile = R-OH

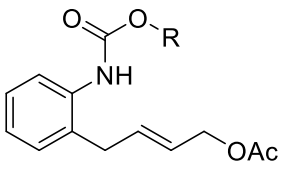

R	Yield (%)
1-Me	32
1-Et	30
1-iPr	29
1-tBu	69
1-nPr	28
1-nBu	28

Nucleophile = R-NH$_2$

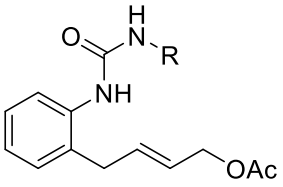

R	Yield (%)
2-Me	32
2-Et	30
2-iPr	35
2-tBu	35
2-nPr	29
2-nBu	28

NMR:

Carbamates

1-Me:

^{1}H NMR (500 MHz, $CDCl_3$) δ 7.75 (s, 1H), 7.27 (td, *J* = 7.6, 1.8 Hz, 1H), 7.15 (dd, *J* = 7.5, 1.7 Hz, 1H), 7.09 (td, *J* = 7.4, 1.3 Hz, 1H), 6.47 (s, 1H), 5.90 (dtt, *J* = 15.3, 6.1, 1.4 Hz, 1H), 5.59 (dtt, *J* = 15.7, 6.3, 1.8 Hz, 1H), 4.55 (dq, *J* = 6.2, 1.2 Hz, 2H), 3.77 (s, 3H), 3.40 – 3.35 (m, 3H), 2.06 (s, 3H), 1.57 (s, 1H).

^{13}C NMR (126 MHz, $CDCl_3$) δ 170.78, 132.58, 130.12, 127.69, 126.19, 77.23, 64.46, 52.44, 34.94, 20.96.

Rf: 0.216 (cyclohexane/AcOEt 8/2)

§

1-Et:

^{1}H NMR (500 MHz, $CDCl_3$) δ 7.76 (s, 1H), 7.26 (dd, *J* = 15.4, 1.7 Hz, 2H), 7.15 (dd, *J* = 7.6, 1.7 Hz, 1H), 7.08 (td, *J* = 7.5, 1.3 Hz, 1H), 6.43 (s, 1H), 5.91 (dtt, *J* = 15.1, 6.1, 1.3 Hz, 1H), 5.59 (dtt, *J* = 15.7, 6.3, 1.7 Hz, 1H), 5.30 (s, 2H), 4.55 (dq, *J* = 6.2, 1.3 Hz, 2H), 4.22 (q, *J* = 7.1 Hz, 2H), 3.41 – 3.35 (m, 2H), 2.06 (s, 3H), 1.31 (t, *J* = 7.1 Hz, 3H).
^{13}C NMR (126 MHz, $CDCl_3$) δ 170.77, 132.59, 130.08, 127.65, 126.14, 64.49, 34.87, 20.96, 14.60.
Rf: 0.304 (cyclohexane/AcOEt 8/2)

1-iPr:

^{1}H NMR (500 MHz, $CDCl_3$) δ 7.77 (s, 1H), 7.25 (td, *J* = 7.7, 1.7 Hz, 1H), 7.14 (dd, *J* = 7.6, 1.7 Hz, 1H), 7.07 (td, *J* = 7.4, 1.3 Hz, 1H), 6.39 (s, 1H), 5.91 (dtt, *J* = 15.1, 6.1, 1.4 Hz, 1H), 5.58 (dtt, *J* = 15.6, 6.3, 1.7 Hz, 1H), 5.01 (hept, *J* = 6.3 Hz, 1H), 4.55 (dq, *J* = 6.3, 1.3 Hz, 2H), 3.37 (dd, *J* = 6.2, 1.6 Hz, 2H), 2.05 (d, *J* = 6.7 Hz, 4H), 1.32 – 1.23 (m, 6H).
^{13}C NMR (126 MHz, $CDCl_3$) δ 170.95, 153.69, 132.59, 130.02, 127.60, 126.10, 124.46, 77.23, 68.80, 64.51, 34.80, 22.11, 21.01 (d, *J* = 12.1 Hz).
Rf: 0.372 (cyclohexane/AcOEt 8/2)

1-tBu:

^{1}H NMR (500 MHz, $CDCl_3$) δ 7.75 (d, *J* = 8.2 Hz, 1H), 7.27 – 7.19 (m, 2H), 7.13 (dd, *J* = 7.6, 1.7 Hz, 1H), 7.05 (td, *J* = 7.5, 1.3 Hz, 1H), 6.32 (s, 1H), 5.91 (dtt, *J* = 15.2, 6.1, 1.4 Hz, 1H), 5.59 (dtt, *J* = 15.6, 6.2, 1.7 Hz, 1H), 4.55 (dq, *J* = 6.2, 1.2 Hz, 2H), 3.37 (dd, *J* = 6.2, 1.5 Hz, 2H), 2.06 (s, 3H), 1.51 (s, 9H).
^{13}C NMR (126 MHz, $CDCl_3$) δ 170.76, 153.21, 136.28, 132.65, 129.96, 127.53, 126.05, 124.25, 80.44, 77.22, 64.54, 34.83, 28.35, 28.35, 20.97.
Rf: 0.451 (cyclohexane/AcOEt 8/2)

1-nPr:

^{1}H NMR (500 MHz, $CDCl_3$) δ 7.76 (s, 1H), 7.29 – 7.21 (m, 1H), 7.15 (dd, *J* = 7.6, 1.7 Hz,

1H), 7.08 (td, *J* = 7.4, 1.3 Hz, 1H), 6.53 – 6.38 (m, 1H), 5.91 (dtt, *J* = 15.2, 6.2, 1.4 Hz, 1H), 5.59 (dtt, *J* = 15.7, 6.3, 1.7 Hz, 1H), 4.55 (dq, *J* = 6.0, 1.2 Hz, 2H), 4.12 (t, *J* = 6.7 Hz, 2H), 3.38 (dd, *J* = 6.4, 1.6 Hz, 2H), 2.05 (s, 3H), 1.70 (h, *J* = 7.2 Hz, 2H), 0.97 (t, *J* = 7.5 Hz, 3H).
^{13}C NMR (126 MHz, $CDCl_3$) δ 170.76, 154.19, 136.00, 132.60, 130.05, 127.64, 126.14, 124.60, 77.23, 66.93, 64.49, 34.88, 22.30, 20.95, 10.34.
Rf: 0.373 (cyclohexane/AcOEt 8/2)

1-nBu:

^{1}H NMR (500 MHz, $CDCl_3$) δ 7.76 (s, 1H), 7.29 – 7.21 (m, 1H), 7.15 (dd, *J* = 7.7, 1.7 Hz, 1H), 7.08 (td, *J* = 7.5, 1.3 Hz, 1H), 6.50 – 6.37 (m, 1H), 5.91 (dtt, *J* = 15.2, 6.2, 1.3 Hz, 1H), 5.59 (dtt, *J* = 15.6, 6.2, 1.7 Hz, 1H), 4.55 (dq, *J* = 6.3, 1.2 Hz, 2H), 4.16 (t, *J* = 6.7 Hz, 2H), 3.38 (dd, *J* = 6.1, 1.5 Hz, 2H), 2.06 (s, 3H), 1.71 – 1.61 (m, 2H), 1.47 – 1.36 (m, 2H), 0.96 (t, *J* = 7.4 Hz, 3H).
^{13}C NMR (126 MHz, $CDCl_3$) δ 170.75, 154.19, 136.00, 132.59, 130.05, 127.64, 126.14, 124.59, 77.23, 65.24, 64.48, 34.87, 31.00, 20.95, 19.09, 13.76.
Rf: 0.412 (cyclohexane/AcOEt 8/2)

Urea-containing molecules:

2-Me:

^{1}H NMR (500 MHz, $CDCl_3$) δ 7.46 (dd, *J* = 8.0, 1.3 Hz, 1H), 7.29 – 7.24 (m, 2H), 7.21 (dd, *J* = 7.6, 1.8 Hz, 1H), 7.16 (td, *J* = 7.4, 1.4 Hz, 1H), 6.08 (s, 1H), 5.88 (dtt, *J* = 15.3, 6.1, 1.4 Hz, 1H), 5.55 (dtt, *J* = 15.6, 6.0, 1.7 Hz, 1H), 4.67 (s, 1H), 4.53 (dq, *J* = 6.1, 1.3 Hz, 2H), 3.39 (dd, *J* = 6.2, 1.5 Hz, 2H), 2.81 (d, *J* = 4.8 Hz, 3H), 2.06 (s, 3H).
^{13}C NMR (126 MHz, $CDCl_3$) δ 171.17, 156.87, 136.31, 133.47, 132.68, 130.66, 127.89, 126.18, 126.06, 125.99, 77.23, 64.79, 34.89, 27.04, 21.05.
Rf: 0.227 (cyclohexane/AcOEt 2/8)

2-Et:

^{1}H NMR (500 MHz, $CDCl_3$) δ 7.47 (dd, *J* = 8.0, 1.3 Hz, 1H), 7.29 – 7.24 (m, 2H), 7.21 (dd, *J* = 7.6, 1.7 Hz, 1H), 7.15 (td, *J* = 7.4, 1.3 Hz, 1H), 6.03 (s, 1H), 5.89 (dtt, *J* = 15.1, 6.1, 1.3 Hz,

1H), 5.55 (dtt, *J* = 15.5, 6.0, 1.7 Hz, 1H), 4.69 (s, 1H), 4.53 (dq, *J* = 6.1, 1.2 Hz, 2H), 3.39 (dd, *J* = 6.1, 1.6 Hz, 2H), 3.27 (qd, *J* = 7.2, 5.6 Hz, 2H), 2.06 (s, 3H), 1.13 (t, *J* = 7.2 Hz, 3H).
^{13}C NMR (126 MHz, $CDCl_3$) δ 171.19, 156.10, 136.38, 133.22, 132.66, 130.65, 127.87, 126.19, 125.89, 125.80, 77.22, 64.83, 35.21, 34.88, 21.06, 15.44.
Rf: 0.386 (cyclohexane/AcOEt 2/8)

2-iPr:

^{1}H NMR (500 MHz, $CDCl_3$) δ 7.50 – 7.45 (m, 1H), 7.30 – 7.23 (m, 4H), 7.20 (dd, *J* = 7.5, 1.7 Hz, 1H), 7.14 (td, *J* = 7.4, 1.3 Hz, 1H), 5.95 (s, 1H), 5.89 (dtt, *J* = 15.1, 6.0, 1.4 Hz, 1H), 5.54 (dtt, *J* = 15.5, 6.1, 1.8 Hz, 1H), 4.54 (dq, *J* = 6.0, 1.3 Hz, 2H), 3.99 (dp, *J* = 7.8, 6.5 Hz, 1H), 3.39 (dd, *J* = 6.2, 1.6 Hz, 2H), 2.06 (s, 3H), 1.15 (d, *J* = 6.5 Hz, 6H).
^{13}C NMR (126 MHz, $CDCl_3$) δ 171.22, 136.47, 132.60, 130.66, 127.86, 126.22, 125.70, 125.54, 64.88, 42.25, 34.90, 23.27, 21.07.
Rf: 0.164 (cyclohexane/AcOEt 1/1)

2-tBu:

^{1}H NMR (500 MHz, $CDCl_3$) δ 7.48 (dd, *J* = 8.0, 1.3 Hz, 1H), 7.24 (dd, *J* = 7.7, 1.7 Hz, 2H), 7.18 (dd, *J* = 7.6, 1.7 Hz, 1H), 7.11 (td, *J* = 7.4, 1.3 Hz, 1H), 5.94 – 5.85 (m, 2H), 5.54 (dtt, *J* = 15.6, 6.1, 1.8 Hz, 1H), 4.66 (s, 1H), 4.54 (dq, *J* = 6.1, 1.3 Hz, 2H), 3.38 (dd, *J* = 6.0, 1.6 Hz, 2H), 2.06 (s, 3H), 1.35 (s, 9H).
^{13}C NMR (126 MHz, $CDCl_3$) δ 171.26, 155.14, 136.79, 132.61, 132.43, 130.58, 127.75, 126.16, 125.33, 125.25, 64.95, 50.69, 34.88, 29.31, 21.09.
Rf: 0.382 (cyclohexane/AcOEt 1/1)

2-nPr:

^{1}H NMR (500 MHz, $CDCl_3$) δ 7.76 (s, 1H), 7.30 – 7.23 (m, 2H), 7.15 (dd, *J* = 7.7, 1.7 Hz, 1H), 7.08 (td, *J* = 7.4, 1.3 Hz, 1H), 6.45 (s, 1H), 5.91 (dtt, *J* = 15.2, 6.1, 1.4 Hz, 1H), 5.59 (dtt, *J* = 15.6, 6.3, 1.7 Hz, 1H), 4.55 (dq, *J* = 6.2, 1.2 Hz, 2H), 4.12 (t, *J* = 6.7 Hz, 2H), 3.41 – 3.35 (m, 2H), 2.06 (s, 3H), 1.75 – 1.65 (m, 2H), 0.97 (t, *J* = 7.4 Hz, 3H).
^{13}C NMR (126 MHz, $CDCl_3$) δ 170.76, 136.01, 132.59, 130.06, 127.64, 126.15, 124.59, 77.22, 66.93, 64.49, 34.89, 22.30, 20.95, 10.34.

§

Rf: 0.181 (cyclohexane/AcOEt 1/1)

2-nBu:

^{1}H NMR (500 MHz, $CDCl_3$) δ 7.76 (s, 1H), 7.26 (td, *J* = 7.9, 1.7 Hz, 1H), 7.15 (dd, *J* = 7.6, 1.7 Hz, 1H), 7.08 (td, *J* = 7.4, 1.2 Hz, 1H), 6.44 (s, 1H), 5.91 (dtt, *J* = 15.2, 6.1, 1.4 Hz, 1H), 5.59 (dtt, *J* = 15.7, 6.3, 1.7 Hz, 1H), 4.55 (dq, *J* = 6.3, 1.3 Hz, 2H), 4.16 (t, *J* = 6.7 Hz, 2H), 3.41 – 3.35 (m, 2H), 2.06 (s, 3H), 1.71 – 1.61 (m, 2H), 1.47 – 1.36 (m, 2H), 0.96 (t, *J* = 7.4 Hz, 3H).
^{13}C NMR (126 MHz, $CDCl_3$) δ 170.75, 154.19, 136.00, 132.59, 132.37, 130.05, 127.64, 126.14, 124.59, 77.23, 65.23, 64.48, 60.06, 34.87, 31.00, 20.95, 19.09, 19.07, 13.76.
Rf: 0.272 (cyclohexane/AcOEt 1/1)

TIPS: It might happen that for the carbamate product, it is difficult to separate the desired product from a side product (probably linked to the quality/eq of DPPA used for the reaction). To purify the batch, it is recommended to proceed through an acetate removal, purify, and then perform the acetylation again.

Example for **1a**

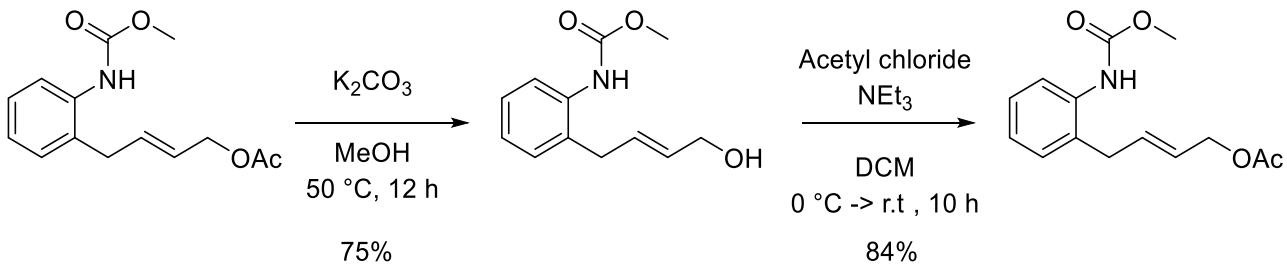

First step:

The methyl carbamate (340 mg, 1.29 mmol, 1 eq) was dissolved in MeOH (5 mL) followed by the addition of K_2CO_3 (71.4 mg, 0.516 mmol, 0.4 eq). The resulting mixture was stirred at 50 °C for 10h. Once by TLC no starting material is detectable, the solution was diluted in DCM to make a solid loading. The crude was then purified by column chromatography using a slow gradient of AcOEt in cyclohexane (from 0% to 30% in 25 CV and then 15 CV at 30%). The pure product was obtained as a pale yellowish oil (213 mg, 75% yield).

§

^{1}H NMR (500 MHz, $CDCl_3$) δ 7.75 (s, 1H), 7.29 – 7.23 (m, 2H), 7.16 (dd, *J* = 7.6, 1.7 Hz, 1H), 7.09 (td, *J* = 7.5, 1.3 Hz, 1H), 6.53 (s, 1H), 5.84 (dtt, *J* = 15.2, 6.1, 1.4 Hz, 1H), 5.66 (dtt, *J* = 15.5, 5.6, 1.6 Hz, 1H), 4.13 (tq, *J* = 5.6, 1.3 Hz, 2H), 3.77 (s, 3H), 3.37 (dq, *J* = 6.2, 1.5 Hz, 2H).

Second step:

The previously obtained free alcohol (105 mg, 0.475 mmol, 1eq) was dissolved in DCM (3 mL) followed by triethylamine (73.4 mL, 0.523 mmol, 1.1 eq) and cooled to 0 °C. Then, acetyl chloride (37.3 mL, 0.523 mmol, 1.1 eq) was added slowly to the cooled solution at 0 °C. The reaction turned slightly yellowish and was stirred at 0°c for an hour and then warmed to room temperature. Silica was added to the solution to form a solid loading, given purification. The crude was then purified by column chromatography using a slow gradient of AcOEt in cyclohexane from 0% to 35% to afford a transparent oil, which, after one night in the freezer, turned into a white solid (105 mg, 74%).

5) Synthesis of methyl (E)-(2-(4-((methylcarbamoyl)oxy)but-2-en-1-yl)phenyl)carbamate **1a**

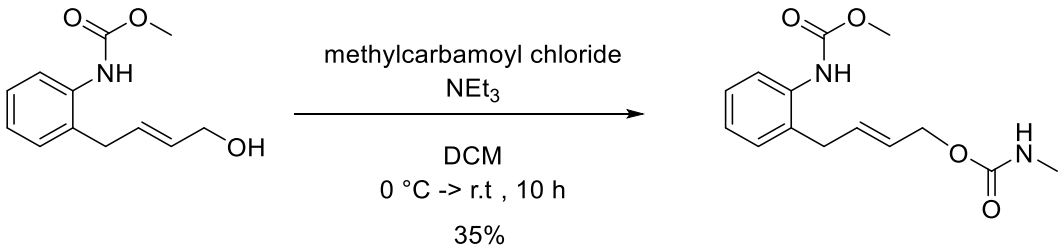

The free alcohol (105 mg, 0.475 mmol, 1 eq) was dissolved in DCM (3 mL), followed by the addition of triethylamine (73.4 mL, 0.523 mmol, 1.1 eq) and the resulting solution was cooled to 0 °C. Then methylcarbamoyl chloride (48.9 mg, 0.523 mmol, 1.1 eq), was added to the cooled solution at 0 °C. The resulting mixture was stirred for 10 h. The crude was turned into a solid loading for further purification. Then, the crude was purified by column chromatography using a gradient of AcOEt in cyclohexane from 0% to 35% to afford a white powder (46 mg, 35%).

NMR:

§

^{1}H NMR (600 MHz, $CDCl_3$) δ 7.78 (s, 1H), 7.28 (s, 7H), 7.17 (d, *J* = 7.4 Hz, 1H), 7.11 (t, *J* = 7.4 Hz, 1H), 6.53 (s, 1H), 5.90 (dt, *J* = 13.4, 6.1 Hz, 1H), 5.68 – 5.54 (m, 1H), 4.61 (s, 1H), 4.56 (d, *J* = 6.1 Hz, 2H), 3.79 (d, *J* = 1.1 Hz, 3H), 3.39 (d, *J* = 6.3 Hz, 2H), 2.82 (d, *J* = 4.9 Hz, 3H).

^{13}C NMR (151 MHz, $CDCl_3$) δ 156.88, 131.86, 130.14, 127.65, 126.95, 64.79, 52.43, 34.95, 27.57.

6) Synthesis of methyl (E)-(2-(4-((diethoxyphosphoryl)oxy)but-2-en-1-yl)phenyl)carbamate **1b**

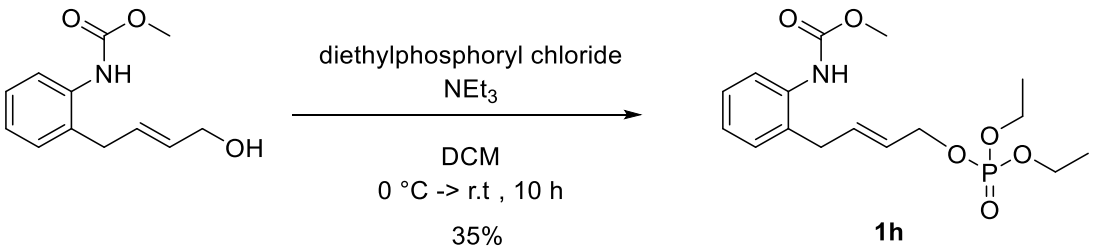

The free alcohol (100 mg, 0.452 mmol, 1 eq) was dissolved in DCM (3 mL), followed by the addition of triethylamine (76.2 mL, 0.542 mmol, 1.2 eq), and the resulting solution was cooled to 0 °C. Then diethyl phosphoryl chloride (78 mL, 0.542 mmol, 1.2 eq) was added to the cooled solution at 0 °C. The resulting mixture was stirred for 10 h. The crude was turned into a solid loading for further purification. Then, the crude was purified by column chromatography using a gradient of AcOEt in cyclohexane from 0% to 35% to afford a white powder (100 mg, 62%).

NMR:

^{1}H NMR (600 MHz, $CDCl_3$) δ 7.74 (s, 1H), 7.28 (d, *J* = 3.3 Hz, 2H), 7.20 – 7.15 (m, 1H), 7.12 (t, *J* = 7.7 Hz, 1H), 6.74 – 6.50 (m, 1H), 6.01 – 5.90 (m, 1H), 5.61 (dtt, *J* = 15.3, 4.5, 1.7 Hz, 1H), 4.56 – 4.46 (m, 2H), 4.17 – 4.04 (m, 4H), 3.78 (dd, *J* = 3.4, 1.4 Hz, 3H), 3.43 – 3.35 (m, 2H), 1.43 – 1.36 (m, 2H), 1.33 (tdd, *J* = 7.0, 4.2, 1.8 Hz, 6H).

^{13}C NMR (151 MHz, $CDCl_3$) δ 154.67, 135.87, 132.78, 130.46, 130.13, 127.70, 126.50, 126.46, 124.96, 83.17, 67.44, 67.41, 65.27, 65.25, 65.23, 63.85, 63.81, 52.43, 34.76, 16.14, 16.10, 16.04, 16.02, 15.99.

§

7) Synthesis of 8-(allyloxy)-N'-(5-((3aS,4S,6aR)-2-oxohexahydro-1H-thieno[3,4-d]imidazol-4-yl)pentanoyl)quinoline-5-carbohydrazide

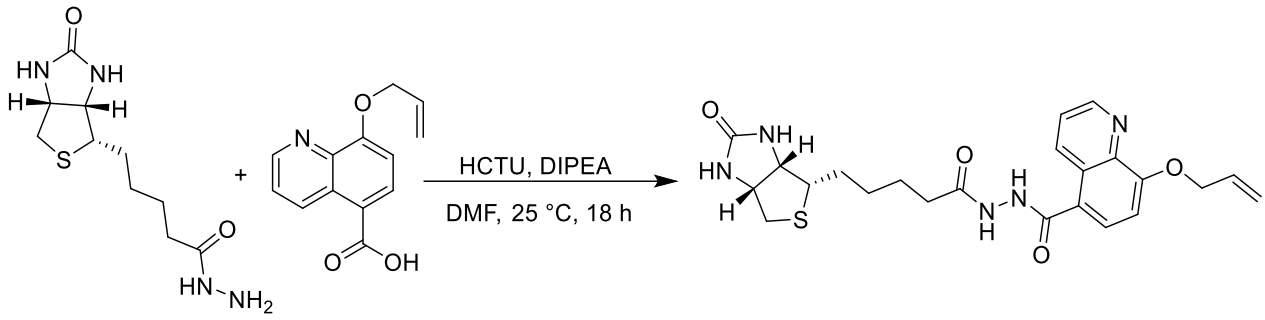

Biotinhydrazide (1.0 eq.), 8-(allyloxy)quinoline-5-carboxylic acid (1.1 eq.), HCTU (1.1 eq.) and DIPEA (2.2 eq.) were dissolved in anhydrous DMF and the mixture was stirred for 3 h at room temperature. The mixture was concentrated *in vacuo*, re-dissolved in DCM and filtered. The crude product **L6** was re-dissolved in MECN:H_2O (2:1) and the product precipitated as a dark solid (5.30 mg, 11.3 µmol, 14%).

NMR:

^{1}H NMR (600 MHz, DMSO) δ 10.24 (s, 1H), 9.95 (s, 1H), 8.91 (d, *J* = 4.1 Hz, 1H), 8.82 (d, *J* = 8.6 Hz, 1H), 7.75 (d, *J* = 8.1 Hz, 1H), 7.63 (dd, *J* = 8.7, 4.0 Hz, 1H), 7.26 (d, *J* = 8.1 Hz, 1H), 6.45 (s, 1H), 6.38 (s, 1H), 6.18 (tt, *J* = 10.9, 6.0 Hz, 1H), 5.53 (d, *J* = 17.2 Hz, 1H), 5.34 (d, *J* = 10.6 Hz, 1H), 4.84 (d, *J* = 5.4 Hz, 2H), 4.32 (t, *J* = 6.4 Hz, 1H), 4.17 (d, *J* = 7.0 Hz, 1H), 3.13 (s, 1H), 2.84 (dd, *J* = 12.8, 5.3 Hz, 1H), 2.59 (d, *J* = 12.6 Hz, 2H), 2.22 (d, *J* = 7.7 Hz, 2H), 1.71 – 1.20 (m, 9H, should be 6H, probable impurities below the signal integrated).

8) Formation of the biotinylated ruthenium cofactors

The ruthenium cofactors **Biot-Ru and Biot-Ru-HQ** were prepared *in situ* by mixing solutions of the respective ligands (16 mM) and $[CpRu(MeCN)_3]PF_6$ (16 mM) in a 1:1 ratio in the co-solvent (de-gassed DMF/DMSO) under inert atmosphere (glovebox station).

9) Allylic amination protocol

Protocol one for carbamate-based substrate

§

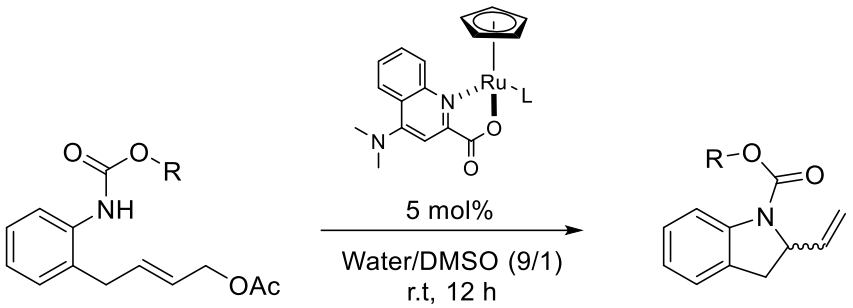

R	Yield (%)
3-Me	45
3-Et	44
3-iPr	45
3-tBu	43
3-nPr	42
3-nBu	41

The experiment was performed in the glovebox. In a sealed tube, the carbamate substrate was followed by degassed water (5 mL per 10 mg). The catalyst solution was prepared in DMSO and then added to the mixture (5% catalytic loading), and the resulting solution was stirred in the glovebox overnight. The reaction was followed via TLC-MS: The right mass was observed in APCI pos mode. The reaction mixture was then dried under vacuum and directly purified on column (gradient of AcOEt in Hexane from 0 to 35%) to afford the corresponding product.

NMR:

3-Me: ^{1}H NMR (500 MHz, $CDCl_3$) δ 7.76 (s, 1H), 7.20 (t, *J* = 7.8 Hz, 1H), 7.14 (d, *J* = 7.4 Hz, 1H), 6.97 (td, *J* = 7.5, 1.0 Hz, 1H), 5.84 (ddd, *J* = 16.9, 10.3, 6.5 Hz, 1H), 5.17 (d, *J* = 17.1 Hz, 1H), 5.08 (d, *J* = 10.3 Hz, 1H), 4.93 (s, 1H), 3.82 (s, 3H), 3.47 – 3.39 (m, 1H), 2.82 (dd, *J* = 16.1, 2.6 Hz, 1H).
^{13}C NMR (126 MHz, $CDCl_3$) δ 153.79, 137.40, 127.60, 124.91, 122.88, 115.19, 114.80, 77.22, 65.86, 61.07, 52.53, 34.73, 29.71, 15.28.

3-Et: ^{1}H NMR (500 MHz, $CDCl_3$) δ 7.76 (s, 1H), 7.23 – 7.17 (m, 1H), 7.14 (ddt, *J* = 7.6, 2.1, 1.3 Hz, 1H), 6.96 (td, *J* = 7.4, 1.0 Hz, 1H), 5.84 (ddd, *J* = 17.0, 10.3, 6.6 Hz, 1H), 5.17 (d, *J* =

17.0 Hz, 1H), 5.08 (d, *J* = 10.4 Hz, 1H), 4.93 (s, 1H), 4.28 (d, *J* = 7.7 Hz, 2H), 3.47 – 3.38 (m, 1H), 2.82 (dd, *J* = 16.1, 2.7 Hz, 1H), 1.33 (t, *J* = 5.9 Hz, 3H).
^{13}C NMR (126 MHz, $CDCl_3$) δ 127.58, 124.90, 122.75, 115.20, 114.84, 77.22, 61.07, 29.71, 14.57.

3-iPr: ^{1}H NMR (500 MHz, $CDCl_3$) δ 7.69 (s, 1H), 7.15 – 7.08 (m, 1H), 7.08 – 7.04 (m, 1H), 6.89 (td, *J* = 7.4, 1.1 Hz, 1H), 5.77 (ddd, *J* = 17.0, 10.2, 6.7 Hz, 1H), 5.09 (d, *J* = 17.0 Hz, 1H), 5.04 – 4.96 (m, 2H), 4.85 (s, 1H), 3.35 (ddt, *J* = 16.0, 10.0, 1.2 Hz, 1H), 2.74 (dd, *J* = 16.1, 2.7 Hz, 1H), 1.25 (dd, *J* = 23.0, 6.3 Hz, 6H).
^{13}C NMR (126 MHz, $CDCl_3$) δ 152.97, 137.56, 127.56, 124.86, 122.64, 115.17, 114.81, 77.23, 61.05, 34.62, 22.29, 22.11.

3-tBu: ^{1}H NMR (500 MHz, $CDCl_3$) δ 7.66 (s, 1H), 7.15 – 7.06 (m, 1H), 7.05 (dq, *J* = 7.3, 1.3 Hz, 1H), 6.86 (td, *J* = 7.4, 1.1 Hz, 1H), 5.76 (ddd, *J* = 17.0, 10.2, 6.7 Hz, 1H), 5.07 (dt, *J* = 17.0, 1.2 Hz, 1H), 4.99 (dt, *J* = 10.3, 1.2 Hz, 1H), 4.79 (s, 1H), 3.33 (ddt, *J* = 16.0, 10.1, 1.2 Hz, 1H), 2.71 (dd, *J* = 16.1, 2.8 Hz, 1H), 1.46 (s, 9H).
^{13}C NMR (126 MHz, $CDCl_3$) δ 152.41, 137.86, 127.49, 124.81, 122.41, 115.10, 114.47, 77.23, 61.18, 28.41.

3-nPr: ^{1}H NMR (500 MHz, $CDCl_3$) δ 7.70 (s, 1H), 7.16 – 7.10 (m, 1H), 7.09 – 7.04 (m, 1H), 6.89 (td, *J* = 7.4, 1.1 Hz, 1H), 5.78 (ddd, *J* = 17.0, 10.2, 6.7 Hz, 1H), 5.10 (d, *J* = 17.0 Hz, 1H), 5.01 (dt, *J* = 10.2, 1.2 Hz, 1H), 4.86 (s, 1H), 4.12 (dq, *J* = 14.1, 8.0 Hz, 2H), 3.37 (ddt, *J* = 16.0, 9.9, 1.2 Hz, 1H), 2.75 (dd, *J* = 16.0, 2.7 Hz, 1H), 1.66 (q, *J* = 7.3 Hz, 2H), 0.92 (t, *J* = 7.4 Hz, 3H).
^{13}C NMR (126 MHz, $CDCl_3$) δ 153.46, 137.56, 127.60, 124.89, 122.75, 115.19, 114.77, 77.23, 61.10, 34.73, 26.93, 22.31, 10.59.

3-nBu: ^{1}H NMR (500 MHz, $CDCl_3$) δ 7.70 (s, 1H), 7.16 – 7.09 (m, 1H), 7.07 (ddt, *J* = 7.5, 2.1, 1.3 Hz, 1H), 6.89 (td, *J* = 7.4, 1.1 Hz, 1H), 5.78 (ddd, *J* = 17.0, 10.2, 6.7 Hz, 1H), 5.09 (d, *J* = 17.0 Hz, 1H), 5.01 (dt, *J* = 10.2, 1.2 Hz, 1H), 4.86 (s, 1H), 4.15 (d, *J* = 6.6 Hz, 2H), 3.36 (ddt, *J* = 16.1, 10.1, 1.3 Hz, 1H), 2.78 – 2.71 (m, 1H), 1.71 – 1.52 (m, 2H), 1.37 (h, *J* = 7.4 Hz, 2H), 0.89 (t, *J* = 7.4 Hz, 3H).

§

^{13}C NMR (126 MHz, $CDCl_3$) δ 153.47, 137.55, 127.60, 124.88, 122.74, 115.18, 114.75, 77.23, 61.09, 34.73, 30.99, 19.23, 13.74.

Protocol one for urea-based substrate

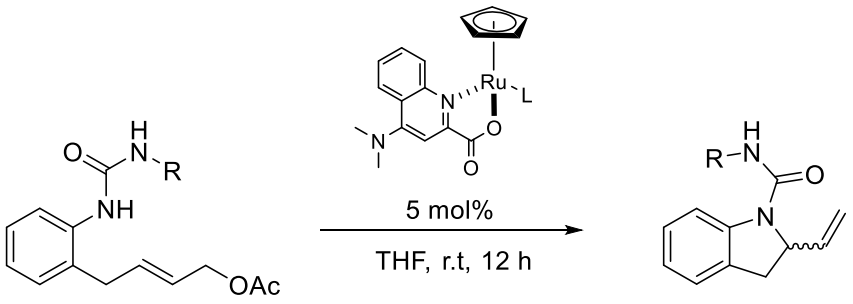

R	Yield (%)
4-Me	32
4-Et	29
4-iPr	34
4-tBu	30
4-nPr	30
4-nBu	31

Dry and degassed THF (1 mL per 10 mg) was added to a nitrogen-filled flask containing the urea substrate compound, the solution was stirred at room temperature. The freshly prepared catalyst was made in the glovebox by mixing the two catalyst precursors ($CpRu(MeCN)_3PF_6$ + lithium 4-(dimethylamino)quinoline-2-carboxylate) in DMF. The freshly prepared cat was added (5% catalytic loading) to the solution of urea substrate in THF, and the resulting dark brown solution was then stirred overnight. The reaction was followed via TLC-MS: The right mass was observed in APCI pos mode. The reaction mixture was then dried under vacuum and directly purified on column (gradient of AcOEt in Hexane from 0 to 35%) to afford the corresponding product.

NMR:

4-Me: ^{1}H NMR (500 MHz, $CDCl_3$) δ 7.90 (d, *J* = 8.0 Hz, 1H), 7.18 (dddt, *J* = 8.3, 7.5, 1.6, 0.9 Hz, 1H), 7.10 (dq, *J* = 7.5, 1.2 Hz, 1H), 6.91 (td, *J* = 7.4, 1.1 Hz, 1H), 5.94 (ddd, *J* = 17.4, 10.2, 7.3 Hz, 1H), 5.31 (dt, *J* = 17.2, 1.0 Hz, 1H), 5.22 (dt, *J* = 10.3, 1.0 Hz, 1H), 4.76 (s, 1H), 4.67

(dddt, *J* = 10.3, 7.3, 3.8, 1.0 Hz, 1H), 3.52 (ddt, *J* = 16.0, 10.3, 1.1 Hz, 1H), 2.86 (d, *J* = 4.6 Hz, 4H).
^{13}C NMR (126 MHz, $CDCl_3$) δ 156.18, 143.55, 138.66, 128.38, 127.72, 124.47, 122.01, 116.01, 115.46, 61.64, 36.07, 27.12.

4-Et: ^{1}H NMR (500 MHz, $CDCl_3$) δ 7.90 (d, *J* = 7.7 Hz, 1H), 7.17 (dddt, *J* = 8.3, 7.4, 1.5, 0.8 Hz, 1H), 7.13 – 7.07 (m, 1H), 6.91 (td, *J* = 7.4, 1.1 Hz, 1H), 5.95 (ddd, *J* = 17.3, 10.2, 7.3 Hz, 1H), 5.31 (dt, *J* = 17.2, 1.1 Hz, 1H), 5.23 (dt, *J* = 10.2, 1.0 Hz, 1H), 4.78 (s, 1H), 4.67 (dddt, *J* = 10.2, 7.2, 3.8, 1.0 Hz, 1H), 3.52 (ddt, *J* = 16.0, 10.3, 1.2 Hz, 1H), 3.33 (qdd, *J* = 7.2, 5.4, 0.9 Hz, 2H), 2.85 (dd, *J* = 16.1, 3.9 Hz, 1H), 1.16 (t, *J* = 7.2 Hz, 3H).
^{13}C NMR (126 MHz, $CDCl_3$) δ 155.47, 143.57, 138.75, 128.40, 127.71, 124.46, 121.96, 115.96, 115.48, 77.22, 61.66, 36.03, 35.26, 15.35.

4-iPr: ^{1}H NMR (500 MHz, $CDCl_3$) δ 7.90 (d, *J* = 8.1 Hz, 1H), 7.17 (ddt, *J* = 8.2, 7.2, 1.1 Hz, 1H), 7.13 – 7.07 (m, 1H), 6.90 (td, *J* = 7.4, 1.0 Hz, 1H), 5.95 (ddd, *J* = 17.4, 10.2, 7.4 Hz, 1H), 5.31 (dt, *J* = 17.1, 1.0 Hz, 1H), 5.23 (dt, *J* = 10.2, 1.0 Hz, 1H), 4.70 – 4.61 (m, 2H), 4.10 – 3.97 (m, *J* = 6.6 Hz, 1H), 3.51 (ddt, *J* = 16.2, 10.3, 1.1 Hz, 1H), 2.84 (dd, *J* = 16.1, 3.9 Hz, 1H), 1.18 (dd, *J* = 9.5, 6.5 Hz, 6H).
^{13}C NMR (126 MHz, $CDCl_3$) δ 154.87, 143.61, 138.88, 128.39, 127.70, 124.44, 121.90, 115.93, 115.46, 77.22, 61.70, 42.30, 35.97, 23.49, 23.03.

4-tBu: ^{1}H NMR (500 MHz, $CDCl_3$) δ 7.90 (d, *J* = 8.1 Hz, 1H), 7.21 – 7.13 (m, 1H), 7.10 (dd, *J* = 7.3, 1.3 Hz, 1H), 6.90 (td, *J* = 7.4, 1.1 Hz, 1H), 5.95 (ddd, *J* = 17.4, 10.2, 7.4 Hz, 1H), 5.31 (dt, *J* = 17.1, 1.1 Hz, 1H), 5.23 (dt, *J* = 10.0, 1.0 Hz, 1H), 4.70 – 4.57 (m, 2H), 4.10 – 3.97 (m, *J* = 6.6 Hz, 1H), 3.51 (dd, *J* = 16.1, 10.3 Hz, 1H), 2.84 (dd, *J* = 16.1, 3.9 Hz, 1H), 1.18 (dd, *J* = 9.5, 6.5 Hz, 6H).
^{13}C NMR (126 MHz, $CDCl_3$) δ 154.87, 143.61, 138.88, 128.39, 127.70, 124.44, 121.90, 115.93, 115.46, 77.22, 61.70, 42.30, 35.98, 23.49, 23.03.

4-nPr: ^{1}H NMR (500 MHz, $CDCl_3$) δ 7.89 (dd, *J* = 8.1, 0.9 Hz, 1H), 7.23 – 7.13 (m, 1H), 7.10 (dq, *J* = 7.3, 1.4 Hz, 1H), 6.91 (td, *J* = 7.4, 1.0 Hz, 1H), 5.95 (ddd, *J* = 17.4, 10.2, 7.4 Hz, 1H), 5.31 (dt, *J* = 17.2, 1.0 Hz, 1H), 5.23 (dt, *J* = 10.2, 1.0 Hz, 1H), 4.86 (t, *J* = 5.3 Hz, 1H), 4.71 –

§

4.63 (m, 1H), 3.51 (ddt, *J* = 16.0, 10.2, 1.1 Hz, 1H), 3.31 – 3.17 (m, 2H), 2.84 (dd, *J* = 16.2, 3.9 Hz, 1H), 1.55 (h, *J* = 7.3 Hz, 2H), 0.93 (t, *J* = 7.4 Hz, 3H).
^{13}C NMR (126 MHz, $CDCl_3$) δ 155.59, 143.55, 138.78, 134.91, 128.39, 127.70, 125.61, 124.45, 121.98, 115.98, 115.49, 77.24, 61.72, 42.15, 42.12, 36.04, 29.71, 23.17, 23.14, 11.44.

4-nBu: ^{1}H NMR (500 MHz, $CDCl_3$) δ 7.93 – 7.87 (m, 1H), 7.17 (ddq, *J* = 9.0, 7.5, 1.0 Hz, 1H), 7.13 – 7.07 (m, 1H), 6.91 (td, *J* = 7.4, 1.0 Hz, 1H), 5.95 (ddd, *J* = 17.4, 10.2, 7.4 Hz, 1H), 5.35 – 5.28 (m, 1H), 5.23 (dt, *J* = 10.2, 1.0 Hz, 1H), 4.82 (s, 1H), 4.67 (dddt, *J* = 10.3, 7.4, 4.0, 1.0 Hz, 1H), 3.56 – 3.44 (m, 1H), 3.29 (tdd, *J* = 7.1, 5.5, 2.4 Hz, 2H), 2.85 (dd, *J* = 16.1, 3.9 Hz, 1H), 1.56 – 1.46 (m, 2H), 1.40 – 1.31 (m, 2H), 0.93 (t, *J* = 7.3 Hz, 3H).
^{13}C NMR (126 MHz, $CDCl_3$) δ 155.57, 143.59, 138.83, 128.37, 127.71, 124.44, 121.95, 115.97, 115.49, 77.22, 61.73, 40.12, 36.04, 32.05, 20.14, 13.79.

II] Ru-catalyzed allylic amination and chiral HPLC monitoring.

Without protein:

In a 2 mL-vial was added 485 μL of PBS buffer solution (pH= 7.4) followed by 5 μL of substrate stock solution (400 mM stock solution in either DMF or DMSO, depending on the experiment). Then, 10 μL of catalyst stock solution (2 mM stock solution in water/DMF (1/1) or water/DMSO (1/1) for 1% catalytic loading experiment; 0.2 mM stock solution was used for the 0.1% catalytic loading experiment). The vial was placed in a thermoshaker at 37 °C and 600 rpm for 15 h. After 15 h, 400 μL of diethylether and 20 μL of standard stock solution (84 mM either in ethyl acetate or cyclohexane depending on the substrate) were added to the vial and vortexed to extract the aqueous phase. Then, 100 μL of this organic was sampled into a vial bearing a conic inlet and submitted to the HPLC.

With protein:

In a 2 mL-vial was added 465 μL of PBS buffer solution (pH= 7.4) followed by 20 μL of protein stock solution (2 mM stock solution for 1% cat load experiment or 0.2 mM stock

solution for 0.1% cat load in water). Then 10 μL of catalyst stock solution (2 mM stock solution in water/DMF (1/1) or water/DMSO (1/1) for 1% catalytic loading experiment; 0.2 mM stock solution was used for the 0.1% catalytic loading experiment) and the vial was incubated for 10 min. Then 5 μL of substrate stock solution (400 mM stock solution in either DMF or DMSO, depending on the experiment) was added to the vial. The vial was placed in a thermoshaker at 37 °C and 600 rpm for 15 h. After 15 h, 400 μL of diethylether and 20 μM of standard stock solution (84 mM either in ethyl acetate or cyclohexane, depending on the substrate) were added to the vial and vortexed to extract the aqueous phase. Then 100 μL of this organic phase was sampled into a vial bearing a conic inlet and submitted to the HPLC.

Screening with Cell Lysate (from BL-21(DE3) *E.coli* cells)

Cell lysate from BL21(DE3) *E.coli* cells was kindly provided by Nico Igareta. It was dissolved in PBS buffer and added to the reaction mixture (final concentration 5 mg/mL). Catalysis was carried out as described in the procedure above using this buffer.

Screening with Glutathione

Glutathione (final concentration 10 mM) was added to the reaction mixture and catalysis was carried out according to the procedure described above. (replace 100 μL of PBS buffer by 100 μL of PBS + GSH 50 mM)

Preparation of BL21(DE3) competent *E.coli* cells

A pre-culture (2 mL of LB medium) was inoculated with a single colony of BL21(DE3) from an agar plate. This pre-culture was incubated overnight (37 °C, 300 rpm). The following day, a main culture (200 mL LB medium (Table 2)) was inoculated with the pre-culture (2 mL) and grown to OD_{600} of around 0.5 (37 °C, 300 rpm, 1–3 h). The main culture was then cooled down on ice (20 min) and centrifuged (2000 g, 4 °C, 10 min). The pellet was carefully re-suspended in TFB1 solution (15 mL, Table 3) and incubated on ice (10 min). Then, the cells were centrifuged again (2000 g, 4 °C, 10 min) and carefully resuspended in TFB2 solution (3 mL, Table 4) on ice. Finally, the cells were aliquoted in

pre-chilled Eppendorf tubes, immediately frozen using liquid nitrogen and stored at −80 °C.

For preparation of competent cells in 96-well plates, the same steps were followed. The well plates were pre-frozen using crushed dry ice and the cells were then distributed directly into the plates (20 µL per well) instead of aliquoting them. The plates were sealed and stored at −80 °C.

Table 1. Composition of LB-medium.[a]

Composition	Amount
Tryptone	10 g
Yeast extract	5 g
NaCl	10 g
dH_2O	Fill up to 1000 mL

[a] Autoclaved (121 °C) and stored at room temperature.

Table 2. Composition of TFB1 buffer.[a]

Composition	Amount
CH_3COOK (30 mM)	0.294 g
$MnCl_2$ (50 mM)	0.989 g
$RbCl_2$ (100 mM)	1.209 g
$CaCl_2.H_2O$ (10 mM)	0.111 g
Glycerol (15% w/v)	15 g
dH_2O	Fill up to 100 mL

[a] Adjusted pH to 6.8 using 0.01 M KOH/HCl, sterile filtered and stored at 4 °C.

Table 3. Composition of TFB2 buffer.[a]

Composition	Amount
MOPS buffer (10 mM)	0.209 mg
$CaCl_2.H_2O$ (10 mM)	1.103 g
$RbCl_2$	0.121 g
Glycerol (15% w/v)	15 g
dH_2O	Fill up to 100 mL

[a] Adjusted pH to 6.8 using 0.01 M KOH/HCl, sterile filtered and stored at 4 °C.

Cytoplasmic expression of Sav in 96-well plates

Competent BL21(DE3) *E.coli* cells in 96-well plates were thawed on ice. Aliquoted cells were also thawed and distributed in 96-well plates (20 μL per well).

Plasmids of the S112x-K121x double mutant library were kindly provided by the Ward group. The selected plasmids (2 μL) were added to the competent cells and the mixture was incubated on ice (15 min). The cells were subjected to heat shock (42 °C, 45 s) and then put back on ice (1 min). LB medium (100 μL) was added and the cells were incubated (37 °C, 1 h, 300 rpm). LB medium (500 μL per well) supplemented with kanamycin (50 μg/mL) was distributed in a new, sterilised 96-well plate and the cell cultures (100 μL) were added. They were incubated overnight (30 °C, 300 rpm). The following day, autoinduction medium (2.4 mL, Table 5) supplemented with kanamycin (50 μg/mL final concentration) was distributed in sterilised 24-well plates. The overnight cultures (150 μL per culture) were added and they were incubated (25 °C, 24 h, 300 rpm).

Finally, the plates were centrifuged (3400 rpm, 25 °C, 5 min) and the supernatant was discarded. The resulting pellets were frozen at −20 °C to facilitate cell lysis. Lysis buffer (1 mL, Table 6) was added to the cell pellets, the plates were incubated (25 °C, 2 h, 300 rpm) and a final centrifugation step was carried out (3400 rpm, 25 °C, 5 min). The resulting supernatant was collected as cell-free lysates and the cell pellet was discarded.

Table 4. Composition of autoinduction medium.[a]

Composition	Volume (mL)
20 x ZYP salts	12.5 mL

§

20 x ZYP sugars	12.5 mL
$MgSO_4$ (0.2 M)	2.5 mL
Kanamycin (50 mg/mL)	250 µL
Yeast-tryptone stock (5 g/L yeast, 10 g/L tryptone)	Fill up to 250 mL

[a] Yeast-tryptone stock was autoclaved, remaining solutions were sterile filtered.

Table 5. Composition of lysis buffer.[a]

Composition	Amount
Tris-HCl (1 M, pH 7.5)	1 mL
Lysozyme	50 mg
DNAse I	Spatula tip
MQ H_2O	49 mL

[a] Adjusted pH to 6.8 using 0.01 M KOH/HCl, sterile filtered and stored at 4 °C.

Determination of biotin-binding sites[30]

A B4F solution (1 µM final concentration) in MOPS buffer (50 mM, pH = 7.4) was prepared. This solution was distributed in a clear micro well-plate (200 µL per well) and cell-free lysate (10 µL per well) was added. The negative control contained lysis buffer (10 µL) only. The positive control (Sav_{STD}) contained a Sav solution (10 µL of 40 µM Sav) as the 100% saturation point. Finally, the fluorescence of each well was measured. Equation 1 was then used to calculate the total concentration of Sav.

$$[Sav_{FBS}] = \frac{\left(F_{CFE} - F_{Sav_{STD}}\right) - \left(F_{LB} - F_{Sav_{STD}}\right)}{\left(-F_{LB} - F_{Sav_{STD}}\right)} * 20$$

§

Equation 1. F_{CFE} is the fluorescence intensity of the cell-free lysate, $F_{Sav_{STD}}$ is the fluorescence intensity of Sav_{STD} to bind all free BF4 and F_{LB} is the fluorescence intensity of the lysis buffer.

The measurement settings for the assay were as follows: Excitation Wavelength 485 nm, Emission Wavelength 520 nm, Excitation Bandwidth 5 nm, Emission Bandwidth 5 nm, Gain 94 (100%), Number of slashes 10, Flash frequency 400 Hz, Integration time 20 µs, Lag time 0 s, Settle Time 100 ms, Z-position 20000 µm.

Mutant Screening with Cell-Free Extracts

The catalysis experiments were carried out according to the procedure above (*In vitro* catalysis), however cell-free extracts were used instead of purified protein. Using the results of the binding assay, the amount of cell-free extract needed to reach a final protein concentration of 8 µM was determined for each mutant. Control experiments were done using empty cell-free extract.

Analytical method to quantify the catalytic performances

The quantification of the catalytic efficiency was based on two value of interest which are the turnover number (TON) and the enantioselectivity (ee). The quantification of the whole catalytic reaction was performed by HPLC using a chiral column OJ-H. Two different analytical method were developed for the analysis of either the carbamates-based molecules or the urea-based one.

Based on Kitamura and co-workers work, we assumed that for carbamates-based product, the fastest enantiomer to come was (S) and the latest (R) since we using the same solvents and the same chiral column CHIRALCEL OJ-H.[231]

Solvent **A**: Hexane/iPrOH (95/5) (Hexan/iPrOH (97/3) was used for **3-iPr/nPr/tBu/nBu**)
Solvent **B**: iPrOH

§

Method one (for carbamates):

Flow rate: 1 mL/min

0 min -> 9 min **0% B**

9 min -> 10 min **0% B** -> **70% B**

10 min -> 12 min **70% B**

12 min -> 13 min **70% B** -> **0% B**

13 min -> 20 min **0% B**

Method Two (for urea):

Flow rate: 1 mL/min

0 min -> 26 min **0% B**

26 min -> 27 min **0% B** -> **60% B**

27 min -> 34 min **60% B**

34 min -> 35 min **70% B** ->**0% B**

35 min -> 50 min **0% B**

Standard curve and UV spectrum (254.16 nm), concentrations are in mM.

§

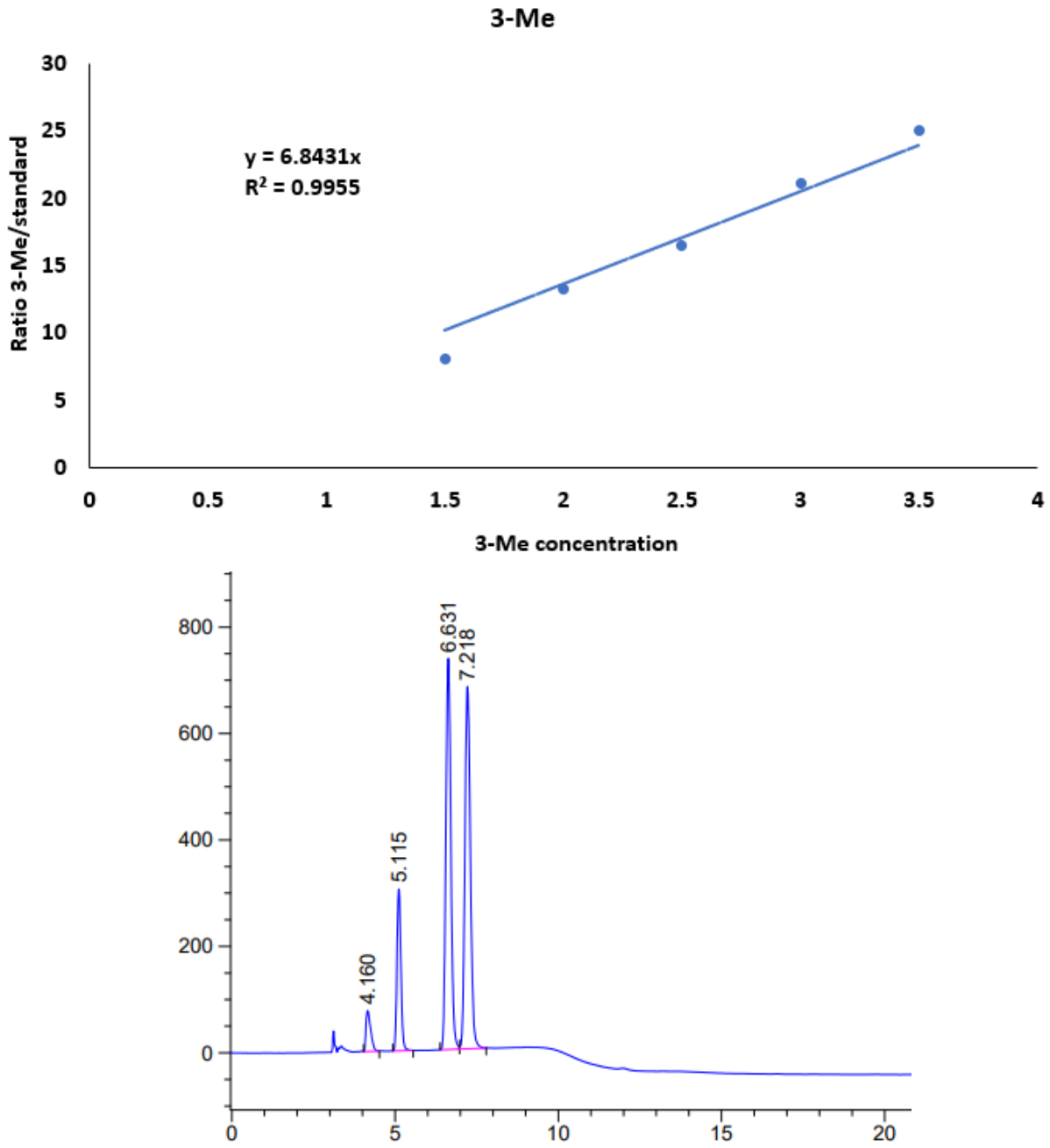

Figure S1: Standard curve and chiral HPLC trace of **3-Me**. t_R 4.160 min is AcOEt, t_R 5.115 min is Anisole (Standard), t_R 6.631 min is (S)-**3-Me** and t_R 7.218 min is (R)-**3-Me**.

§

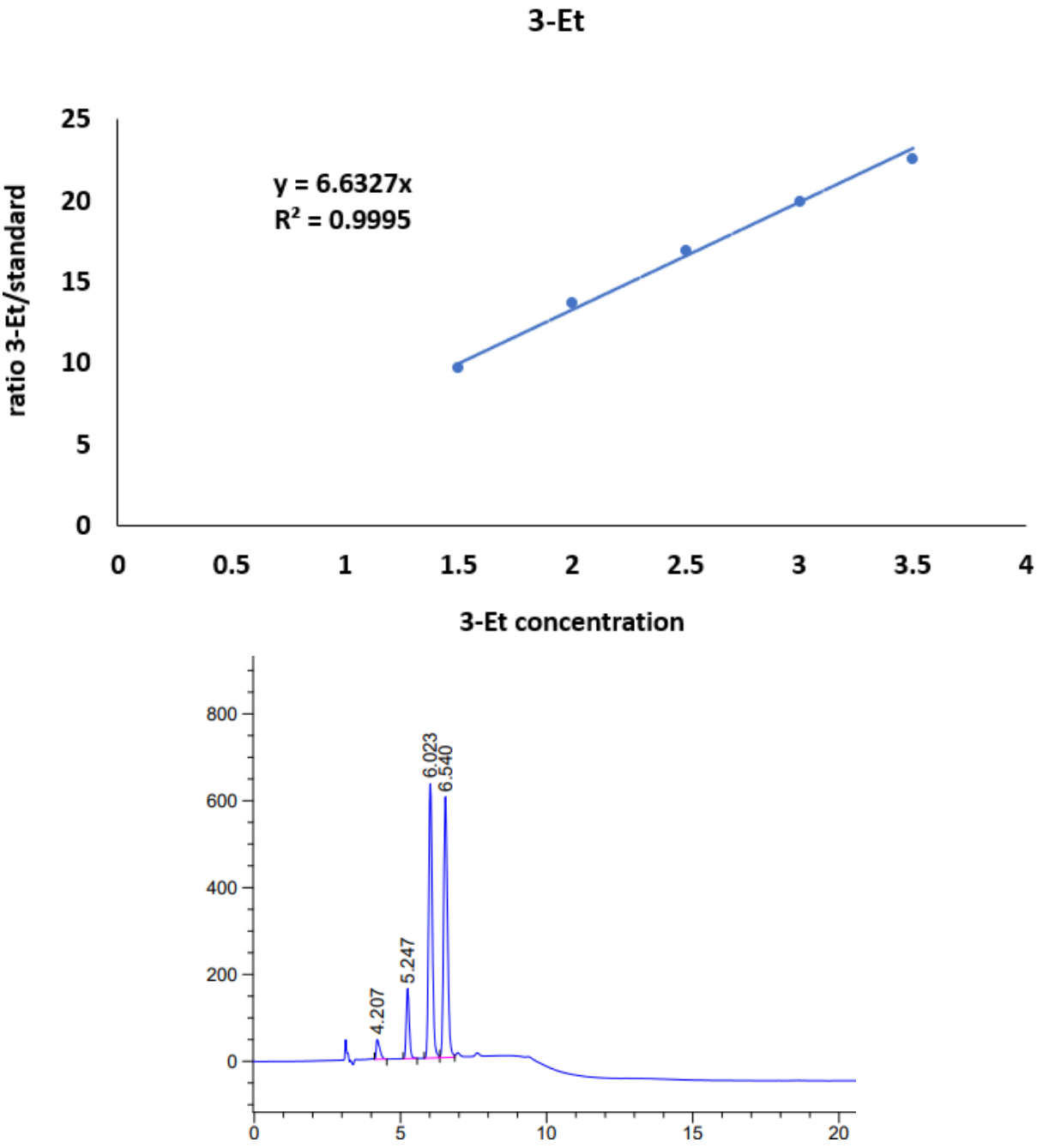

Figure S2: Standard curve and chiral HPLC trace of **3-Et.** t_R 4.207 min is AcOEt, t_R 5.247 min is Anisole and t_R 6.023-6.540 is **3-Et**.

§

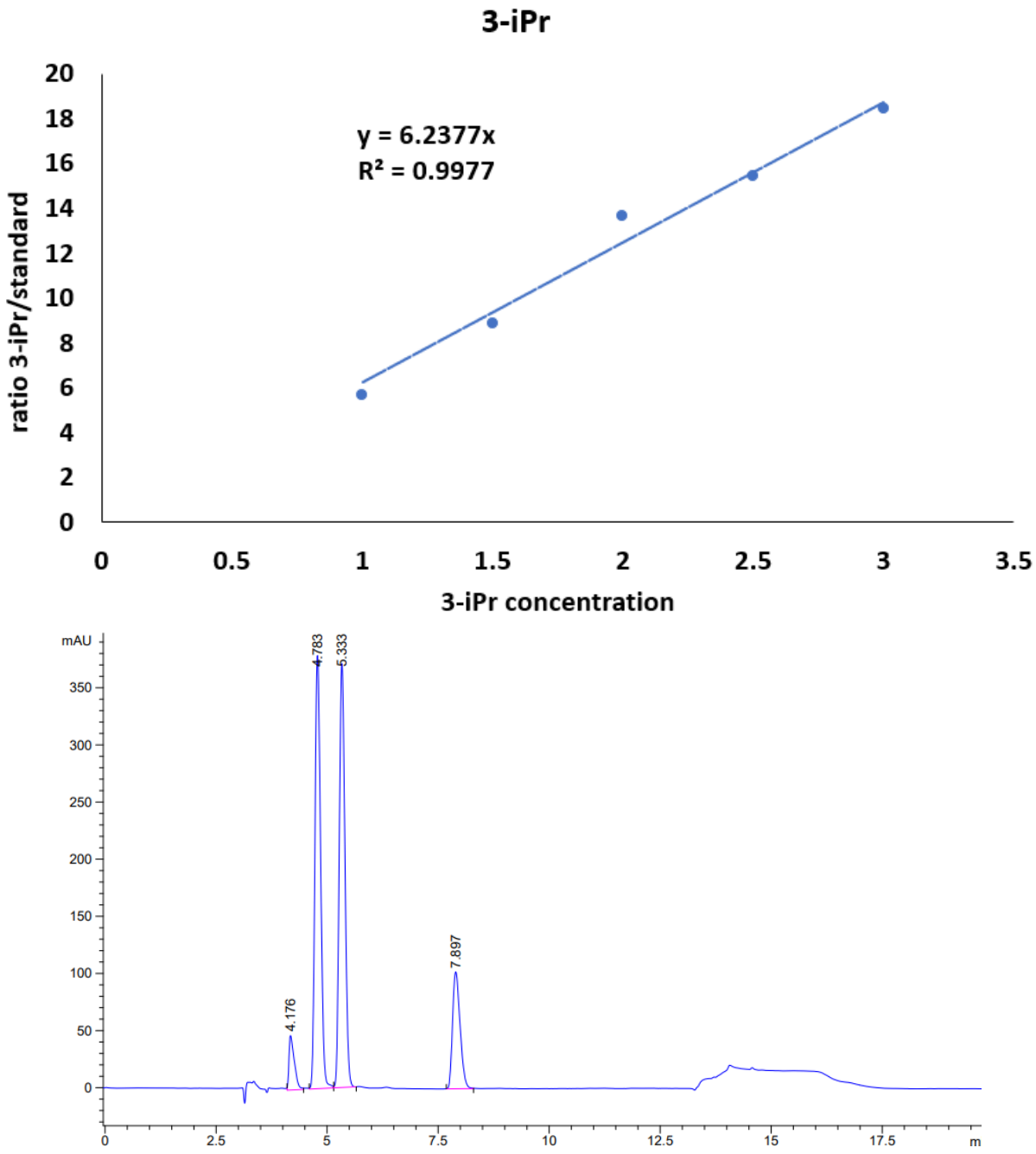

Figure S3: Standard curve and chiral HPLC trace of **3-iPr.** t_R 4.176 min is AcOEt, t_R 4.783-5.33 min is **3-iPr** and t_R 7.897 min is trimethoxybenzene (Standard).

§

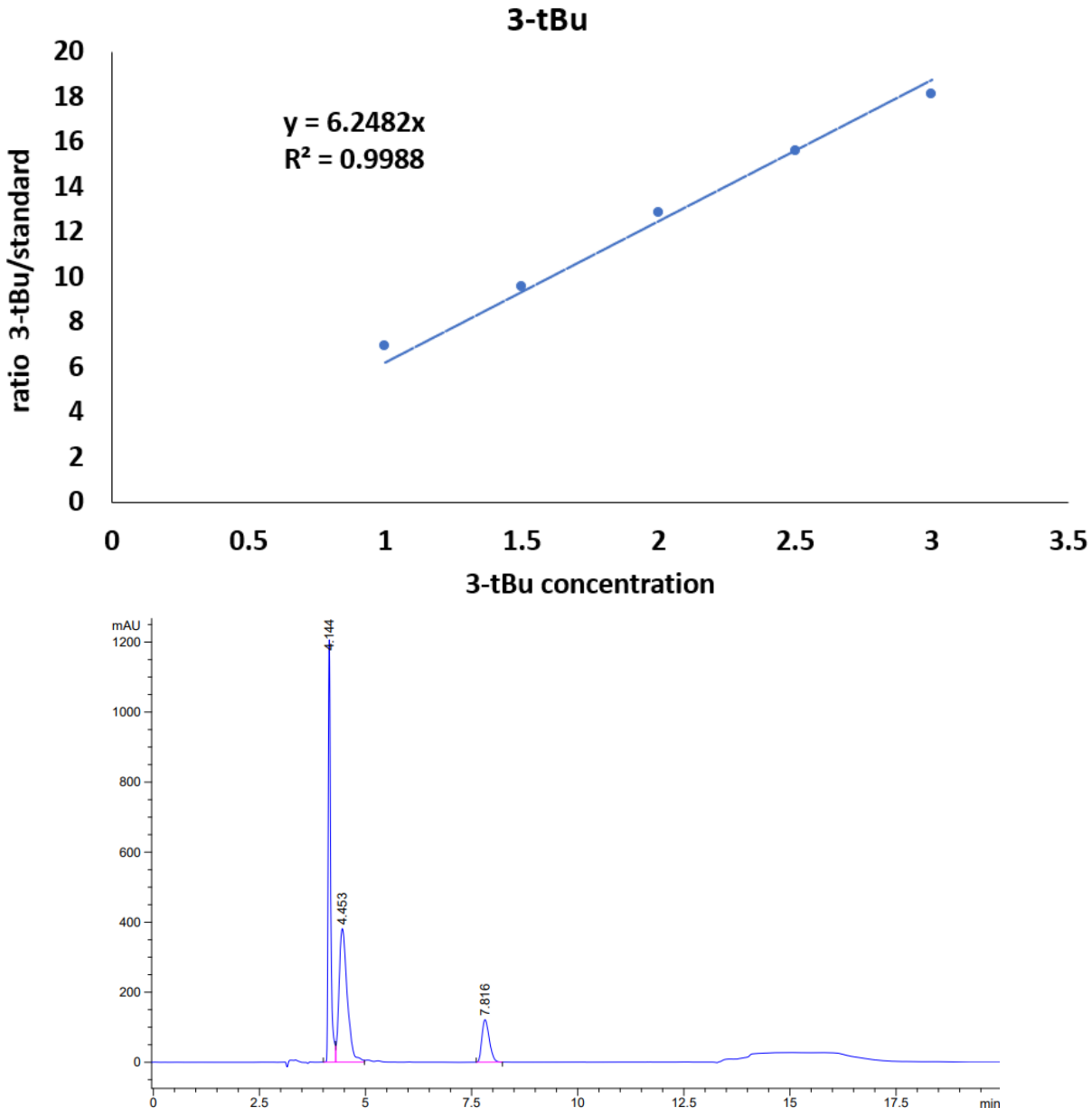

Figure S4: Standard curve and chiral HPLC trace of **3-tBu.** t_R 4.144-4.453 min is **3-tBu** and t_R 7.816 min is trimethoxybenzene (Standard). No AcOEt was used to prepare any stock solution since AcOEt would overlap with **3-tBu**.

§

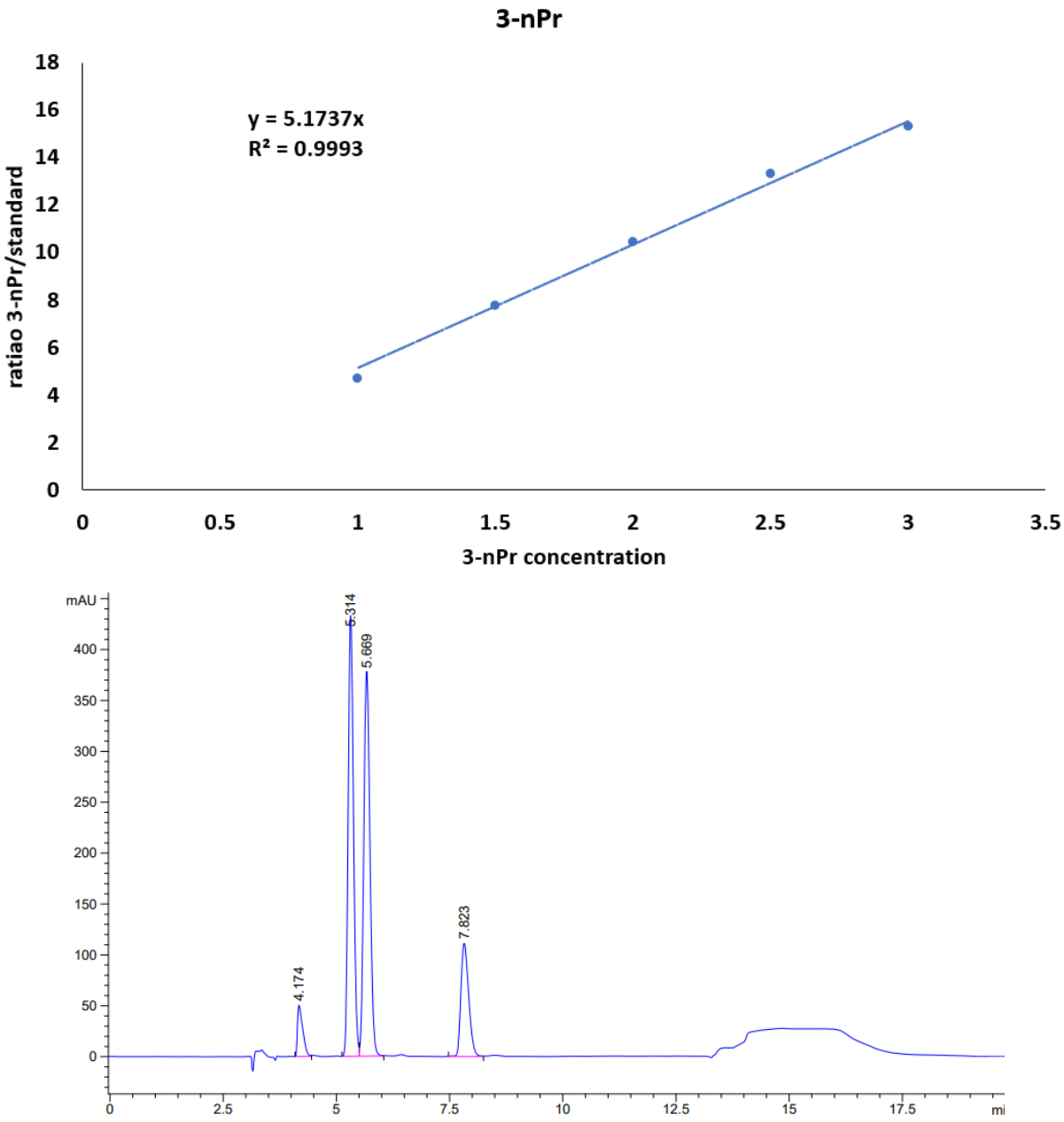

Figure S5: Standard curve and chiral HPLC trace of **3-nPr.** t_R 4.174 is AcOEt, t_R 5.314-5.669 min is **3-nPr** and t_R 7.897 min is trimethoxybenzene (Standard).

§

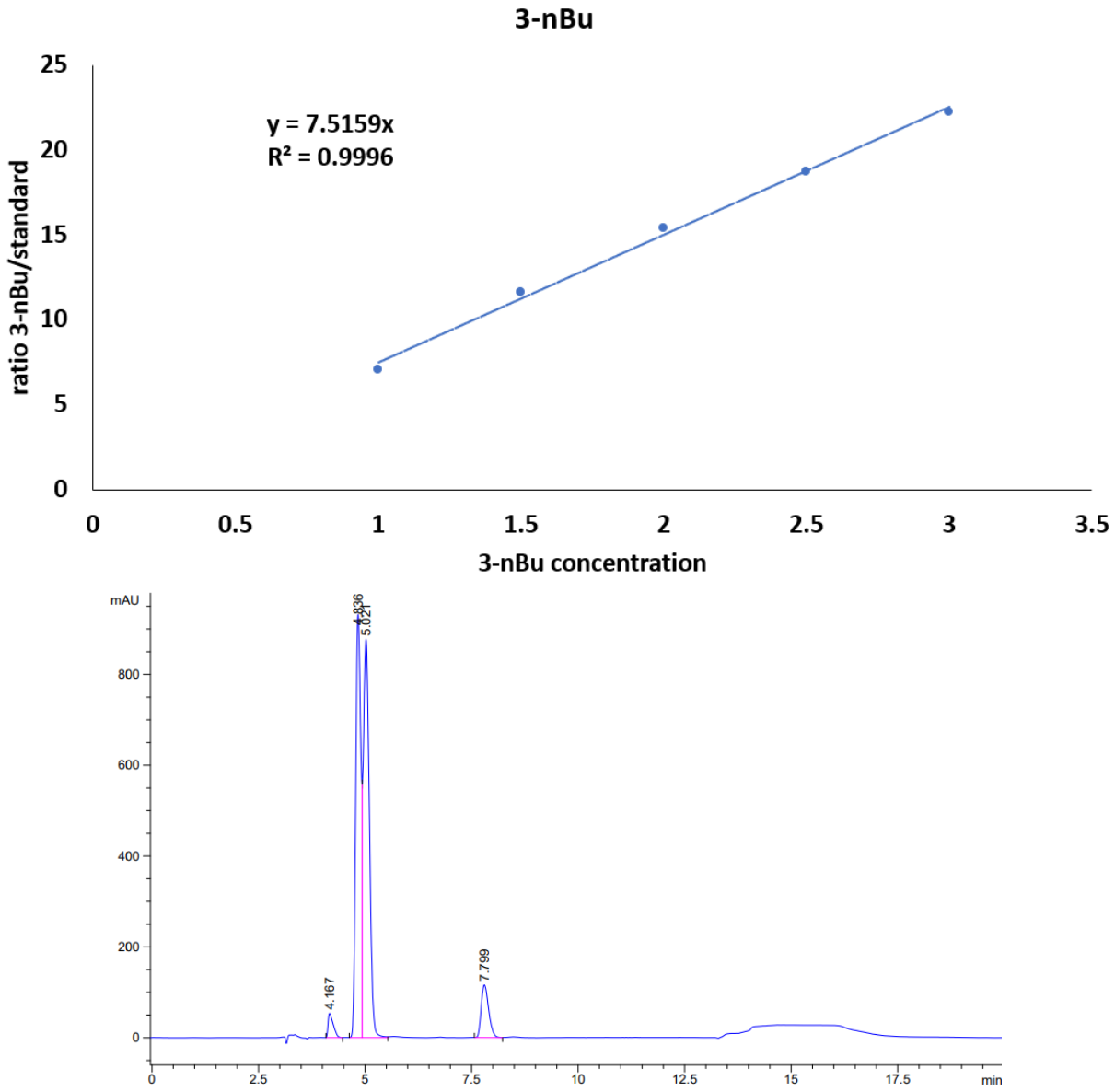

Figure S6: Standard curve and chiral HPLC trace of **3-nBu.** t_R 4.167 is AcOEt, t_R 4.836-5.021 min is **3-nBu** and t_R 7.799 min is trimethoxybenzene (Standard).

Standard curve and UV spectrum (254.4 nm), concentrations are in mM.

§

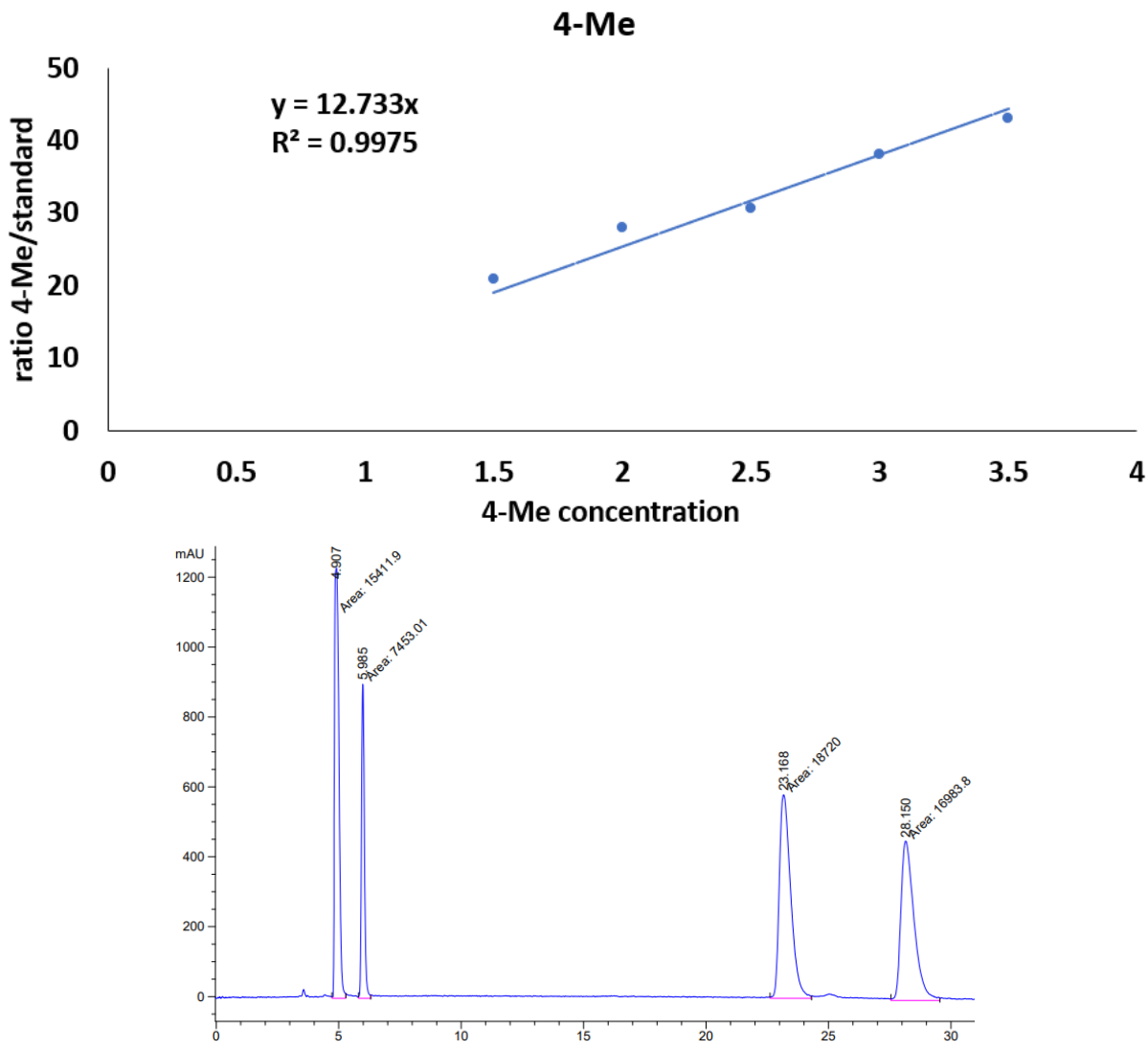

Figure S7: Standard curve and chiral HPLC trace of **4-Me.** t_R 4.907 min is AcOEt, t_R 5.985 min is Anisole and t_R 23.168-28.150 min is **4-Me**.

§

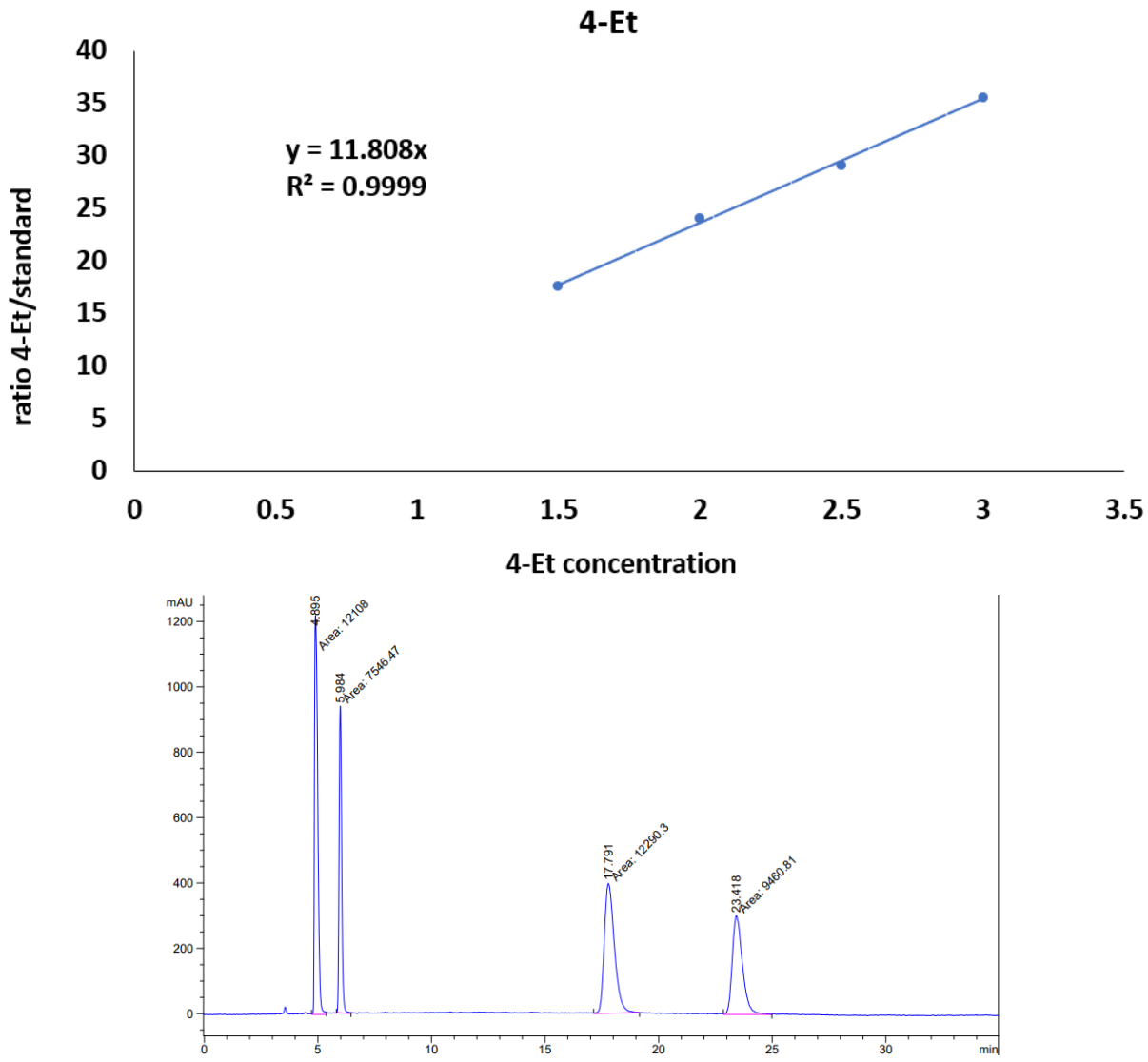

Figure S8: Standard curve and chiral HPLC trace of **4-Et.** t_R 4.895 min is AcOEt, t_R 5.984 min is Anisole and t_R 17.791-23.418 min is **4-Et**.

§

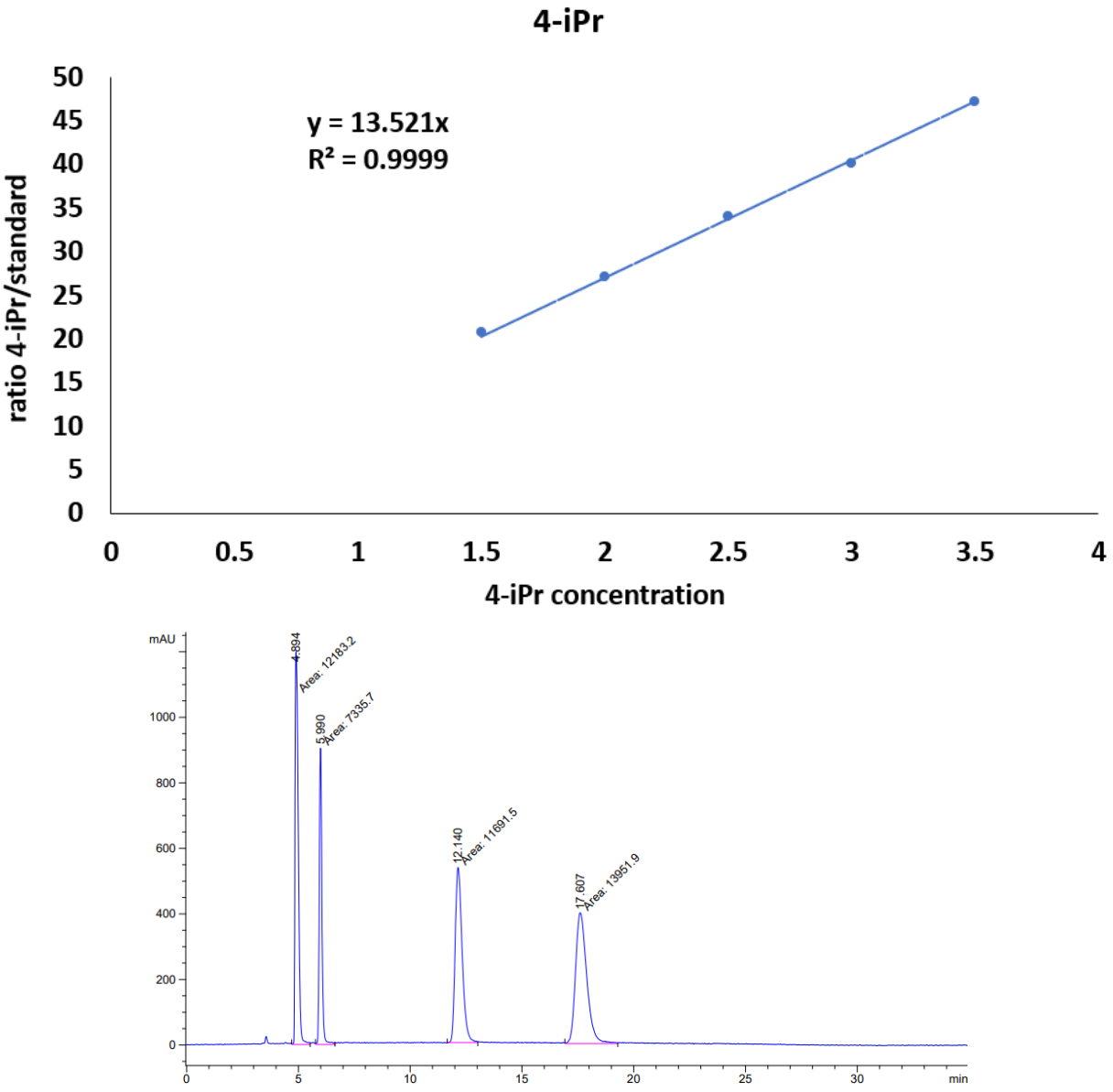

Figure S9: Standard curve and chiral HPLC trace of **4-iPr.** t_R 4.894 min is AcOEt, t_R 5.990 min is Anisole and t_R 12.140-17.607 min is **4-iPr**.

§

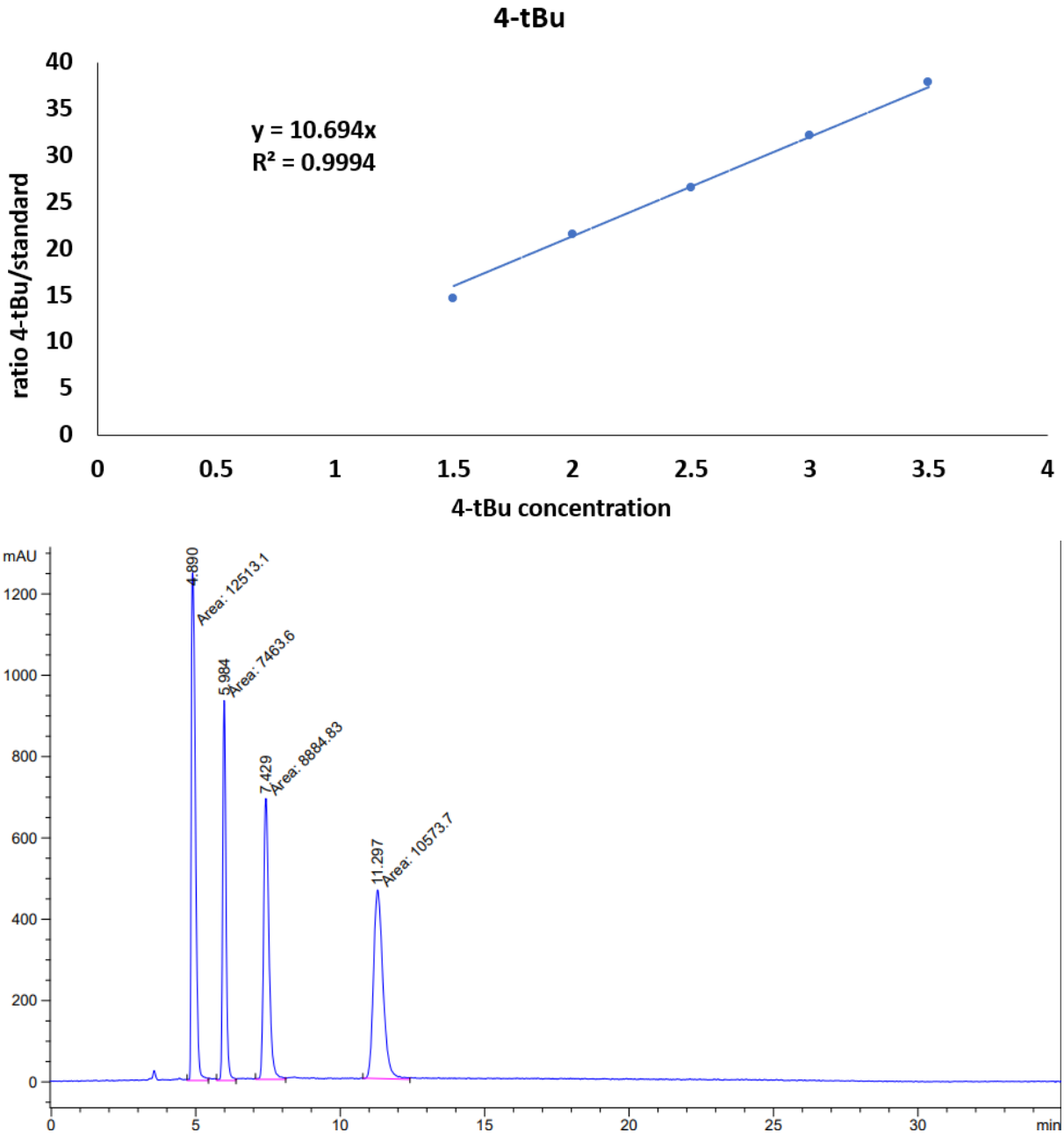

Figure S10: Standard curve and chiral HPLC trace of **4-tBu.** t_R 4.89 min is AcOEt, t_R 5.984 min is Anisole and t_R 7.429-11.297 min is **4-tBu**.

§

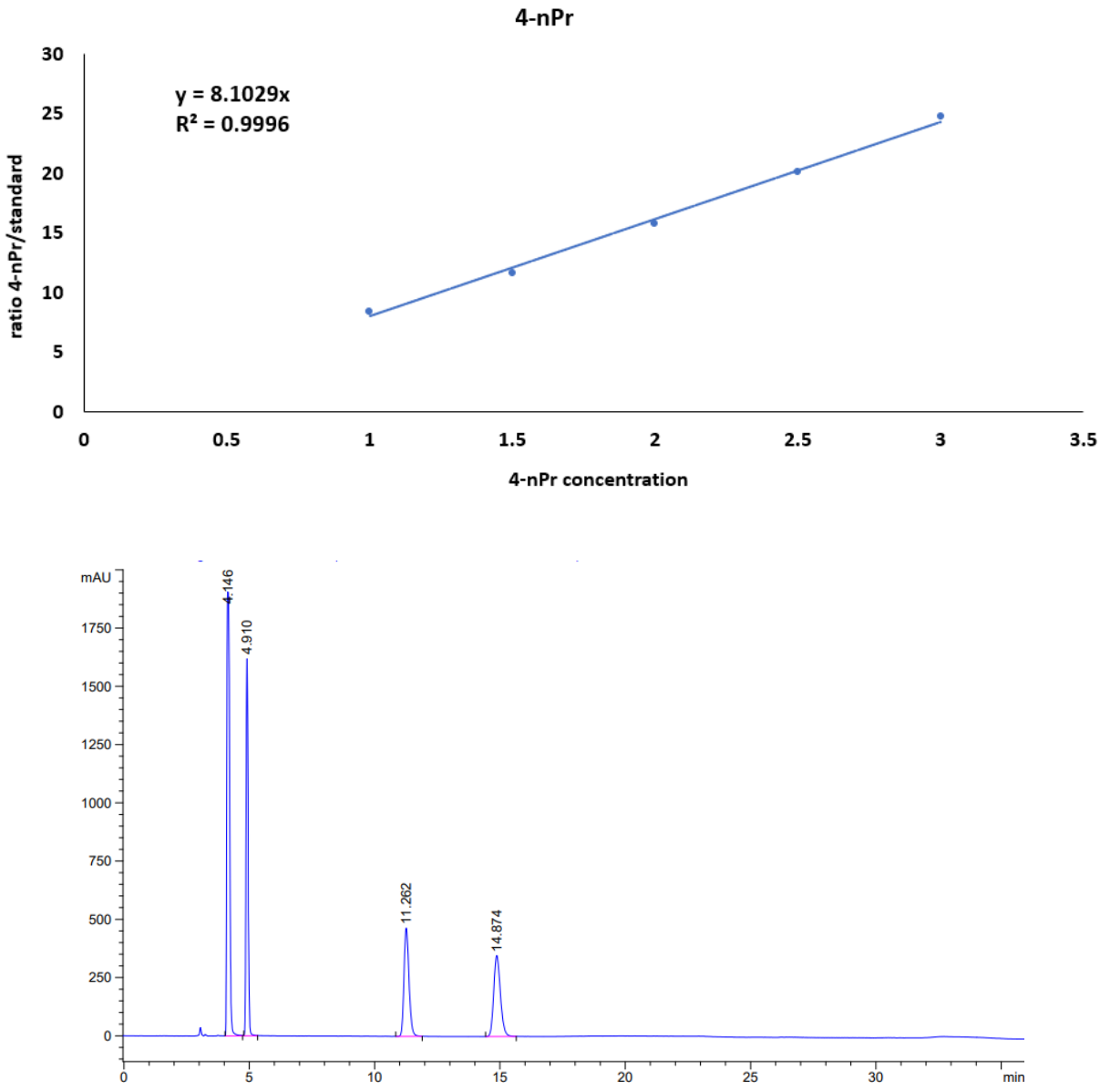

Figure S11: Standard curve and chiral HPLC trace of **4-nPr.** t_R 4.146 min is AcOEt, t_R 4.910min is Anisole and t_R 11.262-14.874 min is **4-nPr**.

§

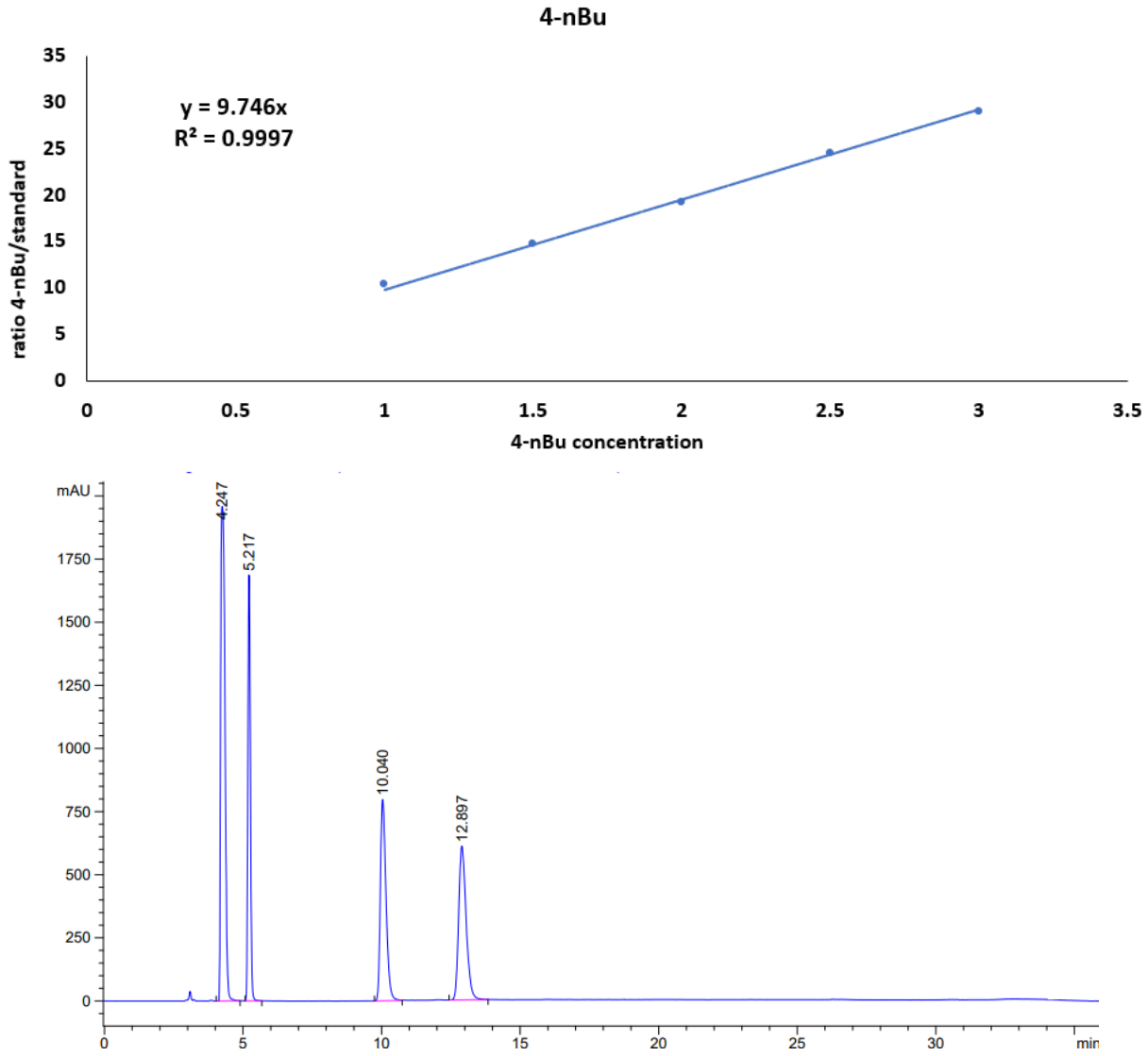

Figure S12: Standard curve and chiral HPLC trace of **4-nBu.** t_R 4.247 min is AcOEt, t_R 5.217 min is Anisole and t_R 10.040-12.897 min is **4-nBu**.

Preliminary results

A quick experiment was performed to determine either DMSO or DMF was the most suitable solvent to work in the presence of protein even though we know that DMSO perform best when used with bare catalyst.

Experience catalyzed by **Ru-biot**:

§

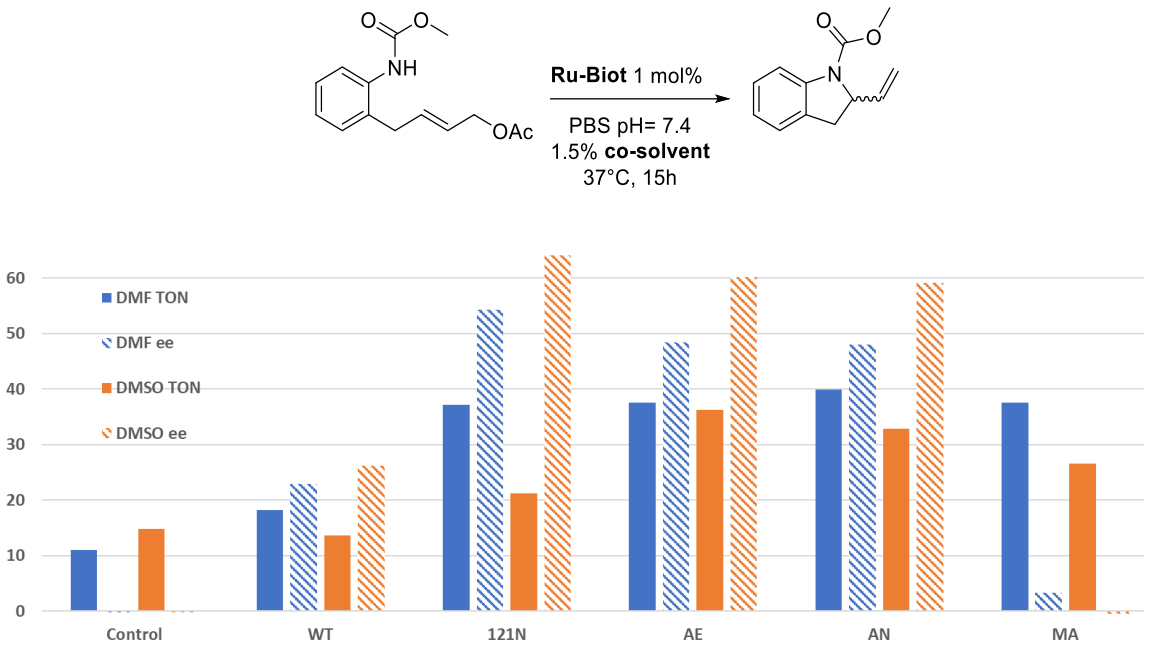

Figure S13: Preliminary result of **Ru-Biot**-ArM catalysis in DMF or DMSO.

Experience catalyzed by **Ru-biot-HQ**:

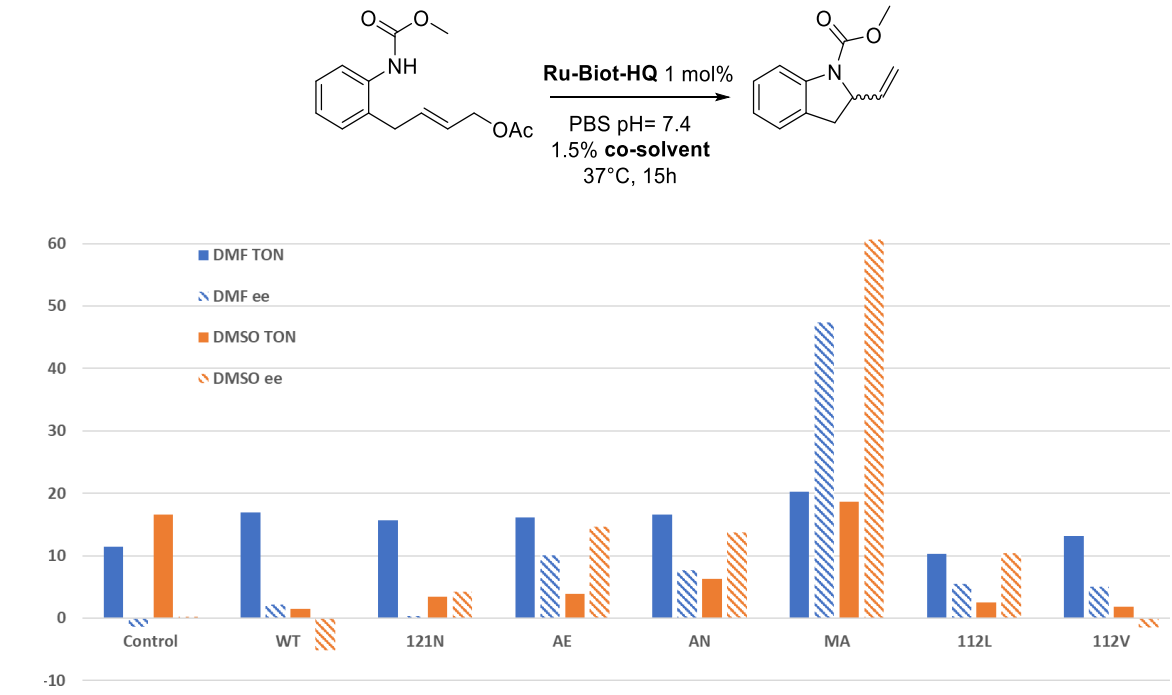

Figure S14: Preliminary result of **Ru-Biot-HQ** ArM catalysis in DMF or DMSO.

III] NMR spectrum and HRMS data:

§

1-Me

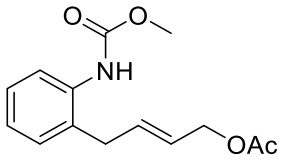

Exact Mass: 263,12
m/z: 263.12 (100.0%), 264.12 (15.5%), 265.12 (2.0%)

§

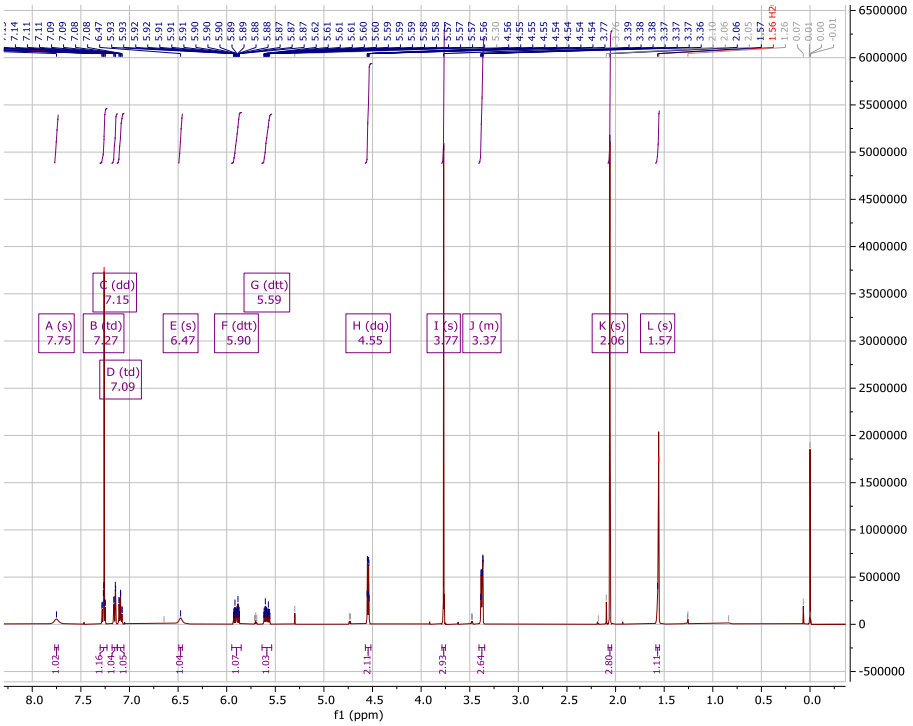
A (s) 7.75
B (td) 7.27
C (dd) 7.15
D (td) 7.09
E (s) 6.47
F (dtt) 5.90
G (dtt) 5.59
H (dq) 4.55
I (s) 3.77
J (m) 3.37
K (s) 2.06
L (s) 1.57
f1 (ppm)

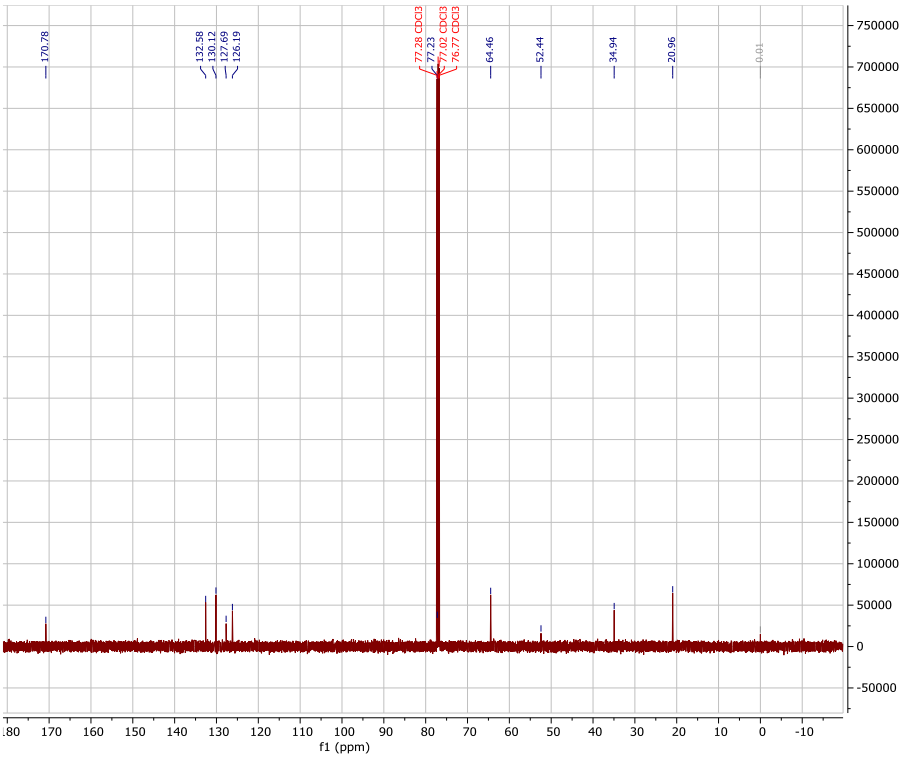
170.78
132.58
130.12
127.69
126.19
77.28 CDCl3
77.23
77.02 CDCl3
76.77 CDCl3
64.46
52.44
34.94
20.96
f1 (ppm)

§

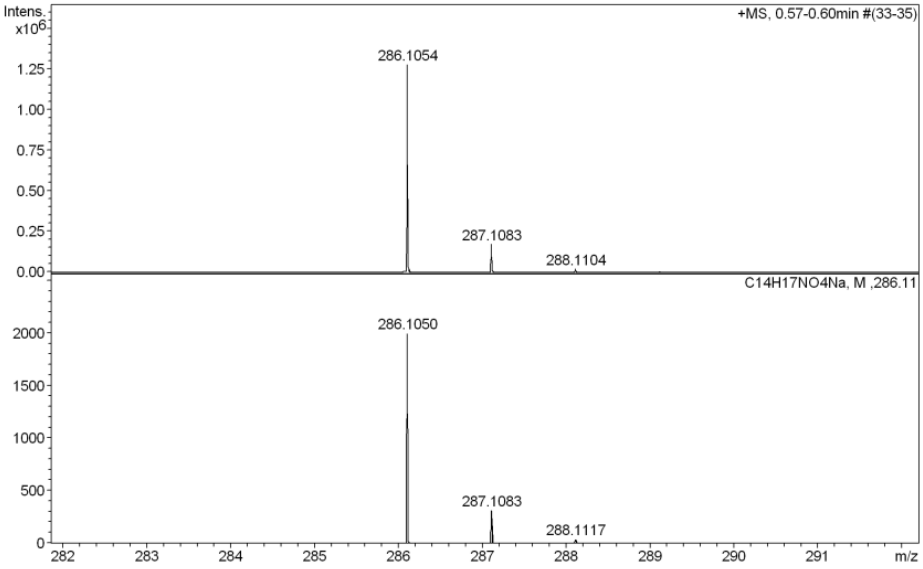

Measured m/z vs. theoretical m/z

Meas. m/z	#	Formula	Score	m/z	err [mDa]	err [ppm]	mSigma	rdb	e⁻ Conf	z
264.1228	1	C 14 H 18 N O 4	100.00	264.1230	0.3	1.0	90.3	6.5	even	1+
286.1054	1	C 14 H 17 N Na O 4	100.00	286.1050	-0.4	-1.4	12.5	6.5	even	
302.0785	1	C 14 H 17 K N O 4	100.00	302.0789	0.4	1.4	6.7	6.5	even	
549.2197	1	C 28 H 34 N 2 Na O 8	100.00	549.2207	1.1	1.9	34.2	12.5	even	

1-Et

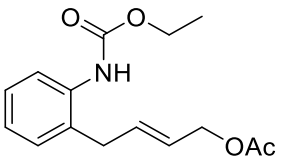

Exact Mass: 277,13
m/z: 277.13 (100.0%), 278.13 (16.6%), 279.14 (2.1%)

§

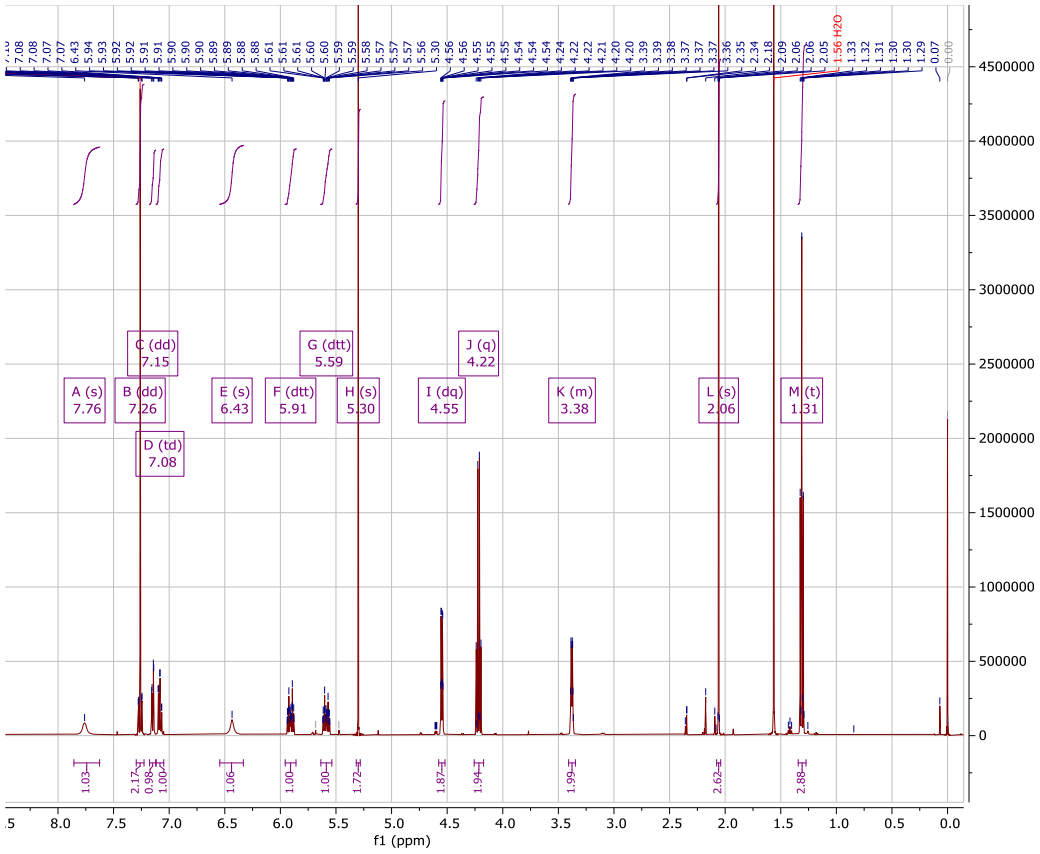
A (s) 7.76
B (dd) 7.26
C (dd) 7.15
D (td) 7.08
E (s) 6.43
F (dtt) 5.91
G (dtt) 5.59
H (s) 5.30
I (dq) 4.55
J (q) 4.22
K (m) 3.38
L (s) 2.06
M (t) 1.31
f1 (ppm)

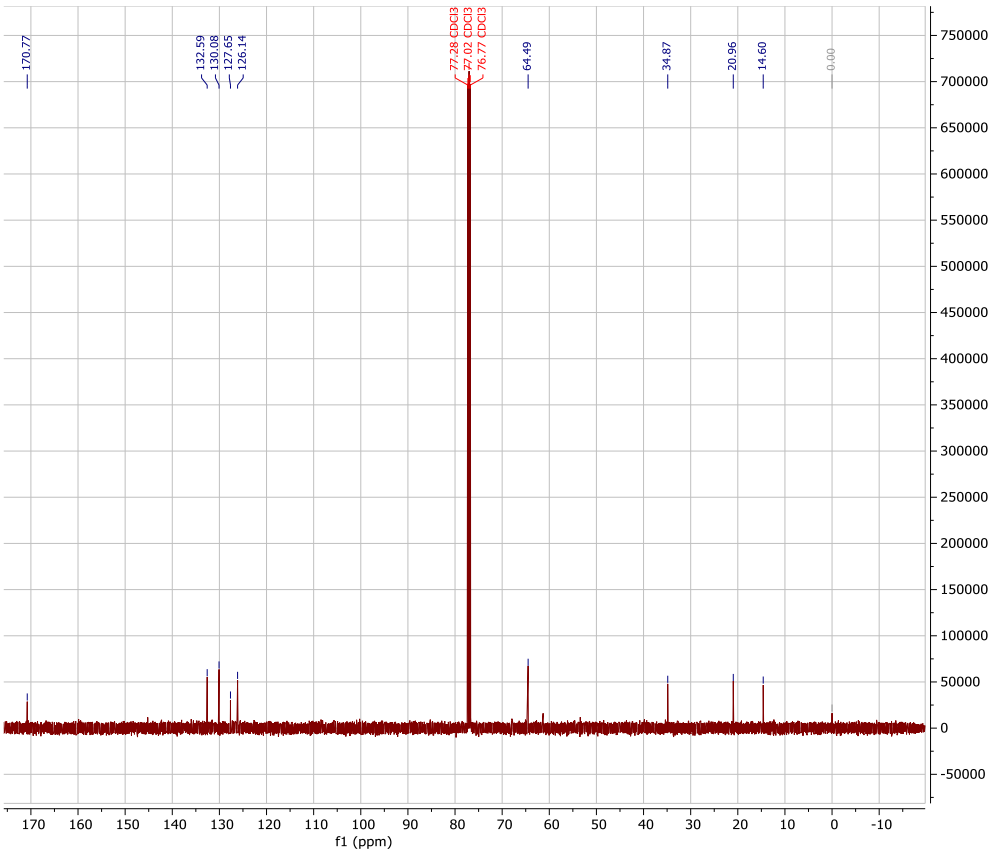
170.77
132.59
130.08
127.65
126.14
77.28 CDCl3
77.02 CDCl3
76.77 CDCl3
64.49
34.87
20.96
14.60
f1 (ppm)

§

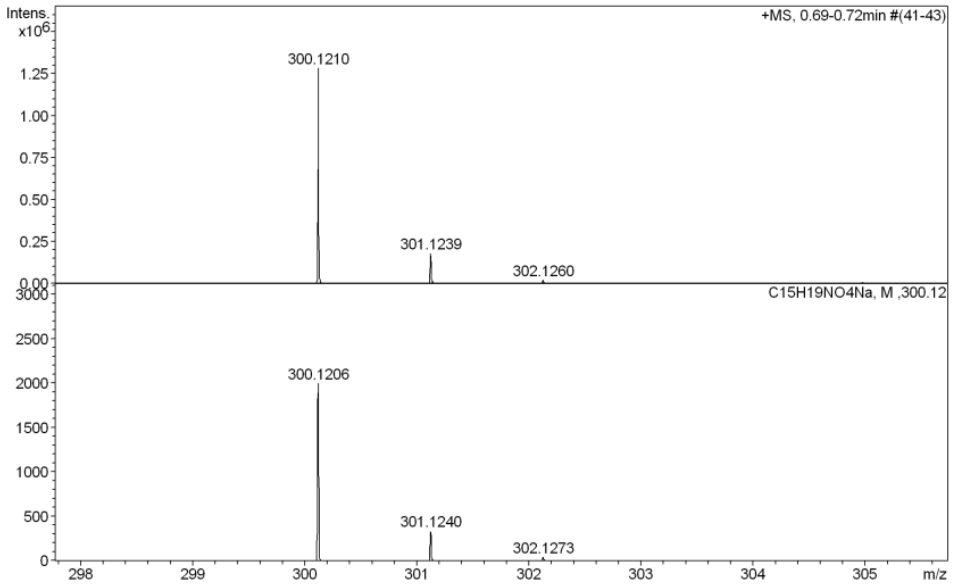

Measured m/z vs. theoretical m/z

Meas. m/z	#	Formula	Score	m/z	err [mDa]	err [ppm]	mSigma	rdb	e⁻ Conf	z
278.1384	1	C 15 H 20 N O 4	100.00	278.1387	0.2	0.9	96.6	6.5	even	1+
300.1210	1	C 15 H 19 N Na O 4	100.00	300.1206	-0.4	-1.2	14.8	6.5	even	
316.0942	1	C 15 H 19 K N O 4	100.00	316.0946	0.3	1.0	11.4	6.5	even	
577.2510	1	C 30 H 38 N 2 Na O 8	100.00	577.2520	1.0	1.7	36.1	12.5	even	

1-iPr

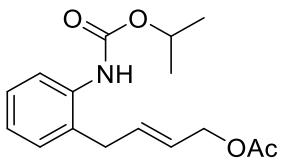

Exact Mass: 291,15
m/z: 291.15 (100.0%), 292.15 (17.7%), 293.15 (2.3%)

§

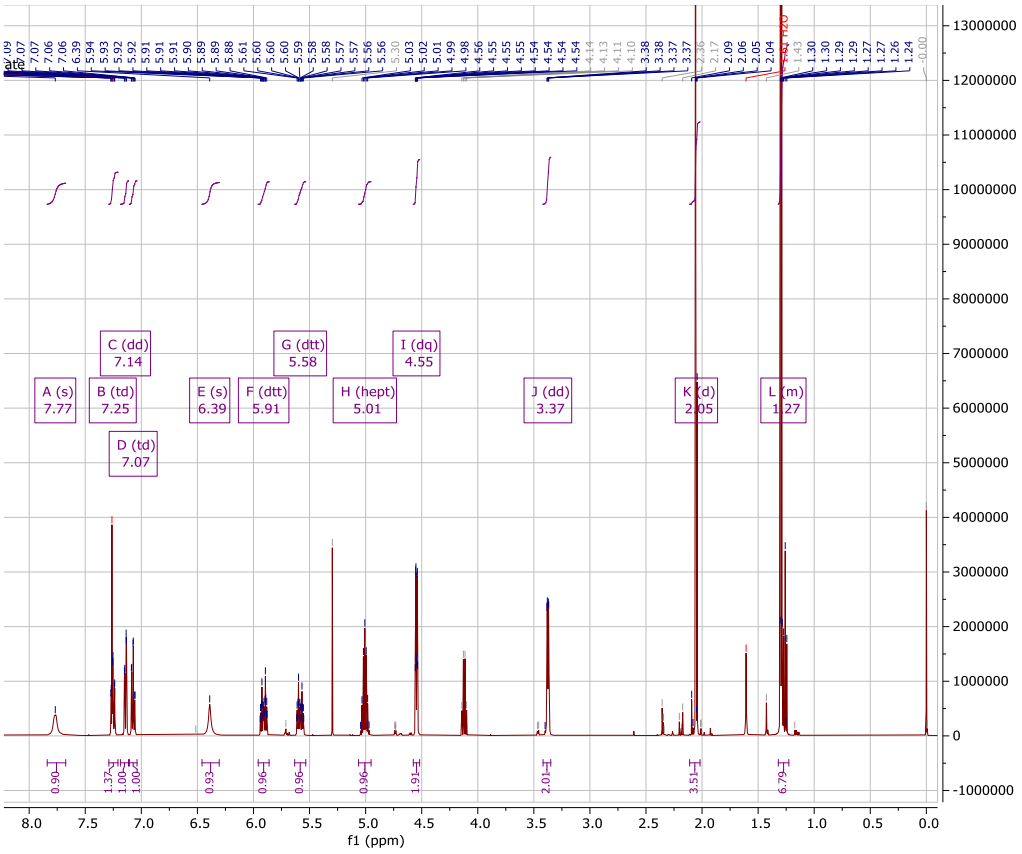
A (s) 7.77
B (td) 7.25
C (dd) 7.14
D (td) 7.07
E (s) 6.39
F (dtt) 5.91
G (dtt) 5.58
H (hept) 5.01
I (dq) 4.55
J (dd) 3.37
K (d) 2.05
L (m) 1.27
f1 (ppm)

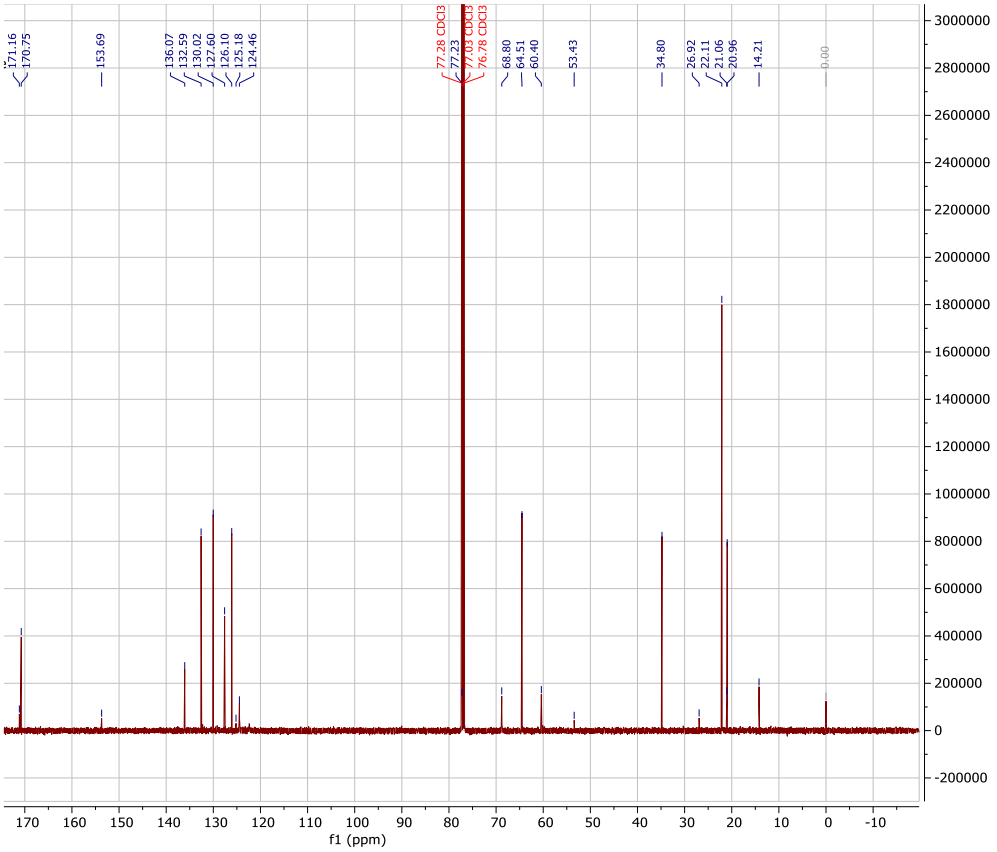
171.16
170.75
153.69
136.07
132.59
130.02
127.60
126.10
125.18
124.46
77.28 CDCl3
77.23
77.03 CDCl3
76.78 CDCl3
68.80
64.51
60.40
53.43
34.80
26.92
22.11
21.06
20.96
14.21
f1 (ppm)

§

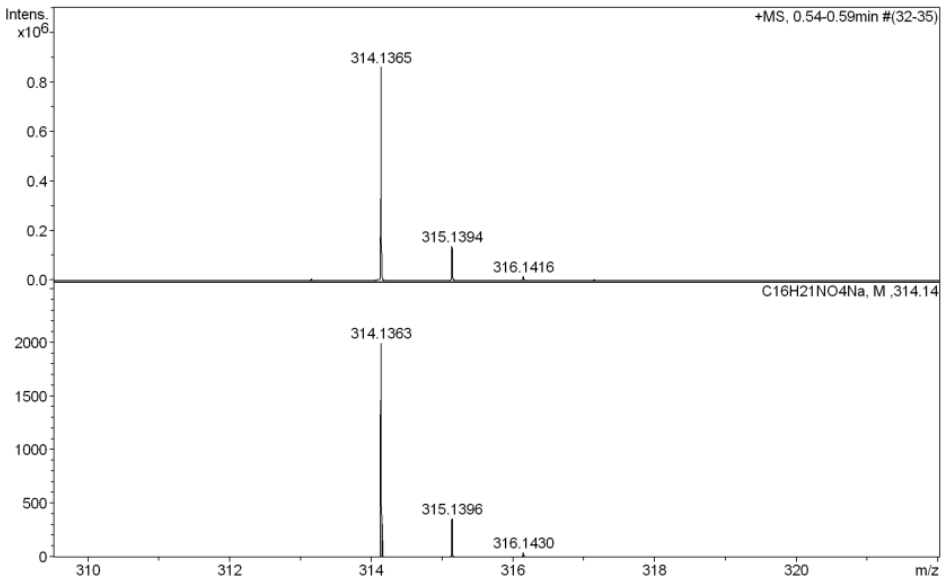

Measured m/z vs. theoretical m/z

Meas. m/z	#	Formula	Score	m/z	err [mDa]	err [ppm]	mSigma	rdb	e⁻ Conf	z
314.1365	1	C 16 H 21 N Na O 4	100.00	314.1363	-0.2	-0.8	9.3	6.5	even	1+
330.1099	1	C 16 H 21 K N O 4	100.00	330.1102	0.3	1.0	7.6	6.5	even	
605.2825	1	C 32 H 42 N 2 Na O 8	100.00	605.2833	0.9	1.4	14.7	12.5	even	

1-tBu

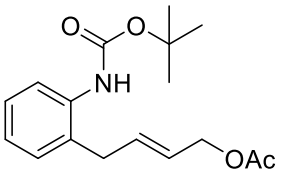

Exact Mass: 305,16
m/z: 305.16 (100.0%), 306.17 (18.8%), 307.17 (2.5%)

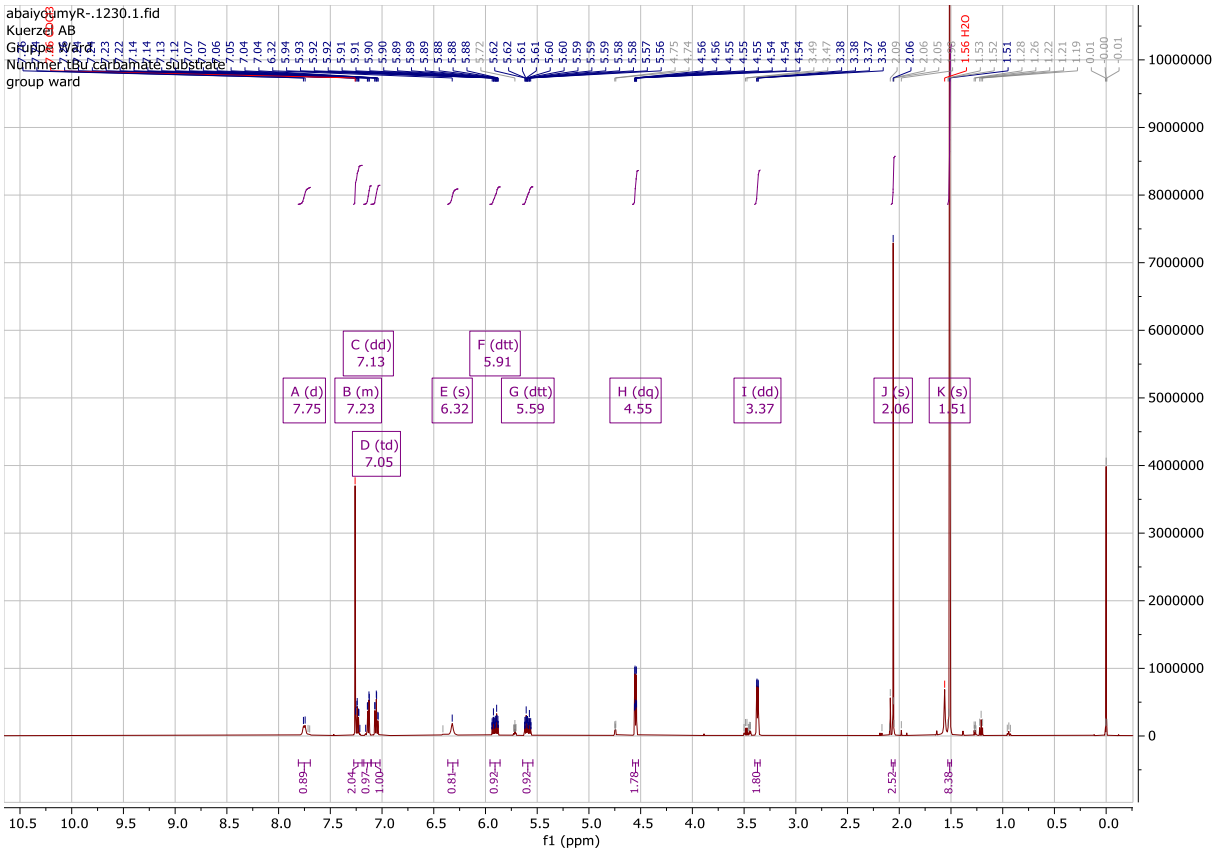
abaiyoumyR-.1230.1.fid
Kuerzel AB
Gruppe Ward,
Nummer tBu carbamate substrate
group ward
A (d) 7.75
B (m) 7.23
C (dd) 7.13
D (td) 7.05
E (s) 6.32
F (dtt) 5.91
G (dtt) 5.59
H (dq) 4.55
I (dd) 3.37
J (s) 2.06
K (s) 1.51
1.56 H2O
f1 (ppm)

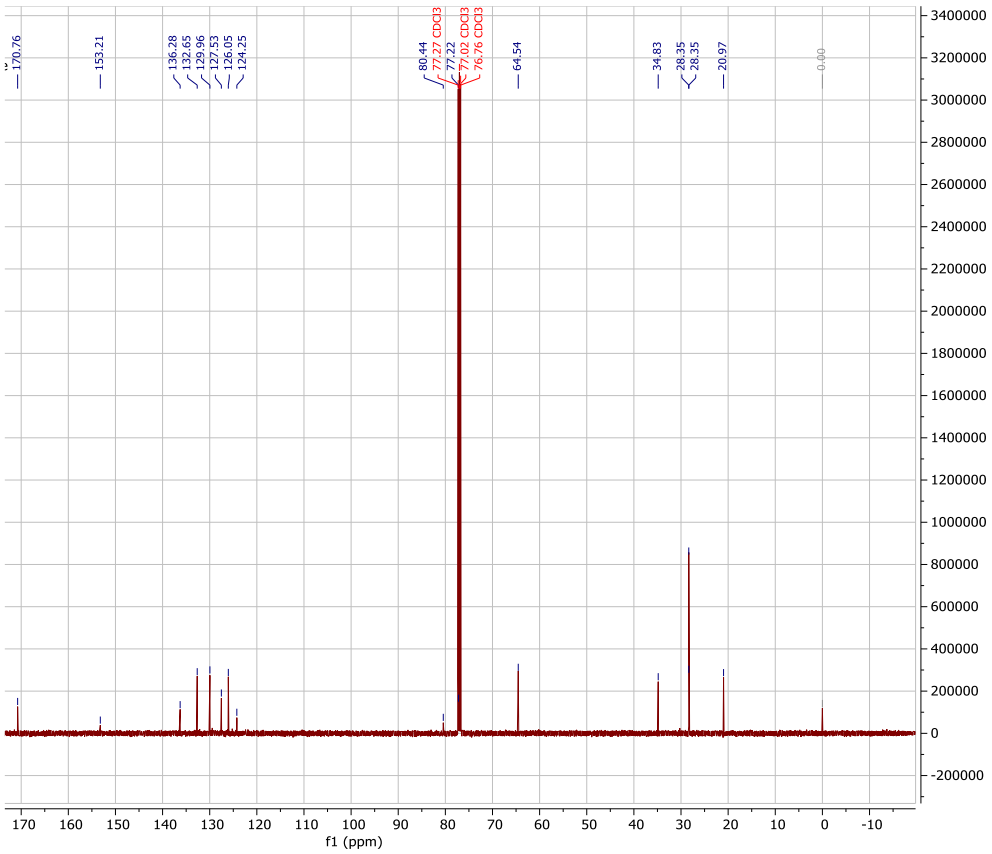
170.76
153.21
136.28
132.65
129.96
127.53
126.05
124.25
80.44
77.27 CDCl3
77.22
77.02 CDCl3
76.76 CDCl3
64.54
34.83
28.35
28.35
20.97
f1 (ppm)

§

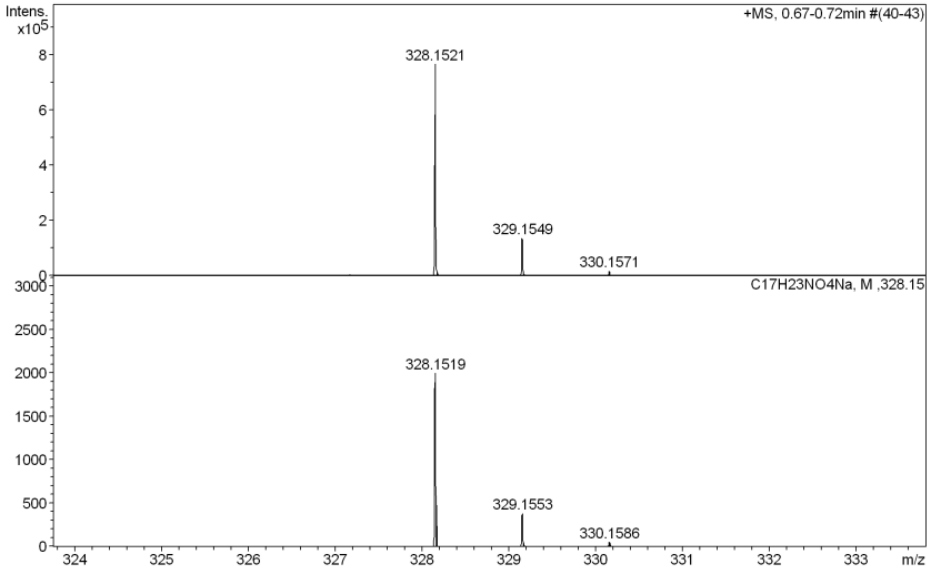

Measured m/z vs. theoretical m/z

Meas. m/z	#	Formula	Score	m/z	err [mDa]	err [ppm]	mSigma	rdb	e⁻ Conf	z
328.1521	1	C 17 H 23 N Na O 4	100.00	328.1519	-0.1	-0.4	5.3	6.5	even	1+
344.1253	1	C 17 H 23 K N O 4	100.00	344.1259	0.6	1.8	26.2	6.5	even	
633.3135	1	C 34 H 46 N 2 Na O 8	100.00	633.3146	1.1	1.8	15.2	12.5	even	

1-nPr

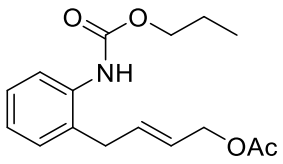

Exact Mass: 291,15
m/z: 291.15 (100.0%), 292.15 (17.7%), 293.15 (2.3%)

§

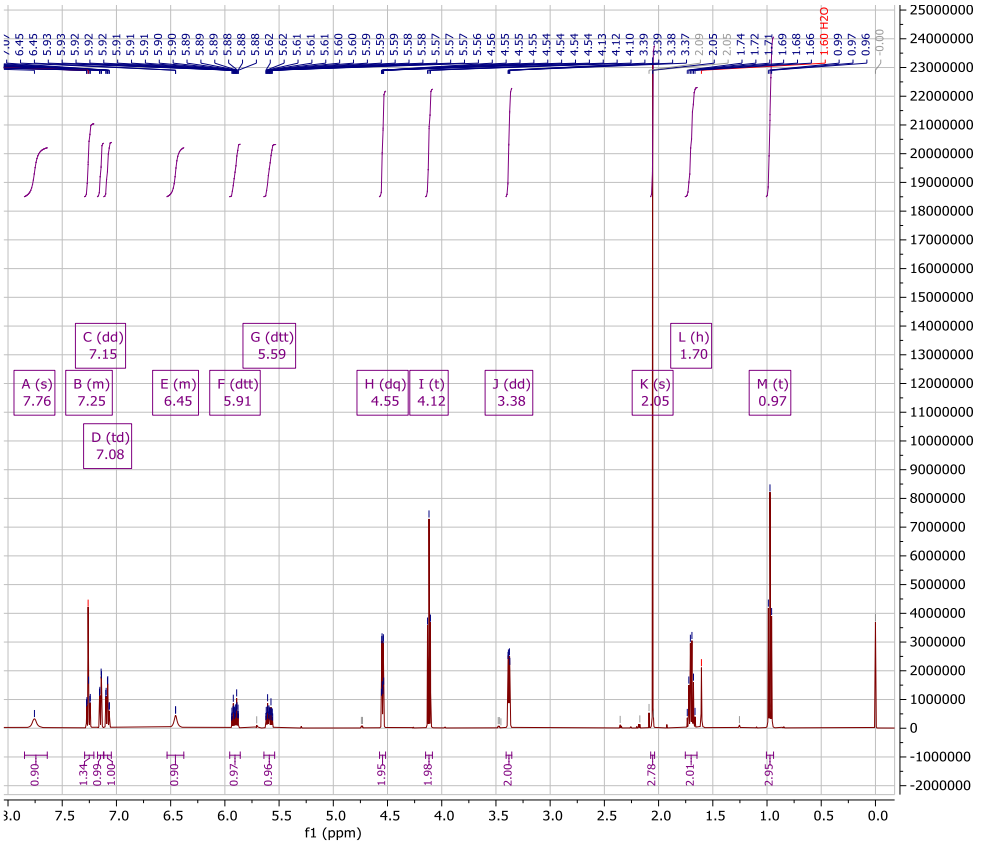
A (s) 7.76
B (m) 7.25
C (dd) 7.15
D (td) 7.08
E (m) 6.45
F (dtt) 5.91
G (dtt) 5.59
H (dq) 4.55
I (t) 4.12
J (dd) 3.38
K (s) 2.05
L (h) 1.70
M (t) 0.97
f1 (ppm)

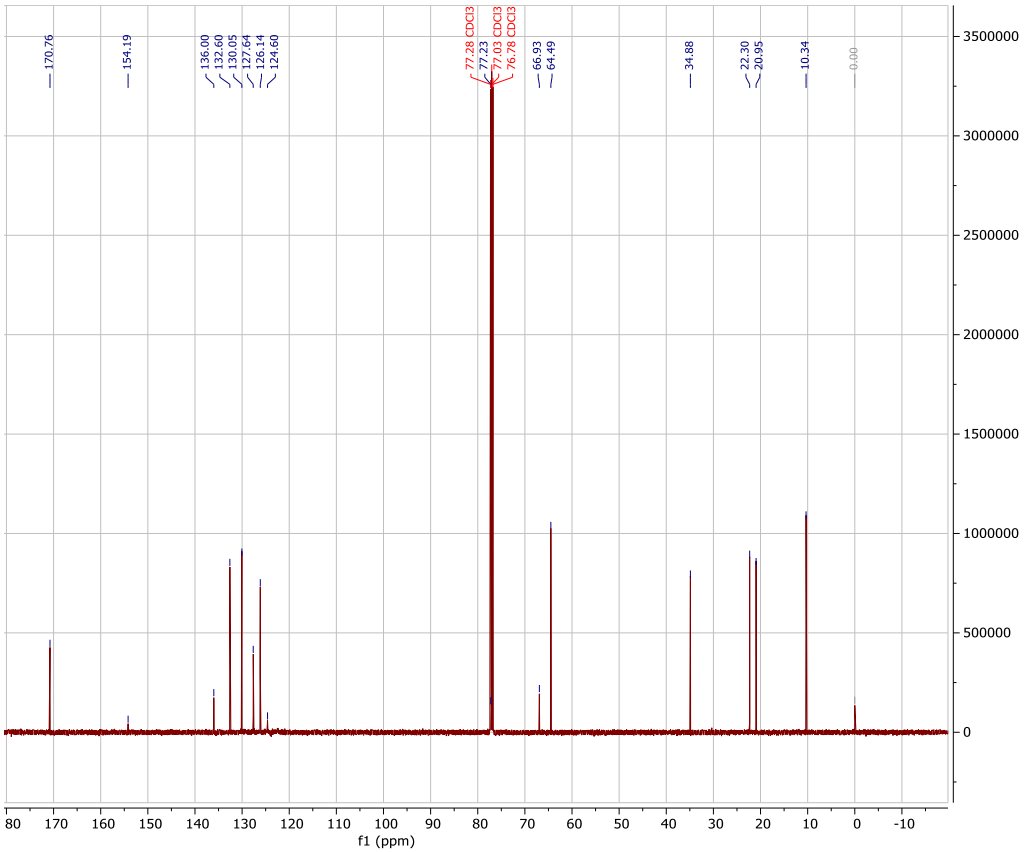
170.76
154.19
136.00
132.60
130.05
127.64
126.14
124.60
77.28 CDCl3
77.23
77.03 CDCl3
76.78 CDCl3
66.93
64.49
34.88
22.30
20.95
10.34
f1 (ppm)

§

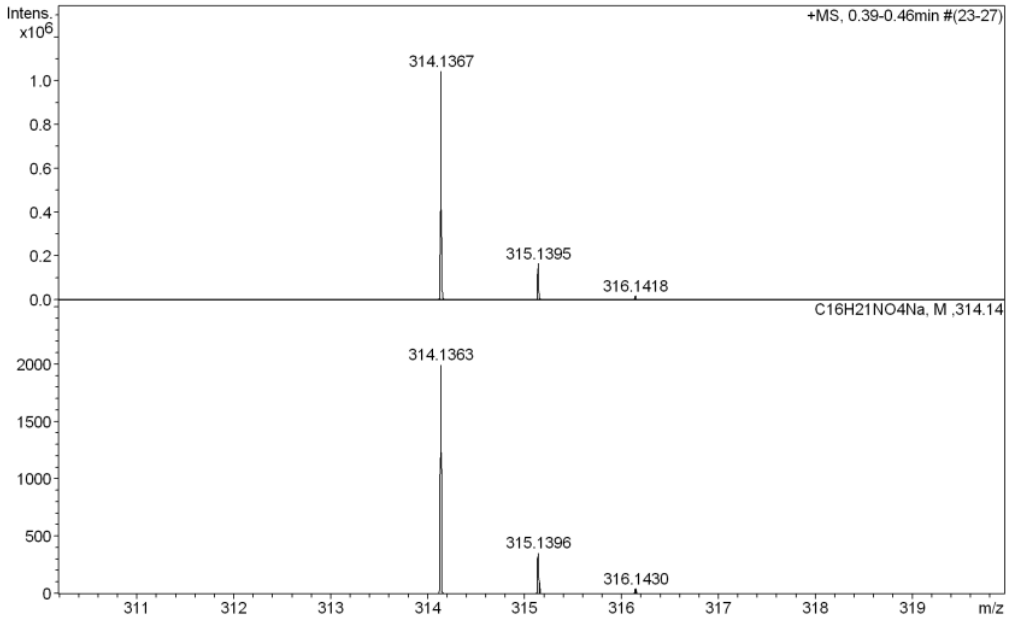

Measured m/z vs. theoretical m/z

Meas. m/z	#	Formula	Score	m/z	err [mDa]	err [ppm]	mSigma	rdb	e⁻ Conf	z
314.1367	1	C 16 H 21 N Na O 4	100.00	314.1363	-0.4	-1.2	10.3	6.5	even	1+
330.1097	1	C 16 H 21 K N O 4	100.00	330.1102	0.5	1.4	7.5	6.5	even	
605.2822	1	C 32 H 42 N 2 Na O 8	100.00	605.2833	1.1	1.8	11.9	12.5	even	

1-nBu

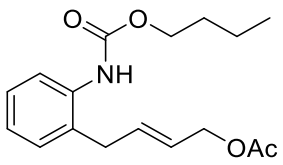

Exact Mass: 305,16
m/z: 305.16 (100.0%), 306.17 (18.8%), 307.17 (2.5%)

§

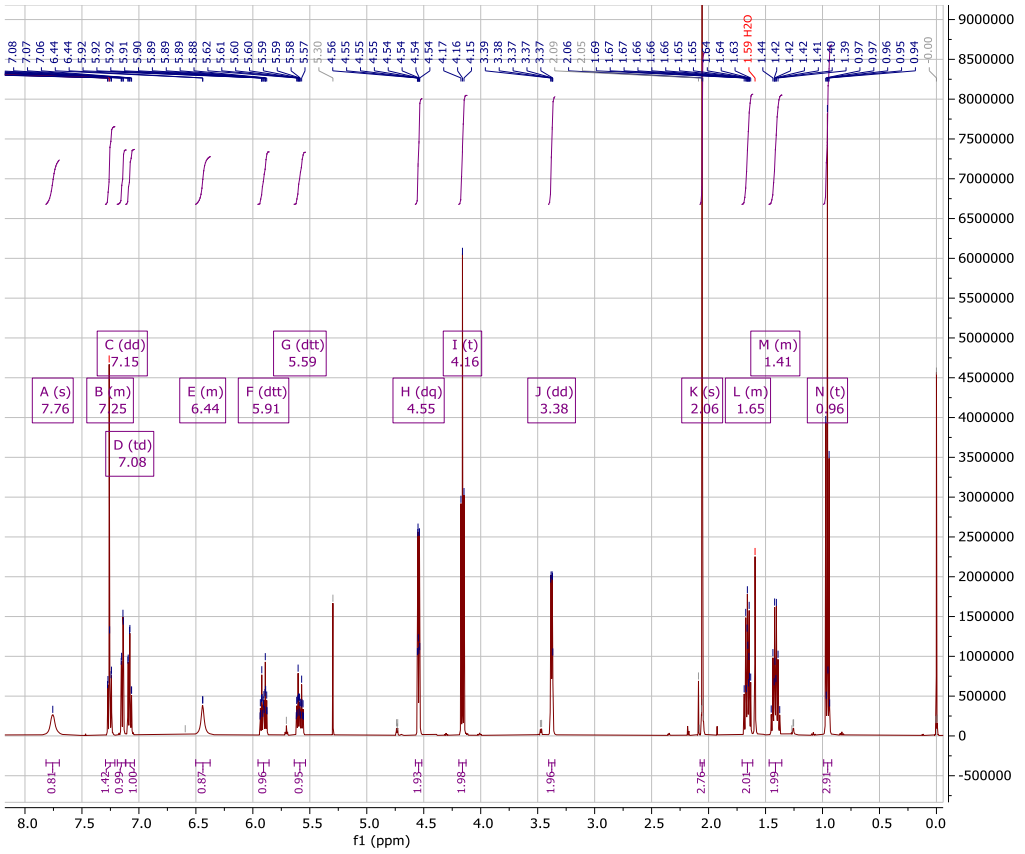
A (s) 7.76
B (m) 7.25
C (dd) 7.15
D (td) 7.08
E (m) 6.44
F (dtt) 5.91
G (dtt) 5.59
H (dq) 4.55
I (t) 4.16
J (dd) 3.38
K (s) 2.06
L (m) 1.65
M (m) 1.41
N (t) 0.96
H2O
f1 (ppm)

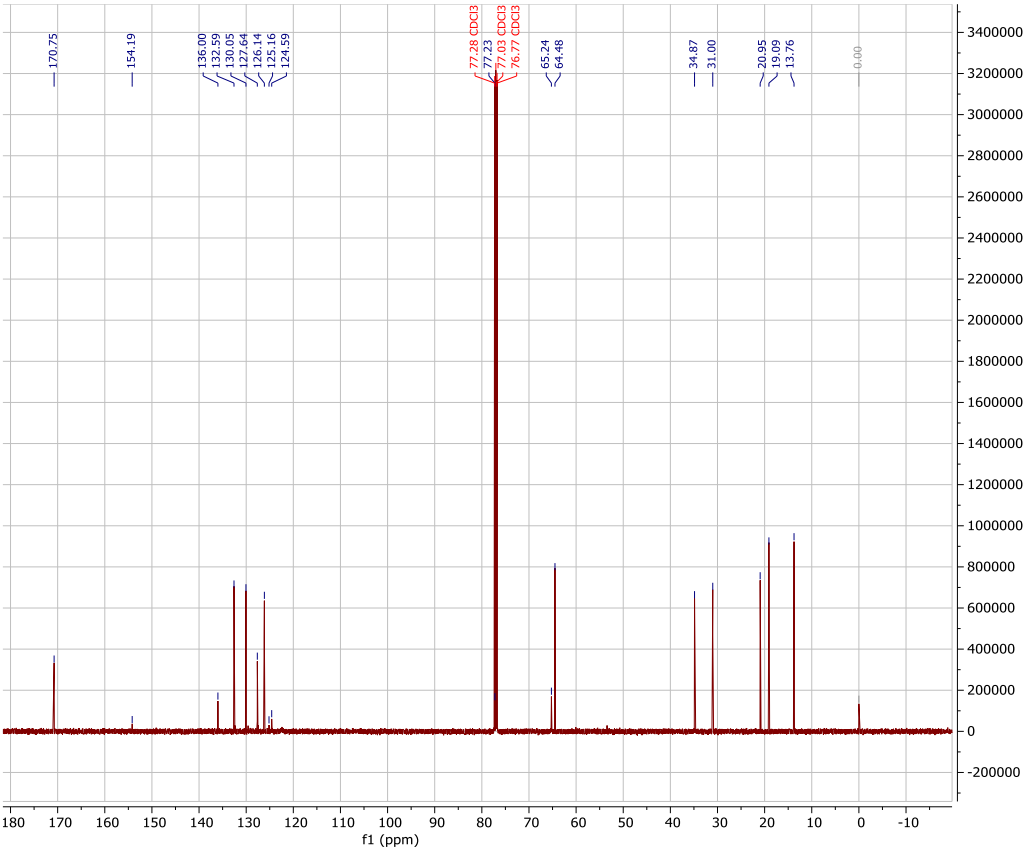
170.75
154.19
136.00
132.59
130.05
127.64
126.14
125.16
124.59
77.28 CDCl3
77.23
77.03 CDCl3
76.77 CDCl3
65.24
64.48
34.87
31.00
20.95
19.09
13.76
f1 (ppm)

§

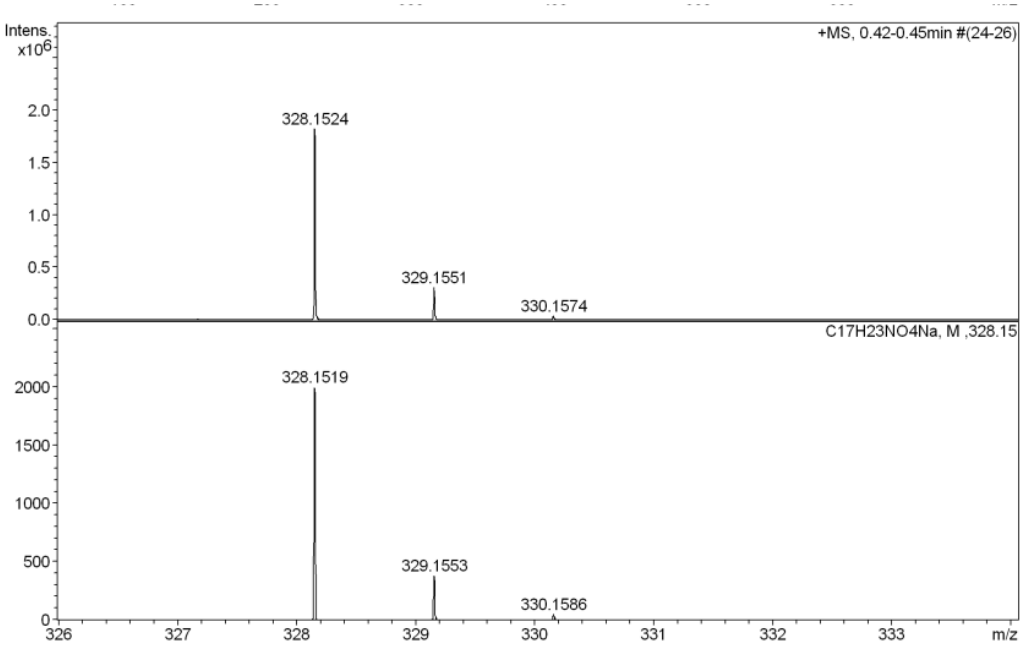

Measured m/z vs. theoretical m/z

Meas. m/z	#	Formula	Score	m/z	err [mDa]	err [ppm]	mSigma	rdb	e⁻ Conf	z
306.1695	1	C 17 H 24 N O 4	100.00	306.1700	0.5	1.6	23.4	6.5	even	1+
328.1524	1	C 17 H 23 N Na O 4	100.00	328.1519	-0.5	-1.4	11.0	6.5	even	
344.1253	1	C 17 H 23 K N O 4	100.00	344.1259	0.6	1.7	14.7	6.5	even	
633.3138	1	C 34 H 46 N 2 Na O 8	100.00	633.3146	0.8	1.3	9.0	12.5	even	

1a

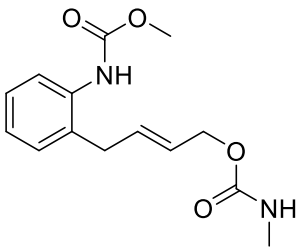

m/z: 278.13 (100.0%), 279.13 (15.5%), 280.13 (2.0%)

§

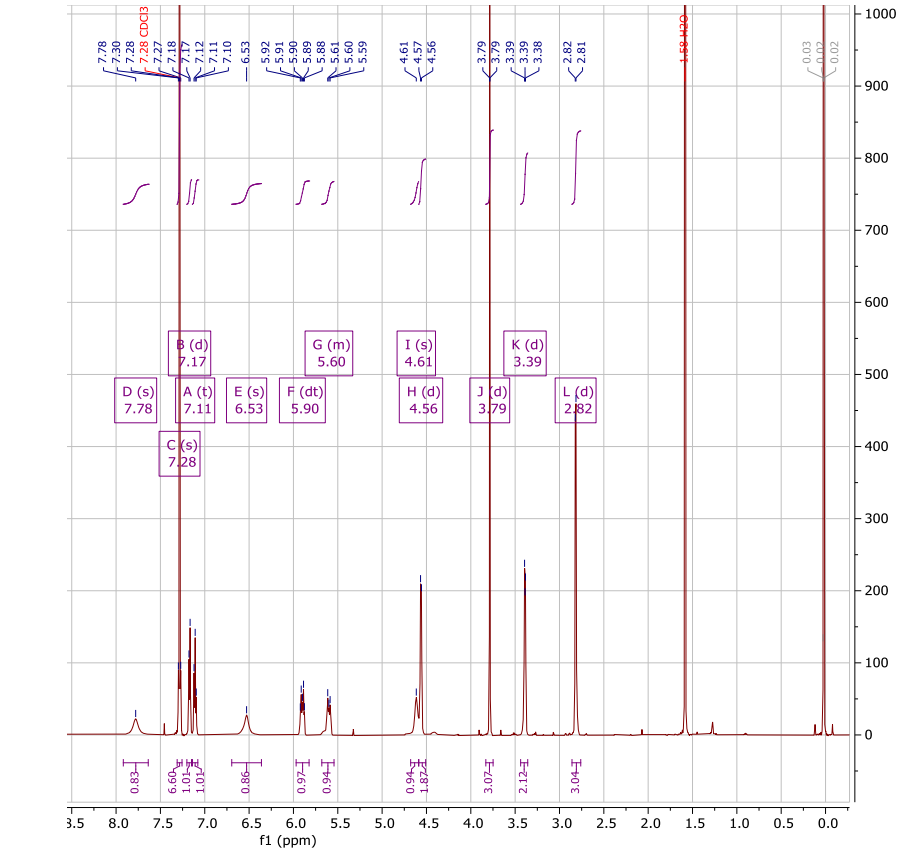
7.78
7.30
7.28
7.28 CDCl3
7.27
7.18
7.17
7.12
7.11
7.10
6.53
5.92
5.91
5.90
5.89
5.88
5.61
5.60
5.59
4.61
4.57
4.56
3.79
3.79
3.39
3.39
3.38
2.82
2.81
1.58 H2O
0.03
0.02
0.02
B (d) 7.17
G (m) 5.60
I (s) 4.61
K (d) 3.39
D (s) 7.78
A (t) 7.11
E (s) 6.53
F (dt) 5.90
H (d) 4.56
J (d) 3.79
L (d) 2.82
C (s) 7.28
0.83
6.60
1.01
1.01
0.86
0.97
0.94
0.94
1.82
3.07
2.12
3.04
f1 (ppm)

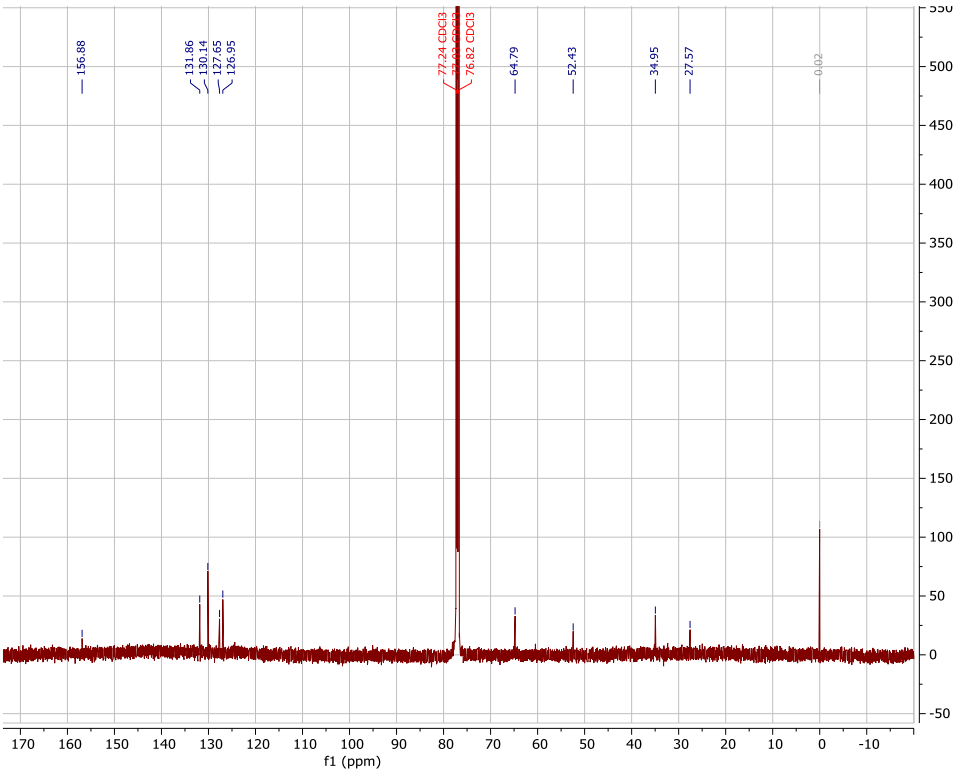
156.88
131.86
130.14
127.65
126.95
77.24 CDCl3
76.82 CDCl3
64.79
52.43
34.95
27.57
0.02
f1 (ppm)

1b

§

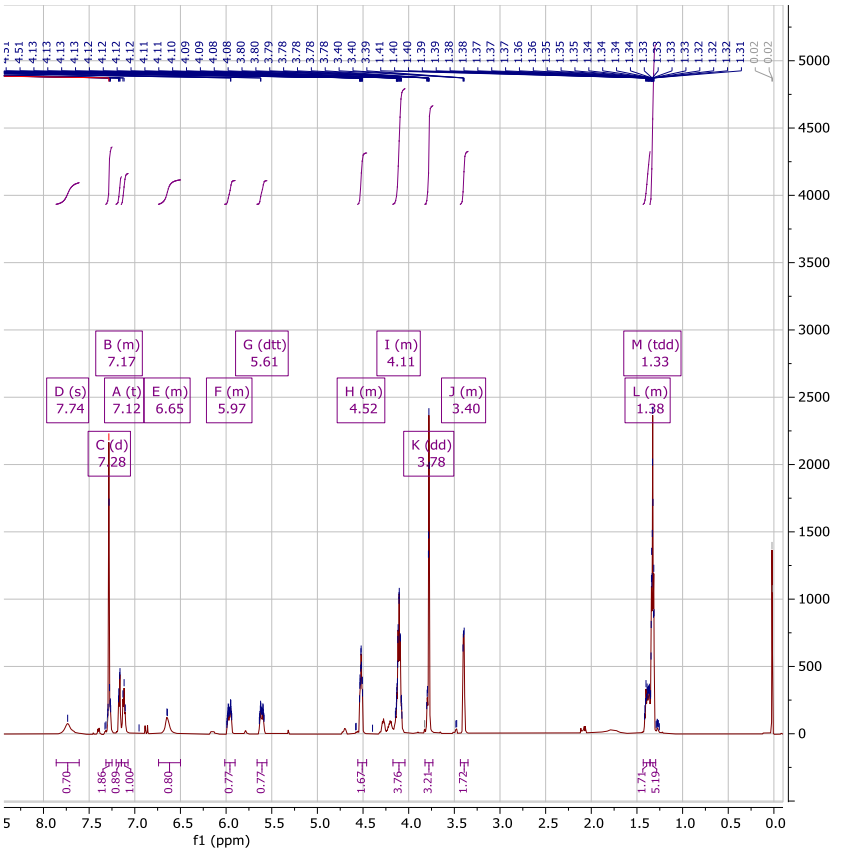
B (m)
7.17
G (dtt)
5.61
I (m)
4.11
M (tdd)
1.33
D (s)
7.74
A (t)
7.12
E (m)
6.65
F (m)
5.97
H (m)
4.52
J (m)
3.40
L (m)
1.38
C (d)
7.28
K (dd)
3.78
f1 (ppm)

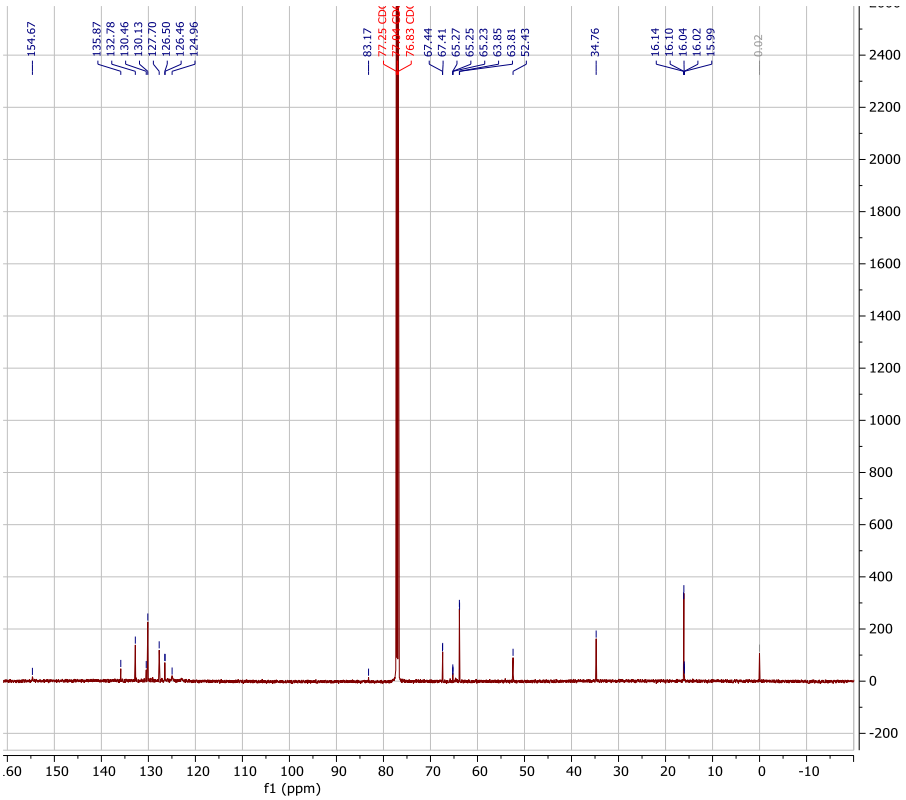
f1 (ppm)

2-Me

§

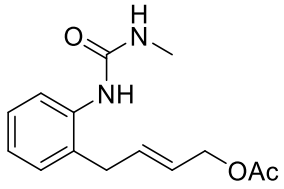

Exact Mass: 262,13
m/z: 262.13 (100.0%), 263.14 (15.5%), 264.14 (1.7%)

§

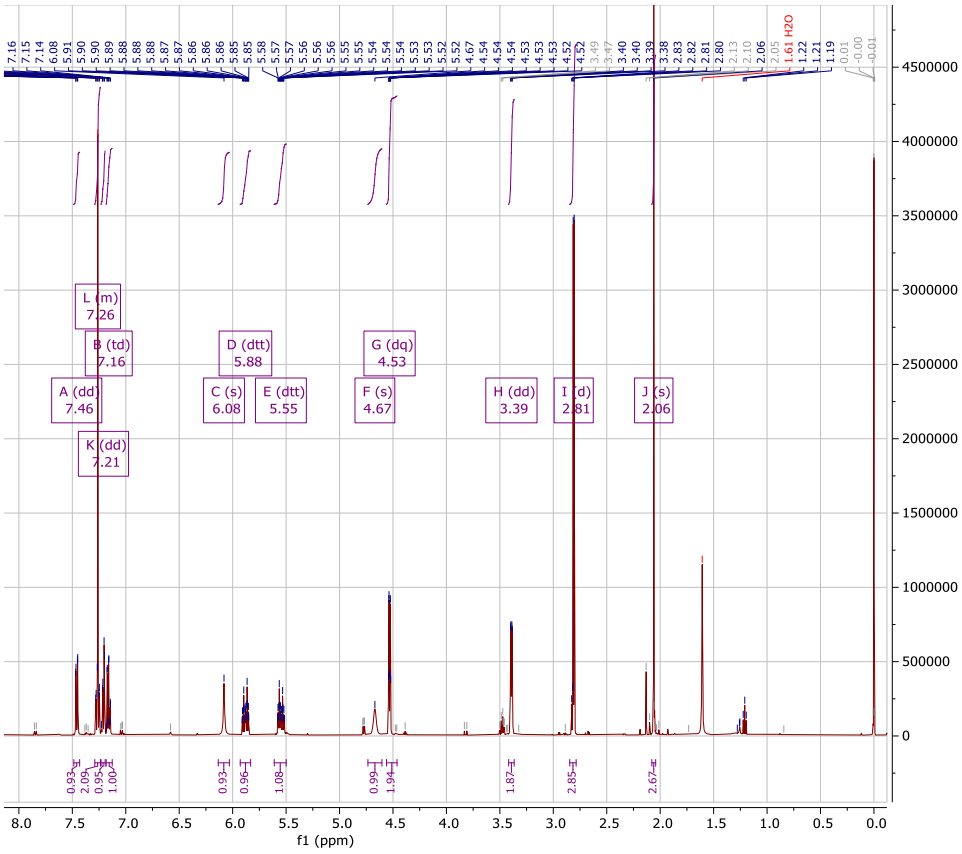
L (m)
7.26
B (td)
7.16
A (dd)
7.46
K (dd)
7.21
D (dtt)
5.88
C (s)
6.08
E (dtt)
5.55
G (dq)
4.53
F (s)
4.67
H (dd)
3.39
I (d)
2.81
J (s)
2.06
f1 (ppm)

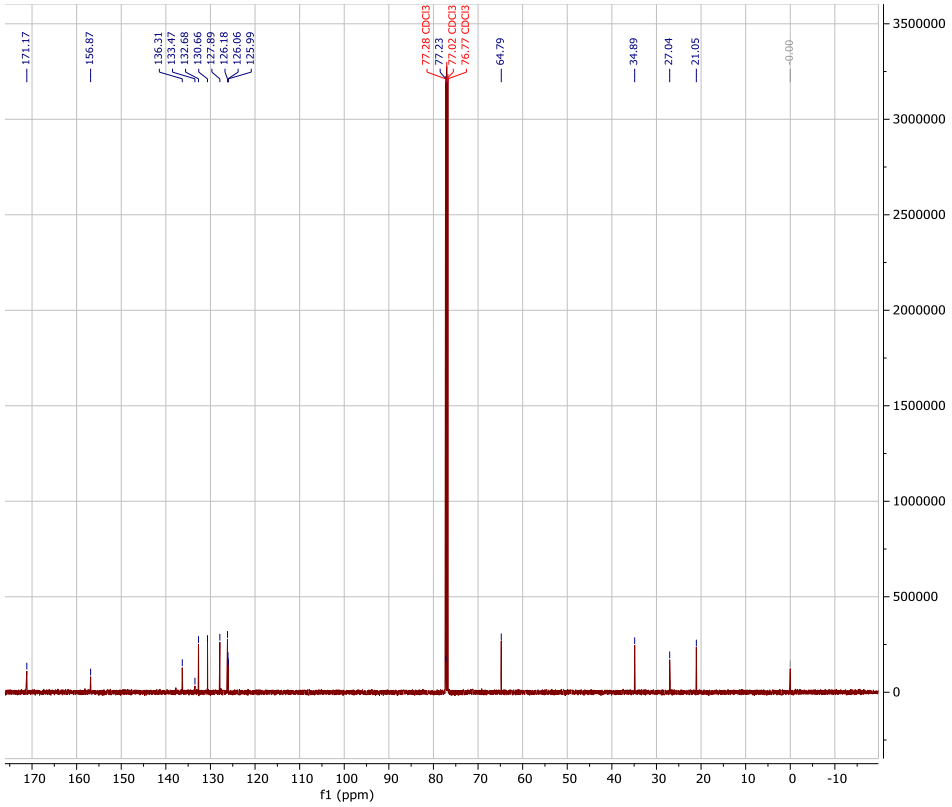
171.17
156.87
136.31
133.47
132.68
130.66
127.89
126.18
126.06
125.99
77.28 CDCl3
77.23
77.02 CDCl3
76.77 CDCl3
64.79
34.89
27.04
21.05
f1 (ppm)

§

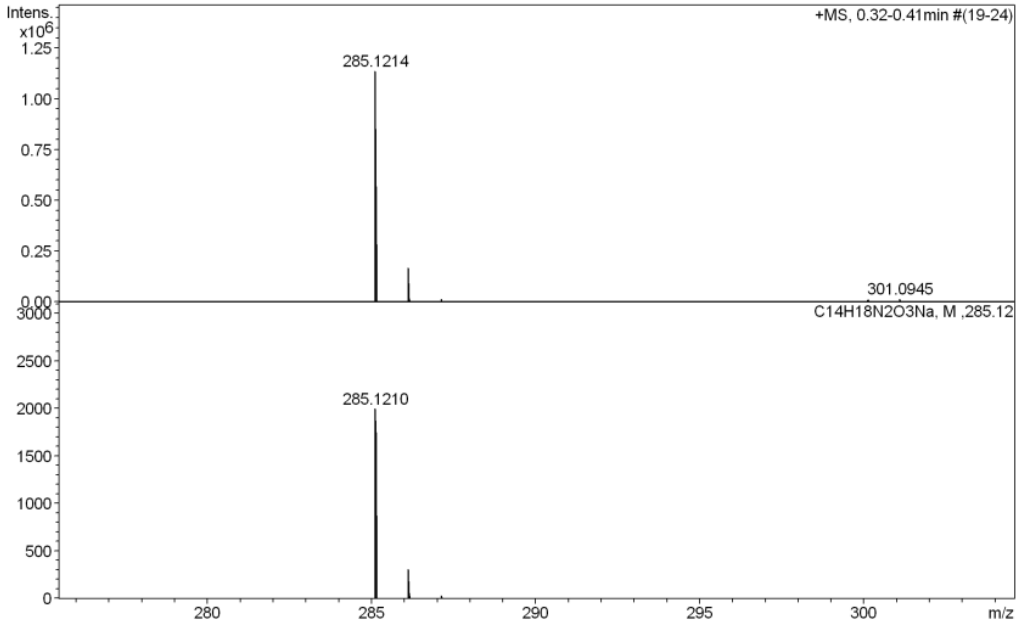

Measured m/z vs. theoretical m/z

Meas. m/z	#	Formula	Score	m/z	err [mDa]	err [ppm]	mSigma	rdb	e⁻ Conf	z
263.1388	1	C 14 H 19 N 2 O 3	100.00	263.1390	0.2	0.8	10.4	6.5	even	1+
285.1214	1	C 14 H 18 N 2 Na O 3	100.00	285.1210	-0.4	-1.5	5.9	6.5	even	
301.0945	1	C 14 H 18 K N 2 O 3	100.00	301.0949	0.4	1.5	11.2	6.5	even	
547.2520	1	C 28 H 36 N 4 Na O 6	100.00	547.2527	0.7	1.3	4.6	12.5	even	

2-Et

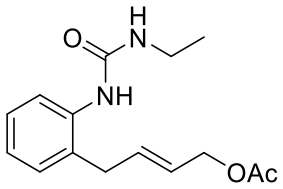

Exact Mass: 276,15
m/z: 276.15 (100.0%), 277.15 (16.6%), 278.15 (2.0%)

§

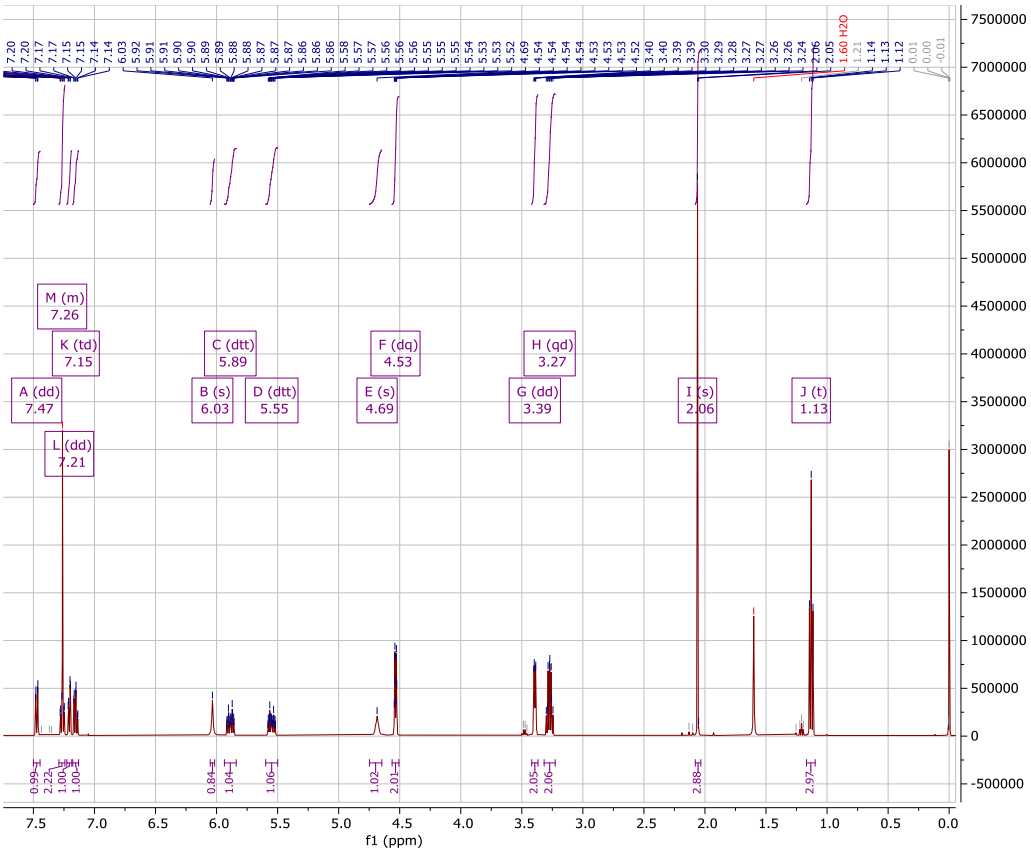
M (m)
7.26
K (td)
7.15
C (dtt)
5.89
F (dq)
4.53
H (qd)
3.27
A (dd)
7.47
B (s)
6.03
D (dtt)
5.55
E (s)
4.69
G (dd)
3.39
I (s)
2.06
J (t)
1.13
L (dd)
7.21
f1 (ppm)

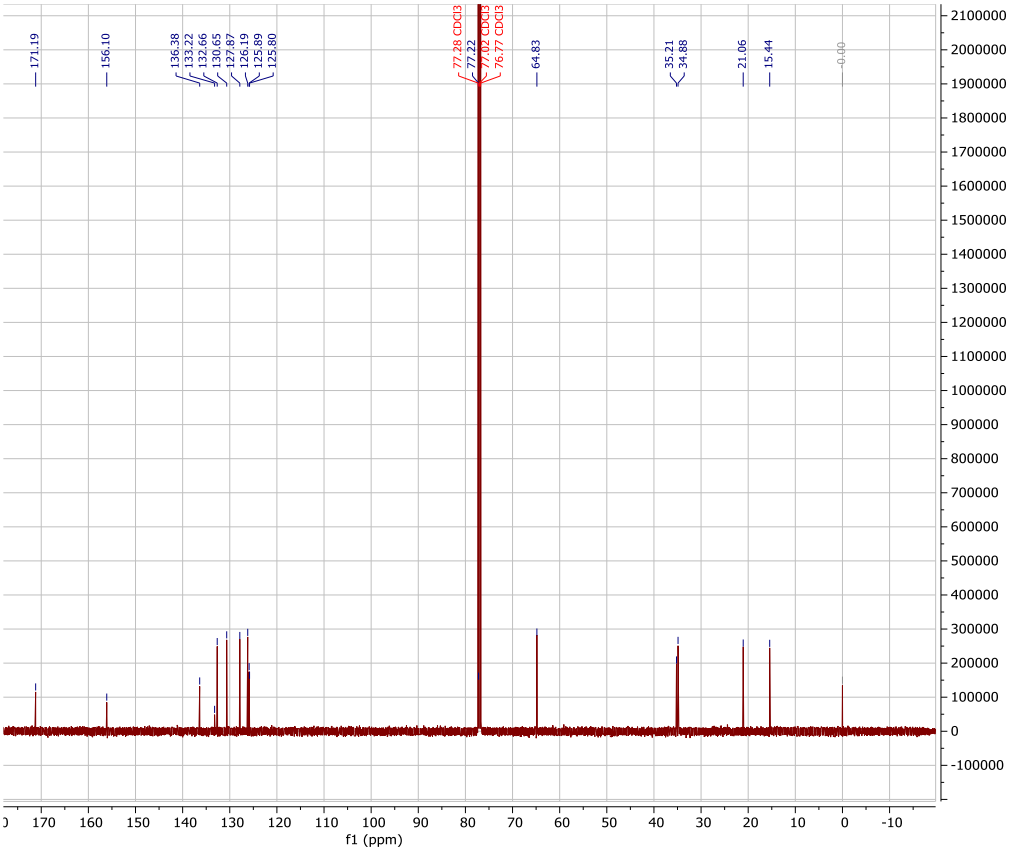
171.19
156.10
136.38
133.22
132.66
130.65
127.87
126.19
125.89
125.80
77.28 CDCl3
77.22
77.07 CDCl3
76.77 CDCl3
64.83
35.21
34.88
21.06
15.44
f1 (ppm)

§

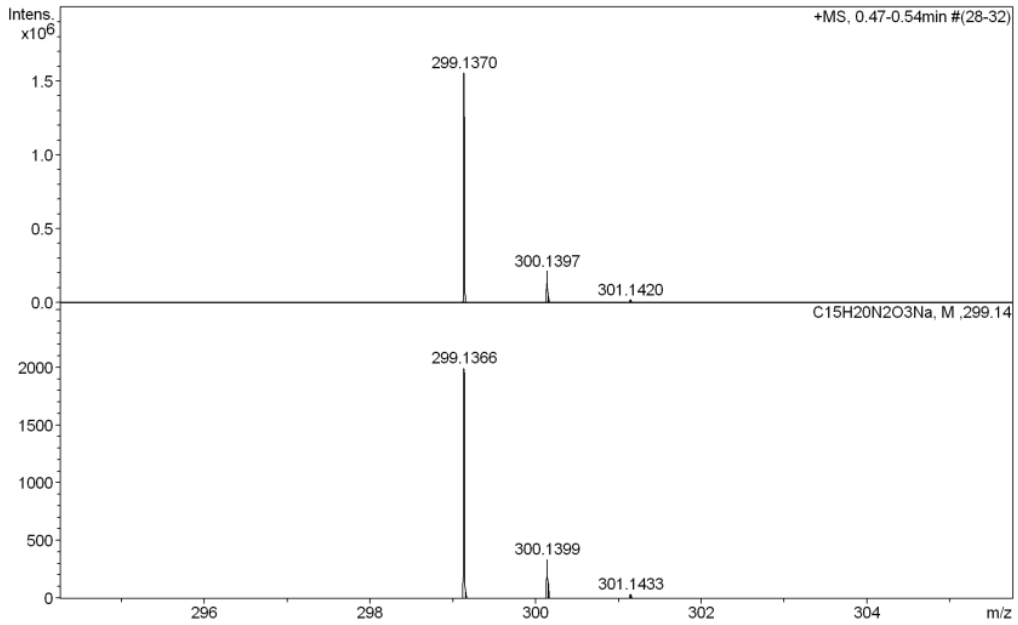

Measured m/z vs. theoretical m/z

Meas. m/z	#	Formula	Score	m/z	err [mDa]	err [ppm]	mSigma	rdb	e⁻ Conf	z
277.1543	1	C 15 H 21 N 2 O 3	100.00	277.1547	0.4	1.3	11.9	6.5	even	1+
299.1370	1	C 15 H 20 N 2 Na O 3	100.00	299.1366	-0.4	-1.2	17.2	6.5	even	
315.1100	1	C 15 H 20 K N 2 O 3	100.00	315.1106	0.6	1.8	11.8	6.5	even	
575.2834	1	C 30 H 40 N 4 Na O 6	100.00	575.2840	0.6	1.1	5.8	12.5	even	

2-iPr

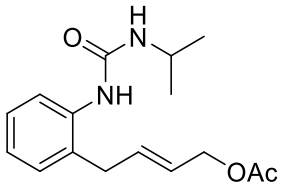

Exact Mass: 290,16
m/z: 290.16 (100.0%), 291.17 (17.7%), 292.17 (2.1%)

§

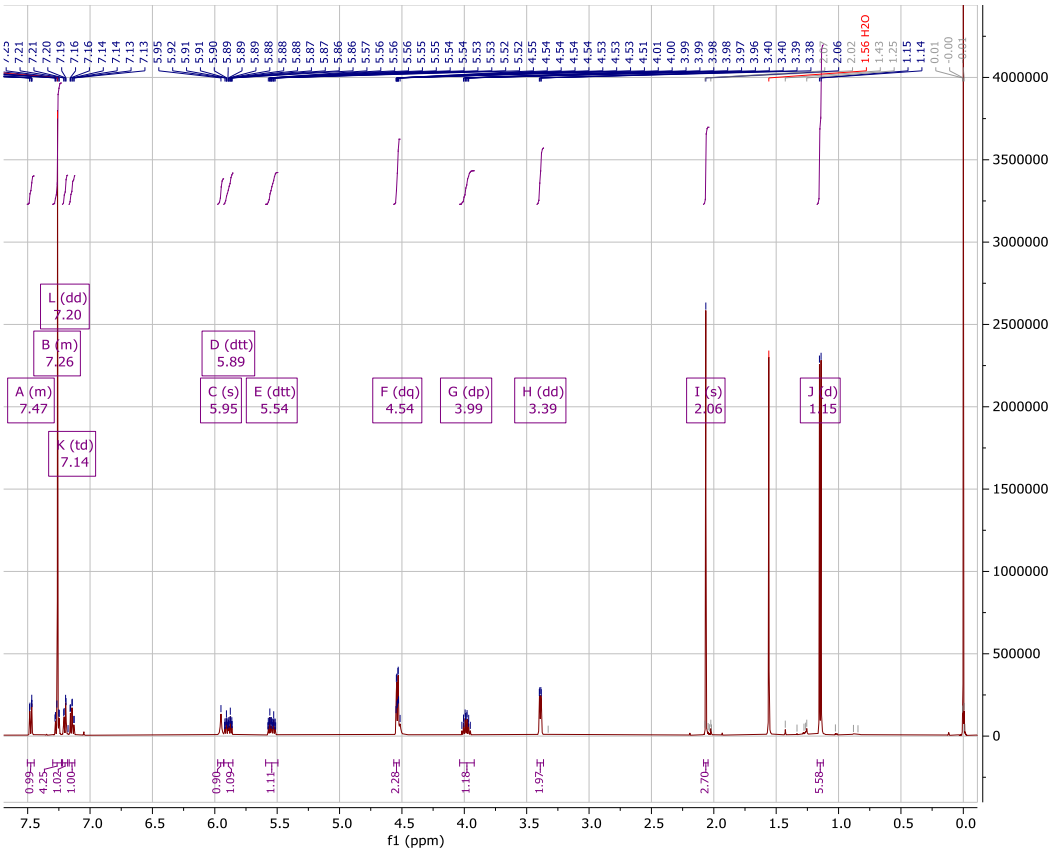
L (dd) 7.20
B (m) 7.26
A (m) 7.47
K (td) 7.14
D (dtt) 5.89
C (s) 5.95
E (dtt) 5.54
F (dq) 4.54
G (dp) 3.99
H (dd) 3.39
I (s) 2.06
J (d) 1.15
1.56 H2O
f1 (ppm)

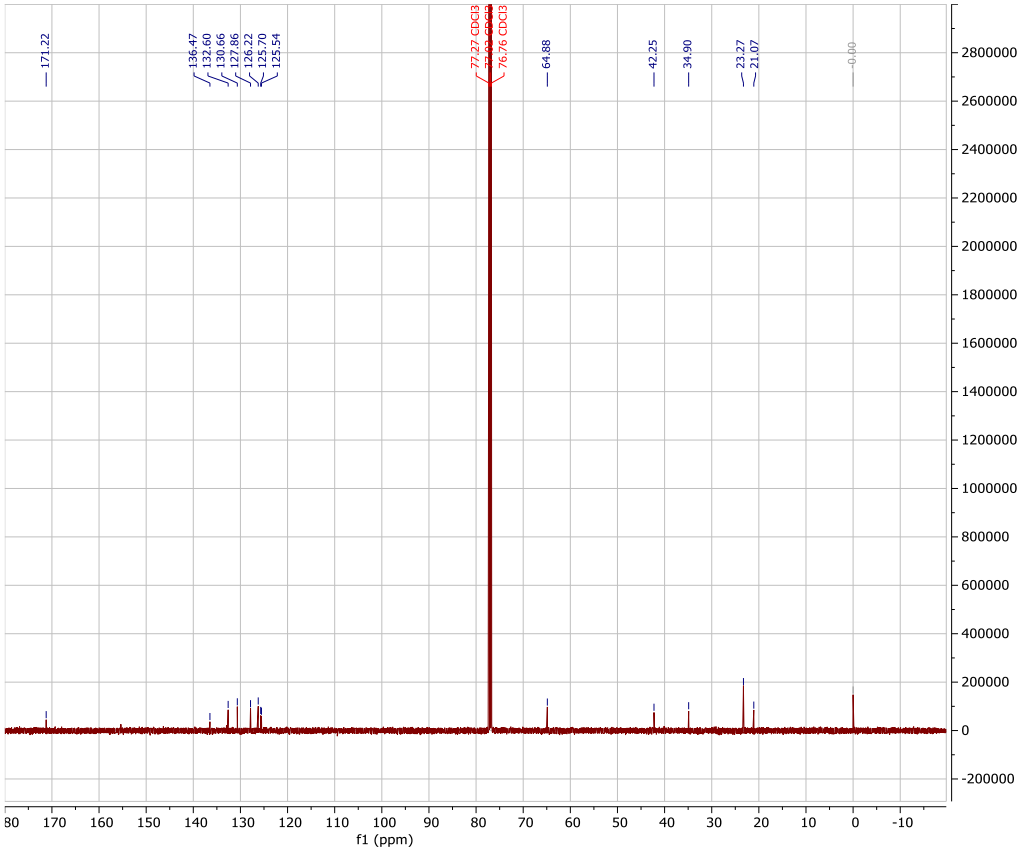
171.22
136.47
132.60
130.66
127.86
126.22
125.70
125.54
77.27 CDCl3
76.76 CDCl3
64.88
42.25
34.90
23.27
21.07
f1 (ppm)

§

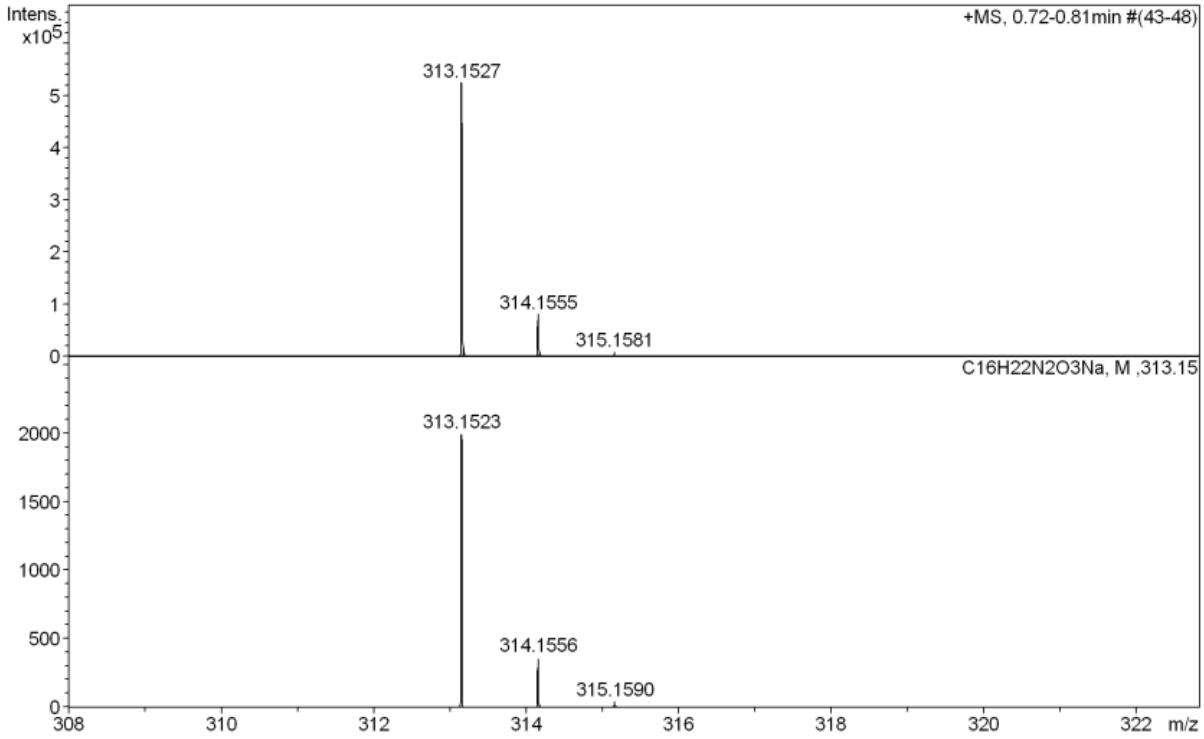

Measured m/z vs. theoretical m/z

Meas. m/z	#	Formula	Score	m/z	err [mDa]	err [ppm]	mSigma	rdb	e⁻ Conf	z
291.1701	1	C 16 H 23 N 2 O 3	100.00	291.1703	0.2	0.7	13.5	6.5	even	1+
313.1527	1	C 16 H 22 N 2 Na O 3	100.00	313.1523	-0.5	-1.5	14.6	6.5	even	
329.1260	1	C 16 H 22 K N 2 O 3	100.00	329.1262	0.2	0.7	47.5	6.5	even	
603.3150	1	C 32 H 44 N 4 Na O 6	100.00	603.3153	0.3	0.5	7.7	12.5	even	

2-tBu

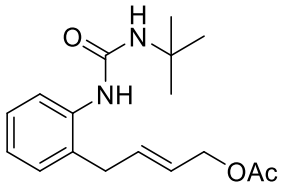

Exact Mass: 304,18
m/z: 304.18 (100.0%), 305.18 (19.5%), 306.19 (1.7%)

§

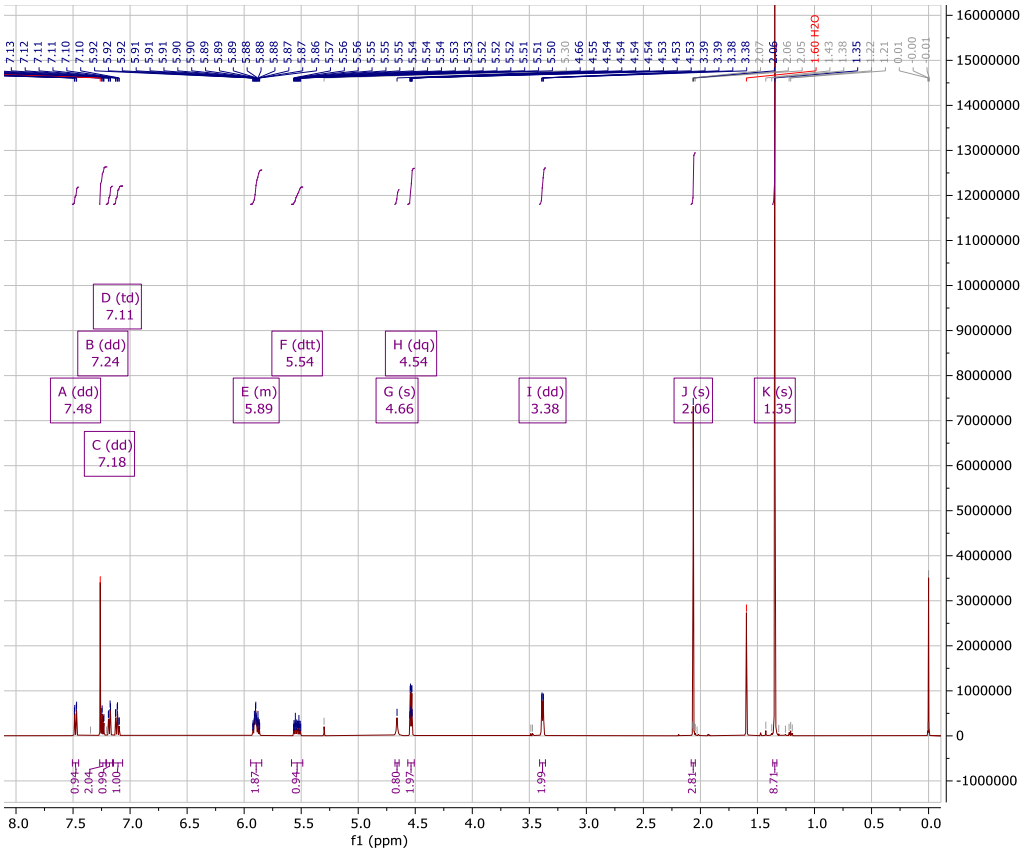
D (td)
7.11
B (dd)
7.24
A (dd)
7.48
C (dd)
7.18
F (dtt)
5.54
E (m)
5.89
H (dq)
4.54
G (s)
4.66
I (dd)
3.38
J (s)
2.06
K (s)
1.35
f1 (ppm)

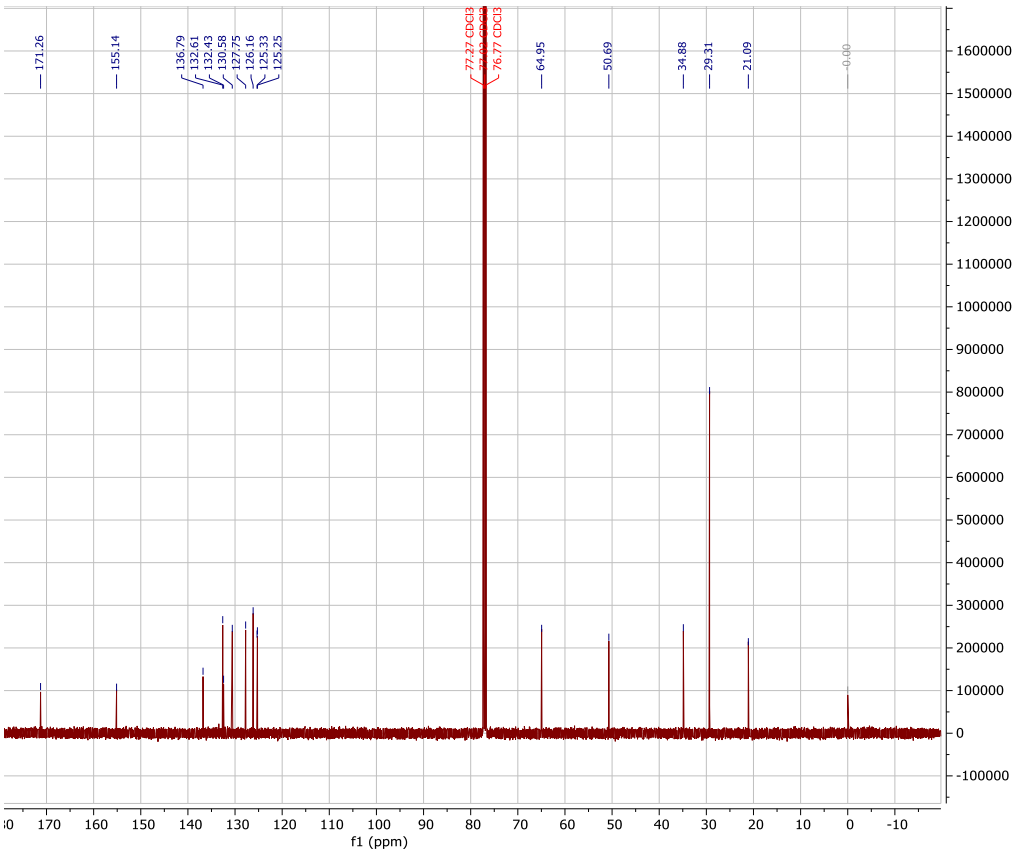
171.26
155.14
136.79
132.61
132.43
130.58
127.75
126.16
125.33
125.25
77.27 CDCl3
76.77 CDCl3
64.95
50.69
34.88
29.31
21.09
f1 (ppm)

§

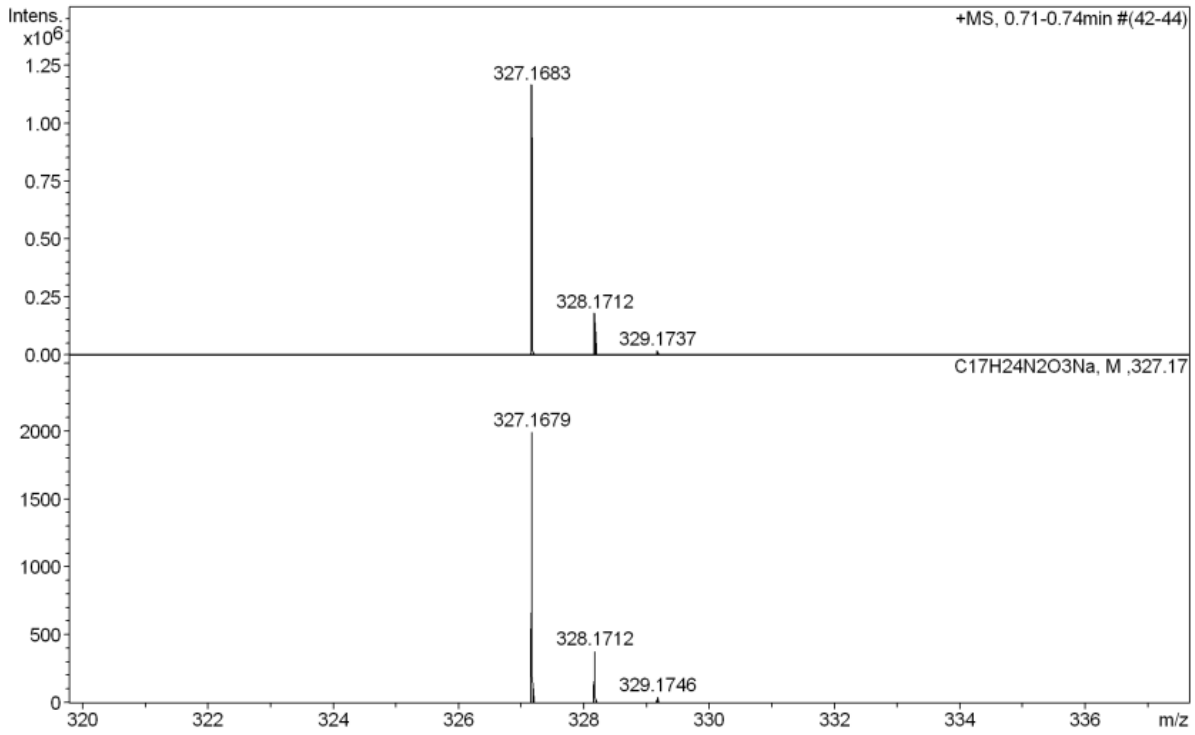

Measured m/z vs. theoretical m/z

Meas. m/z	#	Formula	Score	m/z	err [mDa]	err [ppm]	mSigma	rdb	e⁻ Conf	z
305.1857	1	C 17 H 25 N 2 O 3	100.00	305.1860	0.3	0.9	5.5	6.5	even	1+
327.1683	1	C 17 H 24 N 2 Na O 3	100.00	327.1679	-0.4	-1.1	20.5	6.5	even	
343.1415	1	C 17 H 24 K N 2 O 3	100.00	343.1419	0.3	0.9	48.4	6.5	even	
631.3461	1	C 34 H 48 N 4 Na O 6	100.00	631.3466	0.5	0.8	2.9	12.5	even	

2-nPr

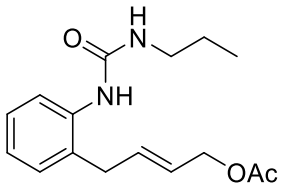

Exact Mass: 290,16
m/z: 290.16 (100.0%), 291.17 (17.7%), 292.17 (2.1%)

§

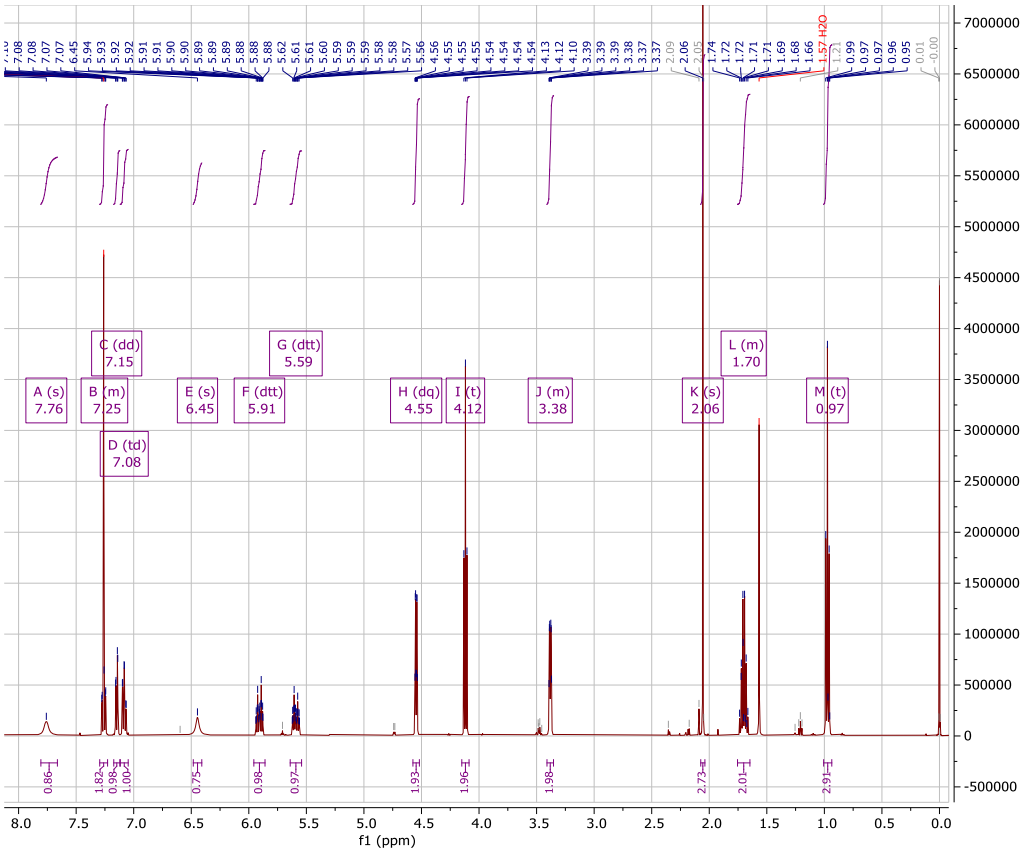
A (s) 7.76
B (m) 7.25
C (dd) 7.15
D (td) 7.08
E (s) 6.45
F (dtt) 5.91
G (dtt) 5.59
H (dq) 4.55
I (t) 4.12
J (m) 3.38
K (s) 2.06
L (m) 1.70
M (t) 0.97
f1 (ppm)

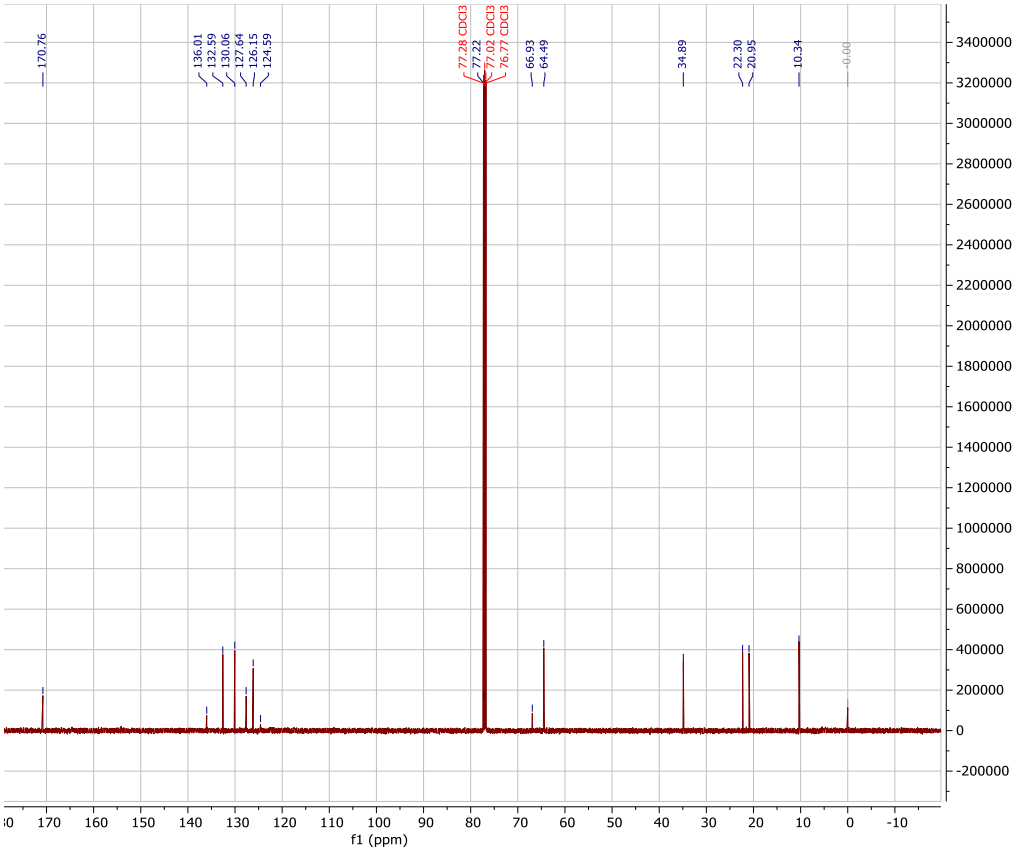
170.76
136.01
132.59
130.06
127.64
126.15
124.59
77.28 CDCl3
77.22
77.02 CDCl3
76.77 CDCl3
66.93
64.49
34.89
22.30
20.95
10.34
f1 (ppm)

§

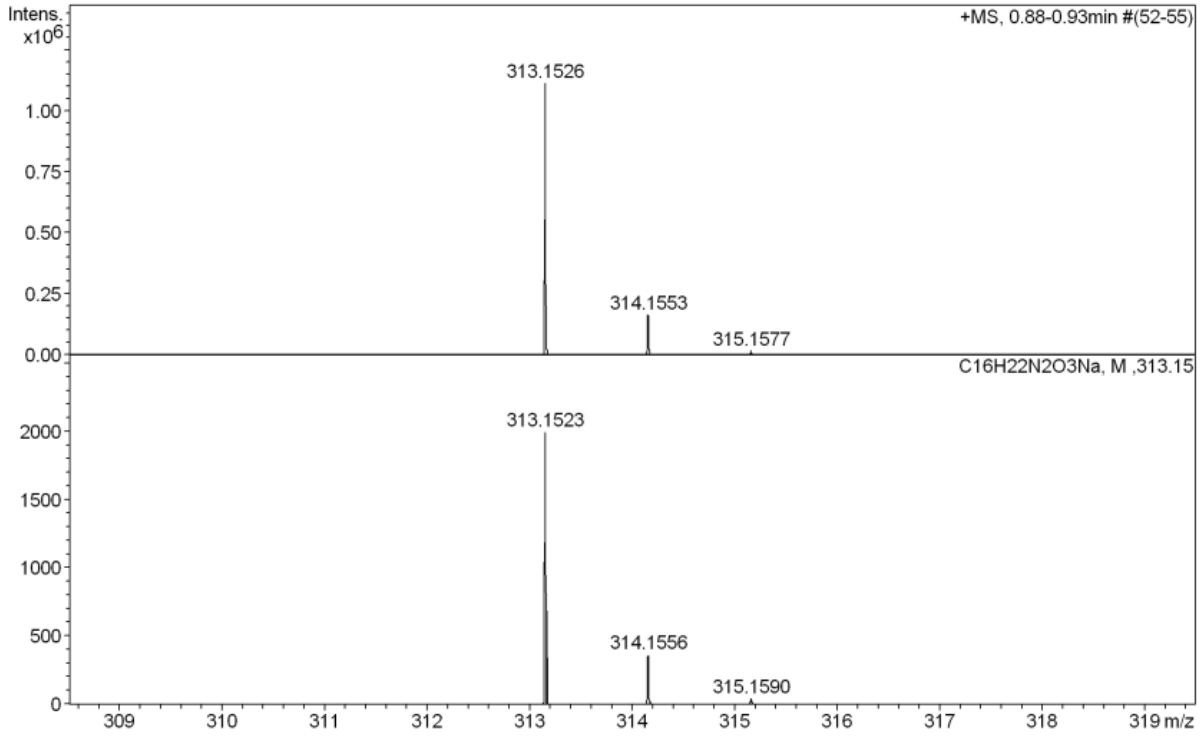

Measured m/z vs. theoretical m/z

Meas. m/z	#	Formula	Score	m/z	err [mDa]	err [ppm]	mSigma	rdb	e¯ Conf	z
291.1700	1	C 16 H 23 N 2 O 3	100.00	291.1703	0.4	1.2	13.1	6.5	even	1+
313.1526	1	C 16 H 22 N 2 Na O 3	100.00	313.1523	-0.4	-1.1	17.7	6.5	even	
329.1256	1	C 16 H 22 K N 2 O 3	100.00	329.1262	0.6	1.7	50.6	6.5	even	
603.3147	1	C 32 H 44 N 4 Na O 6	100.00	603.3153	0.6	1.0	3.2	12.5	even	

2-nBu

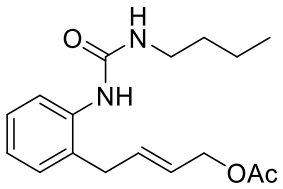

Exact Mass: 304,18
m/z: 304.18 (100.0%), 305.18 (19.5%), 306.19 (1.7%)

§

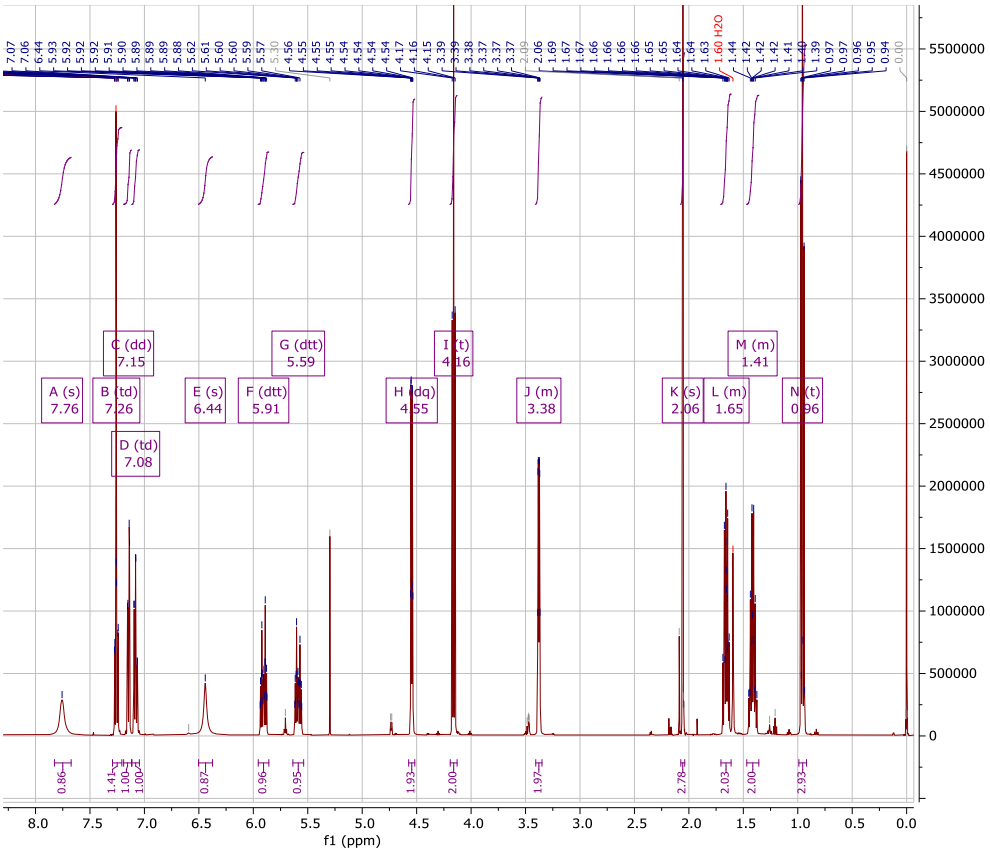
A (s) 7.76
B (td) 7.26
C (dd) 7.15
D (td) 7.08
E (s) 6.44
F (dtt) 5.91
G (dtt) 5.59
H (dq) 4.55
I (t) 4.16
J (m) 3.38
K (s) 2.06
L (m) 1.65
M (m) 1.41
N (t) 0.96
f1 (ppm)

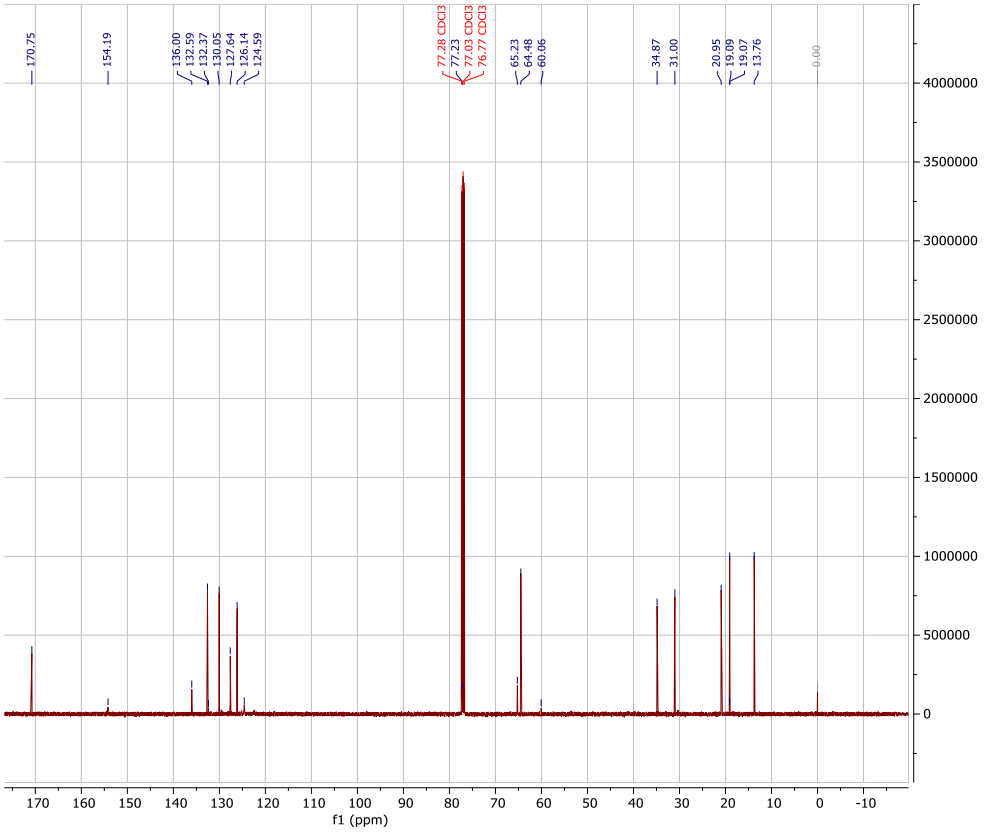
170.75
154.19
136.00
132.59
132.37
130.05
127.64
126.14
124.59
77.28 CDCl3
77.23
77.03 CDCl3
76.77 CDCl3
65.23
64.48
60.06
34.87
31.00
20.95
19.09
19.07
13.76
f1 (ppm)

§

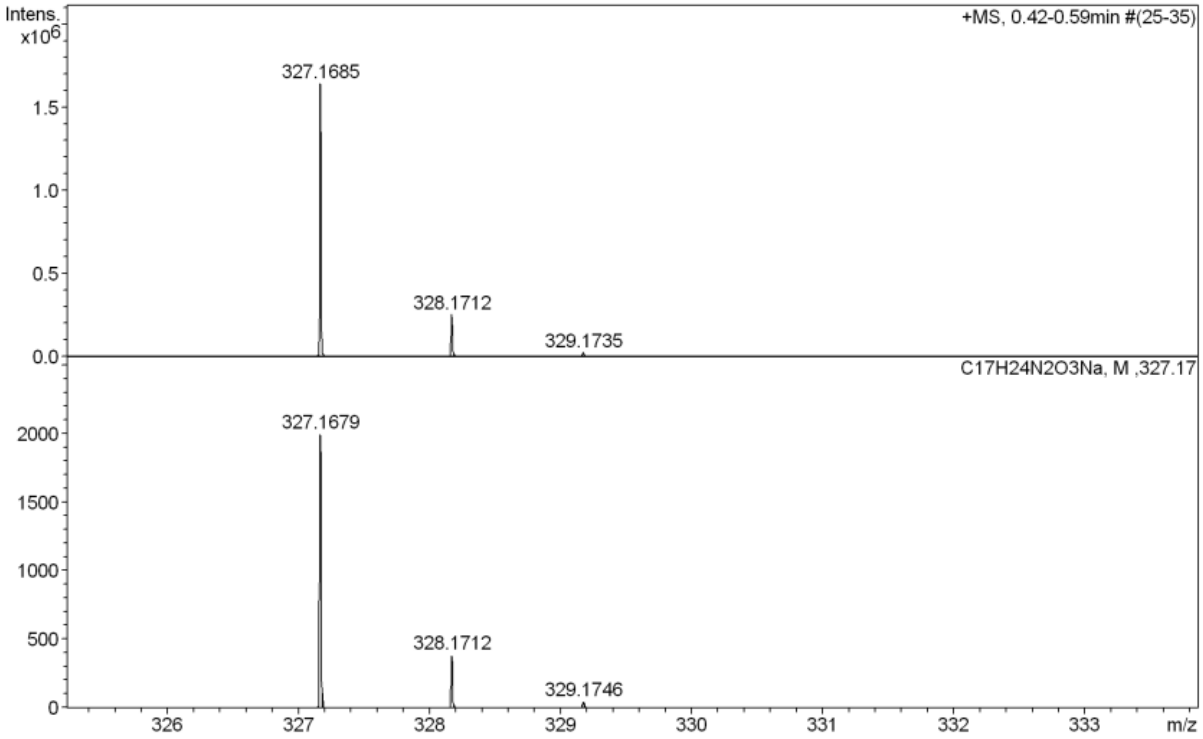

Measured m/z vs. theoretical m/z

Meas. m/z	#	Formula	Score	m/z	err [mDa]	err [ppm]	mSigma	rdb	e⁻ Conf	z
305.1858	1	C 17 H 25 N 2 O 3	100.00	305.1860	0.2	0.6	4.7	6.5	even	1+
327.1685	1	C 17 H 24 N 2 Na O 3	100.00	327.1679	-0.5	-1.6	20.6	6.5	even	
343.1415	1	C 17 H 24 K N 2 O 3	100.00	343.1419	0.4	1.1	48.4	6.5	even	
631.3466	1	C 34 H 48 N 4 Na O 6	100.00	631.3466	0.0	0.0	6.6	12.5	even	

3-Me

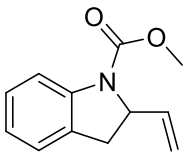

Exact Mass: 203,09
m/z: 203.09 (100.0%), 204.10 (13.2%), 205.10 (1.3%)

§

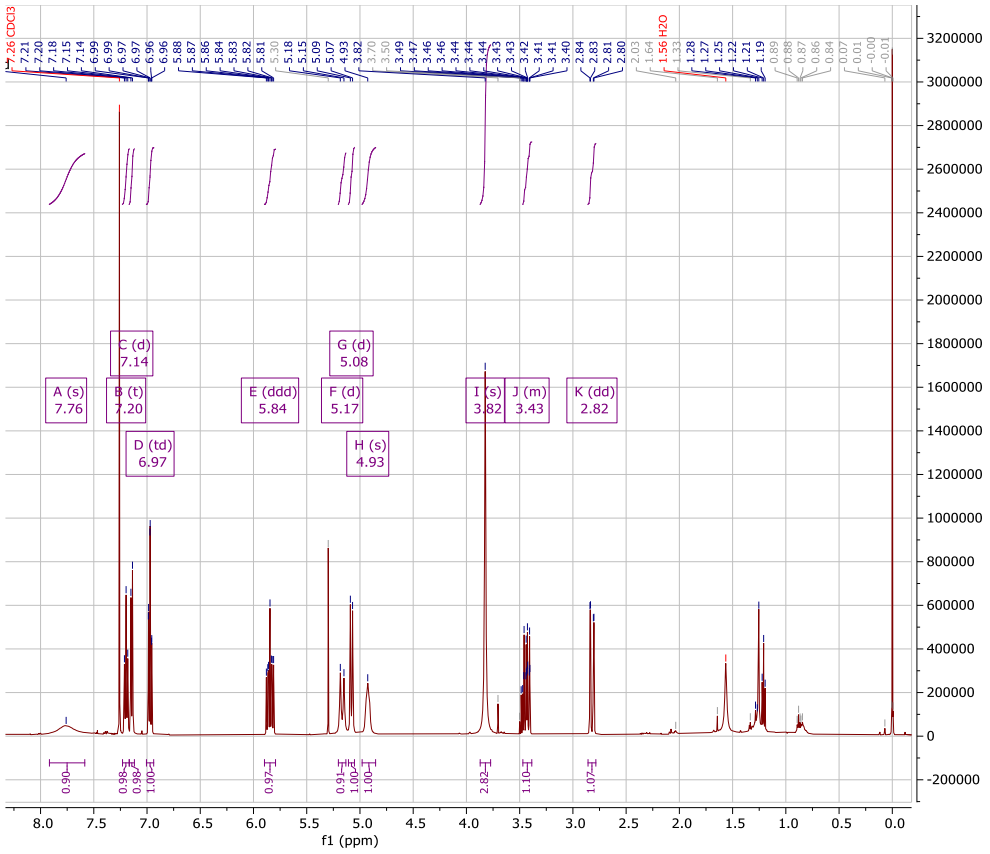
7.26 CDCl3
1.56 H2O
A (s) 7.76
B (t) 7.20
C (d) 7.14
D (td) 6.97
E (ddd) 5.84
F (d) 5.17
G (d) 5.08
H (s) 4.93
I (s) 3.82
J (m) 3.43
K (dd) 2.82
f1 (ppm)

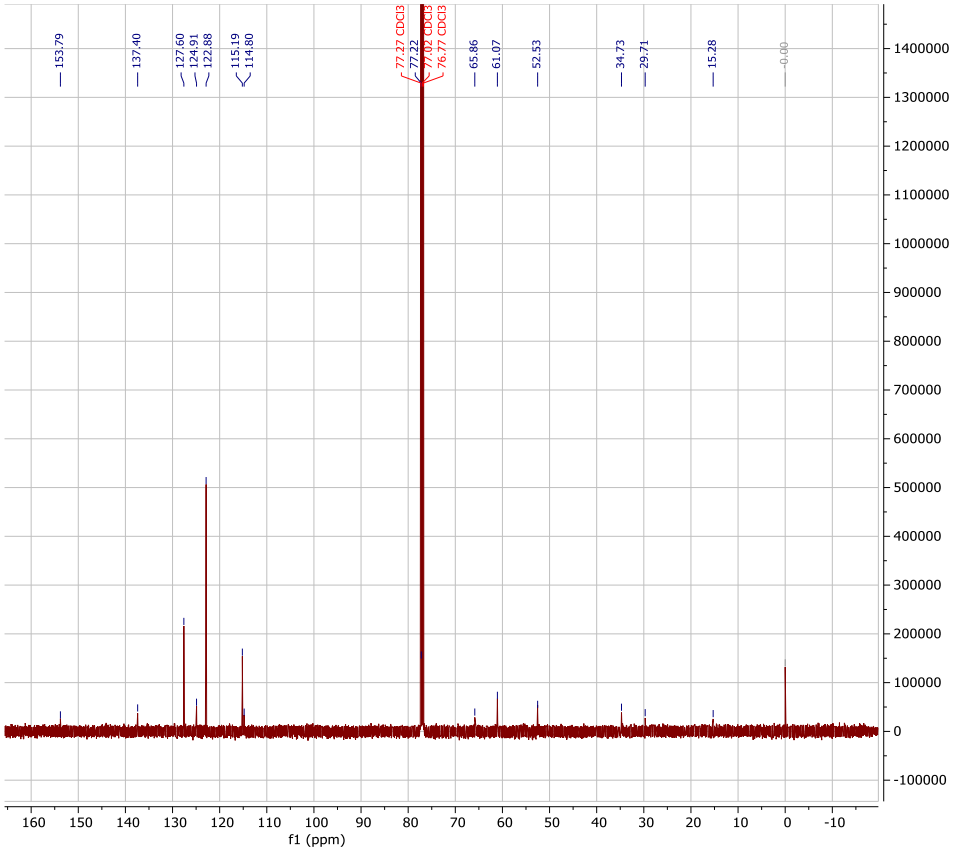
153.79
137.40
127.60
124.91
122.88
115.19
114.80
77.27 CDCl3
77.02 CDCl3
76.77 CDCl3
65.86
61.07
52.53
34.73
29.71
15.28
f1 (ppm)

§

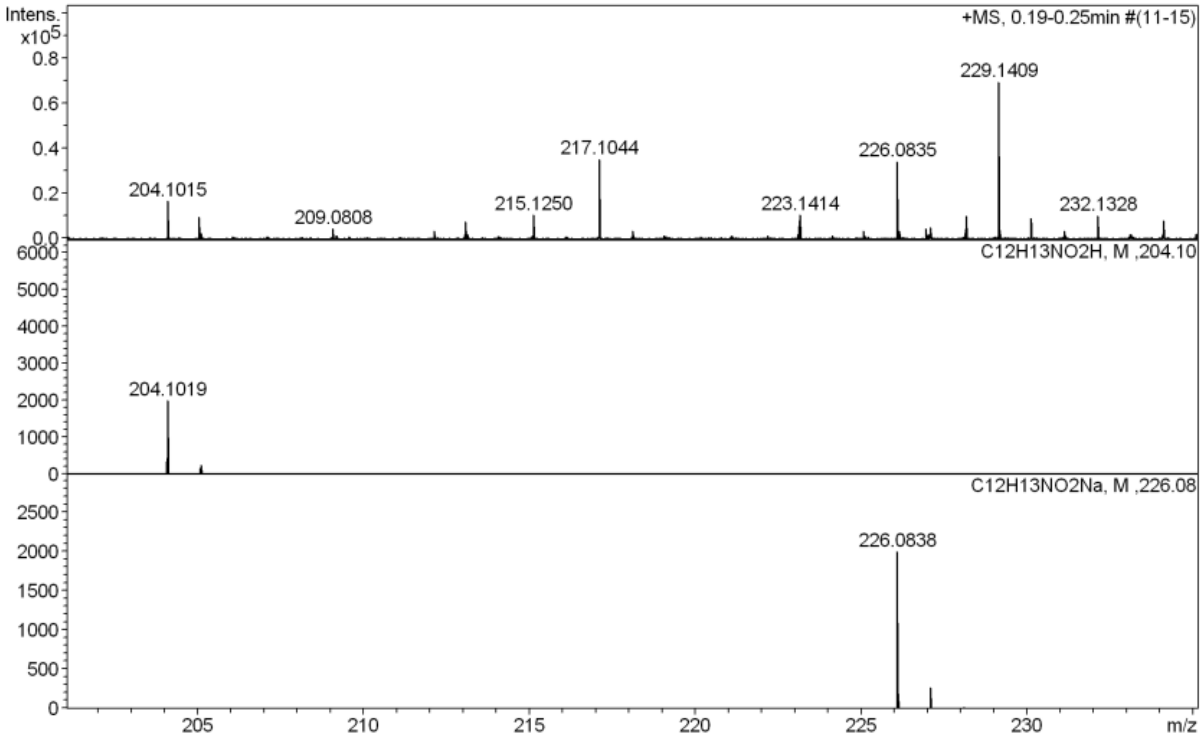

3-Et

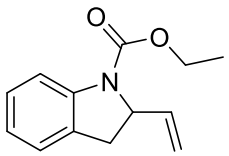

Exact Mass: 217,11
m/z: 217.11 (100.0%), 218.11 (14.5%)

§


A (s) 7.76
B (m) 7.19
C (ddt) 7.14
D (td) 6.96
E (ddd) 5.84
F (d) 5.17
G (d) 5.08
H (s) 4.93
I (d) 4.28
J (m) 3.43
K (dd) 2.82
L (t) 1.33
1.55 H2O
f1 (ppm)

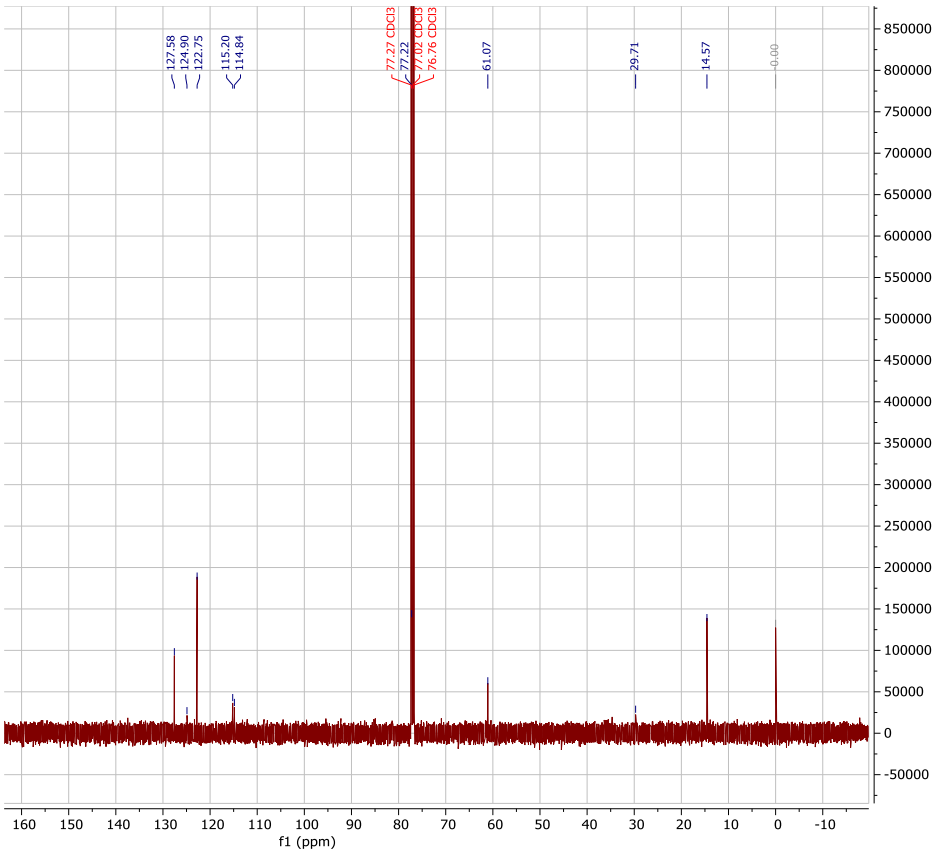
127.58
124.90
122.75
115.20
114.84
77.27 CDCl3
77.22
77.02 CDCl3
76.76 CDCl3
61.07
29.71
14.57
f1 (ppm)

§

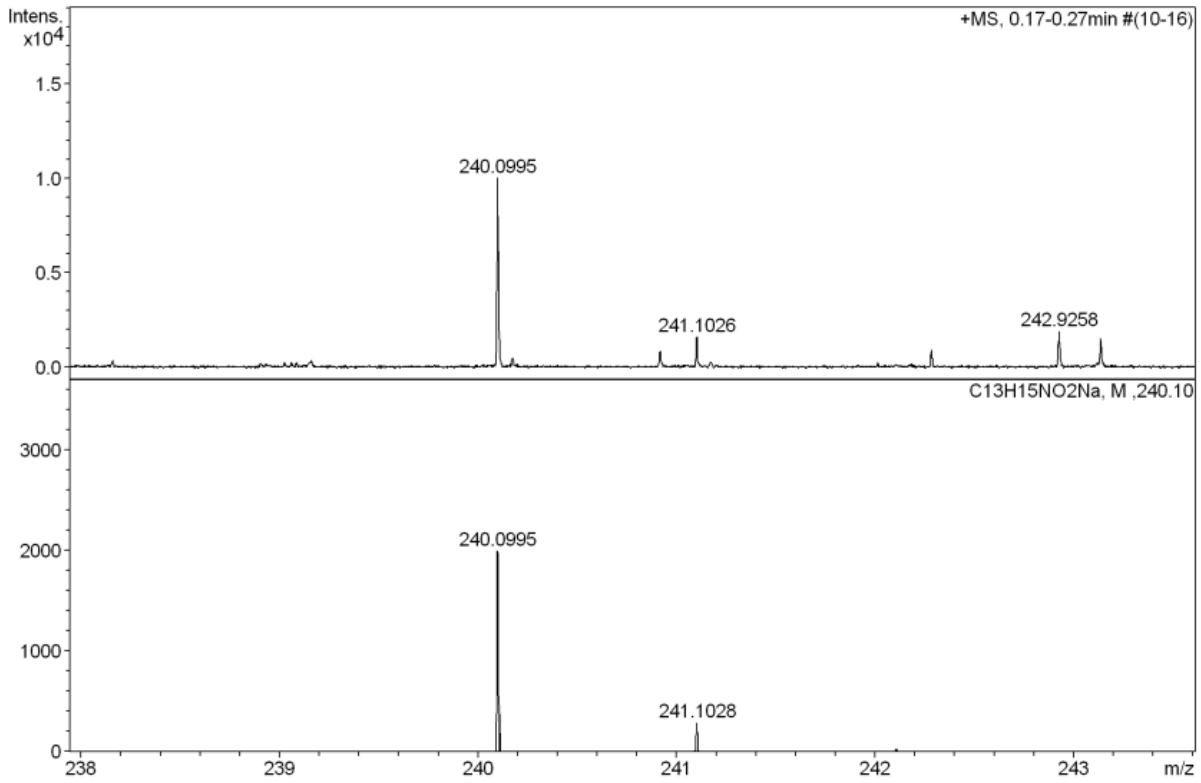

Measured m/z vs. theoretical m/z

Meas. m/z	#	Formula	Score	m/z	err [mDa]	err [ppm]	mSigma	rdb	e⁻ Conf	z
218.1174	1	C 13 H 16 N O 2	100.00	218.1176	0.1	0.6	25.7	6.5	even	1+
240.0995	1	C 13 H 15 N Na O 2	100.00	240.0995	-0.0	-0.2	13.6	6.5	even	

3-iPr

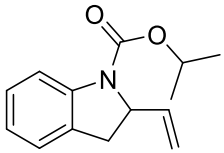

Exact Mass: 231,13
m/z: 231.13 (100.0%), 232.13 (15.4%), 233.13 (1.5%)

§

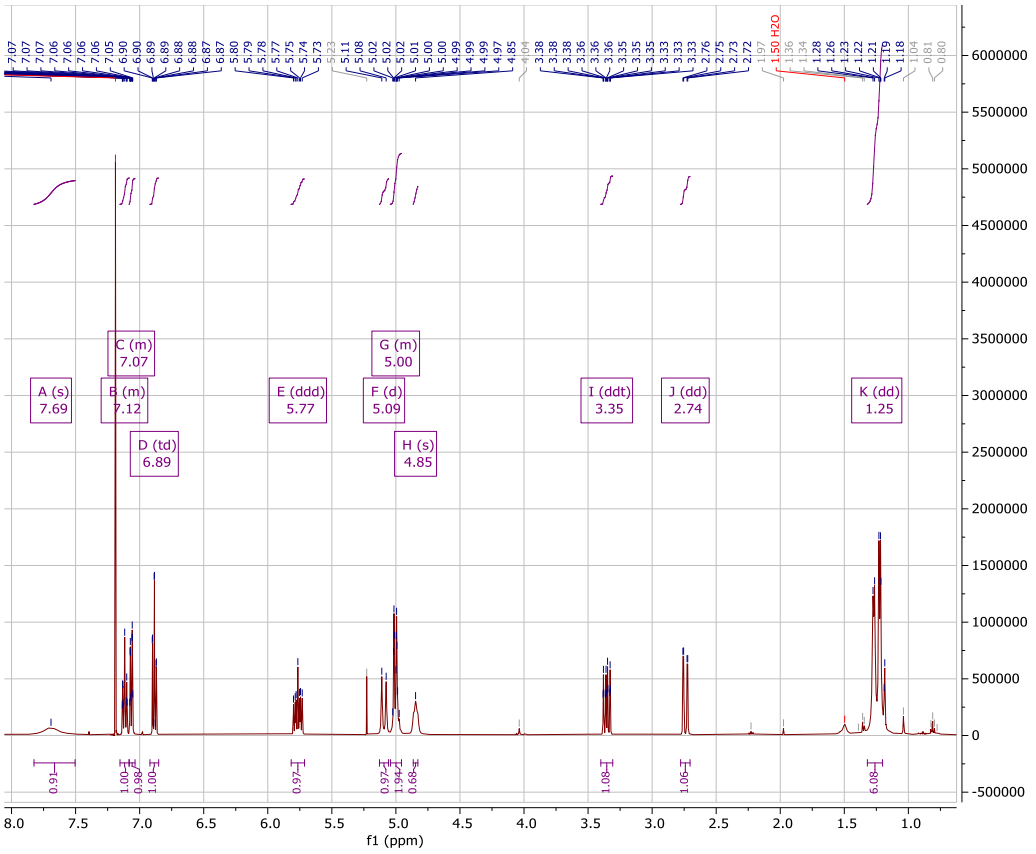
A (s) 7.69
B (m) 7.12
C (m) 7.07
D (td) 6.89
E (ddd) 5.77
F (d) 5.09
G (m) 5.00
H (s) 4.85
I (ddt) 3.35
J (dd) 2.74
K (dd) 1.25
f1 (ppm)

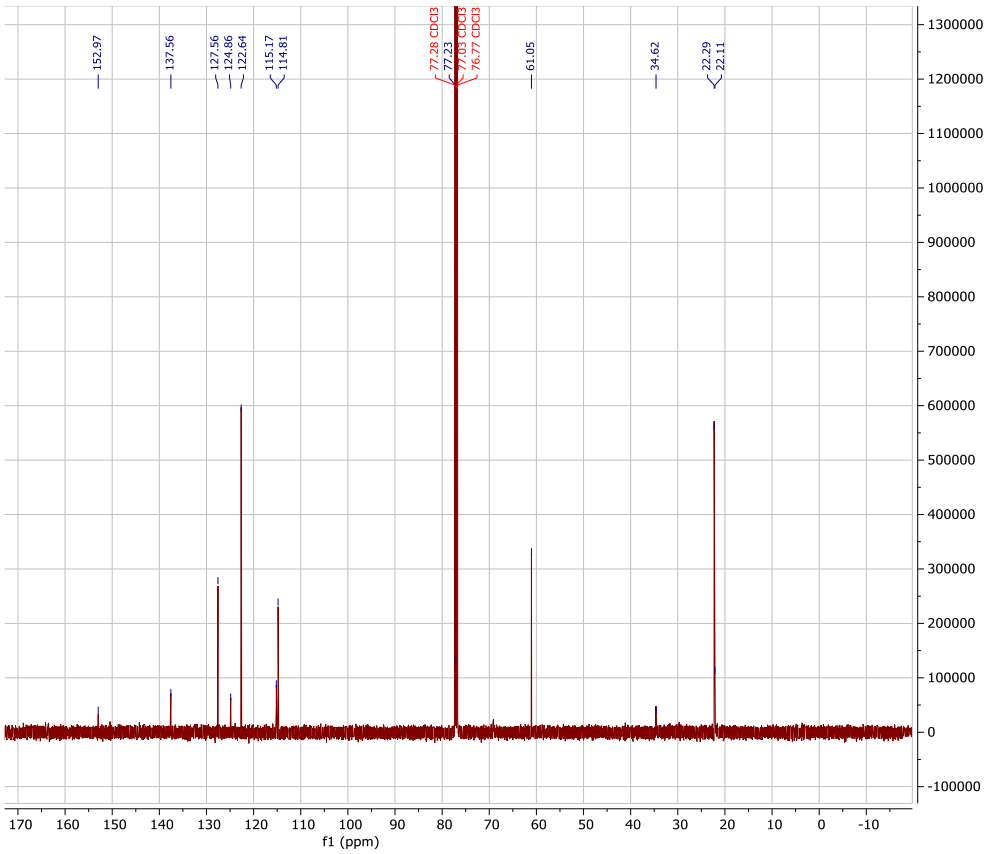
152.97
137.56
127.56
124.86
122.64
115.17
114.81
77.28 CDCl3
77.23
77.03 CDCl3
76.77 CDCl3
61.05
34.62
22.29
22.11
f1 (ppm)

§

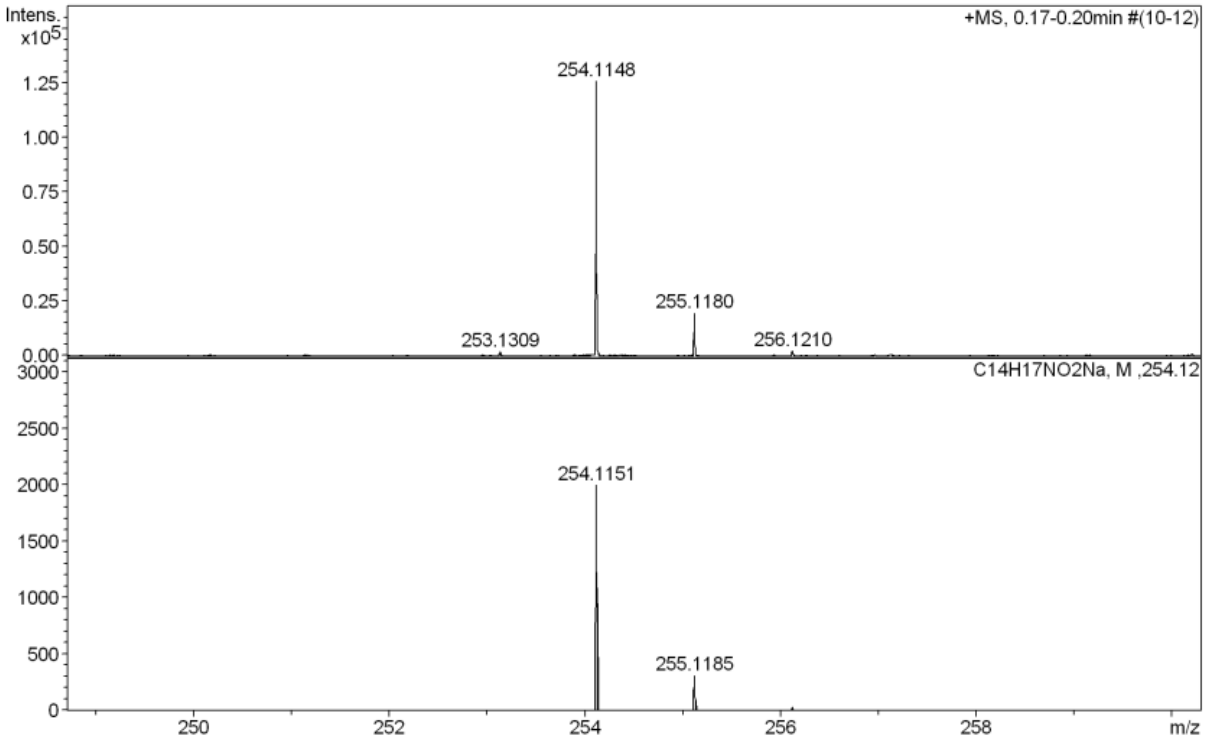

Measured m/z vs. theoretical m/z

Meas. m/z	#	Formula	Score	m/z	err [mDa]	err [ppm]	mSigma	rdb	e⁻ Conf	z
232.1328	1	C 14 H 18 N O 2	100.00	232.1332	0.4	1.8	10.5	6.5	even	1+
254.1148	1	C 14 H 17 N Na O 2	100.00	254.1151	0.3	1.3	1.2	6.5	even	
485.2395	1	C 28 H 34 N 2 Na O 4	100.00	485.2411	1.6	3.3	37.8	12.5	even	

3-tBu

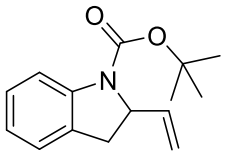

Exact Mass: 245,14
m/z: 245.14 (100.0%), 246.14 (16.6%), 247.15 (1.7%)

§

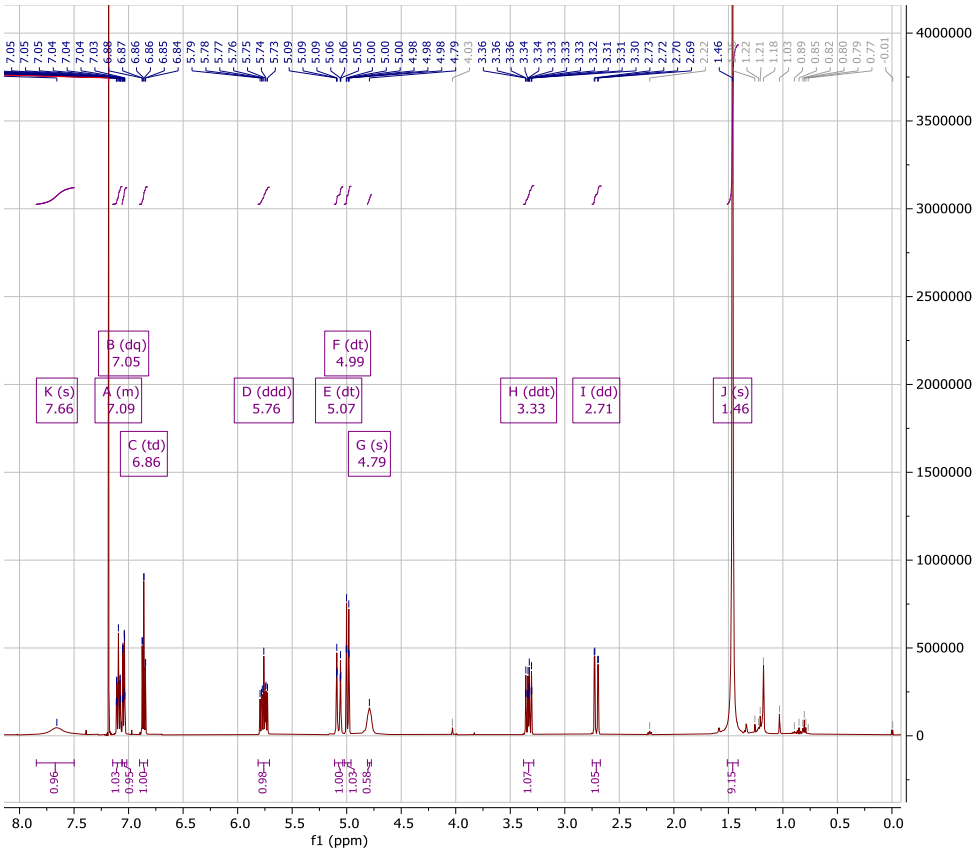
B (dq)
7.05
F (dt)
4.99
K (s)
7.66
A (m)
7.09
D (ddd)
5.76
E (dt)
5.07
H (ddt)
3.33
I (dd)
2.71
J (s)
1.46
C (td)
6.86
G (s)
4.79
f1 (ppm)

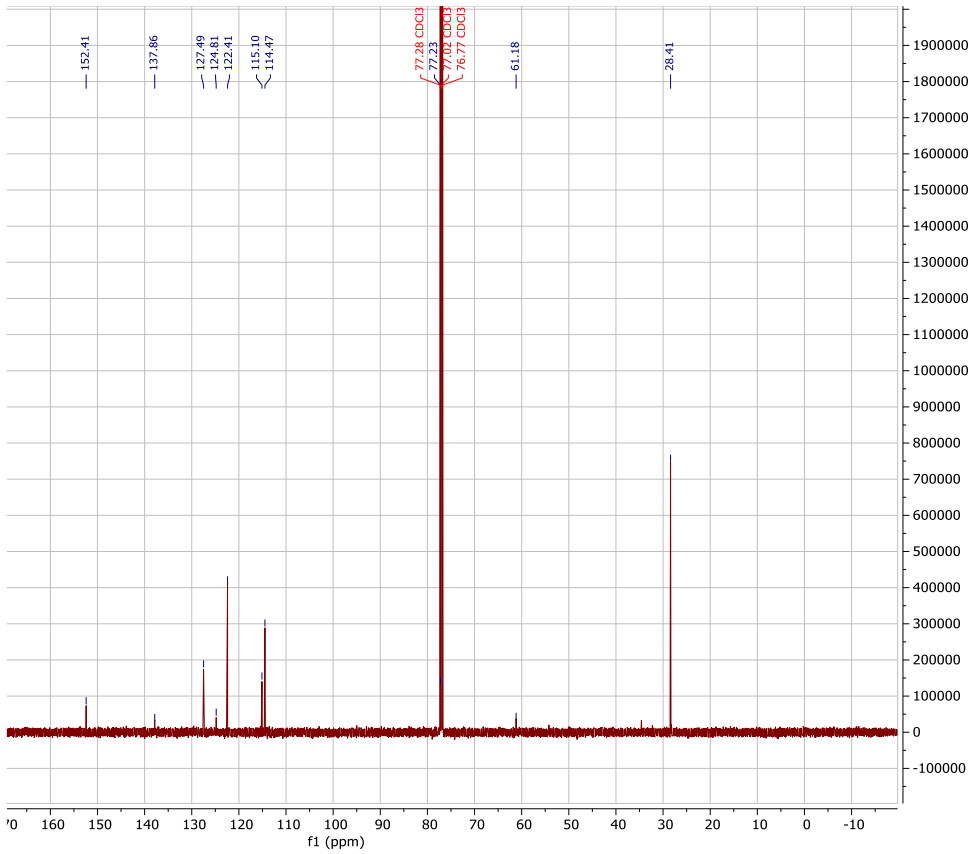
152.41
137.86
127.49
124.81
122.41
115.10
114.47
77.28 CDCl3
77.23
77.02 CDCl3
76.77 CDCl3
61.18
28.41
f1 (ppm)

§

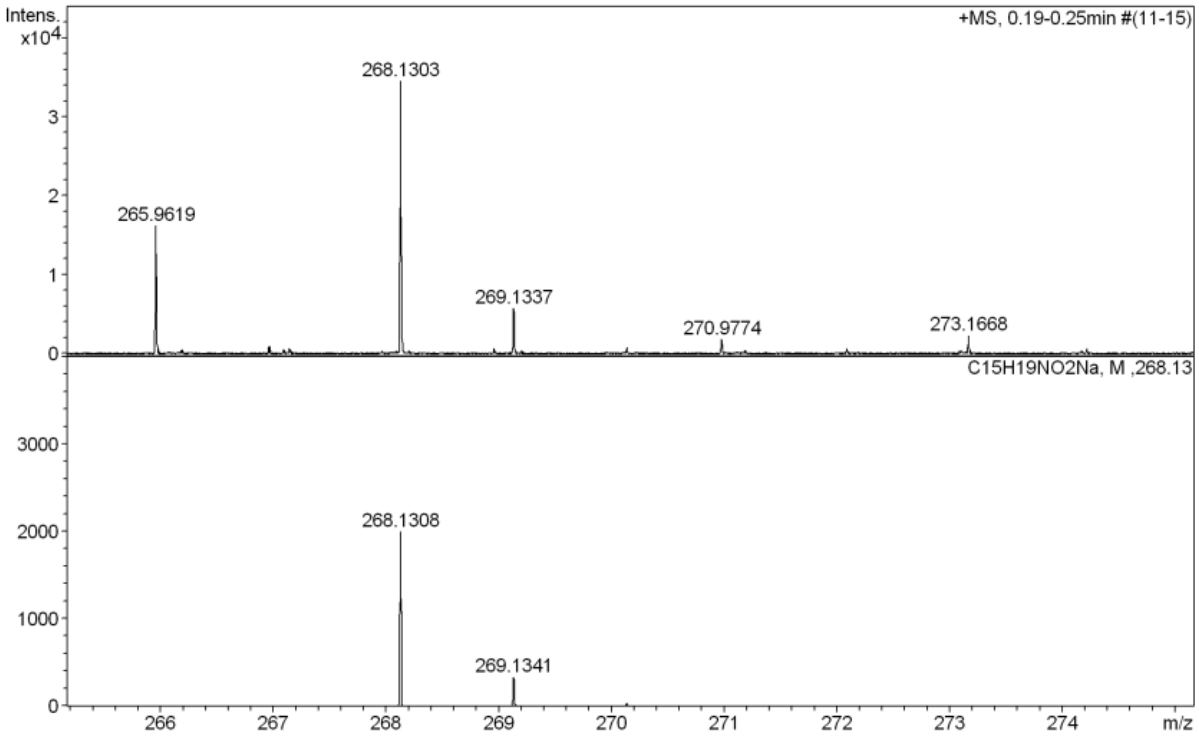

Measured m/z vs. theoretical m/z

Meas. m/z	#	Formula	Score	m/z	err [mDa]	err [ppm]	mSigma	rdb	e⁻ Conf	z
268.1303	1	C 15 H 19 N Na O 2	100.00	268.1308	0.5	1.7	9.8	6.5	even	1+

3-nPr

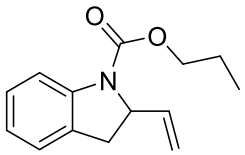

Exact Mass: 231,13
m/z: 231.13 (100.0%), 232.13 (15.4%), 233.13 (1.5%)

§

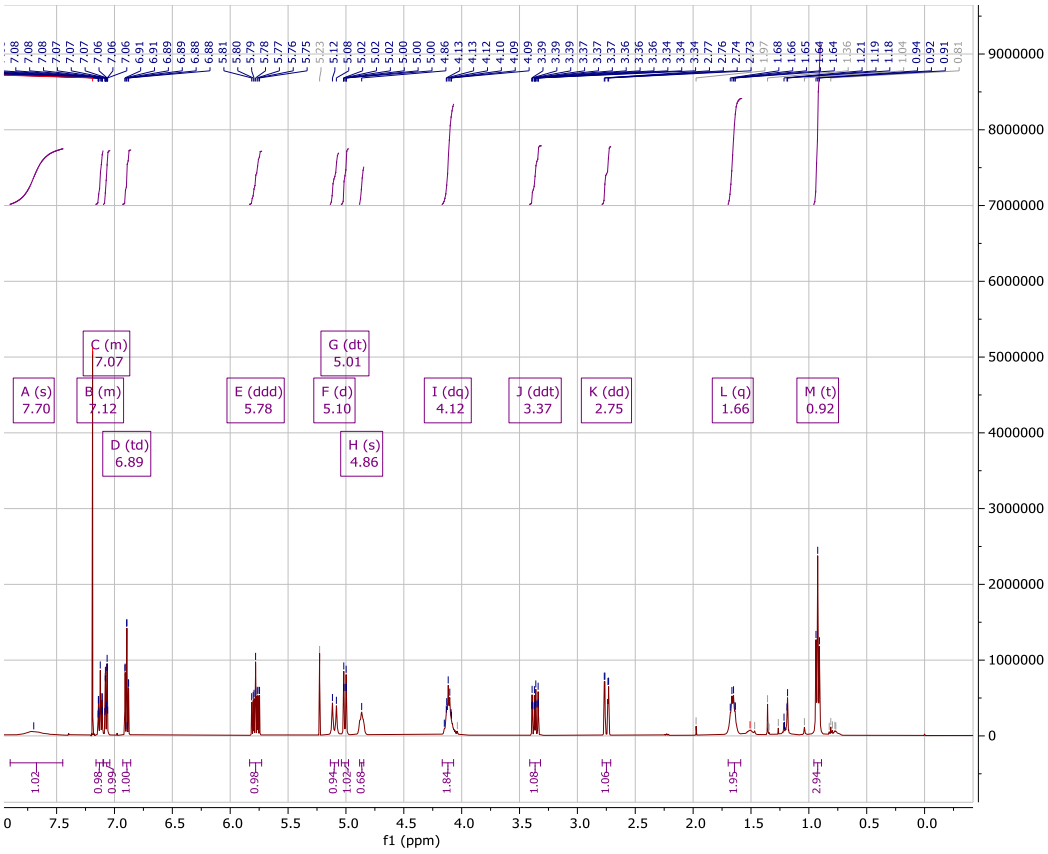
A (s) 7.70
B (m) 7.12
C (m) 7.07
D (td) 6.89
E (ddd) 5.78
F (d) 5.10
G (dt) 5.01
H (s) 4.86
I (dq) 4.12
J (ddt) 3.37
K (dd) 2.75
L (q) 1.66
M (t) 0.92
f1 (ppm)

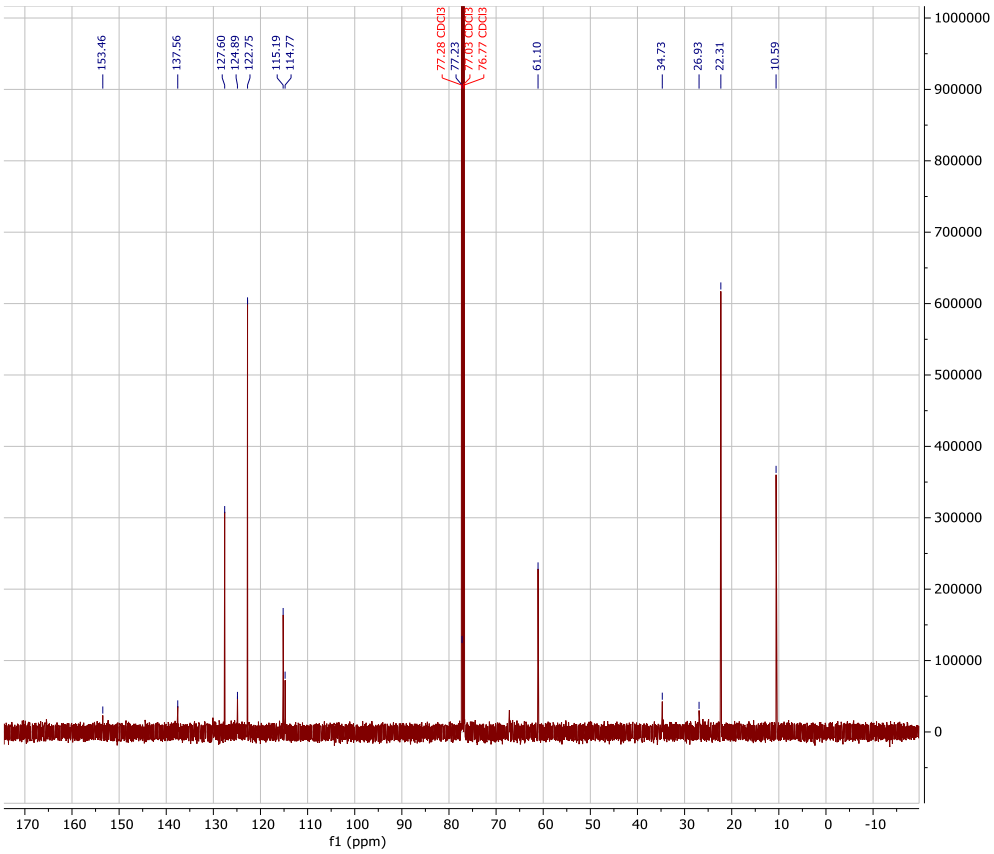
153.46
137.56
127.60
124.89
122.75
115.19
114.77
77.28 CDCl3
77.23
77.03 CDCl3
76.77 CDCl3
61.10
34.73
26.93
22.31
10.59
f1 (ppm)

§

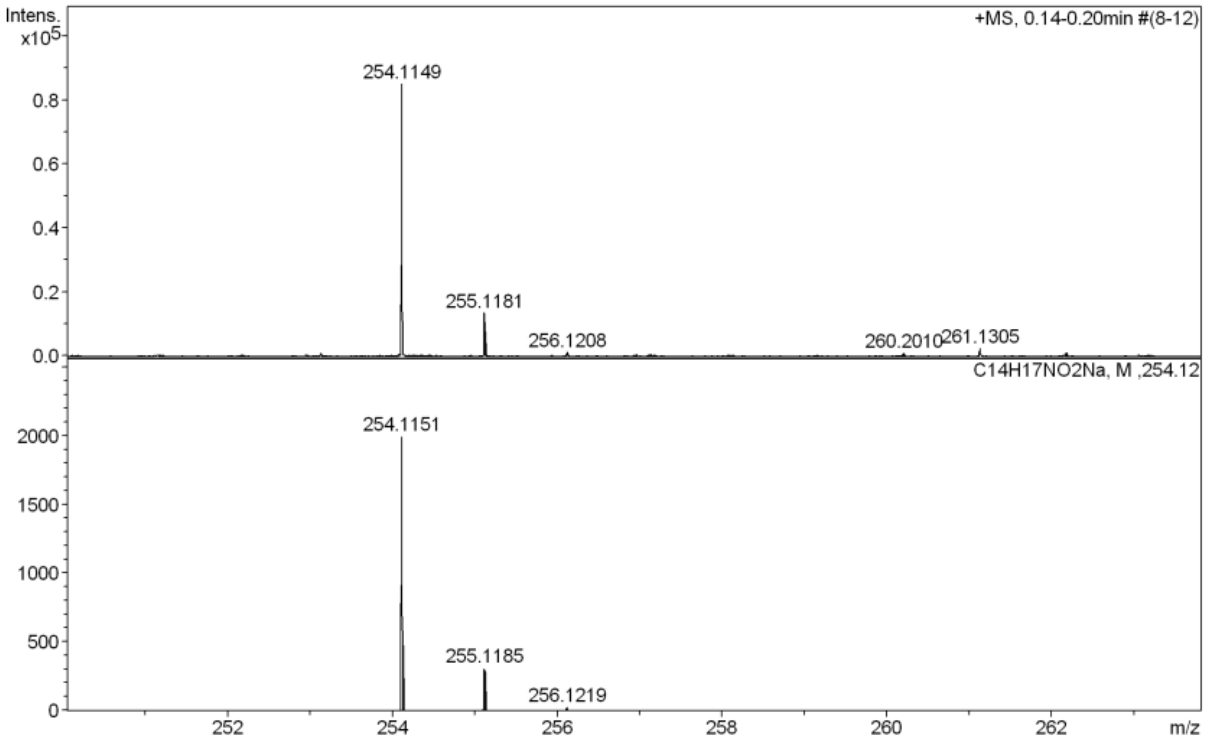

Measured m/z vs. theoretical m/z

Meas. m/z	#	Formula	Score	m/z	err [mDa]	err [ppm]	mSigma	rdb	e⁻ Conf	z
232.1328	1	C 14 H 18 N O 2	100.00	232.1332	0.4	1.8	9.2	6.5	even	1+
254.1149	1	C 14 H 17 N Na O 2	100.00	254.1151	0.3	1.1	2.2	6.5	even	
485.2403	1	C 28 H 34 N 2 Na O 4	100.00	485.2411	0.8	1.6	32.1	12.5	even	

3-nBu

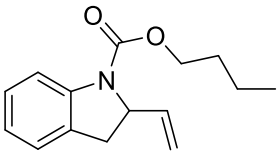

Exact Mass: 245,14
m/z: 245.14 (100.0%), 246.14 (16.6%), 247.15 (1.7%)

§

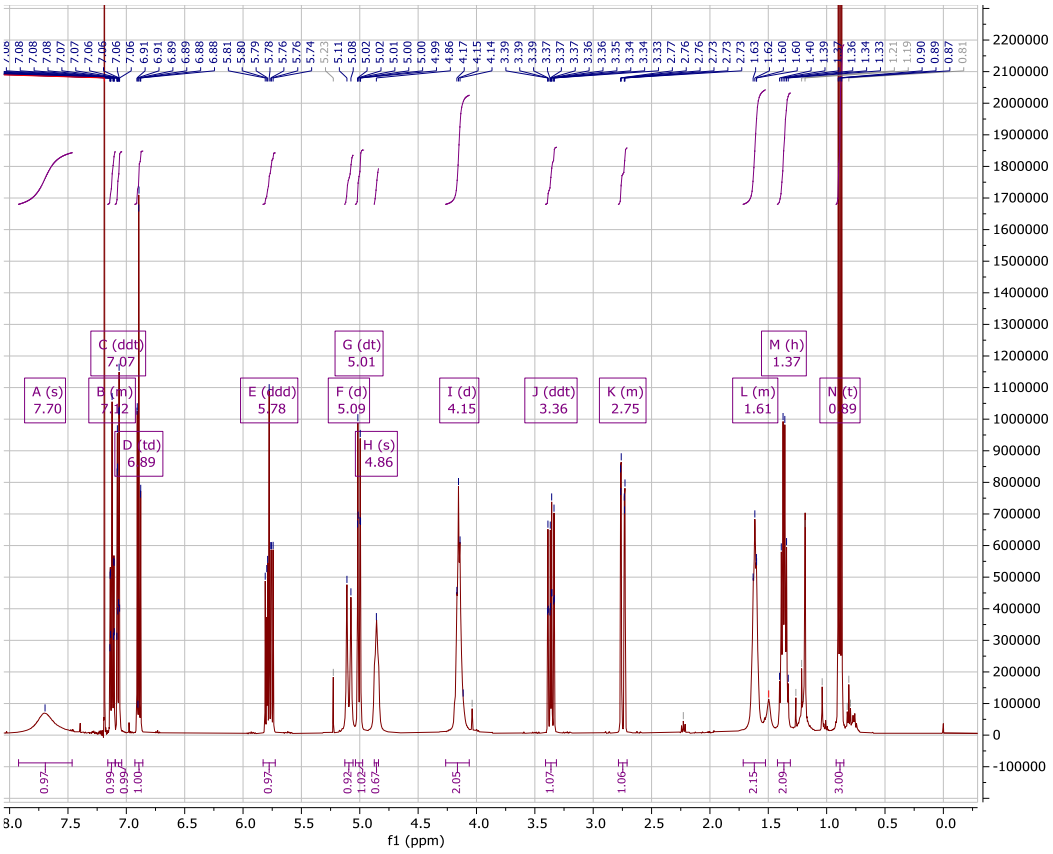
A (s) 7.70
B (m) 7.12
C (ddt) 7.07
D (td) 6.89
E (ddd) 5.78
F (d) 5.09
G (dt) 5.01
H (s) 4.86
I (d) 4.15
J (ddt) 3.36
K (m) 2.75
L (m) 1.61
M (h) 1.37
N (t) 0.89
f1 (ppm)

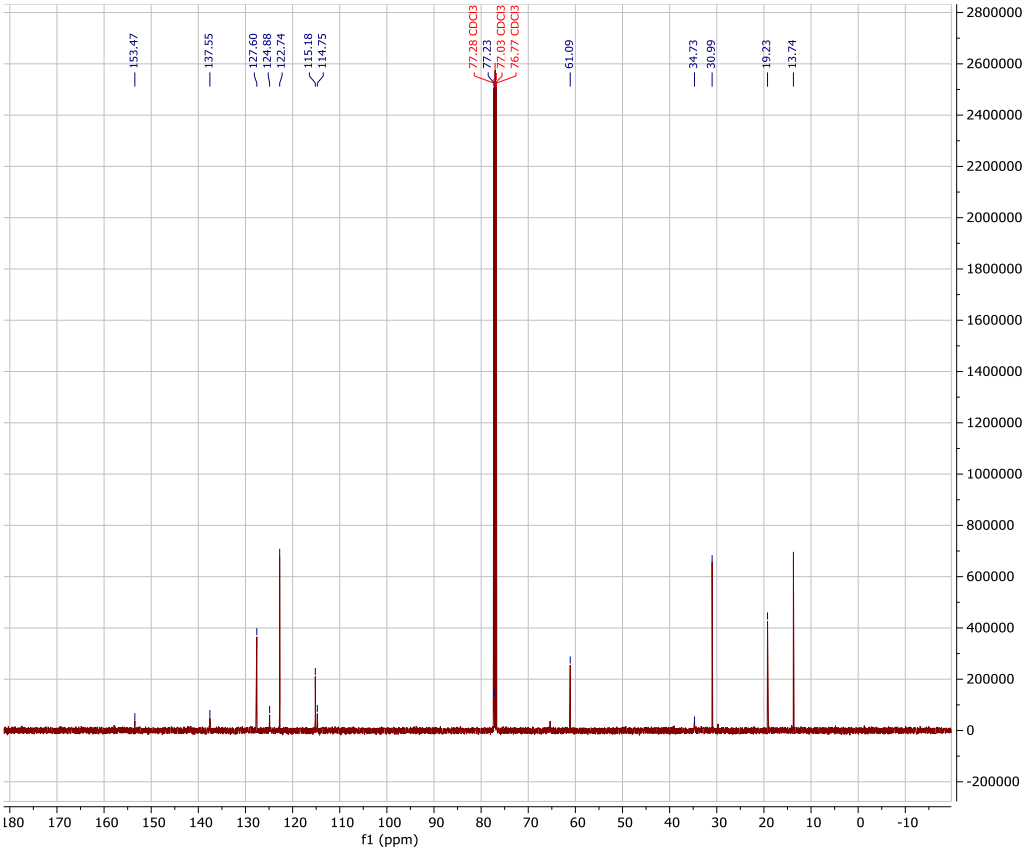
153.47
137.55
127.60
124.88
122.74
115.18
114.75
77.28 CDCl3
77.23
77.03 CDCl3
76.77 CDCl3
61.09
34.73
30.99
19.23
13.74
f1 (ppm)

§

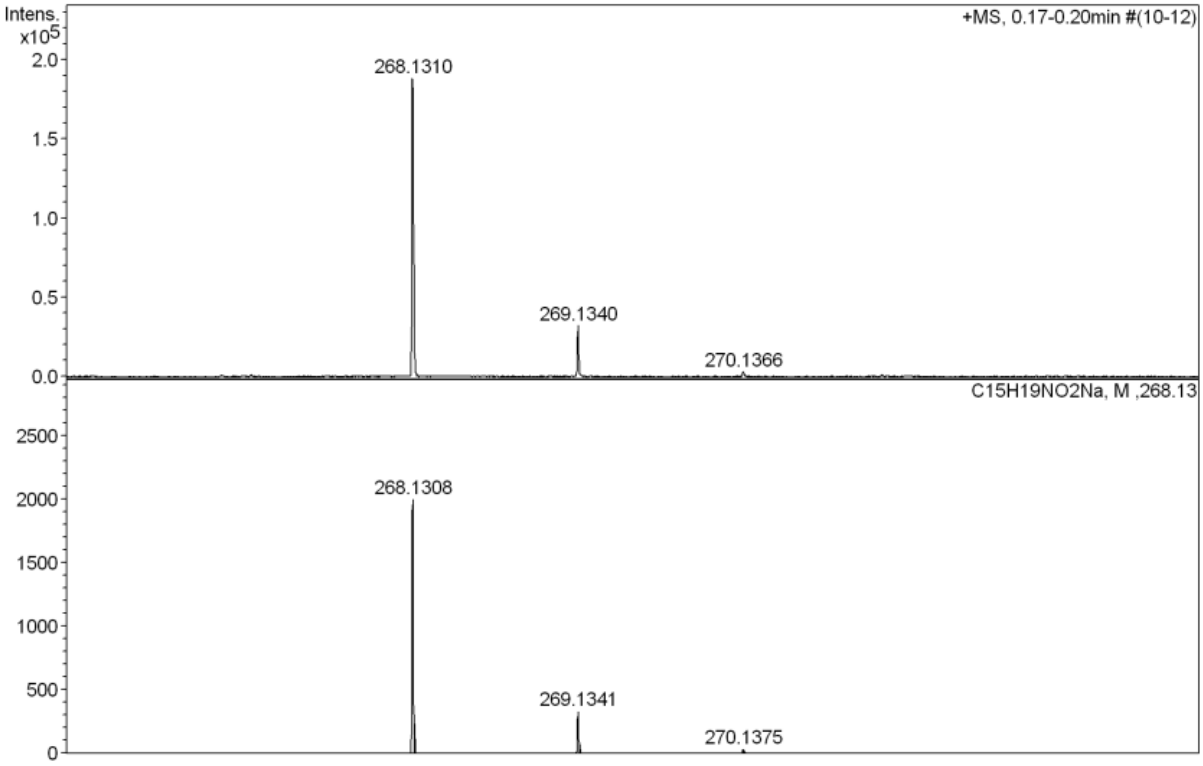

Measured m/z vs. theoretical m/z

Meas. m/z	#	Formula	Score	m/z	err [mDa]	err [ppm]	mSigma	rdb	e⁻ Conf	z
246.1489	1	C 15 H 20 N O 2	100.00	246.1489	-0.1	-0.4	10.0	6.5	even	1+
268.1310	1	C 15 H 19 N Na O 2	100.00	268.1308	-0.2	-0.7	3.0	6.5	even	
513.2718	1	C 30 H 38 N 2 Na O 4	100.00	513.2724	0.6	1.2	15.5	12.5	even	

4-Me

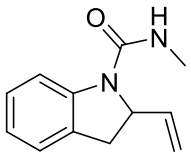

Exact Mass: 202,11
m/z: 202.11 (100.0%), 203.11 (13.8%)

§

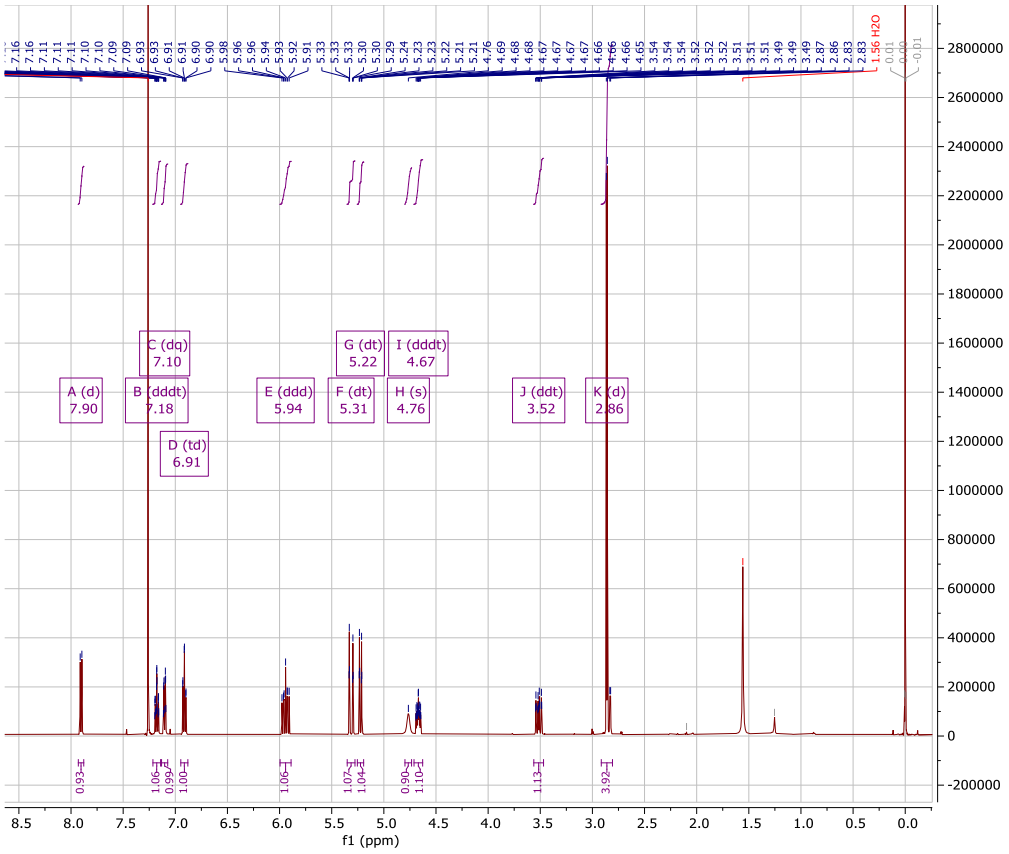
A (d) 7.90
B (dddt) 7.18
C (dq) 7.10
D (td) 6.91
E (ddd) 5.94
F (dt) 5.31
G (dt) 5.22
H (s) 4.76
I (dddt) 4.67
J (ddt) 3.52
K (d) 2.86
1.96 H2O
f1 (ppm)

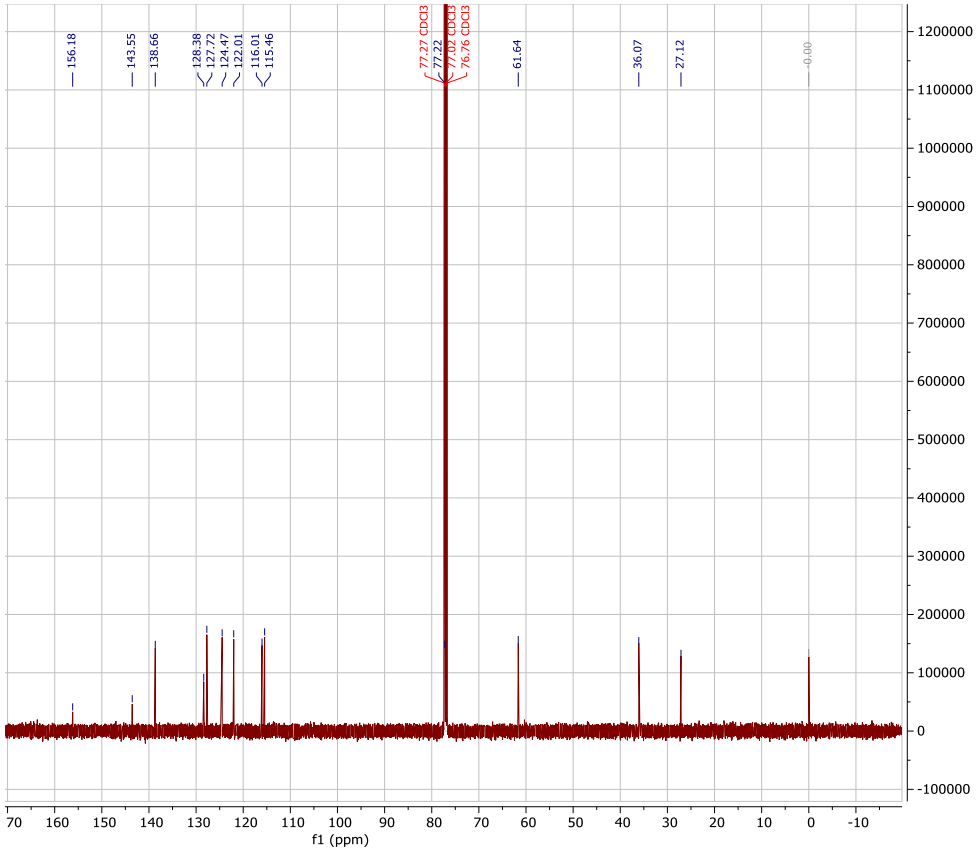
156.18
143.55
138.66
128.38
127.72
124.47
122.01
116.01
115.46
77.27 CDCl3
77.22
77.07 CDCl3
76.76 CDCl3
61.64
36.07
27.12
f1 (ppm)

§

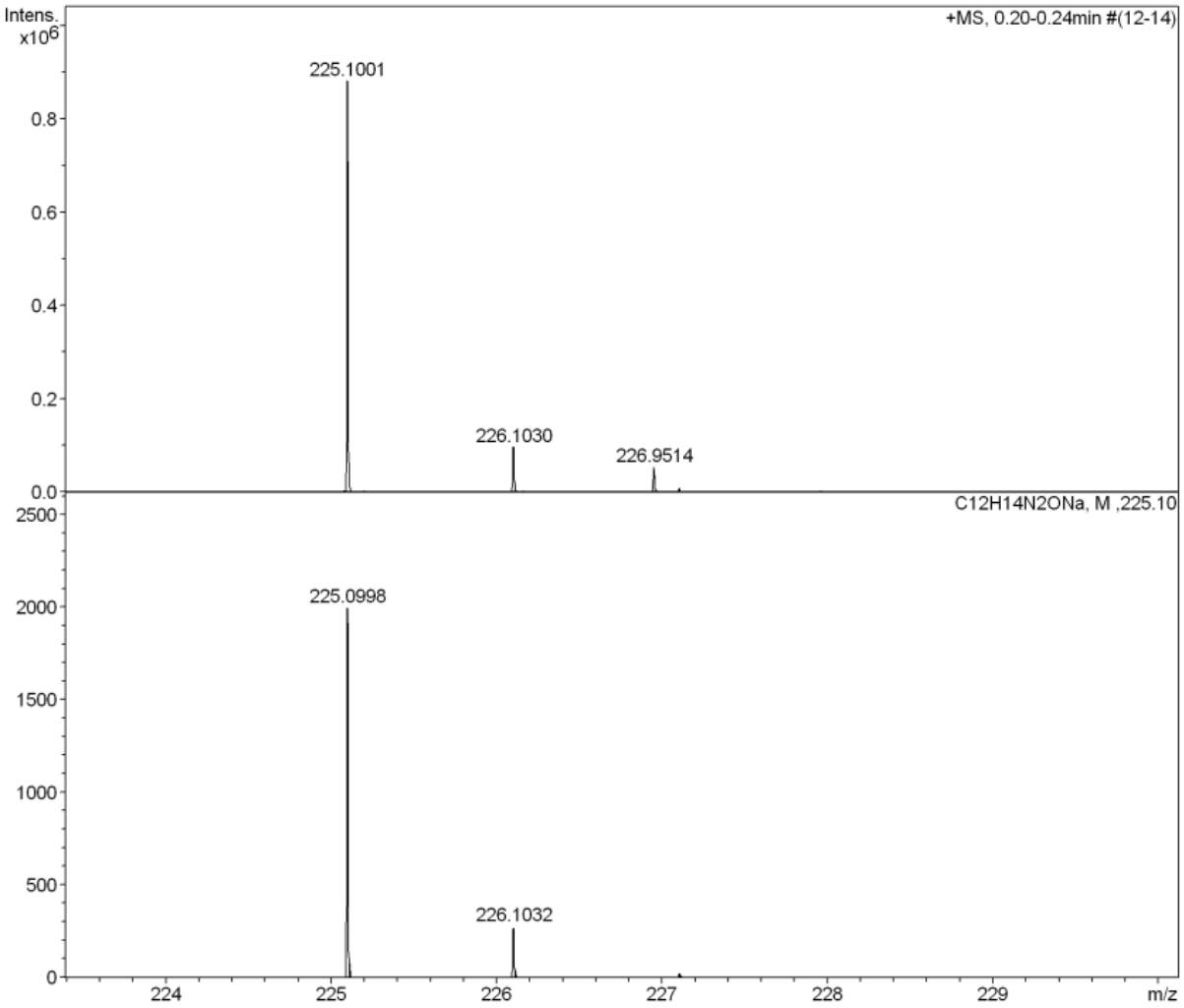

Measured m/z vs. theoretical m/z

Meas. m/z	#	Formula	Score	m/z	err [mDa]	err [ppm]	mSigma	rdb	e⁻ Conf	z
203.1179	1	C 12 H 15 N 2 O	100.00	203.1179	-0.0	-0.1	1.8	6.5	even	1+
225.1001	1	C 12 H 14 N 2 Na O	100.00	225.0998	-0.3	-1.2	15.2	6.5	even	
241.0734	1	C 12 H 14 K N 2 O	100.00	241.0738	0.4	1.5	79.8	6.5	even	
427.2102	1	C 24 H 28 N 4 Na O 2	100.00	427.2104	0.3	0.7	4.3	12.5	even	

4-Et

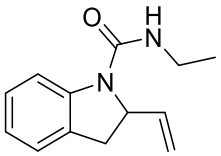

Exact Mass: 216,13
m/z: 216.13 (100.0%), 217.13 (14.3%), 218.13 (1.2%)

§

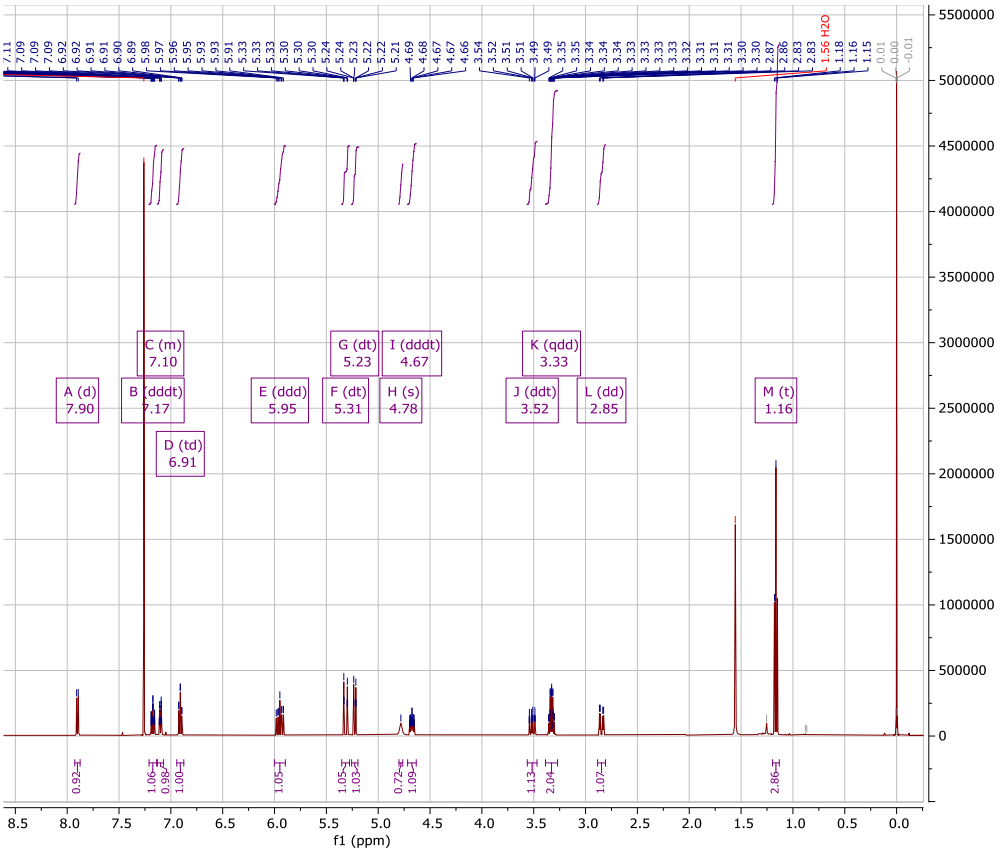
A (d) 7.90
B (dddt) 7.17
C (m) 7.10
D (td) 6.91
E (ddd) 5.95
F (dt) 5.31
G (dt) 5.23
H (s) 4.78
I (dddt) 4.67
J (ddt) 3.52
K (qdd) 3.33
L (dd) 2.85
M (t) 1.16
1.56 H2O
f1 (ppm)

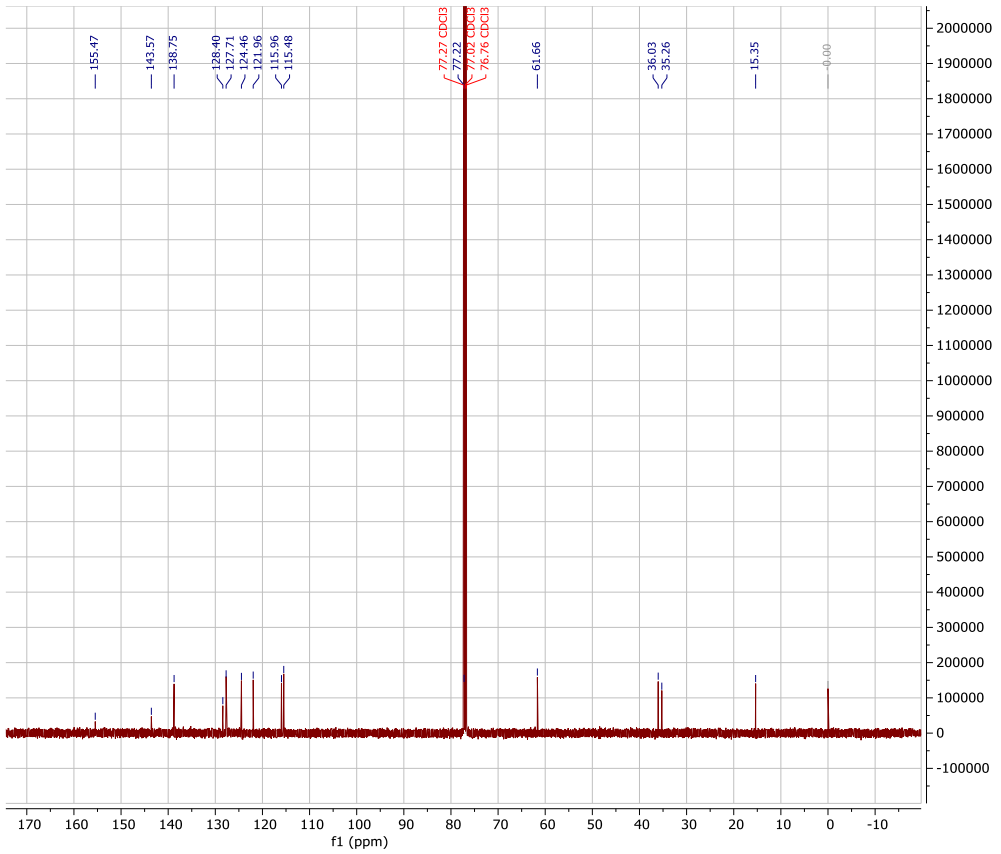
155.47
143.57
138.75
128.40
127.71
124.46
121.96
115.96
115.48
77.27 CDCl3
77.22
77.02 CDCl3
76.76 CDCl3
61.66
36.03
35.26
15.35
f1 (ppm)

§

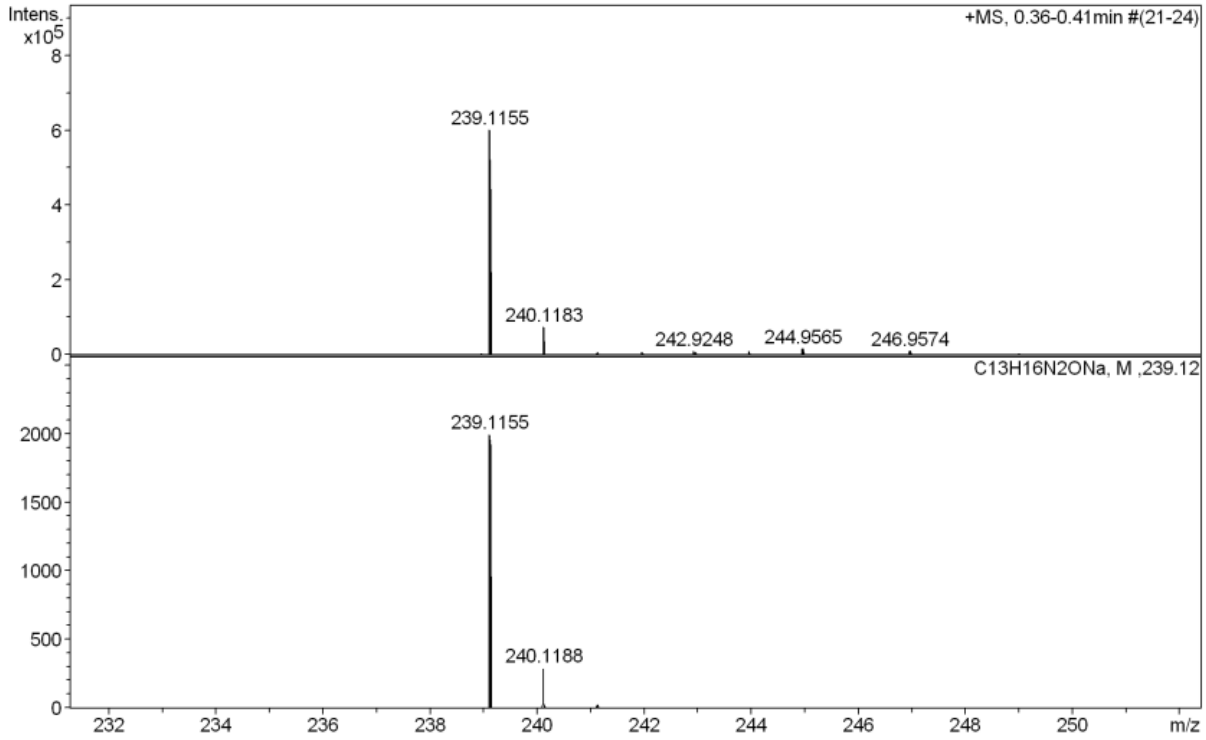

Measured m/z vs. theoretical m/z

Meas. m/z	#	Formula	Score	m/z	err [mDa]	err [ppm]	mSigma	rdb	e¯ Conf	z
217.1332	1	C 13 H 17 N 2 O	100.00	217.1335	0.3	1.5	6.0	6.5	even	1+
239.1155	1	C 13 H 16 N 2 Na O	100.00	239.1155	0.0	0.1	12.9	6.5	even	
455.2410	1	C 26 H 32 N 4 Na O 2	100.00	455.2417	0.7	1.6	12.0	12.5	even	

4-iPr

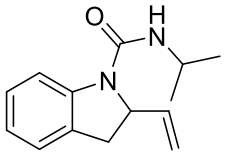

Exact Mass: 230,14
m/z: 230.14 (100.0%), 231.15 (15.4%), 232.15 (1.3%)

§

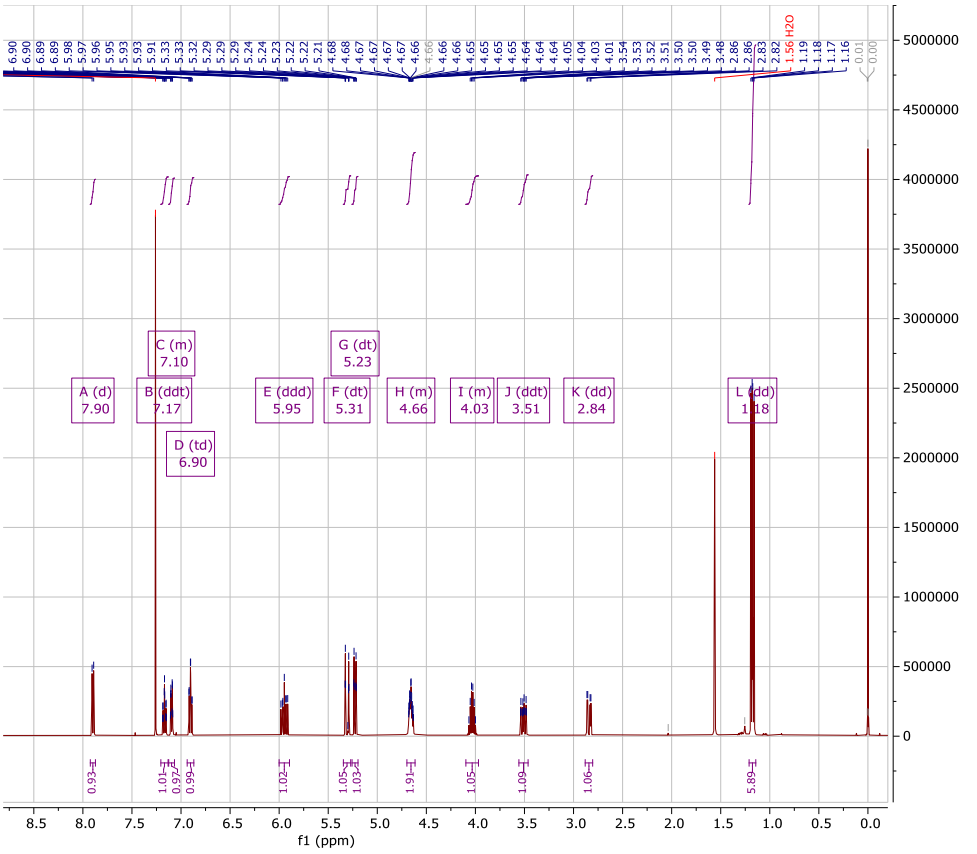
A (d) 7.90
B (ddt) 7.17
C (m) 7.10
D (td) 6.90
E (ddd) 5.95
F (dt) 5.31
G (dt) 5.23
H (m) 4.66
I (m) 4.03
J (ddt) 3.51
K (dd) 2.84
L (dd) 1.18
1.56 H2O
f1 (ppm)

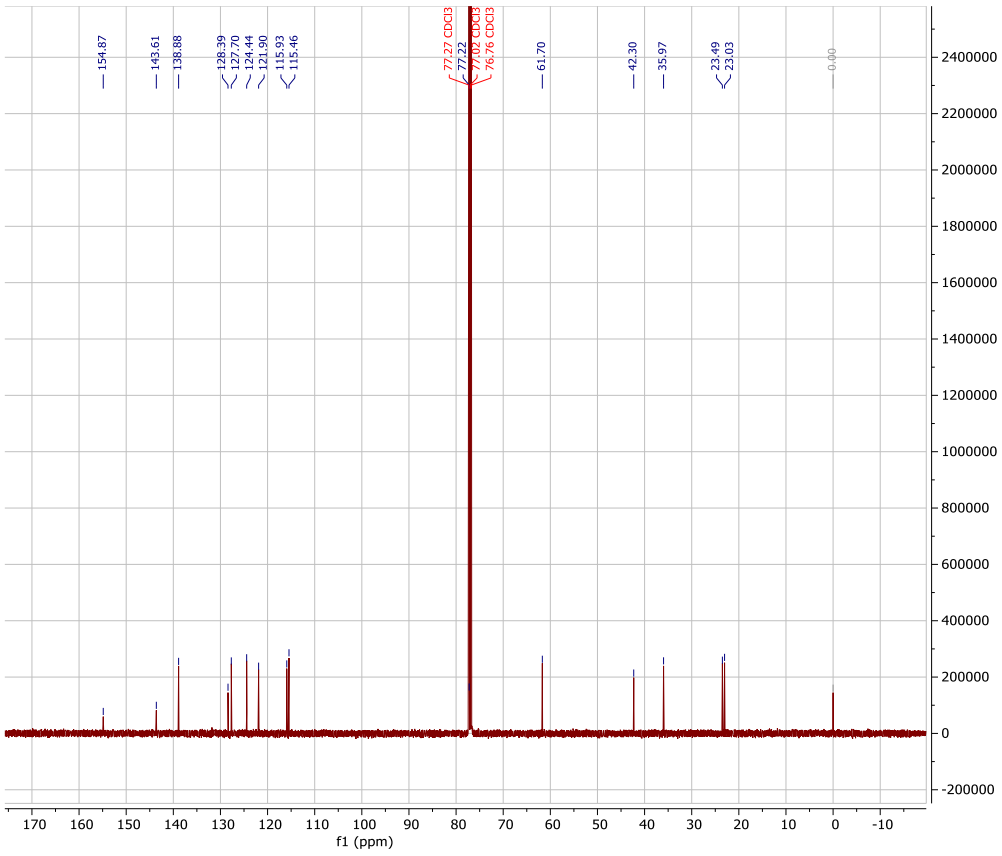
154.87
143.61
138.88
128.39
127.70
124.44
121.90
115.93
115.46
77.27 CDCl3
77.22
77.02 CDCl3
76.76 CDCl3
61.70
42.30
35.97
23.49
23.03
f1 (ppm)

§

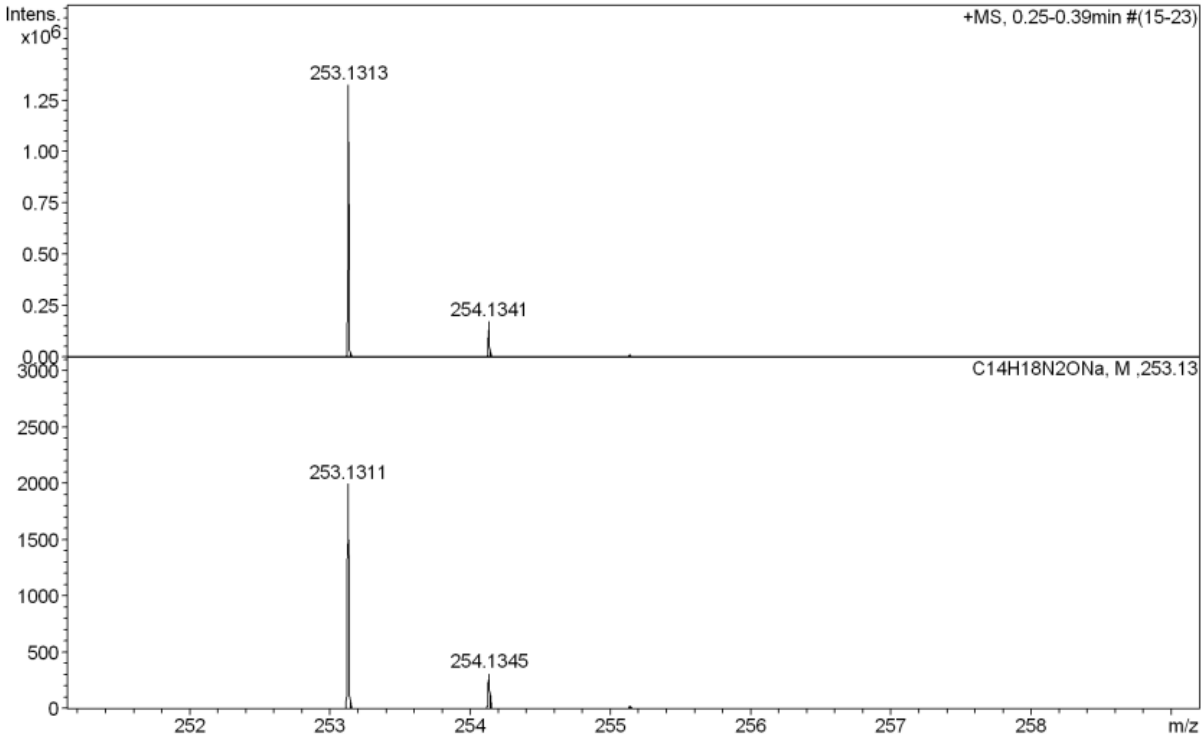

Measured m/z vs. theoretical m/z

Meas. m/z	#	Formula	Score	m/z	err [mDa]	err [ppm]	mSigma	rdb	e¯ Conf	z
231.1491	1	C 14 H 19 N 2 O	100.00	231.1492	0.1	0.5	12.4	6.5	even	1+
253.1313	1	C 14 H 18 N 2 Na O	100.00	253.1311	-0.2	-0.8	15.3	6.5	even	
483.2726	1	C 28 H 36 N 4 Na O 2	100.00	483.2730	0.4	0.9	7.2	12.5	even	

4-tBu

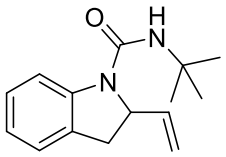

Exact Mass: 244,16
m/z: 244.16 (100.0%), 245.16 (16.5%), 246.16 (1.6%)

§

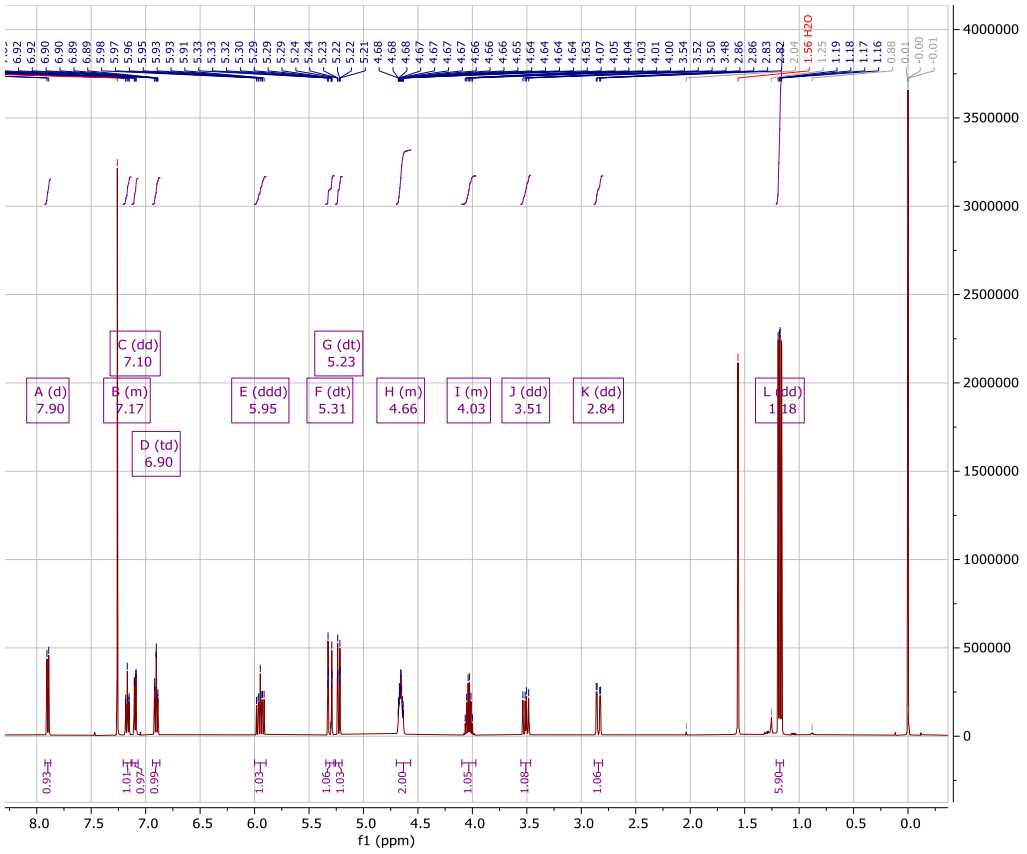
A (d) 7.90
B (m) 7.17
C (dd) 7.10
D (td) 6.90
E (ddd) 5.95
F (dt) 5.31
G (dt) 5.23
H (m) 4.66
I (m) 4.03
J (dd) 3.51
K (dd) 2.84
L (dd) 1.18
1.56 H2O
f1 (ppm)

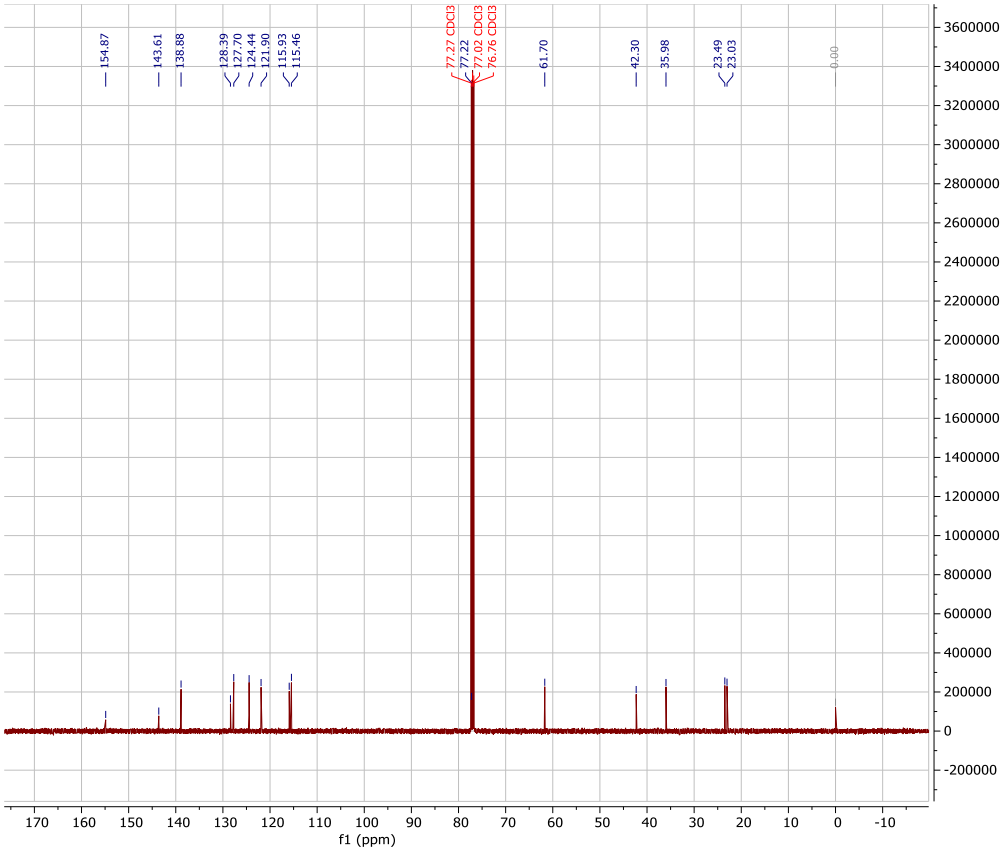
154.87
143.61
138.88
128.39
127.70
124.44
121.90
115.93
115.46
77.27 CDCl3
77.22
77.02 CDCl3
76.76 CDCl3
61.70
42.30
35.98
23.49
23.03
0.00
f1 (ppm)

§

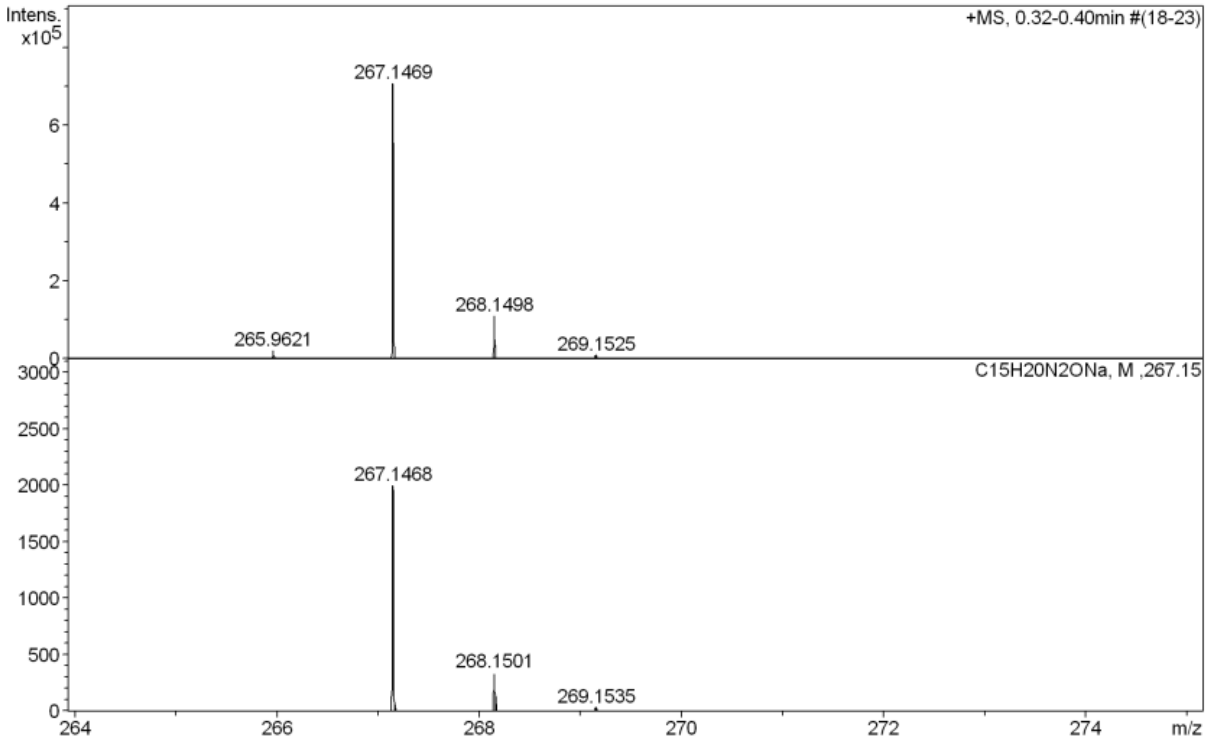

Measured m/z vs. theoretical m/z

Meas. m/z	#	Formula	Score	m/z	err [mDa]	err [ppm]	mSigma	rdb	e⁻ Conf	z
245.1651	1	C 15 H 21 N 2 O	100.00	245.1648	-0.2	-0.9	11.4	6.5	even	1+
267.1469	1	C 15 H 20 N 2 Na O	100.00	267.1468	-0.1	-0.5	7.7	6.5	even	
283.1202	1	C 15 H 20 K N 2 O	100.00	283.1207	0.6	2.0	95.2	6.5	even	
511.3039	1	C 30 H 40 N 4 Na O 2	100.00	511.3043	0.5	0.9	8.5	12.5	even	

4-nPr

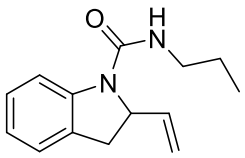

Exact Mass: 230,14
m/z: 230.14 (100.0%), 231.15 (15.4%), 232.15 (1.3%)

§

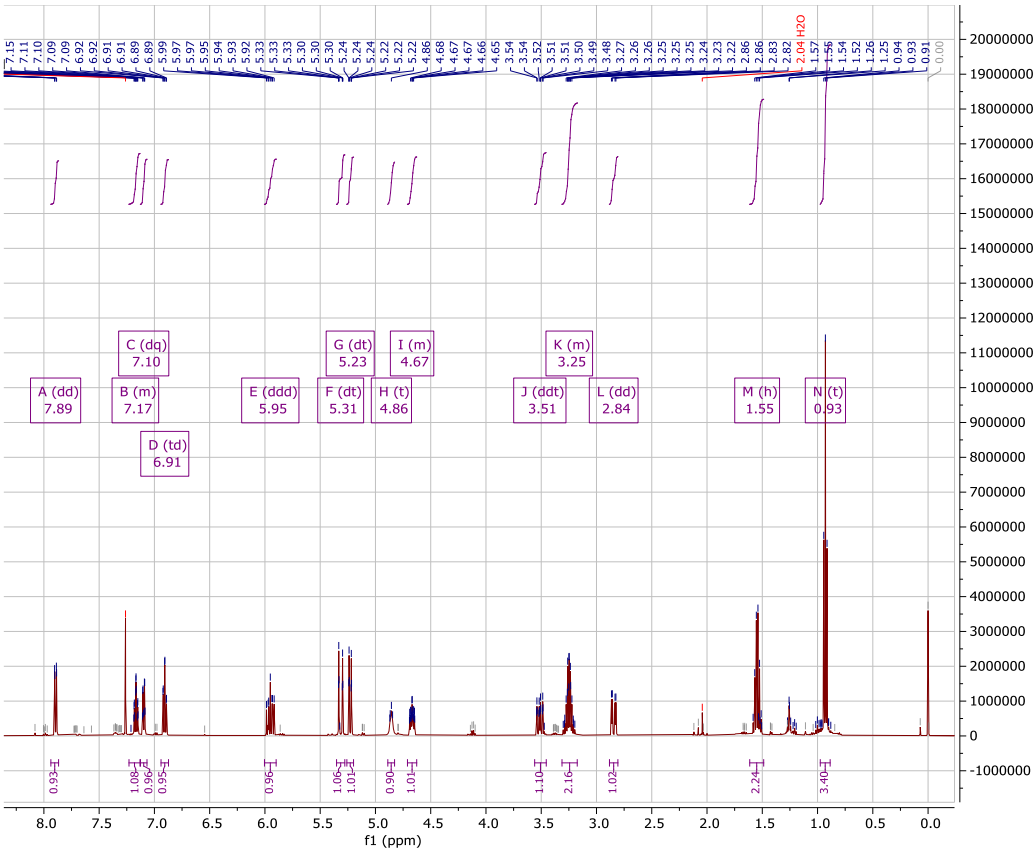
A (dd) 7.89
B (m) 7.17
C (dq) 7.10
D (td) 6.91
E (ddd) 5.95
F (dt) 5.31
G (dt) 5.23
H (t) 4.86
I (m) 4.67
J (ddt) 3.51
K (m) 3.25
L (dd) 2.84
M (h) 1.55
N (t) 0.93
2.04 H2O
f1 (ppm)

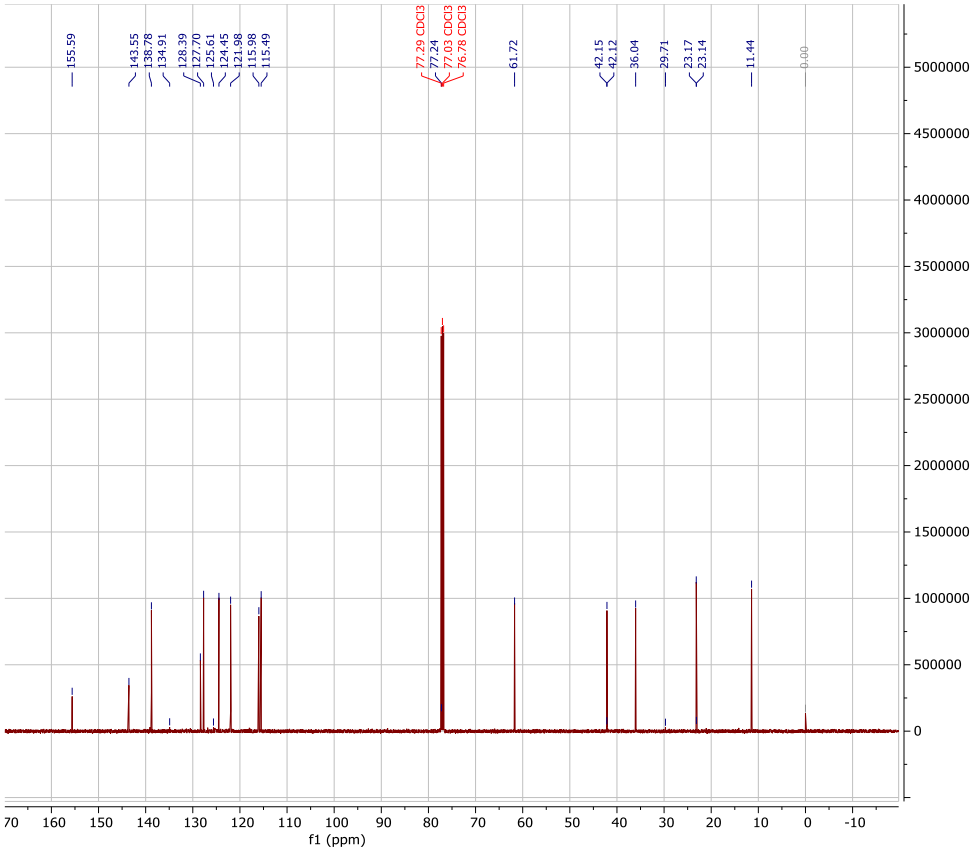
155.59
143.55
138.78
134.91
128.39
127.70
125.61
124.45
121.98
115.98
115.49
77.29 CDCl3
77.24
77.03 CDCl3
76.78 CDCl3
61.72
42.15
42.12
36.04
29.71
23.17
23.14
11.44
f1 (ppm)

§

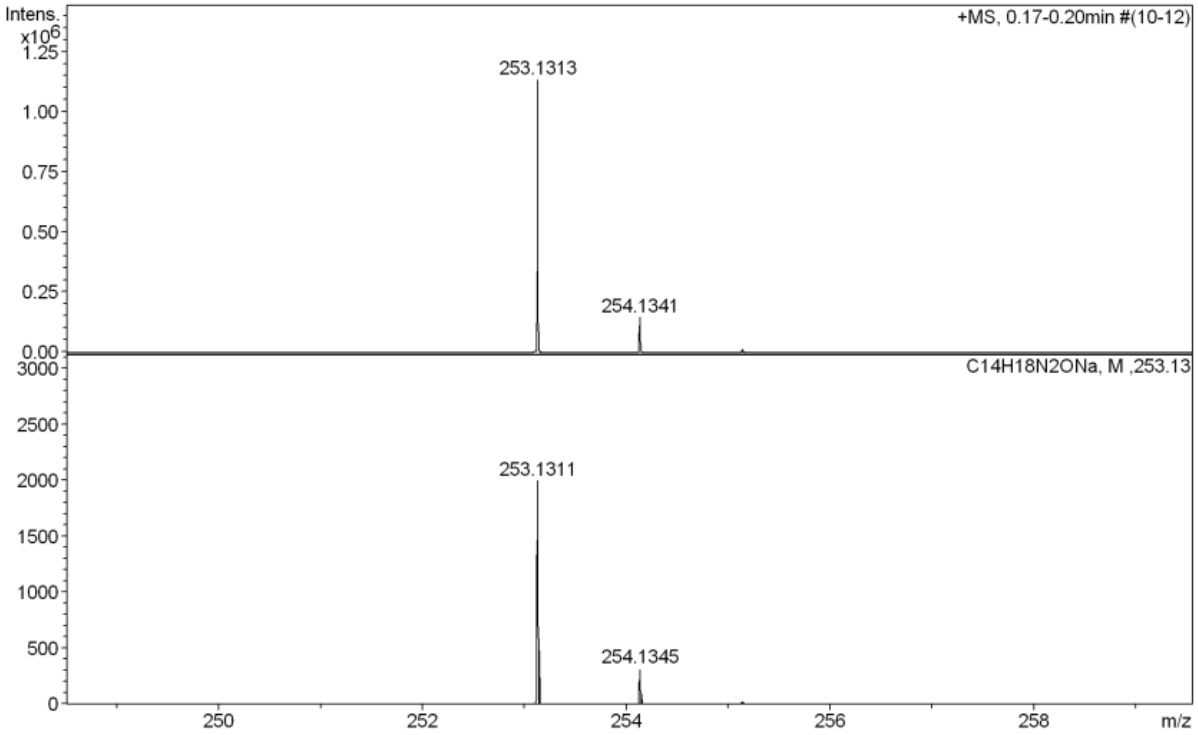

Measured m/z vs. theoretical m/z

Meas. m/z	#	Formula	Score	m/z	err [mDa]	err [ppm]	mSigma	rdb	e⁻ Conf	z
231.1491	1	C 14 H 19 N 2 O	100.00	231.1492	0.0	0.2	11.5	6.5	even	1+
253.1313	1	C 14 H 18 N 2 Na O	100.00	253.1311	-0.2	-0.8	16.9	6.5	even	
269.1049	1	C 14 H 18 K N 2 O	100.00	269.1051	0.2	0.7	90.0	6.5	even	
483.2728	1	C 28 H 36 N 4 Na O 2	100.00	483.2730	0.3	0.6	12.1	12.5	even	

4-nBu

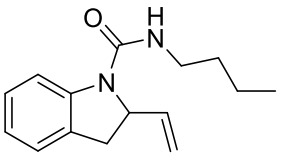

Exact Mass: 244,16
m/z: 244.16 (100.0%), 245.16 (16.5%), 246.16 (1.6%)

§

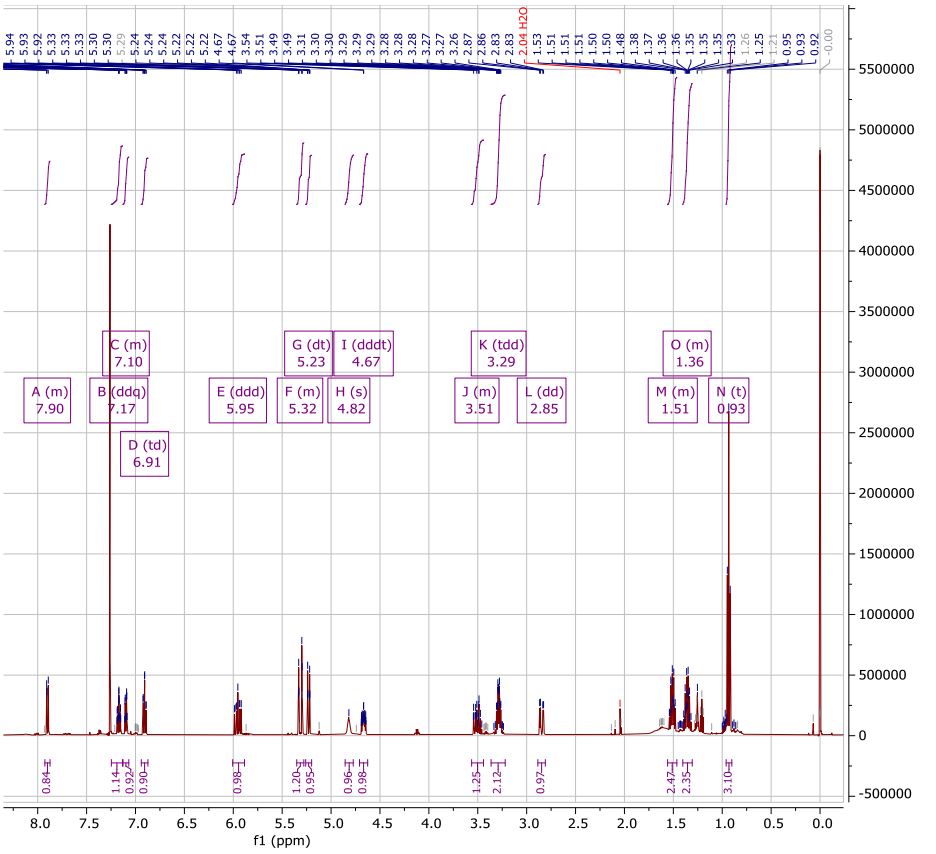
A (m) 7.90
B (ddq) 7.17
C (m) 7.10
D (td) 6.91
E (ddd) 5.95
F (m) 5.32
G (dt) 5.23
H (s) 4.82
I (dddt) 4.67
J (m) 3.51
K (tdd) 3.29
L (dd) 2.85
M (m) 1.51
N (t) 0.93
O (m) 1.36
f1 (ppm)

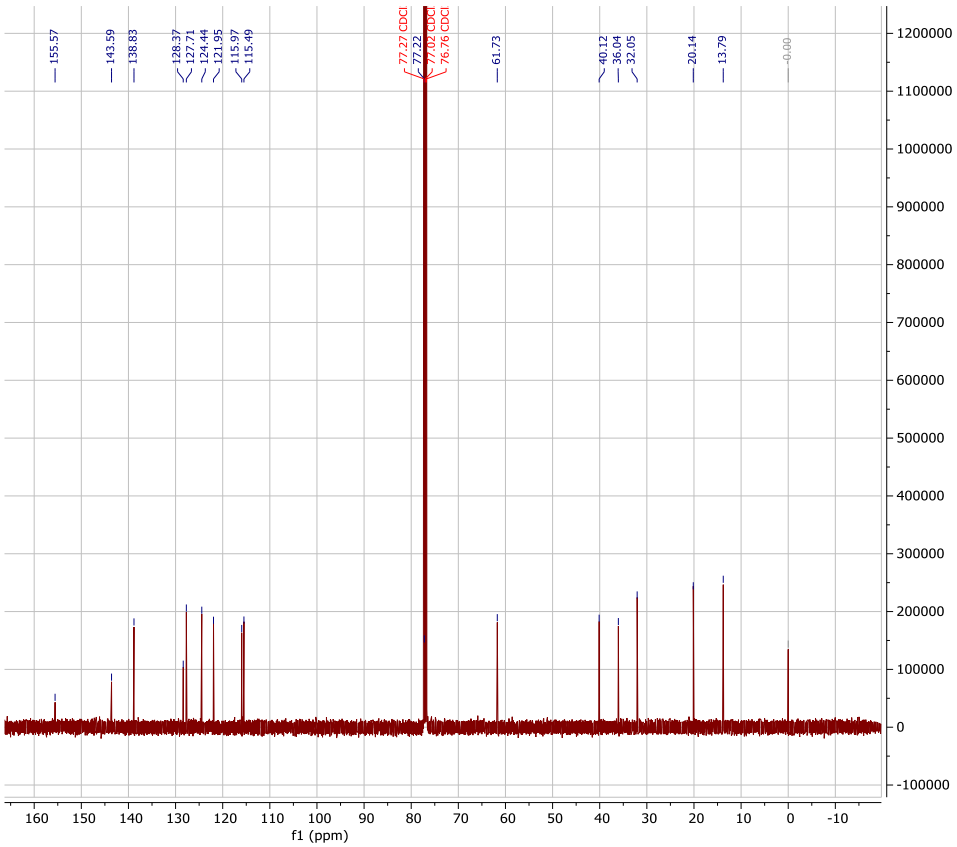
155.57
143.59
138.83
128.37
127.71
124.44
121.95
115.97
115.49
77.27 CDCl
77.22
77.02 CDCl
76.76 CDCl
61.73
40.12
36.04
32.05
20.14
13.79
f1 (ppm)

§

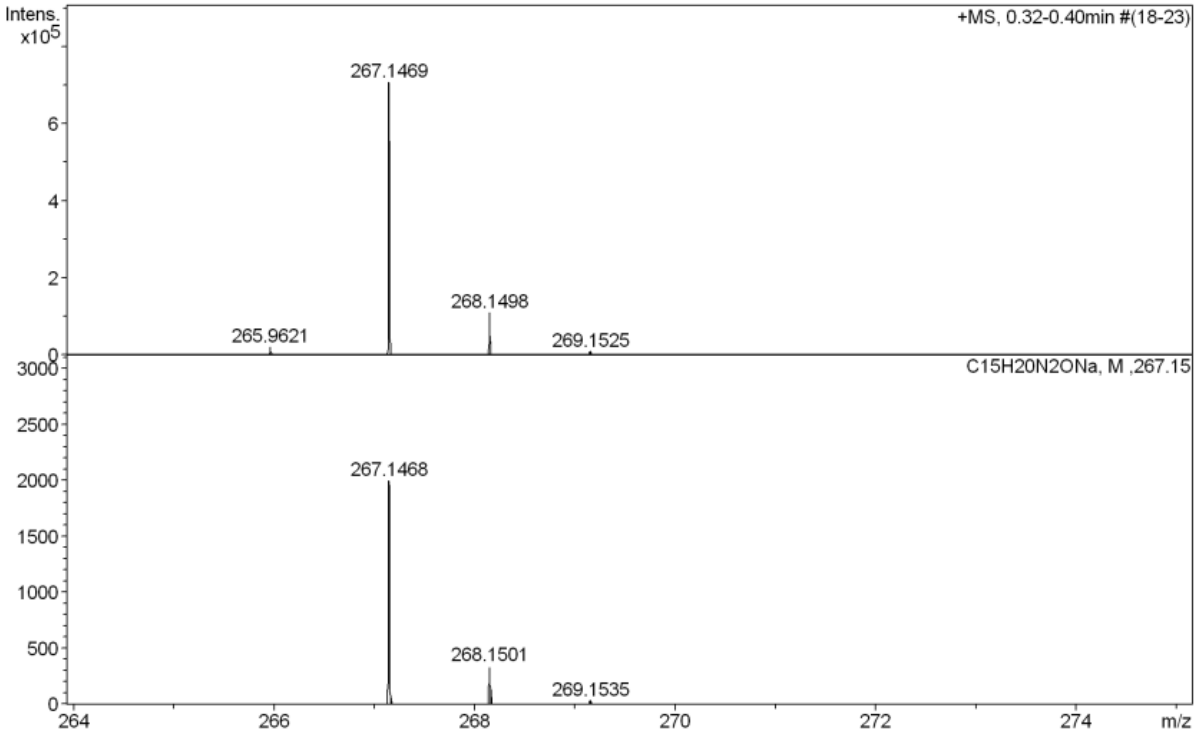

Measured m/z vs. theoretical m/z

Meas. m/z	#	Formula	Score	m/z	err [mDa]	err [ppm]	mSigma	rdb	e⁻ Conf	z
245.1651	1	C 15 H 21 N 2 O	100.00	245.1648	-0.2	-0.9	11.4	6.5	even	1+
267.1469	1	C 15 H 20 N 2 Na O	100.00	267.1468	-0.1	-0.5	7.7	6.5	even	
283.1202	1	C 15 H 20 K N 2 O	100.00	283.1207	0.6	2.0	95.2	6.5	even	
511.3039	1	C 30 H 40 N 4 Na O 2	100.00	511.3043	0.5	0.9	8.5	12.5	even	

§

Chapter 6: Outlook

This thesis presented some applications and limitations encountered using this CpRu-based catalytic system. Solutions were found to circumvent some of these limitations via substrate design or using an anaerobic environment to perform the catalysis. Nevertheless, these solutions drastically narrow the potential application of these catalytic systems. This thesis aimed to develop an artificial allylic aminase for *in vivo* purposes. In Chapter 5, *via* substrate design, the reaction was shown to proceed in cell lysate.

Nevertheless, the transformation efficiency observed was so low that *in vivo* applications would present even more problems. Artificial metalloenzymes improved the stability and, thus, the system's activity but could not render the process efficient enough for further *in vivo* development. Therefore, the author believes that this field's fate resides in a catalyst design campaign that will be better suited for *in vivo* purposes. Specifically, catalysts must be designed with much-increased air and thiol resilience and low cytotoxicity.

§

Chapter 7: References

(1) Serrano-Becerra, J. M.; Morales-Morales, D. *Applications in Catalysis and Organic Transformations Mediated by Platinum Group PCP and PNP Aromatic-Based Pincer Complexes: Recent Advances*; 2009; Vol. 6.

(2) Zhao, K.; Shen, L.; Shen, Z. L.; Loh, T. P. Transition Metal-Catalyzed Cross-Coupling Reactions Using Organoindium Reagents. *Chemical Society Reviews*. Royal Society of Chemistry February 7, 2017, pp 586–602. https://doi.org/10.1039/c6cs00465b.

(3) Cherney, A. H.; Kadunce, N. T.; Reisman, S. E. Enantioselective and Enantiospecific Transition-Metal-Catalyzed Cross-Coupling Reactions of Organometallic Reagents to Construct C-C Bonds. *Chemical Reviews*. American Chemical Society September 9, 2015, pp 9587–9652. https://doi.org/10.1021/acs.chemrev.5b00162.

(4) Lennox, A. J. J.; Lloyd-Jones, G. C. Selection of Boron Reagents for Suzuki-Miyaura Coupling. *Chemical Society Reviews*. Royal Society of Chemistry January 7, 2014, pp 412–443. https://doi.org/10.1039/c3cs60197h.

(5) Nakashima, Y.; Hirata, G.; Sheppard, T. D.; Nishikata, T. The Mizoroki-Heck Reaction with Internal Olefins: Reactivities and Stereoselectivities. *Asian Journal of Organic Chemistry*. Wiley-VCH Verlag April 1, 2020, pp 480–491. https://doi.org/10.1002/ajoc.201900741.

(6) Phapale, V. B.; Cárdenas, D. J. Nickel-Catalysed Negishi Cross-Coupling Reactions: Scope and Mechanisms. *Chem Soc Rev* **2009**, *38* (6), 1598–1607. https://doi.org/10.1039/b805648j.

(7) Wang, D.; Gao, S. Sonogashira Coupling in Natural Product Synthesis. *Organic Chemistry Frontiers*. Royal Society of Chemistry July 1, 2014, pp 556–566. https://doi.org/10.1039/c3qo00086a.

(8) Heravi, M. M.; Zadsirjan, V.; Hajiabbasi, P.; Hamidi, H. Advances in Kumada–Tamao–Corriu Cross-Coupling Reaction: An Update. *Monatshefte fur Chemie*. Springer-Verlag Wien April 4, 2019, pp 535–591. https://doi.org/10.1007/s00706-019-2364-6.

(9) Cordovilla, C.; Bartolomé, C.; Martínez-Ilarduya, J. M.; Espinet, P. The Stille Reaction, 38 Years Later. *ACS Catalysis*. American Chemical Society May 1, 2015, pp 3040–3053. https://doi.org/10.1021/acscatal.5b00448.

(10) Negishi, E.; Meijere, A. de; Jiro Tsuji; Negishi, E.; Meijere, A. de. *Handbook of Organopalladium Chemistry for Organic Synthesis*.

(11) Heravi, M. M.; Kheilkordi, Z.; Zadsirjan, V.; Heydari, M.; Malmir, M. Buchwald-Hartwig Reaction: An Overview. *Journal of Organometallic Chemistry*. Elsevier B.V. April 15, 2018, pp 17–104. https://doi.org/10.1016/j.jorganchem.2018.02.023.

(12) Lin, H.; Sun, D. Recent Synthetic Developments and Applications of the Ullmann Reaction. a Review. *Organic Preparations and Procedures International*. Taylor and Francis Inc. September 3, 2013, pp 341–394. https://doi.org/10.1080/00304948.2013.816208.

(13) Besset, T.; Poisson, T.; Pannecoucke, X. Access to Difluoromethylated Alkynes through the Castro-Stephens Reaction. *European J Org Chem* **2014**, *2014* (32), 7220–7225. https://doi.org/10.1002/ejoc.201402937.

§

(14) Sindhu, K. S.; Anilkumar, G. Recent Advances and Applications of Glaser Coupling Employing Greener Protocols. *RSC Advances*. Royal Society of Chemistry 2014, pp 27867–27887. https://doi.org/10.1039/c4ra02416h.

(15) Foubelo, F.; Nájera, C.; Yus, M. The Hiyama Cross-Coupling Reaction: New Discoveries. *Chemical Record* **2016**, *16* (6), 2521–2533. https://doi.org/10.1002/tcr.201600063.

(16) Sikandar, S.; Zahoor, A. F.; Naheed, S.; Parveen, B.; Ali, K. G.; Akhtar, R. Fukuyama Reduction, Fukuyama Coupling and Fukuyama–Mitsunobu Alkylation: Recent Developments and Synthetic Applications. *Molecular Diversity*. Springer Science and Business Media Deutschland GmbH February 1, 2022, pp 589–628. https://doi.org/10.1007/s11030-021-10194-7.

(17) Sindhu, K. S.; Thankachan, A. P.; Sajitha, P. S.; Anilkumar, G. Recent Developments and Applications of the Cadiot-Chodkiewicz Reaction. *Organic and Biomolecular Chemistry*. Royal Society of Chemistry July 7, 2015, pp 6891–6905. https://doi.org/10.1039/c5ob00697j.

(18) Jablonkai, E.; Keglevich, G. Advances and New Variations of the Hirao Reaction. *Organic Preparations and Procedures International*. Taylor and Francis Inc. July 4, 2014, pp 281–316. https://doi.org/10.1080/00304948.2014.922376.

(19) Johnson. JOHNSON MATTHEY TECHNOLOGY REVIEW SPECIAL ISSUE 12 “PALLADIUM CATALYSED CROSS-COUPLING-PRACTICAL ASPECTS” APRIL 2017. **2017**.

(20) Streu, C.; Meggers, E. Ruthenium-Induced Allylcarbamate Cleavage in Living Cells. *Angewandte Chemie - International Edition* **2006**, *45* (34), 5645–5648. https://doi.org/10.1002/anie.200601752.

(21) Völker, T.; Meggers, E. Chemical Activation in Blood Serum and Human Cell Culture: Improved Ruthenium Complex for Catalytic Uncaging of Alloc-Protected Amines. *ChemBioChem* **2017**, *18* (12), 1083–1086. https://doi.org/10.1002/cbic.201700168.

(22) Völker, T.; Dempwolff, F.; Graumann, P. L.; Meggers, E. Progress towards Bioorthogonal Catalysis with Organometallic Compounds. *Angew Chem Int Ed Engl* **2014**, *53* (39), 10536–10540. https://doi.org/10.1002/anie.201404547.

(23) Tsuji, J.; Takahashi, H.; Morikawa, M. *ORGANIC SYNTHESES BY BEANS OF NOBLEMETALCOMPOUNDS XVII. BEACTION OF h-ALLYLPALLADIUM CBLORIDE WITH NUCLEOPHILES’*; Pergamon Press Ltd, 1965.

(24) Hata, G.; Takahashi, K.; Miyake, A. *Palladium-Catalgsed Exchange of Allylic Groups of Ethers and Esters with Active-Hydrogen Compounds*; 1970.

(25) Atkins, K. E.; Walker, W. E.; Manyik, R. M. *PALLADIUM CATALYZED TRANSFER OF ALLYLIC GROUPS*; 1970; Vol. 43.

(26) BM Trost, T. F. *New Synthetic Reactions. AllylicAlkylation*; 1973; Vol. 94. https://pubs.acs.org/sharingguidelines.

(27) Jiro Tsuji, I. S. I. M. Y. O. T. S. and K. T. *Allylic Carbonates. Efficient Allylating Agents of Carbonucleophiles in Palladium-Catalyzed Reactions under Neutra LConditions*; Springer-Verlag: Berlin, 1985; Vol. 50. https://pubs.acs.org/sharingguidelines.

§

(28) Ryo Takeuchi* and Mikihiro Kashio. *Highly Selective Allylic Alkylation with a Carbon Nucleophile at the More Substituted Allylic Terminus Catalyzed by an Iridium Complex: An Efficient Method for Constructing Quaternary Carbon Centers***; 1997.

(29) Ichiro Minami, I. S. J. T. *REACTIONS OF ALLYLIC CARBONATES CATALYZED BY PALLADIUM, RHODIUM, RUTHENIUM, MOLYBDENUM, AND NICKEL COMPLEXES; ALLYLATION OF CARBONUCLEOPHILES AND DECARBOXYLATION-DEHYDROGENATION * ICHIRO MINAMI, ISA0 SHIMIZU, and JIRO TSUJI l*; 1985.

(30) Green, M. L. H.; Nagmhima, H.; Ohshima, K.; Itoh, K. *Solvated Trlorganotln Catlons. Structure and Use as Catalysts for Dlels-Alder Addltlons to Furan*; 1984; Vol. 3.

(31) Soldevila-Barreda, J. J.; Romero-Canelón, I.; Habtemariam, A.; Sadler, P. J. Transfer Hydrogenation Catalysis in Cells as a New Approach to Anticancer Drug Design. *Nat Commun* **2015**, *6*. https://doi.org/10.1038/ncomms7582.

(32) Chen, F.; Romero-Canelón, I.; Soldevila-Barreda, J. J.; Song, J. I.; Coverdale, J. P. C.; Clarkson, G. J.; Kasparkova, J.; Habtemariam, A.; Wills, M.; Brabec, V.; Sadler, P. J. Transfer Hydrogenation and Antiproliferative Activity of Tethered Half-Sandwich Organoruthenium Catalysts. *Organometallics* **2018**, *37* (10), 1555–1566. https://doi.org/10.1021/acs.organomet.8b00132.

(33) Chen, F.; Soldevila-Barreda, J. J.; Romero-Canelón, I.; Coverdale, J. P. C.; Song, J. I.; Clarkson, G. J.; Kasparkova, J.; Habtemariam, A.; Brabec, V.; Wolny, J. A.; Schünemann, V.; Sadler, P. J. Effect of Sulfonamidoethylenediamine Substituents in RuII Arene Anticancer Catalysts on Transfer Hydrogenation of Coenzyme NAD+ by Formate. *Dalton Transactions* **2018**, *47* (21), 7178–7189. https://doi.org/10.1039/c8dt00438b.

(34) Bruneau, C.; Renaud, J. L.; Demerseman, B. Ruthenium Catalysts for Selective Nucleophilic Allylic Substitution. In *Pure and Applied Chemistry*; 2008; Vol. 80, pp 861–871. https://doi.org/10.1351/pac200880050861.

(35) Bosquain, S. S.; Dorcier, A.; Dyson, P. J.; Erlandsson, M.; Gonsalvi, L.; Laurenczy, G.; Peruzzini, M. Aqueous Phase Carbon Dioxide and Bicarbonate Hydrogenation Catalyzed by Cyclopentadienyl Ruthenium Complexes. *Appl Organomet Chem* **2007**, *21* (11), 947–951. https://doi.org/10.1002/aoc.1317.

(36) Kumar, P.; Gupta, R. K.; Pandey, D. S. Half-Sandwich Arene Ruthenium Complexes: Synthetic Strategies and Relevance in Catalysis. *Chemical Society Reviews*. Royal Society of Chemistry January 21, 2014, pp 707–733. https://doi.org/10.1039/c3cs60189g.

(37) Hsu, H. T.; Trantow, B. M.; Waymouth, R. M.; Wender, P. A. Bioorthogonal Catalysis: A General Method to Evaluate Metal-Catalyzed Reactions in Real Time in Living Systems Using a Cellular Luciferase Reporter System. *Bioconjug Chem* **2016**, *27* (2), 376–382. https://doi.org/10.1021/acs.bioconjchem.5b00469.

(38) Kamo, N.; Kujirai, T.; Kurumizaka, H.; Murakami, H.; Hayashi, G.; Okamoto, A. Organoruthenium-Catalyzed Chemical Protein Synthesis to Elucidate the Functions of Epigenetic Modifications on Heterochromatin Factors. *Chem Sci* **2021**, *12* (16), 5926–5937. https://doi.org/10.1039/d1sc00731a.

(39) Madec, H.; Figueiredo, F.; Cariou, K.; Roland, S.; Sollogoub, M.; Gasser, G. Metal Complexes for Catalytic and Photocatalytic Reactions in Living Cells and Organisms. *Chem Sci* **2022**. https://doi.org/10.1039/d2sc05672k.

§

(40) Tanaka, S.; Saburi, H.; Ishibashi, Y.; Kitamura, M. CpRuIIPF6/Quinaldic Acid-Catalyzed Chemoselective Allyl Ether Cleavage. A Simple and Practical Method for Hydroxyl Deprotection. *Org Lett* **2004**, *6* (11), 1873–1875. https://doi.org/10.1021/ol0493397.

(41) Völker, T.; Dempwolff, F.; Graumann, P. L.; Meggers, E. Progress towards Bioorthogonal Catalysis with Organometallic Compounds. *Angew Chem Int Ed Engl* **2014**, *53* (39), 10536–10540. https://doi.org/10.1002/anie.201404547.

(42) Yong-Kie Wonga, D.; Hsiaoa, Y.-L.; Poona, C.-K.; Kwanb, P.-C.; Chao, S.-Y.; Choud, S.-T.; Yang, C.-S. *CANCER LETTERS Glutathione Concentration in Oral Cancer Tissues*; 1994; Vol. 8.

(43) GSH Roles in Cells.

(44) Tanaka, S.; Saburi, H.; Hirakawa, T.; Seki, T.; Kitamura, M. Dehydrative Allylation of Alcohols and Deallylation of Allyl Ethers Catalyzed by [CpRu(CH 3CN) 3]PF 6 and 2-Pyridinecarboxylie Aeid Derivatives. Effect of π-Accepting Ability and COOH Acidity of Ligand on Reactivity. *Chem Lett* **2009**, *38* (2), 188–189. https://doi.org/10.1246/cl.2009.188.

(45) Saburi, H.; Tanaka, S.; Kitamura, M. Catalytic Dehydrative Allylation of Alcohols. *Angewandte Chemie - International Edition* **2005**, *44* (11), 1730–1732. https://doi.org/10.1002/anie.200462513.

(46) Tanaka, S.; Saburi, H.; Murase, T.; Yoshimura, M.; Kitamura, M. Catalytic Removal of N-Allyloxycarbonyl Groups Using the [CpRu(IV)(π-C3H5)(2-Quinolinecarboxylato)]PF 6 Complex. A New Efficient Deprotecting Method in Peptide Synthesis. *Journal of Organic Chemistry* **2006**, *71* (12), 4682–4684. https://doi.org/10.1021/jo060445r.

(47) Tanaka, S.; Seki, T.; Kitamura, M. Asymmetrie Dehydrative Cyclization of ω-Hydroxy Allyl Alcohols Catalyzed by Ruthenium Complexes. *Angewandte Chemie - International Edition* **2009**, *48* (47), 8948–8951. https://doi.org/10.1002/anie.200904671.

(48) Tanaka, S.; Pradhan, P. K.; Maegawa, Y.; Kitamura, M. Highly Efficient Catalytic Dehydrative S-Allylation of Thiols and Thioic S-Acids. *Chemical Communications* **2010**, *46* (22), 3996–3998. https://doi.org/10.1039/c0cc00096e.

(49) Völker, T.; Meggers, E. Chemical Activation in Blood Serum and Human Cell Culture: Improved Ruthenium Complex for Catalytic Uncaging of Alloc-Protected Amines. *ChemBioChem* **2017**, *18* (12), 1083–1086. https://doi.org/10.1002/cbic.201700168.

(50) Mancuso, F.; Rahm, M.; Dzijak, R.; Mertlíková-Kaiserová, H.; Vrabel, M. Transition-Metal-Mediated versus Tetrazine-Triggered Bioorthogonal Release Reactions: Direct Comparison and Combinations Thereof. *Chempluschem* **2020**, *85* (8), 1669–1675. https://doi.org/10.1002/cplu.202000477.

(51) Hsu, H. T.; Trantow, B. M.; Waymouth, R. M.; Wender, P. A. Bioorthogonal Catalysis: A General Method to Evaluate Metal-Catalyzed Reactions in Real Time in Living Systems Using a Cellular Luciferase Reporter System. *Bioconjug Chem* **2016**, *27* (2), 376–382. https://doi.org/10.1021/acs.bioconjchem.5b00469.

(52) Rubini, R.; Ivanov, I.; Mayer, C. A Screening Platform to Identify and Tailor Biocompatible Small-Molecule Catalysts. *Chemistry - A European Journal* **2019**, *25* (70), 16017–16021. https://doi.org/10.1002/chem.201904808.

§

(53) Lee, Y.; Umeano, A.; Balskus, E. P. Rescuing Auxotrophic Microorganisms with Nonenzymatic Chemistry. *Angewandte Chemie - International Edition* **2013**, *52* (45), 11800–11803. https://doi.org/10.1002/anie.201307033.

(54) Rubini, R.; Mayer, C. Addicting Escherichia Coli to New-to-Nature Reactions. *ACS Chem Biol* **2020**, *15* (12), 3093–3098. https://doi.org/10.1021/acschembio.0c00713.

(55) Sánchez, M. I.; Penas, C.; Vázquez, M. E.; Mascareñas, J. L. Metal-Catalyzed Uncaging of DNA-Binding Agents in Living Cells. *Chem Sci* **2014**, *5* (5), 1901–1907. https://doi.org/10.1039/c3sc53317d.

(56) Tomás-Gamasa, M.; Martínez-Calvo, M.; Couceiro, J. R.; Mascarenãs, J. L. Transition Metal Catalysis in the Mitochondria of Living Cells. *Nat Commun* **2016**, *7*. https://doi.org/10.1038/ncomms12538.

(57) Vidal, C.; Tomás-Gamasa, M.; Destito, P.; López, F.; Mascareñas, J. L. Concurrent and Orthogonal Gold(I) and Ruthenium(II) Catalysis inside Living Cells. *Nat Commun* **2018**, *9* (1). https://doi.org/10.1038/s41467-018-04314-5.

(58) Tomás-Gamasa, M.; Martínez-Calvo, M.; Couceiro, J. R.; Mascarenãs, J. L. Transition Metal Catalysis in the Mitochondria of Living Cells. *Nat Commun* **2016**, *7*. https://doi.org/10.1038/ncomms12538.

(59) Vidal, C.; Tomás-Gamasa, M.; Destito, P.; López, F.; Mascareñas, J. L. Concurrent and Orthogonal Gold(I) and Ruthenium(II) Catalysis inside Living Cells. *Nat Commun* **2018**, *9* (1), 1–9. https://doi.org/10.1038/s41467-018-04314-5.

(60) Southwell, J.; Herman, R.; Raines, D.; Clarke, J.; Boeswald, I.; Dreher, T.; Gutenthaler, S.; Schubert, N.; Seefeldt, J.; Metzler-Nolte, N.; Thomas, G.; Wilson, K.; Duhme-Klair, A.-K. Siderophore-linked Ruthenium Catalysts for Targeted Allyl Ester Prodrug Activation within Bacterial Cells. *Chemistry – A European Journal* **2022**. https://doi.org/10.1002/chem.202202536.

(61) Heinisch, T.; Schwizer, F.; Garabedian, B.; Csibra, E.; Jeschek, M.; Vallapurackal, J.; Pinheiro, V. B.; Marlière, P.; Panke, S.; Ward, T. R. E. Coli Surface Display of Streptavidin for Directed Evolution of an Allylic Deallylase. *Chem Sci* **2018**, *9* (24), 5383–5388. https://doi.org/10.1039/c8sc00484f.

(62) Okamoto, Y.; Kojima, R.; Schwizer, F.; Bartolami, E.; Heinisch, T.; Matile, S.; Fussenegger, M.; Ward, T. R. A Cell-Penetrating Artificial Metalloenzyme Regulates a Gene Switch in a Designer Mammalian Cell. *Nat Commun* **2018**, *9* (1). https://doi.org/10.1038/s41467-018-04440-0.

(63) Cheng, Y.; Zong, L.; López-Andarias, J.; Bartolami, E.; Okamoto, Y.; Ward, T. R.; Sakai, N.; Matile, S. Cell-Penetrating Dynamic-Covalent Benzopolysulfane Networks. *Angewandte Chemie* **2019**, *131* (28), 9622–9626. https://doi.org/10.1002/ange.201905003.

(64) Baiyoumy, A.; Vallapurackal, J.; Schwizer, F.; Heinisch, T.; Kardashliev, T.; Held, M.; Panke, S.; Ward, T. R. Directed Evolution of a Surface-Displayed Artificial Allylic Deallylase Relying on a GFP Reporter Protein. *ACS Catal* **2021**, *11* (17), 10705–10712. https://doi.org/10.1021/acscatal.1c02405.

§

(65) Vornholt, T.; Christoffel, F.; Pellizzoni, M. M.; Panke, S.; Ward, T. R.; Jeschek, M. *Systematic Engineering of Artificial Metalloenzymes for New-to-Nature Reactions*; 2021; Vol. 7. https://www.science.org.

(66) Stein, A.; Liang, A. D.; Sahin, R.; Ward, T. R. Incorporation of Metal-Chelating Unnatural Amino Acids into Halotag for Allylic Deamination. *J Organomet Chem* **2022**, *962*. https://doi.org/10.1016/j.jorganchem.2022.122272.

(67) Szponarski, M.; Schwizer, F.; Ward, T. R.; Gademann, K. On-Cell Catalysis by Surface Engineering of Live Cells with an Artificial Metalloenzyme. *Commun Chem* **2018**, *1* (1). https://doi.org/10.1038/s42004-018-0087-y.

(68) Lohner, P.; Zmyslia, M.; Thurn, J.; Pape, J. K.; Gerasimaitė, R.; Keller-Findeisen, J.; Groeer, S.; Deuringer, B.; Süss, R.; Walther, A.; Hell, S. W.; Lukinavičius, G.; Hugel, T.; Jessen-Trefzer, C. Inside a Shell—Organometallic Catalysis Inside Encapsulin Nanoreactors. *Angewandte Chemie - International Edition* **2021**, *60* (44), 23835–23841. https://doi.org/10.1002/anie.202110327.

(69) Ahmadi, P.; Muguruma, K.; Chang, T. C.; Tamura, S.; Tsubokura, K.; Egawa, Y.; Suzuki, T.; Dohmae, N.; Nakao, Y.; Tanaka, K. In Vivometal-Catalyzed SeCT Therapy by a Proapoptotic Peptide. *Chem Sci* **2021**, *12* (37), 12266–12273. https://doi.org/10.1039/d1sc01784e.

(70) Tonga, G. Y.; Jeong, Y.; Duncan, B.; Mizuhara, T.; Mout, R.; Das, R.; Kim, S. T.; Yeh, Y. C.; Yan, B.; Hou, S.; Rotello, V. M. Supramolecular Regulation of Bioorthogonal Catalysis in Cells Using Nanoparticle-Embedded Transition Metal Catalysts. *Nat Chem* **2015**, *7* (7), 597–603. https://doi.org/10.1038/nchem.2284.

(71) Cao-Milán, R.; He, L. D.; Shorkey, S.; Tonga, G. Y.; Wang, L. S.; Zhang, X.; Uddin, I.; Das, R.; Sulak, M.; Rotello, V. M. Modulating the Catalytic Activity of Enzyme-like Nanoparticles through Their Surface Functionalization. *Mol Syst Des Eng* **2017**, *2* (5), 624–628. https://doi.org/10.1039/c7me00055c.

(72) Das, R.; Landis, R. F.; Tonga, G. Y.; Cao-Milán, R.; Luther, D. C.; Rotello, V. M. Control of Intra- versus Extracellular Bioorthogonal Catalysis Using Surface-Engineered Nanozymes. *ACS Nano* **2019**, *13* (1), 229–235. https://doi.org/10.1021/acsnano.8b05370.

(73) Zhang, X.; Fedeli, S.; Gopalakrishnan, S.; Huang, R.; Gupta, A.; Luther, D. C.; Rotello, V. M. Protection and Isolation of Bioorthogonal Metal Catalysts by Using Monolayer-Coated Nanozymes. *ChemBioChem* **2020**, *21* (19), 2759–2763. https://doi.org/10.1002/cbic.202000207.

(74) Zhang, X.; Liu, Y.; Gopalakrishnan, S.; Castellanos-Garcia, L.; Li, G.; Malassiné, M.; Uddin, I.; Huang, R.; Luther, D. C.; Vachet, R. W.; Rotello, V. M. Intracellular Activation of Bioorthogonal Nanozymes through Endosomal Proteolysis of the Protein Corona. *ACS Nano* **2020**, *14* (4), 4767–4773. https://doi.org/10.1021/acsnano.0c00629.

(75) Garcia, E. S.; Xiong, T. M.; Lifschitz, A.; Zimmerman, S. C. Tandem Catalysis Using an Enzyme and a Polymeric Ruthenium-Based Artificial Metalloenzyme. *Polym Chem* **2021**, *12* (46), 6755–6760. https://doi.org/10.1039/d1py01255j.

(76) Xiong, T. M.; Garcia, E. S.; Chen, J.; Zhu, L.; Alzona, A. J.; Zimmerman, S. C. Enzyme-like Catalysis by Single Chain Nanoparticles That Use Transition Metal Cofactors. *Chemical Communications* **2022**, *58* (7), 985–988. https://doi.org/10.1039/d1cc05578j.

§

(77) Destito, P.; Couceiro, J. R.; Faustino, H.; López, F.; Mascareñas, J. L. Ruthenium-Catalyzed Azide–Thioalkyne Cycloadditions in Aqueous Media: A Mild, Orthogonal, and Biocompatible Chemical Ligation. *Angewandte Chemie - International Edition* **2017**, *56* (36), 10766–10770. https://doi.org/10.1002/anie.201705006.

(78) Miguel-Ávila, J.; Tomás-Gamasa, M.; Mascareñas, J. L. Intracellular Ruthenium-Promoted (2+2+2) Cycloadditions. *Angewandte Chemie - International Edition* **2020**, *59* (40), 17628–17633. https://doi.org/10.1002/anie.202006689.

(79) Adriaenssens, L.; Severa, L.; Vávra, J.; Šálová, T.; Hývl, J.; Čfžková, M.; Pohl, R.; Šaman, D.; Teplý, F. Bio-and Air-Tolerant Carbon-Carbon Bond Formations via Organometallic Ruthenium Catalysis. *Collect Czechoslov Chem Commun* **2009**, *74* (7–8), 1023–1034. https://doi.org/10.1135/cccc2009053.

(80) Vidal, C.; Tomás-Gamasa, M.; Gutiérrez-González, A.; Mascarenas, J. L. Ruthenium-Catalyzed Redox Isomerizations inside Living Cells. *J Am Chem Soc* **2019**, *141* (13), 5125–5129. https://doi.org/10.1021/jacs.9b00837.

(81) Sabatino, V.; Ward, T. R. Aqueous Olefin Metathesis: Recent Developments and Applications. *Beilstein Journal of Organic Chemistry*. Beilstein-Institut Zur Forderung der Chemischen Wissenschaften February 14, 2019, pp 445–468. https://doi.org/10.3762/bjoc.15.39.

(82) Sánchez, M. I.; Penas, C.; Vázquez, M. E.; Mascareñas, J. L. Metal-Catalyzed Uncaging of DNA-Binding Agents in Living Cells. *Chem Sci* **2014**, *5* (5), 1901–1907. https://doi.org/10.1039/c3sc53317d.

(83) Rubini, R.; Mayer, C. Addicting Escherichia Coli to New-to-Nature Reactions. *ACS Chem Biol* **2020**, *15* (12), 3093–3098. https://doi.org/10.1021/acschembio.0c00713.

(84) Rubini, R.; Ivanov, I.; Mayer, C. A Screening Platform to Identify and Tailor Biocompatible Small-Molecule Catalysts. *Chemistry - A European Journal* **2019**, *25* (70), 16017–16021. https://doi.org/10.1002/chem.201904808.

(85) Cao-Milán, R.; He, L. D.; Shorkey, S.; Tonga, G. Y.; Wang, L. S.; Zhang, X.; Uddin, I.; Das, R.; Sulak, M.; Rotello, V. M. Modulating the Catalytic Activity of Enzyme-like Nanoparticles through Their Surface Functionalization. *Mol Syst Des Eng* **2017**, *2* (5), 624–628. https://doi.org/10.1039/c7me00055c.

(86) Tonga, G. Y.; Jeong, Y.; Duncan, B.; Mizuhara, T.; Mout, R.; Das, R.; Kim, S. T.; Yeh, Y. C.; Yan, B.; Hou, S.; Rotello, V. M. Supramolecular Regulation of Bioorthogonal Catalysis in Cells Using Nanoparticle-Embedded Transition Metal Catalysts. *Nat Chem* **2015**, *7* (7), 597–603. https://doi.org/10.1038/nchem.2284.

(87) Zhang, X.; Liu, Y.; Gopalakrishnan, S.; Castellanos-Garcia, L.; Li, G.; Malassiné, M.; Uddin, I.; Huang, R.; Luther, D. C.; Vachet, R. W.; Rotello, V. M. Intracellular Activation of Bioorthogonal Nanozymes through Endosomal Proteolysis of the Protein Corona. *ACS Nano* **2020**, *14* (4), 4767–4773. https://doi.org/10.1021/acsnano.0c00629.

(88) Garcia, E. S.; Xiong, T. M.; Lifschitz, A.; Zimmerman, S. C. Tandem Catalysis Using an Enzyme and a Polymeric Ruthenium-Based Artificial Metalloenzyme. *Polym Chem* **2021**, *12* (46), 6755–6760. https://doi.org/10.1039/d1py01255j.

§

(89) Xiong, T. M.; Garcia, E. S.; Chen, J.; Zhu, L.; Alzona, A. J.; Zimmerman, S. C. Enzyme-like Catalysis by Single Chain Nanoparticles That Use Transition Metal Cofactors. *Chemical Communications* **2022**, *58* (7), 985–988. https://doi.org/10.1039/d1cc05578j.

(90) Szponarski, M.; Schwizer, F.; Ward, T. R.; Gademann, K. On-Cell Catalysis by Surface Engineering of Live Cells with an Artificial Metalloenzyme. *Commun Chem* **2018**, *1* (1). https://doi.org/10.1038/s42004-018-0087-y.

(91) Stein, A.; Liang, A. D.; Sahin, R.; Ward, T. R. Incorporation of Metal-Chelating Unnatural Amino Acids into Halotag for Allylic Deamination. *J Organomet Chem* **2022**, *962*, 122272. https://doi.org/10.1016/j.jorganchem.2022.122272.

(92) Vornholt, T.; Christoffel, F.; Pellizzoni, M. M.; Panke, S.; Ward, T. R.; Jeschek, M. Systematic Engineering of Artificial Metalloenzymes for New-to-Nature Reactions. *Sci Adv* **2021**, *7* (4), 1–12. https://doi.org/10.1126/sciadv.abe4208.

(93) Vallapurackal, J.; Stucki, A.; Liang, A. D.; Klehr, J.; Dittrich, P. S.; Ward, T. R. Ultrahigh-Throughput Screening of an Artificial Metalloenzyme Using Double Emulsions**. **2022**. https://doi.org/10.1101/2021.09.20.460989.

(94) Jeschek, M.; Reuter, R.; Heinisch, T.; Trindler, C.; Klehr, J.; Panke, S.; Ward, T. R. Directed Evolution of Artificial Metalloenzymes for in Vivo Metathesis. *Nature* **2016**, *537* (7622), 661–665. https://doi.org/10.1038/nature19114.

(95) Okamoto, Y.; Kojima, R.; Schwizer, F.; Bartolami, E.; Heinisch, T.; Matile, S.; Fussenegger, M.; Ward, T. R. A Cell-Penetrating Artificial Metalloenzyme Regulates a Gene Switch in a Designer Mammalian Cell. *Nat Commun* **2018**, *9* (1). https://doi.org/10.1038/s41467-018-04440-0.

(96) Baiyoumy, A.; Vallapurackal, J.; Schwizer, F.; Heinisch, T.; Kardashliev, T.; Held, M.; Panke, S.; Ward, T. R. Directed Evolution of a Surface-Displayed Artificial Allylic Deallylase Relying on a GFP Reporter Protein. *ACS Catal* **2021**, *11* (17), 10705–10712. https://doi.org/10.1021/acscatal.1c02405.

(97) Lohner, P.; Zmyslia, M.; Thurn, J.; Pape, J. K.; Gerasimaitė, R.; Keller-Findeisen, J.; Groeer, S.; Deuringer, B.; Süss, R.; Walther, A.; Hell, S. W.; Lukinavičius, G.; Hugel, T.; Jessen-Trefzer, C. Inside a Shell—Organometallic Catalysis Inside Encapsulin Nanoreactors. *Angewandte Chemie - International Edition* **2021**, *60* (44), 23835–23841. https://doi.org/10.1002/anie.202110327.

(98) Mancuso, F.; Rahm, M.; Dzijak, R.; Mertlíková-Kaiserová, H.; Vrabel, M. Transition-Metal-Mediated versus Tetrazine-Triggered Bioorthogonal Release Reactions: Direct Comparison and Combinations Thereof. *Chempluschem* **2020**, *85* (8), 1669–1675. https://doi.org/10.1002/cplu.202000477.

(99) Ai, H. W.; Lee, J. W.; Schultz, P. G. A Method to Site-Specifically Introduce Methyllysine into Proteins in E. Coli. *Chemical Communications* **2010**, *46* (30), 5506–5508. https://doi.org/10.1039/c0cc00108b.

(100) Zhang, X.; Lin, S.; Huang, R.; Gupta, A.; Fedeli, S.; Cao-Milán, R.; Luther, D. C.; Liu, Y.; Jiang, M.; Li, G.; Rondon, B.; Wei, H.; Rotello, V. M. Degradable ZnS-Supported Bioorthogonal Nanozymes with Enhanced Catalytic Activity for Intracellular Activation of Therapeutics. *J Am Chem Soc* **2022**, *144* (28), 12893–12900. https://doi.org/10.1021/jacs.2c04571.

§

(101) Murphy, M. P. Targeting Lipophilic Cations to Mitochondria. *Biochimica et Biophysica Acta - Bioenergetics*. July 2008, pp 1028–1031. https://doi.org/10.1016/j.bbabio.2008.03.029.

(102) Heinisch, T.; Schwizer, F.; Garabedian, B.; Csibra, E.; Jeschek, M.; Vallapurackal, J.; Pinheiro, V. B.; Marlière, P.; Panke, S.; Ward, T. R. E. Coli Surface Display of Streptavidin for Directed Evolution of an Allylic Deallylase. *Chem Sci* **2018**, *9* (24), 5383–5388. https://doi.org/10.1039/c8sc00484f.

(103) Lombardi, A.; Pirro, F.; Maglio, O.; Chino, M.; DeGrado, W. F. De Novo Design of Four-Helix Bundle Metalloproteins: One Scaffold, Diverse Reactivities. *Acc Chem Res* **2019**, *52* (5), 1148–1159. https://doi.org/10.1021/acs.accounts.8b00674.

(104) Lewis, J. C. Beyond the Second Coordination Sphere: Engineering Dirhodium Artificial Metalloenzymes to Enable Protein Control of Transition Metal Catalysis. *Acc Chem Res* **2019**, *52* (3), 576–584. https://doi.org/10.1021/acs.accounts.8b00625.

(105) Rebelein, J. G.; Cotelle, Y.; Garabedian, B.; Ward, T. R. Chemical Optimization of Whole-Cell Transfer Hydrogenation Using Carbonic Anhydrase as Host Protein. *ACS Catal* **2019**, *9* (5), 4173–4178. https://doi.org/10.1021/acscatal.9b01006.

(106) Roelfes, G. LmrR: A Privileged Scaffold for Artificial Metalloenzymes. *Acc Chem Res* **2019**, *52* (3), 545–556. https://doi.org/10.1021/acs.accounts.9b00004.

(107) Oohora, K.; Onoda, A.; Hayashi, T. Hemoproteins Reconstituted with Artificial Metal Complexes as Biohybrid Catalysts. *Acc Chem Res* **2019**, *52* (4), 945–954. https://doi.org/10.1021/acs.accounts.8b00676.

(108) Natoli, S. N.; Hartwig, J. F. Noble-Metal Substitution in Hemoproteins: An Emerging Strategy for Abiological Catalysis. *Acc Chem Res* **2019**. https://doi.org/10.1021/acs.accounts.8b00586.

(109) Mocny, C. S.; Pecoraro, V. L. De Novo Protein Design as a Methodology for Synthetic Bioinorganic Chemistry. *Acc Chem Res* **2015**, *48* (8), 2388–2396. https://doi.org/10.1021/acs.accounts.5b00175.

(110) Liu, Z.; Arnold, F. H. New-to-Nature Chemistry from Old Protein Machinery: Carbene and Nitrene Transferases. *Current Opinion in Biotechnology*. Elsevier Ltd June 1, 2021, pp 43–51. https://doi.org/10.1016/j.copbio.2020.12.005.

(111) Lee, H. S.; Spraggon, G.; Schultz, P. G.; Wang, F. Genetic Incorporation of a Metal-Ion Chelating Amino Acid into Proteins as a Biophysical Probe. *J Am Chem Soc* **2009**, *131* (7), 2481–2483. https://doi.org/10.1021/ja808340b.

(112) Liu, X.; Li, J.; Hu, C.; Zhou, Q.; Zhang, W.; Hu, M.; Zhou, J.; Wang, J. Significant Expansion of the Fluorescent Protein Chromophore through the Genetic Incorporation of a Metal-Chelating Unnatural Amino Acid. *Angewandte Chemie - International Edition* **2013**, *52* (18), 4805–4809. https://doi.org/10.1002/anie.201301307.

(113) Zhang, X.; Fedeli, S.; Gopalakrishnan, S.; Huang, R.; Gupta, A.; Luther, D. C.; Rotello, V. M. Protection and Isolation of Bioorthogonal Metal Catalysts by Using Monolayer-Coated Nanozymes. *ChemBioChem* **2020**, *21* (19), 2759–2763. https://doi.org/10.1002/cbic.202000207.

(114) Zhang, X.; Landis, R. F.; Keshri, P.; Cao-Milán, R.; Luther, D. C.; Gopalakrishnan, S.; Liu, Y.; Huang, R.; Li, G.; Malassiné, M.; Uddin, I.; Rondon, B.; Rotello, V. M. Intracellular Activation of

Anticancer Therapeutics Using Polymeric Bioorthogonal Nanocatalysts. *Adv Healthc Mater* **2021**, *10* (5), 1–5. https://doi.org/10.1002/adhm.202001627.

(115) Han, G.; You, C.; Kim, B.; Turingan, R. S.; Forbes, N. S.; Martin, C. T.; Rotello, V. M. Light-Regulated Release of DNA and Its Deliveryto Nuclei by Means of Photolabile GoldNanoparticles. **2006**, 3237–3241. https://doi.org/10.1002/ange.200600214.

(116) Sandhu, K. K.; Mcintosh, C. M.; Simard, J. M.; Smith, S. W.; Rotello, V. M. Gold Nanoparticle-Mediated Transfection of Mammalian Cells. **2002**, 7–10.

(117) Vivero-escoto, J. L.; Slowing, I. I.; Wu, C.; Lin, V. S. Photoinduced Intracellular Controlled Release Drug Delivery in Human Cells by Gold-Capped Mesoporous Silica Nanosphere. **2009**, 3462–3463.

(118) Cotí, K. K.; Belowich, M. E.; Liong, M.; Ambrogio, M. W.; Lau, Y. A.; Khatib, H. A.; Zink, J. I.; Khashab, N. M.; Stoddart, J. F. Mechanised Nanoparticles for Drug Delivery. *Nanoscale* **2009**, *1* (1), 16–39. https://doi.org/10.1039/b9nr00162j.

(119) Hong, R.; Fischer, N. O.; Verma, A.; Goodman, C. M.; Emrick, T.; Rotello, V. M. Control of Protein Structure and Function through Surface Recognition by Tailored Nanoparticle Scaffolds. *J Am Chem Soc* **2004**, *126* (3), 739–743. https://doi.org/10.1021/ja037470o.

(120) Kim, C.; Agasti, S. S.; Zhu, Z.; Isaacs, L.; Rotello, V. M. Recognition-Mediated Activation of Therapeutic Gold Nanoparticles inside Living Cells. *Nat Chem* **2010**, *2* (11), 962–966. https://doi.org/10.1038/nchem.858.

(121) Angelos, S.; Khashab, N. M.; Yang, Y. W.; Trabolsi, A.; Khatib, H. A.; Stoddart, J. F.; Zink, J. I. PH Clock-Operated Mechanized Nanoparticles. *J Am Chem Soc* **2009**, *131* (36), 12912–12914. https://doi.org/10.1021/ja9010157.

(122) Oudar, J. Sulfur Adsorption and Poisoning of Metallic Catalysts. *Catalysis Reviews* **1980**, *22* (2), 171–195. https://doi.org/10.1080/03602458008066533.

(123) Miguel-Ávila, J.; Tomás-Gamasa, M.; Mascareñas, J. L. Intracellular Ruthenium-Promoted (2+2+2) Cycloadditions. *Angewandte Chemie - International Edition* **2020**, *59* (40), 17628–17633. https://doi.org/10.1002/anie.202006689.

(124) Malik, E. M.; Müller, C. E. Anthraquinones As Pharmacological Tools and Drugs. *Medicinal Research Reviews*. John Wiley and Sons Inc. July 1, 2016, pp 705–748. https://doi.org/10.1002/med.21391.

(125) Vidal, C.; Tomás-Gamasa, M.; Gutiérrez-González, A.; Mascarenas, J. L. Ruthenium-Catalyzed Redox Isomerizations inside Living Cells. *J Am Chem Soc* **2019**, *141* (13), 5125–5129. https://doi.org/10.1021/jacs.9b00837.

(126) Martin, C.; Zhang, Y. The Diverse Functions of Histone Lysine Methylation. *Nature Reviews Molecular Cell Biology*. November 2005, pp 838–849. https://doi.org/10.1038/nrm1761.

(127) Kondo, Y.; Shen, L.; Issa, J.-P. J. Critical Role of Histone Methylation in Tumor Suppressor Gene Silencing in Colorectal Cancer. *Mol Cell Biol* **2003**, *23* (1), 206–215. https://doi.org/10.1128/mcb.23.1.206-215.2003.

§

(128) Evans, R.; Thurber, G. M. Design of High Avidity and Low Affinity Antibodies for in Situ Control of Antibody Drug Conjugate Targeting. *Sci Rep* **2022**, *12* (1). https://doi.org/10.1038/s41598-022-11648-0.

(129) Drago, J. Z.; Modi, S.; Chandarlapaty, S. Unlocking the Potential of Antibody–Drug Conjugates for Cancer Therapy. *Nature Reviews Clinical Oncology*. Nature Research June 1, 2021, pp 327–344. https://doi.org/10.1038/s41571-021-00470-8.

(130) Zacharias, N.; Podust, V. N.; Kajihara, K. K.; Leipold, D.; del Rosario, G.; Thayer, D.; Dong, E.; Paluch, M.; Fischer, D.; Zheng, K.; Lei, C.; He, J.; Ng, C.; Su, D.; Liu, L.; Masih, S.; Sawyer, W.; Tinianow, J.; Marik, J.; Yip, V.; Li, G.; Chuh, J.; Morisaki, J. H.; Park, S.; Zheng, B.; Hernandez-Barry, H.; Loyet, K. M.; Xu, M.; Kozak, K. R.; Phillips, G. L.; Shen, B. Q.; Wu, C.; Xu, K.; Yu, S. F.; Kamath, A.; Rowntree, R. K.; Reilly, D.; Pillow, T.; Polson, A.; Schellenberger, V.; Hazenbos, W. L. W.; Sadowsky, J. A Homogeneous High-DAR Antibody-Drug Conjugate Platform Combining THIOMAB Antibodies and XTEN Polypeptides†. *Chem Sci* **2022**, *13* (11), 3147–3160. https://doi.org/10.1039/d1sc05243h.

(131) Bagshawel, K. D.; Springer', C. J.; Searle', F.; Antoniwl, P.; Sharma', S. K.; Melton2, R. G.; Sherwood2, R. F. *A Cytotoxic Agent Can Be Generated Selectively at Cancer Sites*.

(132) Sharma, S. K.; Bagshawe, K. D. Translating Antibody Directed Enzyme Prodrug Therapy (ADEPT) and Prospects for Combination. *Expert Opinion on Biological Therapy*. Taylor and Francis Ltd January 2, 2017, pp 1–13. https://doi.org/10.1080/14712598.2017.1247802.

(133) Lozhkin, B.; Ward, T. R. Bioorthogonal Strategies for the in Vivo Synthesis or Release of Drugs. *Bioorg Med Chem* **2021**, *45*. https://doi.org/10.1016/j.bmc.2021.116310.

(134) Sabatino, V.; Unnikrishnan, V. B.; Bernardes, G. J. L. Transition Metal Mediated Bioorthogonal Release. *Chem Catalysis*. Cell Press January 20, 2022, pp 39–51. https://doi.org/10.1016/j.checat.2021.12.007.

(135) Chang, T. C.; Tanaka, K. In Vivo Organic Synthesis by Metal Catalysts. *Bioorg Med Chem* **2021**, *46*. https://doi.org/10.1016/j.bmc.2021.116353.

(136) Nasibullin, I.; Smirnov, I.; Ahmadi, P.; Vong, K.; Kurbangalieva, A.; Tanaka, K. Synthetic Prodrug Design Enables Biocatalytic Activation in Mice to Elicit Tumor Growth Suppression. *Nat Commun* **2022**, *13* (1). https://doi.org/10.1038/s41467-021-27804-5.

(137) Beckman, R. A.; Weiner, L. M.; Davis, H. M. Antibody Constructs in Cancer Therapy: Protein Engineering Strategies to Improve Exposure in Solid Tumors. *Cancer*. January 15, 2007, pp 170–179. https://doi.org/10.1002/cncr.22402.

(138) Zhao, Z.; Tao, X.; Xie, Y.; Lai, Q.; Lin, W.; Lu, K.; Wang, J.; Xia, W.; Mao, Z. W. In Situ Prodrug Activation by an Affibody-Ruthenium Catalyst Hybrid for HER2-Targeted Chemotherapy. *Angewandte Chemie - International Edition* **2022**, *61* (26). https://doi.org/10.1002/anie.202202855.

(139) Keizer, R. J.; Huitema, A. D. R.; Schellens, J. H. M.; Beijnen, J. H. *Clinical Pharmacokinetics of Therapeutic Monoclonal Antibodies*.

(140) Wilson, M. E.; Whitesides, G. M. Conversion of a Protein to a Homogeneous Asymmetric Hydrogenation Catalyst by Site-Specific Modification with a Diphosphinerhodium(I) Moiety. *J Am Chem Soc* **1978**, *100* (1), 306–307. https://doi.org/10.1021/ja00469a064.

§

(141) Schwizer, F.; Okamoto, Y.; Heinisch, T.; Gu, Y.; Pellizzoni, M. M.; Lebrun, V.; Reuter, R.; Köhler, V.; Lewis, J. C.; Ward, T. R. Artificial Metalloenzymes: Reaction Scope and Optimization Strategies. *Chem Rev* **2018**, *118* (1), 142–231. https://doi.org/10.1021/acs.chemrev.7b00014.

(142) Davis, H. J.; Ward, T. R. Artificial Metalloenzymes: Challenges and Opportunities. *ACS Cent Sci* **2019**, *5* (7), 1120–1136. https://doi.org/10.1021/acscentsci.9b00397.

(143) Reetz, M. T.; Peyralans, J. J. P.; Maichele, A.; Fu, Y.; Maywald, M. Directed Evolution of Hybrid Enzymes: Evolving Enantioselectivity of an Achiral Rh-Complex Anchored to a Protein. *Chemical Communications* **2006**, No. 41, 4318–4320. https://doi.org/10.1039/b610461d.

(144) Tomás-Gamasa, M.; Martínez-Calvo, M.; Couceiro, J. R.; Mascarenãs, J. L. Transition Metal Catalysis in the Mitochondria of Living Cells. *Nat Commun* **2016**, *7*, 12538–12548. https://doi.org/10.1038/ncomms12538.

(145) Hsu, H. T.; Trantow, B. M.; Waymouth, R. M.; Wender, P. A. Bioorthogonal Catalysis: A General Method to Evaluate Metal-Catalyzed Reactions in Real Time in Living Systems Using a Cellular Luciferase Reporter System. *Bioconjug Chem* **2016**, *27* (2), 376–382. https://doi.org/10.1021/acs.bioconjchem.5b00469.

(146) Völker, T.; Meggers, E. Chemical Activation in Blood Serum and Human Cell Culture: Improved Ruthenium Complex for Catalytic Uncaging of Alloc-Protected Amines. *ChemBioChem* **2017**, *18* (12), 1083–1086. https://doi.org/10.1002/cbic.201700168.

(147) Key, H. M.; Dydio, P.; Clark, D. S.; Hartwig, J. F. Abiological Catalysis by Artificial Haem Proteins Containing Noble Metals in Place of Iron. *Nature* **2016**, *534* (7608), 534–537. https://doi.org/10.1038/nature17968.

(148) Song, W. J.; Tezcan, F. A. A Designed Supramolecular Protein Assembly with in Vivo Enzymatic Activity. **2021**, *346* (6216), 1525–1528.

(149) Grimm, A. R.; Sauer, D. F.; Polen, T.; Zhu, L.; Hayashi, T.; Okuda, J.; Schwaneberg, U. A Whole Cell E. Coli Display Platform for Artificial Metalloenzymes: Poly(Phenylacetylene) Production with a Rhodium-Nitrobindin Metalloprotein. *ACS Catal* **2018**, *8* (3), 2611–2614. https://doi.org/10.1021/acscatal.7b04369.

(150) Blomberg, R.; Kries, H.; Pinkas, D. M.; Mittl, P. R. E.; Grütter, M. G.; Privett, H. K.; Mayo, S. L.; Hilvert, D. Precision Is Essential for Efficient Catalysis in an Evolved Kemp Eliminase. *Nature* **2013**, *503* (7476), 418–421. https://doi.org/10.1038/nature12623.

(151) Srivastava, P.; Yang, H.; Ellis-Guardiola, K.; Lewis, J. C. Engineering a Dirhodium Artificial Metalloenzyme for Selective Olefin Cyclopropanation. *Nat Commun* **2015**, *6*, 7789–7797. https://doi.org/10.1038/ncomms8789.

(152) Ilie, A.; Reetz, M. T. Directed Evolution of Artificial Metalloenzymes. *Isr J Chem* **2015**, *55* (1), 51–60. https://doi.org/10.1002/ijch.201400087.

(153) Bornscheuer, U. T.; Huisman, G. W.; Kazlauskas, R. J.; Lutz, S.; Moore, J. C.; Robins, K. Engineering the Third Wave of Biocatalysis. *Nature* **2012**, *485* (7397), 185–194. https://doi.org/10.1038/nature11117.

(154) Brandenberg, O. F.; Fasan, R.; Arnold, F. H. Exploiting and Engineering Hemoproteins for Abiological Carbene and Nitrene Transfer Reactions. *Curr Opin Biotechnol* **2017**, *47*, 102–111. https://doi.org/10.1016/j.copbio.2017.06.005.

§

(155) Kille, S.; Acevedo-Rocha, C. G.; Parra, L. P.; Zhang, Z. G.; Opperman, D. J.; Reetz, M. T.; Acevedo, J. P. Reducing Codon Redundancy and Screening Effort of Combinatorial Protein Libraries Created by Saturation Mutagenesis. *ACS Synth Biol* **2013**, *2* (2), 83–92. https://doi.org/10.1021/sb300037w.

(156) Ward, T. R. Artificial Metalloenzymes Based on the Biotin - Avidin Technology: Enantioselective Catalysis and Beyond. *Acc Chem Res* **2011**, *44* (1), 47–57. https://doi.org/10.1021/ar100099u.

(157) Blomberg, R.; Kries, H.; Pinkas, D. M.; Mittl, P. R. E.; Grütter, M. G.; Privett, H. K.; Mayo, S. L.; Hilvert, D. Precision Is Essential for Efficient Catalysis in an Evolved Kemp Eliminase. *Nature* **2013**, *503* (7476), 418–421. https://doi.org/10.1038/nature12623.

(158) Key, H. M.; Dydio, P.; Clark, D. S.; Hartwig, J. F. Abiological Catalysis by Artificial Haem Proteins Containing Noble Metals in Place of Iron. *Nature* **2016**, *534* (7608), 534–537. https://doi.org/10.1038/nature17968.

(159) Song, W. J.; Tezcan, F. A. A Designed Supramolecular Protein Assembly with in Vivo Enzymatic Activity. **2021**, *346* (6216), 1525–1528.

(160) Jeschek, M.; Reuter, R.; Heinisch, T.; Trindler, C.; Klehr, J.; Panke, S.; Ward, T. R. Directed Evolution of Artificial Metalloenzymes for in Vivo Metathesis. *Nature* **2016**, *537* (7622), 661–665. https://doi.org/10.1038/nature19114.

(161) Markel, U.; Sauer, D. F.; Schiffels, J.; Okuda, J.; Schwaneberg, U. Towards the Evolution of Artificial Metalloenzymes—A Protein Engineer's Perspective. *Angew Chem Int Ed Engl* **2019**, *131* (14), 4500–4511. https://doi.org/10.1002/ange.201811042.

(162) Obexer, R.; Godina, A.; Garrabou, X.; Mittl, P. R. E.; Baker, D.; Griffiths, A. D.; Hilvert, D. Emergence of a Catalytic Tetrad during Evolution of a Highly Active Artificial Aldolase. *Nat Chem* **2017**, *9* (1), 50–56. https://doi.org/10.1038/nchem.2596.

(163) Völker, T.; Dempwolff, F.; Graumann, P. L.; Meggers, E. Progress towards Bioorthogonal Catalysis with Organometallic Compounds. *Angew Chem Int Ed Engl* **2014**, *53* (39), 10536–10540. https://doi.org/10.1002/anie.201404547.

(164) Streu, C.; Meggers, E. Ruthenium-Induced Allylcarbamate Cleavage in Living Cells. *Angewandte Chemie - International Edition* **2006**, *45* (34), 5645–5648. https://doi.org/10.1002/anie.200601752.

(165) Heinisch, T.; Schwizer, F.; Garabedian, B.; Csibra, E.; Jeschek, M.; Vallapurackal, J.; Pinheiro, V. B.; Marlière, P.; Panke, S.; Ward, T. R. E. Coli Surface Display of Streptavidin for Directed Evolution of an Allylic Deallylase. *Chem Sci* **2018**, *9* (24), 5383–5388. https://doi.org/10.1039/c8sc00484f.

(166) Völker, T.; Dempwolff, F.; Graumann, P. L.; Meggers, E. Progress towards Bioorthogonal Catalysis with Organometallic Compounds. *Angew Chem Int Ed Engl* **2014**, *53* (39), 10536–10540. https://doi.org/10.1002/anie.201404547.

(167) Park, M.; Jose, J.; Thömmes, S.; Kim, J. Il; Kang, M. J.; Pyun, J. C. Autodisplay of Streptavidin. *Enzyme Microb Technol* **2011**, *48* (4–5), 307–311. https://doi.org/10.1016/j.enzmictec.2010.12.006.

§

(168) Reetz, M. T.; Carballeira, J. D. Iterative Saturation Mutagenesis (ISM) for Rapid Directed Evolution of Functional Enzymes. *Nat Protoc* **2007**, *2* (4), 891–903. https://doi.org/10.1038/nprot.2007.72.

(169) Kille, S.; Acevedo-Rocha, C. G.; Parra, L. P.; Zhang, Z. G.; Opperman, D. J.; Reetz, M. T.; Acevedo, J. P. Reducing Codon Redundancy and Screening Effort of Combinatorial Protein Libraries Created by Saturation Mutagenesis. *ACS Synth Biol* **2013**, *2* (2), 83–92. https://doi.org/10.1021/sb300037w.

(170) Vornholt, T.; Christoffel, F.; Pellizzoni, M. M.; Panke, S.; Ward, T. R.; Jeschek, M. Systematic Engineering of Artificial Metalloenzymes for New-to-Nature Reactions. *Sci. Adv* **2021**, *7*, 4208–4230.

(171) Hestericová, M.; Heinisch, T.; Alonso-Cotchico, L.; Maréchal, J.-D.; Vidossich, P.; Ward, T. R. Directed Evolution of an Artificial Imine Reductase. *Angew Chem Int Ed Engl* **2018**, *130* (7), 1881–1886. https://doi.org/10.1002/ange.201711016.

(172) Jose, J.; Bernhardt, R.; Hannemann, F. Functional Display of Active Bovine Adrenodoxin on the Surface of E. Coli by Chemical Incorporation of the [2Fe ± 2S] Cluster. *ChemBioChem* **2001**, *2*, 695–701.

(173) Jose, J.; Von Schwichow, S. Autodisplay of Active Sorbitol Dehydrogenase (SDH) Yields a Whole Cell Biocatalyst for the Synthesis of Rare Sugars. *ChemBioChem* **2004**, *5* (4), 491–499. https://doi.org/10.1002/cbic.200300774.

(174) Peschke, T.; Rabe, K. S.; Niemeyer, C. M. Orthogonale Oberflächenmarkierungen Für Die Ganzzellkatalyse. *Angewandte Chemie* **2017**, *129* (8), 2215–2219. https://doi.org/10.1002/ange.201609590.

(175) Grimm, A. R.; Sauer, D. F.; Polen, T.; Zhu, L.; Hayashi, T.; Okuda, J.; Schwaneberg, U. A Whole Cell E. Coli Display Platform for Artificial Metalloenzymes: Poly(Phenylacetylene) Production with a Rhodium-Nitrobindin Metalloprotein. *ACS Catal* **2018**, *8* (3), 2611–2614. https://doi.org/10.1021/acscatal.7b04369.

(176) Völker, T.; Meggers, E. Chemical Activation in Blood Serum and Human Cell Culture: Improved Ruthenium Complex for Catalytic Uncaging of Alloc-Protected Amines. *ChemBioChem* **2017**, *18* (12), 1083–1086. https://doi.org/10.1002/cbic.201700168.

(177) Völker, T.; Dempwolff, F.; Graumann, P. L.; Meggers, E. Progress towards Bioorthogonal Catalysis with Organometallic Compounds. *Angew Chem Int Ed Engl* **2014**, *53* (39), 10536–10540. https://doi.org/10.1002/anie.201404547.

(178) Hsu, H. T.; Trantow, B. M.; Waymouth, R. M.; Wender, P. A. Bioorthogonal Catalysis: A General Method to Evaluate Metal-Catalyzed Reactions in Real Time in Living Systems Using a Cellular Luciferase Reporter System. *Bioconjug Chem* **2016**, *27*, 376–382. https://doi.org/10.1021/acs.bioconjchem.5b00469.

(179) Tomás-Gamasa, M.; Martínez-Calvo, M.; Couceiro, J. R.; Mascarenãs, J. L. Transition Metal Catalysis in the Mitochondria of Living Cells. *Nat Commun* **2016**, *7*. https://doi.org/10.1038/ncomms12538.

(180) Song, W. J.; Tezcan, F. A. A Designed Supramolecular Protein Assembly with in Vivo Enzymatic Activity Downloaded From. **2021**, *346*, 6216.

§

(181) Vidal, C.; Tomás-Gamasa, M.; Destito, P.; López, F.; Mascareñas, J. L. Concurrent and Orthogonal Gold(I) and Ruthenium(II) Catalysis inside Living Cells. *Nat Commun* **2018**, *9* (1), 1–9. https://doi.org/10.1038/s41467-018-04314-5.

(182) Key, H. M.; Dydio, P.; Clark, D. S.; Hartwig, J. F. Abiological Catalysis by Artificial Haem Proteins Containing Noble Metals in Place of Iron. *Nature* **2016**, *534* (7608), 534–537. https://doi.org/10.1038/nature17968.

(183) Dydio, P.; Key, H. M.; Nazarenko, A.; Rha, J. Y.-E.; Seyedkazemi, V.; Clark, D. S.; Hartwig, J. F. An Artificial Metalloenzyme with the Kinetics of Native Enzymes. *Science (1979)* **2016**, *354* (6308), 102–106. https://doi.org/10.1126/science.aah4427.

(184) Völker, T.; Meggers, E. Chemical Activation in Blood Serum and Human Cell Culture: Improved Ruthenium Complex for Catalytic Uncaging of Alloc-Protected Amines. *ChemBioChem* **2017**, *18* (12), 1083–1086. https://doi.org/10.1002/cbic.201700168.

(185) Rubini, R.; Mayer, C. Addicting Escherichia Coli to New-to-Nature Reactions. *ACS Chem Biol* **2020**, *15* (12), 3093–3098. https://doi.org/10.1021/acschembio.0c00713.

(186) Okamoto, Y.; Kojima, R.; Schwizer, F.; Bartolami, E.; Heinisch, T.; Matile, S.; Fussenegger, M.; Ward, T. R. A Cell-Penetrating Artificial Metalloenzyme Regulates a Gene Switch in a Designer Mammalian Cell. *Nat Commun* **2018**, *9* (1). https://doi.org/10.1038/s41467-018-04440-0.

(187) Shingler, V.; Moore, T. Sensing of Aromatic Compounds by the DmpR Transcriptional Activator of Phenol-Catabolizing Pseudomonas Sp. Strain CF600. *J. Bacteriol.* **1994**, 1555–1560.

(188) Shingler, V.; Bartilson, M.; Moore, T. Cloning and Nucleotide Sequence of the Gene Encoding the Positive Regulator (DmpR) of the Phenol Catabolic Pathway Encoded by PVI150 and Identification of DmpR as a Member of the NtrC Family of Transcriptional Activators. *J Bacteriol* **1993**, 1596–1604.

(189) Choi, S. L.; Rha, E.; Lee, S. J.; Kim, H.; Kwon, K.; Jeong, Y. S.; Rhee, Y. H.; Song, J. J.; Kim, H. S.; Lee, S. G. Toward a Generalized and High-Throughput Enzyme Screening System Based on Artificial Genetic Circuits. *ACS Synth Biol* **2014**, *3* (3), 163–171. https://doi.org/10.1021/sb400112u.

(190) Kwon, K. K.; Lee, D. H.; Kim, S. J.; Choi, S. L.; Rha, E.; Yeom, S. J.; Subhadra, B.; Lee, J.; Jeong, K. J.; Lee, S. G. Evolution of Enzymes with New Specificity by High-Throughput Screening Using DmpR-Based Genetic Circuits and Multiple Flow Cytometry Rounds. *Sci Rep* **2018**, *8* (1), 2659–2668. https://doi.org/10.1038/s41598-018-20943-8.

(191) Earhart, C. F. Use of an Lpp-OmpA Fusion Vehicle for Bacterial Surface Display. *Methods Enzymol.* **2000**, *326*, 506–516.

(192) Reetz, M. T.; Sanchis, J. Constructing and Analyzing the Fitness Landscape of an Experimental Evolutionary Process. *ChemBioChem* **2008**, *9* (14), 2260–2267. https://doi.org/10.1002/cbic.200800371.

(193) Francisco, J. A.; Earhart, C. F.; Georgiou, G. Transport and Anchoring of 8-Lactamase to the External Surface of Escherichia Coli. *Biochemistry* **1992**, *89*, 2713–2717.

(194) Jose, J.; Meyer, T. F. The Autodisplay Story, from Discovery to Biotechnical and Biomedical Applications. *MICROBIOLOGY AND MOLECULAR BIOLOGY REVIEWS* **2007**, *71* (4), 600–619. https://doi.org/10.1128/MMBR.00011-07.

§

(195) Stathopoulos, C.; Georgiou, G.; Earhart, C. F. Characterization of Escherichia Coli Expressing an Lpp'OmpA(46-159)-PhoA Fusion Protein Localized in the Outer Membrane. *Appl Microbiol Biotechnol* **1996**, *45* (1–2), 112–119. https://doi.org/10.1007/s002530050657.

(196) van Bloois, E.; Winter, R. T.; Kolmar, H.; Fraaije, M. W. Decorating Microbes: Surface Display of Proteins on Escherichia Coli. *Trends Biotechnol* **2011**, *29* (2), 79–86. https://doi.org/10.1016/j.tibtech.2010.11.003.

(197) Shi, J. M.; Pei, J.; Liu, E. Q.; Zhang, L. Bis(Sulfosuccinimidyl) Suberate (BS3) Crosslinking Analysis of the Behavior of Amyloid-β Peptide in Solution and in Phospholipid Membranes. *PLoS One* **2017**, *12* (3), 1–13. https://doi.org/10.1371/journal.pone.0173871.

(198) Reinhart A.F., R.; Bragg, P. D. Cross-Linking of the Proteins in the Outer Membrane of Escherichia Coli. *BBA - Biomembranes* **1977**, *466* (2), 245–256. https://doi.org/10.1016/0005-2736(77)90222-X.

(199) Palva, E. T.; Rndall, L. L. Nearest-Neighbor Analysis of Escherichia Coli Outer Membrane Proteins , Using Cleavable Cross-Links. **1976**, *127* (3), 1558–1560.

(200) Angus, B. L.; Hancock, R. E. W. Outer Membrane Porin Proteins F, P, and D1 of Pseudomonas Aeruginosa and PhoE of Escherichia Coli: Chemical Cross-Linking to Reveal Native Oligomers. *J Bacteriol* **1983**, *155* (3), 1042–1051. https://doi.org/10.1128/jb.155.3.1042-1051.1983.

(201) Humbert, N.; Zocchi, A.; Ward, T. R. Electrophoretic Behavior of Streptavidin Complexed to a Biotinylated Probe: A Functional Screening Assay for Biotin-Binding Proteins. *Electrophoresis* **2005**, *26* (1), 47–52. https://doi.org/10.1002/elps.200406148.

(202) Köhler, V.; Mao, J.; Heinisch, T.; Pordea, A.; Sardo, A.; Wilson, Y. M.; Knörr, L.; Creus, M.; Prost, J. C.; Schirmer, T.; Ward, T. R. OsO4•streptavidin: A Tunable Hybrid Catalyst for the Enantioselective Cis-Dihydroxylation of Olefins. *Angewandte Chemie - International Edition* **2011**, *50* (46), 10863–10866. https://doi.org/10.1002/anie.201103632.

(203) Kada, G.; Falk, H.; Gruber, H. J. *Accurate Measurement of Avidin and Streptavidin in Crude Bio£uids with a New, Optimized Biotin^£uorescein Conjugate*.

(204) Reetz, M. T.; Kahakeaw, D.; Lohmer, R. Addressing the Numbers Problem in Directed Evolution. *ChemBioChem* **2008**, *9* (11), 1797–1804. https://doi.org/10.1002/cbic.200800298.

(205) Streu, C.; Meggers, E. Ruthenium-Induced Allylcarbamate Cleavage in Living Cells. *Angewandte Chemie - International Edition* **2006**, *45* (34), 5645–5648. https://doi.org/10.1002/anie.200601752.

(206) Cheng, Y.; Zong, L.; López-Andarias, J.; Bartolami, E.; Okamoto, Y.; Ward, T. R.; Sakai, N.; Matile, S. Cell-Penetrating Dynamic-Covalent Benzopolysulfane Networks. *Angewandte Chemie - International Edition* **2019**, *58* (28), 9522–9526. https://doi.org/10.1002/anie.201905003.

(207) Sánchez, M. I.; Penas, C.; Vázquez, M. E.; Mascareñas, J. L. Metal-Catalyzed Uncaging of DNA-Binding Agents in Living Cells. *Chem Sci* **2014**, *5* (5), 1901–1907. https://doi.org/10.1039/c3sc53317d.

(208) Jaisankar, P.; Tanaka, S.; Kitamura, M. Catalytic Dehydrative S-Allylation of Cysteine-Containing Peptides in Aqueous Media toward Lipopeptide Chemistry. *Journal of Organic Chemistry* **2011**, *76* (6), 1894–1897. https://doi.org/10.1021/jo102278m.

§

(209) Rubini, R.; Ivanov, I.; Mayer, C. A Screening Platform to Identify and Tailor Biocompatible Small-Molecule Catalysts. *Chemistry - A European Journal* **2019**, *25* (70), 16017–16021. https://doi.org/10.1002/chem.201904808.

(210) Bai, Y.; Chen, J.; Zimmerman, S. C. Designed Transition Metal Catalysts for Intracellular Organic Synthesis. *Chemical Society Reviews*. Royal Society of Chemistry March 7, 2018, pp 1811–1821. https://doi.org/10.1039/c7cs00447h.

(211) Garcia, E. S.; Xiong, T. M.; Lifschitz, A.; Zimmerman, S. C. Tandem Catalysis Using an Enzyme and a Polymeric Ruthenium-Based Artificial Metalloenzyme. *Polym Chem* **2021**, *12* (46), 6755–6760. https://doi.org/10.1039/d1py01255j.

(212) Zhang, X.; Liu, Y.; Gopalakrishnan, S.; Castellanos-Garcia, L.; Li, G.; Malassiné, M.; Uddin, I.; Huang, R.; Luther, D. C.; Vachet, R. W.; Rotello, V. M. Intracellular Activation of Bioorthogonal Nanozymes through Endosomal Proteolysis of the Protein Corona. *ACS Nano* **2020**, *14* (4), 4767–4773. https://doi.org/10.1021/acsnano.0c00629.

(213) Kiesewetter, M. K.; Waymouth, R. M. Kinetics of an Air- and Water-Stable Ruthenium(IV) Catalyst for the Deprotection of Allyl Alcohol in Water. *Organometallics* **2010**, *29* (22), 6051–6056. https://doi.org/10.1021/om100892v.

(214) Mascarenas, J. L.; Gutierrez-González, A.; López, F. Ruthenium Catalysis in Biological Habitats. *Helv Chim Acta* **2023**. https://doi.org/10.1002/hlca.202300001.

(215) Franco, R.; Cidlowski, J. A. Apoptosis and Glutathione: Beyond an Antioxidant. *Cell Death and Differentiation*. 2009, pp 1303–1314. https://doi.org/10.1038/cdd.2009.107.

(216) Homer, N. Z. M.; Reglinski, J.; Sowden, R.; Spickett, C. M.; Wilson, R.; Walker, J. J. Dimethylsulfoxide Oxidizes Glutathione in Vitro and in Human Erythrocytes: Kinetic Analysis by 1H NMR. *Cryobiology* **2005**, *50* (3), 317–324. https://doi.org/10.1016/j.cryobiol.2005.04.002.

(217) Kiesewetter, M. K.; Waymouth, R. M. Kinetics of an Air- and Water-Stable Ruthenium(IV) Catalyst for the Deprotection of Allyl Alcohol in Water. *Organometallics* **2010**, *29* (22), 6051–6056. https://doi.org/10.1021/om100892v.

(218) Takenaka, M.; Kikkawa, M.; Matsumoto, T.; Yatabe, T.; Ando, T.; Yoon, K. S.; Ogo, S. Oxidation of Guanosine Monophosphate with O2 via a Ru-Peroxo Complex in Water. *Chem Asian J* **2018**, *13* (21), 3180–3184. https://doi.org/10.1002/asia.201801267.

(219) Albertin, G.; Antoniutti, S.; Bortoluzzi, M.; Castro, J.; Ferraro, V. Preparation and Reactivity of Half-Sandwich Dioxygen Complexes of Ruthenium. *Dalton Transactions* **2018**, *47* (27), 9173–9184. https://doi.org/10.1039/c8dt01871e.

(220) Tronic, T. A.; Kaminsky, W.; Coggins, M. K.; Mayer, J. M. Synthesis, Protonation, and Reduction of Ruthenium-Peroxo Complexes with Pendent Nitrogen Bases. *Inorg Chem* **2012**, *51* (20), 10916–10928. https://doi.org/10.1021/ic3013987.

(221) Wall, A.; Nicholls, K.; Caspersen, M. B.; Skrivergaard, S.; Howard, K. A.; Karu, K.; Chudasama, V.; Baker, J. R. Optimised Approach to Albumin-Drug Conjugates Using Monobromomaleimide-C-2 Linkers. *Org Biomol Chem* **2019**, *17* (34), 7870–7873. https://doi.org/10.1039/c9ob00721k.

(222) Zhao, Z.; Tao, X.; Xie, Y.; Lai, Q.; Lin, W.; Lu, K.; Wang, J.; Xia, W.; Mao, Z. W. In Situ Prodrug Activation by an Affibody-Ruthenium Catalyst Hybrid for HER2-Targeted Chemotherapy.

§

Angewandte Chemie - International Edition **2022**, *61* (26). https://doi.org/10.1002/anie.202202855.

(223) Woronoff, G.; el Harrak, A.; Mayot, E.; Schicke, O.; Miller, O. J.; Soumillion, P.; Griffiths, A. D.; Ryckelynck, M. New Generation of Amino Coumarin Methyl Sulfonate-Based Fluorogenic Substrates for Amidase Assays in Droplet-Based Microfluidic Applications. *Anal Chem* **2011**, *83* (8), 2852–2857. https://doi.org/10.1021/ac200373n.

(224) Pratheebaa, P.; Perumal, P.; Angayarkanni, J.; SundaraBaalaji, N.; Palvannan, T. 4-[2-Allylsulfanyl-1-(Carboxymethyl-Carbamoyl)-Ethylcarbamoyl]-2-Amino-Butyric Acid: Evaluation as Topoisomerase Inhibitor Using in Vitro Assay and Molecular Docking Study. *Medicinal Chemistry Research* **2015**, *24* (5), 1893–1900. https://doi.org/10.1007/s00044-014-1263-y.

(225) Saburi, H.; Tanaka, S.; Kitamura, M. Catalytic Dehydrative Allylation of Alcohols. *Angewandte Chemie - International Edition* **2005**, *44* (11), 1730–1732. https://doi.org/10.1002/anie.200462513.

(226) Tanaka, S.; Saburi, H.; Ishibashi, Y.; Kitamura, M. CpRuIIPF6/Quinaldic Acid-Catalyzed Chemoselective Allyl Ether Cleavage. A Simple and Practical Method for Hydroxyl Deprotection. *Org Lett* **2004**, *6* (11), 1873–1875. https://doi.org/10.1021/ol0493397.

(227) Sabatino, V.; Rebelein, J. G.; Ward, T. R. "Close-to-Release": Spontaneous Bioorthogonal Uncaging Resulting from Ring-Closing Metathesis. *J Am Chem Soc* **2019**, *141* (43), 17048–17052. https://doi.org/10.1021/jacs.9b07193.

(228) Kazuo Yamamura, B.; Thomas Kaiser, E. *Studies on the Oxidase Activity of Copper(I1) Carboxypeptidase A*; 1976.

(229) Lindberg, B.; Klenow, H.; Hansen, K.; Biol Chem, J.; Baughn, R. L.; Adalsteinsson George Whitesides, Ó. M. *A Large Number of Other Nucleosides and Nucleotide Kinases Are Also Known; Cf. E. P. An-Derson In*; Academic Press, 1967; Vol. 242. https://pubs.acs.org/sharingguidelines.

(230) Ward, T. R. Artificial Metalloenzymes Based on the Biotin - Avidin Technology: Enantioselective Catalysis and Beyond. *Acc Chem Res* **2011**, *44* (1), 47–57. https://doi.org/10.1021/ar100099u.

(231) Seki, T.; Tanaka, S.; Kitamura, M. Enantioselective Synthesis of Pyrrolidine-, Piperidine-, and Azepane-Type N -Heterocycles with α-Alkenyl Substitution: The CpRu-Catalyzed Dehydrative Intramolecular N -Allylation Approach. *Org Lett* **2012**, *14* (2), 608–611. https://doi.org/10.1021/ol203218d.

(232) Tanaka, S.; Seki, T.; Kitamura, M. Asymmetrie Dehydrative Cyclization of ω-Hydroxy Allyl Alcohols Catalyzed by Ruthenium Complexes. *Angewandte Chemie - International Edition* **2009**, *48* (47), 8948–8951. https://doi.org/10.1002/anie.200904671.

(233) Destito, P.; Couceiro, J. R.; Faustino, H.; López, F.; Mascareñas, J. L. Ruthenium-Catalyzed Azide-Thioalkyne Cycloadditions in Aqueous Media: A Mild, Orthogonal, and Biocompatible Chemical Ligation. *Angewandte Chemie* **2017**, *129* (36), 10906–10910. https://doi.org/10.1002/ange.201705006.

(234) Helbig, K.; Bleuel, C.; Krauss, G. J.; Nies, D. H. Glutathione and Transition-Metal Homeostasis in Escherichia Coli. *J Bacteriol* **2008**, *190* (15), 5431–5438. https://doi.org/10.1128/JB.00271-08.

§

Acknowledgements

I would like to thank Prof. Dr. Thomas R. Ward for offering me the possibility to work on this topic and in his research group. I would also like to thank my second supervisor, Prof. Dr. Olivier Baudoin, and the external expert Prof. Dr. Clemens Mayer for reading my manuscript and agreeing to examine my thesis.

J'aimerais en premier lieu remercier mon frère Guillaume, sans qui je n'en serais jamais arrivé là où j'en suis aujourd'hui. Il est un modèle de droiture, de respect et de tolérance. Merci pour tout.

J'aimerais remercier Prof. Dr. José Roldan Rivas-Enterrios pour nos échanges scientifiques dans le domaine de la chimie. Une personne toujours ouverte aux discussions et aux idées, au point de m'accompagner pendant mon temps libre au labo pour essayer certaines d'entre elles. Son motto « La Nature est la meilleure des chimistes » m'accompagne encore aujourd'hui.

J'aimerais remercier Prof. Dr. David Virieux qui par ses qualités humaines et pédagogiques, a su me guider dans mon parcours universitaire. J'ai pu profiter de la richesse de son expérience et gagner ainsi en maturité. Merci pour tout David.

J'aimerais remercier Prof. Dr. Jean-Luc Pirat d'avoir été bienveillant durant mon parcours à l'ENSCM. Merci de m'avoir toujours prodigué des conseils même après l'université.

I would like to thanks all my friends who supported me during the whole PhD and without whom, this time would have been much harded. Thanks to you all !

J'aimerais remercier Armand Benmouffok et Lucas.

I would like to thanks Fadri, Nico and Coco for the time we spent in the lab, It was really nice and helping have you in this group, as colleague but mainly as friends. Without you it would not have been that enjoyable!

I would like to thanks Elinor, Manjistha and Simon for joining the lab and for the time we have spent together, you brought back some life in the lab and it was really pleasant to end my time in this lab with you around!

§

I would like to thanks Giacomo Persiani for all the friendly moment we had since we are both in Basel and for teaching me the essence and technics of climbing :D Really looking forward to start Alpinism with you!

I would like to thanks Pascal Rieder, Prof. Dr. Daniel Häussinger, Dr. Michael Pfeffer, Jonas Zurflüh and Dr. Alessandro Prescimone for all their help with the analytics over my PhD time!

I would like to thanks Hala Helmi for all the discussion we had, her time and her advices

§

§